Investigations of small-pore zeolites with complex structural chemistry [Redacted version]

Elliott Leigh Bruce

A thesis submitted for the degree of PhD
at the
University of St Andrews

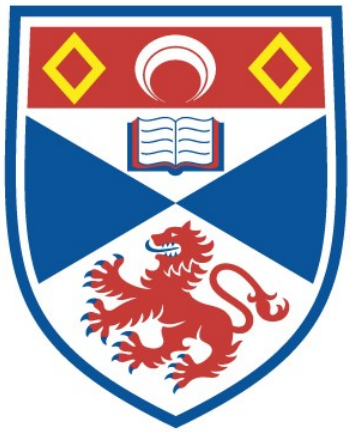

2024

Candidate's declaration

I, Elliott Leigh Bruce, do hereby certify that this thesis, submitted for the degree of PhD, which is approximately 57,000 words in length, has been written by me, and that it is the record of work carried out by me, or principally by myself in collaboration with others as acknowledged, and that it has not been submitted in any previous application for any degree. I confirm that any appendices included in my thesis contain only material permitted by the 'Assessment of Postgraduate Research Students' policy.

I was admitted as a research student at the University of St Andrews in September 2017.

I received funding from an organisation or institution and have acknowledged the funder(s) in the full text of my thesis.

Date 30/09/23 Signature of candidate

Supervisor's declaration

I hereby certify that the candidate has fulfilled the conditions of the Resolution and Regulations appropriate for the degree of PhD in the University of St Andrews and that the candidate is qualified to submit this thesis in application for that degree. I confirm that any appendices included in the thesis contain only material permitted by the 'Assessment of Postgraduate Research Students' policy.

Date 05/10/23 Signature of supervisor

Permission for publication

In submitting this thesis to the University of St Andrews we understand that we are giving permission for it to be made available for use in accordance with the regulations of the University Library for the time being in force, subject to any copyright vested in the work not being affected thereby. We also understand, unless exempt by an award of an embargo as requested below, that the title and the abstract will be published, and that a copy of the work may be made and supplied to any bona fide library or research worker, that this thesis will be electronically accessible for personal or research use and that the library has the right to migrate this thesis into new electronic forms as required to ensure continued access to the thesis.

I, Elliott Leigh Bruce, have obtained, or am in the process of obtaining, third-party copyright permissions that are required or have requested the appropriate embargo below.

The following is an agreed request by candidate and supervisor regarding the publication of this thesis:

Printed copy

No printed copy is supplied.

Electronic copy

Embargo on part (Chapter 8, Chapter 9, Chapter 10, Appendix II) of electronic copy for a period of 3 years on the following ground(s):

- Publication would be commercially damaging to the researcher, or to the supervisor, or the University
- Publication would be in breach of law or ethics

Supporting statement for electronic embargo request

My research was sponsored/funded by a commercial company and there are conditions on my research being made publicly available and they intent to submit a patent.

Title and Abstract

- I require an embargo on the abstract only.

Date 30/09/23 Signature of candidate

Date 05/10/23 Signature of supervisor

Underpinning Research Data or Digital Outputs

Candidate's declaration

I, Elliott Leigh Bruce, understand that by declaring that I have original research data or digital outputs, I should make every effort in meeting the University's and research funders' requirements on the deposit and sharing of research data or research digital outputs.

Date 30/09/23 Signature of candidate

Permission for publication of underpinning research data or digital outputs

We understand that for any original research data or digital outputs which are deposited, we are giving permission for them to be made available for use in accordance with the requirements of the University and research funders, for the time being in force.

We also understand that the title and the description will be published, and that the underpinning research data or digital outputs will be electronically accessible for use in accordance with the license specified at the point of deposit, unless exempt by award of an embargo as requested below.

The following is an agreed request by candidate and supervisor regarding the publication of underpinning research data or digital outputs:

No embargo on underpinning research data or digital outputs.

Date 30/09/23 Signature of candidate

Date 05/10/23 Signature of supervisor

Acknowledgements

I would like to thank my academic supervisor, Prof Paul Wright for providing me with the opportunity to carry out this work within his group, sharing his knowledge and expertise in the course of many discussions, and for supporting me during a long and wide-ranging PhD. Thanks are also due to my industrial supervisor, Dr Alessandro Turrina for his support, in sharing his experience and the chance to see the point of view of industry. Prof Mervyn Shannon is also thanked for tutoring and consulting on all things DIFFaX.

Much of this work is based on that of others within the Wright group. In particular, I am indebted to the hard work and perseverance of Dr Veselina Georgieva in her many, many syntheses of materials and the characterisation that came after. Similarly, Dr Magda Lozinska was always there to turn to for any questions regarding refinement, analysis and experiments, and is thanked too for her samples and help in characterisation. Dr Ruxy Chitac also helped with the synthesis of materials, as well as wading through STEM images with me and talking about what it all meant. She has also been wonderful to talk to throughout my PhD about progress, or lack thereof, and looming deadlines. Dr Abi Watts is also thanked for her materials and her help when I was first starting to learn Rietveld refinement. Previous members Drs Angelica Orsi, Ram Prasad, Amanda Anderson, Alex Greenaway and current members Dr Harpreet Kaur, Qian Jia, Sonia Ndlovu, Malavika Manoj are thanked for their help, suggestions and support.

Thanks are also due to many of the scientific and technical staff at the University of St Andrews, including Drs Yuri Andreev, Daniel Dawson and Ross Blackley. I would also like to thank my reviewers Profs Sharon Ashbrook and John Irvine for their helpful suggestions. Many people outside of the university have also been incredibly helpful, including collaborators and friends at Johnson Matthey, Air Products, the POSTECH and the Universities of Edinburgh and Bath, including Drs Nicholas Batts and Raquel Garcia, Dr Bill Casteel, Dr Hyun June Choi and Prof Suk Bong Hong, Dr Thomas Alexander and Prof Tina Düren, and Drs Claire Hobday, Maarten Verbraeken and Profs Carole Morrison and Stefano Brandani.

I would like to thank my friends, John, Ian and Viktor, as well as all of my family for their love and support, particularly over the last few difficult years: my Mum, Dad and Laraine, and Marie, Bob, Holly and Rory, who have gone above and beyond for me. Oliver, thank you for putting everything into perspective. Finally, I could not have done any of this without the support of Rose, who encouraged, suffered and supported me throughout this journey and for who I will be forever grateful.

Funding

This work was supported by the Engineering and Physical Sciences Research Council [EP/R512199/1], and Johnson Matthey Technology Centre.

Research Data/Digital Outputs access statement

Research data underpinning this thesis are available at https://doi.org/10.17630/ad8c3629-a0ce-439a-80ed-dbc09ea846a4

To Oliver

Publications

Publications arising from this work:

- Verbraeken, M. C.; Mennito, R.; Georgieva, V. M.; Bruce, E. L.; Greenaway, A. G.; Cox, P. A.; Min, J. G.; Hong, S. B.; Wright, P. A.; Brandani, S. Understanding CO_2 Adsorption in a Flexible Zeolite through a Combination of Structural , Kinetic and Modelling Techniques. *Sep. Purif. Technol.* **2021**, *256*, 117846.

Information presented in this thesis has been published and has been adapted with permission from above authors. Copyright 2021, Elsevier B. V.

- Georgieva, V. M.; Bruce, E. L.; Verbraeken, M. C.; Scott, A. R.; Casteel, Jr, W. J.; Brandani, S.; Wright, P. A. Triggered Gate Opening and Breathing Effects during Selective CO_2 Adsorption by Merlinoite Zeolite. *J. Am. Chem. Soc.* **2019**, *141* (32), 12744–12759.

Information presented in this thesis has been published and has been adapted with permission from above authors. Copyright 2019, American Chemical Society.

- Bruce, E. L.; Georgieva, V. M.; Verbraeken, M. C.; Murray, C. A.; Hsieh, M.-F.; Casteel, Jr., W. J.; Turrina, A.; Brandani, S.; Wright, P. A. Structural Chemistry, Flexibility and CO_2 Adsorption Performance of Alkali Metal Forms of Merlinoite with Framework Si/Al Ratio of 4.2. *J. Phys. Chem. C* **2021**, *125* (49), 27403–27419.

Information presented in this thesis has been published and has been adapted with permission from above authors. Copyright 2021, Wiley.

- Georgieva, V. M.; Bruce, E. L.; Chitac, R. G.; Lozinska, M. M.; Hall, A. M.; Murray, C. A.; Smith, R. I.; Turrina, A.; Wright, P. A. Cation Control of Cooperative CO_2 Adsorption in Li-Containing Mixed Cation Forms of the Flexible Merlinoite Zeolite. *Chem. Mater.* **2021**, *33*, 1157–1173.

Information presented in this thesis has been published and has been adapted with permission from above authors. Copyright 2021, American Chemical Society.

- Choi, H. J.; Bruce, E. L.; Kencana, K. S.; Hong, J.; Wright, P. A.; Hong, S. B. Highly Cooperative CO_2 Adsorption *via* a Cation Crowding Mechanism on a Cesium-Exchanged Phillipsite Zeolite. *Angew. Chemie Int. Ed.* **2023**, *62* (36), e202305816.

Information presented in this thesis has been published and has been adapted with permission from above authors. Copyright 2023, Wiley.

In preparation:

- Lozinska, M. M.; Bruce, E. L.; Feverston-Siebel, E.; Bhadra, S. J.; Lau, G. C.; Golden, T. C.; Sorensen, E. M.; Whitley, R. D.; Smith, R. I.; Wright, P. A.; Casteel, Jr, W. J. Optimizing the Flexible Zeolite Rho for Unrivalled Argon Purification Performance.
- Patent relating to Chapter 9.

Outside the scope of this work:

- Lozinska, M. M.; Bruce, E. L.; Mattock, J.; Chitac, R. G.; Cox, P. A.; Turrina, A.; Wright, P. A. Understanding the Anion-Templated, OSDA-Free, Interzeolite Conversion Synthesis of High Silica ZK-5. *Chem. - A Eur. J.* **2022**, *28* (56), e202201689.

Abbreviations

Abbreviation	Meaning
2CLJQ	2-centre Lennard-Jones plus point-quadrupole model
a	Unit cell parameter
aft	AlPO-52 cavity
AlPO	Aluminophosphate
b	Unit cell parameter
Biso	Isotropic thermal dispacement factor
BF	Bright field
c	Unit cell parameter
ca.	Approximately (latin: *circa*)
can	Cancrinite cage
CBU	Composite building unit
CDM	Charge density mismatch
cha	Chabazite cavity
CIT	California Institute of Technology
CMS	Carbon molecular sieve
d6r	Double 6-ring cage
D6R	Double 6-ring cation site
d8r	Double 8-ring cavity
D8R	Double 8-ring cation site
dcc	Double crankshaft chain building unit
diDABCO-C*n*	1,*n*-(1,4-diazabicyclo[2.2.2]octane)*n*-yl
DLS	Diamond Light Source
ED	Electron diffraction
EDX	Electron dispersive X-ray analysis
EM	Electron microscopy
eri	Erionite cavity
ESRF	European Synchrotron Radiation Facility
E-ZLC	Extended zero length column method
FT	Fourier transform

Abbreviation	Meaning
FTC	Framework Type Code
FWHM	Full width at half maximum
gme	Gmelinite cavity
GSAS	General Structure Analysis System
HAADF	High angle annular dark field
HM	Hexamethonium
HRTEM	High resolution transmission electron microscopy
IM	Institut Français du Pétrole and University of Mulhouse
^{i}PrO	Isopropoxide
ISDA	Inorganic structure directing agent
ISIS	Neutron and muon source at the Rutherford Appleton Laboratory
IUPAC	International Union of Pure and Applied Chemistry
IZA	International Zeolite Association
lta	Linde Type A cavity
MAS	Magic angle spinning
MBS	Mean block size
MFWD	Mean free window diameter
MOF	Metal organic framework
MTO	Methanol-to-olefin
NMR	Nuclear magnetic resonance
OSDA	Organic structure directing agent
oto	*t-oto* natural tile, a zeolite cavity
pau	Paulingite cavity
PBU	Primary building unit
phi	Phillipsite cavity
PND	Powder neutron diffraction
PXRD	Powder X-ray diffraction
***R*exp**	Expected *R*-factor
***R*p**	Pattern *R*-factor
***R*wp**	Weighted pattern *R*-factor

Abbreviation	Meaning
S8R	Single 8-ring cation site
SAED	Selected area electron diffraction
SAPO	Silicoaluminophosphate
SBU	Secondary building unit
SCR	Selective catalytic reduction
SDA	Structure directing agent
SEM	Scanning electron microscopy
sfw	SSZ-52 cavity
SSZ	Standard Oil Synthetic Zeolite
STA	St Andrews materials
ste	*t-ste* natural tile, a zeolite cavity
STEM	Scanning tunneling electron microscopy
swy	STA-30 cavity
TEA	Tetraethylammonium
TEM	Transmission electron microscopy
TEPA	Tetraethylenepentamine
TGA	Thermogravimetric analysis
TMA	Tetramethylammonium
TPA	Tetrapropylammonium
TrMA	Trimethylammononium
UOP	Universal Oil Products
VPXRD	Variable pressure X-ray diffraction
XRD	X-ray diffraction
ZLC	Zero length column method

Contents

1. Introduction

1.1. Zeolite materials

Zeolites were first described in 1756 by the Swedish minerologist Axel F. Cronstedt,[1] who is also known for discovering the element nickel.[2] Upon heating a naturally occurring aluminosilicate, believed to be stilbite, a froth formed.[3] As such, he coined the term zeolite from the Greek *zeo-* ("to boil") and *lithos* ("stone").[4] This property arose from the porous nature of zeolites, which leads to adsorption of water. Upon heating, water is released, causing a foam to appear in Cronstedt's sample. Further naturally occurring zeolites have been discovered in the centuries afterwards, as have synthetic materials.

This family of aluminosilicates consist of frameworks composed of corner-sharing tetrahedra (TO_4, T = Si or Al) linked together to define void spaces. This gives rise to their porosity and a diverse range of potential structures can be synthesised. Related materials with additional or alternate elements to Si and Al, such as P or Ge, form their own classes of porous materials, and together are termed zeotypes.

Zeolites and zeotypes have found use as ion exchange materials, as well as adsorbents and catalysts. As such, there has been a great deal of interest in their study. A major part of this has been to understand their crystal structures, as this determines some of the properties of the materials and this can enable samples to be improved for application. This work seeks to investigate the structures of a number of zeolite and zeotypes with a view to rationalise their properties, particularly as CO_2 adsorbents.

1.2. Structures of zeolites

The study of zeolites was initially restricted by the lack of any available structural analysis. In 1896 the first suggestion of an open framework was made to describe the reversible adsorption of water,[5] and it was only in 1930 that the first zeolite structures were reported, using X-ray diffraction techniques.[6–8]

As discussed and as shown in Figure 1.2.1, zeolites are composed of corner sharing tetrahedra $[SiO_4]$ and $[AlO_4]^-$, which form the primary building units (PBUs). The incorporation of Al into the framework introduces a negative charge, which must be

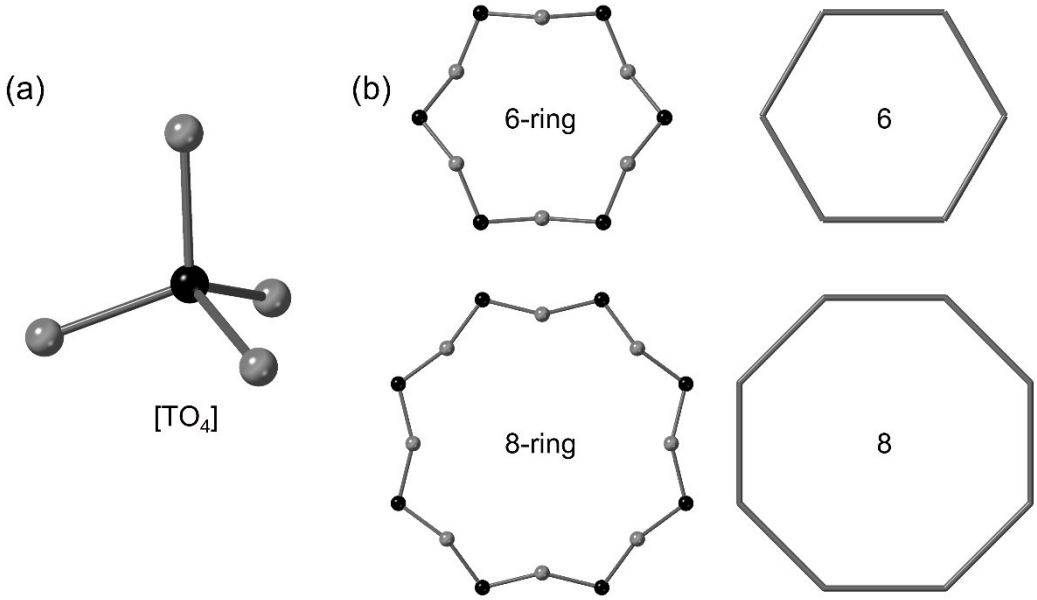

Figure 1.2.1. Smaller building units within zeolite and zeotype frameworks: (a) a PBU and (b) SBUs. SBUs shown are n-rings, classified as n in SBU notation, shown with T-O bonds and in a reduced T-T "bond" representation, with O sites removed for clarity. T and O sites are shown in black and grey, respectively.

compensated by extraframework cations, and gives aluminosilicate zeolites the following composition:

$$M^{m+}_{x/m}[Si_{1-x}Al_xO_2],$$

where M^{m+} represents extra-framework cations. Tetrahedra are rather rigid units, with reasonably predictable bond distances and angles: Si-O, 1.62 Å; Al-O, 1.73 Å; and ∠OTO, 109.7°.[4] The angles made by the bridging T-O-T linkages are more variable, with ∠TOT *ca.* 145°, and a range between 135-180°,[9] though reported angles of 180° are likely due to disorder.[10] This last point highlights that it should be remembered that values obtained from diffraction studies are time-space averages. When Si and Al are disordered, T-O bonds will typically be found to be a weighted average of Si-O and Al-O bond lengths. Experimental values determined by Rietveld refinement should be close to the above values so that the refined structure is realistic. Strong deviation may suggest that the wrong symmetry is being applied to a crystal structure.

Si and Al sites cannot be randomly distributed across the framework. Löwenstein's rule states that Al-O-Al bridges are weak and so do not occur within zeolite structures.[11] As a result, the highest possible aluminium content in a zeolite corresponds to strictly

alternating Si and Al T sites, as is seen in zeolite A.[12] It should be noted that this is not the theoretical maximum for all zeolites, particularly those with an odd number of T atoms in a structural building unit (described below), such as the 5-membered ring containing pentasils. In this case, strict alternation of Al and Si is not possible and the maximum aluminium content is correspondingly lower. Non-Löwensteinian zeolites have been synthesised, however these are unusual, requiring high temperatures to overcome the associated energy barrier in formation of Al-O-Al linkages.[13] However, recent computational studies suggest that Löwenstein's rule may not be as steadfast in zeolites as is commonly believed.[14]

Zeotypes incorporate alternative tri- and tetravalent elements into the framework, such as B, Fe, Ga, Ge, Ti and pentavalent P.[4,15] This gives rise to interesting new properties and can introduce new rules for PBUs, such as strict ordering of $[AlO_4]^-$ and $[PO_4]^+$ in aluminophosphates (AlPOs). Si can be introduced into an AlPO framework to create a silicoaluminophosphate (SAPO), and these have the formula:

$$H_x[AlP_{1-x}Si_xO_4].$$

Some of the materials studied in this work are SAPOs, but the vast majority are aluminosilicate zeolites. Both types of materials adopt frameworks composed of PBUs, which are linked together to form secondary building units (SBUs).[4] These are small motifs that can be used to describe the entire framework structure. Some SBUs relevant to this work are *n*-rings, composed of *n* tetrahedra in a loop, and shown in Figure 1.2.1. These are described as SBUs by simply stating *n*, whilst other SBUs have more involved codes based on the linkages between PBUs. Structures can also be described in terms of composite building units (CBUs), extended assemblies of PBUs which can appear in multiple types of framework. A selection of these encountered in this work are shown in Figure 1.2.2. These are often more practical to describe extended zeolite structures and can aid the description of synthesis or the rationalisation of properties.

The smallest CBU is the *lov* unit, composed of 5 tetrahedra, and larger ones include *aft* and *lta*, both of which contain 48 T sites.[16] Some of these encapsulate pores within materials, and form cages or cavities, as is the case for both *aft* and *lta*, as well as *pau*, *phi* and *cha*. Other methods to describe zeolites include elongated chains, such as the double crankshaft (*dcc*) shown in Figure 1.2.2, or layers, particularly useful in describing

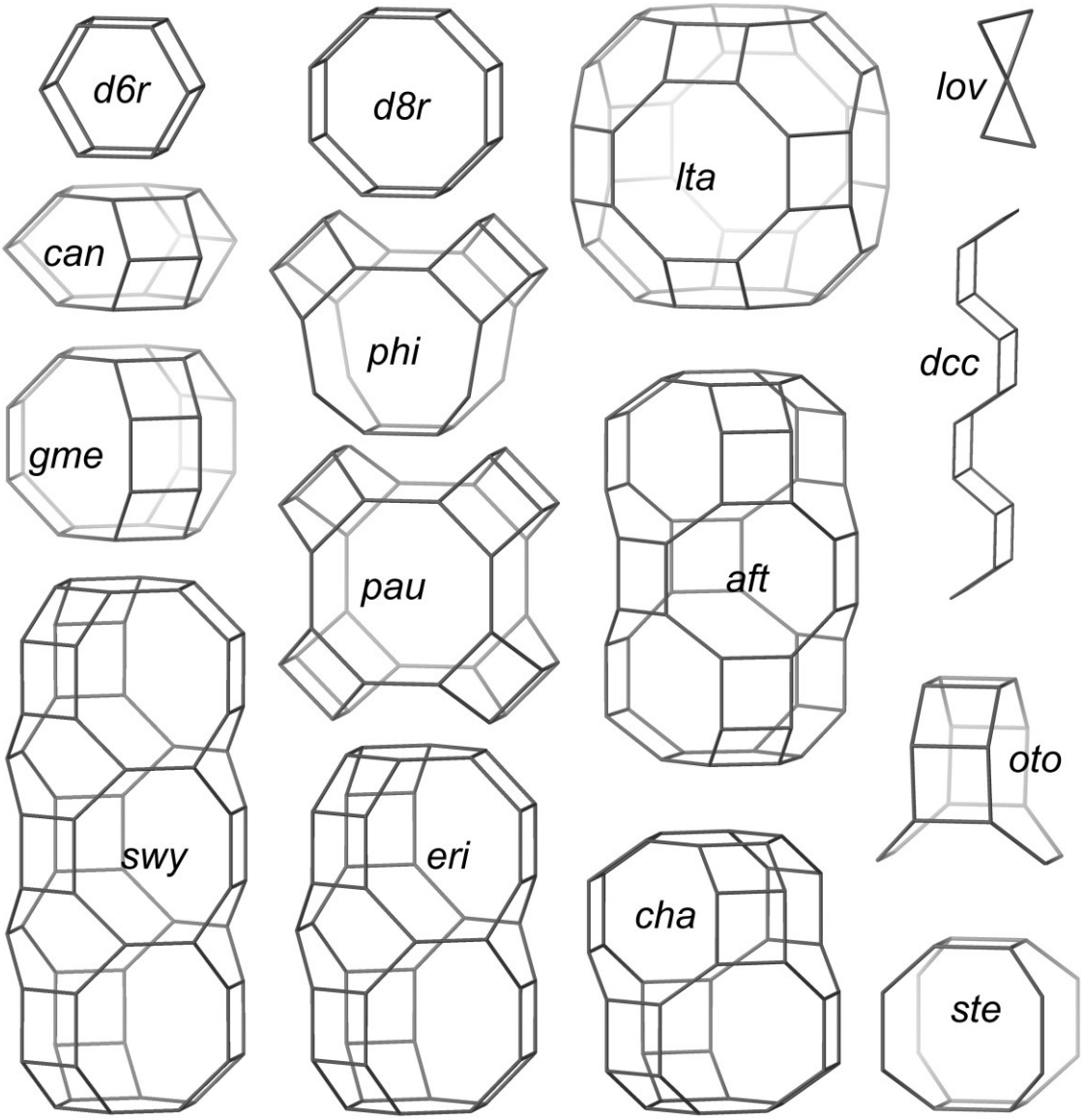

Figure 1.2.2. A selection of CBUs, including some of those encountered in this work. The double crankshaft (dcc) motif is also shown. O sites are omitted for clarity.

materials with stacking faults, discussed in Chapter 8. Cages are defined as units with windows too small to be penetrated by molecules larger than water and so have no *n*-rings larger than $n = 6$.[17] A cavity, on the other hand, is one which can allow the entrance of larger molecules but is not indefinitely extended, this being a channel. The term "channel" also describes an indefinitely extended system of adjacent cavities that allow percolation between them. In practice, the terms "cage" and "cavity" are used somewhat interchangeably.

The completed framework structure is given a 3-letter framework type code (FTC) by the International Zeolite Association (IZA) based on related materials, sometimes obviously, such as for **CHA** (**cha**bazite) and **RHO** (zeolite **Rho**), and sometimes more enigmatically, for instance **SFW** (**S**tandard Oil Synthetic Zeolite - **f**ifty-t**w**o), **AFT** (**A**lPO **f**ifty-**t**wo) and **AFX** (S**A**PO **f**ifty-si**x**).[16] There are 255 FTCs for ordered materials at the time of writing,[16] and new ones are added on a somewhat regular basis as new materials are synthesised. Some frameworks can be synthesized as both zeolites and zeotypes, and the FTC is shared between different samples and synthesis systems, as it only refers to the topology of the framework. Some of the frameworks relevant to this work are presented in Figure 1.2.3.

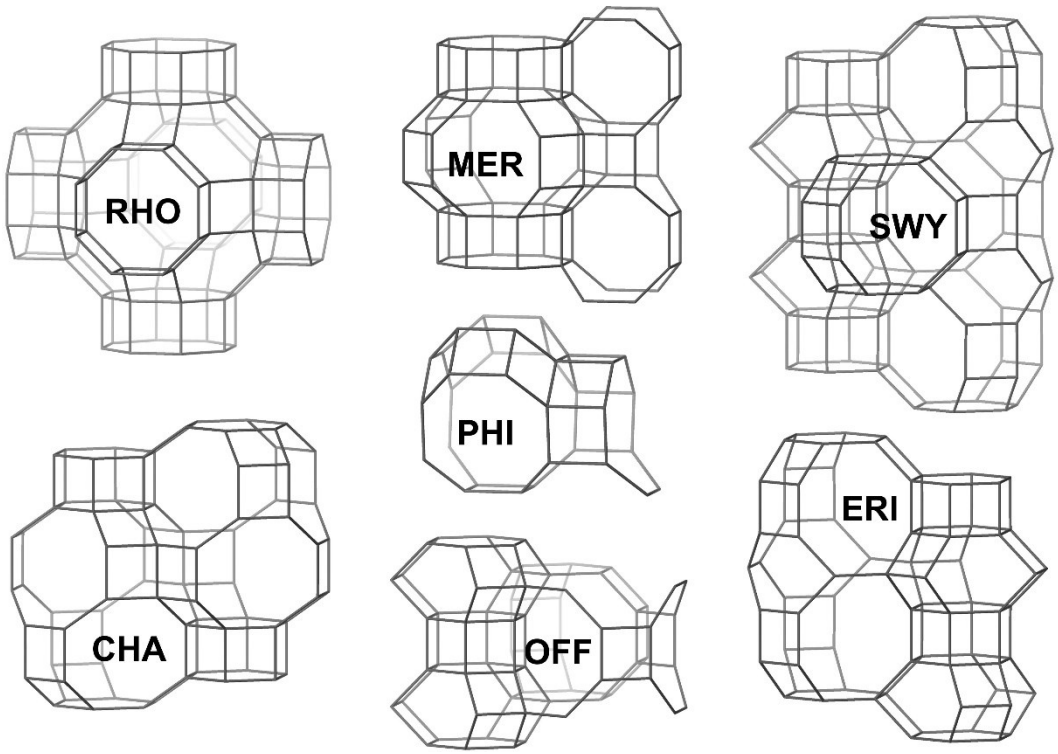

Figure 1.2.3. Illustrative framework structures for some of the materials examined in this work, with their FTCs overlaid. O sites are omitted for clarity.

As well as the framework, zeolites can contain extra-framework species. These include inorganic and organic cations, which counterbalance the framework charge caused by the presence of Al, and guest molecules, such as water, hydrocarbons or CO_2.[18–21] Counterbalancing inorganic cations are readily exchanged from the pores of zeolites, although some may be trapped within cages, as is the case in zeolite L.[22–26] The exchange

of these cations is of potential interest, as it can greatly affect the chemical and physical properties of a zeolite, and have great implications for gas adsorption, catalysis and other potential applications.[27–31] Organic species are typically trapped within cavities, particularly if they have played a role in synthesis as a "space filler" and these are removed by calcination, leaving a proton behind to counterbalance the framework charge.[4] This is particularly relevant for acid catalysis, and inorganic cations can be exchanged with ammonium and subsequently calcined to produce further Brønsted acid sites.

Guest species can also have a significant effect on the framework of flexible zeolites. For example, in the case of hydrated forms of natrolite, the Cs-exchanged form experiences a volume expansion of 18.5% compared to the naturally occurring Na-form.[32] The effect in other flexible zeolites is only observed after dehydration. This is the case for zeolite Rho, for example, which undergoes a framework distortion to better coordinate extraframework cations.[26,33,34] Such a distortion can be accompanied by cation migration and can be reversed with the adsorption of guest species.[9,35–37] This is discussed in greater detail in Chapter 3 and is also observed in zeolites explored throughout Chapters 4-7.

1.3. Synthesis of zeolites

Early research in zeolite science was restricted to natural minerals, with the first synthesis of a zeolite, levynite, reported by the French minerologist Étienne-Henri Saint-Claire-Deville in 1862.[15,38] This was a century after the first discovery of a natural zeolite material by Cronstedt. Work by the pioneering New Zealander Richard M. Barrer, amongst others, in the 1940s and onwards revolutionised zeolite synthesis, through the use of alkali cations in high temperature, high alkalinity hydrothermal syntheses.[4,15,39]

In hydrothermal zeolite syntheses, amorphous reagents are converted to crystalline products in the presence of a base. Hydroxide ions catalyse the breaking apart and reforming of Si-O and Al-O bonds. Syntheses are carried out at high temperatures in autoclaves, under autogenous pressure. Crystalline products precipitate from the thick synthesis gel and are recovered and washed by filtration or centrifugation.

The type of product formed by these syntheses is greatly influenced by cations within the synthesis gel. Initially only inorganic cations, such as Na^+ or K^+, were used in syntheses. These often directed relatively dense or small-pore zeolite frameworks, including analcime, sodalite, cancrinite, edingtonite or chabazite, and the framework contained a large amount of Al.[15,40,41] Barrer and Denny expanded this approach by adding tetramethylammonium hydroxide (TMAOH) to a synthesis system in 1961, forming zeolites A, X and Y.[42] The frameworks of these samples were not new, but were formed with a higher Si/Al ratio. Since then an extensive range of organic species have been included in zeolite syntheses as structure-directing agents (SDAs),[15] a number of which are shown in Figure 1.3.1. Organic and inorganic species are labelled as OSDAs and ISDAs, respectively, and determine the product formed. This may directly "template" pores within the structure or influence the final product through the stabilisation of a desired phase, or the disfavouring of another, competing, phase.[43–45] This was the case in a study by Iwama *et al.*, that showed that in faujasite synthesis, K^+ caused precipitation into the gel of aluminosilicates responsible for the nucleation of zeolite A.[46] This resulted in the crystallisation of pure faujasite.

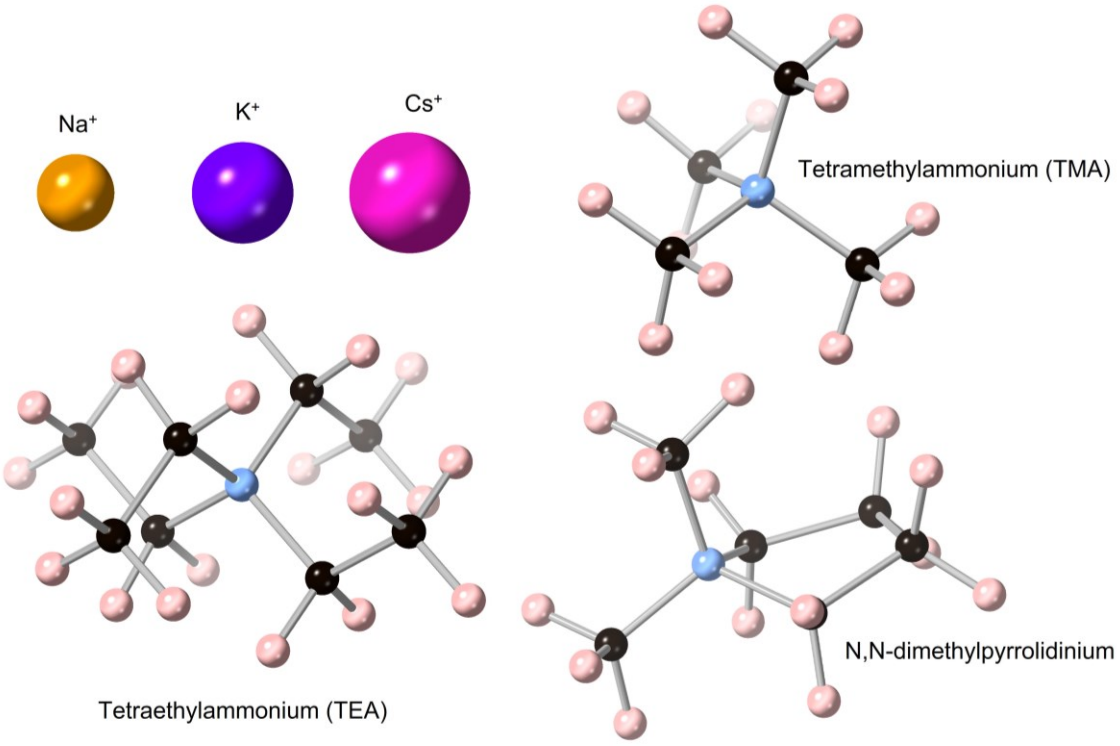

Figure 1.3.1. Examples of SDAs used in zeolite synthesis, both inorganic and organic. C, N and H atoms are shown in black, blue and pink, with inorganic species as labelled.

During synthesis, ISDAs may stabilise specific aluminosilicate ring structures or larger building units, such as *n*-rings or cages. Tuoto *et al*., for instance, showed that both K and Na cations favour the formation of 6-rings.[47] Metal cations have also been shown to affect crystal growth, with Skofteland *et al*. showing that larger crystals of merlinoite were formed in higher concentrations of K cations.[48] The authors also suggested that K cations directed the synthesis of merlinoite through the formation of a K^+ and H_2O H-bonded network, forming a larger "template" for the *pau* cavity.

A more wide ranging investigation by Vaughan suggested that inorganic cations could direct the synthesis of extended structures which condensed to form a final zeolite.[49] The nature of the cation appeared to determine the types of structure formed: Na^+ forming layered species, and K^+ directing column-type aluminosilicate structures. The role of secondary cations, including OSDAs, determined how these species knitted together. This agreed with work by Garcia *et al*. in which a large OSDA appeared to produce faujasite sheets which slowly condensed around smaller OSDAs, in an alkali-metal-free, fluoride medium synthesis.[50]

OSDAs must be of medium hydrophobicity for use in synthesis. This allows them to dissolve within the synthesis mixture and yet interact strongly with silicate species within solution.[51] It has been hypothesised that during synthesis, such interactions leads to silicate species surrounding the OSDA forming cages or cavities which will ultimately make up part of the zeolite structure. One example is that of Ahn *et al.*, who suggested that in the synthesis of silicoaluminophosphates (SAPOs) SSZ-13 and SAPO-34 (both **CHA**) and NU-3 and SAPO-35 (both **LEV**), the large *cha* and *lev* cavities, respectively, are initially formed around OSDAs.[52] These cavities then grow into larger structures, forming viable nuclei for crystallisation. Work by Gies *et al*. found that many SDAs' selectivities are altered with temperature and that the pore size "templated" by an OSDA increases with temperature as a result of thermal motion.[53]

The concept of OSDAs as "space-fillers" has led to the use of multiple OSDAs to target different cavities within the same structure. For instance, Turrina *et al*. successfully synthesised SAPO-56 and 2 novel SAPOs, STA-18 and STA-19, using 2 OSDAs simultaneously.[54] Computer modelling was initially used to determine that trimethylammonium would be a good template for the *gme* cavities in the structures,

whilst bisdiazabiscyclooctane cations and their derivatives could template the remaining cavities and channels within the structures.

As OSDAs have a low charge density, the cavities they template are expected to have a similarly low Al content, with potential consequences on the properties of the final product. Pinar *et al*. found that in alkali-metal-free synthesis in a fluoride media, the choice of OSDA could determine the distribution of Al sites in the framework, with particular relevance to catalysis.[55]

To direct synthesis with large cavities, a similarly large OSDA is required. This is a challenge if zeolites with a lower Si/Al are desired, due to the low charge density of the templating OSDA.[15] A large OSDA alone will not cause the crystallisation of a fully extended solid but rather the aluminosilicate species will remain in solution.[56] For such a zeolite to crystallise, metal or small organic cations must be incorporated into the synthesis. These high charge density species allow negatively charged aluminosilicate species to coalesce and form the extended structure required. This is the basis for the charge density mismatch method (CDM) method, first developed by UOP, which allows larger pore zeolites to be synthesised with a reasonably high Al content.[57] This is discussed further in Chapter 9.

1.4. Applications of zeolites

The porous nature of zeolites enables most of their applications. They have been used for their ion exchange potential, removing heavy metals and even capturing radioactive isotopes after nuclear accidents at both Three Mile Island, USA (1979) and Chernobyl, Ukraine (1986).[58–60] This work examines materials for application predominantly in selective O_2/Ar and CO_2/CH_4 adsorption processes; and to a lesser extent as potential catalysts.

Zeolites are well known as acid catalysts, and are used in cracking, alkylation, protonation and alkane isomerisation reactions.[4] Channels within the structure allow hydrocarbons to percolate through zeolite materials and their well-defined channels enable product selectivity, including size and shape selectivity.[20,61,62] Size selectivity blocks larger molecules (reactants, products or adsorbates) from entering or exiting the

material whilst smaller ones can pass freely. This is due to the dimensions of windows within the zeolite hindering or even excluding potential adsorbates based on their size. Smaller species can percolate relatively freely through the porous structure, and this becomes more difficult as molecules become larger and/or window diameters decrease. Zeolite materials can be described as small, medium, large and extra-large pore based on the free diameters of windows (smallest distance between 2 O sites across the middle of an *n*-ring, minus the 2 radii of O to account for the space occupied by oxygen atoms).[4] These are typically defined as *ca.* 4, 5.5, 7 and >8 Å, respectively. Such descriptions can help to identify suitable applications, with small pore zeolites more relevant for the reaction of small molecules, such as reduction of NO_x, whilst larger pore materials are more suitable for reactions of hydrocarbons, including aromatics.

Shape selectivity is similar to size-selectivity but discriminates molecules based on their geometry, rather than overall size.[4,63]. This applies to molecular diffusion through windows based on minimum molecular widths, and formation of species during catalysis in pores or channels. In the case of the latter, it can limit relative molecular orientations to promote one transition state over others. This is exploited for the selective production of linear alkanes over branched conformers, and another the isomerisation of *m*-xylene to the more streamlined *p*-xylene.[64–66]

Methanol-to-hydrocarbon, including methanol-to-olefin (MTO) catalysis is another application of zeolites and zeotypes, and SAPO-34, with the **CHA** framework, is one example that has been used industrially.[67–69] Extra-framework metal cations can also provide a role as catalytic sites, such as in the selective catalytic reduction (SCR) of NO_x in car exhausts.[12,70] These typically contain Cu^{2+} cations as the active catalyst.[4,71,72]

Much of this work looks at zeolites for application in different selective adsorption processes. Separation and purification of gas streams can be done using temperature-, pressure- or vacuum-swing adsorption processes (TSA, PSA and VSA, respectively).[4,73] In all of these methods, the target gas is adsorbed in a mixed stream, and then undergoes isolated desorption to regenerate the sorbent. A TSA process uses an increased temperature to desorb gas species, whilst PSA and VSA exploit a decrease in pressure. In PSA, the lower pressure is no lower than 1 bar, whilst for VSA a vacuum is used.[73,74] Zeolites and zeotypes have been shown to be useful as such materials in a range of

processes.[75–81] Of particular interest are small-pore zeolites for the separation of CO_2 over N_2 and CH_4.[75,82–84] These are often suggested as potential materials in pre-combustion gas or biogas upgrading processes,[85–88] or post-combustion carbon capture and storage (CCS).[89,90] There are many factors which impact the adsorption behaviour of these materials, including pore size and shape, the number and type of extraframework cations present and physical properties of gas species, as well as the temperature and pressure of the system.[91] Another process of particular interest to this work is O_2/Ar separation, for which zeolite A materials have previously been suggested.[92–96]

1.5. Structural analysis of zeolites

As has been stated, the first crystal structures of zeolites were reported in 1930 by Pauling and Taylor.[6–8] Since then, diffraction techniques have been a major tool in the study of these and other porous materials. Zeolite samples are often polycrystalline, and so require powder diffraction and subsequent Rietveld analysis, a technique first published in 1969 for neutron diffraction,[97] and used extensively in this work. This method is described in greater detail in Chapter 2. This is by no means the only tool that can or should be used to study these materials, nuclear magnetic resonance and electron microscopy techniques can both be used to examine more localised structural behaviour that cannot be observed with diffraction.[4,98]

Refinement of crystal structures is simpler with fewer extraframework species. This includes water in hydrated forms of zeolites, as well as adsorbates, such as CO_2, or OSDAs, such as TEA. Species such as water, methane or ammonia could readily be considered as a single site, but this is more complex for larger molecules, including CO_2. Restraints based on molecular geometries or rigid bodies can be used, as discussed in Chapter 2, to explore such molecules,[99,100] with examples from work outside of the scope of this thesis shown in Figure 1.5.1.[101] Larger molecules can be particularly challenging to study as these typically do not match the symmetry of the crystal as a whole and can be disordered over neighbouring cages, leading to a superposition of multiple, partially occupied, molecular orientations.[99]

Additional complexity is created when studying defects or faults, as these break the long-range order that forms the basis of diffraction-based techniques. Methods to

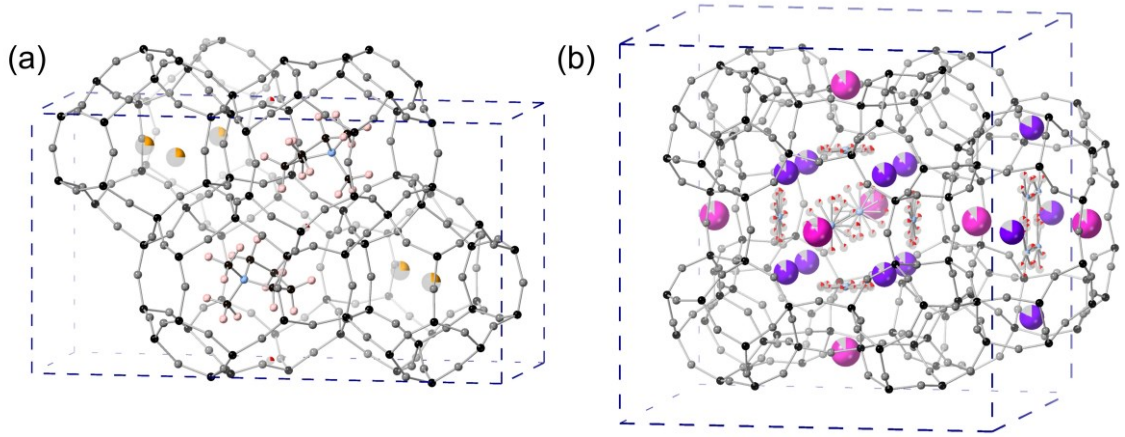

*Figure 1.5.1. Zeolite structures refined using rigid bodies to describe extra-framework species: (a) N,N-dimethylpyrrolidinium in ERS-7 (**ESV**) and (b) nitrates in ZK-5 (**KFI**). Framework T and O sites are shown in black and grey, with extra-framework Na, K, Cs, C, N, O and H shown in orange, purple, pink, black, light blue, red and light pink, respectively. Occupancies are indicated by fractional shading of spheres.*

combat this are covered in greater detail in Chapter 8, and diffraction is often combined with electron microscopy data. The introduction of DIFFaX software by Treacy *et al.* revolutionised the study of faulted materials, enabling the widespread analysis of complex systems such as zeolites.[102] Since then, a wide range of zeolite and zeotype systems has been examined in the literature,[103] and the known families of synthesised intergrowths are provided by the IZA structural commission.[104]

In this work, flexible small-pore zeolites are examined with Rietveld refinement from powder X-ray diffraction data, and with neutron diffraction in the case of zeolite Rho. These structures are said to be flexible as their framework structures distort upon dehydration to better coordinate extra-framework species. These materials are of interest as selective adsorbent materials, primarily for CO_2/CH_4. The effects of sample composition on structural behaviour are explored and used to rationalise gas adsorption behaviour. The second part of this work examines the stacking behaviour of other porous materials, both SAPOs and aluminosilicate zeolites. These systems are composed of members of the ABC-6 family of zeolites, well known to be prone to stacking faults.[105] These show potential as catalysts for which a structural description could be valuable.[106]

1.6. Aims

This work examines a range of small-pore zeolite and zeotype materials, with the following aims:

i. To analyse diffraction data collected on flexible zeolites prepared with different cations, in hydrated, dehydrated and CO_2-loaded states to understand their CO_2 adsorption behaviour.
ii. To prepare disordered materials in the ABC-6 family of zeolites.
iii. To analyse disordered intergrowth structures on the basis of PXRD and STEM data.

1.7. References

(1) Cronstedt, A. F. Rön Och Beskrifning Om En Oberkant Barg Art, Som Kallas Zeolites. *Kongl. Sv. vet. Akad. Handl.* **1756**, *17*, 120–123.

(2) Bartow, V. Axel Fredrik Cronstedt. *J. Chem. Educ.* **1953**, *30* (5), 247–252.

(3) Colella, C.; Gualtieri, A. F. Cronstedt's Zeolite. *Microporous Mesoporous Mater.* **2007**, *105*, 213–221.

(4) Wright, P. A. *Microporous Framework Solids*; Royal Society of Chemistry: Cambridge, 2008.

(5) Friedel, M. G. Sur Des Figures de Corrosion Du Mica et Sur l'Orientation Des Fissures de Glissement Produites Par La Perforation. *Bull. Soc. Fr. Miner. Crystallogr.* **1896**, *19*, 13–22.

(6) Taylor, W. H. The Structure of Analcite ($NaAlSi_2O_6 \cdot H_2O$). *Zeitschrift für Krist. - Cryst. Mater.* **1930**, *74* (1), 1–19.

(7) Pauling, L. The Structure of Some Sodium and Calcium Aluminosilicates. *Proc. Natl. Acad. Sci.* **1930**, *16* (7), 453–459.

(8) Pauling, L. XXII. The Structure of Sodalite and Helvite. *Zeitschrift für Krist. - Cryst. Mater.* **1930**, *74* (1–6), 213–225.

(9) Wright, P. A.; Lozinska, M. Structural Chemistry and Properties of Zeolites. In

Zeolites and Ordered Porous Solids: Fundamentals and Applications; Martinez, C., Pérez-Pariente, J., Eds.; Editorial Universitat Politecnica de Valencia, 2011; pp 1–37.

(10) Wragg, D. S.; Morris, R. E.; Burton, A. W. Pure Silica Zeolite-Type Frameworks : A Structural Analysis. *Chem. Mater.* **2008**, *20* (4), 1561–1570.

(11) Loewenstein, W. The Distribution of Aluminum in the Tetrahedra of Silicates and Aluminates. *Am. Mineral.* **1954**, *39*, 92–96.

(12) Ryu, T.; Ahn, N. H.; Seo, S.; Cho, J.; Kim, H.; Jo, D.; Park, G. T.; Kim, P. S.; Kim, C. H.; Bruce, E. L.; Wright, P. A.; Nam, I. S.; Hong, S. B. Fully Copper-Exchanged High-Silica LTA Zeolites as Unrivaled Hydrothermally Stable NH3-SCR Catalysts. *Angew. Chemie - Int. Ed.* **2017**, *56* (12), 3256–3260.

(13) Robinson, W. L. J. (12) United States Patent. US 8815382 B2, 2014.

(14) Fletcher, R. E.; Ling, S.; Slater, B. Violations of Löwenstein's Rule in Zeolites. *Chem. Sci.* **2017**, 7483–7491.

(15) Millini, R.; Bellussi, G. Zeolite Science and Perspectives. In *Zeolites in Catalysis: Properties and Applications*; Čejka, J., Morris, R. E., Nachtigall, P., Eds.; Royal Society of Chemistry: Croydon, 2017; pp 1–36.

(16) Baerlocher, C.; McCusker, L. B. IZA Database of Zeolite Structures, http://www.iza-structure.org/databases/, accessed October 2023.

(17) McCusker, L. B.; Liebau, F.; Engelhardt, G. Nomenclature of Structural and Compositional Characteristics of Ordered Microporous and Mesoporous Materials with Inorganic Hosts (IUPAC Recommendations 2001). *Pure Appl. Chem.* **2001**, *73* (2), 381–394.

(18) Fuchs, A. H.; Cheetham, A. K. Adsorption of Guest Molecules in Zeolitic Materials: Computational Aspects. *J. Phys. Chem. B* **2001**, *105* (31), 7375–7383.

(19) Morris, R. E.; Wheatley, P. S. Gas Storage in Nanoporous Materials. *Angew. Chemie - Int. Ed.* **2008**, *47* (27), 4966–4981.

(20) Barrer, R. M. Porous Crystals: A Perspective. *Stud. Surf. Sci. Catal.* **1986**, *28* (C), 3–

11.

(21) Paris, C.; Martín, N.; Martínez-Triguero, J.; Moliner, M.; Corma, A. Synthesis of Al-MTW with Low Si/Al Ratios by Combining Organic and Inorganic Structure Directing Agents. *New J. Chem.* **2016**, *40* (5), 4140–4145.

(22) Lozinska, M. M.; Miller, D. N.; Brandani, S.; Wright, P. A. Hiding Extra-Framework Cations in Zeolites L and Y by Internal Ion Exchange and Its Effect on CO_2 Adsorption. *J. Mater. Chem. A* **2020**, *8* (6), 3280–3292.

(23) Barrer, R. M.; Davies, J. A.; Rees, L. V. C. Comparison properties of the ion exchange of zeolites X and Y. *J. Inorg. Nucl. Chem.* **1969**, *31* (1969), 2599–2609.

(24) Barrer, R. M.; Townsend, R. P. Transition Metal Ion Exchange in Zeolites. *J. Chem. Soc. Faraday Trans. 1* **1976**, No. 72, 661–673.

(25) Johnson, G. M.; Reisner, B. A.; Tripathi, A.; Corbin, D. R.; Toby, B. H.; Parise, J. B. Flexibility and Cation Distribution upon Lithium Exchange of Aluminosilicate and Aluminogermanate Materials with the RHO Topology. *Chem. Mater.* **1999**, *11* (10), 2780–2787.

(26) Lozinska, M. M.; Mangano, E.; Mowat, J. P. S.; Shepherd, A. M.; Howe, R. F.; Thompson, S. P.; Parker, J. E.; Brandani, S.; Wright, P. A. Understanding Carbon Dioxide Adsorption on Univalent Cation Forms of the Flexible Zeolite Rho at Conditions Relevant to Carbon Capture from Flue Gases. *J. Am. Chem. Soc.* **2012**, *134* (42), 17628–17642.

(27) Greenaway, A. G.; Shin, J.; Cox, P. A.; Shiko, E.; Thompson, S. P.; Brandani, S.; Hong, S. B.; Wright, P. A. Structural Changes of Synthetic Paulingite (Na,H-ECR-18) upon Dehydration and CO_2 Adsorption. *Zeitschrift fur Krist.* **2015**, *230* (4), 223–231.

(28) Vanelderen, P.; Vancauwenbergh, J.; Sels, B. F.; Schoonheydt, R. A. Coordination Chemistry and Reactivity of Copper in Zeolites. *Coord. Chem. Rev.* **2013**, *257* (2), 483–494.

(29) Babarao, R.; Jiang, J. Unprecedentedly High Selective Adsorption of Gas Mixtures in *Rho* Zeolite-like Metal−Organic Framework: A Molecular Simulation Study. *J.*

Am. Chem. Soc. **2009**, *131* (32), 11417–11425.

(30) Martínez-Franco, R.; Moliner, M.; Corma, A. Direct Synthesis Design of Cu-SAPO-18, a Very Efficient Catalyst for the SCR of NOx. *J. Catal.* **2014**, *319*, 36–43.

(31) Zanota, M. L.; Heymans, N.; Gilles, F.; Su, B. L.; De Weireld, G. Thermodynamic Study of LiNaKLSX Zeolites with Different Li Exchange Rate for N_2/O_2 Separation Process. *Microporous Mesoporous Mater.* **2011**, *143* (2–3), 302–310.

(32) Lee, Y.; Lee, Y.; Seoung, D. Natrolite May Not Be a "Soda-Stone" Anymore: Structural Study of Fully K-, Rb-, and Cs-Exchanged Natrolite. *Am. Mineral.* **2010**, *95* (11–12), 1636–1641.

(33) Parise, J. B.; Abrams, L.; Gier, T. E.; Corbin, D. R.; Jorgensen, J. D.; Prince, E. Flexibility of the Framework of Zeolite Rho - Structural Variation From 11 to 573-K - a Study Using Neutron Powder Diffraction Data. *J. Phys. Chem.* **1984**, *88* (11), 2303–2307.

(34) Parise, J. B.; Gier, T. E.; Corbin, D. R.; Cox, D. E. Structural Changes Occurring upon Dehydration of Zeolite Rho. A Study Using Neutron Powder Diffraction and Distance-Least-Squares Structural Modeling. *J. Phys. Chem.* **1984**, *88* (8), 1635–1640.

(35) Lozinska, M. M.; Mowat, J. P. S.; Wright, P. A.; Thompson, S. P.; Jorda, J. L.; Palomino, M.; Valencia, S.; Rey, F. Cation Gating and Relocation during the Highly Selective "Trapdoor" Adsorption of CO_2 on Univalent Cation Forms of Zeolite Rho. *Chem. Mater.* **2014**, *26* (6), 2052–2061.

(36) Lee, Y.; Reisner, B. A.; Hanson, J. C.; Jones, G. A.; Parise, J. B.; Corbin, D. R.; Toby, B. H.; Freitag, A.; Larese, J. Z. New Insight into Cation Relocations within the Pores of Zeolite Rho: In Situ Synchrotron X-Ray and Neutron Powder Diffraction Studies of Pb- and Cd-Exchanged Rho. *J. Phys. Chem. B* **2001**, *105* (30), 7188–7199.

(37) Choi, H. J.; Hong, S. B. Effect of Framework Si/Al Ratio on the Mechanism of CO_2 Adsorption on the Small-Pore Zeolite Gismondine. *Chem. Eng. J.* **2022**, *433* (P3), 133800.

(38) Saint-Claire-Deville, M. H. Reproduction de La Lévyne. *C. R. Acad. Sci.* **1862**, *54*,

324–327.

(39) Rees, L. V. C. Richard Maling Barrer. *Bibliogr. Mem. Fellows R. Soc.* **1998**, *44*, 37–49.

(40) Barrer, R. M.; White, E. A. D. The Hydrothermal Chemistry of Silicates. Part II. Synthetic Crystalline Sodium Aluminosilicates. *J. Chem. Soc.* **1952**, 1561–1571.

(41) Barrer, R. M.; Baynham, J. W. The Hydrothermal Chemistry of the Silicates. Part VII. Synthetic Potassium Aluminosilicates. *J. Chem. Soc.* **1956**, 2882–2891.

(42) Barrer, R. M.; Denny, P. J. Hydrothermal Chemistry of the Silicates. Part IX. Nitrogenous Aluminosilicates. *J. Chem. Soc.* **1961**, 971–982.

(43) Grand, J.; Awala, H.; Mintova, S. Mechanism of Zeolites Crystal Growth: New Findings and Open Questions. *CrystEngComm* **2016**, *18* (5), 650–664.

(44) Oleksiak, M. D.; Rimer, J. D. Synthesis of Zeolites in the Absence of Organic Structure-Directing Agents: Factors Governing Crystal Selection and Polymorphism. *Rev. Chem. Eng.* **2014**, *30* (1).

(45) Ji, Y.; Wang, Y.; Xie, B.; Xiao, F. S. Zeolite Seeds: Third Type of Structure Directing Agents in the Synthesis of Zeolites. *Comments Inorg. Chem.* **2016**, *36* (1), 1–16.

(46) Iwama, M.; Suzuki, Y.; Plévert, J.; Itabashi, K.; Ogura, M.; Okubo, T. Location of Alkali Ions and Their Relevance to Crystallization of Low Silica X Zeolite. *Cryst. Growth Des.* **2010**, *10* (8), 3471–3479.

(47) Tuoto, C. V.; Nagy, J. B.; Nastro, A. The Role of Na and K on the Synthesis of Levyne-Type Zeolites. In *Zeolites: A Refined Tool for Designing Catalytic Sites*; Bonneviot, L., Kaliaguine, S., Eds.; Elsevier Science B.V.: Amsterdam, 1995; Vol. 97, pp 551–556.

(48) Skofteland, B. M.; Ellestad, O. H.; Lillerud, K. P. Potassium Merlinoite: Crystallization, Structural and Thermal Properties. *Microporous Mesoporous Mater.* **2001**, *43* (1), 61–71.

(49) Vaughan, D. E. W. The Roles of Metal and Organic Cations in Zeolite Synthesis. *Catal. Adsorbtion by Zeolites* **1991**, *65* (6), 275–286.

(50) García, R.; Gómez-Hortigüela, L.; Díaz, I.; Sastre, E.; Pérez-Pariente, J. Synthesis

of Materials Containing Ferrierite Layers Using Quinuclidine and 1-Benzyl-1-Methylpyrrolidine as Structure-Directing Agents. An Experimental and Computational Study. *Chem. Mater.* **2008**, *20* (3), 1099–1107.

(51) Goretsky, A.; Beck, L.; Zones, S. I.; Davis, M. E. Influence of the Hydrophobic Character of Structure-Directing Agents for the Synthesis of Pure-Silica Zeolites. *Microporous Mesoporous Mater.* **1999**, *28* (3), 387–393.

(52) Ahn, S. H.; Lee, H.; Hong, S. B. Crystallization Mechanism of Cage-Based, Small-Pore Molecular Sieves: A Case Study of CHA and LEV Structures. *Chem. Mater.* **2017**, *29* (13), 5583–5590.

(53) Gies, H.; Marker, B. The Structure-Controlling Role of Organic Templates for the Synthesis of Porosils in the Systems SiO_2/Template/H_2O. *Zeolites* **1992**, *12* (1), 42–49.

(54) Turrina, A.; García, R.; Cox, P. A.; Casci, J. L.; Wright, P. A. Retrosynthetic Co-Templating Method for the Preparation of Silicoaluminophosphate Molecular Sieves. *Chem. Mater.* **2016**, *28* (14), 4998–5012.

(55) Pinar, A. B.; García, R.; Gómez-Hortigüela, L.; Pérez-Pariente, J. Synthesis of Open Zeolite Structures from Mixtures of Tetramethylammonium and Benzylmethylalkylammonium Cations: A Step towards Driving Aluminium Location in the Framework. *Top. Catal.* **2010**, *53* (19–20), 1297–1303.

(56) Park, M. B.; Jo, D.; Jeon, H. C.; Nicholas, C. P.; Lewis, G. J.; Hong, S. B. Zeolite Synthesis from a Charge Density Perspective: The Charge Density Mismatch Synthesis of UZM-5 and UZM-9. *Chem. Mater.* **2014**, *26* (23), 6684–6694.

(57) Burton, A. W.; Zones, S. I. Organic Molecules in Zeolite Synthesis: Their Preparation and Structure-Directing Effects. In *Studies in Surface Science and Catalysis*; Čejka, J., Bekkum, H. van, Corma, A., Schüth, F., Eds.; Elsevier B.V.: Amsterdam, 2007; Vol. 168, pp 137–179.

(58) Dabrowski, A.; Hubicki, Z.; Podkocielny, P.; Robens, E. Selective Removal of the Heavy Metal Ions from Waters and Industrial Wastewaters by Ion-Exchange Method. *Chemosphere* **2004**, *56* (2), 91–106.

(59) Misaelides, P. Application of Natural Zeolites in Environmental Remediation : A Short Review. *Microporous Mesoporous Mater.* **2011**, *144* (1–3), 15–18.

(60) Borai, E. H.; Harjula, R.; Malinen, L.; Paajanen, A. Efficient Removal of Cesium from Low-Level Radioactive Liquid Waste Using Natural and Impregnated Zeolite Minerals. *J. Hazard. Mater.* **2009**, *172*, 416–422.

(61) van Donk, S.; Janssen, A. H.; Bitter, J. H.; de Jong, K. P. Generation, Characterization, and Impact of Mesopores in Zeolite Catalysts. *Catal. Rev.* **2003**, *45* (2), 297–319.

(62) Moliner, M.; Martínez, C.; Corma, A. Multipore Zeolites: Synthesis and Catalytic Applications. *Angew. Chemie - Int. Ed.* **2015**, *54* (12), 3560–3579.

(63) Thomas, J. M.; Millward, G. R. Direct, Real-Space Determination of Intergrowths in ZSM-5/ZSM-11 Catalysts. *J .Chem. Soc., Chem Commun.* **1982**, 1380–1383.

(64) González, G.; González, C. S.; Stracke, W.; Reichelt, R.; García, L. New Zeolite Topologies Based on Intergrowths of FAU/EMT Systems. *Microporous Mesoporous Mater.* **2007**, *101* (1-2 SPEC. ISS.), 30–42.

(65) Liu, X.; Luo, Y.; Mao, W.; Jiang, J.; Xu, H.; Han, L.; Sun, J.; Wu, P. 3D Electron Diffraction Unravels the New Zeolite ECNU-23 from the "Pure" Powder Sample of ECNU-21. *Angew. Chemie - Int. Ed.* **2020**, *59* (3), 1166–1170.

(66) Bengoa, J. F.; Marchetti, S. G.; Gallegos, N. G.; Alvarez, a M.; Cagnoli, M. V; Yeramian, a a. Stacking Faults Effects on Shape Selectivity of Offretite. *Ind. Eng. Chem. Res.* **1997**, *36* (1), 83–87.

(67) Stöcker, M. Methanol-to-Hydrocarbons: Catalytic Materials and Their Behavior. *Microporous Mesoporous Mater.* **1999**, *29* (1–2), 3–48.

(68) Ferri, P.; Li, C.; Paris, C.; Vidal-Moya, A.; Moliner, M.; Boronat, M.; Corma, A. Chemical and Structural Parameter Connecting Cavity Architecture, Confined Hydrocarbon Pool Species, and MTO Product Selectivity in Small-Pore Cage-Based Zeolites. *ACS Catal.* **2019**, *9* (12), 11542–11551.

(69) Gallego, E. M.; Li, C.; Paris, C.; Martín, N.; Martínez-Triguero, J.; Boronat, M.; Moliner, M.; Corma, A. Making Nanosized CHA Zeolites with Controlled Al

Distribution for Optimizing Methanol-to-Olefin Performance. *Chem. - A Eur. J.* **2018**, *24* (55), 14631–14635.

(70) Moliner, M.; Martínez, C.; Corma, A.; Mart, C.; Corma, A. Synthesis Strategies for Preparing Useful Small Pore Zeolites and Zeotypes for Gas Separations and Catalysis. *Chem. Mater.* **2014**, *26* (1), 246–258.

(71) Takata, T.; Tsunoji, N.; Takamitsu, Y.; Sadakane, M.; Sano, T. Incorporation of Various Heterometal Atoms in CHA Zeolites by Hydrothermal Conversion of FAU Zeolite and Their Performance for Selective Catalytic Reduction of NO_x with Ammonia. *Microporous Mesoporous Mater.* **2017**, *246*, 89–101.

(72) Deka, U.; Lezcano-gonzalez, I.; Weckhuysen, B. M.; Beale, A. M. Local Environment and Nature of Cu Active Sites in Zeolite-Based Catalysts for the Selective Catalytic Reduction of NO_X. *ACS Catal.* **2013**, *3* (3), 413–427.

(73) Shi, C.; Li, L.; Li, Y. High-Throughput Screening of Hypothetical Aluminosilicate Zeolites for CO_2 Capture from Flue Gas. *J. CO_2 Util.* **2020**, *42* (July).

(74) Liu, Q.; Pham, T.; Porosoff, M. D.; Lobo, R. F. ZK-5: A CO_2-Selective Zeolite with High Working Capacity at Ambient Temperature and Pressure. *ChemSusChem* **2012**, *5* (11), 2237–2242.

(75) Palomino, M.; Corma, A.; Jordà, J. L.; Rey, F.; Valencia, S. Zeolite Rho: A Highly Selective Adsorbent for CO_2/CH_4 Separation Induced by a Structural Phase Modification. *Chem. Commun.* **2012**, *48* (2), 215–217.

(76) Miyamoto, M.; Fujioka, Y.; Yogo, K. Pure Silica CHA Type Zeolite for CO_2 Separation Using Pressure Swing Adsorption at High Pressure. *J. Mater. Chem.* **2012**, *22*, 20186–20189.

(77) Shin, J.; Camblor, M. A.; Woo, H. C.; Miller, S. R.; Wright, P. A.; Hong, S. B. PST-1 : A Synthetic Small-Pore Zeolite That Selectively Adsorbs H_2. *Angew. Chemie - Int. Ed.* **2009**, *48*, 6647–6649.

(78) Gaffney, T. R. Porous Solids for Air Separation. *Curr. Opin. Solid State Mater. Sci.* **1996**, *1* (1), 69–75.

(79) Ansón, A.; Kuznicki, S. M.; Kuznicki, T.; Haastrup, T.; Wang, Y.; Lin, C. C. H.;

Sawada, J. A.; Eyring, E. M.; Hunter, D. Adsorption of Argon, Oxygen, and Nitrogen on Silver Exchanged ETS-10 Molecular Sieve. *Microporous Mesoporous Mater.* **2008**, *109* (1–3), 577–580.

(80) Siriwardane, R. V; Shen, M.; Fisher, E. P. Adsorption of CO_2, N_2, and O_2 on Natural Zeolites. *Energy Fuels* **2003**, *17* (3), 571–576.

(81) Siriwardane, R. V.; Shen, M.; Fisher, E. P.; Poston, J. A. Adsorption of CO_2 on Molecular Sieves and Activated Carbon. *Energy Fuels* **2001**, *15* (2), 279–284.

(82) Remy, T.; Gobechiya, E.; Danaci, D.; Peter, S. A.; Xiao, P.; Van Tendeloo, L.; Couck, S.; Shang, J.; Kirschhock, C. E. A.; Singh, R. K.; Martens, J. A.; Baron, G. V.; Webley, P. A.; Denayer, J. F. M. Biogas Upgrading through Kinetic Separation of Carbon Dioxide and Methane over Rb- and Cs-ZK-5 Zeolites. *RSC Adv.* **2014**, *4* (107), 62511–62524.

(83) Rzepka, P.; Wardecki, D.; Smeets, S.; Müller, M.; Gies, H.; Zou, X.; Hedin, N. CO_2-Induced Displacement of Na^+ and K^+ in Zeolite |NaK|-A. *J. Phys. Chem. C* **2018**, *122* (30), 17211–17220.

(84) Choi, H. J.; Min, J. G.; Ahn, S. H.; Shin, J.; Hong, S. B.; Radhakrishnan, S.; Chandran, C. V.; Bell, R. G.; Breynaert, E.; Kirschhock, C. E. A. Framework Flexibility-Driven CO_2 Adsorption on a Zeolite. *Mater. Horizons* **2020**, *7* (6), 1528–1532.

(85) Zhao, J.; Xie, K.; Singh, R.; Xiao, G.; Gu, Q.; Zhao, Q.; Li, G.; Xiao, P.; Webley, P. A. Li^+/ZSM-25 Zeolite as a CO_2 Capture Adsorbent with High Selectivity and Improved Adsorption Kinetics, Showing CO_2-Induced Framework Expansion. *J. Phys. Chem. C* **2018**, *122* (33), 18933–18941.

(86) Bacsik, Z.; Cheung, O.; Vasiliev, P.; Hedin, N. Selective Separation of CO_2 and CH_4 for Biogas Upgrading on Zeolite NaKA and SAPO-56. *Appl. Energy* **2016**, *162*, 613–621.

(87) Min, J. G.; Kemp, K. C.; Hong, S. B. Zeolites ZSM-25 and PST-20: Selective Carbon Dioxide Adsorbents at High Pressures. *J. Phys. Chem. C* **2017**, *121* (6), 3404–3409.

(88) Palomino, M.; Corma, A.; Rey, F.; Valencia, S. New Insights on CO_2-Methane

Separation Using LTA Zeolites with Different Si/Al Ratios and a First Comparison with MOFs. *Langmuir* **2010**, *26* (3), 1910–1917.

(89) Hedin, N.; Chen, L.; Laaksonen, A. Sorbents for CO_2 Capture from Flue Gas - Aspects from Materials and Theoretical Chemistry. *Nanoscale* **2010**, *2* (10), 1819–1841.

(90) D'Alessandro, D. M.; Smit, B.; Long, J. R. Carbon Dioxide Capture: Prospects for New Materials. *Angew. Chemie - Int. Ed.* **2010**, *49* (35), 6058–6082.

(91) Bonenfant, D.; Kharoune, M.; Niquette, P.; Mimeault, M.; Hausler, R. Advances in Principal Factors Influencing Carbon Dioxide Adsorption on Zeolites. *Sci. Technol. Adv. Mater.* **2008**, *9*, 1–7.

(92) Breck, D. W. *Zeolite Molecular Sieves : Structure, Chemistry, and Use*; Robert E. Krieger Publishing: Malabar, FLA, USA, 1984.

(93) US Pat. 2810454, 1957.

(94) US Pat. 5159816, 1992.

(95) Farooq, S. Sorption and Diffusion of Oxygen and Nitrogen in Molecular Sieve RS-10. *Gas Sep. Purif.* **1995**, *9* (3), 205–212.

(96) Shin, H. -S; Knaebel, K. S. Pressure Swing Adsorption: An Experimental Study of Diffusion-induced Separation. *AIChE J.* **1988**, *34* (9), 1409–1416.

(97) Rietveld, H. M. A Profile Refinement Method for Nuclear and Magnetic Structures. *J. Appl. Crystallogr.* **1969**, *2* (2), 65–71.

(98) Ashbrook, S. E.; Dawson, D. M.; Griffin, J. M. Solid-State Nuclear Magnetic Resonance Spectroscopy. In *Local Structural Characterisation*; Bruce, D. W., O'Hare, D., Walton, R. I., Eds.; John Wiley & Sons Ltd: Chichester, 2014; pp 1–88.

(99) Smeets, S.; McCusker, L. B. Location of Organic Structure-Directing Agents in Zeolites Using Diffraction Techniques. In *Insights into the Chemistry of Organic Structure-Directing Agents in the Synthesis of Zeolitic Materials*; Gómez-Hortigüela, L., Ed.; Cham, Switzerland, 2017; pp 43–74.

(100) Østbø, N. P.; Goyal, R.; Jobic, H.; Fitch, A. N. The Location of Pyridine in Sodium-

Silver-Y Zeolite by Powder Synchrotron X-Ray Diffraction. *Microporous Mesoporous Mater.* **1999**, *30* (2–3), 255–265.

(101) Lozinska, M. M.; Bruce, E. L.; Mattock, J.; Chitac, R. G.; Cox, P. A.; Turrina, A.; Wright, P. A. Understanding the Anion-Templated, OSDA-Free, Interzeolite Conversion Synthesis of High Silica ZK-5. *Chem. - A Eur. J.* **2022**, *28* (56), e202201689.

(102) Treacy, M. M. J.; Newsam, J. M.; Deem, M. W. A General Recursion Method for Calculating Diffracted Intensities from Crystals Containing Planar Faults. *Proc. R. Soc. London, Ser. A Math. Phys. Sci. Soc. London, A* **1991**, *433* (1889), 499–520.

(103) Schwalbe-Koda, D.; Corma, A.; Román-Leshkov, Y.; Moliner, M.; Gómez-Bombarelli, R. Data-Driven Design of Biselective Templates for Intergrowth Zeolites. *J. Phys. Chem. Lett.* **2021**, *12* (43), 10689–10694.

(104) Baerlocher, C.; McCusker, L. B.; Gies, H.; Marler, B. IZA Database of Disordered Zeolite Structures, http://www.iza-structure.org/databases/, accessed October 2023.

(105) Szostak, R.; Lillerud, K. P. Faults, Intergrowths and Random Phases in the ABC-D6R Family of Zeolites. In *Studies in Surface Science and Catalysis*; Weitkamp, J., Karge, H. G., Pfeifer, H., Holderich, W., Eds.; Elsevier B.V.: Amsterdam, 1994; Vol. 84, pp 535–542.

(106) Wang, Y.; Tong, C.; Liu, Q.; Han, R.; Liu, C. Intergrowth Zeolites , Synthesis , Characterization , and Catalysis, Article ASAP. *Chem. Rev.* **2023**, 1–58.

2. Theoretical Background to Analytical Techniques

2.1. Diffraction

2.1.1. Introduction

Zeolite materials typically possess long-range order and are readily examined by diffraction techniques. The most common of these is X-ray diffraction but others are also used when appropriate. Although no technique on its own can provide a full description of a material's behaviour, diffraction can often prove vital.

2.1.2. Basic Crystallography

A crystal consists of a crystallographic lattice with a single motif of atoms on each lattice point. The simplest repeating unit that can be used to generate the entire lattice solely through integer translations along the **a**, **b**, and **c** axes is termed the "unit cell".[1] The unit cell is generated by the asymmetric unit, the smallest repeating piece, *via* a series of symmetry operations, described below.[2] In total, 6 unit cell parameters are used to describe the unit cell: 3 unit cell edges, *a*, *b* and *c*; and 3 interaxial angles, α, β, and γ.[1] Atomic positions within the unit cell are represented by the variables *x*, *y* and *z*.

There are 4 possible lattice types: primitive (P), face-centred (F), body-centred (I) and base-centred (A, B or C).[1] These describe the locations of lattice points within the unit cell, as shown in Figure 2.1.1. The relationship between the 6 lattice parameters are defined by 1 of the 7 crystal systems described in Table 2.1.1. 14 unique Bravais lattices are formed by combining all possible lattice types and crystal systems, as shown in Figure 2.1.2.[2]

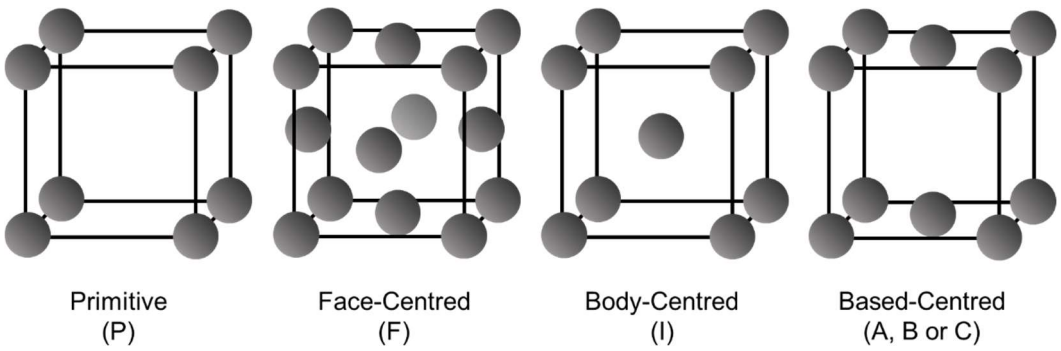

Figure 2.1.1. The 4 types of centring: primitive, face-centred, body-centred and base-centred.

Table 2.1.1. The 7 crystal systems.

Crystal System	Axial Dimensions	Interaxial Angles
Triclinic	$a \neq b \neq c$	$\alpha \neq \beta \neq \gamma$
Monoclinic	$a \neq b \neq c$	$\alpha \neq 90° = \beta = \gamma$
Orthorhombic	$a \neq b \neq c$	$\alpha = \beta = \gamma = 90°$
Tetragonal	$a = b \neq c$	$\alpha = \beta = \gamma = 90°$
Trigonal	$a = b = c$	$\alpha = \beta = \gamma \neq 90°$
Hexagonal	$a = b \neq c$	$\alpha = \beta = 90°, \gamma = 120°$
Cubic	$a = b = c$	$\alpha = \beta = \gamma = 90°$

The symmetry of a crystal can be classified into 1 of 230 space groups by considering translational symmetry operations in addition to the 32 point groups.[3] The point groups contain proper and improper rotations, mirror planes and inversion centres only, whilst space groups also include screw axes and glide planes. Examples of these symmetry

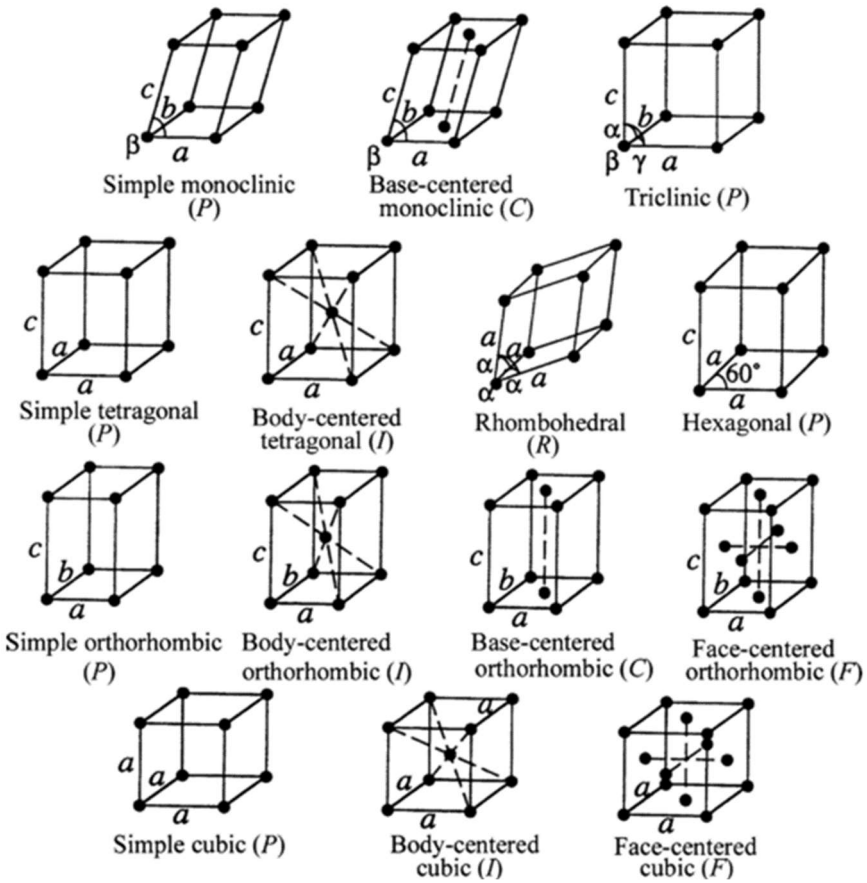

Figure 2.1.2. The 14 unique Bravais lattices, reproduced from Waseda et al,[2] with permission from Springer Nature.

elements are described in Table 2.1.2. Crystal structures can then be identified through individual codes related to their symmetry and lattice type, such as the orthorhombic *Immm* (body centring with mirror planes perpendicular to ***a***, ***b*** and ***c***), tetragonal $P4_2/nmc$ (primitive centring, with a 4_2 screw axis along ***c*** and perpendicular to an *n* glide, a mirror plane perpendicular to ***a*** and ***b*** and a *c* glide perpendicular to the diagonals in the ***ab*** plane) and cubic $I\bar{4}3m$ (body centring with a $\bar{4}$ inversion axis along ***a***, a 3 rotation axis along the body diagonal and a mirror plane along the face diagonal).

It can be convenient when describing diffraction, discussed in the following chapters, to consider a crystal as a series of equally spaced lattice planes. This was introduced in 1839 by the British mineralogist William Hallowes Miller,* and the lattice planes are thus termed "Miller planes".[4] Each set of parallel planes is described by the integers *h*, *k* and *l*, dubbed "Miller indices", with the "*d* spacing" between planes denoted by d_{hkl}. The Miller indices designate a plane's intersection with each crystallographic axis. This is done such that, if a plane passes through the origin of a unit cell, an adjacent one will cut the ***a***, ***b*** and ***c*** axes at a/h, b/k and c/l, respectively.[3]

Table 2.1.2. Symmetry elements and their symbols.

Symmetry element	**Symbol**
Inversion centre	$\bar{1}$
Mirror plane	*m*
Glide plane	*a*, *b*, *c*, *d*, *n*
Rotation axis	2, 3, 4, 6
Screw axis	2_1, 3_1, 3_2, 4_1, 4_2, 4_3, 6_1, 6_2, 6_3, 6_4, 6_5
Inversion axis	$\bar{3}$, $\bar{4}$, $\bar{6}$

2.1.3. Diffraction and Bragg's Law

The British polymath Thomas Young described the wave-like behaviour and interference of light in 1801.[5] Light is diffracted by spaces of a similar size to its wavelength and initially this could not be applied to the study of crystal structures. This

* It is interesting to note that Miller's work comes before the development of X-ray diffraction, discussed below, and was based solely on examination and measurement of crystal faces. Modern crystallography is so reliant on diffraction as to be unrecognisable in comparison with Miller's field.

changed in light of the Nobel prize winning discoveries of German physicists Wilhelm Röntgen and Max von Laue. In 1895, Röntgen discovered the existence of X-rays which enabled von Laue to discover crystal diffraction almost 2 decades later, in 1912.[6,7] Von Laue's attempts to describe the underlying diffraction conditions of crystals ultimately reduce to Bragg's law, devised by Lawrence Bragg in 1913.[8] He confirmed this relationship experimentally with his father, William Bragg, and the two subsequently shared the Nobel Prize in Physics.

As previously discussed, diffraction is a phenomenon observed when a wave meets an object, or gap, with a similar size to its wavelength. This occurs in crystals when d_{hkl} is comparable to the wavelength, λ, of incident X-rays. The periodicity within crystalline solids leads to constructive and destructive interference effects. Constructive interference peaks can be described using the Bragg equation:

$$n\lambda = 2d_{hkl} \sin 2\theta \tag{2.1}$$

where n is a positive integer and θ is the angle between the incident X-rays and the crystal planes.[9] This condition is derived geometrically by considering the setup shown in Figure 2.1.3, when the path difference between reflected X-rays is an integer number of wavelengths. Any X-rays which do not fulfil the Bragg equation will interfere destructively.

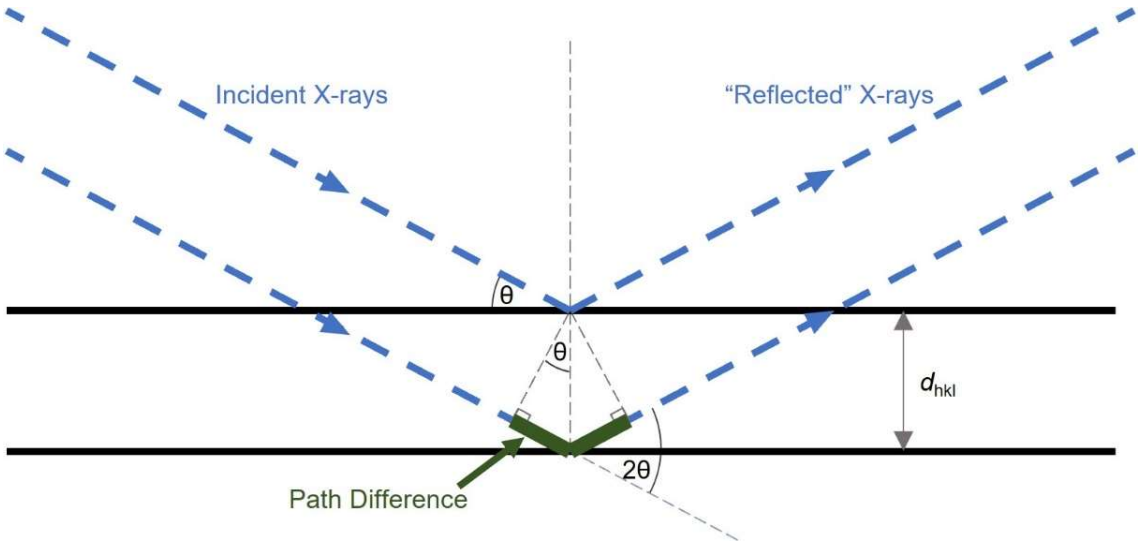

Figure 2.1.3. Schematic representation of the Bragg reflection.

2.1.4. X-ray Sources

In order to carry out X-ray diffraction (XRD) experiments, a beam of X-rays must first be created. The instrument used depends on the analysis needed and availability. Laboratory sources are far more readily available but do not have the same high resolution which synchrotron sources can provide and may be required. Generation of X-rays for both sources are discussed here but a more detailed description of both setups are discussed in Section 2.1.7.

2.1.4.1. Laboratory X-ray Sources

A typical laboratory instrument utilises an X-ray tube, shown in Figure 2.1.4. A current passes through the cathode, a metal wire, heating it and generating electrons.[10] These electrons are accelerated by an electric potential, forming a high energy electron beam and striking a target metal anode. Common anode materials include Cu, Mo and Fe.

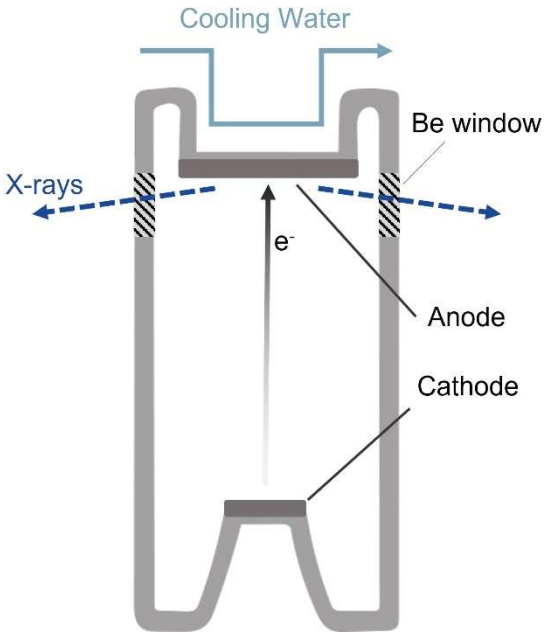

Figure 2.1.4. Schematic depiction of a laboratory X-ray tube.

Upon hitting the anode, 2 modes of X-ray generation can occur. The first is due to the sudden deceleration of the charged electrons and is termed *Bremsstrahlung* (German, literally "braking radiation"). This generates "white" X-rays, with a range of wavelengths. This is utilised in synchrotron instruments, although generated differently, as discussed later.

The second method gives rise to well defined wavelengths which are dependent on the metal used (common anodes are Cu, Mo, Fe and Co). When electrons within the beam hit the anode, some collide with metal atoms, causing the ejection of core electrons, as shown in Figure 2.1.5(a). To fill this core hole, an electron from an outer orbital can drop down, accompanied by a loss of excess energy. This takes the form of a photon, with a wavelength in the X-ray range of the electromagnetic spectrum (0.01 – 10 nm). As the energy of this photon is dependent on the energy levels of the atom, shown in Figure 2.1.5(b), it is dependent on the element. This is exploited in elemental analysis as discussed in Section 2.3. Cu is the most commonly used metal and exhibits multiple characteristic X-rays. As described in Figure 2.1.5(b), K_β arises from the 3p → 1s transition (λ = 1.3922 Å), whilst K_α is due to the 2p → 1s transition and is itself split into $K_{\alpha1}$ (λ = 1.54051 Å) and $K_{\alpha2}$ (λ = 1.54433 Å) due to different spin states of the 2p electron relative to the 1s vacancy.† A selection of characteristic X-rays is shown in Table 2.1.3.

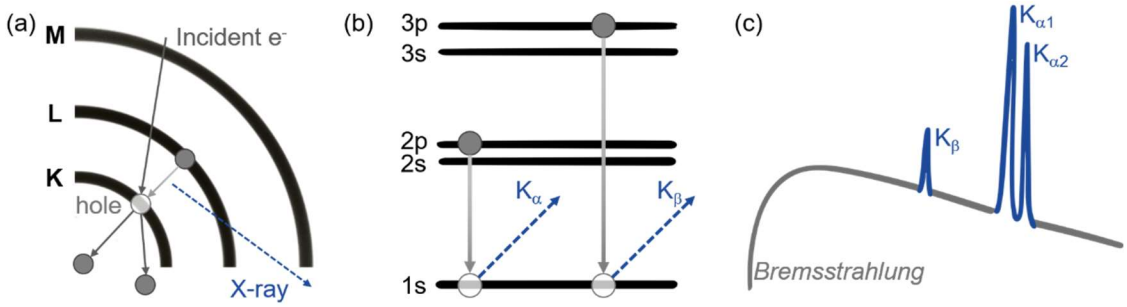

Figure 2.1.5. Laboratory X-ray generation: (a) characteristic X-rays result from the formation of core holes and subsequent recombination with a higher-lying e⁻; (b) the energies of such X-rays are dependent on atomic energy levels; (c) the overall emission spectrum is a superposition of characteristic peaks and a Bremsstrahlung background.

X-ray emission from a laboratory tube is a combination of both *Bremsstrahlung* and characteristic peak phenomena, leading to spectra such as shown in Figure 2.1.5(c). The broad range of wavelengths would be highly problematic for typical X-ray diffraction experiments, as used in this work.‡. As a result, generated X-rays pass often through a monochromator to isolate a given wavelength, typically $K_{\alpha(1)}$ as this is the most intense of those generated. Further details are given in the Section 2.1.7.

† This also occurs for K_β but wavelengths are not sufficiently different and generally overlap in X-ray emission spectra.
‡ Polychromatic beams can be used but alternative experimental setups are required.

Table 2.1.3. Wavelengths of characteristic X-rays for metals commonly used as anodes, taken from the International Tables for Crystallography.[11]

Metal	Wavelength (Å)		
	$K_{\alpha1}$	$K_{\alpha2}$	K_{β}
Mo	0.7093172	0.71361	0.63230
Cu	1.5405929	1.5444274	1.392234
Co	1.788996	1.792835	1.620826
Fe	1.936041	1.939973	1.756604
Cr	2.289726	2.293651	2.084881

2.1.4.2. Synchrotron X-ray sources

Synchrotron radiation is generated in an entirely different method, making use of the phenomenon of *Bremsstrahlung*. There are only approximately 70 such facilities in the world and require funding at a national or international level, and beam time is precious. Electrons are generated by an electron gun and reach speeds close to that of light using a series of particle accelerators (linear accelerator, booster synchrotron and finally a large storage ring). At Diamond Light Source (DLS) in Oxfordshire the storage ring is made up of straight sections angled together using bending magnets to form a polygon 562 m in perimeter, a schematic of which is shown in Figure 2.1.6.[12]

Whilst the bending magnets generate *Bremsstrahlung*, a higher intensity X-ray beam can be formed through the use of insertion devices. These employ magnets within the linear sections of the storage ring, causing the beam to "wiggle", increasing the X-ray intensity at each bend. These high intensity X-rays are well suited for high quality XRD patterns, allowing high resolution and intensity, and an insertion device is used before beamline I11 for this purpose. Each beamline is composed of a front end, extracting X-rays from the storage ring; an optics hutch, filtering and focussing incident X-rays; an experimental hutch, containing the investigational setup; and the control hutch for monitoring and control of the experiment. To minimise energy loss within the storage ring, the electron beam is energised by radio waves in the radiofrequency (RF) cavities. This is insufficient to completely compensate the loss and so new high energy electrons are generated and added to the storage ring routinely, maintaining a constant beam current.

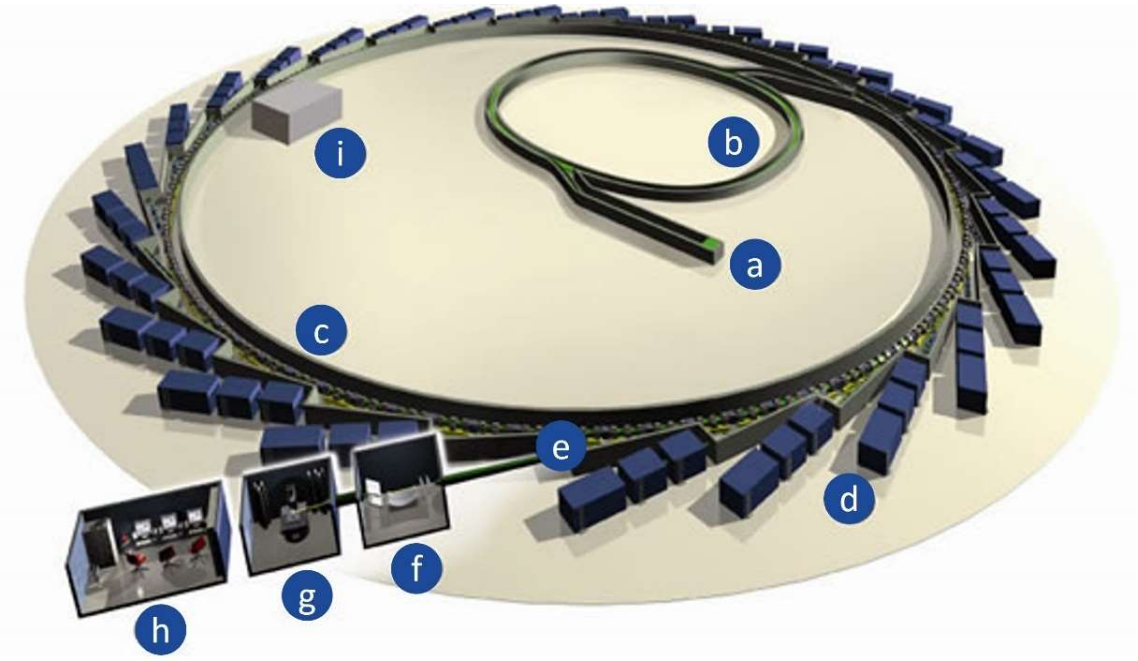

Figure 2.1.6. Schematic of Diamond Light Source (DLS), composed of (a) linear injector, (b) booster ring, (c) storage ring, (d) beamline, (e) front end, (f) optics hutch, (g) experimental hutch, (h) control cabin and (i) RF cavities. Schematic adapted from DLS.[12]

As a result of the high intensity and resolution available, synchrotron facilities are beneficial in the study of samples with complex diffraction patterns or structures, such as samples containing guest molecules, possessing large unit cells or supercells, or fine peak splitting. The wavelengths of synchrotron beamlines used during this study are given in Table 2.1.4.

Table 2.1.4. Beamline parameter ranges available at I11,[12] *ID31,*[13] *9B,*[14] *part of Diamond Light Source (DLS), the European Synchrotron Research Facility (ESRF) and the Pohang Accelerator Laboratory (PAL), respectively.*

Beamline	Energy Range (keV)	Wavelength Range (Å)
DLS I11	6-25	0.5-2.1
ESRF ID31	21-150	0.1-0.6
PAL 9B	8-20	0.6-1.5

2.1.4.3. Monochromation

As diffraction angles are dependent on the X-ray wavelength, as determined by the Bragg equation, it is important that the wavelength distribution is as narrow as possible.

This is done using a monochromator.[15] Here Bragg's law is exploited by passing a polychromatic beam through a single crystal of known structure, often graphite, Si or Ge, and orientated such that only the desired wavelength is directed to the sample under investigation. I11 at DLS uses the (111) peak from 2 successive Si crystals as a double-crystal monochromator, for example,[16] similar to the setup shown in Figure 2.1.7.

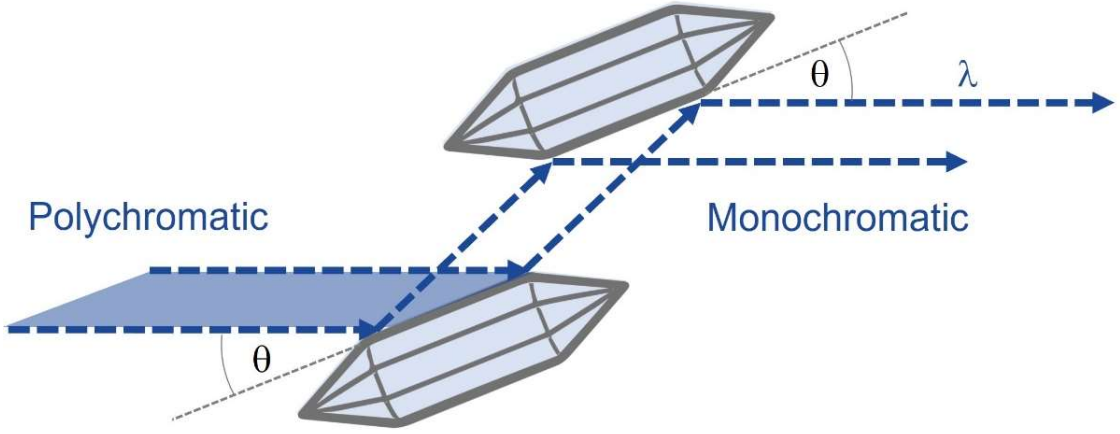

Figure 2.1.7. Schematic of a double-crystal monochromator, filtering only X-rays with wavelength λ from a polychromatic beam by exploitation of the Bragg angle, θ.

2.1.5. Powder X-ray Diffraction

The value of d_{hkl} in the Bragg equation is related to the Miller indices of the plane, as discussed earlier. As *h*, *k* and *l* are integers, diffraction leads to a series of discrete peaks. If the sample of interest is a single crystal, a series of well-defined spots will be produced upon exposure to a monochromatic beam of X-rays. Rotation allows the crystallographer to selectively collect diffraction patterns from individual orientations. Thus, a 3-dimensional pattern can be obtained, and peaks given their respective Miller indices. This is not the case for powder samples.

Within a powder of crystalline material there exists all possible crystallite orientations. Equally, for a given set of Miller planes, all possible orientations relative to the X-ray beam occur. Some of these will fulfil Bragg's law but, instead of discrete peaks as observed in the single crystal case diffraction cones radiate from the sample, termed Debye cones,[2] as shown in Figure 2.1.8.

During a typical diffraction experiment, intensities are measured as a detector radially scans cross-sections of the Debye cones. Collected patterns are then plotted as a

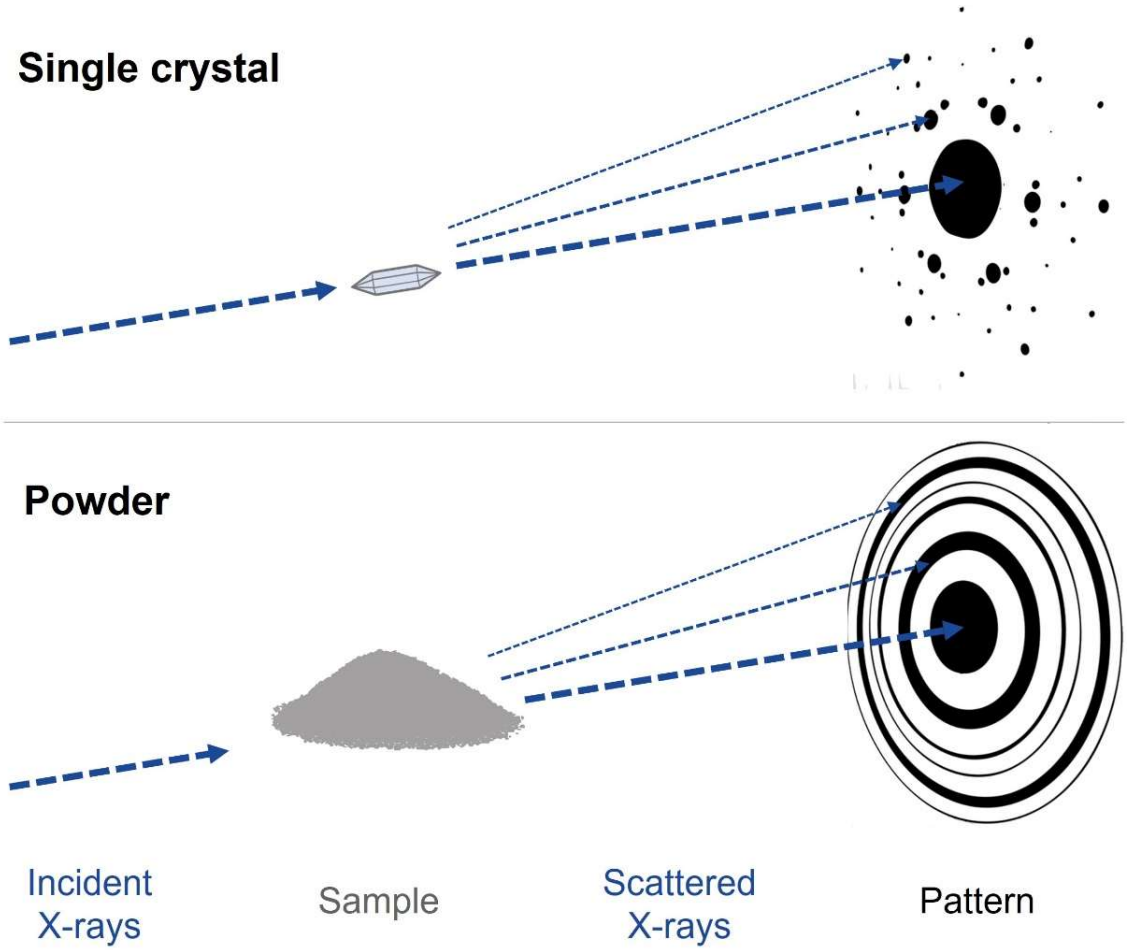

Figure 2.1.8. Comparison of the diffraction patterns collected from single crystal and powder X-ray diffraction.

diffracted intensity against 2θ. Such plots have 2 major uses. The first is termed "fingerprinting", as each crystal structure has a characteristic pattern and hence samples can be identified qualitatively, either for verification of synthesis or analysis of phase composition. The second use of diffraction patterns is structural refinement, the main characterisation method used in this work.

Peak positions in a diffraction pattern are dependent on the unit cell parameters, with the exact relationship determined by the crystal system. The intensities of the peaks are related *via* Fourier transform to the internal structure – the position and type of atoms present in the crystal,[15] described by

$$F_{hkl} = \int \rho(x,y,z).\, e^{2\pi i(hx+ky+lz)}\, dV \qquad (2.2)$$

where $\rho(x,y,z)$ is the electron density and F_{hkl} is the structure factor, which describes the ability of the unit cell to scatter X-rays for a given (*hkl*) and is composed of an amplitude and a phase. The structure factor is related to the intensity of peaks for a given (*hkl*), I_{hkl}, within the diffraction pattern by

$$I_{hkl} \propto |F_{hk}|^2 \tag{2.3}$$

As such, whilst the amplitude of F_{hkl} is recorded during diffraction, information on the phase is lost.

As X-rays are scattered by electrons, higher electron density causes greater scattering. This means that heavier atoms, such as Cs, can greatly influence diffraction pattern intensities, whilst those of light elements, such as Li, have little impact. The scattering ability of an atom, *n*, is described by its scattering factor, f_n, and can be useful to describe F_{hkl}, such that

$$F_{hkl} = \sum_n f_n e^{2\pi i(hx_n+ky_n+lz_n)} \tag{2.4}$$

In single crystal XRD, the intensities of every diffraction peak can be measured, although the relative phase of the reflection is lost in what is known as the "phase problem". A direct Fourier transform from the diffraction data is therefore impossible but many techniques have been developed, such as direct methods approaches, to allow the crystal structure to be determined. This is done in an iterative and statistical manner, and includes utilising physical constraints, such as non-negative electron density and chemical knowledge of bonding geometries amongst other, more specialised, methodologies.[15] These methods allow a structure to be obtained with no or very little prior knowledge of the crystal in question.

In powder X-ray diffraction (PXRD), the 3-dimensional diffraction pattern that would be available for a single crystal collapses into a single dimension. As such, PXRD is not readily used as an *ab initio* method for full crystal structure determination, as this requires highly specialised techniques. Instead, structural refinement is more typical, and is the basis of this work.

2.1.6. Le Bail Fitting and Rietveld Refinement

The initial step in typical structural refinements is often Le Bail fitting. This is a structureless, whole-pattern fitting method which determines unit cell and instrument

parameters and can be useful in the identification of impurity phases.[17] To gain information about the internal structure of the unit cell, Rietveld refinement must be carried out.

The Rietveld method§ was developed at the Netherlands Reactor Centre in the 1960s by Loopstra, van Laar and Rietveld.[18] This is a whole-pattern fitting, least squares structure refinement technique. As it is a refinement technique suitably close starting models must be used. In this work this method is used to refine the structures of zeolites under various conditions using TOPAS-Academic software,[19] with initial structures taken from the Database of Zeolite Structures from the International Zeolite Association Structural Commission,[20] unless otherwise stated.

Rietveld refinement is a least squares method as it attempts to minimise the residual, *s*, between the calculated and observed pattern, such that

$$s = \sum w_i \left| y_{i,obs} - y_{i,calc} \right|^2 \qquad (2.5)$$

where w_i is a weighting factor, and $y_{i,obs}$ and $y_{i,calc}$ are the observed and calculated intensities of the i^{th} step respectively.[21] The weighting factor is related to the standard deviation of the relevant peak, $\sigma_{i,p}$ and background, $\sigma_{i,b}$ by:

$$w_i^{-1} = \sigma_{i,p}^2 + \sigma_{i,b}^2 \qquad (2.6)$$

The "goodness of fit" of a refined structure can be quantified through a variety of criteria.[22] The profile residual, R_p, is one such parameter, which is described by:

$$R_p = \sqrt{\frac{\sum \left| y_{i,obs} - y_{i,calc} \right|}{\sum y_{i,obs}}} \qquad (2.7)$$

This does not account for the weightings of individual points described above, unlike the weighted *R* value, R_{wp}, given by:

$$R_{wp} = \sqrt{\frac{\sum w_i \left| y_{i,obs} - y_{i,calc} \right|^2}{\sum w_i y_{i,obs}^2}} \qquad (2.8)$$

§ The "Rietveld" method was developed by the 3 researchers listed, with Loopstra and van Laar working on much of the theoretical background and Rietveld responsible for coding the method. Without consulting the others, Rietveld published as the sole author, mentioning the other 2 only as acknowledgements and presenting the entire work as his own. The term "Rietveld refinement" is now ingrained in the literature and scientific community at large, and will be used in this work, despite the ethical issues associated with the term.

This is a commonly used parameter in reporting the validity of an individual refinement. The expected residual, R_{exp}, is not affected by refinement and is described by:

$$R_{exp} = \sqrt{\frac{N-P}{\sum w_i {y_{i,obs}}^2}} \quad (2.9)$$

where N and P are the number of data points and parameters, respectively. Comparison of this value with that of R_{wp} determines the goodness of fit, χ^2, as shown here;

$$\chi^2 = \left(\frac{R_{wp}}{R_{exp}}\right)^2 = \frac{\sum w_i \left|y_{i,obs} - y_{i,calc}\right|^2}{N-P} \quad (2.10)$$

Whilst χ^2 is not the most commonly reported value in structural refinement, it is useful as a well-known and understood measure in other fields, aiding interdisciplinary legibility.

The values of the R_{wp} and χ^2 are minimised through the refinement of multiple parameters in an iterative process.[21] It is important to note that whilst low values of residuals and χ^2 are a good quantification of refinement progress, and are reported as such, they are not the be-all and end-all and visual comparison of the calculated pattern with the experimental pattern is always the best method,[23] especially for checking peak profiles and background functions, as well as crystallographic phenomena such as systematic absences and peak splitting. Care must also be taken in ensuring the chemical plausibility of the refined structure.

The refinement process often follows a general systematic technique, such as suggested by McCusker *et al.*, whereby background and peak profile parameters are refined first, followed by structural parameters, such as atomic positions and occupancies.[24] Refinement of parameters continues until no significant improvement is observed. Whilst some parameters, such as atomic coordinates, or positions, and fractional occupancy are readily understood, additional factors and techniques are detailed below.

2.1.6.1. Background

A background function is one of the first parameters to be refined, along with a zero-point correction and scale factor. This is composed of noise, typically due to experimental sources, which can be fitted by various functions. In this work, Chebyshev polynomials of the first kind are used. These take the form

$$T_n(\cos\theta) = \cos n\theta, \quad (2.11)$$

and can be shown to be polynomials by trigonometric identities.[25] Additionally, by recurrence relation,

$$T_{n+1}(x) = 2xT_n(x) - T_{n-1}(x) \quad (2.12)$$

TOPAS-Academic uses such functions to treat the background by first normalising the 2θ range investigated to between -1 and 1 and applying coefficients to each polynomial such that;

$$f_{bkg}(x) = \sum_n^N c_n T_n(x) \quad (2.13)$$

where $f_{bkg}(x)$ is the background function, n denotes the n^{th} term, N the highest term and x the normalised 2θ value.[26] The number of polynomials used can be increased, increasing the value of N, to improve the fit of the background, although using too many terms can lead to the background "fitting" peak intensity and the plausibility of the background function should be checked.

2.1.6.2. Peak profiles

Peak shapes observed in PXRD patterns contain contributions from the wavelength used, the instrumental setup and the sample itself. Some of these may be modelled explicitly, or simply fitted mathematically. The 2 best known types of profiles are Gaussian and Lorentzian (or Cauchy), $G(x)$ and $L(x)$, respectively, described by:

$$G(x) = \frac{2\sqrt{\frac{ln\,2}{\pi}}}{FWHM} e^{\frac{-4\,ln\,2\,x^2}{FWHM^2}} \quad (2.14)$$

$$L(x) = \frac{2\,FWHM}{\pi(FWHM^2+4x^2)} \quad (2.15)$$

where FWHM is the full-width at half-maximum of the peak.[26] The FWHM has an angular dependency and can be described in multiple ways, such as;

$$FWHM = h_a + h_b\,tan\,\theta + h_c\,sec\,\theta \quad (2.16)$$

where h_a, h_b and h_c are refinable parameters.[26] An example of Gaussian and Lorentzian profiles, and their angular dependencies are shown in Figure 2.1.9. From this, the relative shapes of Gaussian and Lorentzian profiles can be seen, as can the profile spread as 2θ increases.

Experimental peak shapes are rarely fully Gaussian or Lorentzian and typically they are combined in some way, such as in a pseudo-Voigt profile, given by:

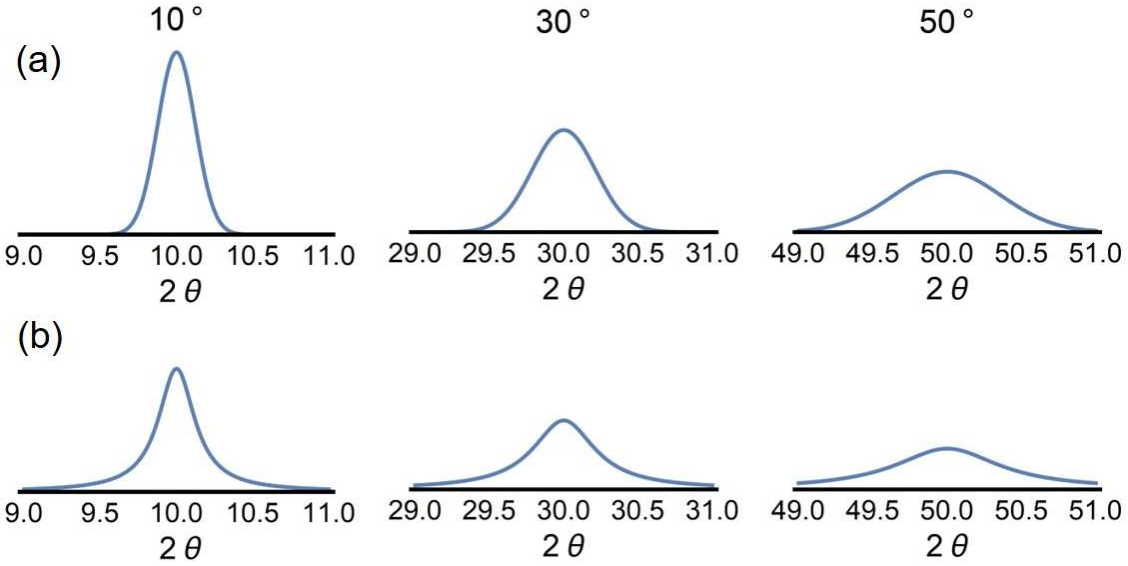

Figure 2.1.9. Examples of (a) Gaussian and (b) Lorentzian profiles, with h_a, h_b, h_c = 0.1, 0.5, 0.1 at varying 2θ. Plots were generated using Mathematica software.[88]

$$PV(x) = \eta L(x) + (1 - \eta)G(x) \tag{2.17}$$

where η is the Lorentz fraction and determines the degree of Lorentzian and Gaussian behaviour.[26] Peaks with varying η are shown in Figure 2.1.10, which illustrates how this parameter can tune the fit of peak profiles.

An additional consideration is the θ dependency of η, which can be described by:

$$\eta = l_a + l_b \tan\theta + l_c \sec\theta \tag{2.18}$$

where l_a, l_b and l_c are refinable parameters.[26] By refinement of these values, in addition to their FWHM analogues, a pseudo-Voigt peak profile can be fitted to an experimental pattern. Other peak profiles include the Pearson VII and modified Thompson-Cox-

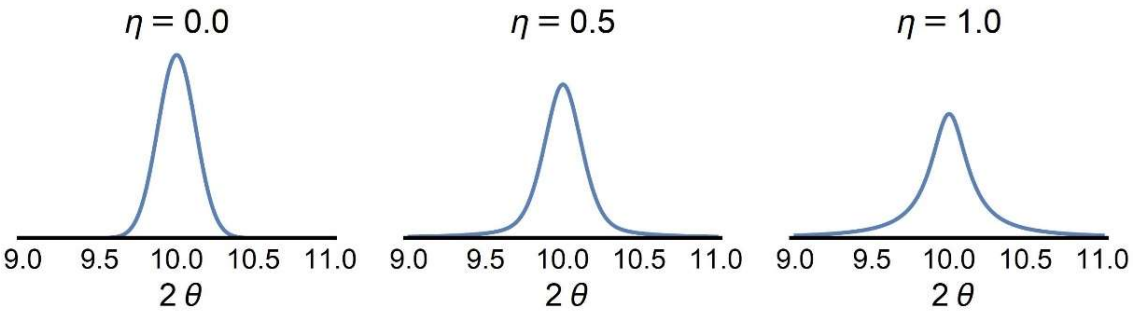

Figure 2.1.10. Peak profiles with varying η and h_a, h_b, h_c = 0.1, 0.5, 0.1. Plots were generated using Mathematica software.[88]

Hastings pseudo-Voigt models, which are described by Pearson and Thompson *et al.*, respectively.[27,28]

2.1.6.3. Peak asymmetry

An additional factor to describe in peak profiles can be asymmetry.[29] Commonly used pseudo-Voigt profiles do not model any peak asymmetry, which is often largely due to axial divergence during data acquisition. This phenomenon is particularly important at very low angles.[30] Due to inherent divergence present in the X-ray source, the X-ray beam spreads out, or diverges, parallel to the axis of the goniometer as it propagates through space, hence axial divergence. The source, sample and detector are not infinitesimally small, and so additional Bragg conditions can be met for these divergent X-rays.[31] In this case, the path required to reach the detector is longer, requiring a different Bragg angle than the angle recorded in the equatorial plane of the diffractometer, 2φ, as shown in Figure 2.1.11. Such Bragg conditions require an angle, 2θ, which is larger than 2φ and so additional intensity is recorded at lower angles ($2\varphi < 2\theta$) causing an asymmetric tail. Other effects contribute to this asymmetry too, such as the curved nature of the footprints of diffraction cones on an X-ray detector of finite

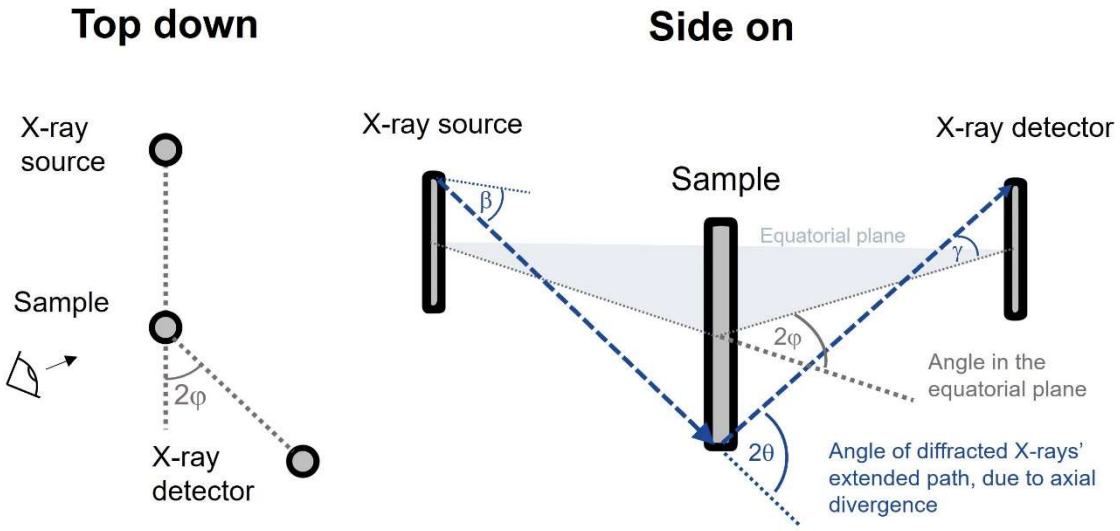

Figure 2.1.11. A schematic diagram illustrating axial divergence in diffractometers from above and side on. The finite length scales of source, sample and detector (shown as rods here), and axial divergence present in the incident beam, β, allows diffracted peaks to be recorded at erroneous values, 2φ. In an ideal case, each rod would be infinitesimally small and axial divergence in the incident and refracted beams (β and γ, respectively) could only be 0. In real world setups however, maximum values of β and γ are non-zero, and so alternate paths can be taken by X-rays scattering with a Bragg angle of 2θ, but recorded at 2φ in the equatorial plane. Of the diffractometer. This introduces an asymmetric tail to diffraction peaks (which occur at the true value $2\varphi = 2\theta$).

width and height. Multiple models have been devised to deal with such effects, such as those of Van Laar and Yelon and Finger *et al.*,[29,32] and in this work refinements are carried out using the simple axial model described by Cheary and Coelho.[33]

2.1.6.4. Thermal parameters

Whilst it is easy to think of a crystalline solid as consisting of atoms frozen in place, in reality atoms within the structure are constantly vibrating due to thermal motion. The atomic scattering factor, *f*, used in equation $F_{hkl} = \sum_n f_n e^{2\pi i(hx_n+ky_n+lz_n)}$ (2.4) is dependent on angle (i.e. $f(\theta)$), with poorer scattering at higher angles due to interference effects. Cromer and Mann fitted this dependency with an analytical function,[34] given by:

$$f(\theta) = \sum_{i=1}^{4} a_i \, e^{\frac{-b_i sin^2(\theta)}{\lambda^2}} + c \qquad (2.19)$$

Values of a_i, b_i and c are given in the International Tables for Crystallography for atoms and ions, giving the best fits for plots determined *via* computational modelling of their electron wavefunctions.[35]

Thermal motion smears out the electron density in space, causing additional interference effects. Assuming equal vibration in all directions, the isotropic displacement parameter, U_{iso}, can be used to describe this effect, as can its alternative, B_{iso}, such that:

$$f'(\theta) = f(\theta) \, e^{\frac{-8\pi^2 U_{iso} sin^2(\theta)}{\lambda^2}} = f(\theta) \, e^{\frac{-B_{iso} sin^2(\theta)}{\lambda^2}} \qquad (2.20)$$

where symbols have their usual meanings.[15] Examples of $f'(\theta)$ and the effect of thermal motion are shown in Figure 2.1.12.

Often powder X-ray data is insufficient to use anything other than an isotropic model of thermal motion.[15] These parameters may remain unrefined as they are strongly correlated with site occupancies in X-ray diffraction patterns, although this is not the case in neutron diffraction, discussed later, and so this may be attempted.[24]

2.1.6.5. Difference Fourier mapping

Additional techniques within Rietveld refinement are important in the structural study of materials. Although the method requires a good starting model, some sites may be missing. Sometimes this can be dealt with by trying to fit appropriate sites reported in the literature, where available. An alternative approach is the use of difference Fourier

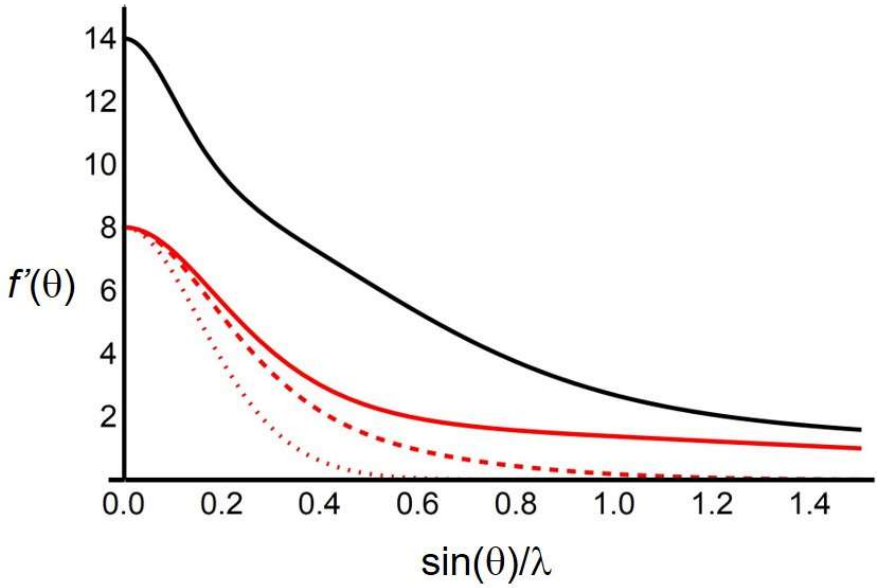

Figure 2.1.12. Atomic scattering factors for Si (black) and O (red) based on values from the International Tables for Crystallography.[35] B_{iso} values of 0, 2 and 10 Å^{-1} are indicated by solid, dashed and dotted lines, respectively. Plots were generated using Mathematica software.[88]

mapping.[24] This compares the "observed" electron density with that of the model, to determine potential additional sites, as described by:

$$\Delta\rho(x,y,z) = \frac{1}{V}\sum_n \left(F_{hkl,o} - F_{hkl,c}\right) e^{-2\pi i(hx_n+ky_n+lz_n)} \qquad (2.21)$$

where terms have their usual meanings and labels o and c relate to observed and calculated variables, respectively.[36] This method has to assume that the phases from the calculated model are close to their true values due to the phase problem, and so difference Fourier methods still require a reasonably close starting model. The difference in electron density, Δρ, can be visualised as a 3-dimensional map, and potential new sites identified. This method is useful in the study of zeolites to find extra-framework cations, and in porous materials in general to find the location of guest species.

2.1.6.6. Restraints, constraints and rigid bodies

To ensure that the refined structure is chemically sensible, restraints and constraints are used.[24] This is of particular importance in larger systems, where the large number of parameters makes convergence to an incorrect structure more likely, but even in less complex setups they are often routine.

Constraints enforce a particular condition upon the model during refinement, such as ensuring all atoms of the same type have identical thermal parameters.[37,38] For less strict

conditions, restraints are used. These penalise models which deviate strongly from an idealised value, without imposing exact conditions upon them. This is routinely used for the refinement of bond lengths and angles.[39–41]

For some systems, including MOFs and zeolites with guest species or OSDAs, it may be useful to enforce spatial relationships between atoms.[42,43] Through the use of rigid bodies, the position and orientation of an assembly of atoms can be refined relative to the structure at large, without altering the relative positions of atoms within the assembly.[44] This approach was used in the refinement of zeolitic imidazolate frameworks (ZIFs), a subset of MOFs, shown in Figure 2.1.13. Such assemblies are represented in the form of a z-matrix or Cartesian matrix. A z-matrix defines sites based on distances, angles and torsion angles relative to other, previously described sites within the assembly, whereas the Cartesian alternative simply uses its eponymous coordinate system. An advantage of a z-matrix is that it can be set up in such a way that meaningful bond lengths, angles and torsion angles can be refined within the assembly whilst retaining a chemically credible structure. In this work, rigid bodies have been applied to both adsorbed CO_2 species and OSDAs.

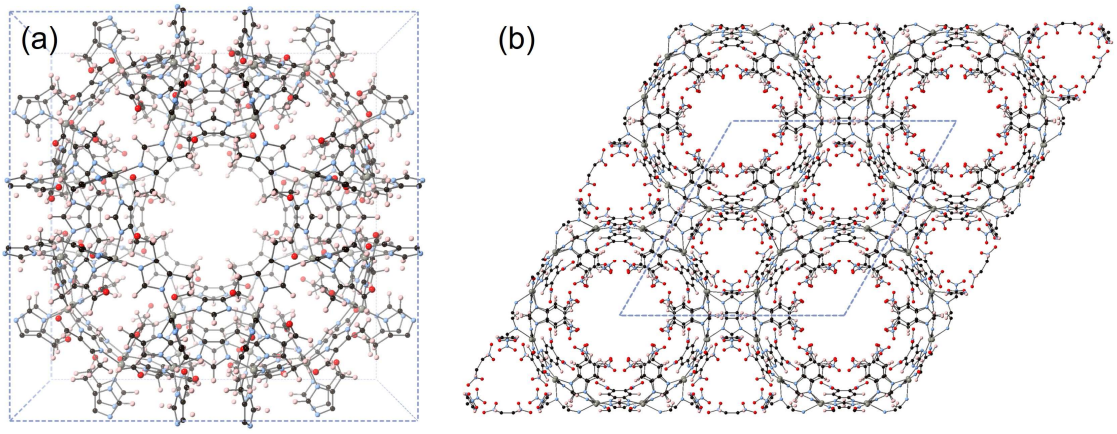

Figure 2.1.13. Structures of ZIFs refined using rigid bodies to describe linker molecules, outside the work of this thesis: (a) ZIF-93 and (b) ZIF-73. Zn, C, N, O and H atoms are depicted in grey, black, light blue, red and pink, respectively.

2.1.6.7. The Rietveld refinement process in this work

The process of Rietveld refinements carried out in this work followed a similar process to that described by McCusker *et al*,[24] with each new step being refined in addition to previously optimised variables such that at the end of the refinement all parameters were refined together. Initial model would be obtained from the IZA database of

framework structures,[20] with additional starting cation locations informed by literature values or if unavailable, as was often the case, predicted by sites deemed suitable based on other sites found for the cation type in the literature. Where occupancy was unknown, sites would initially have an equal fractional matching the experimentally determined cation content whilst not introducing a site bias into refinement of the crystal structure.

First the background was fitted, and the zero-shift error refined. Additional terms were added to the background function for the best results without overfitting the data. In the case of overfitting, fewer terms would be used to prevent this behaviour and the background function could be revisited at a later point once peak intensity was better fitted by refinement of unit cell contents. Next the unit cell parameters were optimised before refining profile parameters, including peak asymmetry. At this point refinement of the unit cell contents could begin.

Extra-framework species were refined first, starting with metal cations. Initially the positions of these species were optimised, one at a time, before refining their occupancies alone and then in concert with their positions all together. Occupancies were often restrained to be close to their experimentally predicted values. A similar process was carried out for CO_2 and other molecular species, including repeatedly examining the optimum orientation of the molecules. Difference Fourier mapping was employed to identify potential additional sites. These would be incorporated into the model and their positions and occupancies refined following the method previously described. Additional sites that provided a reasonable improvement in fit whilst retaining a realistic crystal structure were retained whilst others were rejected.

Subsequently, framework sites could be investigated. These typically utilised restraints to promote reasonable T-O and O-O distances which were consistent with the expected Si/Al ratio of the framework. This involved a weighted average of Si-O (1.6 Å) and Al-O (1.7 Å) bond distances for T-O distances and O-O restraints derived to match a tetrahedral geometry. These restraints would be loosened over the course of refinement, with deviations from expected bond distances and angles reinstating increased weighting of specific restraints. In the case of very sharp T-O-T angles, an additional restraint was added to the relevant T-T distance, but this was typically only required for the exceptionally large unit cells explored in Chapter 3.

At this point, difference Fourier mapping would be carried out again to identify further potential sites, further terms in the background function could be introduced if necessary and alternative peak profile descriptions would be investigated. Thermal parameters were not typically refined, due to their correlation with occupancies. The value of B_{iso} for extraframework species was typically 4, whilst framework T and O sites were prescribed 1 and 2. These values are consistent with the range used in the literature and reflect the relative vibrational freedom of each environment.

2.1.7. Diffractometers

A major impact on powder data quality is the X-ray diffractometer used during acquisition. Some of the effects that a diffractometer can influence have already been discussed, such as axial divergence, but here this is given in more detail.

In the laboratory, 2 geometrical setups exist: reflection and transmission.[10] The experimental details of these are provided below and both have their benefits and the type of analysis required will often determine which setup is used. In this work both types have been used with Stoe STADIP (transmission) and PANalytical Empyrean (reflection) diffractometers.

2.1.7.1. Reflection geometry

This is the most commonly used mode for PXRD data collection, providing high intensity peaks whilst retaining high resolution.[10] Also known as the "Bragg-Brentano" geometry, a divergent beam is reflected from the sample surface to converge at a fixed radius from the sample. The sample is placed in a flat plate, and this typically spins to improve the powder averaging of crystallite orientations. In this geometry, the sample stage is always at an angle θ to the incident beam whilst the detector is at 2θ.[10] Commonly a θ-2θ setup is used, shown in Figure 2.1.14(a), which fixes the source position and rotates the sample and detector around to fulfil the geometrical conditions, as used for reflection diffractometers in this work. An alternate mode is θ-θ which keeps the sample stage fixed and rotates both the source and detector.

A number of additional considerations are required.[10] Söller slits limit the size of the X-ray beam and reduce axial divergence. Additional slits are used to control scattering and

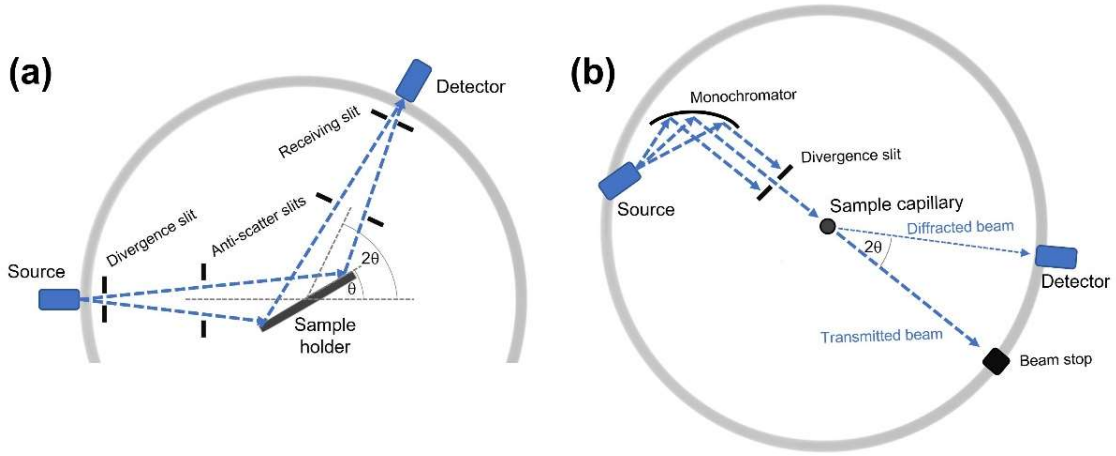

Figure 2.1.14. Schematic representations of the 2 laboratory X-ray diffractometer setups: (a) Reflection (Bragg-Brentano) and (b) transmission (Debye-Scherrer) geometries.

divergence of the incident and diffracted beams in the equatorial plane. Narrower slits improve resolution at the expense of intensity.

2.1.7.2. Transmission geometry

Also known as the Debye-Scherrer geometry, this method involves samples in capillaries or between thin foils. Again, these are spun to improve random sample orientation during data acquisition. The source and sample position remain fixed, whilst the detector is swept around 2θ recording X-ray intensity, as shown in Figure 2.1.14(b).[10] A monochromator and divergence slits are used to control the incident X-ray beam. This setup gives poorer intensity than the reflection mode and so longer collection times are needed for quality data, but it has similar resolution and is far more useful for sensitive samples or specialised experiments.[10]

Transmission diffractometers have been used for most of the work in this thesis. The experimental setup allows for measurement of samples which have been dehydrated or exposed to gas in a capillary and subsequently flame sealed. This geometry is also more readily altered to allow investigation of gas adsorption effects during data acquisition or under different temperature regimes.

2.1.7.3. Beamline I11

As well as lab-based diffractometers, those utilising a synchrotron source should also be considered. The source of these X-rays has already been discussed in Section 2.1.4.2 but here greater detail is given on the primary synchrotron diffractometer used in this work,

Beamline I11. This beamline, illustrated in Figure 2.1.15, is part of Diamond Light Source at the Harwell Science and Innovation Campus in Oxfordshire.

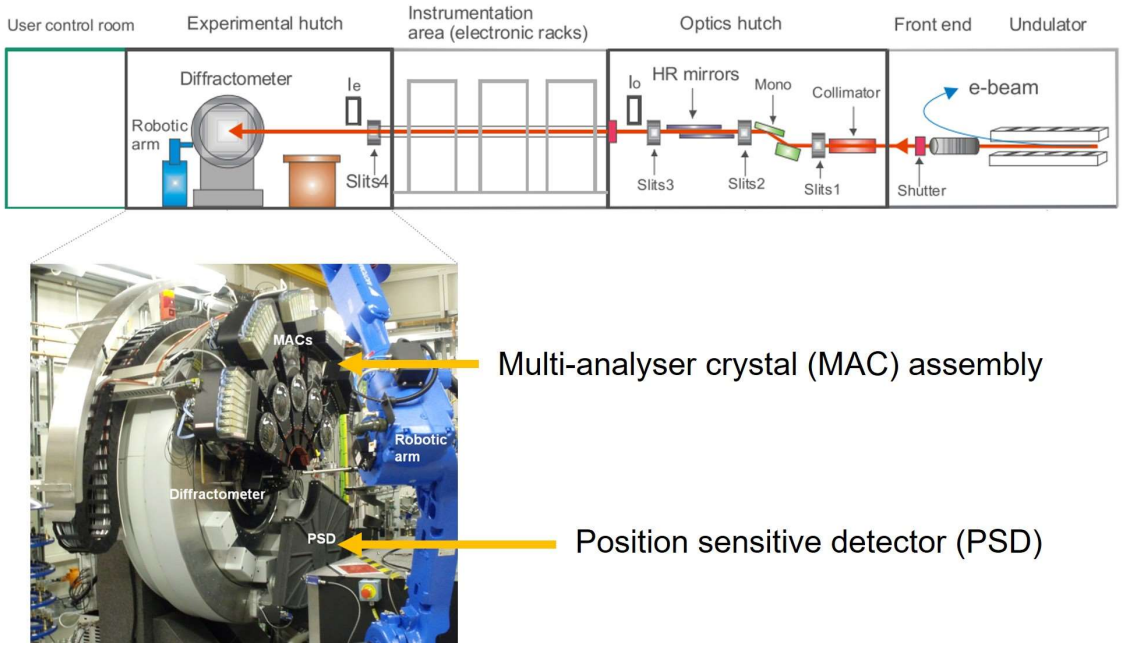

Figure 2.1.15. (Top) Schematic representation of beamline I11 at Diamond Light Source reprinted from Thompson et al,[16] with the permission of AIP publishing. (Bottom) an image of the diffractometer inside the experimental hutch, including MAC and PSD analysers, adapted from Diamond Light Source.[12]

The X-ray beam enters the optics hutch from the storage ring and is conditioned through the use of a collimator, monochromator, harmonic rejection mirrors and an array of slits. The beam then passes through to the experimental hutch and the diffractometer. The sample stage can be set up in a variety of ways but for samples in this work, a capillary approach was used. The diffractometer can use 2 types of detector, shown in Figure 2.1.15 – a multi-analysing crystal (MAC) assembly, consisting of 5 identical 9-crystal MAC arms, each separated by 30° in the 2θ plane, or a position-sensitive detector (PSD), with a 90° aperture.[12,16,45] The MAC assembly records 45 PXRD patterns simultaneously, the angular separation of which allows a whole a very high resolution pattern to be collected rapidly, with little rotation of the MAC assembly. The PSD on the other hand is static but allows for extremely rapid collection of diffraction patterns, whilst retaining a high resolution of $\Delta 2\theta \cong 0.004°$. Both methods allow I11 to provide fast and high quality PXRD data and coworkers found the PSD instrument to be more appropriate for the samples investigated here. The PSD is limited to a maximum 2θ of 90° but this was

found to be sufficient for these materials, as was the resolution. The incident X-ray beam used in examining materials here had an energy of 15 keV, or a wavelength of *ca*. 0.8265 Å.

Another strength of I11 is the range of conditions that samples can be exposed to and measured under, including a range of temperatures and exposure to gas pressure. For materials of interest for adsorption, samples can be dehydrated *in situ* using a heat gun and cryostream and exposed to gas streams of interest, such as CO_2, up to high pressure. Such experiments increase the time required on the beamline due to the length of time required for dehydration and adsorption equilibrium steps.

In this work, I11 was used to collect patterns of samples under hydrated, dehydrated and CO_2 exposed conditions.

2.1.8. Neutron Diffraction

X-ray diffraction is a powerful tool for structural studies but has some significant drawbacks, most obviously the dependency of the scattering factor, *f*, on electron count. As discussed previously, this greatly limits PXRD as a technique for the study of light elements, such as Li. Another probe is therefore required if diffraction is to be useful for materials where these elements are of interest.

Diffraction requires a probe with a wavelength, λ, of similar magnitude to the *d* spacings within the structure, as previously discussed. The appropriate range of λ in the electromagnetic spectrum falls within the X-ray region, hence XRD. The dual wave-particle nature of subatomic species allows other probes, typically considered particles, to be used for diffraction, with λ determined by the de Broglie relation,

$$\lambda = \frac{h}{p} = \frac{h}{m\upsilon} \tag{2.22}$$

where *h* is the Planck constant (6.63×10^{-34} Js) and *p* is the particle's momentum, which is described by its mass, *m*, and velocity, υ.

With acceleration to sufficiently high speeds, neutrons can become an appropriate probe giving rise to the method of powder neutron diffraction (PND). Their neutral nature makes them highly penetrating which has significant consequences.[10] To increase the number of scattering events and signal to noise ratio, a large amount of sample (*ca*. 3 g

for zeolites) is required, as is a high intensity neutron source. The former can be an issue for some materials and the latter means that PND can only be carried out at national facilities. Even with the brightness of such sources, longer acquisition times are required compared to PXRD. For these reasons, PND is typically not a first method of choice.

Despite this, PND is a highly valuable method. The scattering power of elements is dependent on the makeup of nuclei, rather than number of electrons, and can differ greatly between neighbours and isotopes.[10,46] Light atoms within a material may therefore contribute greatly to a PND pattern despite having no measurable effect on a PXRD pattern. A comparison of scattering strength for XRD (atomic scattering factor, *f*) and PND (coherent scattering length, b_c) is detailed in Table 2.1.5 for selected elements.

An additional consideration with PND is that some elements, such as Li, possess a negative scattering length. This somewhat novel property can make these species either easier or far harder to refine, depending on the material in question. In the latter case, it may be essential to gather as much knowledge of the material as possible, such as reliable chemical composition data.

Table 2.1.5. Scattering strength of species for XRD and PND used in this thesis, as determined by their atomic X-ray scattering factors, f, and coherent neutron scattering length, b_c, respectively. Species with larger magnitudes have a greater effect on diffraction patterns. For PND, negative values indicate a phase change of neutrons upon scattering. Values are obtained from the International Tables for Crystallography and Sears, respectively. [35,47]

Element	**XRD: *f***	**PND: b_c (fm)**
Li^+	2	-1.90
Na^+	10	3.63
K^+	18	3.67
Rb^+	36	7.09
Cs^+	54	5.42
Zn^{2+}	28	5.680
C	6	6.6460
N	7	9.36
O	8	5.803
Al	13	3.449
Si	14	4.1491

In this work, PND data was collected on samples of zeolite on the Polaris diffractometer at the ISIS Neutron and Muon Source at the Rutherford Appleton Laboratory in Oxfordshire,[48] adjacent to DLS. To generate neutrons, hydride ions are first produced in batches by ionising hydrogen gas in the presence of Cs vapour. These reach relativistic speeds using 2 linear accelerators before being stripped of their electrons as they enter a synchrotron. The bare protons are further accelerated during circuits of the synchrotron to highly relativistic speeds and released to hit a tungsten target. These protons break tungsten nuclei apart in a process called spallation. Larger fragments deexcite, releasing neutrons with energies of *ca*. 1 MeV in the process, whilst smaller particles can induce further spallation events. The neutrons produced during spallation are at too high energy for diffraction experiments and are slowed down to appropriate energies (and hence wavelengths) with a H_2O moderator. This gives rise a neutrons with a range of energies and hence a polychromatic beam, which travel along flight paths to the available instruments, including Polaris, located 14.0 m away from the tungsten target.[48]

The Polaris diffractometer utilises a time-of-flight (TOF) technique which requires a polychromatic beam of neutrons.[10] As shown by the de Broglie relationship above, the wavelength of neutrons is inversely proportional to their velocity and so higher λ neutrons are slower to travel from the source, through the sample and to the detector. Recording the time at which neutrons impact a fixed angle, 2θ, enables the calculation of the associated *d* spacing using the de Broglie and Bragg equations to get

$$d = \frac{ht}{2mL \sin\theta} \tag{2.23}$$

where *t* is the time of flight, *m* is the mass of a neutron, *L* is the total path length and all other symbols have their usual meaning. Multiple banks of detectors at varying angles improve the quality of data acquired and cover a larger range of *d* spacings. Polaris comprises 5 such banks at 2θ = 10.40°, 25.99°, 52.21°, 92.59° and 146.72°, shown in Figure 2.1.16. These have different flight paths from the sample and hence different *d* spacing resolution (secondary flight paths of 2.25, 2.36-1.31, 1.57-0.925, 1.08-0.710, 1.54-0.795 m; $\Delta d/d$ =2.7, 1.5, 0.85, 0.51, 0.30% for banks 1-5, respectively).[48] Diffraction patterns for each of these banks are plotted as intensity against *d* spacing, as determined by time of flight.

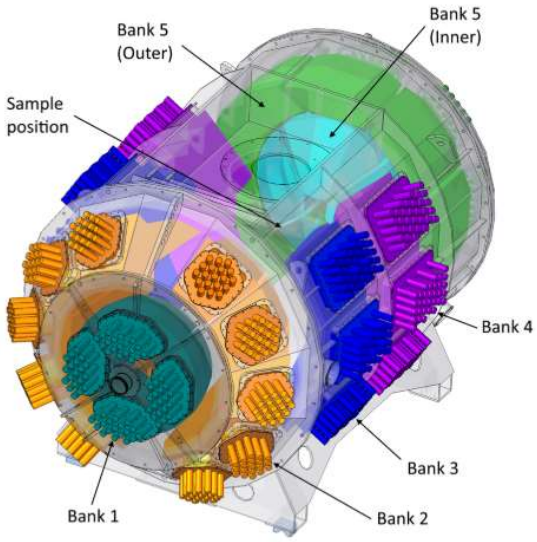

Figure 2.1.16. Schematic of the Polaris diffractometer and its arrangement of detector banks, reproduced from Smith et al.[48].

Samples are packed into vanadium cans, due to the small coherent scattering length, and hence diffraction signal of the element Vanadium (b_c = -0.402 for ^{51}V, 99.75% abundant).[10] As with the I11 beamline at DLS, a range of sample conditions can be explored *in situ*. In this work, dehydrated and CO_2 exposed samples were investigated.

2.1.9. Diffraction Data in this Work

X-ray diffraction data discussed in this work was collected by multiple people. Laboratory data for Rho samples was collected by Dr Magdalena M. Lozinska and myself, for phillipsite samples by Dr Hyun June Choi with assistance from Dr Yuri Andreev, and for merlinoite samples predominantly by Dr Veselina M. Georgieva with additional data collected by Dr Lozinska and myself and with assistance from Dr Andreev. ABC-6 material diffraction data was collected by Ms Ruxandra G. Chitac and myself. Synchrotron data was collected at I11 and ID31 by Drs Georgieva, Lozinska, Alex Greenaway and Prof Paul A. Wright, with aid from Drs Claire Murray and Andy Fitch. PND data was collected by Dr Ron I. Smith after sample preparation carried out by Dr Lozinska with assistance from Dr Julia L. Payne.

2.2. Electron Microscopy

2.2.1. Introduction

Powder X-ray diffraction is a bulk analytical method and is far from sufficient for the complete description of a material. Conversely, electron microscopy (EM) is used for local analysis, although the term "local" spans a broad range of dimensions. EM allows for far higher resolution than optical microscopy,[49] making it well suited to the investigation of materials on micro- and nanoscales. In this study, EM was used to investigate the crystal morphologies on the μm scale, as well as stacking faults at the atomic level. Additionally, EM was 1 method used to determine elemental compositions of materials in the form of elemental dispersive X-ray spectroscopy, discussed later.

2.2.2. Scanning Electron Microscopy

A particle's morphology is often of interest as it can help to elucidate a crystal growth mechanism and can affect a material's properties. Scanning electron microscopy (SEM) is typically used to investigate this. A schematic of a typical SEM setup is shown in Figure 2.2.1.

Electrons are produced at an electron gun and accelerated towards an anode under a high voltage. After passing the anode, condenser lenses make the electron beam coherent and focus it onto the sample. Pairs of scanning coils are used to deflect the beam in x and y directions, and a raster pattern is used to image across the desired sample area.[50,51] The beam can interact with the sample in multiple ways and detectors are placed in different locations, dependent on the type of signal monitored.

Interaction between the sample and the incident beam causes the scattering of electrons (and X-rays). These may be incident (primary) electrons which have been backscattered, or secondary electrons generated within the sample.[50,52] Backscattered electrons are caused by an elastic "slingshot" interaction between the negatively-charged electrons in the beam and positively-charged nuclei within the sample. Secondary electrons, on the other hand, are created in an inelastic process. When primary electrons have sufficiently high energy, ionisation of elements with the sample can occur, with a valance electron emitted. These secondary electrons have low kinetic energy as the energy transferred must overcome the work function. Such electrons readily recombine with the sample

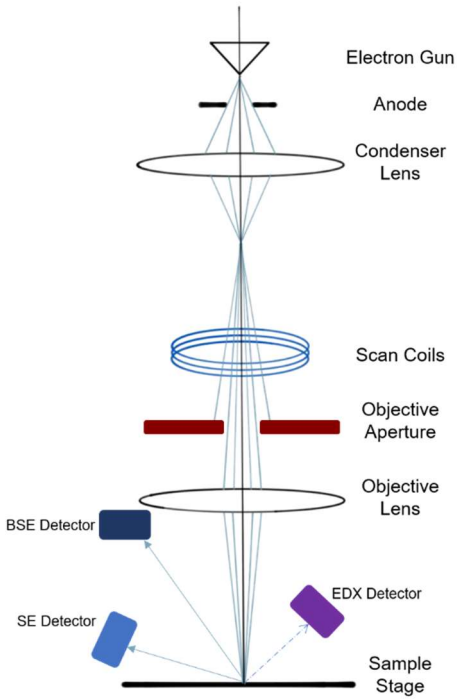

Figure 2.2.1. Schematic representation of a scanning electron microscope.

and thus only those expelled within a few nanometers of the surface are detected.[50,53] As a result, secondary electrons are sensitive only to a sample's surface and provide a way of investigating crystal morphology.

2.2.3. Scanning Transmission Electron Microscopy

In transmission electron microscopy (TEM), an electron beam is incident upon a very thin sample. The thinness of the sample allows electrons to pass through and the effect of the sample upon these transmitted electrons can be recorded in the form of an image.[54] By scanning across the sample in a raster pattern, as for SEM, a picture of an extended area can be formed and gives rise to scanning transmission electron microscopy (STEM). A typical STEM setup is shown in Figure 2.2.2. (S)TEM methods operate at far higher accelerating voltages than SEM, causing shorter electron beam wavelengths. This allows for atomic resolution,[55] which is of great interest in zeolites, particularly faulted materials.[56]

As for SEM, multiple types of interaction occur between the sample and the electron beam.[57] In STEM, inelastic electron scattering events lead to small deflections from the

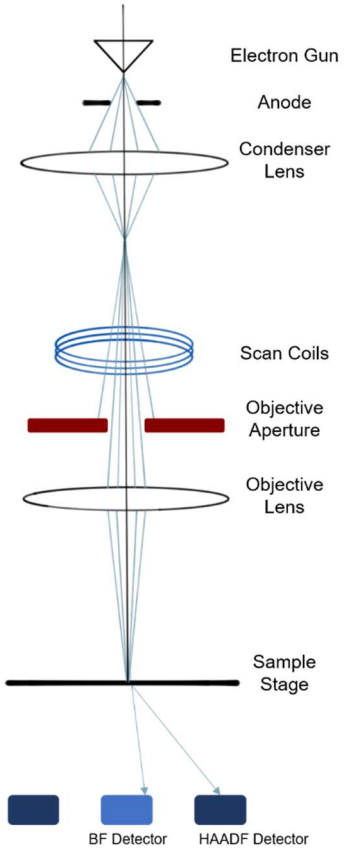

Figure 2.2.2. Schematic representation of a scanning transmission electron microscope.

electron beam and give rise to a bright field (BF) signal. Elastic scattering events cause deflections at higher angles (dark field). Measuring the latter events over a range of angles (i.e. within an annulus) gives rise to the high angle annular dark field (HAADF) signal. The intensity of this signal is more dependent on sample thickness and composition than the BF signal, with HAADF intensity increasing with atomic number.[57]

2.2.4. Electron Diffraction

EM can be used for applications other than imaging. One such use is electron diffraction (ED).[58] When examining a single crystal under the electron microscope this is similar to single crystal XRD but uses an electron beam as opposed to X-rays. ED can also examine individual regions of a crystal, rather than the crystal or sample as a whole, as is the case for single crystal and powder XRD, respectively. The technique is particularly useful for analysing defects present in materials and their spread throughout individual crystals.

One example of this is examining stacking faults, described in Chapter 8, which can cause streaking in a pattern otherwise consisting of sharp spots.

2.2.5. Microscopy Data in this Work

SEM data was collected by Dr Veselina M. Georgieva, Ms Ruxandra G. Chitac and myself. STEM data was collected by Dr Alvaro Mayoral at la Universidad de Zaragoza, as were ED patterns.

2.3. Elemental Analysis

2.3.1. Introduction

An important consideration in studying any material is its chemical composition. In zeolites it is helpful to determine the Si/Al ratio of the sample, the cation content and purity. The following methods have been used during this work to determine the bulk composition of samples.

2.3.2. Elemental Dispersive X-ray Spectroscopy

In SEM, X-rays are generated through the interaction of the beam and the sample, in addition to electrons, discussed previously. After the ejection of core electrons from an atom, a higher lying electron will relax to fill the resultant hole. The associated loss of energy manifests itself in the form of an X-ray, with energy characteristic of the element of the atom of its origin. This allows for the elemental analysis of a sample and is known as elemental dispersive X-ray (EDX) spectroscopy.[59] As a result, the elemental composition of the bulk sample can be found, often useful in following the process of ion exchange, such as that described in Appendix I.

2.3.3. X-ray Fluorescence Spectroscopy

Another method of bulk elemental analysis is X-ray fluorescence (XRF) spectroscopy. This occurs in a very similar process to that of EDX spectroscopy, however, X-rays, rather than electrons, are used to ionise atoms and form an electron hole.[60] Additionally,

incident X-rays have a far longer mean free path than electrons employed by EDX analysis, enabling a greater depth of the sample to be penetrated and ensuring data is more representative of the sample as a whole.

2.3.4. Elemental Analysis in this Work

EDX data was collected by Drs Magdalena M. Lozinska, Veselina M. Georgieva, Hyun June Choi, Ruxandra G. Chitac and myself. XRF data was collected by Dr Alessandro Turrina at Johnson Matthey.

2.4. Adsorption

2.4.1. Porosity

One of the key properties of zeolites is porosity, which is required for many of their applications, most notably in gas separation technologies. The porous nature of zeolites causes surface areas far greater internally than externally. When gas molecules are present in a zeolite, they are attracted to the surface area by induced or permanent dipole or quadrupole interactions. This may lead to the formation of chemical bonds (chemisorption) or merely weak van der Waals interactions (physisorption) between the gas molecule (adsorbate) and material (adsorbent). These 2 processes have significant differences, listed in Table 2.4.1. Access to adsorption sites within zeolites is governed by the diameters of windows and channels within the structure and the properties of the adsorbate, typically size but in some cases also electrostatic properties, such as those shown in Table 2.4.2.

2.4.2. Adsorption Isotherms

To study how a material adsorbs a gas, an adsorption isotherm is measured. This involves monitoring the uptake of gas, either gravimetrically or volumetrically, as pressure is increased. This is carried out at constant temperature to determine the equilibrium uptake of gas as a function of pressure. Multiple models have been proposed for adsorption of gases, including the Langmuir isotherm describing monolayer coverage in 1918,[64,65] and the BET (Brunauer-Emmet-Teller) describing multilayer

adsorption in 1938.[66] BET analysis is often a standard model used to describe pore volumes of zeolites, although it has limitations, as for other models.[67–69]

Table 2.4.1. Comparison of typical properties of physi- and chemisorption.[61–63]

	Physisorption	**Chemisorption**
Strength	Weak (10-40 kJ mol^{-1})	Strong (40-400 kJ mol^{-1})
Desorption	Reversible	Irreversible
Bonding	Van der Waals	Chemical
Sorbate structure	Multilayer possible	Monolayer only
Selectivity	Low	High
Kinetics	Fast	Slow
Temperatures	Low	High
Uses	Gas adsorption	Catalysis

In 1940, Brunauer, Demming, Demming and Teller were the first to attempt to classify adsorption isotherms into 5 distinct classes (Types I-V, described below),[70] with Sing adding a further type for IUPAC in 1985 (Type VI).[71] Slight modifications to this were suggested in 2015,[72] shown in Figure 2.4.1, but much of the literature typically refers to the 1985 classifications with no distinctions between subtypes of I and IV.

Table 2.4.2. Size and electrostatic properties of gas molecules relevant to this thesis.[73–77] *2CLJQ indicates 2-centred Lennard Jones quadrupole pair potential, a model treating linear molecules as 2 sites separated by a short distance, as opposed to as a single sphere.*

Gas	**Spherical kinetic diameter (Å)**	**2CLJQ kinetic diameter (Å)**	**Quadrupole moment ($\times 10^{-40}$ C m^2)**	**Polarisability ($Å^3$)**
O_2	3.46	3.11	-1.33	1.60
N_2	3.64	3.32	-4.91	1.76
CO_2	3.30	2.98	-13.71	2.65
Ar	3.40		0	1.49
CH_4	3.80		0	2.60

Isotherms of Type I are exhibited by microporous materials, with a steep gradient at low pressure and plateauing as adsorption sites are occupied. The maximum uptake is determined by the available pore space, as opposed to surface area. This has been

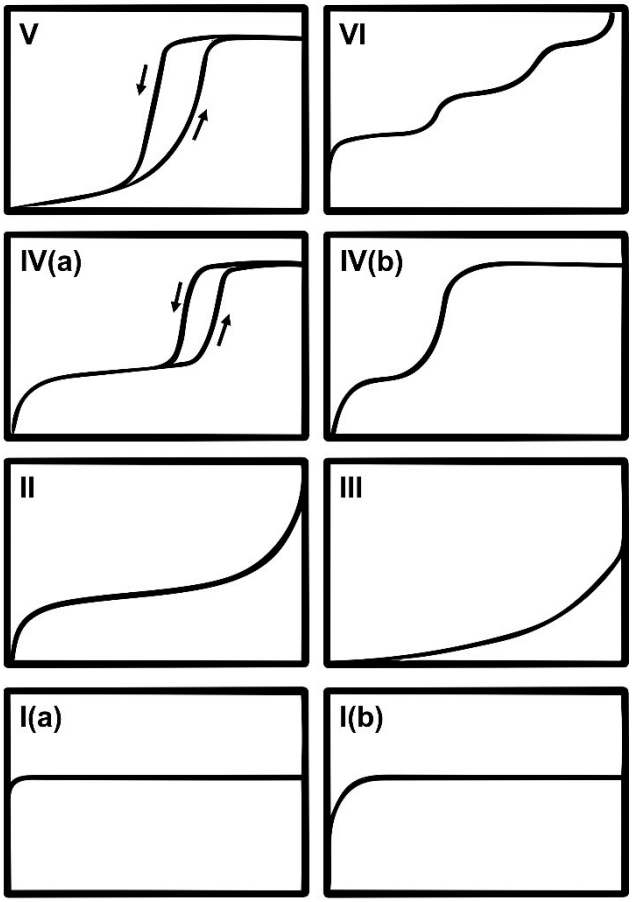

Figure 2.4.1. The 8 types of adsorption isotherm, as described by Thommes et al.[72]

subsequently split into Types I(a), for materials with narrow micropores, and I(b), for materials with larger micropores, the latter showing a less steep initial gradient but still reaching a plateau. Type II isotherms are observed for macro- or non-porous materials, with monolayer formation followed by multilayer adsorption. This is also the case for Type III but interactions between the sorbent and sorbate are much weaker, and so no initial monolayer forms. Mesoporous materials exhibit Type IV isotherms. These are similar to Type II, with initial monolayer formation, followed here by gas condensing to a liquid-like state in the mesopores. This can be further separated into Types IV(a) and (b), with the former including hysteresis in the desorption branch of the isotherm due to larger pore diameters. Type V is similar to Type III, with weak sorbent-sorbate interactions initially causing clustering of sorbate molecules followed by pore filling, either in either mesoporous or microporous materials. Finally, Type VI occurs only for adsorption on highly uniform, non-porous surfaces, with each step corresponding to a new layer of adsorbed molecules.

2.4.3. Adsorption Kinetics

Adsorption isotherms should measure equilibrium gas adsorption, with samples allowed to equilibrate at each dosing pressure. Another factor to consider when investigating potential adsorbents is kinetic adsorption properties, particularly for application in pressure swing adsorption (PSA) technologies.

Zero-length column (ZLC) analysis was devised by Eic and Ruthven in 1988.[78] A material is initially saturated with a known concentration of the desired gas species before switching to an inert carrier gas, such as He.[79] The concentration can be chosen to match an industrial application of interest. This removes the adsorbed species and the concentration of the species in the gas flow is monitored over time by a detector. To gain adsorption parameters, this needs to be repeated under various conditions, such as flow rate and temperature.[80–82]

When considering a binary separation process, such as CO_2/CH_4, it is insufficient to measure the kinetic behaviour of the material for the 2 species separately, as 1 may affect the other. For this reason, binary breakthrough curves are collected. Traditionally these are collected on large columns, which require a significant amount of sample and can suffer from heating, making the system non-isothermal. The extended zero-length column (E-ZLC) method developed by Gibson *et al*. does not suffer from these flaws as a ZLC method but the column is of sufficient length to allow the separation of 2 components to be investigated.[83]

A simpler approach is to observe the uptake curve of a material. In these experiments, the material is exposed to a dosage of gas at a given pressure. The pressure drops as gas is adsorbed until equilibrium is reached and the pressure plateaus. Measuring the pressure over time allows the uptake to be calculated during the adsorption process. This technique was used by collaborators to examine O_2 and Ar adsorption on zeolite materials.

2.4.4. Adsorption Data in this Work

Gas adsorption isotherm data discussed in this work was collected by Drs Veselina M. Georgieva, Magdalena M. Lozinska and Hyun June Choi.

Low- and high-pressure CO_2 adsorption isotherms were measured at 298 K using a Micromeritics ASAP 2020 Gas Adsorption Analyser connected to a Julabo F25 Chiller Unit and a Hiden IGA gravimetric analyser, respectively, after overnight activation. The same analysers were used for N_2 adsorption at 77 K for the same pressure regimes.

Kinetic and breakthrough data was collected by Dr Maarten C. Verbraeken at the University of Edinburgh, using ZLC and E-ZLC apparatus, respectively. Additional kinetic data in the form of uptake curves was collected by Dr William J. Casteel at Air Products.

2.5. Nuclear Magnetic Resonance Spectroscopy

Whilst PXRD studies the long range order of a sample, nuclear magnetic resonance (NMR) spectroscopy examines the local environment of species with a non-zero intrinsic angular momentum.[84] Whilst spins with different alignments are degenerate in the absence of a magnetic field, this degeneracy is lifted upon the introduction of such a field. Resonance occurs when a pulse of electromagnetic radiation is applied with energy equal to the energy gap between spin states.[84]

The exact frequency a nucleus resonates at is determined by multiple interactions with its local environment. An NMR spectrum is typically shown as a plot of intensity *vs* chemical shift, δ, a dimensionless quantity related to the frequency relative to a standard, reported in ppm. In solid state NMR, multiple interactions are present, which leads to the complication of spectra.[85,86] It should be noted however, that these interactions may also provide a way to gain information about a sample.[87]

A major consequence of these phenomena is the broadening of linewidths. To resolve individual peaks, some of these effects must be cancelled out or reduced. For many samples, this can be achieved through the use of magic angle spinning (MAS) NMR spectroscopy.[84] This is carried out through the rapid rotation of sample, packed in a rotor, about an axis at 54.34° relative to the magnetic field, as this reduces the magnitude of multiple interactions to zero.

In zeolites, ^{27}Al and ^{29}Si NMR spectroscopy are routinely used methods. Higher coordinated Al species exhibit a less positive δ, and so non-tetrahedral species,

commonly associated with extra-framework species, can be identified.[84] Significantly different tetrahedral Al environments may also be distinguished. Additionally, ^{29}Si NMR spectroscopy provides an accurate measure of the framework Si/Al ratio. As ^{29}Si δ are sensitive to next-nearest neighbours, and assuming Löwenstein's rule holds, the ratio can be calculated as:

$$Si/Al = 4\ \frac{\sum I_n}{\sum n I_n} \qquad (2.24)$$

where n is the number of adjacent Al tetrahedra and I_n is the intensity of the peak corresponding to Si with n adjacent Al tetrahedra.[84] This method is far more accurate in determining framework Si/Al ratio than bulk techniques, such as elemental dispersive X-ray (EDX) or X-ray fluorescence (XRF) spectroscopy, discussed below, as these latter methods do not discriminate framework and extra-framework species.

2.5.1. NMR Data in this Work

Solid-state NMR data was acquired by Dr Daniel M. Dawson at the University of St Andrews.

2.6. References

(1) Woolfson, M. M. *An Introduction to X-Ray Crystallography*; Cambridge University Press: London, 1970.

(2) Waseda, Y.; Matsubara, E.; Shinoda, K. *X-Ray Diffraction Crystallography; Introduction, Examples and Solved Problems*; Springer: Heidelberg, 2011.

(3) Smart, L. E.; Moore, E. A. *Solid State Chemistry: An Introduction*, 3rd edn.; Taylor & Francis: Boca Raton, Florida, 2005.

(4) Miller, W. H. *A Treatise on Crystallography*; J. & J. J. Deighton: Cambridge, 1839.

(5) Robinson, A. *The Last Man Who Knew Everything*; Pi Press: New York, 2006.

(6) Röntgen, W. C. On a New Kind of Rays. *Nature* **1896**, *53* (1369), 274–276.

(7) Eckert, M. Max von Laue and the Discovery of X-Ray Diffraction in 1912. *Ann. Phys.* **2012**, *524* (5), 83–85.

(8) Bragg, W. H.; Bragg, W. L. The Reflection of X-Rays by Crystals. *Proc. R. Soc. London, Ser. A Math. Phys. Sci.* **1913**, *88* (605), 428–438.

(9) Bragg, W. L. The Specular Reflection of X-Rays. *Nature*. 1912, pp 410–410.

(10) Cockcroft, J. K.; Fitch, A. N. Experimental Setups. In *Powder Diffraction: Theory and Practice*; Dinnebier, R. E., Billinge, S. J. L., Eds.; Royal Society of Chemistry: Cambridge, 2008; pp 20–57.

(11) Deslattes, R. D.; Kessler Jr., E. G.; Indelicato, P.; Lindroth, E. X-Rays Wavelengths. In *International Tables for Crystallography. Volume C: Mathematical, Physical and Chemical Tables*; Prince, E., Ed.; Spring: Dordrecht, The Netherlands, 2004; pp 200–213.

(12) Diamond Light Source https://www.diamond.ac.uk, accessed October 2023.

(13) ESRF https://www.esrf.fr, accessed October 2023.

(14) Pohang Accelerator Laboratory, accessed October 2023.

(15) Clegg, W. *X-Ray Crystallography*, 2nd edn.; Oxford University Press: Oxford, 2015.

(16) Thompson, S. P.; Parker, J. E.; Potter, J.; Hill, T. P.; Birt, A.; Cobb, T. M.; Yuan, F.; Tang, C. C. Beamline I11 at Diamond: A New Instrument for High Resolution Powder Diffraction. *Rev. Sci. Instrum.* **2009**, *80*, 075107.

(17) Le Bail, A. Whole Powder Pattern Decomposition Methods and Applications: A Retrospection. *Powder Diffr.* **2005**, *20* (04), 316–326.

(18) Van Laar, B.; Schenk, H. The Development of Powder Profile Refinement at the Reactor Centre Netherlands at Petten: *Acta Crystallogr. Sect. A Found. Adv.* **2018**, *74* (2), 88–92.

(19) Coelho, A. *TOPAS-Academic*; Coelho Software: Brisbane, Australia, 2016.

(20) Baerlocher, C.; McCusker, L. B. IZA Database of Zeolite Structures, http://www.iza-structure.org/databases/, accessed October 2023.

(21) Young, R. A. *The Rietveld Method*; Oxford University Press: Oxford, 1993.

(22) David, W. I. F. Powder Diffraction: Least-Squares and Beyond. *J. Res. Natl. Inst.*

Stand. Technol. **2004**, *109* (1), 107–123.

(23) Toby, B. H. R Factors in Rietveld Analysis: How Good Is Good Enough? . *Powder Diffr.* **2006**, *21* (1), 67–70.

(24) McCusker, L. B.; Von Dreele, R. B.; Cox, D. E.; Louër, D.; Scardi, P. Rietveld Refinement Guidelines. *J. Appl. Crystallogr.* **1999**, *32* (1), 36–50.

(25) Boyd, J. P. *Chebyshev and Fourier Spectral Methods*, 2nd ed.; Dover Publications, Inc.: Mineola, New York, 2000.

(26) TOPAS wiki http://topas.dur.ac.uk/topaswiki/.

(27) Pearson, K. Mathematical Contributions to the Theory of Evolution . XIX . Second Supplement to a Memoir on Skew Variation. *Philos. Trans. R. Soc. London* **1916**, *216*, 429–457.

(28) Thompson, P.; Cox, D. E.; Hastings, J. B. Rietveld Refinement of Debye-Scherrer Synchrotron X-Ray Data from Al2O3. *J. Appl. Crystallogr.* **1987**, *20*, 79–83.

(29) Finger, L. W.; Cox, D. E.; Jephcoat, A. P. Correction for Powder Diffraction Peak Asymmetry Due to Axial Divergence. *J. Appl. Crystallogr.* **1994**, *27* (pt 6), 892–900.

(30) Prince, E.; Toby, B. H. A Comparison of Methods for Modeling the Effect of Axial Divergence in Powder Diffraction. *J. Appl. Crystallogr.* **2005**, *38* (5), 804–807.

(31) Zuev, A. Instrumental Contributions to the Line Profile in X-Ray Powder Diffraction . Example of the Diffractometer with Bragg-Brentano Geometry. In *Powder Diffraction: Theory and Practice*; Dinnebier, R. E., Billinge, S. J. L., Eds.; Royal Society of Chemistry: Cambridge, 2008; pp 166–205.

(32) Van Laar, B.; Yelon, W. B. The Peak in Neutron Powder Diffraction. *J. Appl. Crystallogr.* **1984**, *17*, 47–54.

(33) Cheary, R. W.; Coelho, A. A. Axial Divergence in a Conventional X-Ray Powder Diffractometer. I. Theoretical Foundations. *J. Appl. Crystallogr.* **1998**, *31* (6), 851–861.

(34) Cromer, D. T.; Mann, J. B. X-Ray Scattering Factors Computed from Numerical Hartree-Fock Wave Functions. *Acta Crystallogr.* **1968**, *A24*, 321–324.

(35) Brown, P. J.; Fox, A. G.; Maslen, E. N.; O'Keefe, M. A.; Willis, T. M. Intensity of Diffracted Intensities. In *International Tables for Crystallography. Volume C: Mathematical, Physical and Chemical Tables*; Prince, E., Ed.; Springer: Dordrecht, The Netherlands, 2004; pp 554–595.

(36) Milanesio, M.; Viterbo, D. Solution and Refinement of Crystal Structures. In *Fundamentals of Crystallography*; Giacovazzo, C., Ed.; Oxford University Press: Oxford, 2011; pp 417–511.

(37) Rojo-Gama, D.; Nielsen, M.; Wragg, D. S.; Dyballa, M.; Holzinger, J.; Falsig, H.; Lundegaard, L. F.; Beato, P.; Brogaard, R. Y.; Lillerud, K. P.; Olsbye, U.; Svelle, S. A Straightforward Descriptor for the Deactivation of Zeolite Catalyst H-ZSM-5. *ACS Catal.* **2017**, 8235–8246.

(38) Kalantzopoulos, G. N.; Lundvall, F.; Lind, A.; Arstad, B.; Chernyshov, D.; Fjellvåg, H.; Wragg, D. S. SAPO-37 Microporous Catalysts: Revealing the Structural Transformations during Template Removal. *Catal. Struct. React.* **2017**, *3* (1–2), 79–88.

(39) Luo, Y.; Smeets, S.; Peng, F.; Etman, A. S.; Wang, Z.; Sun, J.; Yang, W. Synthesis and Structure Determination of Large-Pore Zeolite SCM-14. *Chem. - A Eur. J.* **2017**, *23* (66), 16829–16834.

(40) Lee, J. K.; Turrina, A.; Zhu, L.; Seo, S.; Zhang, D.; Cox, P. A.; Wright, P. A.; Qiu, S.; Hong, S. B. An Aluminophosphate Molecular Sieve with 36 Crystallographically Distinct Tetrahedral Sites. *Angew. Chemie - Int. Ed.* **2014**, *53* (29), 7480–7483.

(41) Turrina, A.; García, R.; Watts, A. E.; Greer, H. F.; Bradley, J.; Zhou, W.; Cox, P. A.; Shannon, M. D.; Mayoral, A.; Casci, J. L.; Wright, P. A. STA-20: An ABC-6 Zeotype Structure Prepared by Co-Templating and Solved via a Hypothetical Structure Database and STEM-ADF Imaging. *Chem. Mater.* **2017**, *29* (5), 2180–2190.

(42) Giacobbe, C.; Lavigna, E.; Maspero, A.; Galli, S. Elucidating the CO_2 Adsorption Mechanisms in the Triangular Channels of the Bis(Pyrazolate) MOF $Fe_2(BPEB)_3$ by in Situ Synchrotron X-Ray Diffraction and Molecular Dynamics Simulations. *J. Mater. Chem. A* **2017**, *5* (32), 16964–16975.

(43) Fateeva, A.; Chater, P. A.; Ireland, C. P.; Tahir, A. A.; Khimyak, Y. Z.; Wiper, P. V.; Darwent, J. R.; Rosseinsky, M. J. A Water-Stable Porphyrin-Based Metal-Organic Framework Active for Visible-Light Photocatalysis. *Angew. Chemie - Int. Ed.* **2012**, *51* (30), 7440–7444.

(44) Margiolaki, I.; Giannopoulou, A. E.; Wright, J. P.; Knight, L.; Norrman, M.; Schluckebier, G.; Fitch, A. N.; Von Dreele, R. B. High-Resolution Powder X-Ray Data Reveal the T6 Hexameric Form of Bovine Insulin. *Acta Crystallogr. Sect. D Biol. Crystallogr.* **2013**, *69* (6), 978–990.

(45) Thompson, S. P.; Parker, J. E.; Marchal, J.; Potter, J.; Birt, A.; Yuan, F.; Fearn, R. D.; Lennie, A. R.; Street, S. R.; Tang, C. C. Fast X-Ray Powder Diffraction on I11 at Diamond. *J. Synchrotron Radiat.* **2011**, *18* (4), 637–648.

(46) Bernardo, P. L.; Amorim, H. S. De. Neutron Diffraction : A Tool for the Magnetic Properties. In *Handbook of Materials Characterization*; Sharma, S. K., Ed.; Springer, 2018; pp 1–35.

(47) Sears, V. F. Neutron Scattering Lengths and Cross Sections. *Neutron News* **1992**, *3* (3), 26–37.

(48) Smith, R. I.; Hull, S.; Tucker, M. G. The Upgraded Polaris Powder Diffractometer at the ISIS Neutron Source. *Rev. Sci. Instrum.* **2019**, *90* (11), 115101.

(49) Scherzer, O. The Theoretical Resolution Limit of the Electron Microscope. *J. Appl. Phys.* **1949**, *20* (1), 20–29.

(50) Goldstein, J. I.; Newbury, D. E.; Michael, J. R.; Ritchie, N. W. M.; Scott, J. H. J.; Joy, D. C. *Scanning Electron Microscopy and X-Ray Microanalysis*, 4th ed.; Springer: New York, 2018.

(51) Egerton, R. F. *Physical Principles of Electron Microscopy*, 1st ed.; Springer: Boston, MA, 2005.

(52) Michler, G. H. Scanning Electron Microscopy (SEM). In *Electron Microscopy of Polymers*; Springer Berlin Heidelberg: Berlin, Heidelberg, 2008; pp 87–120.

(53) Seiler, H. Secondary Electron Emission in the Scanning Electron Microscope. *J. Appl. Phys.* **1983**, *54* (11).

(54) Michler, G. H. Transmission Electron Microscopy: Fundamentals of Methods and Instrumentation. In *Electron Microscopy of Polymers*; Springer Berlin Heidelberg: Berlin, Heidelberg, 2008; pp 15–51.

(55) Pennycook, S. J. A Scan Through the History of STEM. In *Scanning Transmission Electron Microscopy*; Pennycook, S. J., Nellist, P. D., Eds.; Springer: New York, 2011; pp 1–90.

(56) Mayoral, A.; Sakamoto, Y.; Diaz, I. Zeolites and Mesoporous Crystals Under the Electron Microscope. In *Advanced Transmission Electron Microscopy: Applications to Nanomaterials*; Deepak, F. L., Mayoral, A., Arenal, R., Eds.; Springer, Cham: Cham, 2015; pp 93–138.

(57) Nellist, P. D. The Principles of STEM Imaging. In *Scanning Transmission Electron Microscopy*; Pennycook, S. J., Nellist, P. D., Eds.; Springer: New York, 2011; pp 91–116.

(58) Zou, X.; Hovmöller, S.; Oleynikov, P. *Electron Crystallography: Electron Microscopy and Electron Diffraction*; Oxford University Press: Oxford, 2011.

(59) Walker, C. G. H. Electron Probe Techniques. In *Handbook of Spectroscopy*; Gauglitz, G., Moore, D. S., Eds.; Wiley-VCH: Weinheim, Germany, 2014; pp 709–740.

(60) Janssens, K. X-Ray Fluorescence Analysis. In *Handbook of Spectroscopy*; Gauglitz, G., Moore, D. S., Eds.; Wiley-VCH: Weinheim, Germany, 2014; pp 451–506.

(61) Wright, P. A. *Microporous Framework Solids*; Royal Society of Chemistry: Cambridge, 2008.

(62) Keller, J.; Staudt, R. *Gas Adsorption Equilibria - Experimental Methods and Adsorption Isotherms*; 2005.

(63) Pourhakkak, P.; Taghizadeh, A.; Taghizadeh, M.; Ghaedi, M.; Haghdoust, S. Fundamentals of Adsorption Technology. In *Adsorption: Fundamental Processes and Applications*; Elsevier Ltd., 2021; Vol. 33, pp 1–70.

(64) Langmuir, I. The Constitution and Fundamental Properties of Solids and Liquids Part I. Solids. *J. Am. Chem. Soc.* **1916**, *38* (11), 2221–2295.

(65) Langmuir, I. The Constitution and Fundamental Properties of Solids and Liquids Part II. Liquids. *J. Am. Chem. Soc.* **1917**, *39* (9), 1848–1906.

(66) Brunauer, S.; Emmett, P. H.; Teller, E. Adsorption of Gases in Multimolecular Layers. *J. Am. Chem. Soc.* **1938**, *60* (2), 309–319.

(67) Sing, K. S. W. Adsorption Methods for the Characterization of Porous Materials. *Adv. Colloid Interface Sci.* **1998**, *76–77*, 3–11.

(68) Sing, K. The Use of Nitrogen Adsorption for the Characterisation of Porous Materials. *Colloids Surfaces A Physicochem. Eng. Asp.* **2001**, *187–188*, 3–9.

(69) Rouquerol, J.; Llewellyn, P.; Rouquerol, F. *Is the BET Equation Applicable to Microporous Adsorbents?*; Elsevier B.V., 2007; Vol. 160.

(70) Brunauer, S.; Deming, L. S.; Deming, W. E.; Teller, E. On a Theory of the van Der Waals Adsorption of Gases. *J. Am. Chem. Soc.* **1940**, *62* (7), 1723–1732.

(71) Sing, K. S. W. Reporting Physisorption Data for Gas/Solid Systems with Special Reference to the Determination of Surface Area and Porosity. *Pure Appl. Chem.* **1985**, *57* (4), 603–619.

(72) Thommes, M.; Kaneko, K.; Neimark, A. V.; Olivier, J. P.; Rodriguez-Reinoso, F.; Rouquerol, J.; Sing, K. S. W. W. Physisorption of Gases, with Special Reference to the Evaluation of Surface Area and Pore Size Distribution (IUPAC Technical Report). *Pure Appl. Chem.* **2015**, *87* (9–10), 1051–1069.

(73) Miller, K. J. Additivity Methods in Molecular Polarizability. *J. Am. Chem. Soc.* **1990**, *112* (23), 8533–8542.

(74) Miller, K. J. Calculation of Molecular Polarizability Tensor. *J. Am. Chem. Soc.* **1990**, *112* (23), 8543–8551.

(75) Vrabec, J.; Stoll, J.; Hasse, H. A Set of Molecular Models for Symmetric Quadrupolar Fluids. *J. Phys. Chem. B* **2001**, *105* (48), 12126–12133.

(76) Stoll, J.; Vrabec, J.; Hasse, H. Vapor-Liquid Equilibria of Mixtures Containing Nitrogen, Oxygen, Carbon Dioxide, and Ethane. *AIChE J.* **2003**, *49* (8), 2187–2198.

(77) Rallapalli, P.; Prasanth, K. P.; Patil, D.; Somani, R. S.; Jasra, R. V.; Bajaj, H. C.

Sorption Studies of CO_2, CH_4, N_2, CO, O_2 and Ar on Nanoporous Aluminum Terephthalate [MIL-53(Al)]. *J. Porous Mater.* **2011**, *18*, 205–210.

(78) Eic, M.; Ruthven, D. M. A New Experimental Technique for Measurement of Intracrystalline Diffusivity. *Zeolites* **1988**, *8* (1), 40–45.

(79) Brandani, S.; Mangano, E. The Zero Length Column Technique to Measure Adsorption Equilibrium and Kinetics: Lessons Learnt from 30 Years of Experience. *Adsorption* **2021**, *27* (3), 319–351.

(80) Brandani, S.; Ruthven, D. M. Analysis of ZLC Desorption Curves for Gaseous Systems. *Adsorption* **1996**, *2* (2), 133–143.

(81) Brandani, S. Effects of Nonlinear Equilibrium on Zero Length Column Experiments. *Chem. Eng. Sci.* **1998**, *53* (15), 2791–2798.

(82) Brandani, S.; Jama, M. A.; Ruthven, D. M. ZLC Measurements under Non-Linear Conditions. *Chem. Eng. Sci.* **2000**, *55* (7), 1205–1212.

(83) Gibson, J. A. A.; Mangano, E.; Shiko, E.; Greenaway, A. G.; Gromov, A. V.; Lozinska, M. M.; Friedrich, D.; Campbell, E. E. B.; Wright, P. A.; Brandani, S. Adsorption Materials and Processes for Carbon Capture from Gas- Fired Power Plants : AMPGas. *Ind. Eng. Chem. Res.* **2016**, *55* (13), 3840–3851.

(84) Ashbrook, S. E.; Dawson, D. M.; Griffin, J. M. Solid-State Nuclear Magnetic Resonance Spectroscopy. In *Local Structural Characterisation*; Bruce, D. W., O'Hare, D., Walton, R. I., Eds.; John Wiley & Sons Ltd: Chichester, 2014; pp 1–88.

(85) Bakhmutov, V. I. *Solid State NMR in Materials Science*; CRC: Boca Raton, Florida, 2012.

(86) Keeler, J. *Understanding NMR Spectroscopy*; Wiley: Oxford, 2002.

(87) Koller, H.; Weiß, M. Solid State NMR of Porous Materials. In *Topics in Current Chemistry*; Chan, J. C. C., Ed.; Springer: Heidelberg, 2012; pp 189–228.

(88) Wolfram Research, I. , Mathematica, Version 11.0. Wolfram Research, Inc.: Champaign, Illinois, 2016.

3 The Extended RHO Family

3.1 Introduction

Zeolite Rho is a small pore zeolite with framework topology **RHO**, which adopts cubic, body-centred symmetry and is composed of only *lta* and *d8r* cavities,[1] shown as G1 in the RHO family in Figure 3.1.1. The framework of zeolite Rho is flexible, adopting the *Im*-3*m* space group in hydrated forms and typically distorting upon dehydration in the presence of extra-framework metal cations to *I*-43*m*. Guo *et al*. realised that the further framework types, **PAU** (paulingite, ECR-18) and **MWF** (ZSM-25), could be described as expansions of **RHO**.[2] A simple way of describing this is by increasing the number of *d8r* units between *lta* cavities, as shown in Figure 3.1.1. These scaffolds require additional *pau* cavities and further space between interpenetrating scaffolds is filled or embedded by supplementary cages. Such related materials have been termed embedded isoreticular zeolites.[2,3]

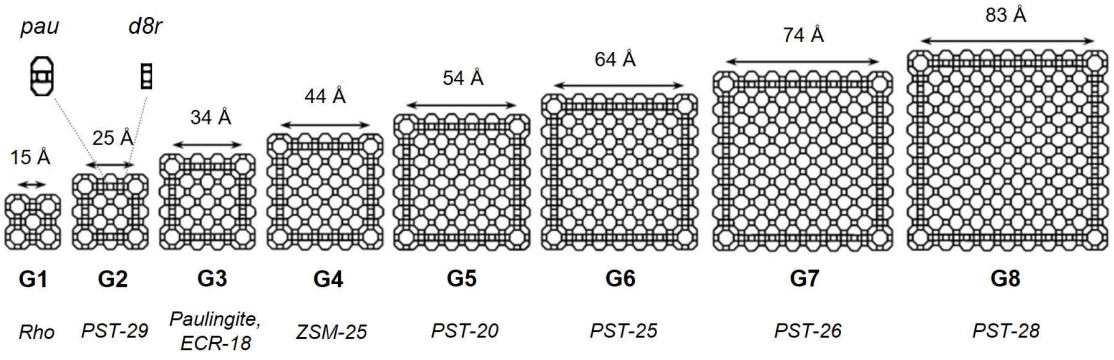

Figure 3.1.1. The extended RHO family of zeolites, showing their generation (G), and approximate unit cell parameter. Materials that adopt these framework structures are given at the bottom. Individual pau and d8r cavities are also shown. Reproduced from Shin et al,[5] with permission from Wiley.

The group of Prof Suk Bong Hong at POSTECH, South Korea, used this as a guide for the synthesis of larger structures, PST-20, 25, 26 and 28 as well as the missing member of the sequence, PST-29, the second smallest.[4–6] As can be seen in Figure 3.1.1, the incorporation of further *d8r* and *pau* units into the scaffold increases the unit cell parameter by *ca* 10 Å at a time, such that RHO-G8 (PST-28) has a unit cell volume *ca*. 180 × greater than that of G1 (zeolite Rho).

The following chapter looks at members of this series of zeolites and examines how far the structures of these materials can be investigated through PXRD analysis to describe adsorption behaviour, starting with the simplest family member, zeolite Rho.

3.2 Zeolite Rho

3.2.1 Introduction

Zeolite Rho is a small-pore zeolite with a 3-dimensional pore system connected *via* 8-ring windows, first synthesised by Robson *et al.*[7] The **RHO** framework, shown in greater detail in Figure 3.2.1 is composed of a body-centred cubic arrangement of *lta* cavities linked *via d8r* units,[1] and the relatively simple structure has only 3 different extra-framework cation sites. These sites are the S6R (single 6-ring) within *lta* cavities, the S8R between *d8r* and *lta* units and the D8R at the centre of the *d8r* cavity.

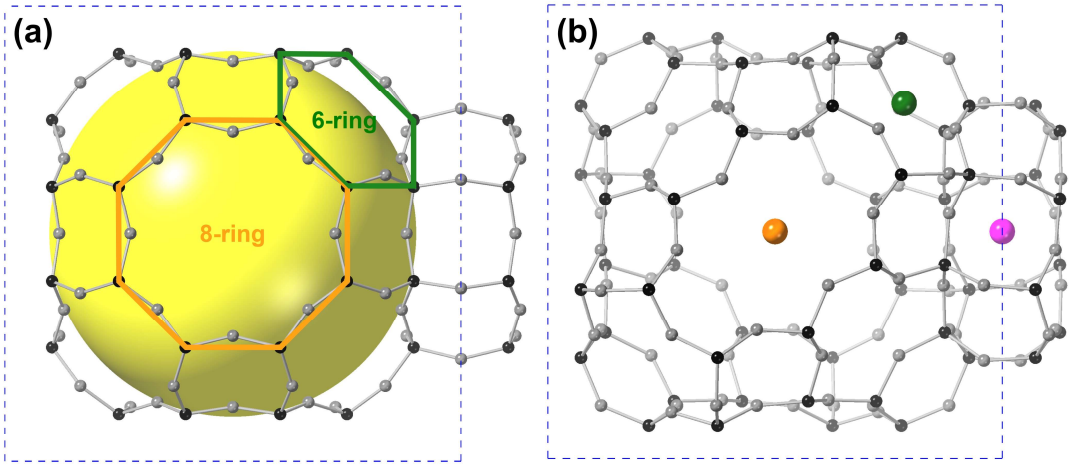

*Figure 3.2.1. The **RHO** framework in (a) undistorted Im-3m and (b) distorted I-43m symmetry. Pore space is indicated by the yellow sphere in (a), as are 6- and 8-ring moieties, and cation sites are shown in (b): S6R (green), S8R (orange) and D8R (pink). Framework T and O sites are depicted in black and grey, respectively.*

Rho is a highly flexible zeolite, distorting upon dehydration from *Im-3m* to *I-43m* symmetry to better coordinate extra-framework cations, as shown in Figure 3.2.1. There are some exceptions to this, discussed later. The degree of distortion is dependent on the cation content of the material,[8–11] and the dehydrated structures of a many cation forms have been investigated, including Li-, Na-, K-, Cs-, NH_4-, Pd- and Cd-exchanged Rho.[9,10,12–14] The nature of cation siting depends on the cations in question, for instance

Johnson *et al*. found Na and Cs cations sit in the S8R and D8R, respectively, in an as-prepared Na,Cs-form of Rho.[9] Upon partial exchange of these cations for Li^+, these small cations were found with powder neutron diffraction (PND) to sit in the S6R site. The H- and Cu^{II}-forms of Rho do not undergo any distortion upon dehydration, and instead remain in the *Im*-3*m* symmetry.[15] In H-Rho materials, framework O species become protonated and so H^+ cations are bound to the framework rather than occupying a window site. Cu^{2+} species, on the other hand, exclusively sit in the S6R site, which has been found to have no effect on framework distortion. Instead, S8R and D8R occupancy drives the shrinkage of the unit cell and change in symmetry.[15]

The crystal structure of zeolite Rho can be modified through cation exchange to alter gas adsorption behaviour. This can be through 2 separate phenomena: varying window size (or diameter) and window occupancy. Some of the main applications suggested for zeolite Rho are selective CO_2/N_2 and CO_2/CH_4 adsorptive separations.[16,17] Lozinska *et al*. have shown that the material can possess high selectivity in such processes through a "cation gating" or "trapdoor" process,[10,12] also observed in other zeolites such as chabazite.[18] In this mechanism, whilst windows are large enough for species to pass through, cations block the site and prohibit adsorption. However, species with relatively large quadrupolar or dipolar moments or polarizability, such as CO_2, can interact with cations to move them from the window site, whilst other potential adsorbates, such as N_2, CH_4, O_2 or Ar, cannot. This gives rise to a high selectivity in separation processes where only a specific molecule has the required physical characteristics for adsorption and such materials have been suggested for pre- and post-combustion applications.[19,20] Li-rich Rho materials have been identified as of particular interest in the past.[13]

To separate other mixtures, such as O_2/Ar or O_2/N_2, the cation gating mechanism cannot be relied upon, and instead more traditional molecular sieving becomes important. This limits the percolation of gas species based on their kinetic diameter relative to windows within the framework.[21] The cases given above are important sources of Ar and N_2 by selectively separating them from O_2 in the air but the kinetic diameters of these species are very similar, making molecular sieving challenging. Kovak *et al*. proposed zeolite adsorbents for isolating Ar from N_2 and O_2 *via* a temperature swing adsorption process but this requires cryogenic conditions.[22] Similarly, Breck used zeolite 4A for kinetic

O_2/N_2 and O_2/Ar separations at sub-ambient temperatures.[23] The low temperature requirements of these processes greatly increase the cost of any potential application.

More recent studies have examined potential adsorbents for ambient temperature O_2-selective separations, including the zeolite-like Ba-RPZ-3,[24] a titanosilicate, and zeolite 4A-based RS-10 from UOP.[25] The former possesses slow kinetics and selectivity of O_2/Ar is relatively low (< 10) whilst the latter exhibits properties that are consistent with carbon molecular sieves (CMSs), benchmark materials though not especially selective due to their irregular pore structure.[26–28] Coe *et al*. have subsequently shown in chabazite zeolites that O_2/Ar kinetic selectivity can be significantly improved over CMS materials by controlling framework window size.[29]

During the course of my undergraduate degree, my penultimate year research project within the group examined Li,Zn-Rho materials with Si/Al = 3.9 (M_x-Rho (3.9) materials),[30] building on the work of Dr Magdalena M. Lozinska. A subsequent summer project on the structures of related materials for Air Products and Chemicals, Inc. formed part of a successful patent application for Rho materials as selective O_2/Ar and O_2/N_2 adsorbents.[31] Again, Li-Rho had been identified as of particular interest for such applications, and has since been examined by Xia *et al*.[32] Subsequent samples were investigated by the group and collaborators at Air Products to improve the performance of the Li-exchanged material but structural data was limited to PXRD analysis.

To provide a more robust rationale for the selective O_2/Ar behaviour of these materials in particular, larger batches of selected samples were prepared by Dr Lozinska and submitted for powder neutron diffraction (PND) to enable the elucidation of Li cation siting, as discussed in Chapter 2. The 3 materials examined are $Li_{9.8}$-, $Li_{7.3}Cs_{2.5}$- and $Li_{5.5}Zn_{2.2}$-Rho (3.9). It is the PND datasets of these materials that form the basis of the work presented in this chapter, with additional previous data re-examined only to reduce or balance systematic errors. The aim of the work presented here is to use PND data to provide a fuller structural explanation of selective O_2/Ar and CO_2/CH_4 adsorption.

3.2.2 Acknowledgements

As-prepared Rho samples contributed by Dr Alessandro Turrina at Johnson Matthey were ion exchanged to the NH_4-form by myself but subsequent exchanges to forms examined by PND analysis were carried out by Dr Lozinska. Other samples were synthesised by Dr Lozinska or myself or sourced from Air Products and Chemicals, Inc., and their dehydration and PXRD data collection was carried out by Dr Lozinska or myself prior to this work. PND samples were prepared and packaged by Drs Lozinska and Julia L. Payne, with Dr Ron I. Smith supervising experiments at ISIS.

Equilibrium adsorption data was obtained by Dr Lozinska, whilst O_2 and Ar kinetic data was collected and analysed by Drs Elizabeth Feverston, Garret C. Lau and William Casteel, Jr. at Air Products and Chemicals, Inc. and CO_2 and CH_4 kinetic data was recorded by Dr Enzo Mangano at the University of Edinburgh.

Background data showing the behaviour of materials is presented in the following section of this chapter, having been obtained by collaborators listed above. This is to allow such behaviour to be explained by structural effects later.

3.2.3 Underlying experimental work

Samples of zeolite Rho (3.9) were obtained from the sources given above, with the general composition of $M^{z+}_{9.8/z}[Si_{38.2}Al_{9.8}O_{96}]$, where symbols have their usual meaning. Example O_2 and Ar uptake curves collected by collaborators at Air Products and Chemicals, Inc. are presented in Figure 3.2.2 for materials similar to those investigated

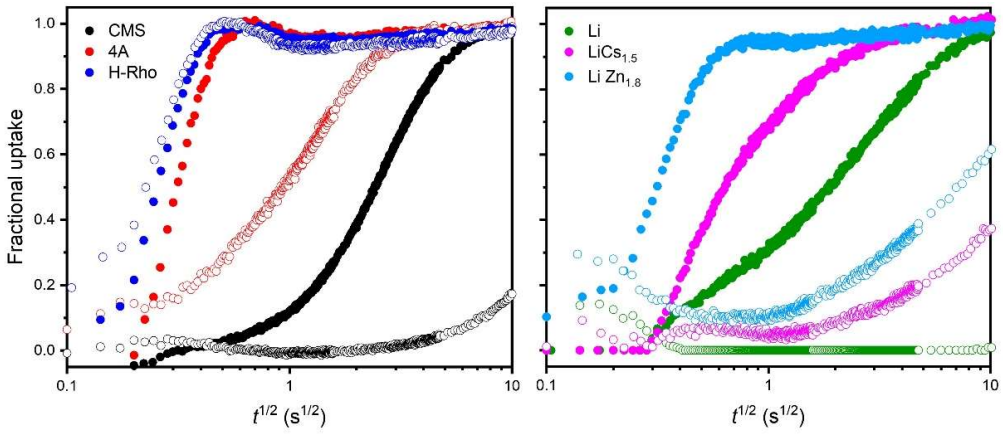

Figure 3.2.2. Uptake curves of (left) $H_{9.8}$-Rho (3.9), 4A and CMS and (right) $Li_{9.8}$-, $Li_{8.3}Cs_{1.5}$- and $Li_{6.2}Zn_{1.8}$-Rho (3.9) in blue, red, black, green, pink and cyan, respectively. Closed and open symbols indicate O_2 and Ar adsorption, respectively.

in this chapter. The values of O_2 and Ar uptake for selected materials are presented in Table 3.2.1.

Table 3.2.1. Uptake of O_2 and Ar at end of uptake experiment. Note that for less selective samples uptakes are very similar for both species, whilst more selective samples, such as Li-Rho, have much lower Ar uptakes. P_∞ is the equilibrium pressure after dosing of gas and subsequent adsorption.

Sample	O_2 uptake at P_∞ (mmol g^{-1})	Ar uptake at P_∞ (mmol g^{-1})
$Li_{9.8}$-Rho	0.10	0.03
$Li_{8.3}Cs_{1.5}$-Rho	0.10	0.08
$Li_{7.4}Zn_{1.2}$-Rho	0.10	0.04
$Li_{6.2}Zn_{1.8}$-Rho	0.11	0.10
$Li_{1.6}Zn_{4.1}$-Rho	0.11	0.11
$Zn_{4.9}$-Rho	0.10	0.10
$H_{9.8}$-Rho	0.14	0.16
4A[31]	0.09	0.08
CMS[31]	0.22	0.22
Ba-RPZ-3[24]	0.17	

The O_2 diffusivity and kinetic O_2/Ar selectivity for various Rho materials determined from these curves are plotted in Figure 3.2.3. Whilst most reference materials are relatively slow and unselective, the zeolite Rho samples shown exhibit a range of behaviours from rapid but unselective ($H_{9.8}$-Rho (3.9)), to highly selective but slow ($Li_{9.8}$-Rho (3.9)). Introducing small amounts of other cations to $Li_{9.8}$-Rho (3.9) increases the diffusivity of materials whilst retaining high selectivity, and this is especially the case for the $Li_{9.8-2x}Zn_x$-Rho (3.9) series, discussed later. Samples most similar to the $Li_{7.3}Cs_{2.5}$- and $Li_{5.5}Zn_{2.2}$-Rho (3.9) materials investigated through PND and PXRD are $Li_{8.3}Cs_{1.5}$- and $Li_{6.2}Zn_{1.8}$-Rho (3.9), respectively. Breakthrough curves obtained through E-ZLC analysis by Dr Mangano at the University of Edinburgh for selected samples are presented in Figure 3.2.4

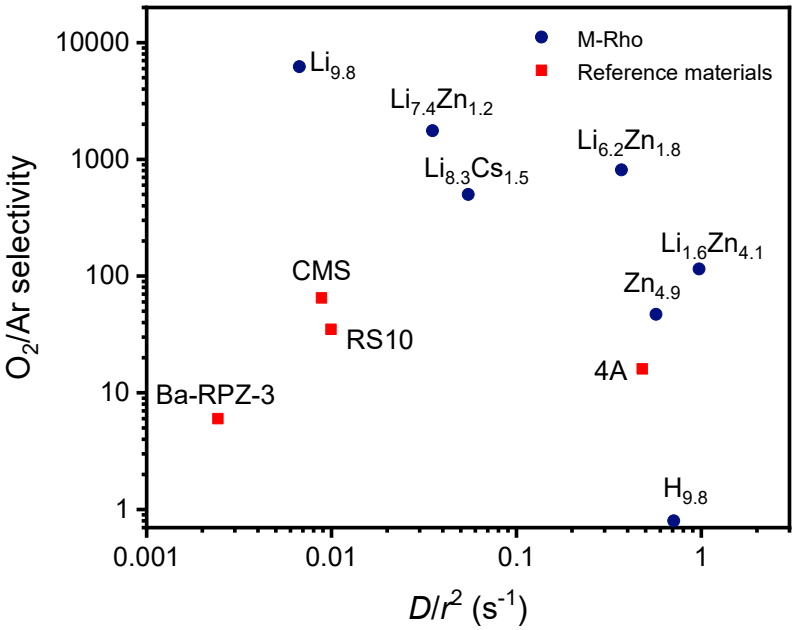

Figure 3.2.3. O_2/Ar Selectivity vs O_2 uptake rate for (blue) M_x-Rho (3.9) materials, where M is as indicated by data labels, and (red) other kinetic adsorbents.

Equilibrium CO_2 adsorption isotherms, shown in Figure 3.2.5 were collected up to 5 bar at 298 K by Dr Lozinska for the materials analysed by PND analysis. These were used to inform Rietveld refinement of these samples under exposure to CO_2 gas at various pressures.

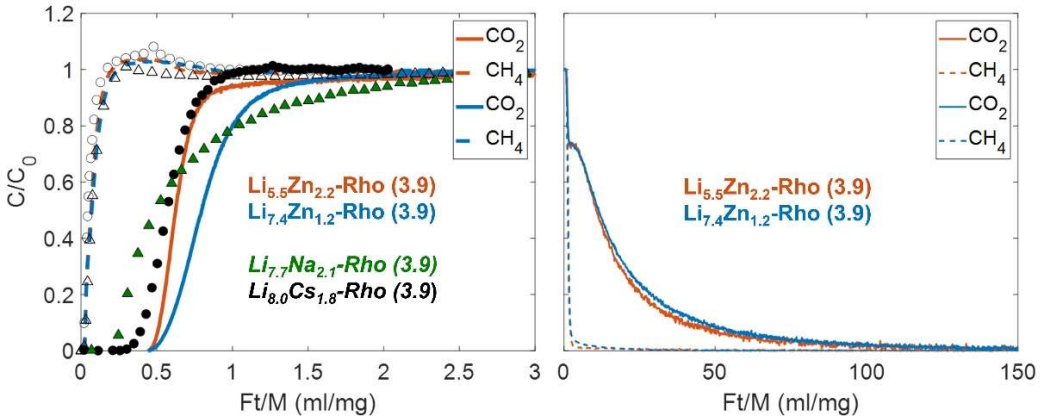

Figure 3.2.4. E-ZLC data for $Li_{5.5}Zn_{2.2}$- and $Li_{7.4}Zn_{1.2}$-Rho (3.9) including (left) adsorption and (right) desorption branches. CO_2 and CH_4 data are indicated by solid and dashed lines, respectively. $Li_{8.0}Cs_{1.8}$- and $Li_{7.7}Na_{2.1}$-Rho (3.9) are also shown, previously published in Lozinska et al,[13] with solid and empty symbols depicting CO_2 and CH_4 data, respectively.

3.2.4 Dehydrated Li-based Rho Structures

$Li_{9.8}$-Rho (3.9) has previously been found to be of interest for both selective O_2/Ar and CO_2/CH_4 adsorption. Lozinska *et al.* have published a structure of $Li_{9.8}$-Rho (3.9) from

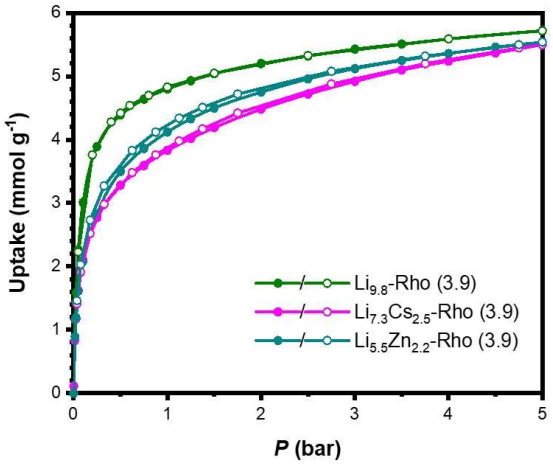

Figure 3.2.5. CO_2 adsorption isotherms up to 5 bar at 298 K for $Li_{9.8}$- (green), $Li_{7.3}Cs_{2.5}$- (pink) and $Li_{5.5}Zn_{2.2}$-Rho (3.9) (cyan). Adsorption and desorption branches are indicated by closed and open symbols, respectively.

PXRD data but this assumed that all Li cations occupy S6R sites, with surplus Li^+ found in the S8R site.[10,13] The poor scattering of X-rays by Li cations makes refinement of cation occupancy and position highly unreliable. Johnson *et al*. found such data using PND in a partially exchanged material, with composition $Li_{7.6}Na_{2.0}Cs_{1.3}$-Rho (3.2) but no such study has been carried out on a fully exchanged Li-Rho form.

A combined Rietveld refinement of both neutron and X-ray data of dehydrated $Li_{9.8}$-Rho (3.9) was performed and associated crystallographic data is given in Table 3.2.2 with other Li-based materials, with Rietveld plots shown in Figure 3.2.6. Further details relevant to adsorption processes are given in Table 3.2.3. The structure of the material is shown in Figure 3.2.7 beside the other Li-based samples investigated here. Dehydrated forms describe the material upon activation in preparation for any adsorption process. For O_2/Ar adsorption, due to the properties of the species previously discussed, guest species do not strongly bind to cations and so do not cause the structures to alter during adsorption. This has been shown to be the case by Georgieva for N_2 at room temperature using variable pressure XRD (VPXRD) analysis.[33] In essence, the dehydrated forms are relevant throughout the O_2/Ar adsorption process, which may not be true in the presence of species such as CO_2, discussed later.

The S6R site is found to be the preferred site for Li cations, as previously observed by neutron diffraction of Li-exchanged aluminogermanate Rho,[34] the partially Li-exchanged aluminosilicate of Johnson *et al*.,[9] and as proposed by Lozinska *et al*.[10] Unlike

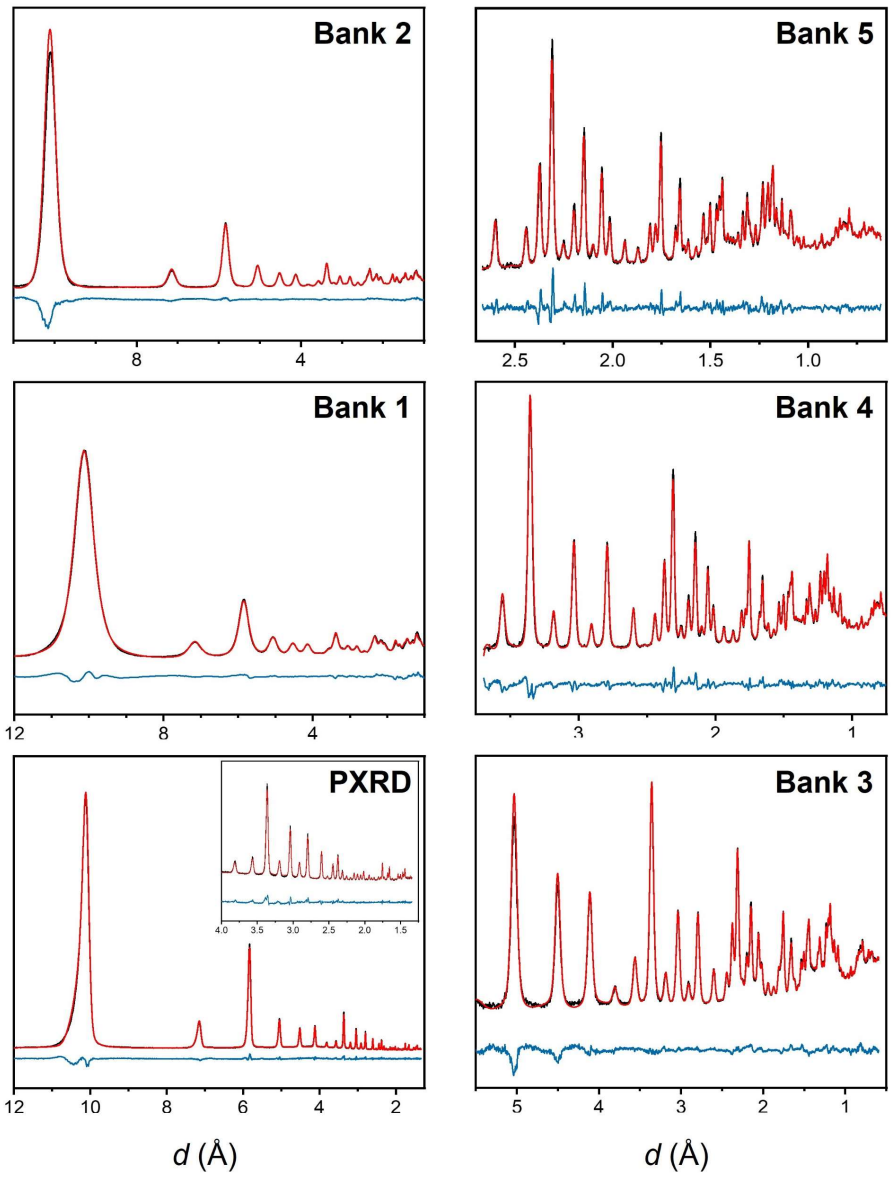

Figure 3.2.6. Rietveld plots of PXRD (Stoe, λ = 1.54056 Å) and PND (Polaris, ISIS) patterns of dehydrated $Li_{9.8}$-Rho (3.9) as a function of d-spacing, with observed, calculated and difference curves shown in black, red and blue, respectively. Dataset identifiers are as labelled.

the latter however, only 6.6 of the 8 S6R sites are occupied. This can be reasoned to be due to Al-free 6-rings which possess no significant negative charge. For a random distribution of Al sites fulfilling Löwenstein's rule in a material with Si/Al = 3.9, this would be the case for *ca*. 32% of the 6-rings. If there is a drive to further separate Al sites within the framework, this value is likely to be lower and from this refinement it would appear to be *ca*. 20%, using the logic of Kim and Seff for Zn siting in zeolite A.[35] A further 3.6 Li cations were found in the S8R. This strongly distorts the 8-ring window, with a

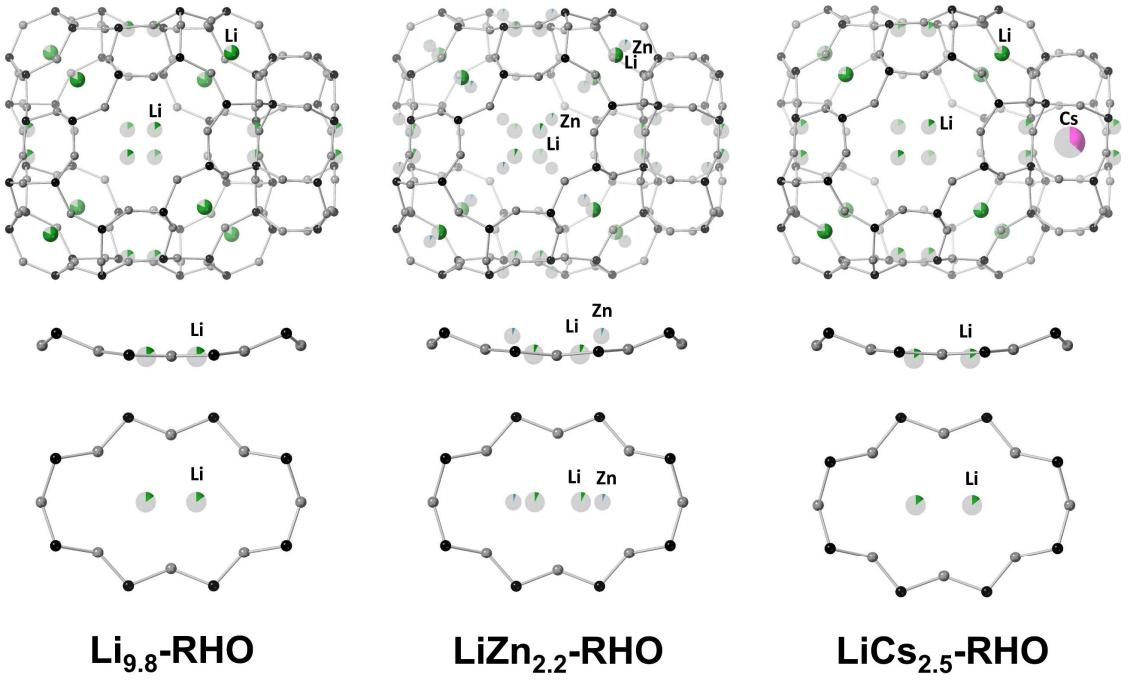

Figure 3.2.7. Structures of Li-based Rho materials obtained from combined refinement of PND and PXRD data, with 8-ring windows shown in the plane and normal to the plane of the ring. Li, Zn and Cs cations are shown in green, blue and pink, respectively, with fractional occupancies indicated by partial shading.

free diameter of 2.0 Å (the shortest distance between 2 O sites across the 8-ring, minus 2 O radii (2 × 1.35 Å)), due to coordination between cations and the framework (Li – O = 2.5(1) Å), which causes a significant distortion of the unit cell (a = 14.255(1) Å compared with 15.017 Å for $H_{9.8}$-Rho (3.9)). Similarly, Lozinska *et al.* reported the unit cell parameter variation with x for a mixed $Li_{9.8-x}H_x$-Rho (3.9) series, which showed the unit cell only distorted with Li^+ content above 6 cations per unit cell.[10] This suggests that *ca.* 6 Li cations sit in the S6R site before surplus cations begin to fill the S8R site, causing framework distortion upon dehydration.

Table 3.2.2. Crystallographic details of dehydrated samples refined with combined PND and PXRD data: $Li_{9.8}$-, $Li_{5.5}Zn_{2.2}$- and $Li_{7.3}Cs_{2.5}$-Rho (3.9) samples, including Rwp, unit cell parameter and cations per unit cell in each site.

Sample	R_{wp}	a (Å)	S6R	S8R	D8R
$Li_{9.8}$	3.2%	14.255(1)	6.6(1) Li	3.6(2) Li	
$Li_{5.5}Zn_{2.2}$	3.6%	14.365(1)	3.8(2) Li, 0.6(1) Zn	1.7(2) Li, 1.4(1) Zn	
$Li_{7.3}Cs_{2.5}$	2.9%	14.444(1)	5.8(1) Li	1.9(2) Li	2.3(1) Cs

Table 3.2.3. Crystallographic details of dehydrated samples refined with combined PND and PXRD data: $Li_{9.8}$-, $Li_{5.5}Zn_{2.2}$- and $Li_{7.3}Cs_{2.5}$-Rho (3.9) samples, the minimum number of open windows and free window diameter. Also included are O_2/Ar kinetic data collected on relevant samples.

Sample	Open windows	Free window diameter (Å)	O_2 D/r^2 (s^{-1})	Kinetic O_2/Ar selectivity
$Li_{9.8}$	2.4(2)	2.0(1)	6.7×10^{-3}	3600
$Li_{5.5}Zn_{2.2}$	2.9(2)	2.2(1)	3.70×10^{-1}	813
$Li_{7.3}Cs_{2.5}$	1.8(2)	2.4(1)	5.49×10^{-2}	500

Previous work by Lozinska *et al.* found that by introducing limited Cs cations (1-2 per unit cell) to $Li_{9.8}$-Rho (3.9), the kinetics of CO_2/CH_4 separation was improved.[13] The presence of large Cs cations in the D8R site led to more open windows throughout the structure, without blocking too many of the *d8r* windows. As such, a $Li_{7.3}Cs_{2.5}$-Rho (3.9) sample was investigated.

Rietveld refinement of this sample upon dehydration was carried out, and the related fits are shown in Figure 3.2.8. Crystallographic parameters are detailed in Table 3.2.2 and its structure is shown in Figure 3.2.7. In keeping with previous studies, all refined Cs cations were found to occupy the D8R, and fewer Li cations were found in the S8R (1.9 per unit cell), although their position remained the same. The unit cell is expanded relative to the $Li_{9.8}$-form, with an *a* parameter of 14.444(1) Å, and a minimum window diameter of 2.4(1) Å. These effects are attributed to the presence the large Cs^+ in D8R sites and fewer Li^+ species in the S8R site.

A higher proportion of Li cations sit in the S6R site within this material than in the pure Li-form and this is to be expected as Li is preferentially, though not exclusively, removed from the S8R site over the S6R with the incorporation of Cs cations. Within this material, the windows are still distorted relative to the H-form or the hydrated form of the material and so the S8R is still a somewhat favourable site, although the S6R is preferred by Li.

Another attempt to improve the performance of $Li_{9.8}$-Rho (3.9), originally suggested by Dr Lozinska, was the introduction of divalent Zn cations. These are similar in size to Li

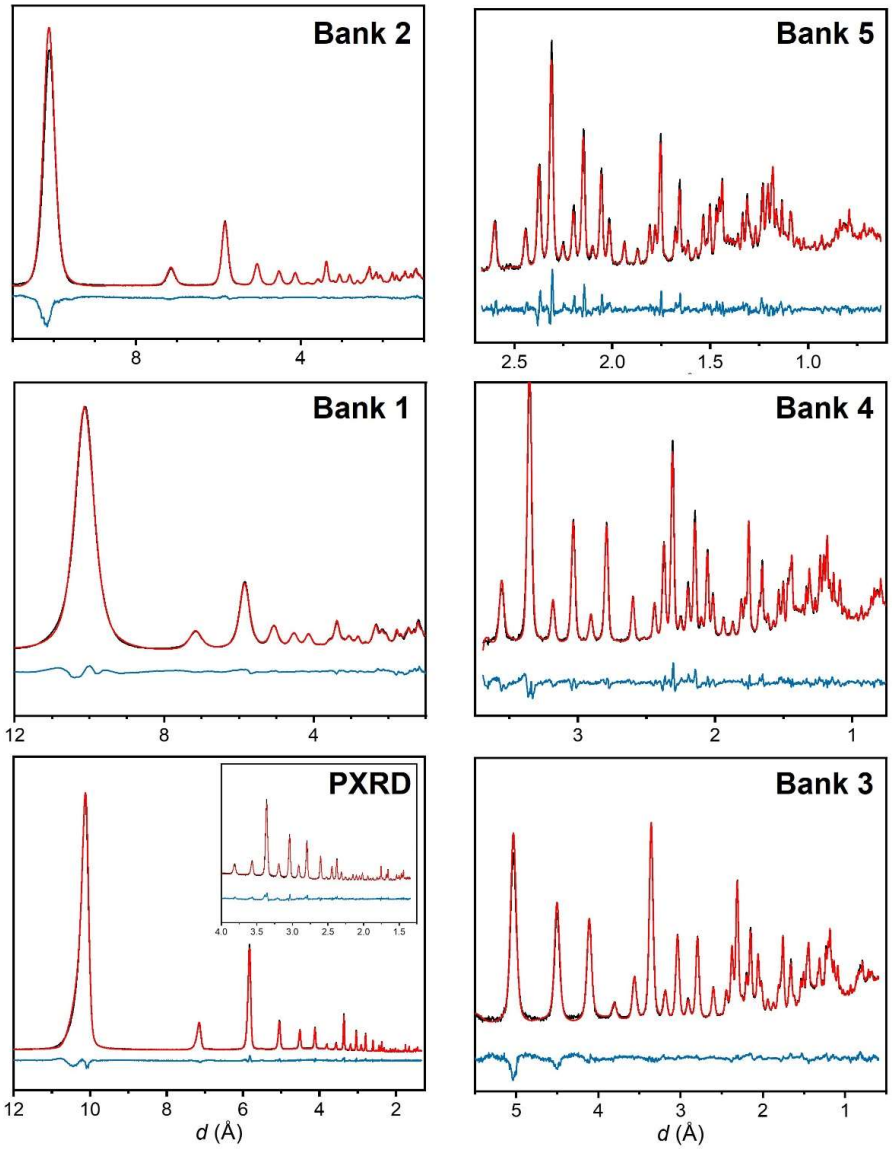

Figure 3.2.8. Rietveld plots of PXRD (Stoe, λ = 1.54056 Å) and PND (Polaris, ISIS) patterns of dehydrated $Li_{7.3}Cs_{2.5}$-Rho (3.9) as a function of d-spacing, with observed, calculated and difference curves shown in black, red and blue, respectively. Dataset identifiers are as labelled.

(0.74 Å for Zn^{2+} *vs*. 0.73 Å for Li^{+}) and hence were expected to prefer S6R sites.[9,10,15,36–38] As a divalent cation, the overall number of zinc species within the structure decreases as they replace counterbalancing Li^{+} cations and had the potential to reduce window blockage, and hence increase diffusivity of desired species within the material. A series of $Li_{9.8-2x}Zn_x$-Rho materials was prepared during my undergraduate studies with additional samples produced by Dr Lozinska, with $x \approx 1$, 2, 4 and 5. Revisiting the PXRD data of these materials upon dehydration using TOPAS-Academic software found the same trend as previously.[30] The introduction of Zn^{2+} results in a measured increase of

the unit cell parameter (and correspondingly of window size) up to 14.541(1) Å for the fully exchanged $Zn_{4.9}$-Rho (3.9), presented in Figure 3.2.9.

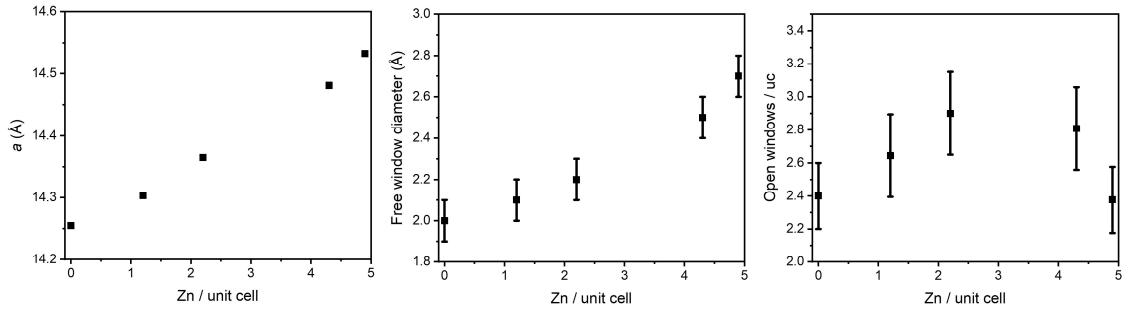

Figure 3.2.9. Unit cell parameter, free window diameter and open windows per unit cell in Li,Zn-Rho materials with varying Zn content.

PXRD analysis of the Zn-material reveals Zn cations are distributed over both S6R and S8R sites, with 1.2 and 3.6 Zn cations per unit cell found in each site, respectively (see Appendix VI.I.I). As Li-content increases in the series, Zn cations are removed from both sites. PXRD data alone could not reveal the behaviour of Li within these materials, however. Examination of a $Li_{5.5}Zn_{2.2}$-Rho (3.9) sample using combined PXRD and PND material was carried out, therefore. Rietveld plots of the sample are given in Figure 3.2.10, and the structure is shown in Figure 3.2.7 and selected structural data is presented in Table 3.2.2.

Within the $Li_{9.8-2x}Zn_x$-Rho (3.9) series, typically Zn cations only have a slight preference for the S8R over the S6R, showing only a narrow bias compared to the relative multiplicities of the 2 sites. PND data allows for the identification of Li cation positions and occupancies but it is not as straightforward as would be desired. The positions of the sites they occupy are very similar, as would be expected based on their similar cation size, but Zn and Li possess positive and negative neutron scattering lengths, respectively.[39] This leads to destructive interference, partially cancelling out scattered intensity from the cations. This obscures the true locations and occupancies of the sites. PXRD provides a reliable account of Zn cation siting, and combined refinement greatly improves the accuracy of the final refined structure. To complement this, the total number of Li and Zn cations were restrained to closely match experimentally expected values, as determined by elemental analysis by coworkers (a combination of EDX and inductively coupled plasma atomic emission spectroscopy (ICP-AES).

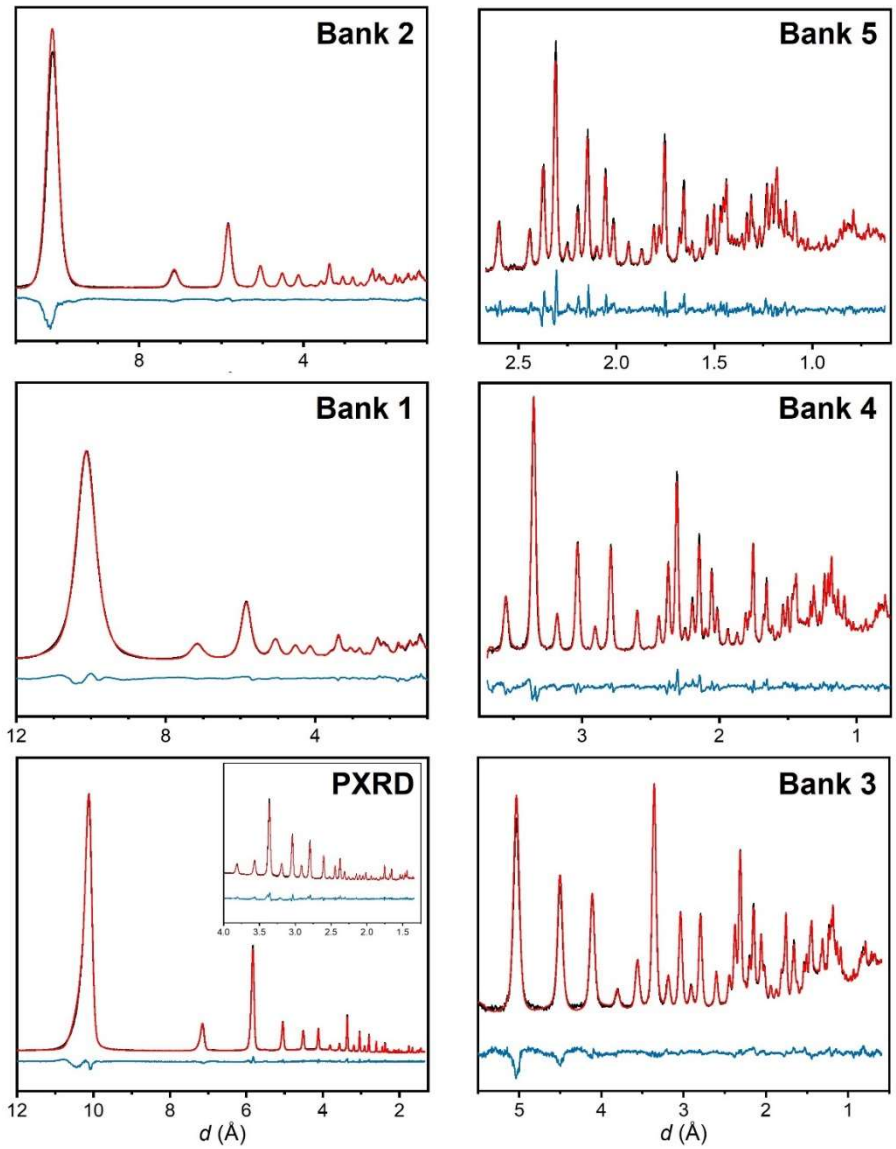

Figure 3.2.10. Rietveld plots of PXRD (Stoe, λ = 1.54056 Å) and PND (Polaris, ISIS) patterns of dehydrated $Li_{5.5}Zn_{2.2}$-Rho (3.9) as a function of d-spacing, with observed, calculated and difference curves shown in black, red and blue, respectively. Dataset identifiers are as labelled.

With this method, Li cations were found to preferentially occupy the S6R in $Li_{5.5}Zn_{2.2}$-Rho (3.9), with fewer cations adopting the S8R site. Additionally, Zn^{2+} species are found projected further out from the planes of the 6-ring and 8-ring sites. The result of partial Zn-exchange is that the number of cations in 8-ring windows drops from 3.6 per unit cell in the Li-form to 3.1 in $Li_{5.5}Zn_{2.2}$-Rho (3.9). Further incorporation of Zn introduces further cations in these sites, with 3.6 per unit cell again in the $Zn_{4.9}$-sample. A model of the number of open windows can be obtained with informed fitting of refined Li and Zn occupancies. This is inaccurate due to the low number of samples examined and only 2

of these, at low Zn concentration, provide Li occupancy data. Such a model is detailed in Appendix VII and suggests the greatest number of open windows at *ca*.2 Zn cations per unit cell, close to the sample investigated. This is due to balancing the greater preference of Li cations for S6R sites with the reduced number of cations associated with divalent Zn-exchange.

3.2.5 Li-based Rho materials as selective O_2/Ar adsorbents

O_2/Ar adsorption data was presented in Section 3.2.3 which showed that $Li_{9.8}$-Rho (3.9) was the most selective composition for these materials, and far exceled other materials such as CMS or Ba-RPZ-3. However, this sample also had the slowest kinetics. This was improved with the incorporation of Zn or Cs cations but at the expense of selectivity. The $Li_{7.4}Zn_{1.2}$- and $Li_{6.2}Zn_{1.8}$-Rho (3.9) materials seemed to be good compromises between the selectivity and diffusivity. The latter sample is close to that of the $Li_{5.5}Zn_{2.2}$-form examined by combined PND and PXRD refinement, whilst the $Li_{8.3}Cs_{1.5}$-Rho (3.9) is the closest to the $Li_{7.3}Cs_{2.5}$-material, the structure of which is presented above.

To isolate the effects of structural features on O_2/Ar separation behaviour, the measured selectivity and diffusivity were plotted for a range of materials against the free diameter of 8-ring windows, as well as the number of open windows determined or deduced from Rietveld refinement, as shown in Figure 3.2.11. From this, it can be seen that the free window diameter greatly impacts O_2/Ar selectivity and diffusivity, particularly between 2.0 and 2.5 Å, with increasing diameter improving diffusivity at the expense of

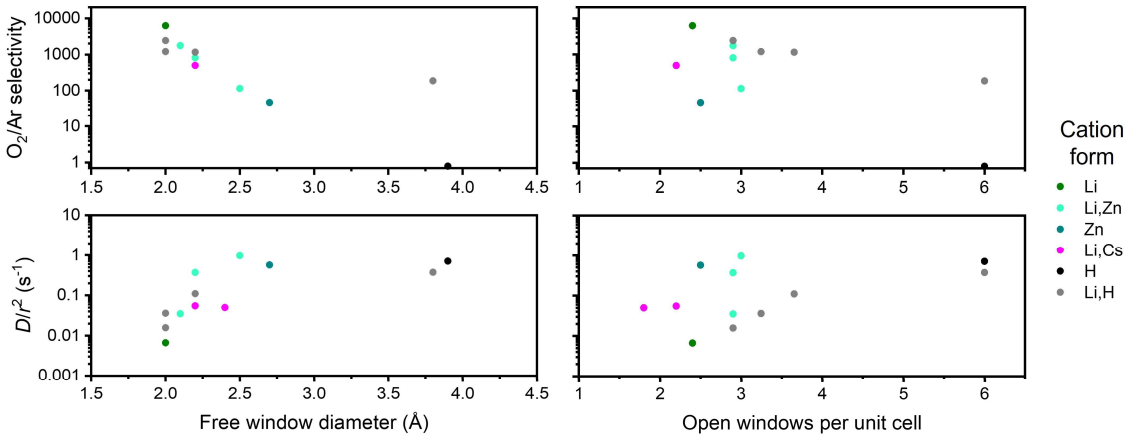

Figure 3.2.11. O_2/Ar selectivity and D/r^2 for Rho (3.9) samples vs. free window diameters and open windows per unit cell as found or inferred from Rietveld refinement. Cation forms or their families are depicted by colours as detailed on the right.

lower selectivity. Whilst $Li_{9.8}$-Rho (3.9), with a free window diameter of 2.0 Å, has a selectivity close to 4000, the Zn-form (free diameter = 2.7 Å) has a value of just 45. Simultaneously, the latter has a diffusivity *ca*. 500 times higher than that of the former.

Comparing the diameters reported here with those of O_2 and Ar (kinetic diameters of 3.1 and 3.4 Å, respectively),[40] neither species would be expected to pass through the material. Cook and Connor, however, suggested that zeolite windows experience thermal vibration, causing the window to be *ca*. 0.7 Å larger than would be expected.[41] This was proposed for "rigid" zeolite frameworks, but it is possible that the flexible nature of the **RHO** framework enables a greater vibrational effect, further expanding the effective window diameter. If this were the case, the sensitive range of window diameters is shifted slightly above that of the 2.7 – 3.2 Å expected from the original proposal of Cook and Connor. This is illustrated by the ability of $Li_{9.8}$-Rho (3.9) to adsorb some O_2, as the free window diameter must be ≥ 3.1 Å locally for some length of time to permit this, even though its crystallographic free diameter is 2.0 Å.

A similar, though far weaker, relationship may be present with varying the number of open windows. Higher diffusivity and lower selectivity results from a greater proportion of open windows but this is a weak correlation compared to the effect as that of the window diameter. This may in part be due to the complicated interdependency of the 2 factors, as cation siting and type influences the free window diameter. Consequently, the type of cation occupying a window is as important as whether the window is occupied.

For example, $Li_{6.2}Zn_{1.8}$-Rho (3.9) has an O_2/Ar selectivity between that of the $Li_{9.8}$- and $Li_{7.3}Cs_{1.5}$-forms. The latter has a larger unit cell than $Li_{6.2}Zn_{1.8}$-Rho (3.9), yet the presence of an additional 0.7 cations in 8-ring windows greatly inhibits O_2 diffusion (D/r^2 = 0.055 and 0.37 s^{-1} for the $Li_{7.3}Cs_{1.5}$- and $Li_{6.2}Zn_{1.8}$-forms, respectively). O_2 uptake on the $Li_{6.2}Zn_{1.8}$-material is also *ca*. 55 times faster than on the $Li_{9.8}$-analogue, which can be attributed to both larger window diameter and the presence of fewer cations in the S8R site compared to the latter. By adding divalent Zn^{2+} to zeolite Rho, 8-ring window occupancy is brought down, enhancing uptake rate, whilst retaining a high degree of 8-ring distortion, which is required to maintain high O_2/Ar selectivity. To some extent, the

degree of Zn-exchange can be tailored to balance higher selectivity with greater diffusivity, as required.

3.2.6 Li-based Rho materials as selective CO_2/CH_4 adsorbents

As previously discussed, the Rietveld analysis of dehydrated materials investigated are indicative of the structure throughout an O_2/Ar separation process. By contrast, CO_2 has an appreciable quadrupole moment and polarizability, enabling the species to interact with cations, as seen in the cation gating process,[18] and this enables the unit cell to expand and undergo cation relocation as CO_2 is adsorbed.[10,12] As such, the materials submitted for PND analysis were also exposed to doses of CO_2 pressure and their neutron diffraction patterns obtained. Unfortunately, associated PXRD patterns were not obtained and so a combined refinement using both probes could not be carried out.

Rigid bodies were used to describe CO_2 molecules in locations previously found in the literature, off the body diagonal in the *lta* cavity and close to the S8R site between *lta* and *d8r* units,[10,12] shown in Figure 3.2.12. The former was found to be preferred over the latter, and refined CO_2 content matched experimental values well, as described in Table 3.2.4. Higher pressure data could not be adequately described through refinement, with the exception of the $Li_{9.8}$-Rho (3.9) sample at 1.2 bar. As the pressure at which data was collected increased, further tools were required to maintain a reasonable chemical structure, particularly at much higher pressures which included the restraining of cation positions and occupancies, as they tended to stray towards the centre of the *lta* cavity.

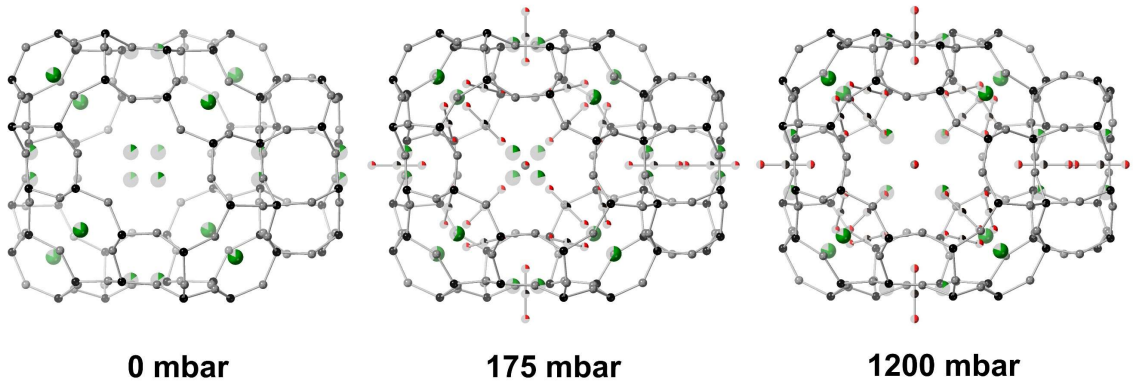

Figure 3.2.12. Structures of $Li_{9.8}$-Rho (3.9) at varying pressures of CO_2, as labelled. Framework T and O sites are shown in black and grey, with Li cations and CO_2 species shown in green and black and red, respectively. Fractional occupancies are indicated by partial filling of spheres.

Pressures at which structures were successfully refined spanned the region of interest for E-ZLC experiments discussed later (0 – 100 mbar pCO_2). The results are detailed in Table 3.2.4, with further discussion below. Rietveld plots for these samples are provided in Appendix IV.

The structures of $Li_{9.8}$-Rho (3.9) were successfully refined at all pressures, including above 1 bar of CO_2, a selection of which are shown in Figure 3.2.12. Upon adsorption of CO_2 at 175 mbar, the unit cell parameter increases by *ca*. 0.2 Å. Another 1 bar of CO_2 is required to observe a further expansion of the same magnitude. At this pressure, the unit cell has yet to reach the fully relaxed state of the hydrated form (*ca*. 15 Å).[9,10] This agrees very well with work by Lozinska *et al*. which found a = 14.6136(1) Å at 1.174 bar of CO_2.[13] Furthermore, from their synchrotron analysis, even at 9 bar of CO_2 the material did not reach the fully relaxed state.

Table 3.2.4. Crystallographic details of samples refined with PND data under varying pCO_2: $Li_{9.8}$-, $Li_{5.5}Zn_{2.2}$- and $Li_{7.3}Cs_{2.5}$-Rho (3.9) samples, including CO_2 pressure, R_{wp}, unit cell parameter and CO_2 content experimentally determined from the relevant CO_2 adsorption isotherm and from refinement.

Sample	P (mbar)	R_{wp}	a (Å)	CO_2/uc experimental	CO_2/uc refinement
$Li_{9.8}$	0	3.3%	14.255(1)	0	0
	26	4.9%	14.297(1)	4.6	3.6(3)
	70	5.7%	14.340(1)	7.8	6.5(3)
	175	5.9%	14.480(1)	10.4	8.9(3)
	1200	7.8%	14.642(1)	14.4	14.0(3)
$Li_{7.3}Cs_{2.5}$	0	2.9%	14.444(1)	0	0
	1	2.7%	14.470(1)	0.4	0
	25	3.2%	14.517(1)	3.7	3.5(3)
	190	4.6%	14.566(1)	8.2	8.6(3)
$Li_{5.5}Zn_{2.2}$	0	3.6%	14.365(1)	0	0
	24	3.6%	14.438(1)	3.6	3.1(3)
	159	4.3%	14.523(1)	7.4	7.1(3)

The changes in unit cell volume for all 3 samples are provided in Figure 3.2.13, along with free window diameters. The expansion of the $Li_{7.3}Cs_{2.5}$-Rho (3.9) framework found here is consistent with previous studies of Lozinska *et al*. on a similar Li,Cs-Rho (3.9)

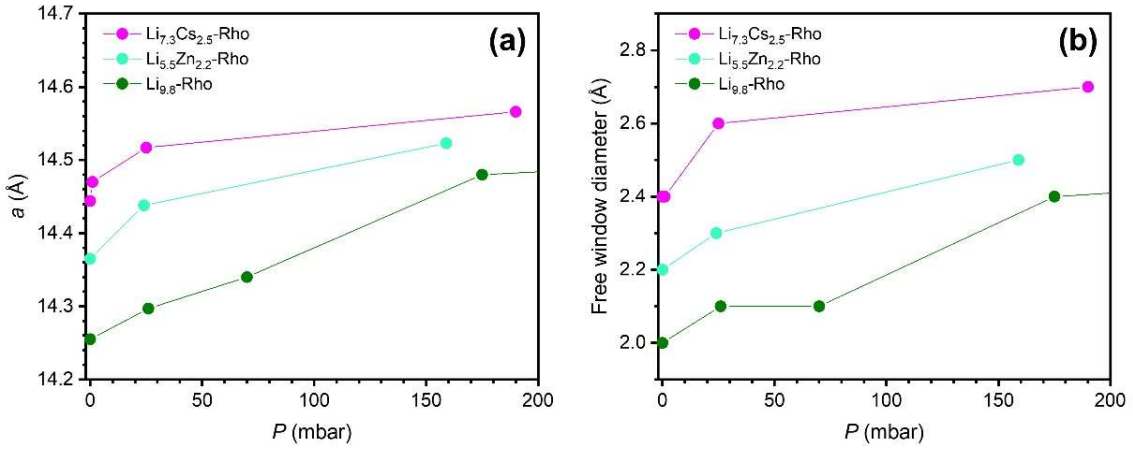

Figure 3.2.13. Structural parameters of Li-based Rho materials using PND data below 200 mbar of CO_2: (a) unit cell parameter and (b) free window diameter. Samples are as identified in the legend.

sample using synchrotron data which found a = 14.5331 Å at 190 mbar of CO_2.[13] The $Li_{5.5}Zn_{2.2}$-structure is the intermediate of the other 2 at all pressures investigated and the gap between the samples narrows for both parameters as CO_2 pressure increases. Each material undergoes an increase in window diameter of *ca*. 0.3 Å, which could have impacts on both diffusivity and selectivity of CO_2 over other gaseous species. This would have less of an impact on separations with a significantly larger species, such as CH_4 with a kinetic diameter of 3.7 Å, compared to 3.0 Å for CO_2.[40]

Cation occupancies within the materials are detailed in Table 3.2.5, and values are found to be very similar across the pressures of CO_2 investigated. As a result, the number of open windows remains very similar for individual materials as CO_2 pressure varies. Cations may become more labile however, as window diameters increase, weakening the overall cation-framework interaction.

Lozinska *et al.* previously reported the kinetic behaviour of CO_2/CH_4 separation on select Li-containing samples of zeolite Rho using breakthrough curves, and some of these were produced in Figure 3.2.4.[13] They found that incorporating Na cations gave slightly improved, though very similar, kinetic behaviour, evidenced by a sharper CO_2 curve at breakthrough compared to $Li_{9.8}$-Rho (3.9). They attributed this to a slightly wider window size. The incorporation of 1.8 Cs cations was found to greatly improve the properties of the sample, with both a steeper curve for CO_2 adsorption and a shift to a later time (broadly equivalent to the x axis when flow rates are constant between samples) for CO_2 breakthrough to occur. The latter was given as proof of better dynamic

separation of CO_2/CH_4 and attributed to the larger window size again, here enabling unhindered CO_2 percolation, whilst retaining high CO_2/CH_4 selectivity.

Table 3.2.5. Crystallographic details of $Li_{9.8}$-, $Li_{5.5}Zn_{2.2}$- and $Li_{7.3}Cs_{2.5}$-Rho (3.9) samples refined with PND data under varying pCO_2, including CO_2 pressure, R_{wp}, unit cell parameter, cation content per unit cell (cations/uc) of each site, the number of open windows per unit cell and free window diameter.

Sample	*P* (mbar)	R_{wp}	*a* (Å)	Cations/uc			Open windows	Free window diameter (Å)
				S6R	S8R	D8R		
$Li_{9.8}$	0	3.3%	14.255(1)	6.6(1) Li	3.6(2) Li		2.4(2)	2.0(1)
	26	4.9%	14.297(1)	6.1(2) Li	3.8(5) Li		2.2(5)	2.1(1)
	70	5.7%	14.340(1)	6.4(2) Li	3.6(5) Li		2.4(5)	2.1(1)
	175	5.9%	14.480(1)	6.4(3) Li	3.4(7) Li		2.6(7)	2.4(1)
	1200	7.8%	14.642(1)	6.4(5) Li	3.4(10) Li		2.6(10)	2.8(1)
$Li_{7.3}Cs_{2.5}$	0	2.9%	14.444(1)	5.8(1) Li	1.9(2) Li	2.3(1) Cs	1.8(2)	2.4(1)
	1	2.7%	14.470(1)	6.1(1) Li	1.9(2) Li	2.5 Cs	1.6(2)	2.4(1)
	25	3.2%	14.517(1)	6.4(1) Li	1.9(2) Li	2.5 Cs	1.6(2)	2.6(1)
	190	4.6%	14.566(1)	6.2(2) Li	1.4(2) Li	2.5 Cs	2.1(2)	2.7(1)
$Li_{5.5}Zn_{2.2}$	0	3.6%	14.365(1)	3.8(2) Li, 0.6(1) Zn	1.7(2) Li, 1.4(1) Zn		2.9(2)	2.2(1)
	24	3.6%	14.438(1)	3.6(3) Li, 0.4(1) Zn	1.9(5) Li, 1.7(2) Zn		2.4(5)	2.3(1)
	159	4.3%	14.523(1)	3.6(6) Li, 0.4(2) Zn	1.9(7) Li, 1.7(2) Zn		2.4(7)	2.5(1)

Additional data for $Li_{5.5}Zn_{2.2}$-Rho (3.9) is also provided in Figure 3.2.4, showing CO_2 breakthrough shifted further to the right compared to the $Li_{8.0}Cs_{1.8}$-Rho (3.9) material previously reported and with an even sharper curve. The free window diameter of this material is smaller than the investigated $Li_{7.3}Cs_{2.5}$-Rho (3.9) and so window size alone does not seem able to be responsible for the improved CO_2 kinetics of the $Li_{5.5}Zn_{2.2}$-material. The $Li_{8.0}Cs_{1.8}$-Rho (3.9) sample refined by Lozinska *et al*. however was found to have a unit cell parameter of 14.4113(1) Å, compared with that of 14.444 Å for the $Li_{7.3}Cs_{2.5}$-sample investigated here, and so will have narrower windows, more similar to that of the $Li_{5.5}Zn_{2.2}$-material with *a* = 14.365 Å. It may in fact be that the windows of the latter sample, whilst smaller, are sufficiently large to enable relatively uninhibited CO_2 percolation whilst the divalent Zn cations lead to increased open windows, further enabling CO_2 diffusion. Indeed, for the materials investigated here, $Li_{5.5}Zn_{2.2}$-Rho (3.9) has 2.9 open windows per unit cell, compared to just 1.8 for the $Li_{7.3}Cs_{2.5}$-form. Another

consideration is the lability of the species, with the steric bulk of the Cs cations likely hindering the dispersal of CO_2 within the structure compared to the smaller Zn^{2+} species, although an unoccupied window would be faster to traverse than one containing a labile cation. As such, the larger number of open windows seems to be an important additional factor, along with the size of the window.

3.2.7 Summary

Samples of Li-containing zeolite Rho with Si/Al = 3.9 were successfully investigated as potential selective sorbent materials. The use of PND enabled refinement of Li^+ positions and occupancies within zeolite Rho, even in the presence of adsorbed CO_2. However, there were limitations to this, with refinement becoming progressively more challenging as further adsorbates were introduced. Whilst co-refinement of Li and Zn cations in similar positions was possible, despite opposed neutron scattering lengths, this was ultimately found unreliable for data obtained at higher pressures of CO_2.

Li cations were found using PND data to sit in S6R and S8R sites in all materials, as was Zn^{2+} in $Li_{9.8-2x}Zn_x$-Rho (3.9) materials, whilst Cs^+ species were located solely in the D8R site. The $Li_{5.5}Zn_{2.2}$-Rho (3.9) material was found to be an optimum composition for the kinetic separation of O_2 from Ar, with a window diameter enabling selective separation whilst exhibiting good O_2 diffusion kinetics. Upon exposure to CO_2, all 3 samples investigated with PND experienced unit cell expansion as CO_2 was adsorbed. Breakthrough experiments also showed $Li_{5.5}Zn_{2.2}$-Rho (3.9) to be a good candidate for selected CO_2/CH_4 adsorption, possessing larger windows than the $Li_{9.8}$-form and more open windows than the $Li_{7.3}Cs_{2.5}$-sample.

3.3 Larger family members

3.3.1 Introduction

The previous part of this chapter looked at the rather simple **RHO** structure and the structural behaviour of the zeolite Rho (3.9) material under different conditions. As has been discussed, the **RHO** framework is the first in a broader family of embedded isoreticular framework types. The following looks specifically at the members ZSM-25

and PST-20 or RHO-G4 and G5, respectively. In 2015, these were the largest zeolites by unit cell volume, after PST-25 (RHO-G6).[2]

Lee *et al*. found that the larger members of the family (G > 1) had improved CO_2 adsorption kinetics, which they attributed to the presence of additional 8-ring windows between cavities.[6] Cations in these windows were thought to be more labile than those in *d8r* units, present in every channel within zeolite Rho, enabling more rapid CO_2 percolation. Min *et al*. also found that these materials could possess non-Type I adsorption, with a "kink" in their CO_2 adsorption isotherms, particularly for Na-ZSM-25 and Na-PST-20.[42] Similar behaviour was observed by Lozinska *et al*. in Na-Rho, but only at very low pressure,[10] and was not observed in Na,TEA-forms (TEA = tetraethylammonium) of the materials by Min *et al*.[43]

The presence of further cavities in the structure relative to the **RHO** framework clearly impacts adsorption properties yet investigation of the materials is hindered by their large size and distortion upon dehydration. This makes an accurate starting model for Rietveld refinement a problem, as the relaxed framework initially discovered is not close enough. Greenaway *et al*. investigated a fully dehydrated form of Na,H-ECR-18 (RHO-G3) for the first time and used a computational modelling approach to generate an initial starting model.[44] This was done using by fixing the unit cell parameter at progressively smaller values and minimising the energy of the structure by varying framework positions.

Impressively, Guo *et al*. reported the refined structures of hydrated ZSM-25 and PST-20 samples.[2] Previously the structure of ZSM-25, synthesised in 1979,[45] had remained unknown. The flexible nature of these zeolites upon dehydration however requires knowledge of their dehydrated structures to better understand their behaviour, particularly for application in gas adsorption. Prior to this work, the dehydrated structures of any materials in the RHO family of zeolites had not been reported. In this chapter, the refinement of ZSM-25 and PST-20 was attempted using the same method of Greenaway *et al*. for ECR-18.[44]

3.3.2 Acknowledgements

Samples of ZSM-25 and PST-20 were obtained from collaborators in the group of Prof Suk Bong Hong at POSTECH, South Korea. Ion exchange and calcination of samples was carried out by Dr Alex Greenaway. PXRD patterns of Na,H- and Na,TEA-ZSM-25 materials were collected by Dr Greenaway and Prof Paul A. Wright at beamline ID31, ESRF, Grenoble with assistance from Dr Andrew N. Fitch, and at beamline I11 at DLS, Oxfordshire aided by Dr Stephen S. Thompson, respectively. Na,TEA-ZSM-25 was dehydrated in place by coworkers at DLS, whilst the Na,H-form was dehydrated on a glass line and flame sealed before analysis at ESRF. Dr Paul A. Cox provided energy minimised silica frameworks at reduced unit cell volumes for the materials, following the same method used in the study of dehydrated Na,H-ECR-18.[44] Laboratory VPXRD data of ZSM-25 samples was obtained by Dr Veselina M. Georgieva with aid from Dr Yuri Andreev. PST-20 data was collected at beamline I11 at DLS, Oxfordshire aided by Dr Greenaway and Prof Wright, with assistance from Dr Thompson.

3.3.3 ZSM-25

As discussed previously, Guo *et al*. reported the structures of hydrated forms of ZSM-25, specifically the as-prepared $Na_{285}TEA_{40}$- and calcined $Na_{285}H_{40}$-materials (framework composition $Si_{1115}Al_{325}O_{2880}$), found to also contain 600 and 800 molecules of water per unit cell, respectively. These samples possess unit cell volumes of *ca*. 91,125 Å^3, with 1440 T sites per unit cell and Si/Al = 3.4. No structure has previously been reported for dehydrated forms, however, with unit cell volumes *ca*. 78,000 Å^3. The refinement process for such a material is complicated by the distortion in 2 ways: the change in framework positions and the loss of symmetry. Displacement within the large unit cell of framework sites from the hydrated positions quickly renders the hydrated form inadequate as a starting model for refinement of the dehydrated structure. This is exacerbated by the decrease in symmetry from *Im*-3*m to I*-43*m*, also observed for other Rho-family materials. This increases the number of symmetry-inequivalent sites, with the number of framework T and O sites increasing from 16 and 40 to 30 and 70, respectively.

Models provided by Dr Cox at artificially reduced unit cell volumes served as good starting points for the framework structures of dehydrated Na,H- and Na,TEA-ZSM-25,

in particular a model with a unit cell parameter of 43.0 Å, respectively. The same technique was used to provide a basic structure for a PST-20 impurity present within the sample. Sites previously reported by Guo *et al*. in the hydrated forms of the materials also served as potential extraframework sites.[2] TEA^+ species were reported as sitting in the *pau* cavities along the length of the scaffold moiety, and in *plg* cavities along the unit cell body diagonal and these positions, orientations and occupancies were replicated in the starting model. Placement of Na cations was less straightforward, however. Window geometries change as the framework distorts and there are no solvating water species, altering the energetics of cation sites. As such, all potential 8-ring and 6-ring sites within the structure were identified by analysing the framework in the asymmetric unit. These may be reasonably expected to host Na^+ species, and were prescribed low levels of occupancy in starting models.

The refinement process followed the same overall process as other materials described in this work, with a few additional considerations. Investigation of cation occupancies were often repeated to validate the occupancies found. Cation positions could stray from their intended site to another within the structure, and framework sites could wander significantly from idealised corner-sharing tetrahedra. Both required the implementation of strong restraints, with relative strengths varied iteratively. This was required as increasing the weighting of restraints to ensure a reasonable structure in one part of the unit cell could cause a new part to stray from an idealised geometry. This is because as one restraint is weighted more heavily, the relative weights of other restraints in use are effectively lowered. Ultimately, structures for both dehydrated materials were refined successfully, as shown in Figure 3.3.1 with associated Rietveld plots presented in Figure 3.3.2. Refinement details are provided in Table 3.3.1.

Table 3.3.1. Crystallographic details of refined dehydrated ZSM-25 samples, including space group, unit cell parameter, volume and goodness of fit. Hydrated data is reproduced from Guo et al. for comparison.[2] Dehydrated and hydrated data is indicated by dh and h, respectively.

Sample	R_{wp}	**Space Group**	***a* (Å)**	***V* (Å^3)**
Na,H-ZSM-25 (dh)	2.4%	*I*-43*m*	42.631(1)	77480(5)
Na,TEA-ZSM-25 (dh)	3.1%	*I*-43*m*	42.980(1)	79396(6)
Na,H-ZSM-25 (h)		*Im*-3*m*	44.924(2)	90665(6)
Na,TEA-ZSM-25 (h)		*Im*-3*m*	45.0711(3)	91558(2)

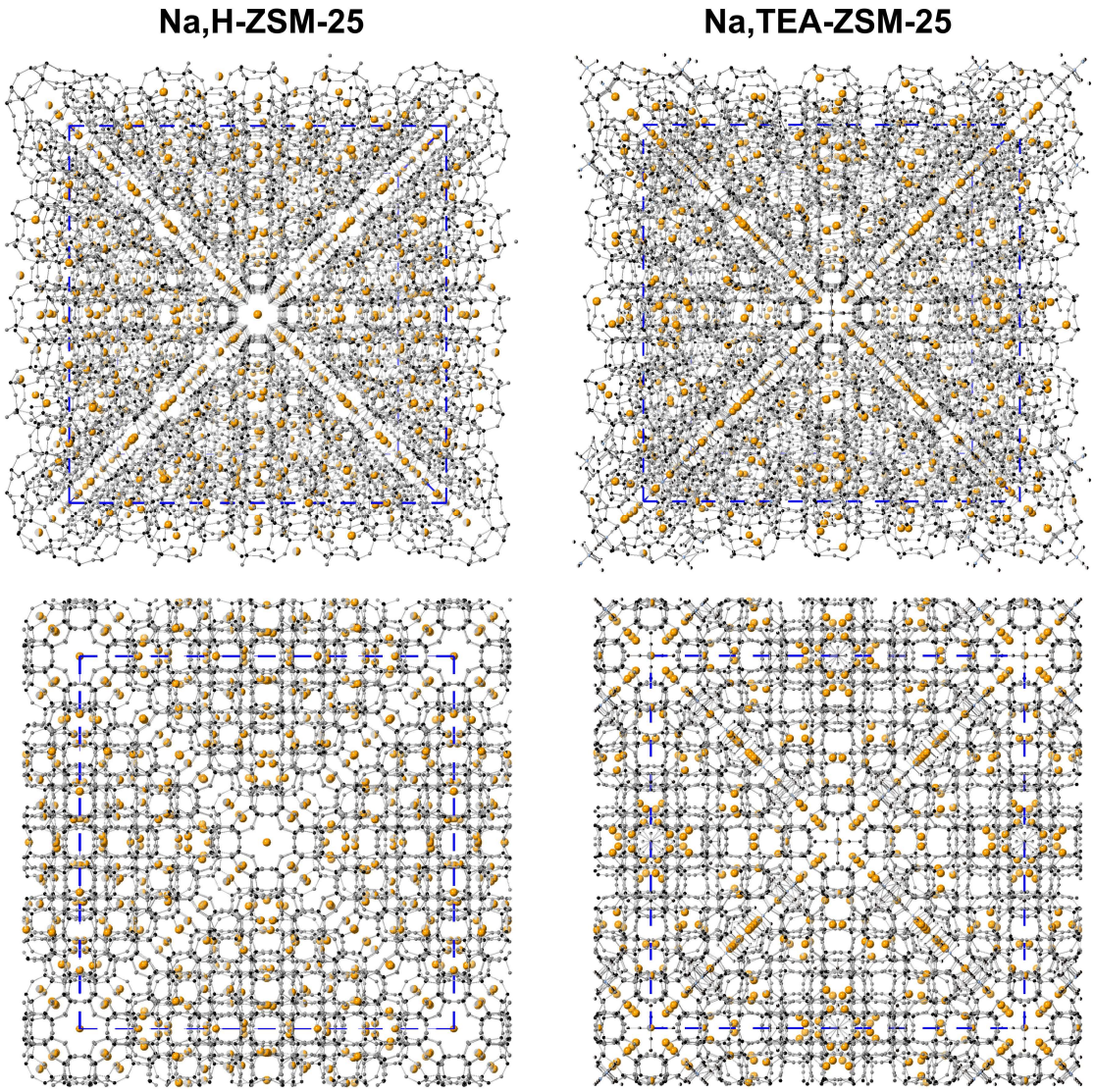

Figure 3.3.1. Refined structures of dehydrated (left) Na,H- and (right) Na,TEA-ZSM-25, with and without perspective. T and O sites are shown in black and grey, with extraframework Na, C and N sites shown in orange, black and blue, respectively, and fractional occupancy indicated by partial shading. The unit cell is indicated by the dashed blue line.

As can be seen in Table 3.3.1, the unit cells undergo significant distortions relative to the hydrated structures reported by Guo *et al.*,[2] which equates to a 15% and 13% reduction in unit cell volume for the Na,H- and Na,TEA-forms, respectively. This distortion has an impact on all window geometries within the materials, a selection of which is given in Figure 3.3.3, along with comparable experimental and computationally acquired structures. The less distorted as-prepared Na,TEA-form can be attributed to the presence of the larger TEA cations, propping open the structure slightly, or to a lower number of high charge density metal cations interacting with the framework.

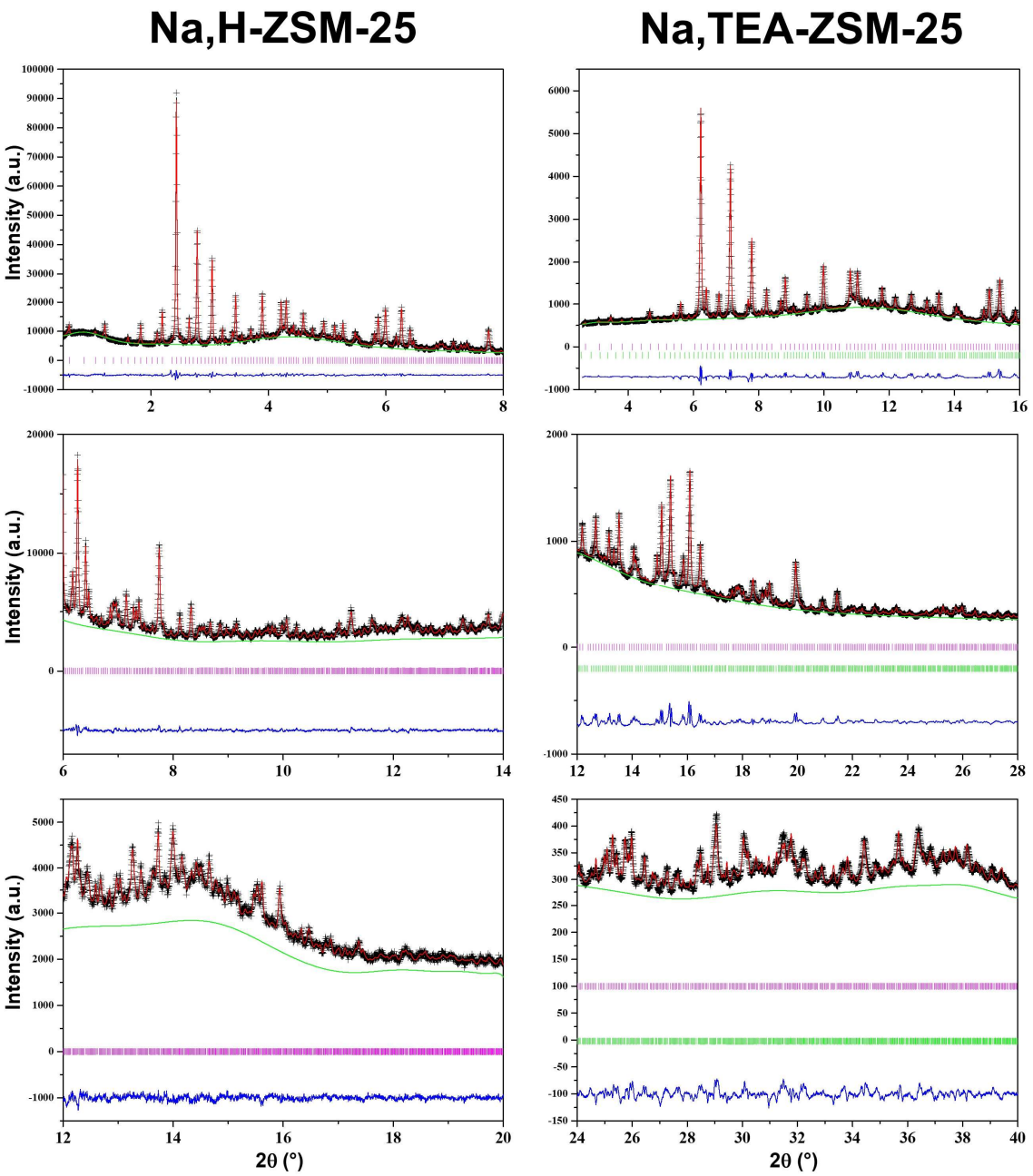

Figure 3.3.2. Rietveld plots of dehydrated (left) Na,H- and (right) Na,TEA-ZSM-25. Observed and calculated patterns are shown in black and red, with background and difference curves depicted in green and blue, respectively. Tick marks are given in pink with additional PST-20 impurity tick marks given in green for the Na,TEA-ZSM-25 sample. ((left) ID31, ESRF, λ = 0.320012 Å, (right) I11, DLS, λ = 0.0.826956 Å).

Synchrotron data, shown in Appendix III.I.I, obtained by Dr Greenaway and Prof Wright of the Na,TEA-material under CO_2 pressure found that the unit cell had expanded with adsorption, as with zeolite Rho, but attempts to refine the sample were unsuccessful. The size of the structure and the large number of extra-framework species, including

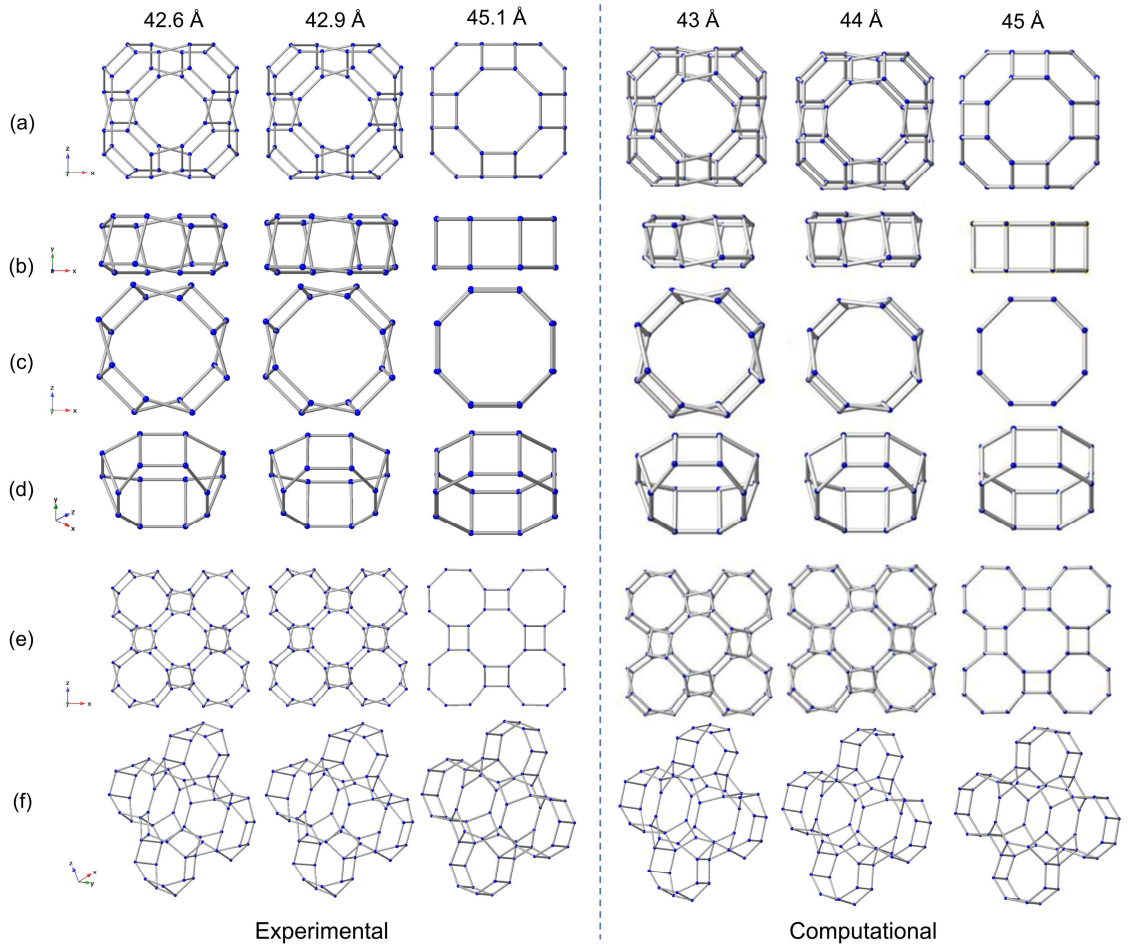

Figure 3.3.3. A selection of structural units present in ZSM-25, from left to right, in dehydrated Na,H-; dehydrated Na,TEA-; hydrated Na,TEA- and computationally modelled structural forms. Corresponding unit cell parameters displayed at the top. Structural units include (a) lta cages, (b,c,d) d8r units, (e,f) pau and adjacent oto cavities. Reproduced from Verbraeken et al.[46]

CO_2, proved too much despite using a computational model similar in unit cell parameter (44 Å) and implementing many restraints.

Instead, to examine how the structure responds to CO_2, variable pressure PXRD (VPXRD) patterns were obtained by Dr Georgieva. These were fitted using either the dehydrated or hydrated structures as a rough model and refining the unit cell parameter whilst keeping the unit cell contents constant. Dr Georgieva investigated data at 298 K whilst I examined 328 K data. Both data sets show a step in unit cell parameter at *ca.* 43.55 Å, as shown in Figure 3.3.4. Similar behaviour is observed in the CO_2 adsorption isotherm, with a step occurring at a CO_2 uptake *ca.* 0.6 mmol g^{-1}.[46]

Analysis of the free window diameters present in the material obtained from synchrotron data is shown in Figure 3.3.5. Almost all of the windows are smaller in the

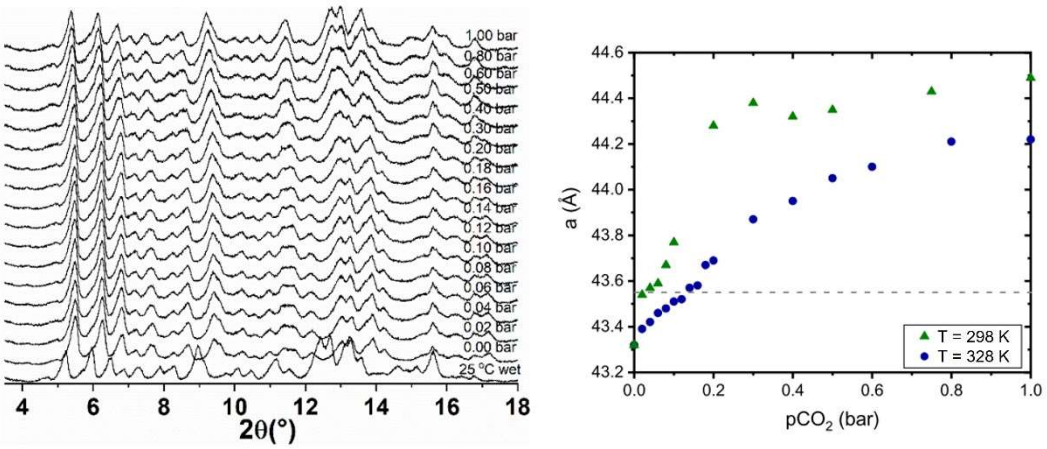

Figure 3.3.4. ZSM-25 VPXRD data: (left) patterns obtained at 328 K, with CO_2 pressures as labeled and (right) unit cell parameters obtained by Dr Veselina M. Georgieva and myself from such data. Reproduced from Verbraeken et al.[46] *(PANalytical, Mo K$\alpha_{1,2}$, λ = 0.711 Å).*

dehydrated form than in the hydrated state of the material. All of the windows are found to be above the 2.3 Å threshold thought to be required after considering the work of Cook and Conner for the percolation of CO_2 throughout the structure. Considering the 2.0 Å found in the related $Li_{9.8}$-Rho (3.9) material, which still allows CO_2 adsorption, these may be considered more than sufficient for CO_2 percolation. The cavities within the material are highly connected in an intricate pore structure, which makes it impossible to attribute adsorption behaviour to any given set of windows.

3.3.4 PST-20

The complexities of the ZSM-25 structure is exacerbated when looking at the even larger PST-20 structure. As for ZSM-25, Guo *et al*. published the structure of the hydrated as-prepared form of PST-20, with composition $Na_{194}Sr_{194}TEA_{56}[Si_{2002}Al_{638}O_{5280}].(H_2O)_{600}$.[2] The reported unit cell volume of the material is 166,772 Å^3, with 2640 T sites per unit cell and Si/Al = 3.1. Again, the hydrated form adopts the *Im*-3*m* space group, whilst the dehydrated material fits *I*-43*m*, and the number of symmetry-inequivalent sites increases from 29 to 55 and from 70 to 125 for framework T and O sites, respectively. The aim of this work was to successfully refine the structure of a Na-exchanged sample, with composition $Na_{388}TEA_{56}[Si_{2002}Al_{638}O_{5280}]$ after dehydration.

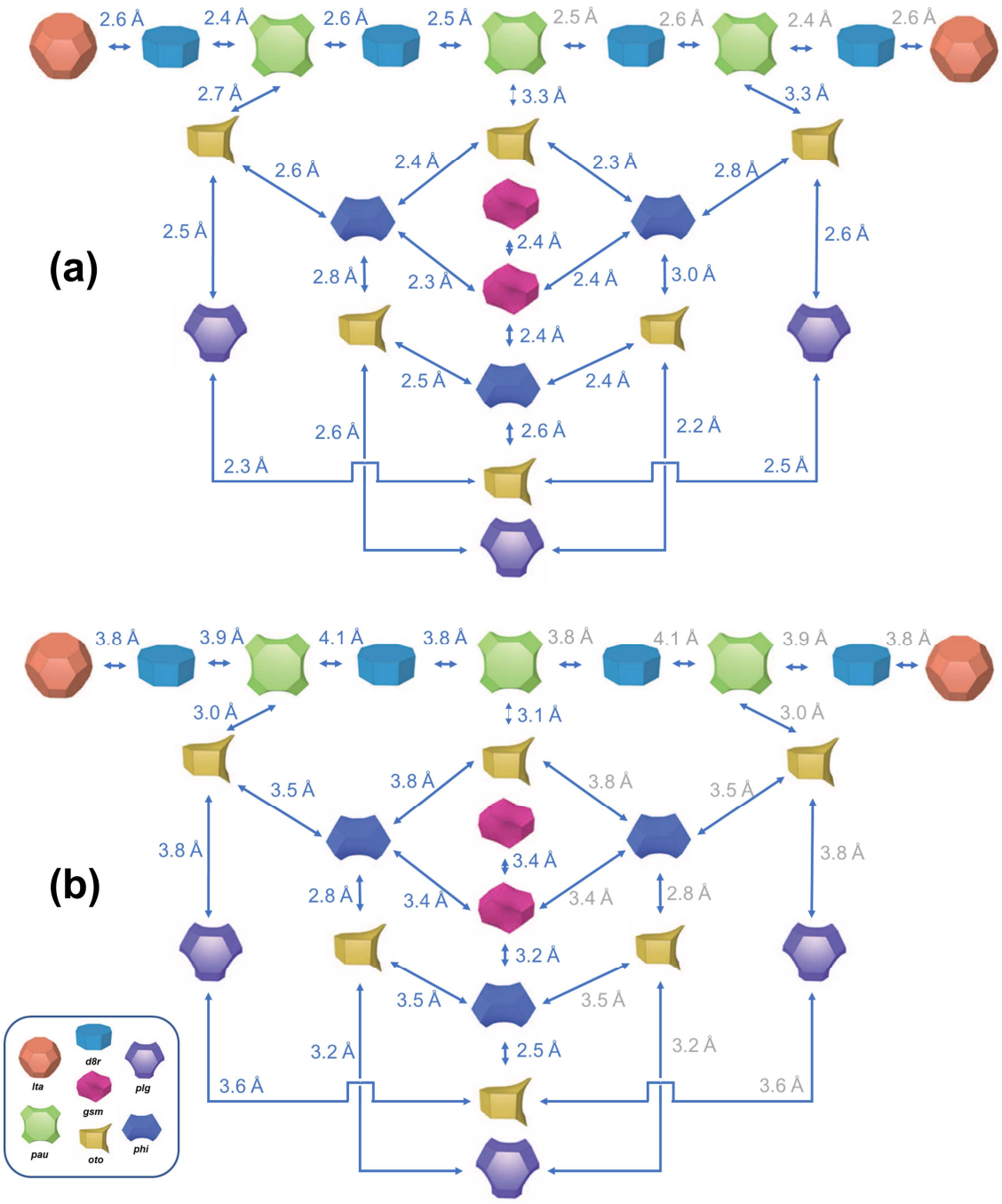

Figure 3.3.5. Free diameters of windows between cavities in (a) dehydrated and (b) hydrated Na,TEA-ZSM-25. Cavities are as given in the key and arrows depict connectivity. Greyed out numbers indicate symmetry related to an already shown window size.

The same approach was used as for ZSM-25, using a computational modelled structure with a = 51.0 Å as a starting model for dehydrated a Na,TEA-form of PST-20. Initial refinement of the PXRD data shown in Appendix III.I.II, however, found a = 52.720 Å. Whilst the model used is closer than the framework of the hydrated form reported by Guo *et al.* (a = 55.044 Å),[2] the difference in unit cell parameter may be too large for

accurate refinement of the structure. The ultimate structure found after refinement of this model is shown in Figure 3.3.6, with the Rietveld plot given in Appendix IV.V and a corresponding R_{wp} = 2.4%.

Unfortunately, the T-O distances spanned too wide a range, from 1.50 – 1.96 Å. Iterative tightening of problematic distances became a Sisyphean task, as new distances would stray from the ideal to replace those that had improved. As such, the refinement of the initial PST-20 model was unsuccessful as, whilst it provided a good fit of the experimental diffraction data, the structure contained multiple unrealistic bond lengths and angles. The refinement of this structure may be possible with an initial framework structure closer to that of the experimental material.

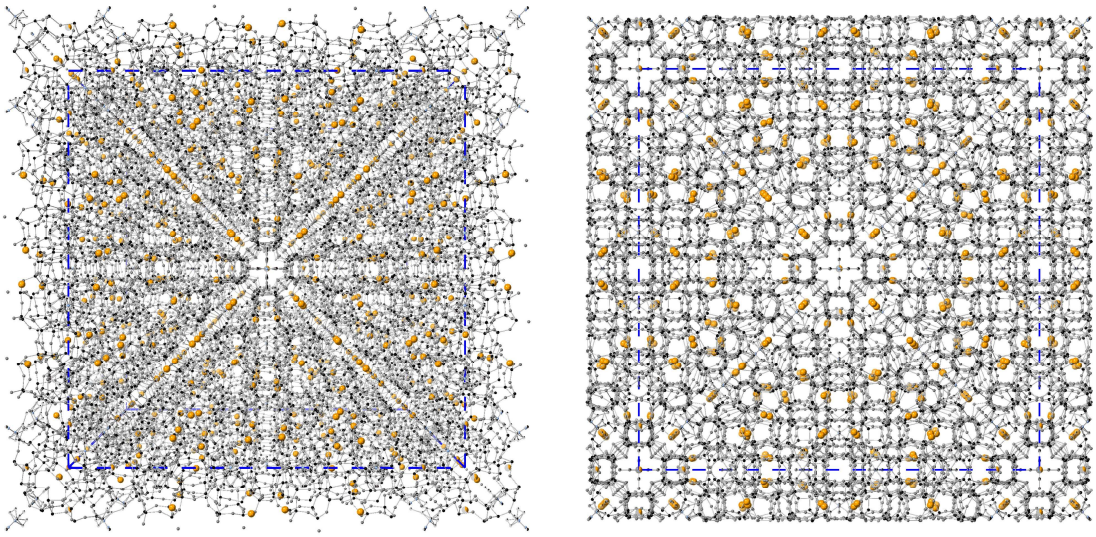

Figure 3.3.6. Refined structure of dehydrated Na,TEA-PST-20, with and without perspective. T and O sites are shown in black and grey, with extraframework Na, C and N sites shown in orange, black and blue, respectively, and fractional occupancy indicated by partial shading. The unit cell is indicated by the dashed blue line.

3.3.5 Summary

The structures of dehydrated forms of ZSM-25 were successfully refined but their large size makes a detailed analysis of the materials complex, particularly with a view to explaining experimental behaviour. A detailed examination of the crystal structures under CO_2 adsorption could not be carried out, as the increased consideration of CO_2 molecules throughout the structure, along with likely cation migration, meant that

refinement proved impossible. Instead, fitting of the unit cell parameter alone was the only choice for samples under pressure of CO_2.

PST-20 proved too complex a structure to be readily refined, as framework bond distances in the dehydrated form of the material investigated erred from desired values. The refinement of this structure could prove to be possible if the initial starting model was closer, improving initial framework positions. Indeed, as the volume of a given structure in this family increases, the starting model must be closer to the true structure as the number of variables increases greatly with each generation.

3.4 Conclusion

This chapter looked at a range of materials within the extended Rho family of zeolites. In the small unit cell Rho material, PND enabled the refinement of Li-containing materials, finding Li^+ positions and occupancies. This proved more challenging, though still doable, in the presence of adsorbed CO_2 species, and with the co-refinement of Li and Zn cations in similar positions. Refinement of structures at high pressures of CO_2 were less reliable, particularly in the mixed Li,Zn-form. Analysis of these structures enables the explanation of the relative behaviours of the materials as selective O_2/Ar and CO_2/CH_4 adsorbents. In both cases this could be related to the size of 8-rings in the structure and their occupancy, rendering the $Li_{5.5}Zn_{2.2}$-Rho (3.9) material particularly good for both applications.

The larger materials ZSM-25 and PST-20 were more problematic under more simple conditions. Whilst the structures of both materials have been reported in their hydrated forms, the challenge is significantly greater upon dehydration due to the change in symmetry from *Im*-3*m* to *I*-43*m*. Dehydrated forms of ZSM-25 were successfully refined but the incorporation of CO_2 proved too demanding. Similarly, the structure of dehydrated PST-20 could not be refined with a truly meaningful structure, which may in part be due to using an inadequate starting model, a problem itself aggravated by the large size of the structure.

Whilst significant problems and complications can be tackled and investigated with the smaller **RHO** framework, this is not the case for the larger structures investigated here.

A relatively simple case of dehydration is extremely challenging and further considerations, such as adsorbates or mixed cation systems, are even more so. Furthermore, the large size of the later structures hinders structural understanding of their behaviour.

3.5 References

(1) Baerlocher, C.; McCusker, L. B. IZA Database of Zeolite Structures, http://www.iza-structure.org/databases/, accessed October 2023.

(2) Guo, P.; Shin, J.; Greenaway, A. G.; Min, J. G.; Su, J.; Choi, H. J.; Liu, L.; Cox, P. A.; Hong, S. B.; Wright, P. A.; Zou, X. A Zeolite Family with Expanding Structural Complexity and Embedded Isoreticular Structures. *Nature* **2015**, *524* (7563), 74–78.

(3) Cho, J.; Choi, H. J.; Guo, P.; Shin, J.; Zou, X.; Hong, S. B. Embedded Isoreticular Zeolites: Concept and Beyond. *Chem. - A Eur. J.* **2017**, 1–9.

(4) Min, J. G.; Choi, H. J.; Shin, J.; Hong, S. B. Crystallization Mechanism of a Family of Embedded Isoreticular Zeolites. *J. Phys. Chem. C* **2017**, *121* (30), 16342–16350.

(5) Shin, J.; Xu, H.; Seo, S.; Guo, P.; Min, J. G.; Cho, J.; Wright, P. A.; Zou, X.; Hong, S. B. Targeted Synthesis of Two Super-Complex Zeolites with Embedded Isoreticular Structures. *Angew. Chemie - Int. Ed.* **2016**, *128* (16), 5012–5016.

(6) Lee, H.; Shin, J.; Choi, W.; Choi, H. J.; Yang, T.; Zou, X.; Hong, S. B. PST-29: A Missing Member of the RHO Family of Embedded Isoreticular Zeolites. *Chem. Mater.* **2018**, *30* (19), 6619–6623.

(7) Robson, H. E.; Shoemaker, D. P.; Ogilvie, R. A.; Manor, P. C. Synthesis and Crystal Structure of Zeolite Rho—A New Zeolite Related to Linde Type A. In *Molecular Sieves*; Meier, W. M., Uytterhoeven, J. B., Eds.; American Chemical Society: Washington DC, 1973; Vol. 121, pp 106–115.

(8) Parise, J. B.; Abrams, L.; Gier, T. E.; Corbin, D. R.; Jorgensen, J. D.; Prince, E. Flexibility of the Framework of Zeolite Rho - Structural Variation From 11 to 573-K - a Study Using Neutron Powder Diffraction Data. *J. Phys. Chem.* **1984**, *88* (11), 2303–2307.

(9) Johnson, G. M.; Reisner, B. A.; Tripathi, A.; Corbin, D. R.; Toby, B. H.; Parise, J. B. Flexibility and Cation Distribution upon Lithium Exchange of Aluminosilicate and Aluminogermanate Materials with the RHO Topology. *Chem. Mater.* **1999**, *11* (10), 2780–2787.

(10) Lozinska, M. M.; Mangano, E.; Mowat, J. P. S.; Shepherd, A. M.; Howe, R. F.; Thompson, S. P.; Parker, J. E.; Brandani, S.; Wright, P. A. Understanding Carbon Dioxide Adsorption on Univalent Cation Forms of the Flexible Zeolite Rho at Conditions Relevant to Carbon Capture from Flue Gases. *J. Am. Chem. Soc.* **2012**, *134* (42), 17628–17642.

(11) Nenoff, T. M.; Parise, J. B.; Jones, G. A.; Galya, L. G.; Corbin, D. R.; Stucky, G. D. Flexibility of the Zeolite RHO Framework. In Situ X-Ray and Neutron Powder Structural Characterization of Cation-Exchanged BePO and BeAsO RHO Analogs. *J. Phys. Chem.* **1996**, *100* (33), 14256–14264.

(12) Lozinska, M. M.; Mowat, J. P. S.; Wright, P. A.; Thompson, S. P.; Jorda, J. L.; Palomino, M.; Valencia, S.; Rey, F. Cation Gating and Relocation during the Highly Selective "Trapdoor" Adsorption of CO_2 on Univalent Cation Forms of Zeolite Rho. *Chem. Mater.* **2014**, *26* (6), 2052–2061.

(13) Lozinska, M. M.; Mangano, E.; Greenaway, A. G.; Fletcher, R.; Thompson, S. P.; Murray, C. A.; Brandani, S.; Wright, P. A. Cation Control of Molecular Sieving by Flexible Li-Containing Zeolite Rho. *J. Phys. Chem. C* **2016**, *120* (35), 19652–19662.

(14) Lee, Y.; Reisner, B. A.; Hanson, J. C.; Jones, G. A.; Parise, J. B.; Corbin, D. R.; Toby, B. H.; Freitag, A.; Larese, J. Z. New Insight into Cation Relocations within the Pores of Zeolite Rho: In Situ Synchrotron X-Ray and Neutron Powder Diffraction Studies of Pb- and Cd-Exchanged Rho. *J. Phys. Chem. B* **2001**, *105* (30), 7188–7199.

(15) Lozinska, M. M.; Jamieson, S.; Verbraeken, M. C.; Miller, D. N.; Bode, B. E.; Murray, C. A.; Brandani, S.; Wright, P. A. Cation Ordering and Exsolution in Copper-Containing Forms of the Flexible Zeolite Rho (Cu,M-Rho; M=H, Na) and Their Consequences for CO_2 Adsorption. *Chem. - A Eur. J.* **2021**, *27* (51), 13029–13039.

(16) Palomino, M.; Corma, A.; Jordà, J. L.; Rey, F.; Valencia, S. Zeolite Rho: A Highly

Selective Adsorbent for CO_2/CH_4 Separation Induced by a Structural Phase Modification. *Chem. Commun.* **2012**, *48* (2), 215–217.

(17) Araki, S.; Kiyohara, Y.; Tanaka, S.; Miyake, Y. Crystallization Process of Zeolite Rho Prepared by Hydrothermal Synthesis Using 18-Crown-6 Ether as Organic Template. *J. Colloid Interface Sci.* **2012**, *376* (1), 28–33.

(18) Shang, J.; Li, G.; Singh, R.; Gu, Q.; Nairn, K. M.; Bastow, T. J.; Medhekar, N.; Doherty, C. M.; Hill, A. J.; Liu, J. Z.; Webley, P. A. Discriminative Separation of Gases by a "Molecular Trapdoor" Mechanism in Chabazite Zeolites. *J. Am. Chem. Soc.* **2012**, *134* (46), 19246–19253.

(19) Shang, J.; Hanif, A.; Li, G.; Xiao, G.; Liu, J. Z.; Xiao, P.; Webley, P. A. Separation of CO_2 and CH_4 by Pressure Swing Adsorption Using a Molecular Trapdoor Chabazite Adsorbent for Natural Gas Purification. *Ind. Eng. Chem. Res.* **2020**, *59* (16), 7857–7865.

(20) Du, T.; Fang, X.; Liu, L.; Shang, J.; Zhang, B.; Wei, Y.; Gong, H.; Rahman, S.; May, E. F.; Webley, P. A.; Li, G. An Optimal Trapdoor Zeolite for Exclusive Admission of CO_2 at Industrial Carbon Capture Operating Temperatures. *Chem. Commun.* **2018**, *54* (25), 3134–3137.

(21) Wright, P. A. *Microporous Framework Solids*; Royal Society of Chemistry: Cambridge, 2008.

(22) US Pat. 5159816, 1992.

(23) Breck, D. W. *Zeolite Molecular Sieves : Structure, Chemistry, and Use*; Robert E. Krieger Publishing: Malabar, FLA, USA, 1984.

(24) Ansón, A.; Kuznicki, S. M.; Kuznicki, T.; Dunn, B. G.; Eyring, E. M.; Hunter, D. B. Separation of Argon and Oxygen by Adsorption on a Titanosilicate Molecular Sieve. *Sep. Sci. Technol.* **2009**, *44* (7), 1604–1620.

(25) Farooq, S. Sorption and Diffusion of Oxygen and Nitrogen in Molecular Sieve RS-10. *Gas Sep. Purif.* **1995**, *9* (3), 205–212.

(26) Yang, R. T. *Gas Separation by Adsorption Processes*; Butterworths: Boston, 1987.

(27) US Pat. 7501009, 2009.

(28) Rege, S. U.; Yang, R. T. Kinetic Separation of Oxygen and Argon Using Molecular Sieve Carbon. *Adsorption* **2000**, *6* (1), 15–22.

(29) US Pat. 9925514 B2, 2018.

(30) Bruce, E. L. Small Pore Zeolites for Carbon Capture, MChem Thesis, Univerisity of St Andrews, 2016.

(31) US Pat. 10646848 B2, 2020.

(32) Xia, H.; Hu, Y.; Bao, Q.; Zhang, J.; Sun, P.; Liang, D.; Wang, B.; Qiao, X.; Wang, X. Adsorption Separation of O_2/N_2 by Li-RHO Zeolite with High Oxygen Selectivity. *Microporous Mesoporous Mater.* **2023**, *350* (July 2022), 112442.

(33) Georgieva, V. M. Unpublished Work.

(34) Lee, Y.; Vogt, T.; Hriljac, J. A.; Parise, J. B. Discovery of a Rhombohedral Form of the Li-Exchanged Aluminogermanate Zeolite RHO and Its Pressure-, Temperature-, and Composition-Induced Phase Transitions. *Chem. Mater.* **2002**, *14* (8), 3501–3508.

(35) Kim, Y.; Seff, K. Crystal Structure of Hydrated Partially Zlnc(II)-Exchanged Zeolite A, Zn_5Na_2-A. *J. Phys. Chem* **1980**, *84*, 2823–2827.

(36) Smith, L. J.; Eckert, H.; Cheetham, A. K. Potassium Cation Effects on Site Preferences in the Mixed Cation Zeolite Li, Na-Chabazite. *Chem. Mater.* **2001**, *13* (2), 385–391.

(37) Newsam, J. M.; Jarman, R. H.; Jacobson, A. J. A Study of the Mixed $Na_{1-x}Li_x$ Zeolite A System by Powder X-Ray Diffraction. *J. Solid State Chem.* **1985**, *58* (3), 325–334.

(38) Shannon, R. D. Revised Effective Ionic Radii and Systematic Studies of Interatomic Distances in Halides and Chalcogenides. *Acta Crystallogr. Sect. A* **1976**, *32* (5), 751–767.

(39) Sears, V. F. Neutron Scattering Lengths and Cross Sections. *Neutron News* **1992**, *3* (3), 26–37.

(40) Vrabec, J.; Stoll, J.; Hasse, H. A Set of Molecular Models for Symmetric

Quadrupolar Fluids. *J. Phys. Chem. B* **2001**, *105* (48), 12126–12133.

(41) Cook, M.; Conner, W. C. How Big Are the Pores of Zeolites? In *Proceedings of the 12th International Zeolite Conference*; Treacy, M. M. J., Marcus, B. K., Bisher, M. E., Higgins, J. B., Eds.; Materials Research Society: Warrendale, PA, USA, 1999; pp 409–414.

(42) Min, J. G.; Kemp, K. C.; Lee, H.; Hong, S. B. CO_2 Adsorption in the RHO Family of Embedded Isoreticular Zeolites. *J. Phys. Chem. C* **2018**, *122* (50), 28815–28824.

(43) Min, J. G.; Kemp, K. C.; Hong, S. B. Zeolites ZSM-25 and PST-20: Selective Carbon Dioxide Adsorbents at High Pressures. *J. Phys. Chem. C* **2017**, *121* (6), 3404–3409.

(44) Greenaway, A. G.; Shin, J.; Cox, P. A.; Shiko, E.; Thompson, S. P.; Brandani, S.; Hong, S. B.; Wright, P. A. Structural Changes of Synthetic Paulingite (Na,H-ECR-18) upon Dehydration and CO_2 Adsorption. *Zeitschrift fur Krist.* **2015**, *230* (4), 223–231.

(45) US Pat. 4247416, 1981.

(46) Verbraeken, M. C.; Mennito, R.; Georgieva, V. M.; Bruce, E. L.; Greenaway, A. G.; Cox, P. A.; Min, J. G.; Hong, S. B.; Wright, P. A.; Brandani, S. Understanding CO_2 Adsorption in a Flexible Zeolite through a Combination of Structural , Kinetic and Modelling Techniques. *Sep. Purif. Technol.* **2021**, *256*, 117846.

4 Zeolite Merlinoite: Si/Al = 3.8

4.1 Introduction

In 1977, Passaglia *et al.*, reported the discovery of a new naturally-occurring zeolite found in central Italy.[1] They named it merlinoite in honour of the Italian crystallographer Prof Stefano Merlino and the refined structure was later reported by Galli *et al.*[2] Interestingly the authors noted that this material was already known, with Breck and Barrer *et al*. each synthesising phases such as "Linde W" and "K-M" in the 1950s.[3–5] This was only the second time that a natural zeolite had been found after its synthetic analogue, the first being mazzite.[1,6] Naturally occurring merlinoite has since been found throughout Europe as well as North America and the Indian and Pacific Oceans.[7]

A range of applications have been proposed for merlinoite materials, including removal of radioactive cations,[8] catalysis,[9–11] as fertilisers,[12–14] and as selective CO_2 adsorbents.[15–17] Industrial interest in applying merlinoite in separation technologies can be seen in the patent literature,[18–20] and the focus of this chapter is to examine materials for such applications.

The framework structure of zeolite merlinoite (framework type code **MER,** and henceforth "MER" is used as a shorthand for merlinoite materials) is composed of 8-rings connected by 4-rings. These form *pau*, *d8r* and *ste* cavities, shown in Figure 4.1.1. The connectivity of these building units forms a 3-dimensionally connected channel system, allowing for percolation of small guest species. The topology of the **MER** framework has maximum symmetry with space group *I*4/*mmm* but this is typically reduced to a lower symmetry with the incorporation of extra-framework cations.[21]

Flexible zeolites, such as zeolite Rho discussed in the previous chapter, distort upon dehydration to better coordinate extra-framework cations.[22] Merlinoite is another such material, with dehydration altering window size and geometry and consequently altering adsorption properties, as seen later. The site preference and charge density of different cations can be expected to alter window sizes and diffusivity, making it important in understanding gas adsorption behaviour.[23]

Before the first structural investigation of natural merlinoite by Galli *et al*. in 1979,[2] Solov'eva *et al*. produced a synthetic material which adopted the parent space group,

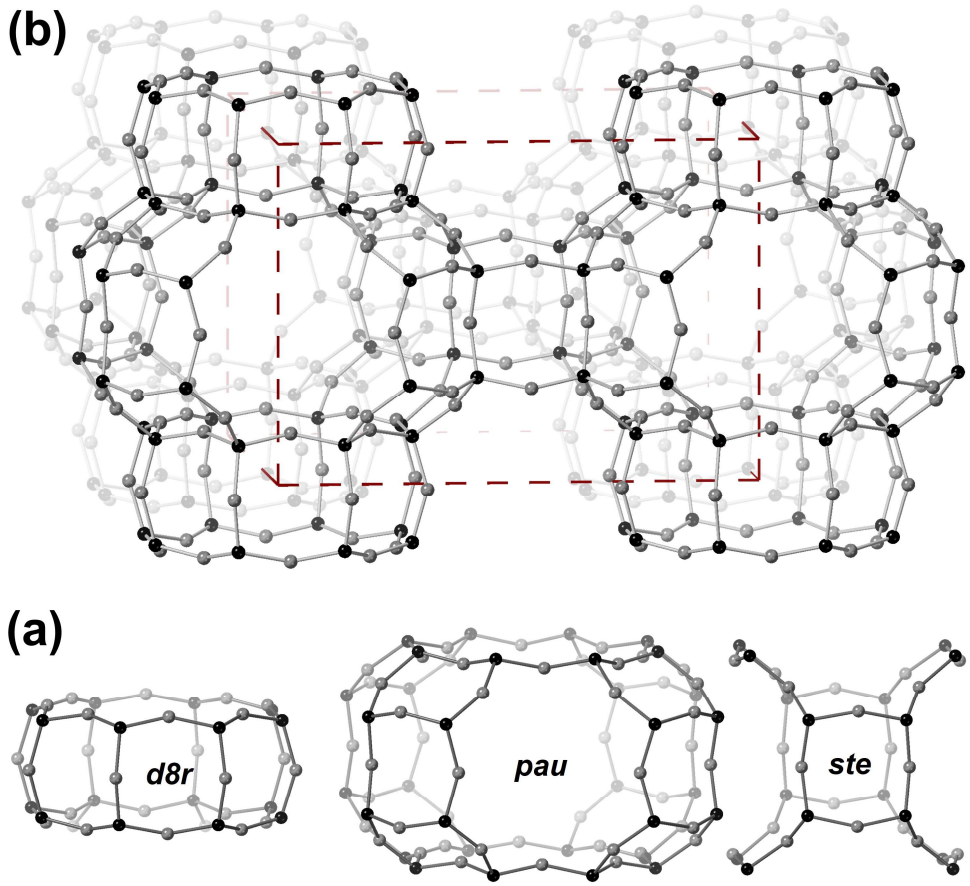

*Figure 4.1.1. Structural representation of zeolite merlinoite (framework type **MER**). (a) Cavity types present in **MER** and (b) the extended **MER** framework. Tetrahedral and O atoms are represented in black and grey, respectively, with the unit cell indicated by dashed red lines.*

*I*4/*mmm*.[24] Subsequent investigations of both natural and synthetic zeolites of varying compositions have more often been described using the *Immm* symmetry found by Galli *et al*., as detailed in Table 4.1.1.[25–28] Skofteland *et al*. reported the potential for phase changes in merlinoite upon dehydration, with a low Si/Al ratio material changing from the *Immm* space group to *Pnnm*, along with significant unit cell volume contraction of 12%.[29] Similar results were found by Pakhomova *et al*. on a naturally occurring form, again with a low Si/Al ratio, and a phase transition from *Immm* to $P4_2/nmc$.[7]

As can be seen from Table 4.1.1, whilst structural data has been reported for a range of merlinoite samples, most of these have high K^+ content, typically due to synthesis or natural formation conditions. Studies on a variety of cation forms of the same MER materials, and the subsequent effect on structure and adsorption, had not been reported until this work and the simultaneous work of Choi *et al*.[16]

*Table 4.1.1. Summary of literature studies of merlinoite samples, including Si/Al ratio, cation content temperature of data collection (T), hydration (H and DH refer to hydrated to dehydrated, respectively), space group (SG) and unit cell volume (V). Dashes indicate information not given. *reported as $Ba_{12}Cl_8(O,OH)_4$.*

Ref	Si/Al	Cations	T (K)	H/DH	SG	V (Å^3)
Solov'eva[24]	2.6	Ba_{12}*		H	*I*4/*mmm*	1860.4
Galli[2]	2.5	K_5Ca_2		H	*Immm*	1997.7
Baturin[25]	1.7	$Na_1K_5Ba_3$	298	H	*Immm*	2023.9
Bieniok[26]	2.1	$K_{10.3}$	298	H	*Immm*	2010.3
Barrett[27]	3.8	$K_{5.2}TEA_{0.8}H_{0.7}$	298	H	*Immm*	1982.1
Yakubovich[28]	1.7	Na_5K_7	298	H	*Immm*	1968.7
Skofteland[29]	1.8	$K_{11.5}$	298	H	*Immm*	2003.7
			298	DH	*Pnnm*	1762.8
	2.4	$K_{9.5}$	298	H	*Pnnm*	-
Pakhomova[7]	1.7	Na_1K_{11}	298	H	*Immm*	2019.4
			498	DH	*P*4$_2$/*nmc*	1727.7

Whilst **MER** is a reasonably simple zeolite framework, with a unit cell volume of *ca.* 1750-2000 Å^3, there are multiple potential cation sites, shown in Figure 4.1.2. For some of the materials presented in this work, this will be simplified as sites become symmetrically equivalent and it can be useful to group sites into 3 major types: I* and Ia, close to the *d8r* unit; II*, occupying the boundary between *ste* and *pau* cavities; and III*, sitting in the *ste* cavity. Galli *et al.*, Skofteland *et al.* and Pakhomova *et al.* reported sites II* as the most highly occupied by K^+ cations, under all conditions, with the exception of the hydrated form reported by Pakhomova *et al.* which saw site I most highly occupied. Cations sitting in sites I* and Ia can hinder percolation of gas molecules along the *pau-d8r* channel, whilst II* slows movement along the *pau-ste* channel. For some symmetries, sites II* are split into site IIa and IIb, with labels indicating the crystallographic axis the 8-rings are perpendicular to, and 2 sets of *pau-ste* channels form. Sites III* also hinder diffusion through such channels in addition to the *ste-ste* channel. The size and charge density of cations alters site preference, which can alter the framework geometry and block percolation of gas molecules, hence the need to study different cation forms and their structural and adsorption properties.

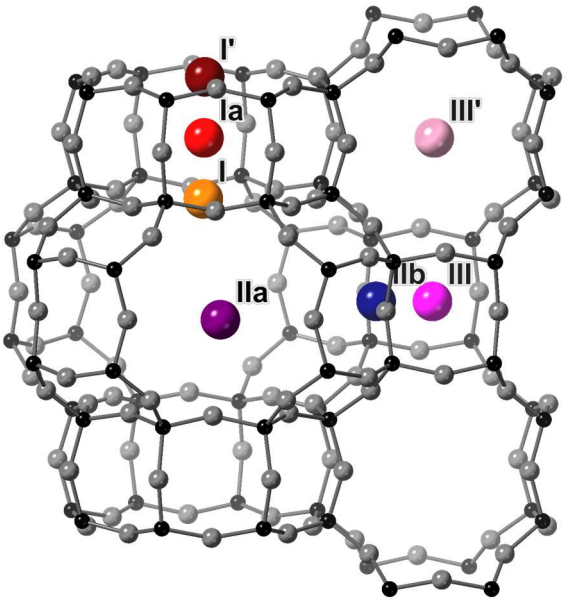

*Figure 4.1.2. The **MER** Framework with labelling schemes used for cation sites. Tetrahedral and O sites are shown in black and grey, respectively. Extra-framework cation sites are shown as I and I' (together termed I* for ease), S8Rs between d8r and pau (orange and dark red); Ia, D8R (bright red); IIa and IIb (II*), S8R between pau and ste cavities (purple and blue); III and III' (III*), inside the ste cavity (bright and pastel pink).*

4.2 Acknowledgements

The work reported here would have been impossible without Dr Veselina M. Georgieva and her dedication and hard work synthesising and preparing the materials investigated. Along with Dr Magdalena M. Lozinska, she also dehydrated samples, and collected equilibrium adsorption and laboratory and synchrotron PXRD data, the latter also assisted by Prof Paul A. Wright and Dr Claire A. Murray. Kinetic adsorption data in the form of ZLC measurements was collected by Dr Maarten C. Verbraeken as part of Prof Stefano Brandani's group at the University of Edinburgh, and kinetic Ar uptake data was obtained by Dr William J. Casteel, Jr. at Air Products & Chemicals, Inc.

Whilst the work carried out personally in this chapter is entirely structural, the properties and adsorption behaviour of these materials is highly relevant and closely related. Therefore, these are detailed at the beginning of the following sections of this chapter, after measurement by the collaborators listed above.

4.3 Underlying experimental work

Zeolite K,TEA-MER (TEA = tetraethylammonium) was synthesised by Dr Georgieva following the method of Barrett *et al*,[27] and found through a combination of EDX, TGA and NMR analysis to have the chemical composition $K_{5.9}TEA_{0.8}[Si_{25.3}Al_{6.7}O_{64}].(H_2O)_x$. An SEM image of the as-prepared material obtained by Dr Georgieva is shown in Figure 4.3.1.

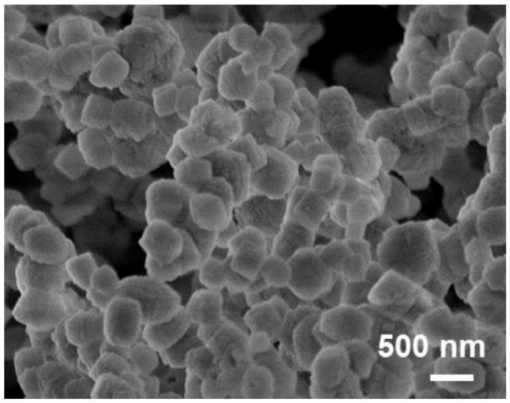

Figure 4.3.1. SEM images of as-prepared $K_{5.9}TEA_{0.8}$-MER (3.8).

Samples of different cation forms were created from this initial material using ion exchange. These samples formed 2 families: $M_{5.9}TEA_{0.8}$-MER (3.8) and $M_{6.7}$-MER (3.8), where M indicates a cation, which included Li-, Na-, K- and Cs-forms. PXRD patterns of these samples and their hydrated and dehydrated forms are shown in Figure 4.3.2.

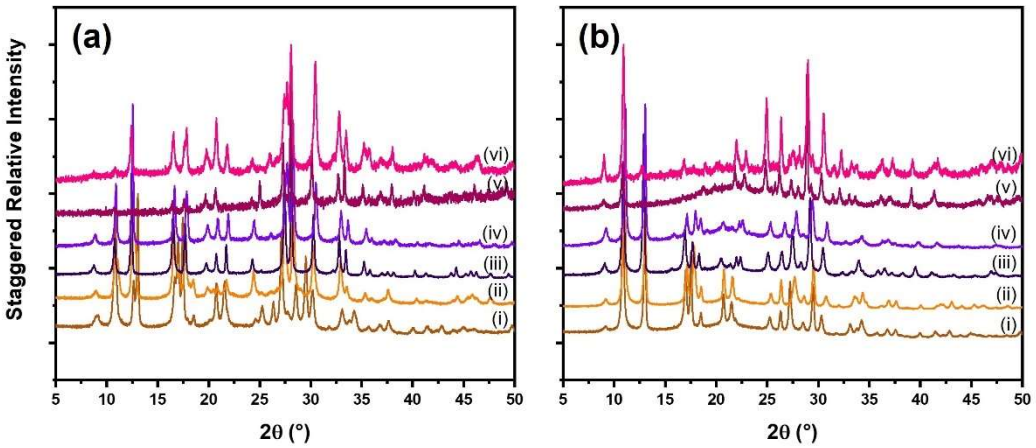

Figure 4.3.2. PXRD patterns of (a) hydrated and (b) dehydrated MER (3.8) materials at 298 K: (i) $Na_{5.9}TEA_{0.8}$-, (ii) $Na_{6.7}$-, (iii) $K_{5.9}TEA_{0.8}$-, (iv) $K_{6.7}$-, (v) $Cs_{5.9}TEA_{0.8}$-, (vi) $Cs_{6.2}K_{0.5}$-MER (3.8). (Stoe, λ = 1.54056 Å).

The CO_2 sorption isotherms up to 1 bar at 298 K were collected for these different cation forms, as shown in Figure 4.3.3. Some samples exhibited non-Type I adsorption behaviour. Higher pressure isotherms up to 5 bar at varying temperatures were also collected for the "pure-cation" forms $Na_{6.7}$-, $K_{6.7}$- and $Cs_{6.2}K_{0.5}$-MER (3.8), shown in Figure 4.3.4, in which Na- and Cs-forms showed non-Type I steps or kinks.

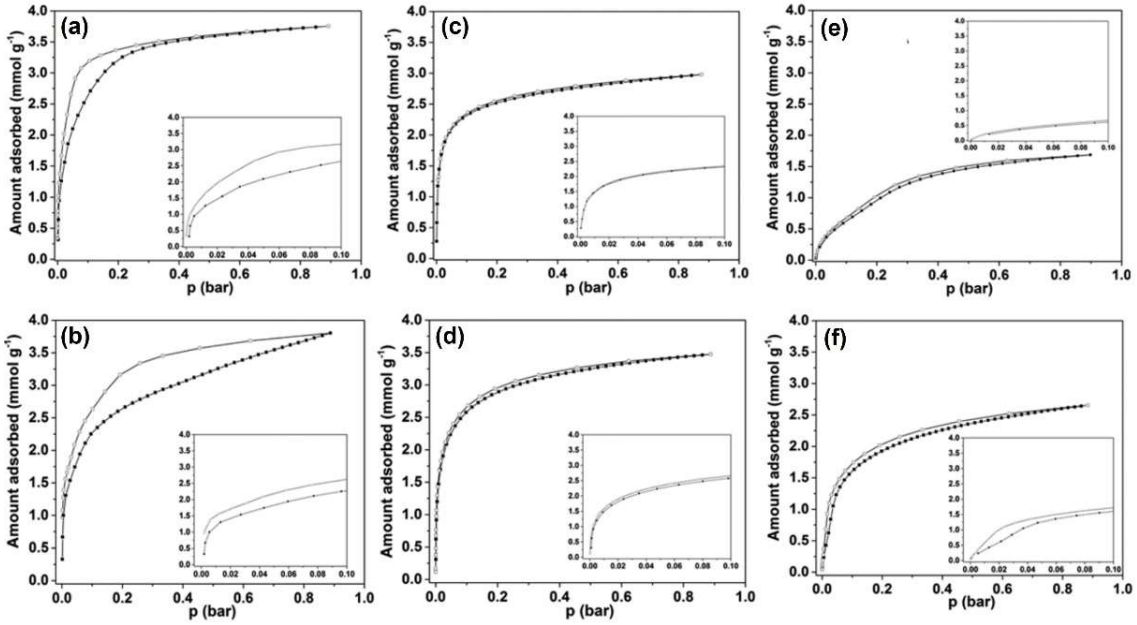

Figure 4.3.3. CO_2 adsorption isotherms up to 1 bar at 298 K for MER (3.8) samples: (a) $Na_{5.9}TEA_{0.8}$-, (b) $Na_{6.7}$-, (c) $K_{5.9}TEA_{0.8}$-, (d) $K_{6.7}$-, (e) $Cs_{5.9}TEA_{0.8}$-, (f) $Cs_{6.2}K_{0.5}$-MER (3.8). Adsorption and desorption branches are indicated by closed and open symbols; respectively. Lower pressures isotherm regions (up to 0.1 bar) are shown inset.

Ar uptake experiments, measuring adsorption over time after an initial dose of pressure, were carried for the pure-cation samples, as a measure of "openness" of the structure upon activation. Ar diffusivities (more correctly, the scaled inverse of the diffusional time constant), and related uptake timescales,[30] are presented in Table 4.3.1.

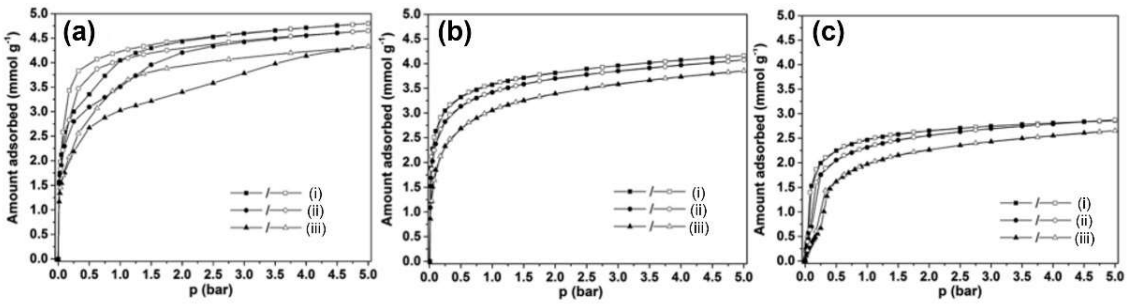

Figure 4.3.4. CO_2 adsorption isotherms up to 5 bar at (i) 298, (ii) 308 and (iii) 328 K for MER (3.8) samples: (a) $Na_{6.7}$-, (b) $K_{6.7}$-, (c) $Cs_{6.2}K_{0.5}$-MER (3.8). Adsorption and desorption branches are indicated by closed and open symbols; respectively.

Table 4.3.1. Ar diffusivity data for MER (3.8) materials

Material	Ar D/r^2 (s^{-1})	Uptake timescale (s)
$Na_{6.7}$-MER (3.8)	8.0×10^{-5}	2500
$K_{6.7}$-MER (3.8)	6.3×10^{-4}	317
$Cs_{6.2}K_{0.5}$-MER (3.8)	2.3×10^{-4}	870

Breakthrough curves were collected for these pure-cation materials with a gas stream of a 10:40:50 CO_2/CH_4/He mixture, as were their subsequent desorption curves, both shown in Figure 4.3.5. Uptakes of CO_2 and CH_4 from these experiments are listed in Table 4.3.2, as are the selectivities of these materials. To analyse desorption kinetics at low CO_2 loadings, ZLC measurements were carried out at 1% or 10% CO_2 in ambient pressure of He and 308 K. These showed diffusivities of D/r^2 = 2.2 and 9.0×10^{-4} s^{-1} for $Na_{6.7}$- and $Cs_{6.2}K_{0.5}$-MER (3.8), respectively, as determined by collaborators by fitting data

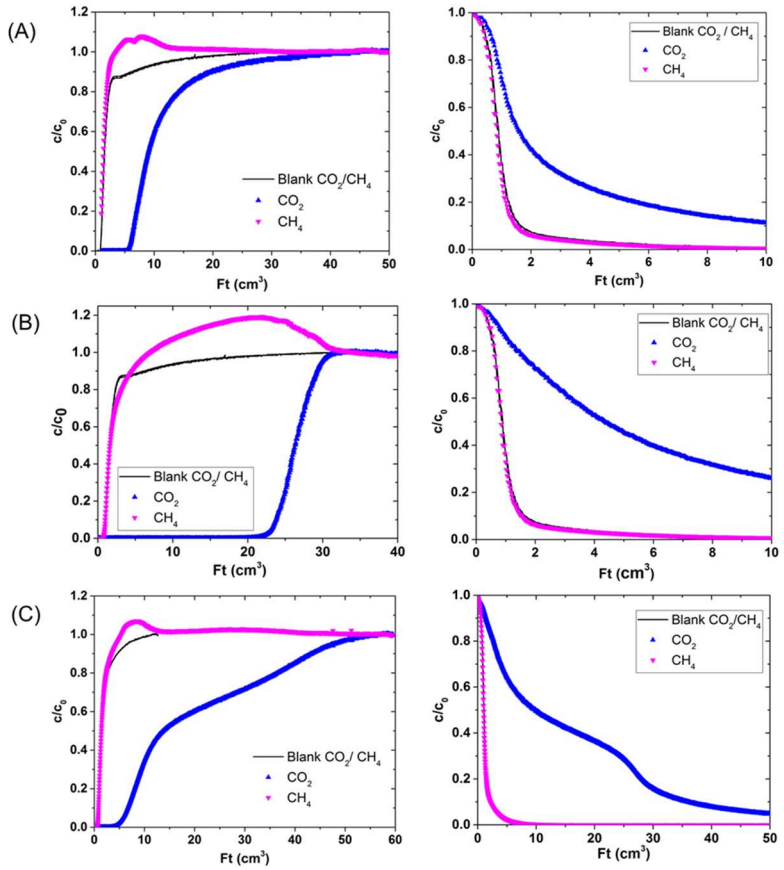

Figure 4.3.5. Breakthrough curves for (A) $Na_{6.7}$-, (B) $K_{6.7}$-, and (C) $Cs_{6.2}K_{0.5}$-MER (3.8) in a flow of 10:40:50 CO_2/CH_4/He at 298 K, with adsorption and desorption curves shown on the left and right, respectively. Curves are shown as a function of volume of gas that has flowed over the sample.

to models described in greater detail in Georgieva *et al*.[31] $K_{6.7}$-MER (3.8) was found to be under thermodynamic control initially, showing rapid percolation of CO_2, with kinetic control becoming established as further CO_2 was released.

Table 4.3.2. Uptakes and selectivities of MER (3.8) materials determined by mixed component E-ZLC experiments at 298 K.

Material	CO_2 uptake (mmol g^{-1})	CH_4 uptake (mmol g^{-1})	CO_2/CH_4 selectivity
$Na_{6.7}$-MER (3.8)	1.174	0.0156	303
$K_{6.7}$-MER (3.8)	1.912	0.0090	850
$Cs_{6.2}K_{0.5}$-MER (3.8)	1.157	0.0136	340

4.4 Structural studies of MER (3.8) materials

MER (3.8) materials and their response to dehydration were investigated using Rietveld refinement, using the IZA framework structure and literature models already discussed for initial framework and cation positions. Subsequent Rietveld refinement followed the principles given in Chapter 2. Samples investigated here include both $M_{6.7}$- and $M_{5.9}TEA_{0.7}$-forms of the MER (3.8) material.

4.4.1 Hydrated $M_{5.9}TEA_{0.8}$-MER (3.8)

The material discussed here was first formed as $K_{5.9}TEA_{0.8}$-MER (3.8) and so the broader family of samples including the TEA SDA are discussed first. Rietveld plots of the hydrated forms of these $M_{5.9}TEA_{0.8}$-MER (3.8) materials are shown in Figure 4.4.1. Crystallographic details of materials are given in Appendix VI.II.I.

As discussed previously, multiple space groups have been used in the literature for zeolite MER. The materials here were synthesised following the method of Barrett et al., who fitted their as-made $K_{5.2}TEA_{0.8}H_{0.7}$-MER material in the *Immm* space group,[27] agreeing with previously reported structures of lower Si/Al materials.[2,26] Here it was found that the reduction in symmetry from the parent *I*4/*mmm* symmetry was not warranted, with daughter space groups providing very similar goodness of fit. The $Cs_{5.9}TEA_{0.8}$-MER data was rather poor due to X-ray absorption by Cs cations but

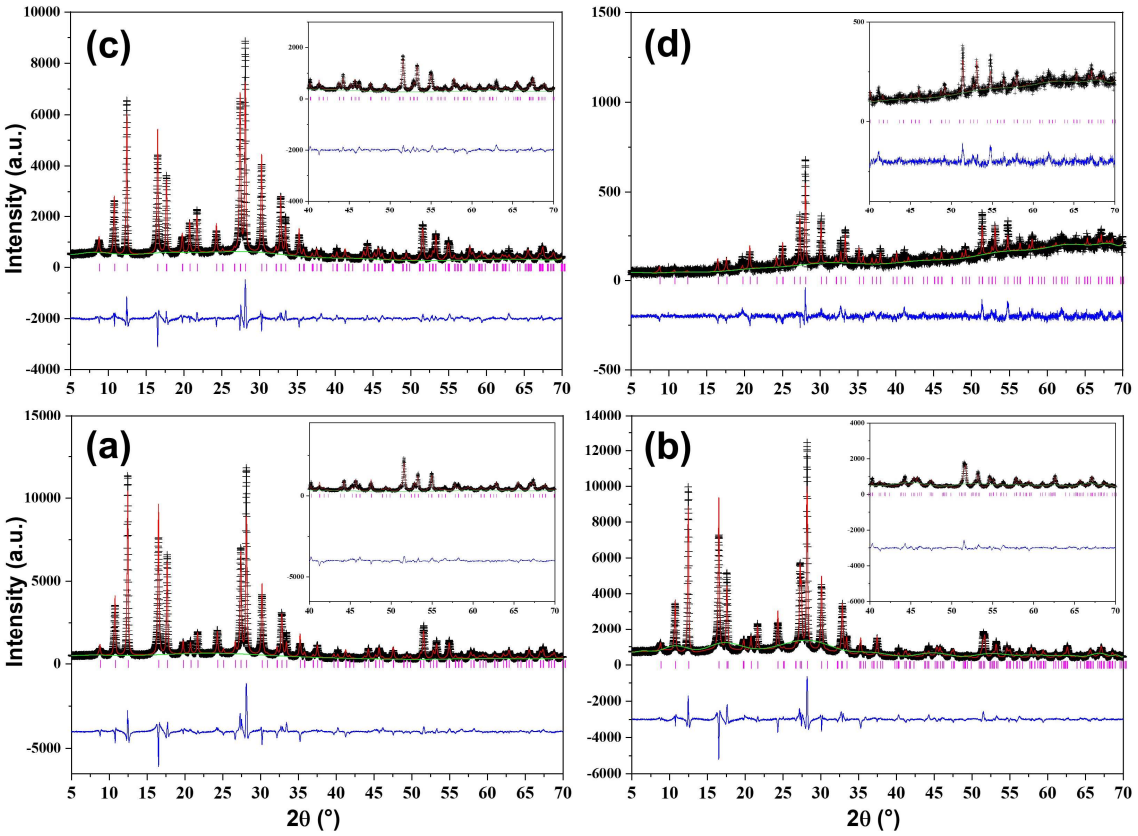

Figure 4.4.1. Rietveld plots of hydrated $M_{5.9}TEA_{0.8}$-MER (3.8) samples, with M = (a) Li, (b) Na, (c) K and (d) Cs. (Stoe, λ = 1.54056 Å).

refinement was possible.[32] Unit cell parameters are given in Table 4.4.1, with the refined structures of these 4 materials are shown in Figure 4.4.2.

Table 4.4.1. Space group (SG), unit cell parameters and R_{wp} from refinement of hydrated $M_{5.9}TEA_{0.8}$-MER samples.

Material	SG	*a* (Å)	*c* (Å)	*V* (Å³)	R_{wp}
$Li_{5.9}TEA_{0.8}$	*I*4/*mmm*	14.157(1)	10.016(1)	2008(1)	11.9%
$Na_{5.9}TEA_{0.8}$	*I*4/*mmm*	14.131(1)	10.067(1)	2010(1)	9.8%
$K_{5.9}TEA_{0.8}$	*I*4/*mmm*	14.167(1)	9.990(1)	2005(1)	9.7%
$Cs_{5.9}TEA_{0.8}$	*I*4/*mmm*	14.192(1)	10.042(1)	2023(1)	10.3%

Unit cell parameters show that hydrated samples have very similar unit cell volumes regardless of cation content. Similar effects were observed for various cation forms of zeolite Rho,[33] with a relaxed framework adopted for all materials in the presence of solvating water molecules. There is also no strong cation ordering as shown by the

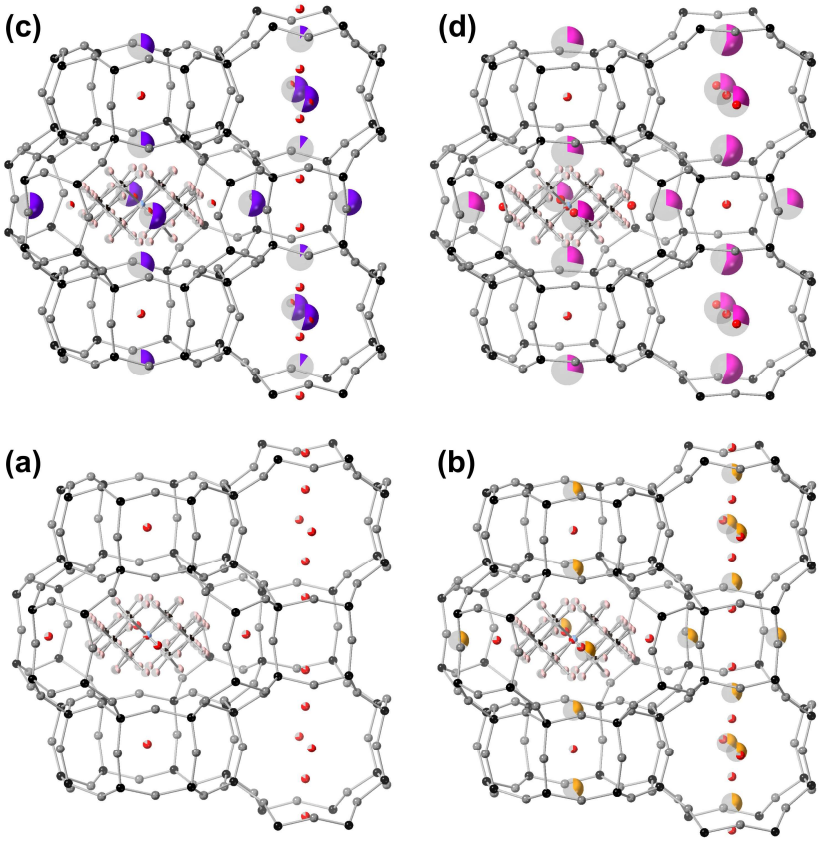

Figure 4.4.2. Refined structures of hydrated $M_{5.9}TEA_{0.8}$-MER (3.8) materials. M = (a) Li, (b) Na, (c) K and (d) Cs. Framework T and O sites are shown in black and grey, respectively. Na, K and Cs cations are shown in orange, purple and pink, with extraframework O, C, N and H shown in red, black, light blue and light pink, respectively. Fractional occupancies are indicated by partial shading of sphere.

retention of *I*4/*mmm* symmetry. The goodness of fits for these samples are wanting and difference Fourier analysis did not provide any insight into additional or alternative water or SDA sites, which was also the case when exploring other potential symmetries. There is also no evidence of additional peaks to suggest supercells or obvious breaking of body-centring.

4.4.2 Dehydrated $M_{5.9}TEA_{0.8}$-MER (3.8)

Differences between the dehydrated forms of these materials were more apparent and Rietveld plots of the dehydrated $M_{5.9}TEA_{0.8}$-MER (3.8) samples are shown in Figure 4.4.3. Further crystallographic details can be found in Appendix VI.II.I.

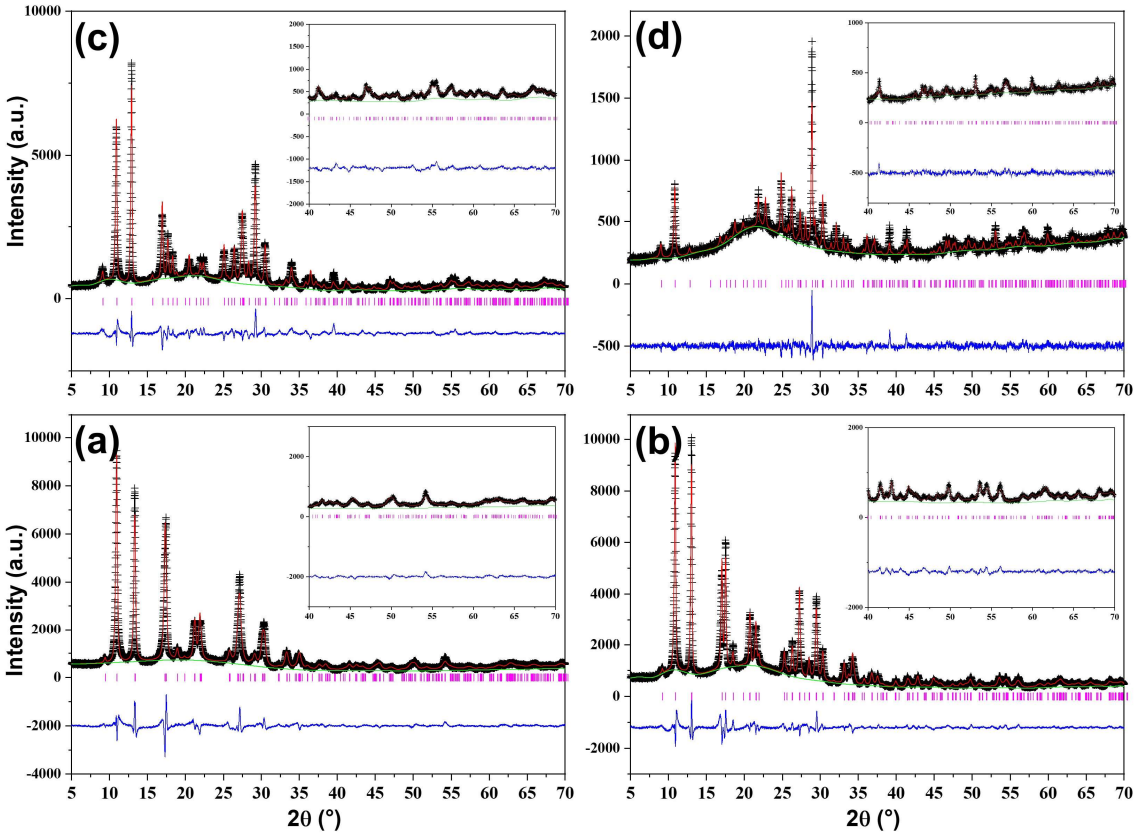

Figure 4.4.3. Rietveld plots of dehydrated $M_{5.9}TEA_{0.8}$-MER (3.8) samples, with M = (a) Li, (b) Na, (c) K and (d) Cs. (Stoe, λ = 1.54056 Å).

Analysis of the PXRD pattern of $K_{5.9}TEA_{0.8}$-MER revealed multiple peaks absent in the hydrated data. These peaks occur at *ca.* 16°, 19°, 23° and 33° and correspond to {201}, {102}. {311} and {412} reflections respectively, all forbidden by body centring. The *Pnnm* space group suggested by Skofteland *et al.* for some of their K-MER samples, including a dehydrated form, also gave a relatively poor fit. Multiple daughter space groups of *I*4/*mmm* and *Immm* were trialled, with the $P4_2/nmc$ space group previously used by Pakhomova *et al.* giving the best fit.[7]

Table 4.4.2. Space group (SG), unit cell parameters and R_{wp} from refinement of dehydrated $M_{5.9}TEA_{0.8}$-MER samples.

Cation form	SG	*a* (Å)	*b* (Å)	*c* (Å)	*V* (Å³)	R_{wp}
$Li_{5.9}TEA_{0.8}$	*Immm*	13.262(2)	13.198(1)	10.142(1)	1775(1)	8.9%
$Na_{5.9}TEA_{0.8}$	*Immm*	13.554(1)	13.525(1)	10.100(1)	1852(1)	7.2%
$K_{5.9}TEA_{0.8}$	$P4_2/nmc$	13.652(1)		9.999(1)	1863(1)	8.8%
$Cs_{5.9}TEA_{0.8}$	$P4_2/nmc$	13.788(1)		10.039(1)	1909(1)	6.5%

No body-centred symmetry breaking peaks were observed for the other samples in their dehydrated forms. $Li_{5.9}TEA_{0.8}$- and $Na_{5.9}TEA_{0.8}$-MER were fitted best by the *Immm* space group used by much of the literature, although the unit cell parameters *a* and *b* remained reasonably close, essentially adopting a "pseudo-tetragonal" unit cell. Fitting of the $Cs_{5.9}TEA_{0.8}$-form was found to be optimal when using $P4_2/nmc$ as opposed to $I4/mmm$ and related space groups, though no peaks breaking body-centring were observed. The fitting of dehydrated samples was significantly improved relative to their hydrated forms, as evidenced in Table 4.4.2. Also tabulated are the unit cell volumes of all materials, which shrink upon dehydration. The degree of contraction increased with smaller cations, with a 12, 8, 7 and 6% reduction in unit cell volume for Li-, Na-, K- and Cs-analogues, respectively. In all cases, materials moved to a lower symmetry space group upon dehydration, with smaller cations adopting *Immm* and larger cations $P4_2/nmc$, both sub-groups of the framework $I4/mmm$ symmetry. These refined structures are shown in Figure 4.4.4.

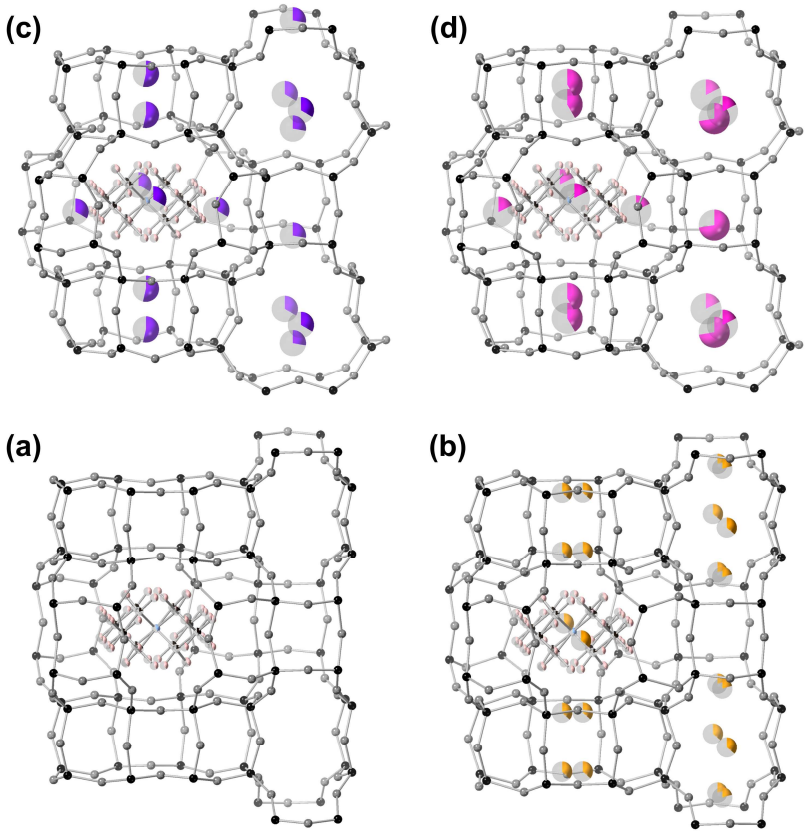

Figure 4.4.4. Refined structures of dehydrated $M_{5.9}TEA_{0.8}$-MER (3.8) materials. M = (a) Li, (b) Na, (c) K and (d) Cs. Framework T and O sites are shown in black and grey, respectively. Na, K and Cs cations are shown in orange, purple and pink, with C, N and H shown in black, light blue and light pink, respectively. Fractional occupancies are indicated by partial shading of spheres.

4.4.3 Hydrated $M_{6.7}$-MER (3.8)

Through calcination and ion exchange of $K_{5.9}TEA_{0.8}$-MER (3.8), "pure" cation forms were synthesised by Dr Georgieva. Attempts to form a $Li_{6.7}$-MER (3.8) material resulted in loss of crystallinity and so no Li-form is discussed for this material. Additionally, the Cs-form was found to have a slight K^+ impurity, and this sample is designated $Cs_{6.2}K_{0.5}$-MER (3.8) accordingly. Rietveld plots of the hydrated forms of these samples are shown in Figure 4.4.5 and crystallographic details are given in Appendix VI.II.I.

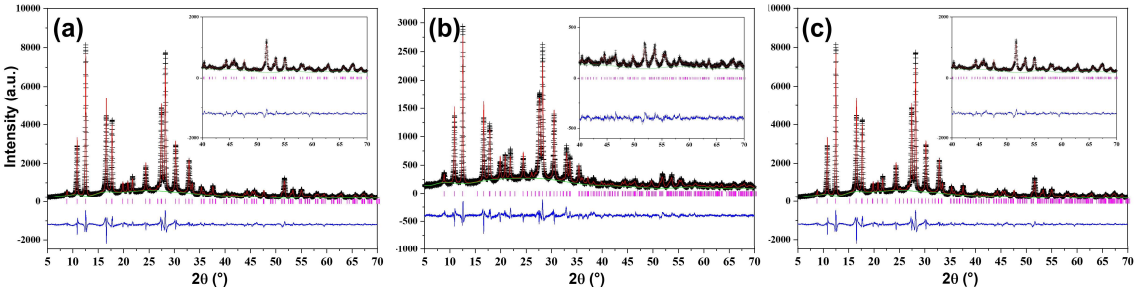

Figure 4.4.5. Rietveld plots of hydrated M-MER (3.8) samples, with M = (a) $Na_{6.7}$, (b) $K_{6.7}$ and (c) $Cs_{6.2}K_{0.5}$. (Stoe, λ = 1.54056 Å).

Unit cell parameters and refinement details are given in Table 4.4.3. All $M_{6.7}$-MER (3.8) materials adopted the same space group as their dehydrated $M_{5.9}TEA_{0.8}$-analogues, and their fits were greatly improved relative to their hydrated $M_{5.9}TEA_{0.8}$-MER (3.8) equivalents. Here, the K-form showed a peak at *ca*. 26° and a minor one at *ca*. 15° which disallowed body centring, corresponding to {302} and {201} reflections, respectively. The $P4_2/nmc$ space group fitted both hydrated $K_{6.7}$- and $Cs_{6.2}K_{0.5}$-MER (3.8) materials best, whilst *Immm* gave the best fit for $Na_{6.7}$-MER (3.8).

Table 4.4.3. Space group (SG), unit cell parameters and R_{wp} from refinement of hydrated $M_{6.7}$-MER samples.

Cation form	SG	*a* (Å)	*b* (Å)	*c* (Å)	*V* (Å^3)	R_{wp}
$Na_{6.7}$	*Immm*	14.144(2)	14.141(2)	10.022(1)	2005(1)	9.4%
$K_{6.7}$	$P4_2/nmc$	14.136(1)		9.930(1)	1984(1)	6.7%
$Cs_{6.2}K_{0.5}$	$P4_2/nmc$	14.209(1)		10.006(1)	2020(1)	7.4%

The refined structures of hydrated $M_{6.7}$-MER (3.8) samples are shown in Figure 4.4.6. The framework geometry of the K-form is slightly distorted despite hydration, which may

be a factor in the need for a lower symmetry space group than *I4/mmm*. This is not the case in the other cation-forms however, with cation ordering responsible in the Na-form, as site IIa is occupied, whilst IIb is left vacant. The cause in the Cs-exchanged material appears to be the relative positions of cations in site III, which are better described with the loss of a mirror plane with reduced symmetry.

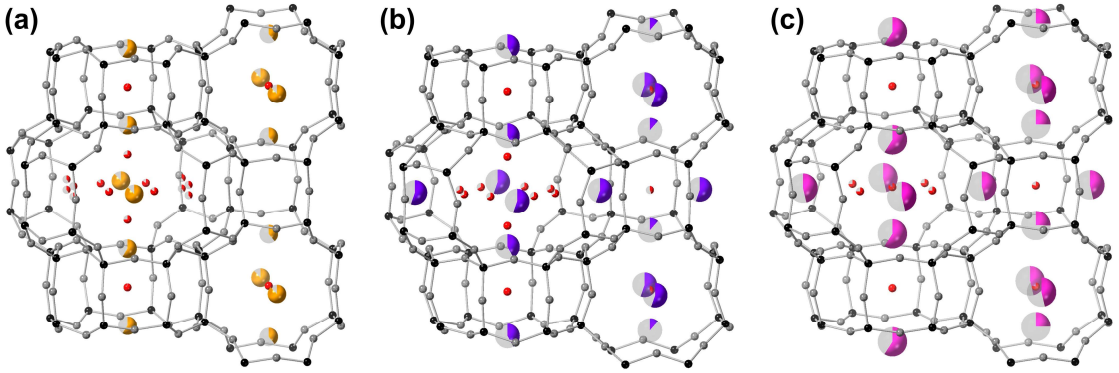

Figure 4.4.6. Refined structures of hydrated (a) $Na_{6.7}$-, (b) $K_{6.7}$-, and (c) $Cs_{6.2}K_{0.5}$-MER (3.8). Na, K and Cs cations are shown in pink, purple, and orange, respectively, water molecule O sites are shown in red. Framework T and O sites are shown in black and grey, respectively. Partial shading of spheres represents fractional occupancies.

4.4.4 Dehydrated $M_{6.7}$-MER (3.8)

Distortions of the frameworks of these materials are far more obvious upon dehydration. Rietveld plots of the dehydrated $M_{6.7}$-MER (3.8) materials are shown in Figure 4.4.7, and crystallographic details are given in Appendix VI.II.I. Here, materials adopted the same space group as their hydrated forms, with refined unit cell parameters of the materials given in Table 4.4.4. $Na_{6.7}$-, $K_{6.7}$- and $Cs_{6.2}K_{0.5}$-MER (3.8) samples exhibited a decrease in unit cell volume of 9.8, 7.7 and 7.8%, respectively. This shows once more a higher level of distortion for the smaller-cation form of the material. The impacts of this on framework structures can be seen in Figure 4.4.8. There are significant differences

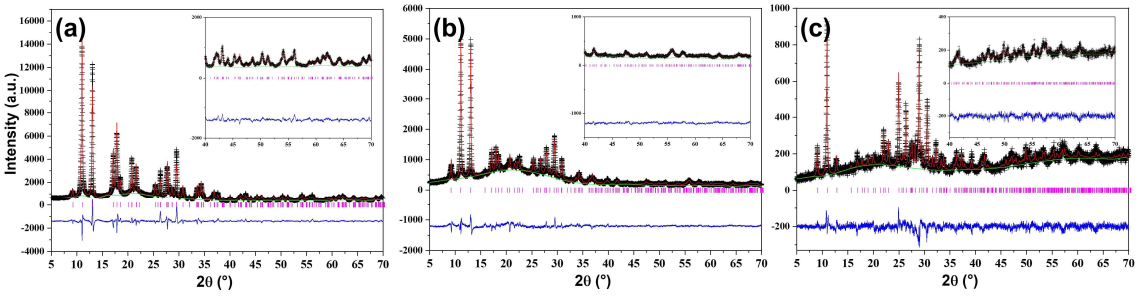

Figure 4.4.7. Rietveld plots of dehydrated M-MER (3.8) samples, with M = (a) $Na_{6.7}$, (b) $K_{6.7}$ and (c) $Cs_{6.2}K_{0.5}$. (Stoe, λ = 1.54056 Å).

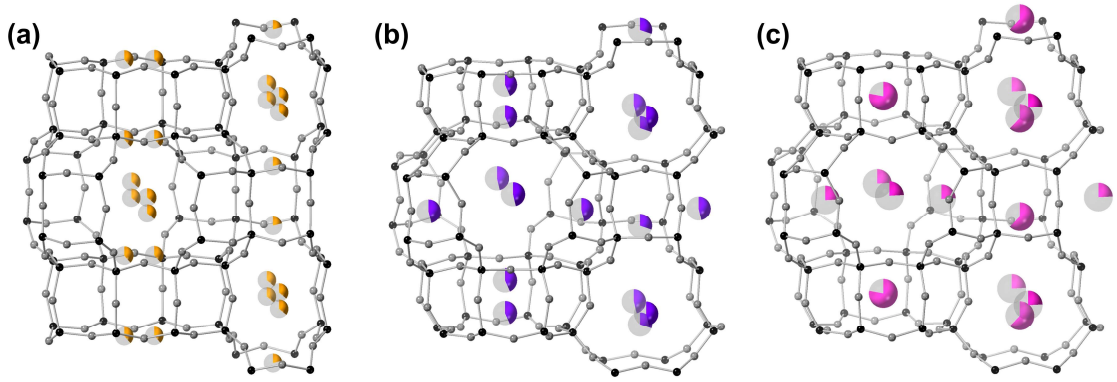

Figure 4.4.8. Refined structures of dehydrated (a) $Na_{6.7}$-, (b) $K_{6.7}$-, and (c) $Cs_{6.2}K_{0.5}$-MER (3.8). Framework T and O sites are shown in black and grey, and extraframework Na, K and Cs cations are shown in pink, purple, and orange, respectively. Fractional occupancies are indicated by partial shading of spheres.

between the different modes of distortion, as described by differences in space group, on both window size and cation siting, and as discussed below.

Table 4.4.4. Space group (SG), unit cell parameters and R_{wp} from refinement of dehydrated $M_{6.7}$-MER samples.

Cation form	SG	*a* (Å)	*b* (Å)	*c* (Å)	*V* (Å^3)	R_{wp}
$Na_{6.7}$	*Immm*	13.519(1)	13.493(1)	9.913(1)	1808(1)	8.2%
$K_{6.7}$	*P*4$_2$/*nmc*	13.587(1)		9.877(1)	1824(1)	7.7%
$Cs_{6.2}K_{0.5}$	*P*4$_2$/*nmc*	13.751(1)		9.950(1)	1881(1)	9.3%

4.4.5 Comparison of MER (3.8) structures

Unit cell sizes of all MER (3.8) materials decreased upon dehydration. Whilst the unit cell volumes of hydrated materials were reasonably similar, dehydrated materials showed greater differences, with volumes shrinking according to the size of cationic radii. Dehydrated forms of $M_{5.9}TEA_{0.8}$-MER (3.8) possessed unit cells which were *ca*. 2% larger than their $M_{6.7}$-equivalents, showing that the steric bulk of the organic TEA cation "props open" the MER structure, despite occupying less than half of the *pau* cavities.

Differences are also observed for cation sitings within the MER (3.8) materials, given in Table 4.4.5. Due to the poor X-ray scattering of Li^+, no cation positions were refined. Pure cation forms and their $M_{5.9}TEA_{0.8}$-MER (3.8) equivalents broadly possess comparable

cation sitings, with changes likely due to differences in unit cell volume. More significant differences, as seen with the hydrated Na-containing materials, may be due to additional inorganic cations altering the energetic favourability of sites, and the availability to better coordinate to H_2O molecules in the absence of TEA cations in the *pau* cavity. In the hydrated materials, site II (between *pau* and *ste* cavities) possesses the highest absolute occupancy for all cation forms. This may be because this site could allow the greatest degree of solvation by H_2O molecules. Cation sitings diverge in dehydrated materials, as the highest occupied sites in the Na-, K- and Cs-forms are I*, II* and III, respectively.

*Table 4.4.5. Absolute site occupancies of M^+ in MER (3.8) materials. *denotes merging of related but symmetry inequivalent positions. [a] denotes site Ia occupancy i.e. D8R site. For $Cs_{6.2}K_{0.5}$-MER (3.8), occupancies given are for Cs^+.*

Cation form	dh/h	I*	II*	III	Total
$Na_{5.9}TEA_{0.8}$	h	1.6(1)	2.8(1)	1.6(1)	6.0(1)
	dh	2.9(1)	1.4(1)	1.7(1)	6.0(1)
$K_{5.9}TEA_{0.8}$	h	1.4(1)	4.3(1)	0.4(1)	6.1(1)
	dh	2.2(1)	2.6(1)	1.1(1)	5.9(1)
$Cs_{5.9}TEA_{0.8}$	h	1.1(1)	2.4(1)	2.2(1)	5.7(1)
	dh	1.7(1)[a]	1.4(1)	2.9(1)	6.0(1)
$Na_{6.7}$	h	1.5(1)	3.8(2)	1.4(1)	6.7(2)
	dh	3.2(2)	2.6(1)	0.9(1)	6.7(2)
$K_{6.7}$	h	1.6(1)	4.4(1)	0.5(1)	6.5(2)
	dh	1.5(1)	3.8(1)	1.1(1)	6.4(2)
$Cs_{6.2}K_{0.5}$	h	2.2(1)	3.4(1)	0.8(1)	6.3(2)
	dh	1.6(1)[a]	1.9(1)	2.5(1)	6.0(2)

The variety of unit cell volumes displayed by MER (3.8) materials is complemented by an array of window sizes, further complicated by differences in space group. Due to the 4_2-screw axis in $P4_2/nmc$, all buckled 8-rings in the *pau* cavity are equivalent. In *Immm*, this relationship is lost and these 8-rings are only equivalent to windows directly opposite in the *pau* cavity, forming 2 sets of windows. These are labelled according to the crystallographic axis they are perpendicular to, as previously detailed. Free window

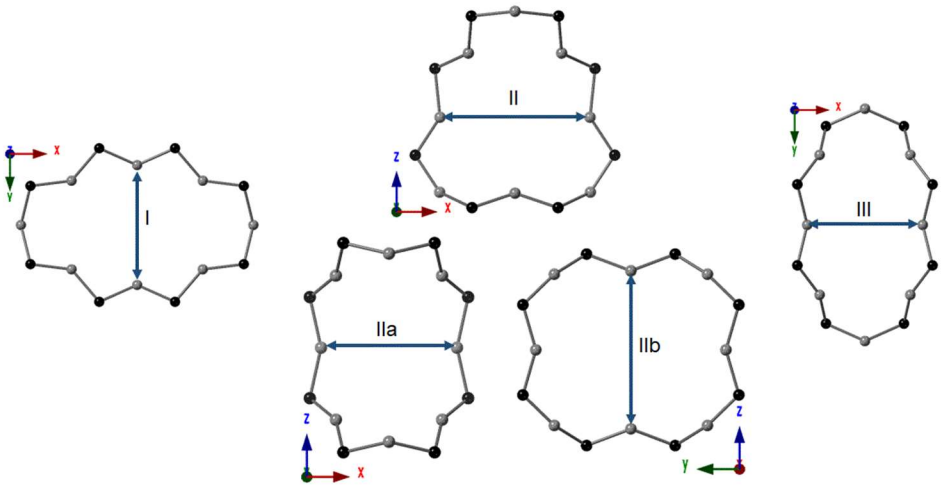

Figure 4.4.9. Estimation of the free diameter of windows within the MER structure, as described above. The O-O distances were taken from the crystallographic structure, and twice the van der Waals radius of O, 2 × 1.35 Å,[34] was subtracted to give the reported free diameters.

diameters are given in Table 4.4.6, determined following the same method as in Chapter 3, the shortest possible path between O sites across the centre of an 8-ring, less 2 O radii (2 × 1.35 Å),[34] and depicted in Figure 4.4.9. As discussed in Chapter 3, Cook and Conner suggest that thermal motion of zeolite framework effectively increases the free diameter of windows by 0.7 Å compared to the crystallographically expected value.[35] As discussed in Chapter 3, CO_2 has a kinetic diameter of 3.0 Å,[36] and so window sizes smaller than 2.3 Å would be expected to block percolation of CO_2 through the structure.

A graphical summary of window sizes is shown in Figure 4.4.10. Window sizes are broadly similar between hydrated samples, reflecting the comparable unit cell volumes. Free diameters of 8-rings generally follow the size of cations present in the structure for both hydrated and dehydrated samples, with the exception of hydrated $K_{5.9}TEA_{0.8}$-MER (3.8), which has slightly smaller windows than expected. The hydrated Cs-containing materials show a significant increase in window size compared to the other hydrated materials.

Upon dehydration, differences increase dramatically and more obviously agree with cation size. Samples with Li^+ and Na^+ display the smallest windows with the exception of window IIb, which is far larger than the accompanying 8-rings present in the materials. This is shown by the large range in window sizes for these samples in Figure 4.4.10. Additionally, the effect of TEA on the structure can be seen, with all bar hydrated $K_{5.9}TEA_{0.8}$-MER (3.8) possessing an array of wider windows than their wholly-inorganic

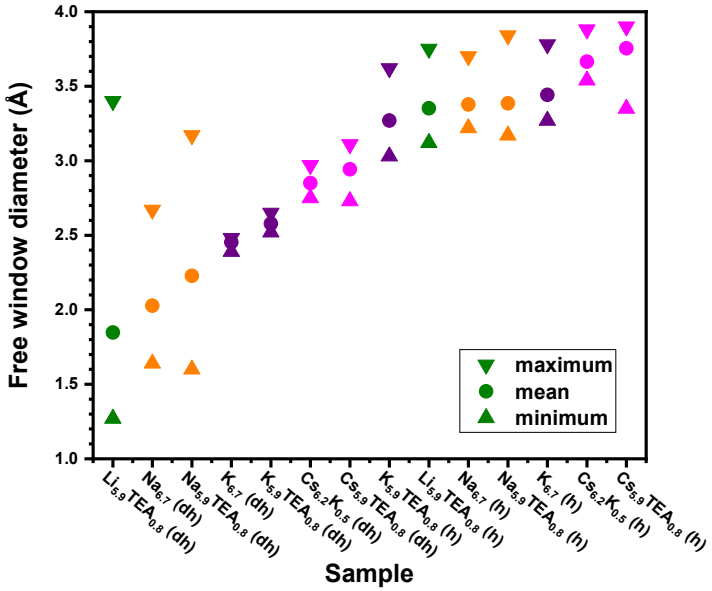

Figure 4.4.10. Free window diameters of MER (3.8) samples. Mean, maximum and minimum values are depicted as shown in the key. Samples and conditions are as indicated on the x axis.

counterparts. The high degree of distortion shown by the $Li_{5.9}TEA_{0.8}$-MER (3.8) sample is therefore likely less than a pure Li-form would experience.

*Table 4.4.6. Free window diameters in MER (3.8) materials. Windows that would be closed to CO_2 percolation (<2.3 Å) are denoted by *.*

Cation form	dh/h	I	II(a)	IIb	III
$Li_{5.9}TEA_{0.8}$	h	3.8(1)	3.1(1)		3.4(1)
	dh	1.4(1)*	1.3(1)*	3.4(1)	1.3(1)*
$Na_{5.9}TEA_{0.8}$	h	3.8(1)	3.2(1)		3.4(1)
	dh	2.0(1)*	1.6(1)*	3.3(1)	2.1(1)*
$K_{5.9}TEA_{0.8}$	h	3.6(1)	3.0(1)		3.4(1)
	dh	2.5(1)	2.6(1)		2.7(1)
$Cs_{5.9}TEA_{0.8}$	h	3.9(1)	3.9(1)		3.4(1)
	dh	2.8(1)	3.1(1)		2.7(1)
$Na_{6.7}$	h	3.7(1)	3.4(1)	3.2(1)	3.2(1)
	dh	2.1(1)*	1.6(1)*	2.7(1)	1.7(1)*
$K_{6.7}$	h	3.3(1)	3.4(1)		3.8(1)
	dh	2.4(1)	2.5(1)		2.5(1)
$Cs_{6.2}K_{0.5}$	h	3.9(1)	3.6(1)		3.5(1)
	dh	3.0(1)	2.8(1)		2.8(1)

The unit cell shrinkage upon dehydration caused by the presence of cations can be said to take 2 forms, termed mode I and mode II, depicted in Figure 4.4.11. In the MER (3.8) material, this is equivalent to the *Immm* and $P4_2/nmc$ space groups respectively, adopted by both the framework and the material as a whole, though this is not the case in Chapter 5, which examines further merlinoite materials.

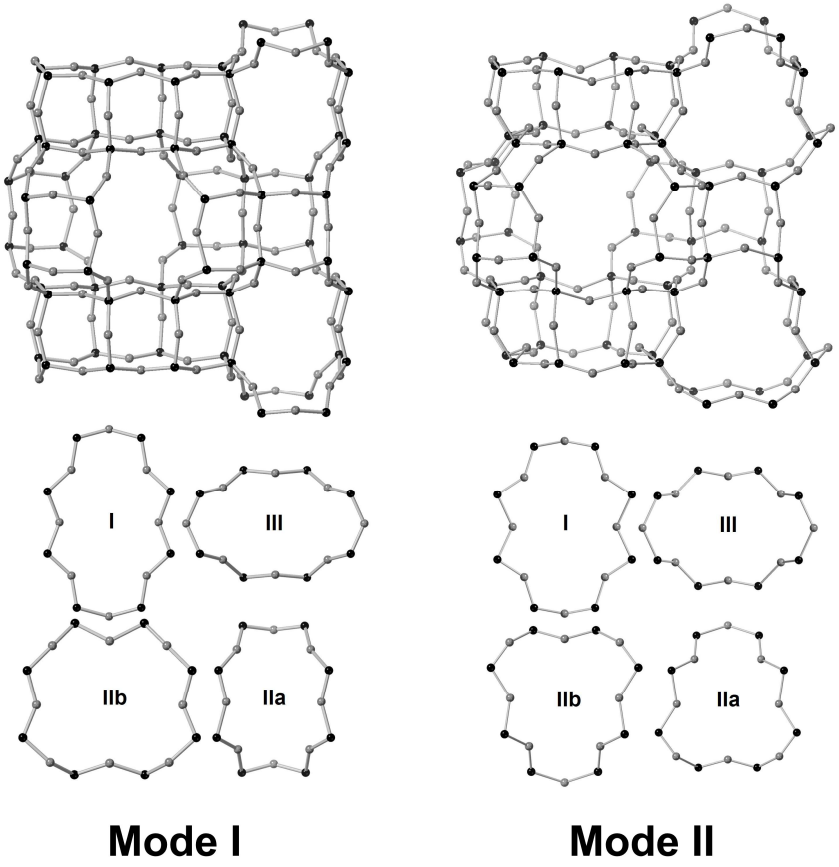

Figure 4.4.11. Depictions of different distortion modes adopted by MER materials, including the extended framework and individual windows, labelled according to the scheme discussed.

In mode I, 8-rings in *d8r* and *ste* units (windows I and III), separated along the *c* axis, are related by mirror planes and align "in phase". By contrast, a 4_2-screw axis describes their relation in mode II, as they alternate in orientation along the *c* axis "out of phase". Due to the connectivity of the framework, these differences manifest themselves with related window shape changes elsewhere. The windows between the *pau* and *ste* cavities along the *a* and *b* axes can be said to be "elliptical" or "ovate". These are type II windows due to their related cation sites.

In mode I, 2 sets of elliptical windows are seen, 1 narrow and 1 wide, defining channels along *a* and *b* axes. The wide window is unoccupied in $Na_{6.7}$-MER (3.8). In mode II, all *pau*/*ste* windows are related and adopt an ovate geometry. In each *pau* cavity, these windows tessellate in such a way that the wide part of the 8-ring is placed at alternating ends in adjacent rings. In this way, the framework distorts to form 4 reasonably large window sites in a *pau* cavity, whereas in mode I there are 2 large and 2 small.

Mode I is adopted by smaller Li and Na cations, whilst larger K and Cs cations direct mode II frameworks. It is known in the literature that small cations, such as Li^+ and Na^+, tend to prefer sites close to bridging O atoms, whilst larger cations like Cs^+ prefer larger sites, such as wide S8Rs and D8Rs, or sit at a greater distance from the framework.[22,33,37–42] This includes in the zeolite chabazite, where preference for S6R over S8R sites is observed for Li and Na cations, whilst K prefers the larger S8R sites.[37,43] Perhaps more pertinently, in zeolite Rho progressively smaller cations were shown to shrink the diameter of 8-rings within the structure.[22,33,44]

Whilst Li^+ sites could not be found in MER (3.8) using Rietveld refinement of PXRD data, upon dehydration, Na^+ was found to favour narrow 8-ring sites. These Na-containing structures host an assembly of exceptionally narrow 8-rings, as does the $Li_{5.9}TEA_{0.8}$-MER (3.8) framework. Mode I allows for the formation of very narrow 8-rings along the *c* axis and also half of the type II windows, whilst the other half are very wide. In some of these materials, this reduces the channel system to 1-dimensional connectivity. The formation of such narrow window sites creates favourable bonding between the framework O sites and smaller cations and as the wide 8-ring is unoccupied, any energetic penalty is reduced. Mode II however enables the formation of many sites which are favourable to larger K and Cs cations. In this way the choice of cation content determines not just the window size, as is the case in other flexible zeolites, such as zeolite Rho,[33,44] but also the mode of framework distortion. This is unknown in other flexible zeolites. Such effects would be expected to have impacts on the adsorption behaviour of these samples, detailed below.

It is worth comparing flexible zeolites merlinoite and Rho, as *d8r* units are present in both. The *d8r* moiety is known to be a flexible building unit, with different modes of distortion.[45] In $Na_{6.7}$-MER (3.8), the structure adopts mode I and as such the 8-rings in

the *d8r* are "in phase" (i.e. aligned). In $Na_{9.8}$-Rho (3.9) however, the windows are out of phase (rotated 90° to each other), consistent with those in mode II in MER (3.8).[33] Curiously these both have very similar 8-ring geometries, with free semi-major by semi-minor diameters (longest and shortest dimension across the ring) of 5.5 Å × 3.3 Å and 5.6 Å × 3.4 Å for the **RHO** and **MER** frameworks, respectively, as shown in Figure 4.4.12.[33] This indicates both the flexibility of these units and also the importance in considering zeolite structures as a whole. For Rho, the out of phase mode, seen for all cation forms, allows every *d8r* unit in the structure to distort to best accommodate cations present. In MER, the distortion of the *d8r* is concomitant with other *pau* 8-ring distortions and so the energetics of these window sites is also to be considered. Interestingly $Na_{132}H_{28}$-ECR-18 (3.2), formed of a **PAU** framework and part of the extended Rho family of zeolites, possesses 1 *pau* cavity and 2 symmetry-inequivalent *d8r* cavities. Due to symmetry, there are 3 sets of 8-rings, all with narrower window dimensions than $Na_{6.7}$-MER (3.8) of 6.0 Å × 2.6 Å, 6.4 Å × 2.3 Å and 6.1 Å × 2.2 Å, and yet the material adopts an out of phase *d8r* alignment, consistent with that of Rho, also

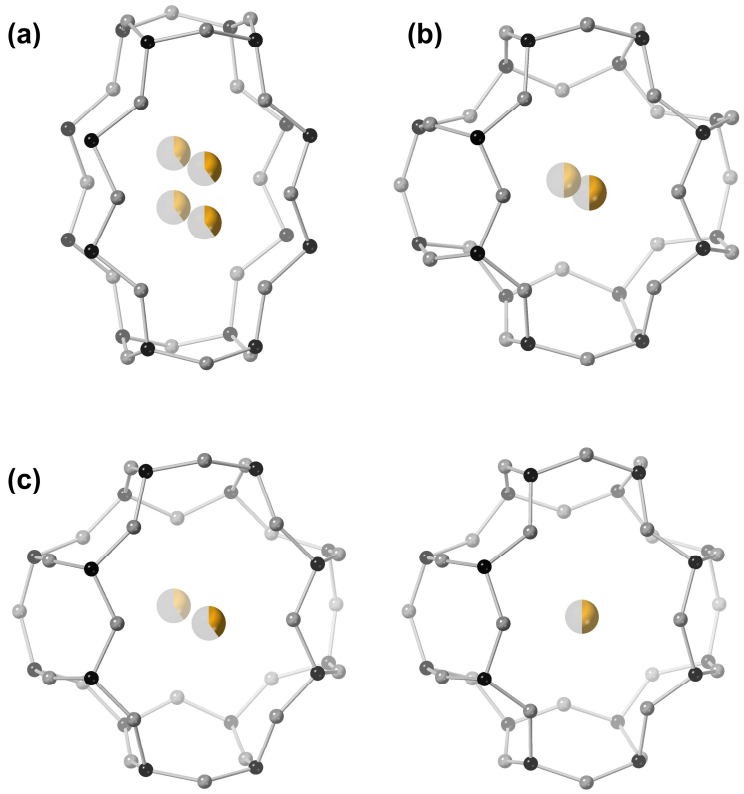

Figure 4.4.12. d8r units in Na forms of (a) ***MER****, (b)* ***RHO*** *and (c)* ***PAU****. T, O and Na are shown in black, grey and orange, respectively, with Na fractional occupancy indicated by fractional filling of sphere. Structures of (a,b,c) are taken from this work, Lozinska et al.,[33] and Greenaway et al.,[46] respectively.*

shown in Figure 4.4.12.[46] Here, the size of the structure and number of cavity types present makes consideration of the overall framework a daunting task.

4.5 MER (3.8) materials as CO_2 sorbents

When examining materials as adsorbents, investigating their dehydrated forms is most relevant as these better replicate the condition of materials upon activation for any subsequent adsorption process. As discussed previously, the framework of zeolite merlinoite can allow percolation of gases along multiple channels. The channel system extends in all 3 dimensions along 2 perpendicular *pau-ste* channels and 2 parallel *pau-d8r* and *ste-ste* channels. As can be seen from Table 4.4.6, smaller cation forms of the MER (3.8) material distort to such an extent upon dehydration that diffusion of CO_2 can only occur along a single *pau-ste* channel. Limiting diffusion to only 1 dimension would be expected to restrict the kinetics of gas diffusion within the material, and comparison of the kinetic behaviour of these materials, detailed in Section 4.3, with analogous K-MER (3.8) materials shows this is the case. This cannot be attributed to window size of the available channel or cation siting as these windows are larger than any window in the corresponding K-form and are wholly unoccupied.

As cation size increases, so does the mean free diameter of 8-rings within the dehydrated MER (3.8) materials. If adsorption kinetics were solely influenced by the framework, $Cs_{6.2}K_{0.5}$-MER (3.8) would be expected to possess the most rapid adsorption properties. As has been seen in Section 4.3 however, $K_{6.7}$-MER (3.8) is the fastest selective CO_2 adsorbent of these materials. Cation content is therefore an important factor in the properties of these materials. From Table 4.4.5 it can be seen that for the dehydrated Cs-material, there is a high occupancy of site III. This is a vital site as occupation hinders gas percolation along both the *pau-ste* channel and the *ste-ste* channel. With 4 *ste* cavities in a unit cell, the 2.5 Cs^+ per unit cell block more than half of these sites. Additionally, Cs^+ sits in more than half of the D8R sites (site Ia), impeding diffusion along the *pau-d8r* channel too.

K cations show a preference for site II, occupying slightly less than half of these buckled 8-rings in the *pau* cavity. Low occupancy of site III may be a large factor in the improved kinetics of the $K_{6.7}$-MER (3.8) material, as may the relative sizes of K^+ and Cs^+. Even with

high site occupancy, gas species may be able to percolate through the structure, as is the case in the cation gating mechanism exhibited in zeolites such as chabazite and Rho.[44,47] The bulkier Cs^+ is rather well confined within sites Ia and III and may be unable to move sufficiently to allow the movement of guest species, or their movement may be far slower. K cations in site II on the other hand may be able to move into the *pau* cavity or hop into an adjacent site II with little thermodynamic penalty.

Studies of the pure-cation materials therefore suggests that $K_{6.7}$-MER (3.8) experiences promising adsorption kinetics due to a balance of larger window sizes and preference for optimum cation sites. Ar adsorption data suggests that this is the case, with percolation in the K-material more rapid than both the Cs- and particularly the Na-form as shown in Table 4.3.1. As Ar is an inert guest, this data can be seen to be a measure of the "openness" of the structures, as previously discussed, and this trend follows a combination of window size and cation occupancy in the dehydrated materials.

To investigate the behaviour of these materials upon CO_2 adsorption, 2 sets of PXRD experiments were carried out. The first was *in situ* variable pressure PXRD (VPXRD) carried out on a laboratory instrument by Dr Georgieva with assistance from Dr Andreev. This gave low quality PXRD data across a range of pressures of CO_2. The second method, "snapshot" experiments, carried out in association with Dr Georgieva, involved dehydration of samples on a gas line, followed by exposure to sub-atmospheric pressure of CO_2, flame sealing and subsequent PXRD data collection. This gave data suitable use in for Rietveld refinement.

Patterns from *in situ* VPXRD experiments at 298 K are shown in Figure 4.5.2. Whilst the quality of this data is poor, it does allow some observations to be made. This can be aided by structured fits of the patterns, to obtain unit cell parameters. The unit cell volumes determined from this method are shown in Figure 4.5.1. The initial and final unit cell volumes of $K_{6.7}$- and $Cs_{6.2}K_{0.5}$-MER (3.8) agree reasonably well with those of the dehydrated and hydrated values, respectively, but not so for the Na-form. There may be experimental reasons for this, such as incomplete dehydration and equilibration, and the dehydrated pattern has differences in relative intensities compared to the synchrotron data.

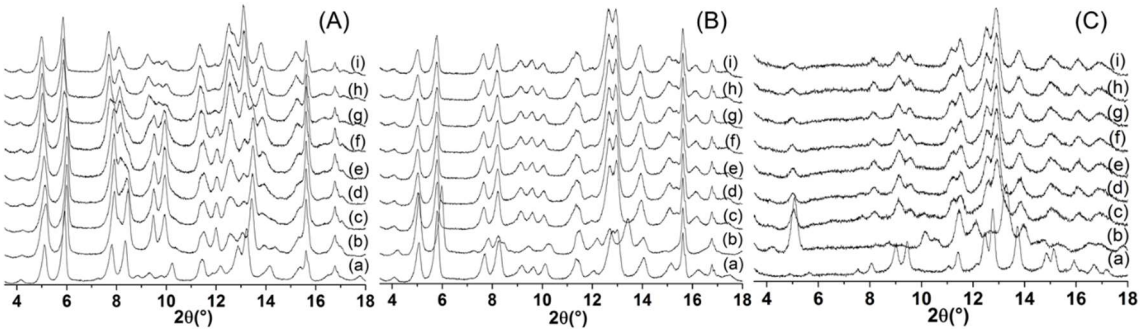

Figure 4.5.2. VPXRD data for (A) $Na_{6.7}$-, (B) $K_{6.7}$- and (C) $Cs_{6.2}K_{0.5}$-MER (3.8) at 298 K under (a) hydrated, (b) dehydrated and (c-i) adsorption conditions, with (c) 0.1, (d) 0.2, (e) 0.3, (f) 0.4, (g) 0.6, (h) 0.8 and (i) 1.0 bar of CO_2. (PANalytical, Mo $K\alpha_{1,2}$, λ = 0.711 Å).

$Na_{6.7}$-MER (3.8) undergoes minor changes in intensity at lower pressures of CO_2 before a more significant, but gradual, change in PXRD pattern at higher pressures. Further examination of this transitional region reveals that these patterns consist of 2 separate phases, corresponding to the structures present at low and high pressure of CO_2. The higher-pressure phase is similar in appearance to the hydrated pattern, indicative of an undistorted framework structure. The pressure at which this occurs increases with temperature, as evidenced by additional VPXRD data shown in Appendix III.II.I. This is consistent with the non-Type I adsorption isotherm observed for this material and indicates a phase change at a critical uptake of CO_2 with associated increased pore volume. This uptake requires a higher pressure of CO_2 as temperature increases. The step in the CO_2 adsorption isotherm at 298 K occurs at *ca.* 0.05 bar, which is consistent

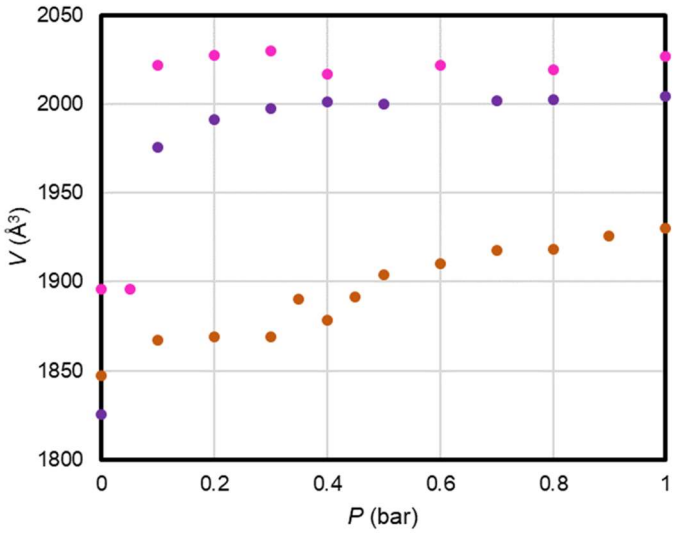

Figure 4.5.1. Unit cell volumes of M-MER (3.8) materials as obtained from VPXRD analysis. $Na_{6.7}$-, $K_{6.7}$- and $Cs_{6.2}K_{0.5}$-MER (3.8) data is plotted in orange, purple and pink, respectively. Note that data between 0.1 and 0.5 bar, values for the Na-form are a weighted average of 2 phases.

with the VPXRD data, which shows the introduction of a wide-pore phase at the first pressure examined, 0.1 bar. Due to the shallow sample depth and relatively large volume of dosing gas, the presence of 2 phases is unlikely to be due to the experimental setup except for equilibration time. As the sample was allowed to equilibrate for an hour after each pressure step before pattern acquisition, the transition from narrow- to wide-pore phases must incur an extreme kinetic penalty.

$K_{6.7}$-MER (3.8) exhibits different behaviour. At the lowest uptake of CO_2 investigated, the structure has switched to a larger pore form, even at higher temperature. This suggests that the phase change occurs with very little CO_2 present and is relatively rapid. This is accompanied by a Type I CO_2 adsorption isotherm. The behaviour of $Cs_{6.2}K_{0.5}$-MER (3.8) appears to lie somewhere in between the other 2 materials. At 298 K, the material adopts a wide-pore form upon exposure to low pressure of CO_2, similar to the K-analogue. At higher temperature however, the distorted structure is shown to be adopted at progressively higher pressure. This is consistent with the adsorption isotherm data which shows a kink at low pressures of CO_2 which moves to higher pressure as temperature increases. At 298 K, the VPXRD data shows opening to the wide-pore form below 0.1 bar, whilst the appropriate adsorption isotherm shows a kink at 0.03 bar of CO_2. Unlike the Na-form, the change in phase is well separated, suggesting a relatively rapid phase change.

In situ data allowed the trend in unit cell volume to be examined but not the contents of the cell. The use of snapshot experiments allowed refinable quality data but only at a single pressure of CO_2. Selected refinement data is detailed in Table 4.5.1. Patterns, Rietveld plots and structures of these materials are shown in Figures 4.5.3, 4.5.4 and 4.5.5, respectively.

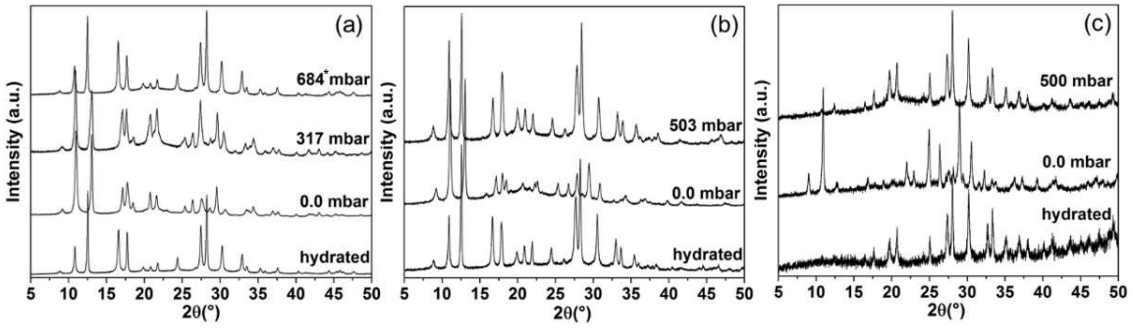

*Figure 4.5.3. Snapshot PXRD patterns of (a) $Na_{6.7}$-, (b) $K_{6.7}$- and (c) $Cs_{6.2}K_{0.5}$-MER (3.8) with hydrated and dehydrated patterns also given for comparison. * denotes extended time experiment. (Stoe, λ = 1.54056 Å).*

*Table 4.5.1. Space group (SG), unit cell parameters and R_{wp} from refinement of snapshot $M_{6.7}$-MER experiments. * denotes extended time experiment.*

Cation form	P (mbar)	SG	*a* (Å)	*b* (Å)	*c* (Å)	*V* (Å³)	R_{wp}
$Na_{6.7}$	317	*Immm*	13.477(1)	13.441(1)	10.015(1)	1814(1)	7.8%
	684	*Immm*	13.485(1)	13.474(1)	10.019(1)	1821(1)	6.4%
	684*	*Immm*	14.121(1)	14.122(1)	10.031(1)	2000(1)	7.0%
$K_{6.7}$	503	$P4_2/nmc$	13.990(1)		9.832(1)	1924(1)	8.3%
$Cs_{6.2}K_{0.5}$	500	$P4_2/nmc$	14.197(1)		10.016(1)	2019(1)	7.5%

The $Na_{6.7}$-MER (3.8) material remains in a narrow-pore form under pressure of CO_2 initially. At 317 mbar, this is as anticipated from *in situ* experiments which show a gradual change to the wide-pore form above 300 mbar of CO_2 at 298 K. By 684 mbar, this is expected to be complete and yet early data collection (overnight on the same day as exposure to gas) showed the sample to still exhibit a narrow-pore form. Only after re-

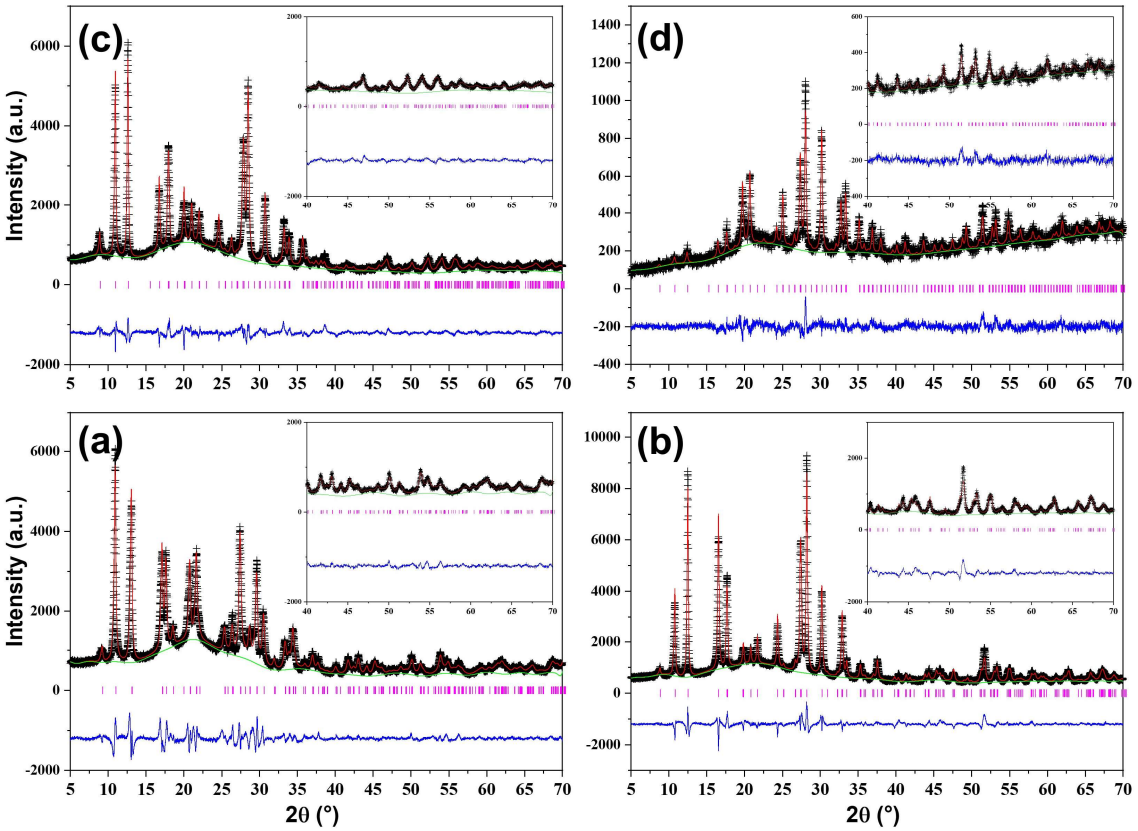

Figure 4.5.4. Rietveld plots of M-MER (3.8) samples under pressure of CO_2, with M = (a,b) $Na_{6.7}$, (c) $K_{6.7}$ and (d) $Cs_{6.2}K_{0.5}$ and CO_2 pressure of (a) 317, (b) 684, (c) 503 and (d) 500 mbar. * denotes extended time experiment. (Stoe, λ = 1.54056 Å).*

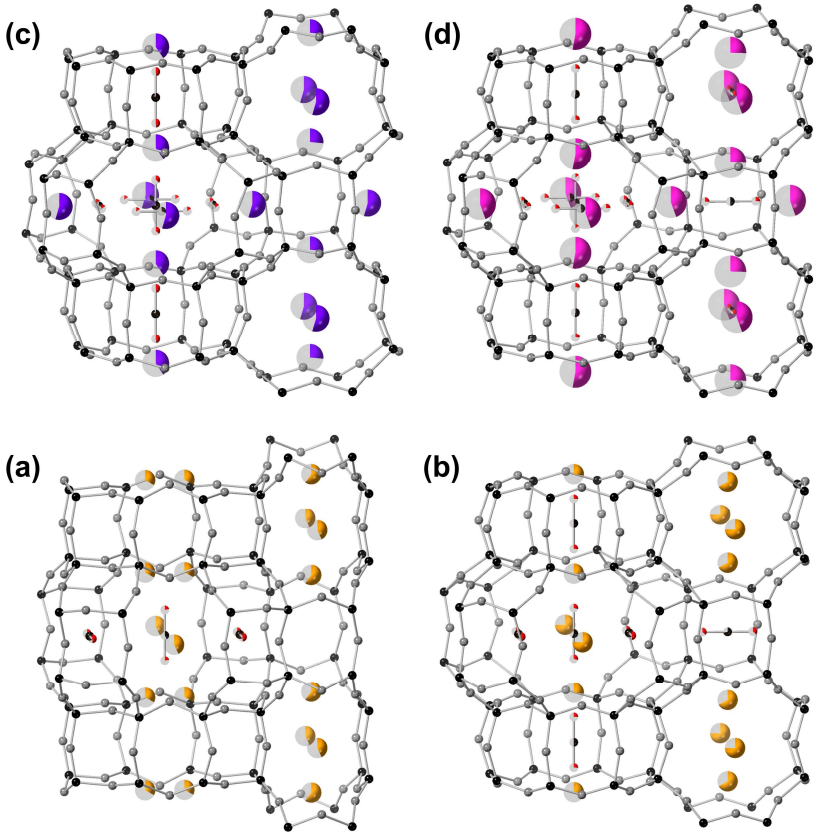

Figure 4.5.5. Refined structures of M-MER (3.8) samples under pressure of CO_2, with M = (a,b) $Na_{6.7}$, (c) $K_{6.7}$ and (d) $Cs_{6.2}K_{0.5}$ and CO_2 pressure of (a) 317, (b) 684, (c) 503 and (d) 500 mbar. * denotes extended time experiment. Framework T and O sites shown in black and grey, CO_2 molecules in red and white and Na, K and Cs cations depicted in orange, purple and pink, respectively. Fractional occupancies are indicated by partial shading.*

examination of the sample one month later was the wide-pore form seen to be adopted. The initial PXRD pattern and refinement data are given in Appendices III.II.I and VI.II.I, respectively, though it is near identical to the 317 mbar data.

This behaviour differs from the expansion behaviour observed in earlier VPXRD data for the sample and these differences are due to the relative setups of the 2 experiments. In the *in situ* case, the sample is exposed to a fixed pressure in a flat plate arrangement. An hour of equilibration was allowed for each pressure dose, and the sample was subject to consecutive gas exposure, equilibration and pattern acquisition steps. In these capillary experiments, the sample was allowed to equilibrate for an hour and the subsequent equilibrium pressure recorded before sealing the sample and any gas present in the capillary. Further equilibration could occur before and during data

acquisition, with the pressure dropping slightly within the capillary as further gas was adsorbed.

High angle data, collected towards the end of pattern acquisition, does not disagree with earlier unit cell parameters, and thus the initial pattern collected can be said to be a narrow-pore form throughout acquisition. Transition to the wide-pore form must therefore have occurred at some point between 20 hrs and a month after dosing of CO_2. Regardless of the exact point at which this occurred, the transition is a slow one, which was also seen in the *in situ* data. Such an extended equilibration time also suggests that both the *in situ* VPXRD data and any gas adsorption isotherms should be viewed with caution, as the sample may not have reached equilibrium and thus be under kinetic control.

Snapshot data for the other samples was more straightforward. $K_{6.7}$-MER (3.8) adopts a wide-pore form at 503 mbar of CO_2 at 298 K, as expected from the previous VPXRD data and the CO_2 adsorption isotherm. The unit cell is smaller than that refined for the hydrated form, with a unit cell volume of 1924 $Å^3$ compared to 1984 $Å^3$ but substantially larger than the 1823 $Å^3$ dehydrated form. This is smaller than expected from the *in situ* data but exact comparisons are difficult due to differences in the respective setups and quality, including peak shape, but perhaps most significantly dehydration, which is likely poorer in the *in situ* experiments and would lead to an expanded unit cell. By contrast, the 500 mbar capillary data for the $Cs_{6.2}K_{0.5}$-MER (3.8) material agrees well with the *in situ* data and clearly shows the adoption of the wide-pore framework structure.

The cation site occupancies for these materials are shown in Table 4.5.2. Comparison with those given previously in Table 4.4.5 for dehydrated and hydrated forms, occupying narrow- and wide-pore forms, respectively, can show if there are substantial differences during adsorption. It can be seen that these values agree strongly with equivalent refinements, with the exception of a higher degree of occupancy in site III at the expense of site IIa for the $Na_{6.7}$-material in both narrow- and wide-pore forms refined during adsorption. The other 2 samples, both in an expanded form, show near identical cation occupancies to their respective hydrated structures.

*Table 4.5.2. Absolute site occupancies of M^+ in MER (3.8) materials under CO_2 adsorption. *denotes merging of related but symmetry inequivalent positions. [a] denotes site Ia occupancy i.e. D8R site. For $Cs_{6.2}K_{0.5}$-MER (3.8), occupancies given are for Cs^+.*

Cation form	P (mbar)	I	II*	III	Total
$Na_{6.7}$	317	3.0(1)	1.6(1)	2.2(1)	6.7(2)
	684	3.2(1)	1.9(1)	1.6(1)	6.7(2)
	684*	1.1(1)	3.0(1)	2.7(1)	6.8(2)
$K_{6.7}$	503	1.6(1)	4.3(1)	1.0(1)	7.0(1)
$Cs_{6.2}K_{0.5}$	500	2.1(1)	3.5(1)	1.0(1)	6.7(1)

Greater differences are observed in terms of window sizes, listed in Table 4.5.3. $Na_{6.7}$-MER (3.8) appears to have smaller windows I and III, and a larger IIb in the narrow-pore form than the dehydrated refinement. This is particularly marked for window I, with a free diameter in both narrow-pore refinements here *ca*. 1.7 Å, as opposed to 2.1 Å. This is reversed in the wide-pore 684 mbar refinement which shows larger windows I and III. Windows IIa and b, by contrast, are smaller than their hydrated counterparts. $K_{6.7}$-MER (3.8) also shows a larger window I, with the $Cs_{6.2}K_{0.5}$-material having smaller windows I and II, with a larger III in comparison to their hydrated forms. Many of these differences are less significant and may suggest simply that the associated errors should be reported as larger values. The more significant differences for window I in both $Na_{6.7}$- and $K_{6.7}$-MER (3.8) under adsorption could be due to unrecognised differences in activation conditions, particularly levels of hydration.

*Table 4.5.3. Free window diameters in MER (3.8) materials under CO_2 adsorption. Windows that would be closed to CO_2 percolation (<2.3 Å) are denoted by *.*

Cation form	P (mbar)	I	II(a)	IIb	III
$Na_{6.7}$	317	1.7(1)*	1.7(1)*	3.0(1)	1.6(1)*
	684	1.7(1)*	1.7(1)*	3.0(1)	1.6(1)*
	684*	3.9(1)	3.2(1)	3.1(1)	3.4(1)
$K_{6.7}$	503	3.5(1)	3.4(1)		3.7(1)
$Cs_{6.2}K_{0.5}$	500	3.8(1)	3.2(1)		3.7(1)

Under pressure of CO_2, $Na_{6.7}$-MER (3.8) initially behaved much like its dehydrated form, in terms of both site occupancies and window sizes. Thus, any initial adsorption would be expected to subject to the same kinetics as the activated form, slow due to the extremely narrow window sizes and resultant 1-dimensional pore network. It is only upon further adsorption of CO_2, and sufficient equilibration time, that the framework switches to the wide-pore form, which sees a great increase in window sizes and 3-dimensional channel connectivity. This explains the poor kinetic behaviour found by ZLC analysis, detailed in Section 4.3, as the measurement was carried out under the narrow-pore regime.

From the *in situ* experiments, it was seen that the $K_{6.7}$-material almost immediately opened to a wide pore form upon adsorption of CO_2. Whilst at initial pressures of CO_2 there appears to be a slight increase in unit cell volume, and therefore likely window size, 503 mbar CO_2 capillary data shows that once fully opened there is little change in the structure. *In situ* experiments suggest this occurs at *ca*. 300 mbar but it is likely that earlier structures are reasonably similar as they adopt the wide-pore form. ZLC data was obtained at 0.1 bar pressure of CO_2, which would adopt the wide-pore form according to *in situ* data. The wide windows and relatively low occupancy of all window sites aids in explaining the rapid diffusion kinetics observed, so rapid that the sample is found to be under equilibrium control. The occupancy of site II is approximately half, which may be expected to begin to limit diffusion through the *pau* and *ste* cavities, although the size of the windows and adjacent, locally-vacant sites I and II may aid cation hopping upon the approach of guest species, as modelled by Mace *et al*. in zeolite A.[48] As cation occupancy is approximately half in this site, and less than half in other sites, it may be that no form of cation gating mechanism is required, and that traditional molecular sieving behaviour dominates for this material, with some windows blocked by cations on a rapid diffusion timescale.

Similar behaviour is observed in the $Cs_{6.2}K_{0.5}$-MER (3.8) material, with some differences. Unlike the K-form, the narrow-pore form of the Cs-material is adopted at low partial pressure of CO_2 before transition to the wide-pore form at a critical uptake. This transition appears to occur relatively quickly, with only single phases observed in the *in situ* VPXRD data at any given pressure. This data also suggests that under the ZLC conditions used the wide-pore structure is the relevant one. This form possesses wide

windows, although bulky Cs cations have quite high occupancy in both sites I and II. This is not significantly different from the $K_{6.7}$-MER (3.8) material under similar conditions and so the size of the cations is most likely to blame for the slower kinetics observed, possibly slowing percolation through *pau* cavities.

4.6 Conclusion

Merlinoite is a flexible zeolite, exhibiting interesting adsorption and structural behaviour, with MER (3.8) samples adopting narrow-pore forms upon dehydration. Steps in CO_2 adsorption isotherms have been shown to be caused by breathing behaviour, with the transition to wide-pore phases upon increased CO_2 pressure. The type of cation present within the MER (3.8) material determines the mode of distortion adopted, as well as the extent, with smaller cations directing a more distorted framework structure, with narrower windows. The degree of distortion caused by Na and Li cations examined here, leads to the formation of 1-dimensional pore structures, limiting the diffusion of gas molecules. The sites that these cations adopt, as well as the size of cations, also determines the kinetic properties of the materials, by combining traditional molecular sieving and pore blocking effects.

4.7 References

(1) Passaglia, E.; Pongiluppi, D.; Rinaldi, R. Merlinoite, a New Mineral of the Zeolite Group. *Neues Jahrb. Fur Mineral. - Monatshefte* **1977**, *8*, 355–364.

(2) Galli, E.; Gottardi, G.; Pongiluppi, D. The Crystal Structure of the Zeolite Merlinoite. *Neues Jahrb. Fur Mineral. - Monatshefte* **1979**, *10*, 1–9.

(3) Sherman, J. D. Identification and Characterization of Zeolites Synthesized in the K_2O-Al_2O_3-SiO_2-H_2O System. In *Molecular Sieves-II*; Katzer, J. R., Ed.; American Chemical Society: Washington DC, 1977; pp 30–42.

(4) Barrer, R. M.; Baynham, J. W. The Hydrothermal Chemistry of the Silicates. Part VII. Synthetic Potassium Aluminosilicates. *J. Chem. Soc.* **1956**, 2882–2891.

(5) Barrer, R. M.; Baynham, J. W.; Bultitude, F. W.; Meier, W. M. Hydrothermal

Chemistry of the Silicates. Part VIII. Low-Temperature Crystal Growth of Aluminosilicates, and of Some Gallium and Germanium Analogues. *J. Chem. Soc.* **1959**, 195–208.

(6) Galli, E.; Passaglia, E.; Pongiluppi, D.; Rinaldi, R. Mazzite, a New Mineral, the Natural Counterpart of the Synthetic Zeolite Ω. *Contrib. to Mineral. Petrol.* **1974**, *45*, 99–105.

(7) Pakhomova, A. S.; Armbruster, T.; Krivovichev, S. V.; Yakovenchuk, V. N. Dehydration of the Zeolite Merlinoite from the Khibiny Massif, Russia: An *in Situ* Temperature-Dependent Single-Crystal X-Ray Study. *Eur. J. Mineral.* **2014**, *26* (3), 371–380.

(8) Kakutani, Y.; Weerachawanasak, P.; Hirata, Y.; Sano, M.; Suzuki, T.; Miyake, T. Highly Effective K-Merlinoite Adsorbent for Removal of Cs^{+} and Sr^{2+} in Aqueous Solution. *RSC Adv.* **2017**, *7*, 30919–30928.

(9) Chen, W.; Song, G.; Lin, Y.; Qiao, J.; Wu, T.; Yi, X.; Kawi, S. A Green and Efficient Strategy for Utilizing of Coal Fly Ash to Synthesize K-MER Zeolite as Catalyst for Cyanoethylation and Adsorbent of CO_2. *Microporous Mesoporous Mater.* **2021**, *326*, 111353.

(10) Cheong, Y.; Rigolet, S.; Daou, T. J.; Wong, K.; Chuan, T.; Ng, E. Crystal Growth Study of Nanosized K-MER Zeolite from Bamboo Leaves Ash and Its Catalytic Behaviour in Knoevenagel Condensation of Benzaldehyde with Ethyl Cyanoacetate. *Mater. Chem. Phys.* **2020**, *251* (April), 123100.

(11) Seo, Y.; Adi, E.; Jiang, N.; Oh, S.; Park, S. Catalytic Dehydration of Methanol over Synthetic Zeolite W. *Microporous Mesoporous Mater.* **2010**, *128*, 108–114.

(12) Li, J.; Zhuang, X.; Font, O.; Moreno, N.; Vallejo, V. R.; Querol, X.; Tobias, A. Synthesis of Merlinoite from Chinese Coal Fly Ashes and Its Potential Utilization as Slow Release K-Fertilizer. *J. Hazard. Mater.* **2014**, *265*, 242–252.

(13) Estevam, S. T.; Fernandes, T.; Tainá, D. A.; Raiane, S. Synthesis of K - Merlinoite Zeolite from Coal Fly Ash for Fertilizer Application. *Brazilian J. Chem. Eng.* **2022**, *39*, 631–643.

(14) Hermassi, M.; Valderrama, C.; Font, O.; Moreno, N.; Querol, X.; Harrouch, N.; Luis, J. Science of the Total Environment Phosphate Recovery from Aqueous Solution by K-Zeolite Synthesized from Fly Ash for Subsequent Valorisation as Slow Release Fertilizer. *Sci. Total Environ.* **2020**, *731*, 139002.

(15) Mirfendereski, S. M. Synthesis and Application of High-Permeable Zeolite MER Membrane for Separation of Carbon Dioxide from Methane. *J. Aust. Ceram. Soc.* **2019**, *55*, 103–114.

(16) Choi, H. J.; Jo, D.; Min, J. G.; Hong, S. B. The Origin of Selective Adsorption of CO_2 on Merlinoite Zeolites. *Angew. Chemie - Int. Ed.* **2021**, *60* (8), 4307–4314.

(17) Yeo, Z. Y.; Chai, S. P.; Zhu, P. W.; Mah, S. K.; Mohamed, A. R. Preparation of Self-Supported Crystalline Merlinoite-Type Zeolite W Membranes through Vacuum Filtration and Crystallization for CO_2/CH_4 Separations. *New J. Chem.* **2015**, *39* (5), 4135–4140.

(18) KR Pat. 20170137999A, 2017.

(19) JP Pat. 2006150239, 2006.

(20) WIPO Pat. 2021024045A1, 2021.

(21) Baerlocher, C.; McCusker, L. B. IZA Database of Zeolite Structures, http://www.iza-structure.org/databases/, accessed October 2023.

(22) Lozinska, M. M.; Mangano, E.; Greenaway, A. G.; Fletcher, R.; Thompson, S. P.; Murray, C. A.; Brandani, S.; Wright, P. A. Cation Control of Molecular Sieving by Flexible Li-Containing Zeolite Rho. *J. Phys. Chem. C* **2016**, *120* (35), 19652–19662.

(23) Balestra, S. R. G.; Hamad, S.; Ruiz-Salvador, A. R.; Domínguez-García, V.; Merkling, P. J.; Dubbeldam, D.; Calero, S. Understanding Nanopore Window Distortions in the Reversible Molecular Valve Zeolite RHO. *Chem. Mater.* **2015**, *27* (16), 5657–5667.

(24) Solov'eva, L. P.; Borisov, S. V.; Bakakin, V. V. New Skeletal Structure in the Crystal Structure of Barium Chloroaluminosilicate $BaAlSi_2O_6(Cl,OH)$ -> $Ba_2[X]BaCl_2[(Si,Al)_8O_{18})$. *Kristallografiya* **1971**, *16*, 1179.

(25) Baturin, S. V.; Malinovskii, Y. A.; Runovoa, I. B. Crystalline Structure of the Low-Silica Merlinoite from the Kola Peninsula. *Mineral. Zhurnal* **1985**, *7*, 67–74.

(26) Bieniok, A.; Bornholdt, K.; Brendel, U.; Baur, W. H. Synthesis and Crystal Structure of Zeolite W, Resembling the Mineral Merlinoite. *J. Mater. Chem.* **1996**, *6* (2), 271.

(27) Barrett, P. A.; Valencia, S.; Camblor, M. A. Synthesis of a Merlinoite-Type Zeolite with an Enhanced Si/Al Ratio via Pore Filling with Tetraethylammonium Cations. *J. Mater. Chem.* **1998**, *23* (10), 2263–2268.

(28) Yakubovich, O. V.; Massa, W.; Pekov, I. V.; Kucherinenko, Y. V. Crystal Structure of a Na,K-Variety of Merlinoite. *Crystallogr. Reports* **1999**, *44*, 776–782.

(29) Skofteland, B. M.; Ellestad, O. H.; Lillerud, K. P. Potassium Merlinoite: Crystallization, Structural and Thermal Properties. *Microporous Mesoporous Mater.* **2001**, *43* (1), 61–71.

(30) Wang, J. Y.; Mangano, E.; Brandani, S.; Ruthven, D. M. A Review of Common Practices in Gravimetric and Volumetric Adsorption Kinetic Experiments. *Adsorption* **2021**, *27* (3), 295–318.

(31) Georgieva, V. M.; Bruce, E. L.; Verbraeken, M. C.; Scott, A. R.; Casteel, Jr, W. J.; Brandani, S.; Wright, P. A. Triggered Gate Opening and Breathing Effects during Selective CO_2 Adsorption by Merlinoite Zeolite. *J. Am. Chem. Soc.* **2019**, *141* (32), 12744–12759.

(32) Waseda, Y.; Matsubara, E.; Shinoda, K. *X-Ray Diffraction Crystallography; Introduction, Examples and Solved Problems*; Springer: Heidelberg, 2011.

(33) Lozinska, M. M.; Mangano, E.; Mowat, J. P. S.; Shepherd, A. M.; Howe, R. F.; Thompson, S. P.; Parker, J. E.; Brandani, S.; Wright, P. A. Understanding Carbon Dioxide Adsorption on Univalent Cation Forms of the Flexible Zeolite Rho at Conditions Relevant to Carbon Capture from Flue Gases. *J. Am. Chem. Soc.* **2012**, *134* (42), 17628–17642.

(34) Shannon, R. D. Revised Effective Ionic Radii and Systematic Studies of Interatomic Distances in Halides and Chalcogenides. *Acta Crystallogr. Sect. A* **1976**,

32 (5), 751–767.

(35) Cook, M.; Conner, W. C. How Big Are the Pores of Zeolites? In *Proceedings of the 12th International Zeolite Conference*; Treacy, M. M. J., Marcus, B. K., Bisher, M. E., Higgins, J. B., Eds.; Materials Research Society: Warrendale, PA, USA, 1999; pp 409–414.

(36) Vrabec, J.; Stoll, J.; Hasse, H. A Set of Molecular Models for Symmetric Quadrupolar Fluids. *J. Phys. Chem. B* **2001**, *105* (48), 12126–12133.

(37) Smith, L. J.; Eckert, H.; Cheetham, A. K. Site Preferences in the Mixed Cation Zeolite, Li,Na-Chabazite: A Combined Solid-State NMR and Neutron Diffraction Study. *J. Am. Chem. Soc.* **2000**, *122* (8), 1700–1708.

(38) Newsam, J. M.; Jarman, R. H.; Jacobson, A. J. A Study of the Mixed $Na_{1-x}Li_x$ Zeolite A System by Powder X-Ray Diffraction. *J. Solid State Chem.* **1985**, *58* (3), 325–334.

(39) Johnson, G. M.; Reisner, B. A.; Tripathi, A.; Corbin, D. R.; Toby, B. H.; Parise, J. B. Flexibility and Cation Distribution upon Lithium Exchange of Aluminosilicate and Aluminogermanate Materials with the RHO Topology. *Chem. Mater.* **1999**, *11* (10), 2780–2787.

(40) Norby, P.; Poshni, F. I.; Gualtieri, A. F.; Hanson, J. C.; Grey, C. P. Cation Migration in Zeolites: An in Situ Powder Diffraction and MAS NMR Study of the Structure of Zeolite Cs(Na)−Y during Dehydration. *J. Phys. Chem. B* **1998**, *102* (5), 839–856.

(41) Su, B.; Martens, J. A. An Infrared Study on the Location of Benzene Molecules and Cations in Cs^+-Exchanged EMT Zeolite. **1998**, *25*, 151–167.

(42) Vance, T. B. J.; Seff, K. Hydrated and Dehydrated Crystal Structures of Seven-Twelfths Cesium-Exchanged Zeolite A. *J. Phys. Chem.* **1975**, *79* (20), 2163–2167.

(43) Smith, L. J.; Eckert, H.; Cheetham, A. K. Potassium Cation Effects on Site Preferences in the Mixed Cation Zeolite Li, Na-Chabazite. *Chem. Mater.* **2001**, *13* (2), 385–391.

(44) Lozinska, M. M.; Mowat, J. P. S.; Wright, P. A.; Thompson, S. P.; Jorda, J. L.; Palomino, M.; Valencia, S.; Rey, F. Cation Gating and Relocation during the Highly Selective "Trapdoor" Adsorption of CO_2 on Univalent Cation Forms of

Zeolite Rho. *Chem. Mater.* **2014**, *26* (6), 2052–2061.

(45) Bieniok, A.; Bürgi, H.-B. Deformation Analysis of the D8R-Unit in Zeolite Structures. In *Studies in Surface Science and Catalysis*; Weitkamp, J., Karge, H. G., Pfeifer, H., Hölderich, W., Eds.; Elsevier B.V.: Amsterdam, 1994; Vol. 84, pp 567–574.

(46) Greenaway, A. G.; Shin, J.; Cox, P. A.; Shiko, E.; Thompson, S. P.; Brandani, S.; Hong, S. B.; Wright, P. A. Structural Changes of Synthetic Paulingite (Na,H-ECR-18) upon Dehydration and CO_2 Adsorption. *Zeitschrift fur Krist.* **2015**, *230* (4), 223–231.

(47) Shang, J.; Li, G.; Singh, R.; Gu, Q.; Nairn, K. M.; Bastow, T. J.; Medhekar, N.; Doherty, C. M.; Hill, A. J.; Liu, J. Z.; Webley, P. A. Discriminative Separation of Gases by a "Molecular Trapdoor" Mechanism in Chabazite Zeolites. *J. Am. Chem. Soc.* **2012**, *134* (46), 19246–19253.

(48) Mace, A.; Hedin, N.; Laaksonen, A. Role of Ion Mobility in Molecular Sieving of CO_2 over N_2 with Zeolite NaKA. *J. Phys. Chem. C* **2013**, *117* (46), 24259–24267.

5 Zeolite Merlinoite: Si/Al = 4.2

5.1 Introduction

After investigation of the previously reported MER (3.8) material, Dr Veselina M. Georgieva developed the synthesis of a higher Si/Al form. This was found by EDX and NMR analysis to possess a framework Si/Al of 4.2. Whilst this may not seem a substantial increase, it decreases the number of extraframework monovalent cations within the structure from 6.7 to 6.2 per unit cell, 7% less. The following details the underlying analysis collected for samples prepared from this material and investigation of their structural behaviour, comparison with the MER (3.8) material previously discussed, and with the contemporaneous work of Choi *et al*. on MER (2.3) and (2.9).[1,2]

5.2 Acknowledgements

Much of the work done by coworkers and collaborators in Chapter 4 is replicated in this chapter. Dr Georgieva was invaluable in synthesising and preparing almost all of the merlinoite materials investigated in this chapter, aided by Dr Alessandro Turrina at Johnson Matthey. Both Drs Veselina M. Georgieva and Magdalena M. Lozinska dehydrated samples and collected equilibrium adsorption, laboratory and synchrotron PXRD data. Prof Paul A. Wright and Dr Claire A. Murray assisted with synchrotron data collection. Kinetic adsorption data described here was again collected by Dr Maarten C. Verbraeken in the group of Prof Stefano Brandani at the University of Edinburgh, and Ar adsorption data was obtained by Dr William J. Casteel, Jr. at Air Products & Chemicals, Inc.

5.3 Underlying experimental work

Higher Si/Al zeolite K,TEA-MER was synthesised by Drs Veselina Georgieva and Alessandro Turrina and found through a combination of EDX, TGA and NMR analysis to have the chemical composition $K_{5.2}TEA_{1.0}[Si_{25.8}Al_{6.2}O_{64}].(H_2O)_x$. SEM images of the as-prepared material collect by Dr Veselina Georgieva are shown in Figure 5.3.1.

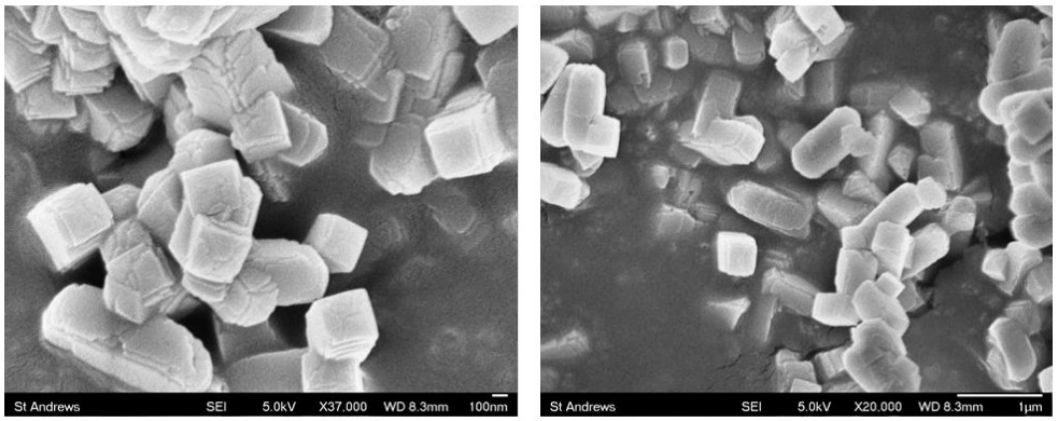

Figure 5.3.1. SEM images of as-prepared $K_{5.2}TEA_{1.0}$-MER (4.2).

Samples of different cation forms were created from this initial material using ion exchange: $M_{6.2}$-MER (4.2), where M indicates a cation, which included Li-, Na-, K- and Cs-forms. Li-MER (4.2) and related materials are discussed in Chapter 6, whilst this chapter focusses on the remaining samples. PXRD patterns of these materials in their hydrated and dehydrated forms are shown in Figure 5.3.2.

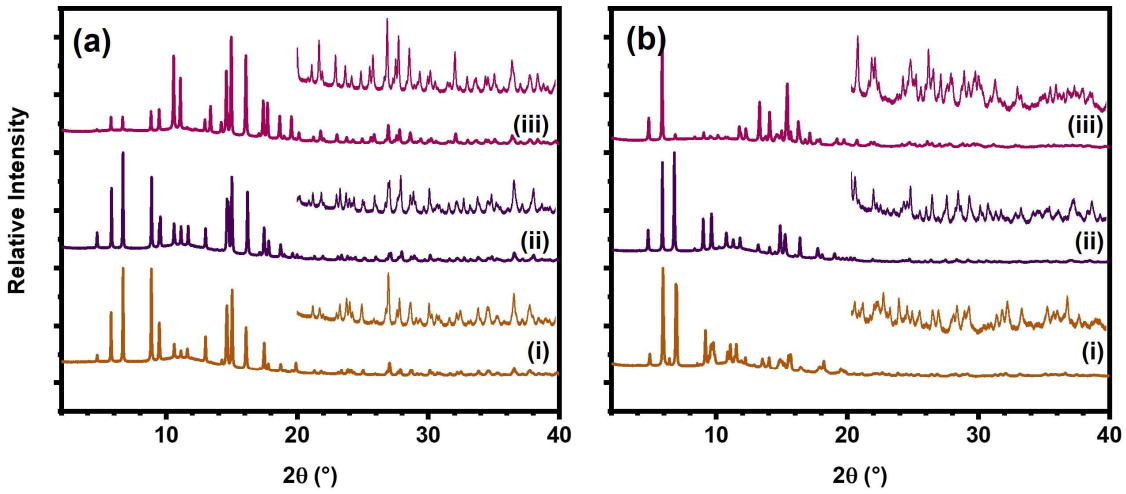

Figure 5.3.2. PXRD patterns of MER (4.2) materials at 298 K under (a) hydrated and (b) dehydrated conditions: (i) $Na_{6.2}$-, (ii) $K_{6.2}$- and (iii) $Cs_{6.2}$-MER (4.2) data (I11, DLS, λ = 0.826398 Å).

CO_2 sorption isotherms up to 1 bar at 298 K and at higher pressure at varying temperatures were collected, as shown in Figure 5.3.3 . Non-type I behaviour is observed for both Na- and Cs-forms of the material.

Ar uptake experiments were also carried out for the samples, as a measure of "openness", as previously discussed in Chapter 4. Ar diffusivities and related uptake timescales,[3] are presented in Table 5.3.1.

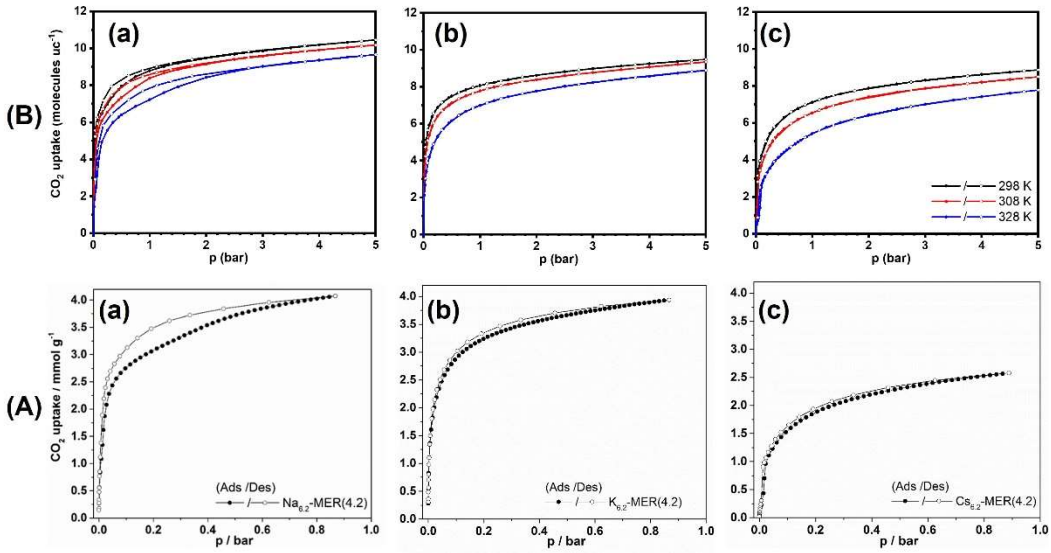

Figure 5.3.3. CO_2 adsorption isotherms of $M_{6.2}$-MER (4.2) materials, (A) up to 1 bar at 298 K and (B) up to 10 bar at 298, 308 and 328 K. M = (a) Na, (b) K and (b) Cs. Note maximum uptakes are more similar when plotted as molecules per unit cell (uc) than as mmol g^{-1}.

Table 5.3.1. Ar diffusivity data for MER (4.2) materials

Material	Ar D/r^2 (s^{-1})	Uptake timescale (s)
$Na_{6.2}$-MER (4.2)	4.6×10^{-3}	43
$K_{6.2}$-MER (4.2)	4.1×10^{-1}	0.5
$Cs_{6.2}$-MER (4.2)	2.1×10^{-3}	95

Breakthrough curves were also collected for these materials with a gas stream composition of 10:40:50 CO_2/CH_4/He, as were their subsequent desorption curves in a flow of He, both shown in Figure 5.3.4. Uptakes of CO_2 and CH_4 from these experiments are listed in Table 5.3.2, as are the selectivities of these materials. To analyse desorption kinetics at low CO_2 loadings, ZLC measurements were carried out at 10% CO_2 in ambient pressure of He and 308 K. These showed diffusivities of D/r^2 = 0.9 and 6.9×10^{-3} s^{-1} for $Na_{6.2}$- and $Cs_{6.2}$-MER (4.2), respectively, as calculate by coworkers following methods more fully described in Bruce *et al.*[4] Again, the K-form was found to be under

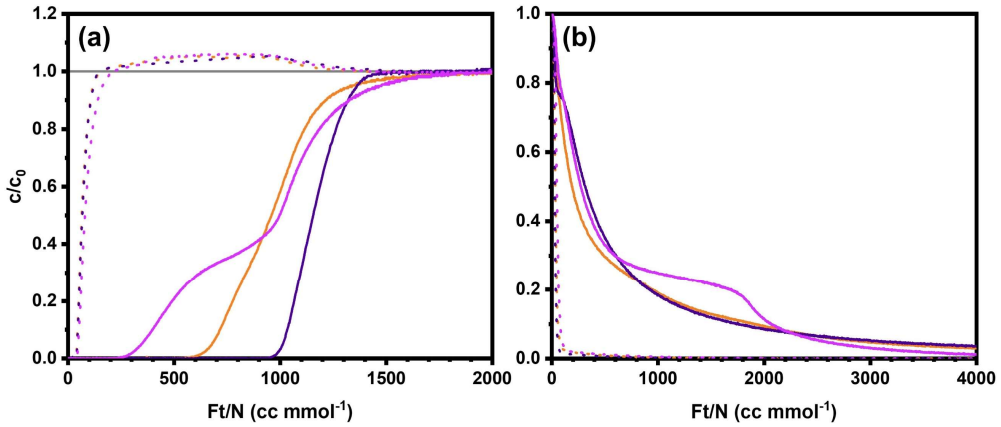

Figure 5.3.4. Breakthrough curves for $M_{6.2}$-MER (4.2) materials in a flow of 10:40:50 CO_2/CH_4/He at 298 K, under (a) adsorption and (b). Data for Na-, K- and Cs-forms are shown in orange, purple and pink, respectively. CO_2 and CH_4 sorption data is shown by solid and dashed lines, respectively. Curves are shown as a function of volume of gas that has flowed over the sample.

thermodynamic control initially under conditions used, showing rapid percolation of CO_2, with kinetic control becoming established as CO_2 was released.

Table 5.3.2. Uptakes and selectivities of MER (4.2) materials determined by mixed component E-ZLC experiments at 298 K.

Material	**CO_2 uptake (mmol g^{-1})**	**CH_4 uptake (mmol g^{-1})**	**CO_2/CH_4 selectivity**
$Na_{6.2}$-MER (4.2)	1.41	0.02	282
$K_{6.2}$-MER (4.2)	1.73	0.05	154
$Cs_{6.2}$-MER (4.2)	1.01	0.005	808

5.4 Structural studies of MER (4.2) materials

5.4.1 Hydrated $M_{6.2}$-MER (4.2)

Once samples were ion exchanged to their desired forms, the samples exist in a hydrated state, before any subsequent dehydration required for adsorption purposes. Rietveld plots of hydrated $M_{6.2}$-MER (4.2) materials are shown in Figure 5.4.1 and crystallographic details are given in Appendix VI.II.II.

Unit cell parameters and refinement details obtained from Rietveld analysis are given in Table 5.4.1. Here all samples adopted the *I*4/*mmm* space group, as was the case in Chapter 4 for the $M_{5.9}TEA_{0.8}$-MER (3.8) materials, and whilst $P4_2/nmc$ was trialled for the

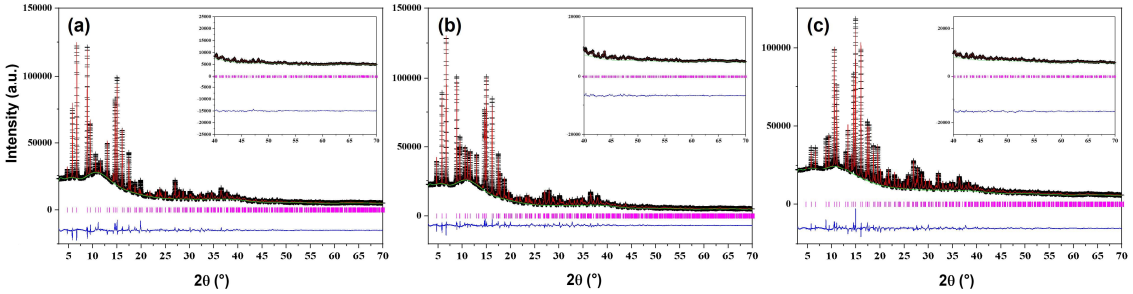

Figure 5.4.1. Rietveld plots of hydrated $M_{6.2}$-MER (4.2) samples, with M = (a) Na, (b) K and (c) Cs. (I11, DLS, λ = 0.826398 Å).

heavier cation forms, improvements were insignificant. Along with the lack of any peaks breaking body centring, this provided no need to invoke the lower symmetry space group. Fits for these samples are much improved over those discussed in Chapter 4.

The refined structures of hydrated $M_{6.2}$-MER (4.2) samples are shown in Figure 5.4.2. These also show the relaxed state of the refined framework associated with the *I*4/*mmm* space group. Visual inspection of the cation locations shows that site positions are very similar between the materials, though they differ slightly in fractional occupancy.

Table 5.4.1. Space group (SG), unit cell parameters and R_{wp} from refinement of hydrated $M_{6.2}$-MER (4.2) samples.

Cation form	SG	*a* (Å)	*c* (Å)	*V* (Å^3)	R_{wp}
$Na_{6.2}$	*I*4/*mmm*	14.127(1)	10.016(1)	1999(1)	3.9%
$K_{6.2}$	*I*4/*mmm*	14.149(1)	9.925(1)	1987(1)	3.4%
$Cs_{6.2}$	*I*4/*mmm*	14.194(1)	10.016(1)	2018(1)	3.3%

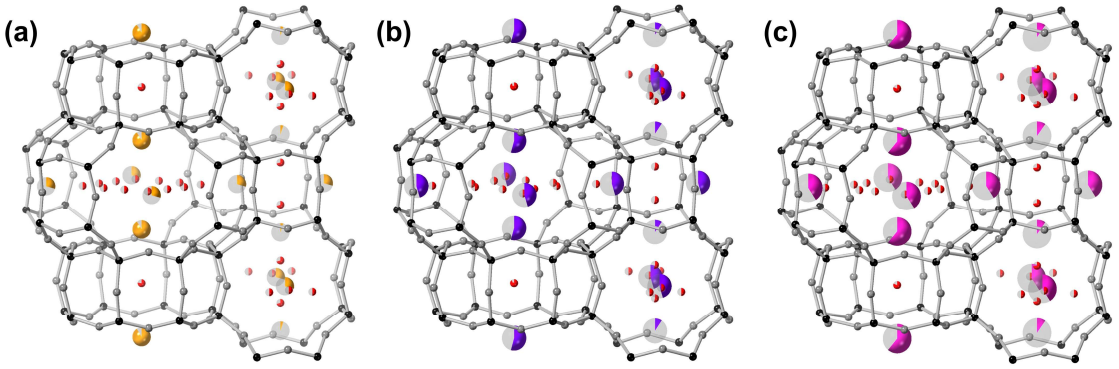

Figure 5.4.2. Structures of hydrated (a) $Na_{6.2}$-, (b) $K_{6.2}$-, and (c) $Cs_{6.2}$-MER (4.2). Na, K and Cs cations are shown in pink, purple, and orange, respectively, with the fractional occupancy indicated by filled proportion of sphere. Water molecule O sites are shown in red. Framework T and O sites are shown in black and grey, respectively.

5.4.2 Dehydrated $M_{6.2}$-MER (4.2)

The samples were subsequently dehydrated and their PXRD patterns obtained to enable Rietveld analysis of the materials. The $Na_{6.2}$-MER (4.2) sample showed a peak which could not be explained using *Immm*, $P4_2/nmc$ or any related space group trialled. A series of $Na_{6.2-x}K_x$-MER (4.2) was prepared by Dr Georgieva, discussed in greater detail in Section 5.5. The sample from this series with the highest Na^+ content, $Na_{5.0}K_{1.2}$-MER (4.2), which does not exhibit the problematic peak, was chosen to discuss the effect of Na cations on the MER structure in this section.

Rietveld plots of the dehydrated $M_{6.2}$-MER (4.2) materials are shown in Figure 5.4.3, with crystallographic details given in Appendix VI.II.II and unit cell parameters and refinement details given in Table 5.4.2. The unit cell volume for the $Na_{5.0}K_{1.2}$-MER (4.2) sample was found to be 1815(1) $Å^3$, very similar to the value of 1808 $Å^3$ obtained when using the same space group to try to fit the pure Na-form. All materials assume a lower symmetry than their hydrated forms, similar to previous merlinoite materials discussed in Chapter 4. Here however, the samples adopt *Pmmn*, rather than $P4_2/nmc$, as evidenced by a much improved fit of the data. There is no obvious separation of peaks which would appear to necessitate the use of an orthorhombic space group, and indeed the values of *a* and *b* parameters are close for all samples detailed here. The use of the reduced symmetry *Pmmn* space group does significantly improve the fit, however, as peak shapes are better described. Re-examination of the samples fitted with $P4_2/nmc$ in the MER (3.8) material show no such improvement, giving very similar measures of fit, as would be expected from a subgroup that provides no further benefit to the structural description, and hence kept.

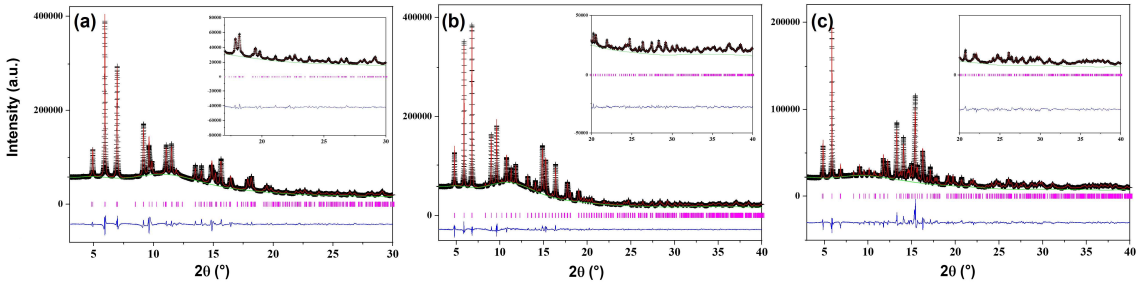

Figure 5.4.3. Rietveld plots of dehydrated M-MER (4.2) samples, with M = (a) $Na_{5.0}K_{1.2}$, (b) $K_{6.2}$ and (c) $Cs_{6.2}$. (I11, DLS, λ = 0.826398 Å).

Table 5.4.2. Space group (SG), unit cell parameters and R_{wp} from refinement of dehydrated $M_{6.2}$-MER samples.

Cation form	SG	*a* (Å)	*b* (Å)	*c* (Å)	*V* (Å^3)	R_{wp}
$Na_{5.0}K_{1.2}$	*Pmmn*	13.606(1)	13.551(1)	9.845(1)	1815(1)	3.4%
$K_{6.2}$	*Pmmn*	13.950(1)	13.894(1)	9.831(1)	1905(1)	2.4%
$Cs_{6.2}$	*Pmmn*	13.794(1)	13.776(1)	9.940(1)	1889(1)	5.1%

$Na_{5.0}K_{1.2}$-, $K_{6.2}$- and $Cs_{6.2}$-MER (4.2) samples exhibited a decrease in unit cell volume upon dehydration of 9.2, 4.1 and 6.4%, respectively. The $Na_{5.0}K_{1.2}$-form shows a far higher level of distortion than the other materials, whilst the K-form sees an unexpectedly small decrease in unit cell volume based on behaviour observed in MER (3.8) materials. The impacts of such distortions are evidenced in the refined structures of dehydrated $M_{6.2}$-MER (4.2) samples, shown in Figure 5.4.4. The hydrated materials exhibit circular windows but upon dehydration, this changes. $Na_{5.0}K_{1.2}$-MER (4.2) shows a set of narrow and wide 8-rings, as was seen previously for small cation samples found to adopt the *Immm* space group in MER (3.8). Although the $Na_{5.0}K_{1.2}$-material assumes *Pmmn* symmetry, the sample adopts distortion mode I, previously detailed in Chapter 4. Whilst the $K_{6.2}$- and $Cs_{6.2}$-forms also exhibit the *Pmmn* symmetry, they adopt distortion mode II, with buckled 8-ring windows in the *pau* cavity forming ovate geometries and an accompanied twisting of *d8r* units. Moreover, the windows along *a* and *b* axes are very similar in diameter (enforced under $P4_2/nmc$ symmetry, though free to differ under

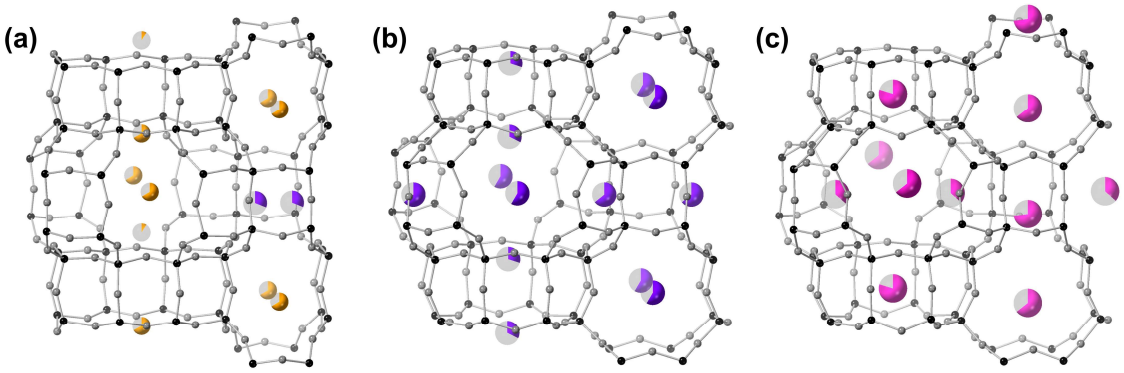

Figure 5.4.4. Structures of dehydrated (a) $Na_{5.2}K_{1.0}$-, (b) $K_{6.2}$-, and (c) $Cs_{6.2}$-MER (4.2). Na, K and Cs cations are shown in pink, purple, and orange, respectively, with the fractional occupancy indicated by filled proportion of sphere. Framework T and O sites are shown in black and grey, respectively.

Pmmn), in juxtaposition to the vastly different values seen in $Na_{5.0}K_{1.2}$-MER (4.2). It is a pleasing observation that a single space group, *Pmmn,* can treat distortion modes I and II observed in these materials, though this is perhaps unsurprising as it is a daughter of both $P4_2/nmc$ and *Immm*.

Examination of the relative cation occupancies in Figure 1.4.4 also shows the need for a lower symmetry space group, as the $Na_{5.0}K_{1.2}$-form exhibits cation ordering in the *d8r* 8-rings, and the Cs-form shows cation ordering in site IIa and IIb, and to a lesser extent between neighbouring *ste* cavities. These behaviours could not be described in either *Immm* or $P4_2/nmc$ space groups used for the related MER (3.8) materials. $K_{6.2}$-MER (4.2) also shows limited ordering between sites IIa and IIb, though this is less marked than in the other cation forms.

5.4.3 Comparison of MER (4.2) structures

Cation sitings for the materials are presented in Table 5.4.3. The nomenclature for both cation sites and windows within the material follow that introduced in Chapter 4. Na cations were found mainly in site I in the hydrated form of the pure Na-form of the material, in the plane of the 8-rings within the *d8r* unit. In the $Na_{5.0}K_{1.2}$-MER (4.2) sample, upon dehydration this preference switches to site II*. Na cations sit within the narrower IIa window, whilst K occupies the wider IIb window. Similarly in the K-form of the material, K^+ species preferentially adopt site II* under both hydrated and dehydrated conditions. Larger Cs cations also prefer this site in the hydrated form, with high occupancy also in site I but upon dehydration and cell contraction, Cs cations move to site III*, at the centre of the *ste* cavities, and occupancy in the *d8r* unit moves to the centre of the cavity, at site Ia.

As for the MER (3.8) material, reduced window sizes are observed as unit cell volumes decrease. These are listed in Table 5.4.4. Some of the window sizes present in the $Na_{5.0}K_{1.2}$-material are very narrow after dehydration, as was observed in $Na_{6.7}$-MER (3.8). Figure 5.4.5 shows a graphical summary of these window sizes. As for the MER (3.8) material, hydrated samples show similar values, due to comparable unit cell volumes. The free diameters of dehydrated samples are not ordered by cation size as windows within $K_{6.2}$-MER (4.2) are more in line with the hydrated samples than would be expected

from the trend observed in MER (3.8) materials. This illustrates that in the tuning of structural parameters of these materials, they cannot be wholly treated as solid solutions.

*Table 5.4.3. Absolute site occupancies of M^+ in MER (4.2) materials. *denotes merging of related but symmetry inequivalent positions. [a] denotes site Ia occupancy i.e. D8R site.*

Cation form	dh/h	I*	II*	III*	Total
$Na_{6.2}$	h	3.7(1)	2.3(2)	0.2(1)	6.2(2)
$Na_{5.0}K_{1.2}$	dh	1.5(1) Na	2.6(1) Na, 1.2(1) K		4.1(2) Na, 1.2(1) K
$K_{6.2}$	h	2.2(1)	3.6(1)	0.4(1)	6.2(2)
	dh	1.2(1)	4.9(2)		6.1(2)
$Cs_{6.2}$	h	2.4(1)	3.3(1)	0.4(1)	6.1(2)
	dh	1.6(1)[a]	1.5(2)	2.8(1)	5.9(2)

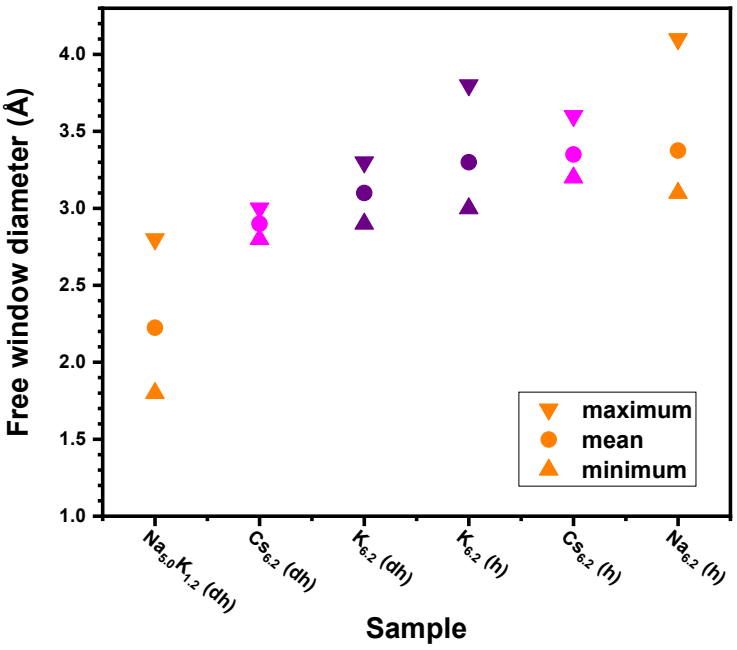

Figure 5.4.5. Window diameters of MER (4.2) samples. Points show minimum, mean and maximum free window diameters, as described in the key. Na-, K- and Cs-forms are denoted by orange, purple and pink, respectively.

*Table 5.4.4. Free window diameters in MER (4.2) materials. Windows that would be closed to CO_2 percolation (<2.3 Å) are denoted by *.*

Cation form	dh/h	I*	II(a)	IIb	III*
$Na_{6.2}$	h	4.1(1)	3.1(1)		3.2(1)
$Na_{5.0}K_{1.2}$	dh	2.2(1)*	1.8(1)*	2.8(1)	2.1(1)*
$K_{6.2}$	h	3.8(1)	3.0(1)		3.4(1)
	dh	3.2(1)	3.0(1)	2.9(1)	3.3(1)
$Cs_{6.2}$	h	3.6(1)	3.2(1)		3.4(1)
	dh	2.9(1)	3.0(1)	2.9(1)	2.8(1)

5.5 $Na_{6.2-x}K_x$-MER (4.2)

5.5.1 Underlying experimental work

As discussed, the structure of the pure Na-form of the MER (4.2) material could not be readily understood through Rietveld analysis, and as such a $Na_{6.2-x}K_x$-MER (4.2) family was created. This was done in the hope of better understanding the impact of Na cations in this material, and potentially revealing the structural behaviour of the pure-cation form. Unfortunately, the latter was unsuccessful. These samples were synthesised, their cation content determined through EDX and dehydrated by Dr Georgieva. Laboratory PXRD patterns of dehydrated samples were collected by Dr Georgieva, as were synchrotron patterns, with help from Prof Wright and Dr Lozinska. These are shown in Figure 5.5.2. Note none of the samples containing K cations shown here exhibit the anomalous peak at *ca*. 12° observed in the $Na_{6.2}$-MER (4.2) sample.

Low pressure CO_2 adsorption isotherms were obtained by Dr Georgieva at 298 K up to 1 bar of CO_2, as presented in Figure 5.5.1. These materials show a smooth transition between adsorption behaviour of the end members of the family. The pressure at which an adsorption step occurs and the level of hysteresis decrease as K^+ content increases. No kinetic data were obtained for these materials.

5.5.2 Dehydrated $Na_{6.2-x}K_x$-MER (4.2) structures

These materials were created to elucidate the impact of Na cations on the crystal structures of MER (4.2) materials. As such, the Rietveld plots and refined structures of

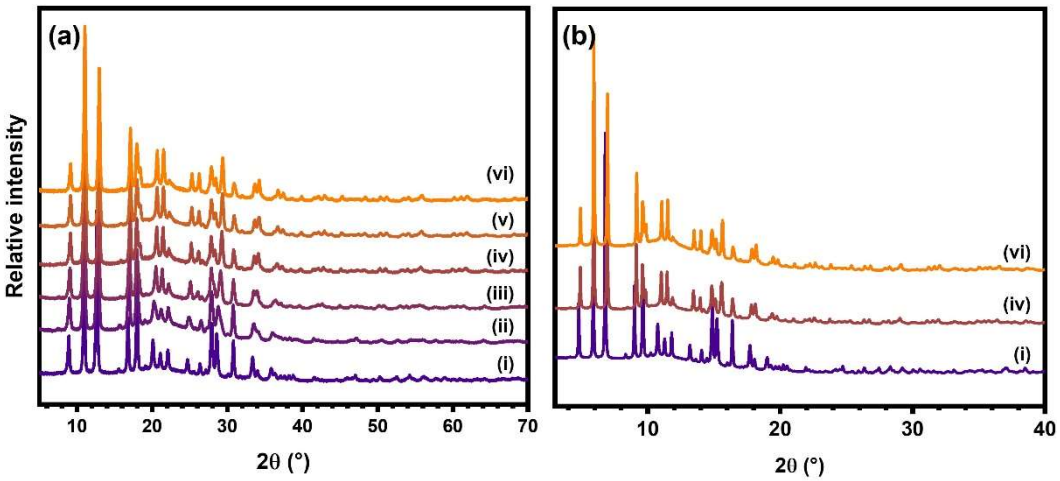

Figure 5.5.2. PXRD patterns of the dehydrated $Na_{6.2-x}K_x$-MER (4.2) series collected with (a) laboratory (Stoe, λ = 1.54056 Å) and (b) synchrotron X-rays (I11, DLS, λ = 0.826398 Å): (i) $Na_{0.5}K_{5.7}$-, (ii) $Na_{1.0}K_{5.2}$-, (iii) $Na_{2.0}K_{4.2}$-, (iv) $Na_{3.0}K_{3.2}$-, (v) $Na_{4.0}K_{2.2}$-, (vi) $Na_{5.0}K_{1.2}$-MER (4.2).

the dehydrated $Na_{6.2-x}K_x$-MER (4.2) samples are shown in Figure 5.5.3 and Figure 5.5.4, respectively. Refinement data is listed in Table 5.5.1.

From unit cell volume data, given in Table 5.5.1 and presented graphically in Figure 5.5.5, it can be seen that as Na^+ content increases in these materials the structure contracts further upon dehydration. Moreover, from the structures shown in Figure 5.5.4, the samples clearly adopt the 2 modes of distortion previously encountered. At high values of x, the $Na_{6.2-x}K_x$-MER (4.2) materials adopt a framework structure very similar to that of $K_{6.2}$-MER (4.2), which itself adopts a unit cell with *Pmmn* symmetry and a volume of 1905 Å^3, or the $P4_2/nmc$ symmetry of $K_{6.7}$-MER (3.8). At values of $x \leq 4.2$, the structure is

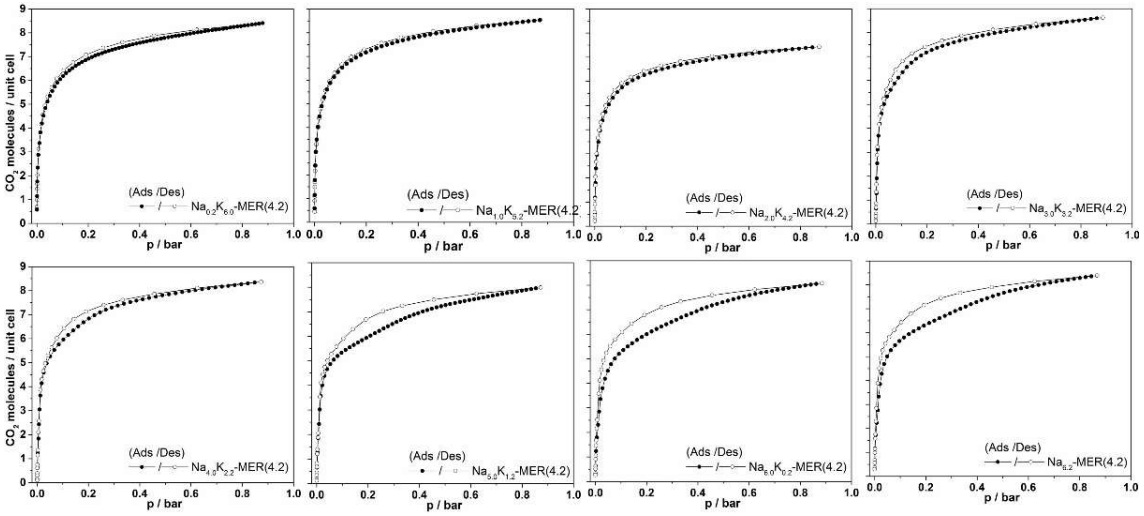

Figure 5.5.1. Low pressure CO_2 adsorption isotherms of $Na_{6.2-x}K_x$-MER (4.2) obtained at 298 K up to 1 bar of CO_2. Samples are as labelled, with adsorption and desorption branches are indicated by closed and open symbols, respectively.

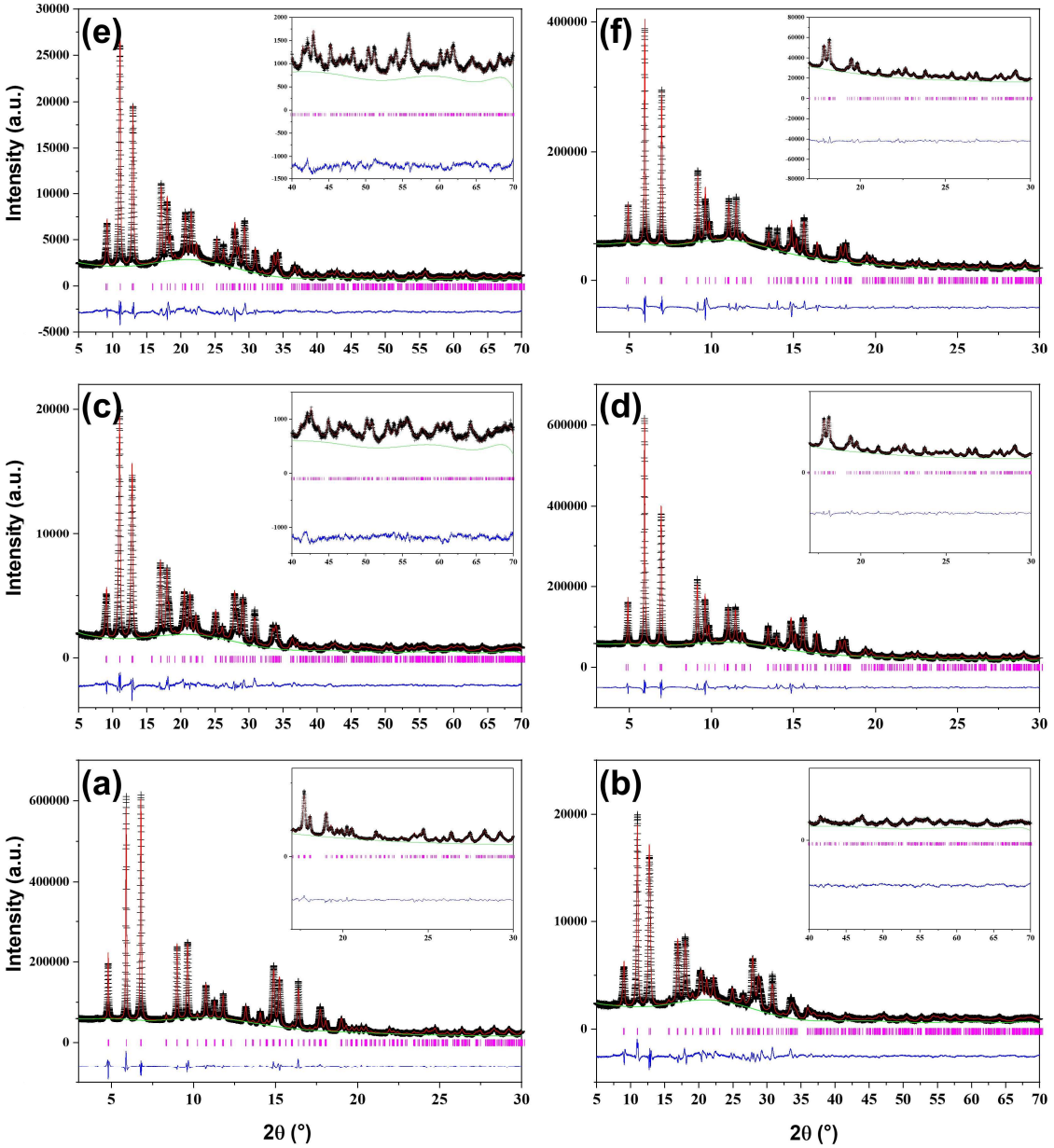

Figure 5.5.3. Rietveld plots of $Na_{6.2-x}K_x$-MER (4.2) samples: (a) $Na_{0.5}K_{5.7}$-, (b) $Na_{1.0}K_{5.2}$-, (c) $Na_{2.0}K_{4.2}$-, (d) $Na_{3.0}K_{3.2}$-, (e) $Na_{4.0}K_{2.2}$- and (f) $Na_{5.0}K_{1.2}$-MER (4.2). ((a, d, f) I11, DLS, λ = 0.826398 Å, (b, c, e) Stoe, λ =1.54056 Å).

more reminiscent of $Na_{6.7}$-MER (3.8), described in Chapter 4, which adopts the *Immm* symmetry. As can be seen in Figure 5.5.5, the trend in unit cell volume is non-linear, and is suggestive of an exponential decay with increasing Na^+ content, with a significant difference in unit cell volume at the point at which a change in the mode of distortion occurs. Again, this shows that these materials cannot be treated as simple solid solutions.

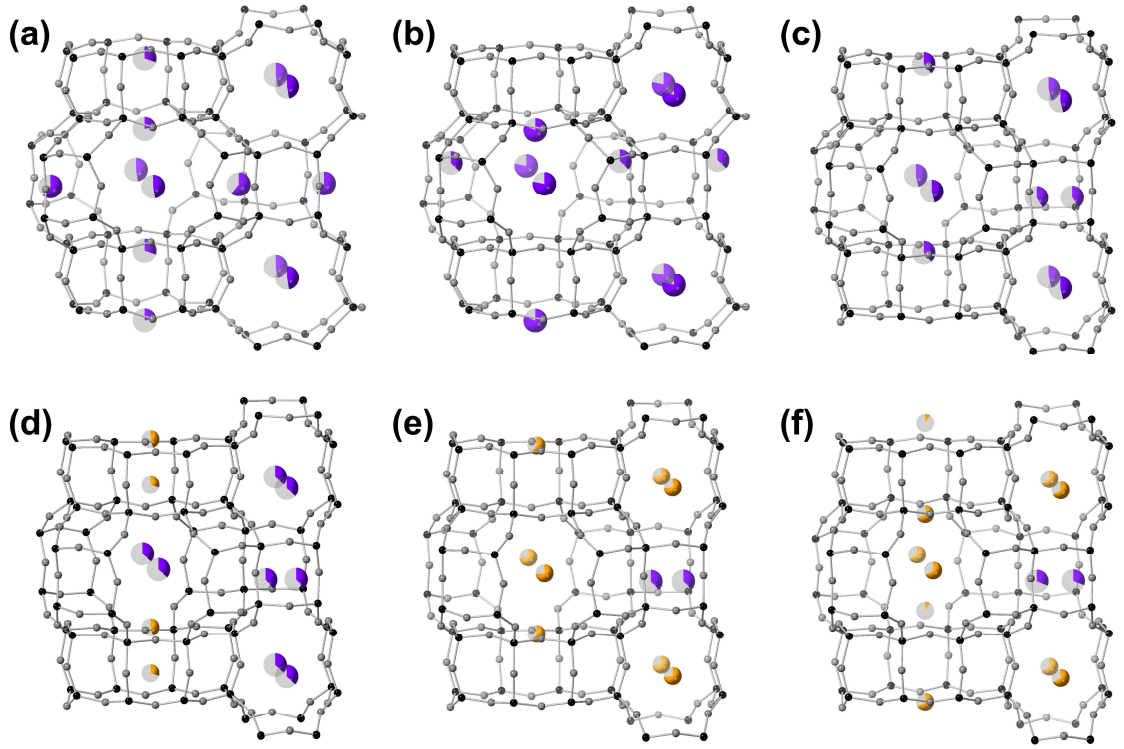

Figure 5.5.4. Refined structures of $Na_{6.2-x}K_x$-MER (4.2) samples: (a) $Na_{0.5}K_{5.7}$-, (b) $Na_{1.0}K_{5.2}$-, (c) $Na_{2.0}K_{4.2}$-, (d) $Na_{3.0}K_{3.2}$-, (e) $Na_{4.0}K_{2.2}$- and (f) $Na_{5.0}K_{1.2}$-MER (4.2). Framework T and O sites are shown in black and grey, and Na and K in orange and potassium, respectively. Partial shading of spheres indicated fractional occupancies of sites.

Table 5.5.1. Unit cell parameters and volumes for $Na_{6.2-x}K_x$-MER (4.2) samples, with diffractometer used, space groups (SGs) and Rietveld R_{wp} and χ^2 values.

Cation form	Diff.	SG	*a* (Å)	*b* (Å)	c (Å)	V (Å^3)	R_{wp} (%)	χ^2
$Na_{0.5}K_{5.7}$	*I11*	*Pmmn*	13.978(1)	13.913(1)	9.820(1)	1910(1)	3.3	48
$Na_{1.0}K_{5.2}$	*Stoe*	*Pmmn*	13.917(1)	13.746(1)	9.862(1)	1887(1)	6.2	8
$Na_{2.0}K_{4.2}$	*Stoe*	*Pmmn*	13.753(1)	13.647(1)	9.851(1)	1849(1)	5.7	5
$Na_{3.0}K_{3.2}$	*I11*	*Pmmn*	13.671(1)	13.598(1)	9.864(1)	1833(1)	3.3	48
$Na_{4.0}K_{2.2}$	*Stoe*	*Pmmn*	13.629(1)	13.564(1)	9.846(1)	1820(1)	5.8	7
$Na_{5.0}K_{1.2}$	*I11*	*Pmmn*	13.606(1)	13.551(1)	9.845(1)	1815(1)	3.4	47

Cation sitings are shown in Table 5.5.2 and graphically in Figure 5.5.7. Due to the greater X-ray scattering power of K cations, the positions of Na^+ species were difficult to determine in many of the materials in this series, particularly samples with low Na^+ content. The sample with the lowest content at which Na cations are refined is $Na_{2.0}K_{4.2}$-MER (4.2), and these are found in site I*. This is also the first sample to adopt a mode I

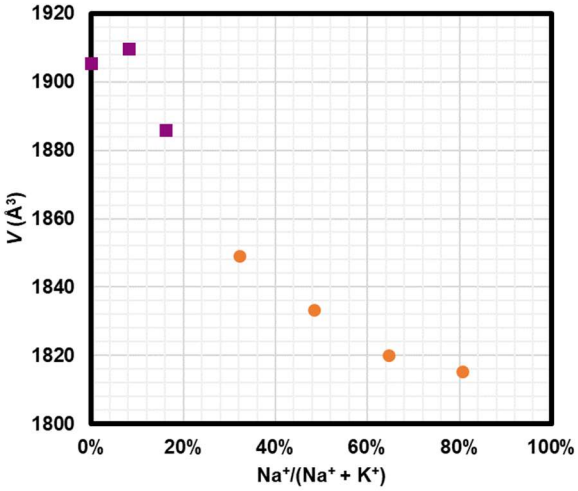

Figure 5.5.5. Plot of unit cell volume vs Na^+ content in the $Na_{6.2-x}K_x$-MER (4.2) series. Samples adopting an open structure are plotted as purple squares, whilst narrow-pore structures are plotted as orange circles.

distortion, as K content decreases. As Na^+ content increases, species are also found in the narrower of the different site II* types. This site is then preferentially occupied compared to site I*. Throughout the series, site II* is found to contain the majority of K cations, with additional occupancy in site I* at higher K^+ loading. It is only at such high loadings that the mode II framework distortion is adopted and it suggests that occupancy of site I* by K cations is controlling factor in determining the mode of distortion adopted by these materials. Alternatively, a threshold site II* occupancy is reached at which point a mode II distortion is adopted, enabling K^+ occupancy of site I*, in a more favourable *d8r* unit geometry.

Table 5.5.2.Refined cation sitings in $Na_{6.2-x}K_x$-MER (4.2) materials.

Cation form	I*	IIa	IIb	Total
$K_{6.2}$	1.2(1) K	2.3(1) K	2.6(1) K	6.1(2) K
$Na_{0.5}K_{5.7}$	1.0(1) K	1.9(1) K	2.4(1) K	5.4(2) K
$Na_{1.0}K_{5.2}$	1.4(1) K	1.3(1) K	2.9(1) K	5.6(2) K
$Na_{2.0}K_{4.2}$	1.3(1) Na	1.6(1) K	1.8(1) K	1.3(1) Na, 3.5(2) K
$Na_{3.0}K_{3.2}$	1.5(1) Na	1.5(1) K	1.5(1) K	1.5(1) Na, 3.0(2) K
$Na_{4.0}K_{2.2}$	1.2(1) Na	1.6(1) K	2.8(1) Na	4.0(2) Na, 1.6(1) K
$Na_{5.0}K_{1.2}$	1.5(1) Na	1.2(1) K	2.6(1) Na	4.1(2) Na, 1.2(1) K

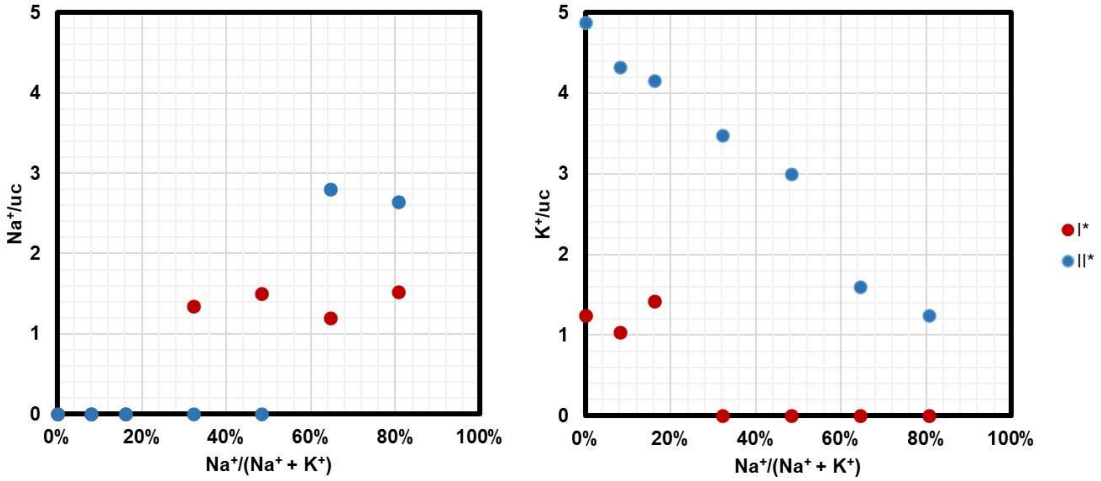

Figure 5.5.7. Cation siting in the $Na_{6.2-x}K_x$-MER (4.2) series. Absolute cations/uc are shown for sites I (red) and II* (blue) for Na^+ (left) and K^+ (right) with varying Na^+ content.*

Another important aspect to investigate in these materials is window size. As shown in Figure 5.5.5, the unit cell volume varies by 5% over the course of the series, and this would be expected to influence window sizes within the materials. Window sizes are given in Table 5.5.3 and shown graphically in Figure 5.5.6. From this, it can be seen that window sizes decrease with increasing Na^+ content, and the associated higher levels of distortion. The introduction of a small amount of Na^+ doping in $K_{6.2}$-MER (4.2) has a limited effect on window dimensions but with only 1 Na^+/uc, window sizes are altered

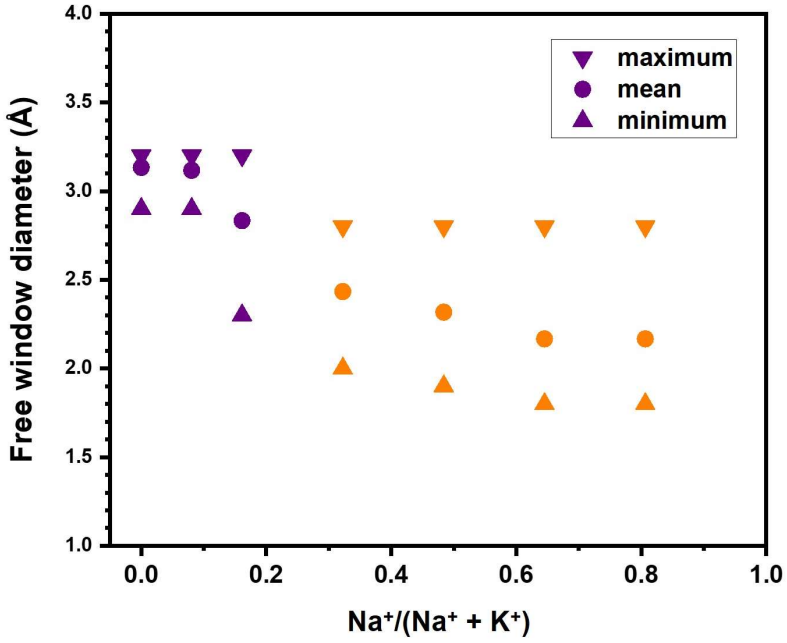

Figure 5.5.6. Window diameters of $Na_{6.2-x}K_x$-MER (4.2) samples. Points show minimum, mean and maximum free window diameters, as described in the key. Mode I and II distortions are indicated by orange and purple, respectively.

significantly. This is particularly true for window IIa which, with a free diameter of 2.3 Å, would only just be expected to allow CO_2 percolation after considering the vibrational effect suggested by Cook and Conner,[5] previously discussed in Chapters 3 and 4.

*Table 5.5.3. Window sizes within the $Na_{6.2-x}K_x$-MER (4.2) series. Windows that would be closed to CO_2 percolation (<2.3 Å) are denoted by *.*

Cation form	I	I′	IIa	IIb	III	III′	Connectivity
$K_{6.2}$	3.1(1)	3.2(1)	2.9(1)	3.0(1)	3.4(1)	3.2(1)	3D
$Na_{0.5}K_{5.7}$	3.0(1)	3.3(1)	3.0(1)	2.9(1)	3.3(1)	3.2(1)	3D
$Na_{1.0}K_{5.2}$	2.7(1)	3.1(1)	2.3(1)	3.2(1)	3.0(1)	2.7(1)	3D
$Na_{2.0}K_{4.2}$	2.7(1)	2.3(1)	2.0(1)*	2.8(1)	2.5(1)	2.3(1)	2D
$Na_{3.0}K_{3.2}$	2.4(1)	2.3(1)	1.9(1)*	2.8(1)	2.2(1)*	2.3(1)	2D
$Na_{4.0}K_{2.2}$	2.3(1)	2.0(1)*	1.8(1)*	2.8(1)	2.2(1)*	1.9(1)*	1D
$Na_{5.0}K_{1.2}$	2.3(1)	2.0(1)*	1.8(1)*	2.8(1)	1.9(1)*	2.2(1)*	1D

Windows I* and III* allow percolation along the *c* direction, whilst IIa and IIb determine percolation along *a* and *b* axes, respectfully. As windows narrow with increasing Na^+ content, channel connectivity drops from 3-dimensional, to 2-dimensional for $Na_{2.0}K_{4.2}$-MER (4.2), to 1-dimensional for the $Na_{4.0}K_{2.2}$-form, as illustrated in Figure 5.5.8. The initial drop in connectivity is concurrent with the change to the more distorted structure. Significant levels of distortion are observed, therefore, as materials approach $Na_{6.2}$-MER

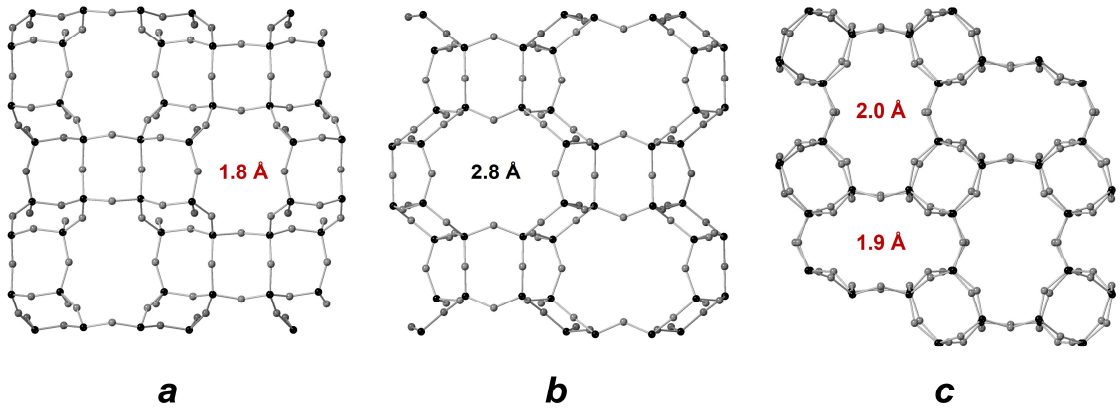

*Figure 5.5.8. Window dimensions in $Na_{4.0}K_{2.2}$-MER (4.2) along **a**, **b** and **c** axes, showing values of the narrowest mean free window diameter in a channel. Red values indicate those too narrow to allow the passage of CO_2 even when considering the additional vibrational effect suggested by Cook and Conner.[4]*

(4.2). Although the structure of this material remains undetermined, it is expected that this material would adopt very narrow windows. The driving force for such an odd structure is likely the same for mode I materials: to create a sufficient number of narrow 8-rings to more favourably bind Na cations and this would also establish a number of wide and unoccupied 8-rings.

5.6 MER (4.2) materials as CO_2 sorbents

5.6.1 Adsorption in pure cation forms of MER (4.2)

As stated previously, cation sitings and window sizes within materials greatly affect adsorption behaviour, and dehydrated forms are particularly relevant to the activated forms of sorbates. $Na_{5.0}K_{1.2}$-MER (4.2) shows severe distortion upon dehydration, as detailed in Table 5.4.4, collapsing the accessible channel system down to 1-dimensional connectivity for CO_2 percolation. This is consistent with kinetic data obtained for the $Na_{6.2}$-MER (4.2) material in the form of E-ZLC data, with diffusion rates far slower than $K_{6.2}$-MER (4.2). It is, however, similar in behaviour to $Cs_{6.2}$-MER (4.2), which possesses window sizes that are comparable to those of the K-form. As was the case in the MER (3.8) material, this shows the importance of cation occupancies, with 2.8 Cs^+ per unit cell in *ste* cavities, blocking almost 75% of these vital positions.

By contrast, K^+ prefers site II* and low occupancy of site III* may contribute greatly to the rapid kinetics of this material, in addition to large window sizes. These windows are very similar to those of the hydrated form. Ar uptake data also shows this structure to be far more open than related materials, consistent with these observations, as shown in Table 5.3.1. $K_{6.2}$-MER (4.2) therefore has promising kinetic behaviour for CO_2/CH_4 or CO_2/N_2 separation processes but, as shown in Table 5.3.2, this comes at the expense of selectivity. In such processes a balance between rapid diffusion and selectivity is often needed as they can be inversely correlated.

In order to examine CO_2 adsorption behaviour, PXRD experiments were carried out. For some of these materials VPXRD data was obtained on I11 at Diamond Light Source, Oxfordshire by Drs Georgieva, Lozinska and Prof Wright. Additional low quality VPXRD data was obtained where further data was necessary, on a laboratory instrument by Dr Georgieva with assistance from Dr Andreev.

Synchrotron VPXRD data is shown in Figure 5.6.1 for $Na_{6.2}$-, $K_{6.2}$- and $Cs_{6.2}$-MER (4.2) samples. Initial inspection of the patterns shows that the Na- and Cs-forms both undergo significant structural changes upon adsorption, as evidenced by both peak positions and intensities, whilst the K-form shows only minor movement of peaks consistent with gradual cell expansion. This agrees with the observed kinks, or lack thereof, in CO_2 adsorption isotherms of the materials.

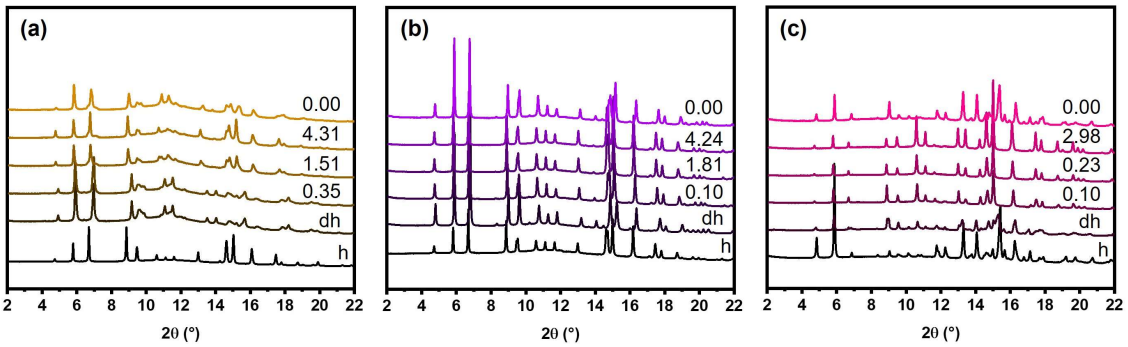

Figure 5.6.1. Synchrotron VPXRD patterns for (a) $Na_{6.2}$-, (b) $K_{6.2}$-, and (c) $Cs_{6.2}$-MER (4.2) at 298 K. Sample conditions during data acquisition on the right. Numbers indicate pressure of CO_2 in bar, and h and dh indicate hydrated and dehydrated, respectively. Patterns denoted 0.00 are those obtained upon desorption. (I11, DLS, λ = 0.826398 Å).

Multiple space groups were trialled for the high pressure $Na_{6.2}$-MER (4.2) phase but, as for the dehydrated sample, none described the patterns successfully. This phase, occurring at and above 1.51 bar of CO_2, seems to show the adoption of a wide-pore structure, as demonstrated by similar peak positions, and to a lesser extent intensities, to the hydrated form. To further investigate this material, laboratory VPXRD patterns were obtained, shown in Figure 5.6.2. This method allows for longer equilibration times between data acquisition steps but is far poorer in terms of resolution, as has previously been discussed in Chapters 3 and 4. By fitting the pattern with an *Immm* distorted framework and refining unit cell parameters accordingly, it could be seen that no unit cell expansion occurs below 0.2 bar of CO_2, as shown in Figure 5.6.2. Above this pressure, a relatively rapid increase in unit cell volume occurs from *ca.* 1840 to 1920 $Å^3$. This suggests a transition from a narrow- to a wide-pore phase and is consistent with stepped adsorption behaviour in the CO_2 adsorption isotherm of the material.

No such behaviour is observed in CO_2 adsorption on $K_{6.2}$-MER (4.2) and subsequently no phase change is seen in the VPXRD data. Instead, a more gentle cell expansion occurs, from 1906 $Å^3$ in the activated form to 1977 $Å^3$ at 4.24 bar of CO_2, as shown in Figure 5.6.3.

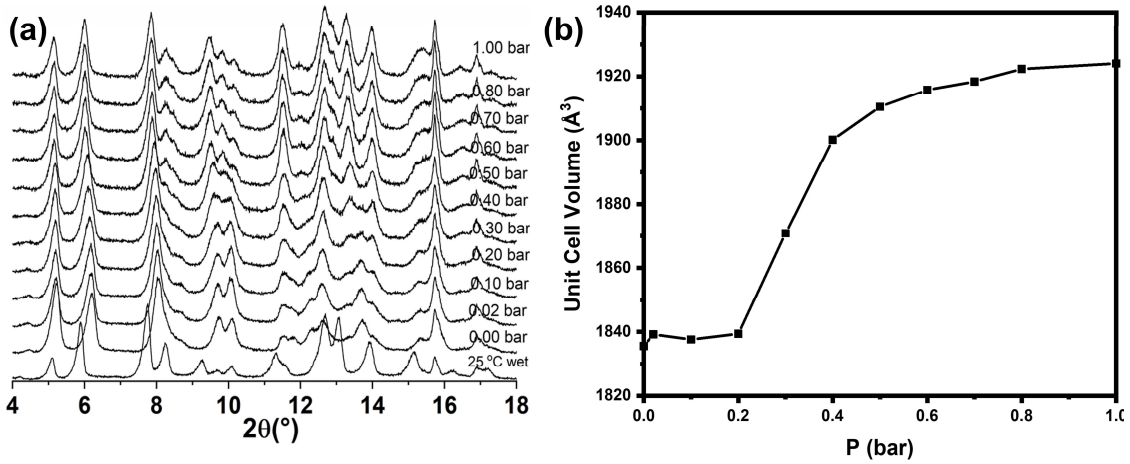

Figure 5.6.2. Laboratory VPXRD data for $Na_{6.2}$-MER (4.2): (a) patterns obtained, with relevant CO_2 pressure indicated on the right, and (b) refined unit cell volume as a function of CO_2 pressure. (PANalytical, Mo $K\alpha_{1,2}$, λ = 0.711 Å).

This trend also follows that of CO_2 uptake. Low pressure data is best fitted by *Pmmn* but above 20 mbar the $P4_2/nmc$ gives the most appropriate fit. This shows that there is a small but noticeable change in the structure upon adsorption of CO_2. It is also at this point that CO_2 molecules can be refined within the structure, also shown in Figure 5.6.3, which relates well to the values expected from CO_2 adsorption isotherm data. Comparison of Rietveld refinements of data obtained at the lowest and highest pressures investigated are also shown in Figure 5.6.3. There is little change in the structure despite the large difference in pressure, with minor cation movement and the adoption of a less distorted framework, evidenced by more circular windows within the structure, though this change is rather insubstantial.

$Cs_{6.2}$-MER (4.2) is expected from CO_2 adsorption isotherm data to exhibit a transition from narrow- to wide-pore structures, as was the case for $Na_{6.2}$-MER (4.2), and this does indeed occur in the VPXRD data, as seen in Figure 5.6.4. The material initially adopts a narrow-pore phase until under 0.1 bar of CO_2, at which point 2 phases are observed concurrently. These phases possess a unit cell volume of 1911 and 1965 $Å^3$ and map to structures present under low- and high-pressure regimes, respectively. The presence of 2 phases simultaneously may be indicative of their relative favourability at this CO_2 potential, or potential slow kinetics of such a transition. Finally, it may be due to limitations of the experimental setup, in particular the formation of a pressure gradient within the sample capillary under adsorption. Mirroring the behaviour of the $K_{6.2}$-MER

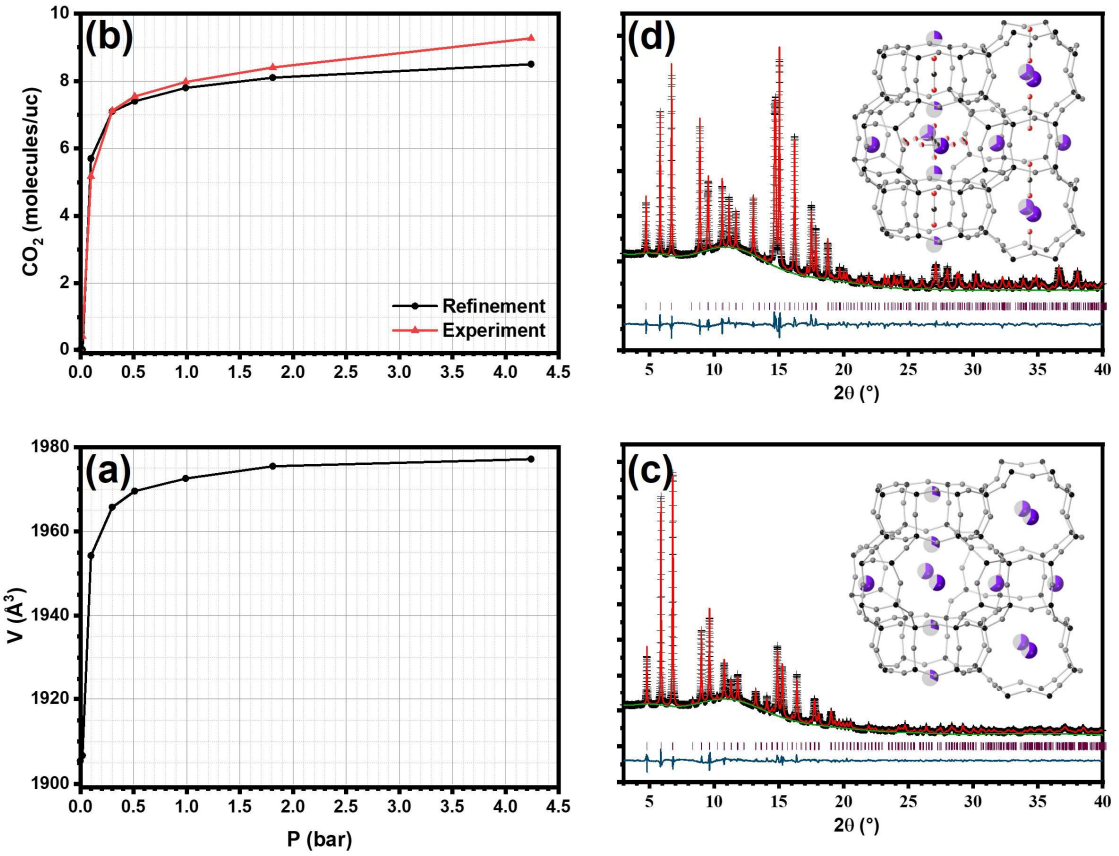

Figure 5.6.3. Synchrotron VPXRD refinement data for $K_{6.2}$-MER (4.2), including (a) unit cell volume and (b) refined and experimental CO_2 uptake with pressure. Rietveld plots under (c) dehydration and (d) 4.24 bar pressure of CO_2, with resultant structures shown inset. Framework T and O sites are shown by black and grey, respectively, K^+ in purple and CO_2 molecules shown in black and red. Partial filling of sites indicates fractional occupancy. (I11, DLS, λ = 0.826398 Å).

(4.2) material, the dehydrated Cs-form adopts the *Pmmn* space group but with exposure to CO_2, $P4_2/nmc$ is found to be an appropriate symmetry. Comparison of data obtained at low and high pressure allows greater insight into the structural change observed by $Cs_{6.2}$-MER (4.2) upon adsorption, and the structures relevant to these 2 regimes in the adsorption isotherm.

Occupancies of cation sites of $K_{6.2}$- and $Cs_{6.2}$-MER (4.2) are shown in Figure 5.6.5. and it can immediately be seen that there is little change within the K-form during adsorption of CO_2, with K cations preferring site II* and additional occupancy in site I*, as was the case for the dehydrated material. This is perhaps unsurprising as the material adopts the wide-pore phase under all conditions investigated. It does however show that cation occupancy within this material is dominated by interactions with the aluminosilicate

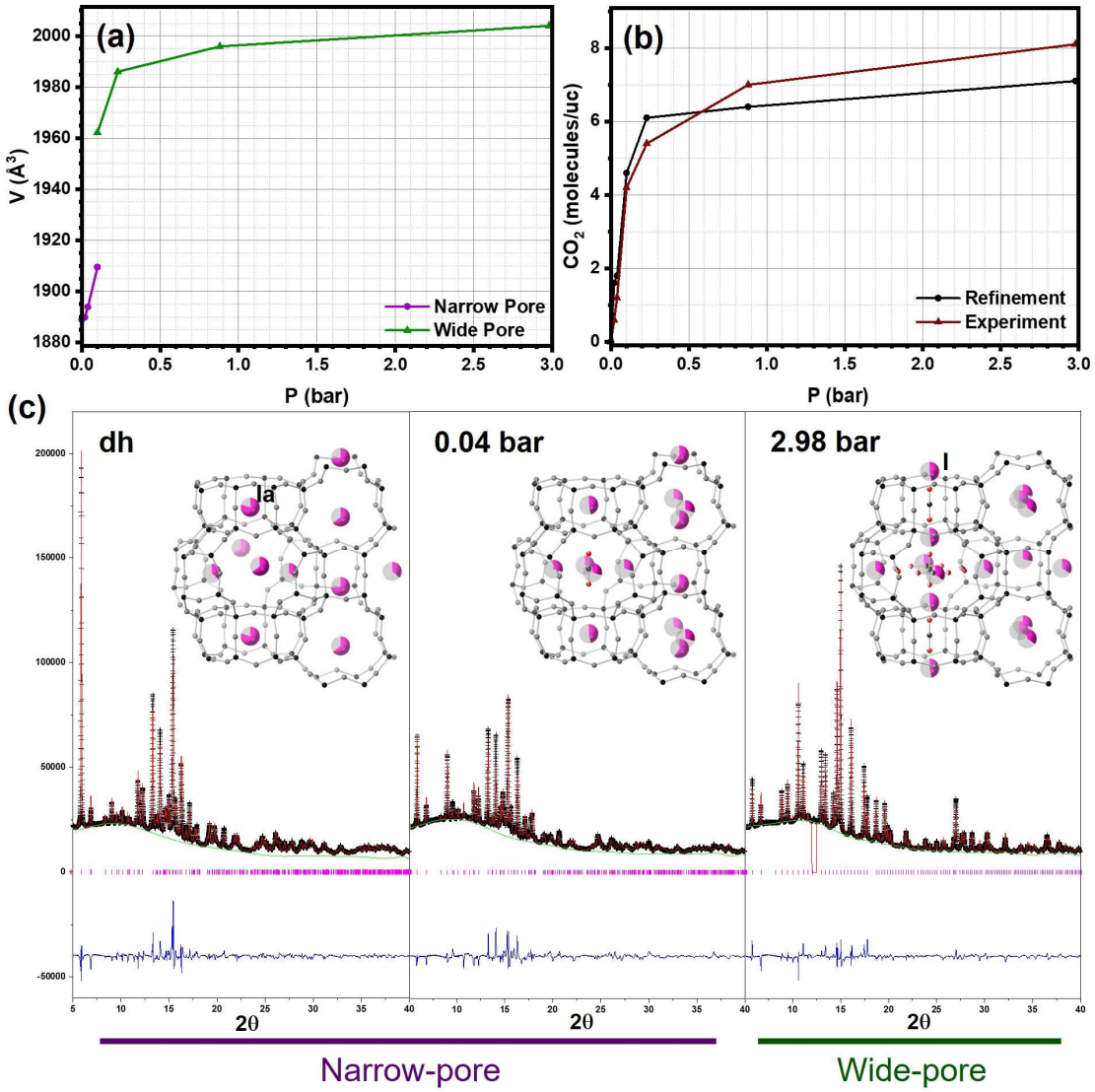

Figure 5.6.4. Synchrotron VPXRD refinement data for $Cs_{6.2}$-MER (4.2) including (a) unit cell volume and (b) refined and experimental CO_2 uptake with pressure. (c) Rietveld plots under dehydration, 0.04 and 2.98 bar pressure of CO_2, with corresponding structures shown inset. Framework T and O sites are shown by black and grey, Cs^+ in pink and CO_2 molecules shown in black and red, respectively. Partial shading of spheres indicates fractional occupancy. Sites Ia and I are highlighted. (I11, DLS, λ = 0.826398 Å).

framework, with guest CO_2 species causing very little change in cation siting. The $Cs_{6.2}$-MER (4.2) does not behave in such a way and shows 3 separate occupancy regimes. The first is the dehydrated material, in which site Ia has the highest fractional occupancy, but the most populous site is site III*, with 2.8 Cs^+ per unit cell. The latter is thought to be a vital site as it sits as a crossroads along both the *pau-ste* and the *ste-ste* channel systems. At low pressure of CO_2, whilst the material adopts a narrow-pore structure, initial

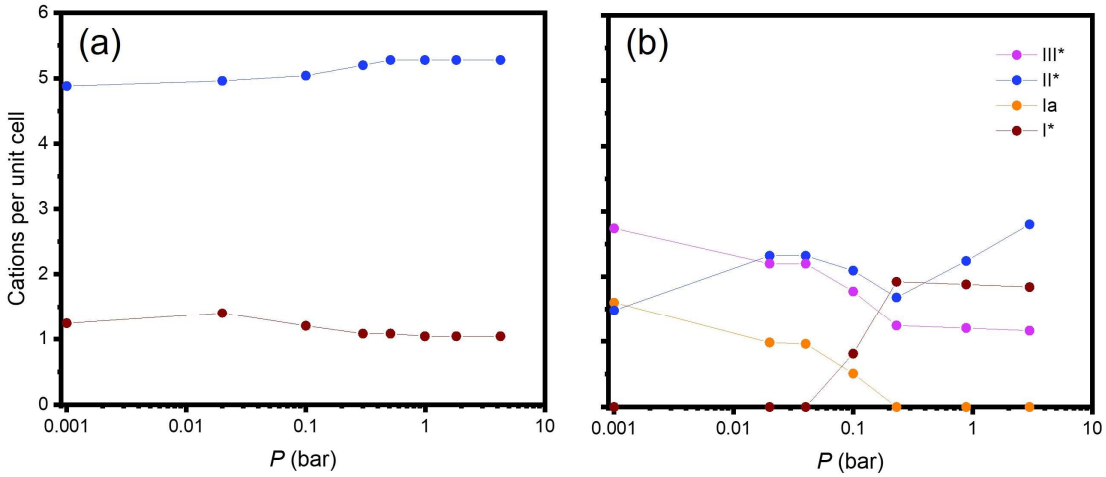

Figure 5.6.5. Cation occupancies in (a) K- and (b) Cs-forms of MER (4.2) with pressure, note logarithmic axis. Site types I, Ia, II* and III* are shown in red, orange, blue and pink, respectively. $Cs_{6.2}$-MER (4.2) data at 0.1 bar is a weighted average of both refined phases. Dehydrated data is plotted on the logarithmic axis at 0.001 bar.*

adsorption leads to Cs^+ redistribution from site Ia to site II*, driven by favourable interactions between the Cs cations and the guest species.

The material sees a more significant transition at 0.1 bar, as the material begins to adopt the wide-pore phase. The data presented in Figure 5.6.5 at this pressure is a weighted average of the 2 phases refined at this pressure, below which only the narrow-pore phase is observed, and only the wide-pore form above. In the wide-pore form, site Ia is vacant of cations, with this space inhabited by CO_2 molecules. Sites I and II become favoured instead. The continued increase in occupancy of site II as pressure increases may be due to errors in refinement at higher pressure, as opposed to a meaningful trend. The occupancy of site I is too high to be due exclusively to relocation from site Ia and cations are redistributed from site III, a site with the highest occupancy in the low-pressure regime but the least favoured of those occupied at high pressure.

A mechanism is suggested whereby Cs cations are rearranged from site III to site I (a direct distance of 7.3 Å) *via* cations hopping from site II to I (4.8 Å) and site III to II (4.2 Å). This may be a concerted mechanism, as shown in Figure 5.6.6, or occur in separate steps, extremely rapid on the timescale of VPXRD equilibration and data acquisition. The presence of CO_2 within the *d8r* unit may give an energetic driving force for occupancy of site I, and CO_2 molecules within the structure and their movement may aid cation redistribution by reducing kinetic barriers.

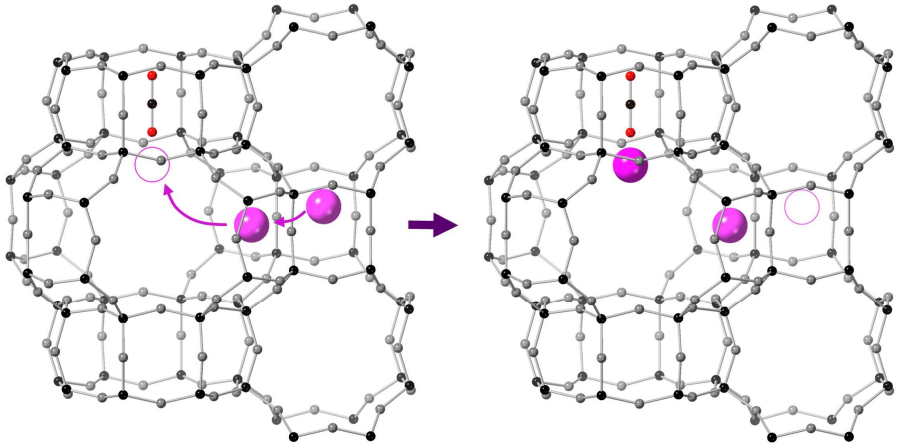

Figure 5.6.6. A postulated Cs cation migration mechanism involves concerted movement from sites II and III to sites I and II, respectively. CO_2 occupying the d8r unit may give a thermodynamic driving force or accelerate such a migration. Framework T and O sites are shown in black and grey, respectively; Cs^+ in pink and CO_2 molecules in black and red.

Window sizes of the materials under pressure of CO_2 are shown in Figure 5.6.7. As was the case for cation occupancies, the mean free window diameter within the $K_{6.2}$-MER (4.2) structure is relatively constant, remaining at *ca.* 3.2 Å over all pressures investigated. By contrast, the mean free diameter increases from 2.9 to 3.5 Å over the course of adsorption in the $Cs_{6.2}$-MER (4.2) material. The increase of 0.6 Å is due solely to the expansion in unit cell volume upon adoption of the wide-pore form and would be expected to have a marked impact on kinetic properties but blocking of channels by bulky Cs cations must also be considered. Lower occupancy of site III at higher pressures

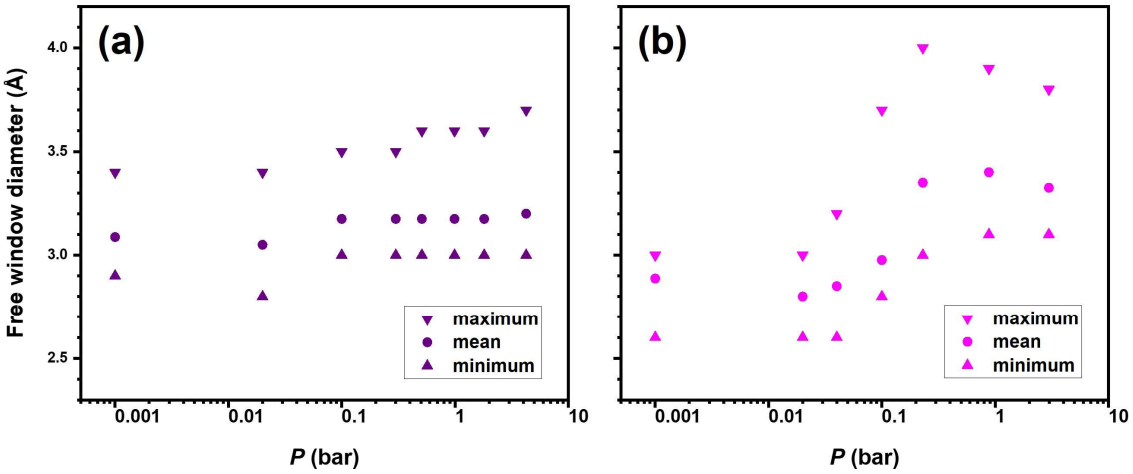

Figure 5.6.7. Window diameters of $M_{6.2}$-MER (4.2) samples: M = (a) K and (b) Cs. Points show minimum, mean and maximum free window diameters, as described in the key. $Cs_{6.2}$-MER (4.2) data at 0.1 bar is a weighted average of both refined phases. Dehydrated data is plotted on the logarithmic axis at 0.001 bar.

also suggests that the kinetics of this material are improved with increased pressure of CO_2.

5.6.2 Adsorption in the mixed cation $Na_{6.2-x}K_x$-MER (4.2) family

The $Na_{6.2-x}K_x$-MER (4.2) samples span a range of structural and adsorption behaviour and such a family could be used to better balance selectivity and diffusion. Whilst the K-form of the MER (4.2) material exhibits rapid CO_2 percolation, it loses selectivity due to its wide window dimensions. The increased distortion witnessed for samples with higher Na^+ content, and subsequent reduced window size and channel connectivity, would be expected to have significant effects on kinetic properties and in some of these samples the positioning of larger K cations may also be an important factor. Unfortunately, no kinetic data was available for these materials at the time of writing, though structural data can still be examined for potential effects on adsorption behaviour.

Examination of the structural response to CO_2 adsorption using a laboratory VPXRD experimental setup was carried out for a single sample in this series, $Na_{4.0}K_{2.2}$-MER (4.2), carried out by Drs Georgieva and Andreev. This sample is more similar to the $Na_{6.2}$-MER (4.2) sample than the K-form, as previously described. Additionally, the sample was exposed to 845 mbar of CO_2 in a "snapshot" experiment by Dr Georgieva, previously described for MER (3.8) samples in Chapter 4.

As for previously reported samples investigated in laboratory VPXRD experiments, unit cell volumes cannot be taken as accurate measurements, as can be seen for the $Na_{4.0}K_{2.2}$-MER (4.2) sample in Figure 5.6.9, by comparing the apparent value upon dehydration of 1860 $Å^3$ and the previous value of 1820 $Å^3$, obtained from higher resolution capillary PXRD data. Instead, the overall trend must be observed and here unit cell expansion follows a curve similar to a Langmuir isotherm. This expansion mirrors the behaviour of $K_{6.2}$-MER (4.2), although here the change in volume is larger, 130 $Å^3$ compared to *ca.* 70 $Å^3$ for the K-form across the same pressure range. By comparison, $Na_{6.2}$-MER (4.2) was seen to maintain the same unit cell volume over the initial 200 mbar region, before expansion was observed. That agreed well with the pressure at which a step was observed in the CO_2 adsorption isotherm of the material, signifying additional available

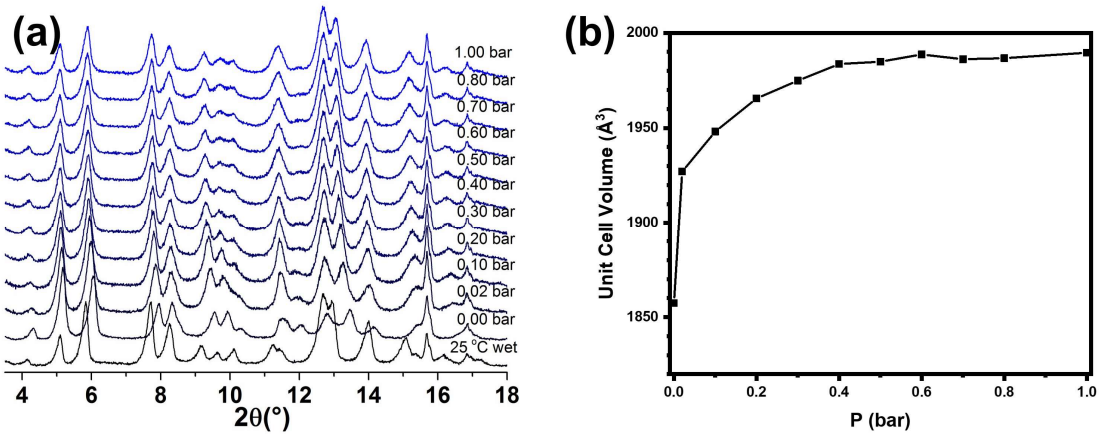

Figure 5.6.8. Laboratory VPXRD data for $Na_{4.0}K_{2.2}$-MER (4.2): (a) patterns obtained, with relevant CO_2 pressure indicated on the right, and (b) refined unit cell volume as a function of CO_2 pressure. (PANalytical, Mo $K\alpha_{1,2}$, λ = 0.711 Å).

pore volume as the framework of the material expanded. Examination of the isotherms of the binary cation materials presented in Figure 5.5.1 shows that there is no obvious step for the $Na_{4.0}K_{2.2}$-form, although hysteresis is present upon desorption at low pressure of CO_2.

The patterns shown in Figure 5.6.8 suggest that the material occupies only 1 phase at any given pressure, and the pattern at 20 mbar resembles higher pressure data in terms of both peak positions and intensities. This suggests that a wide-pore form may be adopted at this low pressure of CO_2. The incorporation of K cations into the $Na_{6.2}$-MER (4.2) material can therefore be said to shift the position of the step in the CO_2 adsorption isotherm to such a low pressure as to cause a triggered opening with exposure to CO_2 molecules, as seen for the $K_{6.7}$-MER (3.8) material in Chapter 4. This occurs by reducing the energetic difference between narrow- and wide-pore structures with the presence of larger cations, and fewer small cations. Rather than a material trapped in a highly distorted form until higher pressure, the structure opens relatively rapidly, with a change between the 2 structure types occurring at very low pressure.

Results of the additional "snapshot" experiment, obtained for the same $Na_{4.0}K_{2.2}$-form under 845 mbar of CO_2 are shown in Figure 5.6.9. In this wide-pore form, Na cations are hard to locate but may occupy site I* in the *d8r*, which is unoccupied by K cations. Instead, K^+ species are dispersed across remaining sites in the structure as window sizes have expanded relative to the dehydrated material. The difference in window sizes and

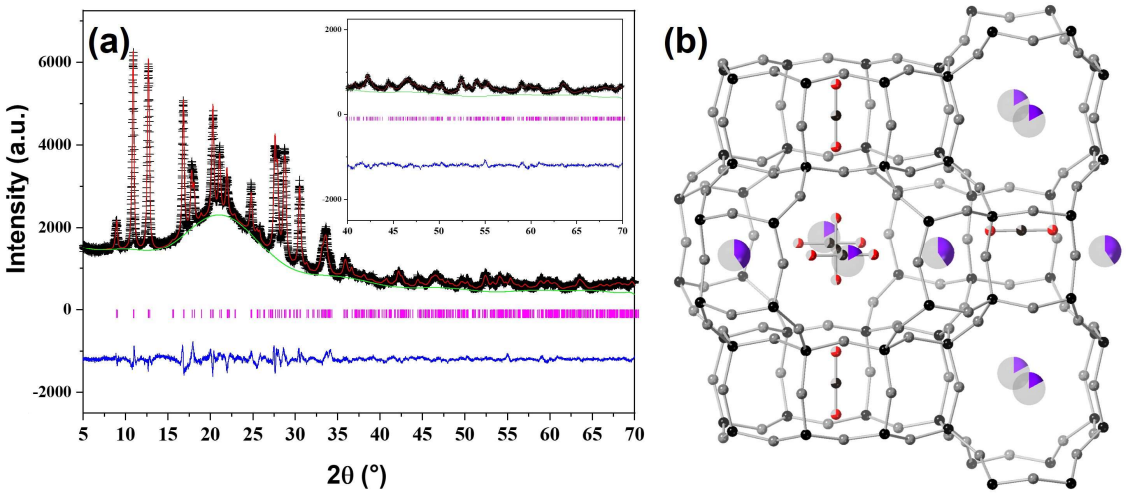

Figure 5.6.9. (a) Refinement plot for $Na_{4.0}K_{2.2}$-MER (4.2), obtained under 845 mbar of CO_2, and (b) the associated structure. Framework T and O sites are shown by black and grey, K^+ in purple, with CO_2 molecules shown in black and red, respectively. Fractional occupancies are indicated by partial shading of spheres. (Stoe, λ = 1.54056 Å).

cation sitings within the 2 types of structure adopted by this material would be expected to greatly affect its kinetic properties. In the wide-pore form, by reducing the number of bulkier cations within the material relative to the pure K-form, the presence of Na^+ species may improve CO_2 percolation if operating at a non-vacuum partial pressure of CO_2. More likely however due to the rapid diffusion observed in $K_{6.2}$-MER (4.2), the narrower windows observed here would make this material slower, though still rapid, and potentially more selective. As such, this material would be of interest to investigate further with kinetic analysis.

5.6.3 Summary of materials under adsorption conditions

Whilst the Na-form of MER (4.2) is highly distorted upon dehydration, initial PXRD analysis showed that the $K_{6.2}$-MER (4.2) material retained a wide-pore form, with minor distortions, upon dehydration. Further VPXRD measurements indicate that this structure is representative of the material upon adsorption too, with little change in window size or cation location across experiments. With the wide-pore form adopted under activation conditions, rapid percolation occurs, as evidenced by both Ar diffusivity measurements and CO_2 kinetic data. The K-form is the only material shown to behave in this way, hence the improved diffusivity relative to the other cation forms. Incorporation of Na cations into this sample altered the structural and adsorption

properties of the material and may provide a way to fine-tune its adsorption behaviour for desired conditions.

As discussed, $Cs_{6.2}$-MER (4.2) undergoes limited cation rearrangement with initial adsorption of CO_2, but window sizes remain constant until expansion to the wide-pore form begins at 0.1 bar. The narrow-pore form is relevant to the initial part of the CO_2 adsorption isotherm, and to the Ar diffusivity measurement, which showed that the material was less open than the $K_{6.2}$-MER (4.2) material. It is also relevant to the breakthrough data, measured at 0.1 bar of CO_2, with the initial part of the breakthrough curve following the filling of a narrow-pore structure. This corresponds to less than 40% of the total CO_2 uptake capacity of the material. The subsequent part of the breakthrough curve tracks the filling of additional pore volume in the expanded form of the material. 2 phases are observed in the VPXRD data for this material, although only at a single investigated pressure, and this may indicate the fine energetic balance of the 2 forms at that pressure. This behaviour makes the Cs-form a poor material for selective kinetic separation processes under these conditions. Above 0.1 bar, the material possesses wide windows, larger than that of the $K_{6.2}$-MER material, which may improve the rate of percolation within the material, although again the size of the bulky Cs cations may limit any gains due to window size expansion.

5.7 Comparison of materials

The work described in this and the previous chapter covers a range of materials, in terms of both framework and extra-framework compositions. A consequence of this is the broad range of structural and adsorption properties observed. This section is dedicated to comparing these materials and their properties. Materials prepared by Choi *et al*. will also be examined closely, as these provide additional data at lower Si/Al ratios which can be beneficial for determining a clearer trend for merlinoite materials.[1,2]

Cation types present in merlinoite materials have a vital role in determining framework distortion upon dehydration, transitions between narrow- and wide-pore forms and kinetic behaviour. One of the apparently simpler observations is that the unit cell shows a greater contraction upon dehydration with decreasing cation size, as shown by the plot in Figure 5.7.1. This is very similar to behaviour seen in zeolite Rho, with small cations

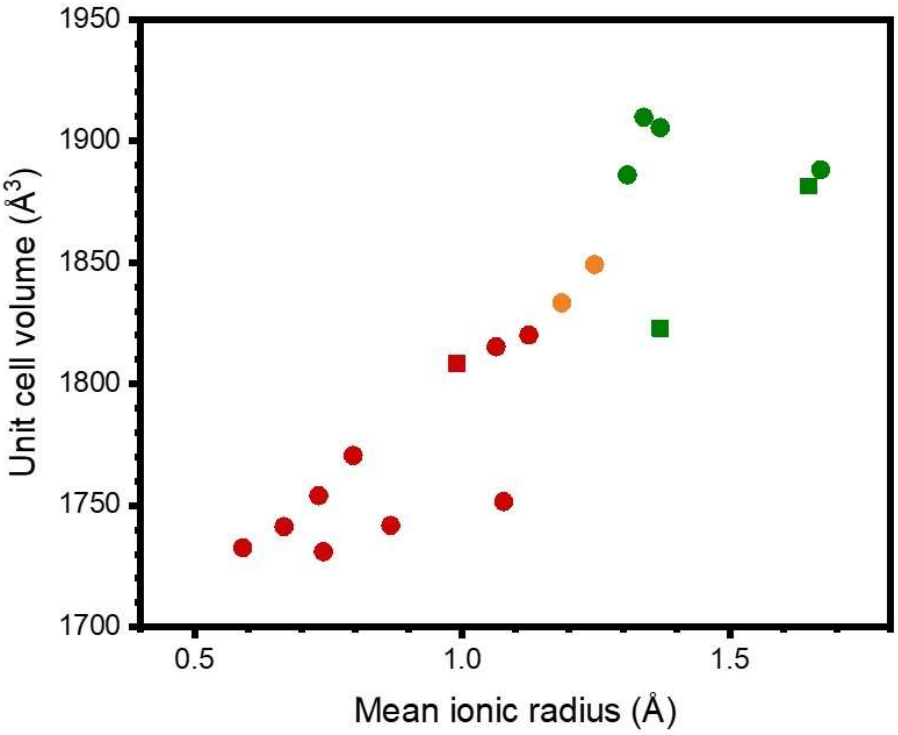

Figure 5.7.1. Unit cell volume of dehydrated MER materials in this work against mean ionic radii of cations present in the material. Si/Al = 3.8 and 4.2 are shown as squares and circles, and 1-, 2- and 3-dimensional channel connectivity is shown in red, orange and green, respectively. Data plotted at lower radii are discussed in Chapter 6.

such as Li^+ causing the greatest cell contraction.[6–8] Complications arise in Rho however, due to cations, such as Cu^{2+}, occupying sites which do not affect cell contraction.[9] Similar can be said for zeolite merlinoite. Whilst there is clearly an overall trend, there are specific points which diverge, and this can also be linked to cation site preferences. The number of site types available in merlinoite is higher than in zeolite Rho, previously discussed in Chapter 3, clouding causal links. It appears that between the 2 Si/Al ratios plotted in Figure 5.7.1, unit cell volumes are quite similar with the same mean ionic radius, with the exception of the points at 1.37 Å, which are the pure K-forms, in which the higher Si/Al does not adopt the narrow-pore form upon dehydration.

Similar to unit cell volumes, cations also alter window sizes within materials. A plot of the mean free window diameter of materials investigated against mean ionic radius is shown in Figure 5.7.2. The overall trend of increasing window size with larger cations is near linear, again with the obvious, though less significant, exceptions of some of the $K_{6.2}$-MER (4.2)-like materials. It may be expected that those materials with a value below the 2.3 Å threshold for CO_2 percolation may be unable to adsorb any gas, however this

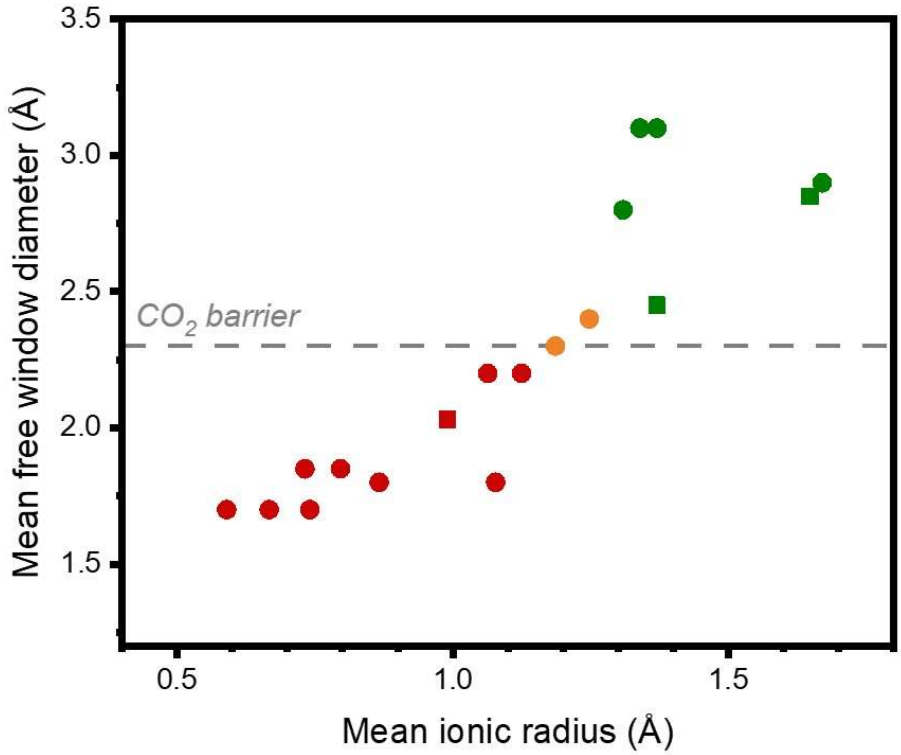

Figure 5.7.2. Mean free window diameter of MER materials in this work against mean ionic radii of cations present in the material. Si/Al = 3.8 and 4.2 are shown as squares and circles, and 1-, 2- and 3-dimensional channel connectivity is shown in red, orange and green, respectively. Data plotted at lower radii are discussed in Chapter 6. The 2.3 Å window diameter required for CO_2 percolation is shown as a grey, dashed line.

is a mean value. In fact, as has been shown for the $Na_{6.2-x}K_x$-MER (4.2) materials, structures with very narrow windows also contain a very large window. Lower values of mean free window diameter can instead be an illustration of the degree of channel connectivity, with samples greatly below the CO_2 percolation line 1-dimensionally connected, above the line 3-dimensionally connected, and 2-dimensional channel systems occurring very close to this line.

Not only does cation siting affect framework distortion but it is also important for adsorption properties in its own right. For the case of small cations, the occupation of windows which are too small to allow CO_2 percolation does not affect CO_2 adsorption, although it affects the energetic balance of narrow- and wide-pore forms and as such alters the position of the adsorption step in CO_2 isotherms. By contrast, Cs-forms of MER have high occupancies within *ste* and *d8r* cavities hindering CO_2 percolation. In these cases, however, as the materials adopt a 3-dimensionally connected channel system and not all sites are fully occupied, this merely lengthens the path taken by CO_2 species, as

opposed to blocking it entirely. Additionally, the less distorted framework could be expected to reduce energy barriers to cation movement and make cation gating more favourable, if still slow for these materials.

So far only 2 Si/Al ratios in merlinoite materials have been investigated in this work. The concurrent work of Choi *et al*. is useful to compare lower silica materials and gain a broader understanding of MER materials.[1,2] In their work, they reported the structures and adsorption behaviour of different cation forms of merlinoite zeolites with Si/Al = 2.3, and additional $K_{11.8}$-MER (1.7) and $K_{8.2}$-MER (2.9) samples. An immediate effect of the Si/Al ratio of materials is the number of metal cations present within the structure of a fully ion-exchanged sample. One consequence of this is the pore volume occupied by cations and hence unavailable to CO_2 molecules. This is shown in Figure 5.7.3, with a comparison of the CO_2 uptake of K-MER materials at 1 bar. Similar behaviour has also been observed in gismondine (**GIS**), with less than 1 mmol g^{-1} of CO_2 adsorbed at 298 K and 1 bar of CO_2 by samples with Si/Al < 2.5, initially followed by increased uptake as cation content decreases.[10]

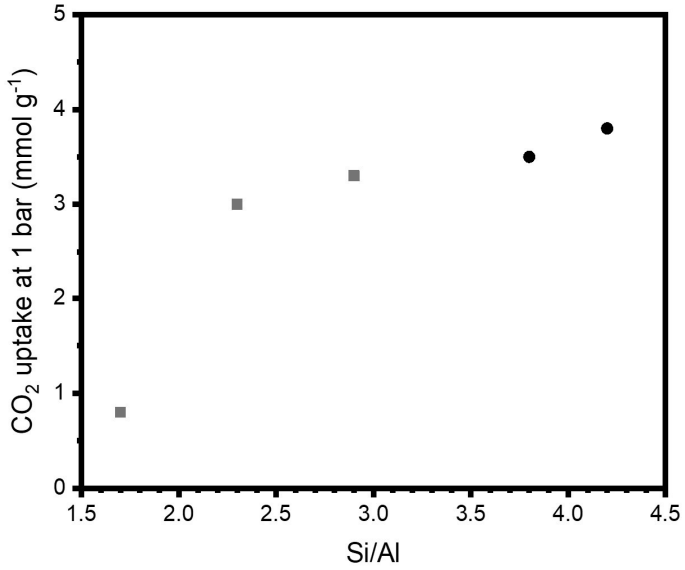

Figure 5.7.3. Uptake at 1 bar of CO_2 for K-MER materials with various Si/Al ratios. Data shown from materials presented in this work and by Choi et al. are indicated by round and square points, respectively.[1,2]

An additional effect of lower cation content within the material and lower framework charge is that there are less interactions that cause the framework to distort. This creates a more open structure as the unit cell volume increases, as does the mean window size,

as shown in Figure 5.7.4. One of the interesting points from this plot is the highly contracted unit cell of $Na_{9.7}$-MER (2.3). This is because the material adopts the $P4_2/nmc$ space group and consequently a mode II distortion. This is different from the Na-materials previously discussed and is due to the additional cations present in the material. For the lower silica material, a mode I distortion is disfavoured as this contains large *pau*/*ste* windows, unoccupied in the structures reported in this work. As more cation sites are required, these windows are unsuitable and so an extremely contracted mode II distortion is observed. There must be a boundary Si/Al ratio above which a mode I distortion is adopted.

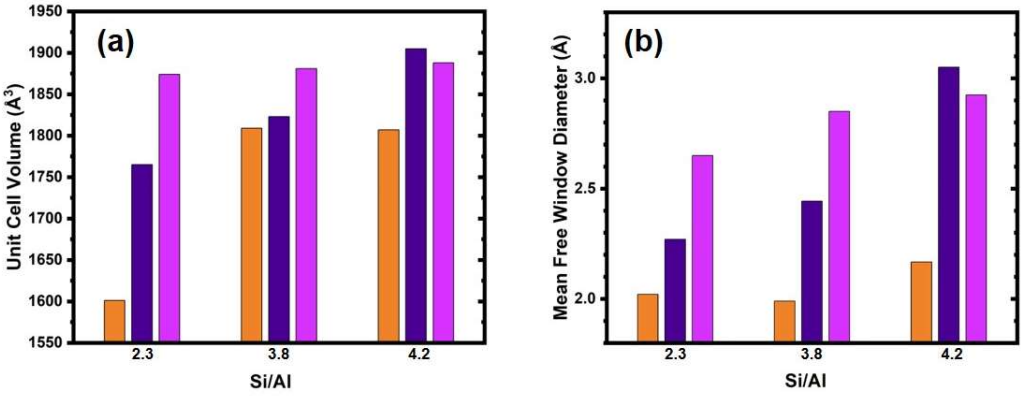

Figure 5.7.4. Comparison of (a) unit cell volumes and (b) mean window free diameters of MER materials with Si/Al = 2.3, 3.8, and 4.2. Na-, K- and Cs-forms are indicated by orange, purple and pink, respectively. Data for MER (2.3) materials is taken from Choi et al.[1] $Na_{5.0}K_{1.2}$-data is shown in place of $Na_{6.2}$-MER (4.2) due to unresolved symmetry of the latter.

Another point of interest is the large unit cell volume and window diameters observed for $K_{6.2}$-MER (4.2). For materials with lower Si/Al, the Cs-form adopts the largest unit cell volume and possesses the widest windows, yet this is not the case for the MER (4.2) material. This is explained by the retention of the wide-pore form upon dehydration observed for this K-material and again suggests a critical content of K^+ required to hold the structure closed. No step was observed in the adsorption isotherm for this material or the MER (3.8) analogue, although the latter did adopt a narrow-pore form upon dehydration. This indicates that both of these materials are very close to any such critical K^+ content. By contrast, the work of Choi *et al*. found that for K-MER materials with Si/Al = 1.7, 2.3 and 2.9, and hence 11.8, 9.7 and 8.2 K cations per unit cell, exhibited steps at 0.3, 0.05 and 0.01 bar of CO_2 at 298 K, respectively.[1,2] Finally, unlike the other cation forms, the Cs-MER materials show relatively minor increases in unit cell volume and

window diameter as Si/Al increases. This is likely due to the preference of Cs cations for site Ia (at the centre of the *d8r)* and site III (in the *ste* cavities), which may cause relatively minor distortion whilst prohibiting further contraction of the extended structure.

As has been mentioned, the $Na_{9.7}$-MER (2.3) material was found by Choi *et al*. to adopt the $P4_2/nmc$ space group,[1] whilst in the Si/Al = 3.8 material *Immm* was adopted. This changes the mode of framework distortion from mode II to I, as shown in Figure 5.7.5. Samples obtained from the MER (4.2) material presented in this chapter adopted the *Pmmn* space group, with the exception of $Na_{6.2}$-MER (4.2), the symmetry of which was not resolved. The *Pmmn* space group is a daughter of both *Immm* and $P4_2/nmc$ and as such can accommodate both modes of distortion. For these higher silica materials, the same mode is adopted relative to their MER (3.8) analogues, with the loss of symmetry due to cation ordering as the number of cations within the material decreases.

Si/Al	2.3	3.8	4.2
Na	$P4_2/nmc$	*Immm*	*Pmmn**
K	$P4_2/nmc$	$P4_2/nmc$	*Pmmn*
Cs	$P4_2/nmc$	$P4_2/nmc$	*Pmmn*

*Figure 5.7.5. Space groups adopted by dehydrated M-MER materials with varying Si/Al. Yellow and blue shading indicates distortion mode I and II, respectively. * $Na_{5.0}K_{1.2}$-MER (4.2) data is shown in place of the pure Na-form as the symmetry of the latter is unresolved. Data for MER (2.3) materials is taken from Choi et al.*[1]

As has been shown, the step or kink in CO_2 adsorption isotherms is due to expansion from narrow- to wide-pore forms. As the Si/Al ratio increases, the pressure at which this step occurs shifts to higher pressure, at any given temperature. This is illustrated in Figure 5.7.6, with Na-forms possessing the highest inflection point of materials for all Si/Al ratios. This is due to the strong preference of such small cations for narrow windows.

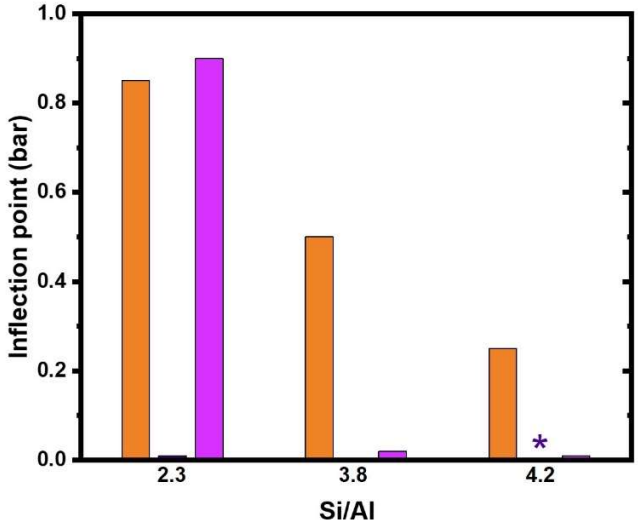

*Figure 5.7.6. Inflection points of steps in CO_2 adsorption isotherms at 298 K with varying cation content and Si/Al. Data for MER (2.3) materials is taken from Choi et al.[1] Na-, K- and Cs-materials are indicated by orange, purple, and pink bars, respectively. *$K_{6.2}$-MER (4.2) retains a wide-pore form upon dehydration, hence no inflection point is observed.*

Whilst for the Na-materials decrease in transition pressure is gradual, for the Cs- and K-containing materials, there is a significant change in breathing behaviour between MER (2.3) and (3.8) samples. Choi *et al.* also report for their $K_{11.8}$-MER (1.7) material a step at *ca*. 0.25 bar.[1] Similarly, a step at very low pressure of CO_2 (*ca*. 0.001 bar) can be seen for their $K_{8.2}$-MER (2.9) material.[2] In the case of $K_{6.7}$-MER (3.8), the step occurs at 0 bar, as the dehydrated form adopts a narrow-pore structure which opens to a wide-pore form with very low doses of CO_2. At the higher Si/Al of 4.2, the structure no longer adopts the narrow-pore form upon activation. It would be expected that there is such a point for all materials, if all Si/Al ratios were available, as the pure silica framework would remain fully open. Such behaviour would be expected to improve adsorption kinetics as wider windows ease CO_2 percolation but, as is observed for the $K_{6.2}$-MER (4.2) material, selectivity would suffer.

5.8 Conclusion

This chapter continued examining the flexible zeolite merlinoite, here with a higher Si/Al than found in the material discussed in Chapter 4. The position of steps in CO_2 adsorption isotherms previously encountered decreased in pressure relative to their MER (3.8) counterparts. The same modes of distortion were encountered for different

cation forms, despite the reduction in symmetry. Mixing cation types present within the material, as in the $Na_{6.2-x}K_x$-MER (4.2) series, enables the tuning of structural parameters, which may provide a route to balancing adsorption properties for any potential application. The flexible nature of the **MER** framework is exemplified by comparing the extremely distorted $Na_{4.0}K_{2.2}$-form, containing a 1-dimensional channel system, with the K-analogue, which retains a wide-pore form upon dehydration, and possesses rapid CO_2 sorption kinetics though at the expense of reduced selectivity. As such, the latter was incorporated into a binder and pelletised by Drs Alessandro Turrina and Ming-Feng Hsieh at Johnson Matthey with a view towards potential application.

5.9 References

(1) Choi, H. J.; Jo, D.; Min, J. G.; Hong, S. B. The Origin of Selective Adsorption of CO_2 on Merlinoite Zeolites. *Angew. Chemie - Int. Ed.* **2021**, *60* (8), 4307–4314.

(2) Choi, H. J.; Jo, D.; Hong, S. B. Effect of Framework Si/Al Ratio on the Adsorption Mechanism of CO_2 on Small-Pore Zeolites: II. Merlinoite. *Chem. Eng. J.* **2022**, *446* (P2), 137100.

(3) Wang, J. Y.; Mangano, E.; Brandani, S.; Ruthven, D. M. A Review of Common Practices in Gravimetric and Volumetric Adsorption Kinetic Experiments. *Adsorption* **2021**, *27* (3), 295–318.

(4) Bruce, E. L.; Georgieva, V. M.; Verbraeken, M. C.; Murray, C. A.; Hsieh, M.-F.; Casteel, Jr, W. J.; Turrina, A.; Brandani, S.; Wright, P. A. Structural Chemistry, Flexibility and CO_2 Adsorption Performance of Alkali Metal Forms of Merlinoite with Framework Si/Al Ratio of 4.2. *J. Phys. Chem. C* **2021**, *125* (49), 27403–27419.

(5) Cook, M.; Conner, W. C. How Big Are the Pores of Zeolites? In *Proceedings of the 12th International Zeolite Conference*; Treacy, M. M. J., Marcus, B. K., Bisher, M. E., Higgins, J. B., Eds.; Materials Research Society: Warrendale, PA, USA, 1999; pp 409–414.

(6) Lozinska, M. M.; Mangano, E.; Mowat, J. P. S.; Shepherd, A. M.; Howe, R. F.; Thompson, S. P.; Parker, J. E.; Brandani, S.; Wright, P. A. Understanding Carbon Dioxide Adsorption on Univalent Cation Forms of the Flexible Zeolite Rho at

Conditions Relevant to Carbon Capture from Flue Gases. *J. Am. Chem. Soc.* **2012**, *134* (42), 17628–17642.

(7) Lozinska, M. M.; Mangano, E.; Greenaway, A. G.; Fletcher, R.; Thompson, S. P.; Murray, C. A.; Brandani, S.; Wright, P. A. Cation Control of Molecular Sieving by Flexible Li-Containing Zeolite Rho. *J. Phys. Chem. C* **2016**, *120* (35), 19652–19662.

(8) Lozinska, M. M.; Mowat, J. P. S.; Wright, P. A.; Thompson, S. P.; Jorda, J. L.; Palomino, M.; Valencia, S.; Rey, F. Cation Gating and Relocation during the Highly Selective "Trapdoor" Adsorption of CO_2 on Univalent Cation Forms of Zeolite Rho. *Chem. Mater.* **2014**, *26* (6), 2052–2061.

(9) Lozinska, M. M.; Jamieson, S.; Verbraeken, M. C.; Miller, D. N.; Bode, B. E.; Murray, C. A.; Brandani, S.; Wright, P. A. Cation Ordering and Exsolution in Copper-Containing Forms of the Flexible Zeolite Rho (Cu,M-Rho; M=H, Na) and Their Consequences for CO_2 Adsorption. *Chem. - A Eur. J.* **2021**, *27* (51), 13029–13039.

(10) Choi, H. J.; Hong, S. B. Effect of Framework Si/Al Ratio on the Mechanism of CO_2 Adsorption on the Small-Pore Zeolite Gismondine. *Chem. Eng. J.* **2022**, *433* (P3), 133800.

6 Zeolite Merlinoite: Effect of Li

6.1 Introduction

The work of previous chapters has shown that cation type has a large impact on the behaviour of materials structurally and hence as potential sorbents. Li cations were found to greatly impact window sizes in zeolite Rho (3.9), discussed in Chapter 3, and a Li-MER (4.2) sample could be expected to be a highly selective adsorbent. Just as for Rho (3.9) materials in Chapter 3, the subsequent introduction of some larger cations could be expected to modify structural and adsorption behaviour, as also observed in $Na_{6.2-x}K_x$-MER (4.2) materials in Chapter 5. Therefore, $Li_{6.2-x}M_x$-MER (4.2) materials were also investigated, as the higher Si/Al merlinoite material described in Chapter 5 enabled a stable Li-form to be synthesised.

6.2 Acknowledgements

The materials described here were prepared by Dr Veselina M. Georgieva *via* ion exchange from the as-prepared material described in Chapter 5, after calcination. Additional samples were prepared by Ms Anna M. Hall. Drs Georgieva and Magdalena M. Lozinska dehydrated samples, as well as collecting adsorption and PXRD data. Prof Paul A. Wright and Dr Claire A. Murray also aided with data collected at the DLS synchrotron. PND samples were prepared and packaged by Drs Lozinska and Julia L. Payne, with Dr Ron I. Smith running experiments at ISIS.

6.3 Underlying experimental work

Hydrated and dehydrated PXRD patterns of selected $Li_{6.2-x}Na_x$-, $Li_{6.2-x}K_x$- and $Li_{6.2-x}Cs_x$-MER (4.2) materials, including $Li_{6.2}$-MER (4.2), collected by Dr Georgieva, are shown in Figure 6.3.1. Dehydrated patterns of the complete $Li_{6.2-x}M_x$-MER (4.2) series, also collected by Dr Georgieva, are presented in Figure 6.3.2. Additional peaks are obvious for $Li_{6.2-x}K_x$- and $Li_{6.2-x}Cs_x$-MER (4.2) at higher values of x.

Additional neutron diffraction data for dehydrated $Li_{6.2}$-MER (4.2) was collected at the ISIS neutron and muon source, in Didcot, Oxfordshire by Dr Smith after sample

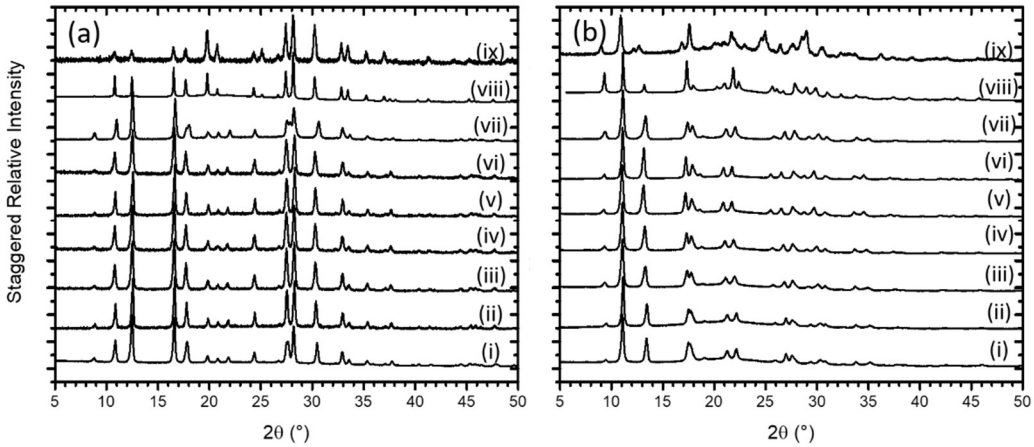

Figure 6.3.1. Scaled PXRD patterns of (a) hydrated and (b) dehydrated MER samples: (i) $Li_{6.2}$-, (ii) $Li_{5.0}Na_{1.2}$-, (iii) $Li_{4.0}Na_{2.2}$-, (iv) $Li_{3.0}Na_{3.2}$-, (v) $Li_{2.0}Na_{4.2}$-, (vi) $Li_{1.0}Na_{5.2}$-, (vii) $Li_{4.0}K_{2.2}$-, (viii) $Li_{3.4}Cs_{2.8}$- and (ix) $Li_{1.0}Cs_{5.2}$-MER. (Stoe, λ = 1.54056 Å).

preparation and packing by Drs. Lozinska and Payne. This data is shown in Figure 6.3.3, along with laboratory PXRD data.

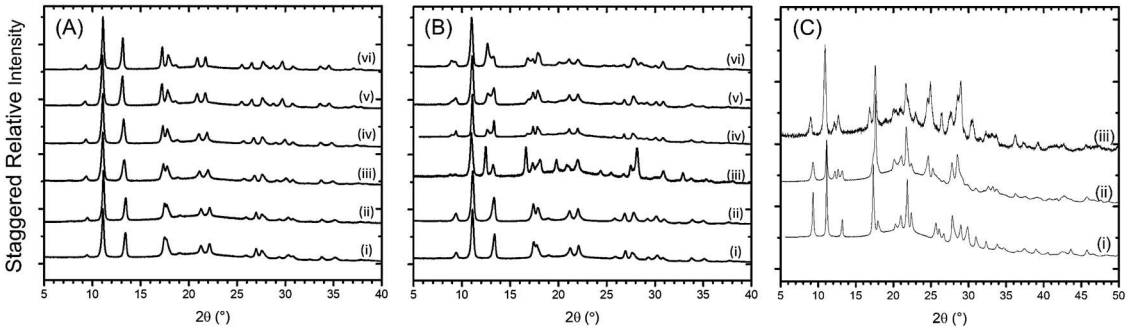

Figure 6.3.2. Dehydrated PXRD patterns of $Li_{6.2-x}M_x$-MER (4.2) series where M = (A) Na, (B) K and (C) Cs. Samples within series are (A): (i) $Li_{6.2}$-, (ii) $Li_{5.0}Na_{1.2}$-, (iii) $Li_{4.0}Na_{2.2}$-, (iv) $Li_{3.0}Na_{3.2}$-, (v) $Li_{2.0}Na_{4.2}$- and (vi) $Li_{1.0}Na_{5.2}$-MER (4.2); (B): (i) $Li_{5.0}K_{1.2}$-, (ii) $Li_{4.0}K_{2.2}$-, (iii) $Li_{3.7}K_{2.5}$-, (iv) $Li_{3.0}K_{3.2}$-, (v) $Li_{2.0}K_{4.2}$- and (vi) $Li_{1.0}K_{5.2}$-MER (4.2); and (C): (i) $Li_{3.4}Cs_{2.8}$-, (ii) $Li_{3.0}Cs_{3.2}$- and (iii) $Li_{1.0}Cs_{5.2}$-MER (4.2). (Stoe, λ = 1.54056 Å).

High pressure CO_2 adsorption isotherms for $Li_{6.2-x}Na_x$- and $Li_{6.2-x}K_x$-MER (4.2) samples were measured by Dr Georgieva and shown in Figure 6.3.4. A comparison of samples from $Li_{6.2-x}M_x$-MER (4.2) series with similar M content is shown in Figure 6.3.6.

Unfortunately, no ZLC or E-ZLC measurements were obtained for these samples. In the place of such quantitative experiments, metadata obtained during high pressure CO_2 equilibrium isotherm acquisition was examined. By evaluating the gradient of CO_2

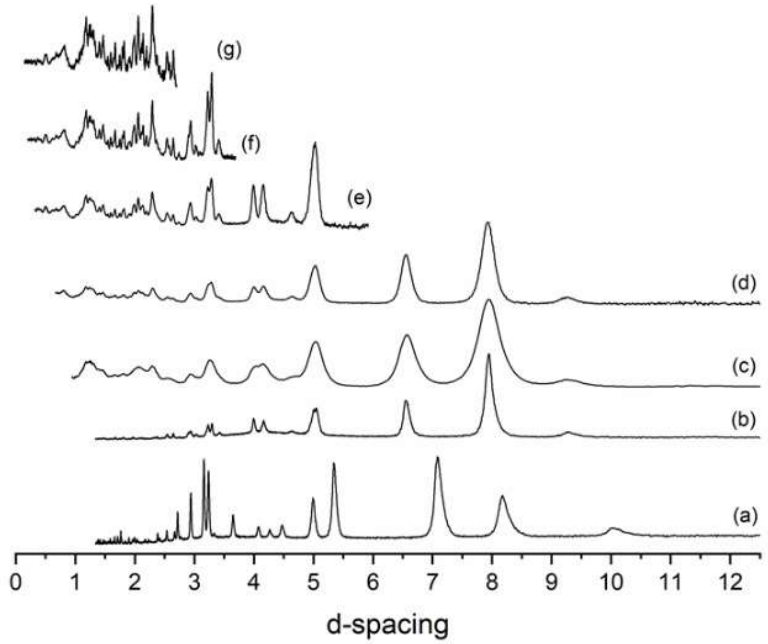

Figure 6.3.3. Comparison of (a) hydrated and (b) dehydrated $Li_{6.2}$-MER (4.2) PXRD data (Stoe, λ = 1.54056 Å) with PND data (Polaris, ISIS) for the dehydrated sample: (c) bank 1, (d) bank 2, (e) bank 3, (f) bank 4 and (g) bank 5.

uptake during equilibration steps, the relative diffusivities of materials could be gauged. Such metadata is shown in Figure 6.3.5.

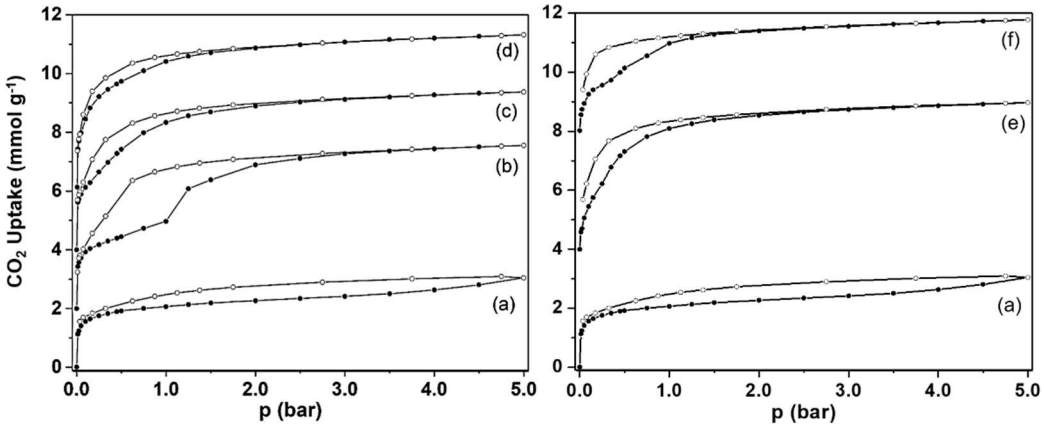

Figure 6.3.4. Stacked CO_2 sorption isotherms at 298 K up to 5 bar for $Li_{6.2-x}Na_x$- and $Li_{6.2-x}K_x$-MER (4.2), offset by (left) 2 and (right) 4 mmol g^{-1}, respectively: (a) $Li_{6.2}$-, (b) $Li_{5.0}Na_{1.2}$-, (c) $Li_{4.0}Na_{2.2}$-, (d) $Li_{3.0}Na_{3.2}$-, (e) $Li_{5.0}K_{1.2}$-, and (f) $Li_{3.7}K_{2.5}$-MER (4.2). Adsorption and desorption curves are shown by open and closed circles, respectively. Note that (f) $Li_{3.7}K_{2.5}$-MER (4.2) undergoes exsolution upon dehydration.

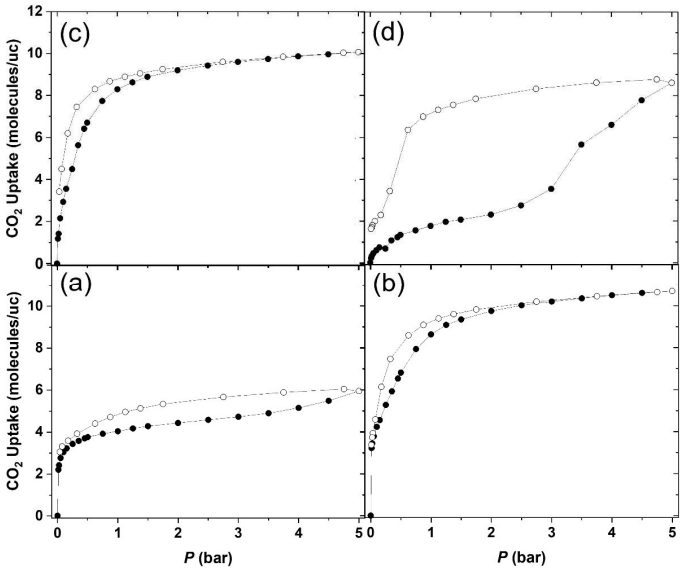

Figure 6.3.5. CO_2 adsorption isotherms at 298 K up to 5 bar for (a) $Li_{6.2}$-, (b) $Li_{4.0}Na_{2.2}$-, (c) $Li_{4.0}K_{2.2}$-, and (d) $Li_{3.4}Cs_{2.8}$-MER (4.2). Adsorption, closed symbols; desorption, open symbols.

Dr Georgieva also obtained multiple CO_2 adsorption isotherms on $Li_{3.4}Cs_{2.8}$-MER (4.2) without heating in between each cycle. This reduced the step pressure as the number of

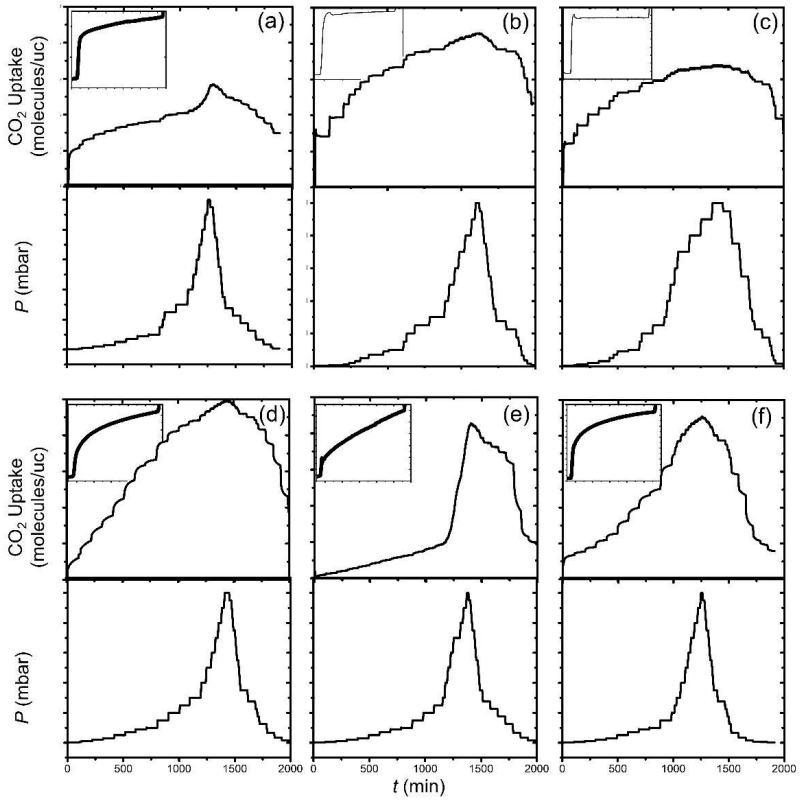

Figure 6.3.6. (a–e) CO_2 uptake over the course of adsorption experiments with relevant dosing pressure steps shown below for $Li_{6.2}$-, $Na_{6.2}$-, $K_{6.2}$-, $Li_{4.0}K_{2.2}$-, and $Li_{3.4}Cs_{2.8}$-MER (4.2), with up to 5 bar pressure of CO_2. (f) Corresponding plots for $Li_{3.4}Cs_{2.8}$-MER (4.2) after consecutive adsorption experiments without thermal activation. Individual adsorption steps for a given low-pressure dose are shown in the inset. T = 298 K for all plots, except (c) where T = 308 K.

cycles increased, but the initial isotherm could be replicated once the sample was evacuated with heating, as shown in Figure 6.3.7.

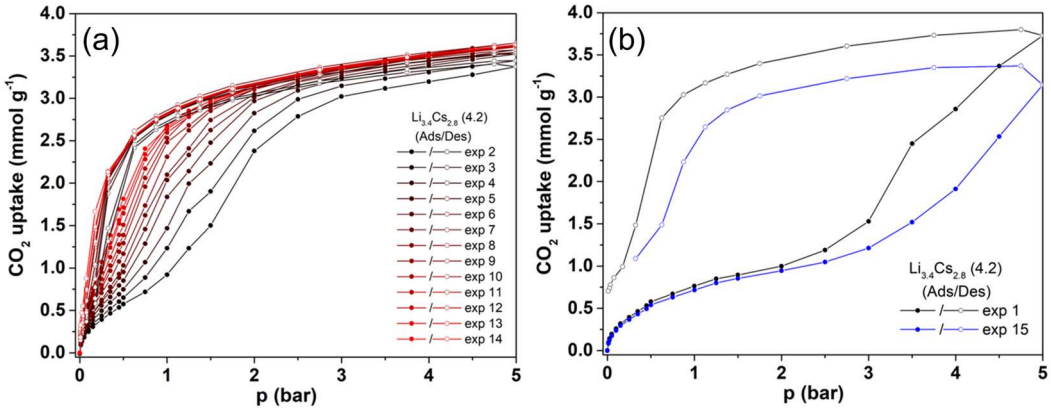

Figure 6.3.7. Cyclical CO_2 adsorption experiments on $Li_{3.4}Cs_{2.8}$-MER (4.2): (a) obtained with only evacuatation and no heating between cycles and (b) isotherms collected with both heating and evacuation, during the first and last cycles.

6.4 $Li_{6.2}$-MER (4.2)

Like previous merlinoite samples discussed in Chapters 4 and 5, $Li_{6.2}$-MER (4.2) undergoes distortion upon dehydration, as evidenced by PXRD patterns shown in Figure 6.3.1. The hydrated and dehydrated forms of the material were refined from similar structures found in Chapter 5, using PXRD alone and combined with PND data, respectively. Rietveld plots and their related structures are given in Appendix IV.VII and Figure 6.4.1, and Figure 6.4.2, respectively.

The hydrated form was found to adopt the *I*4/*mmm* space group, whilst upon dehydration *Immm* was required. Unlike other MER (4.2) samples described in Chapter 5, there was no need to choose the *Pmmn* symmetry, which gave no improvement in fit. Dehydration of the pure Li-material causes a decrease in unit cell volume of 12.8%, as indicated in Table 6.4.1, far higher than previous merlinoite materials investigated. The fit is poorest for banks at higher angles, particularly banks 4 and 5, due to the equal weighting given to each pattern during refinement. Bank 5 gives the highest resolution data, and it could be argued that the information present in bank 1 provides nothing further than that already available in bank 2, effectively doubling the weighting of high *d* spacing data. This should be re-examined in the future, either removing bank 1 or adjusting the weighting of the banks. The good fit with PXRD data may suggest that the framework positions are especially reliable but that Li positions, which do not contribute

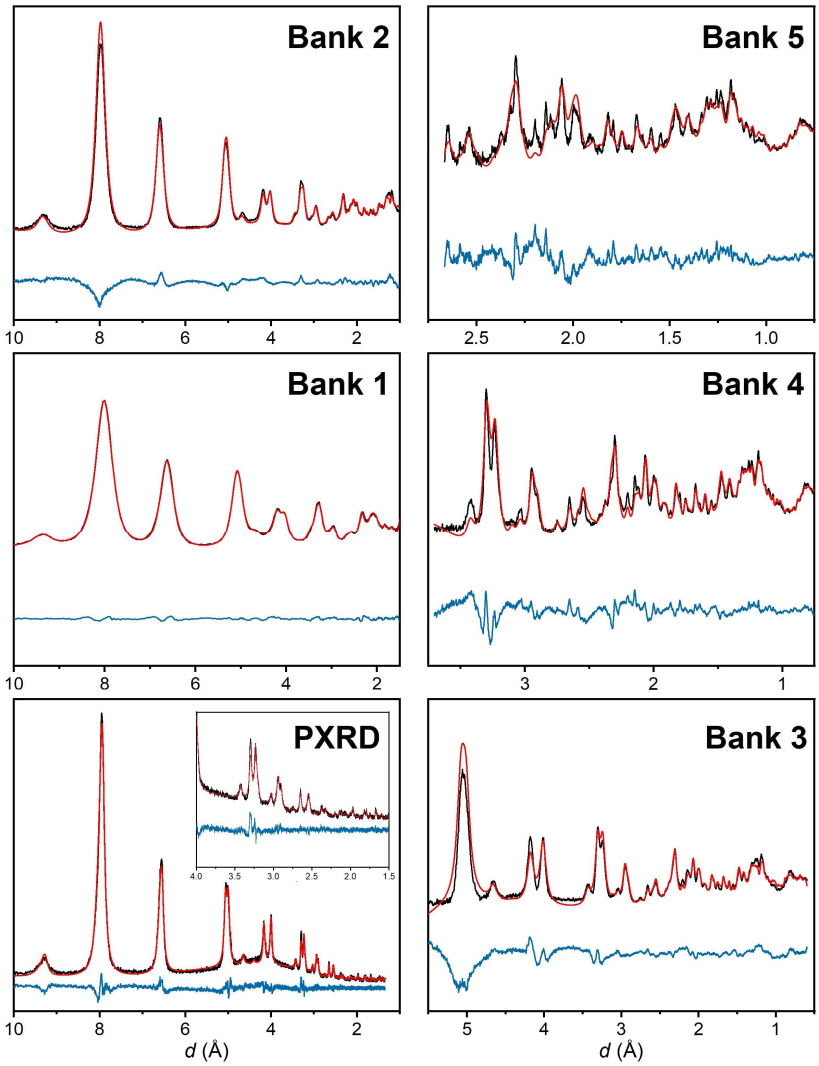

Figure 6.4.1. Combined Rietveld fit of $Li_{6.2}$-MER (4.2) of laboratory PXRD (Stoe, λ = 1.54056 Å) and PND data (Polaris, ISIS), as a function of d spacing. Observed, calculated and difference curves are shown in black, red and blue, respectively with datasets as labelled.

significantly to X-ray diffraction, may be more sensitive to the weighting of different banks.

Table 6.4.1. Space group (SG), unit cell parameters and R_{wp} from refinement of $Li_{6.2}$-MER (4.2) samples under hydrated and dehydrated conditions.

Condition	**SG**	***a* (Å)**	***b* (Å)**	***c* (Å)**	***V* (Å³)**	**R_{wp}**
Hydrated	*I*4/*mmm*	14.147(1)		9.926(1)	1986(1)	5.9%
Dehydrated	*Immm*	13.206(1)	13.141(1)	9.976(1)	1731(1)	3.5%

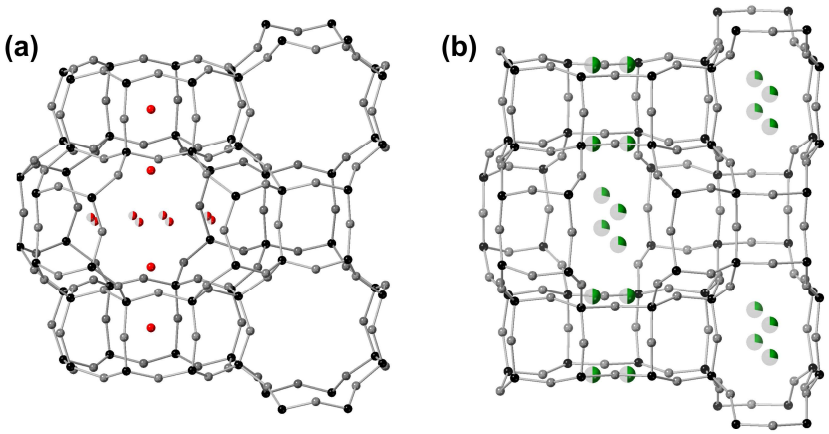

Figure 6.4.2. Refined structures of $Li_{6.2}$-MER (4.2) in the (a) hydrated and (b) dehydrated form. Framework T and O sites are indicated by black and grey, with extraframework O and Li species depicted in red and green, respectively. Fractional occupancies are shown by partial shading of spheres.

The high level of framework distortion is evidenced numerically in the relative window diameters given in Table 6.4.2. Cation sites and framework windows follow the nomenclature used in both Chapters 4 and 5. All windows are very strongly reduced in size upon dehydration, with the exception of window IIb, which is very similar to window II in the hydrated form. The distortion is so extreme that the free diameters of the remaining windows are reduced to almost 1 Å which, if the framework were rigid, would preclude all gas species larger than hydrogen. This is very similar to the behaviour observed for $Na_{4.0}K_{2.2}$-MER (4.2), shown in Figure 5.5.8.

As PND data was acquired for the dehydrated $Li_{6.2}$-MER (4.2) sample, it was possible to refine the positions and occupancies of Li cations in this form. This was not obtained for the hydrated form and for ease of discussion, Li cations sites are discussed in greater depth relative to those of heavier cations refined in $Li_{6.2-x}M_x$-samples, detailed below.

*Table 6.4.2. Free window diameters in $Li_{6.2}$-MER (4.2) materials under hydrated and dehydrated conditions. Windows that would be closed to CO_2 percolation (<2.3 Å) are denoted by *.*

Condition	dh/h	I (Å)	II(a) (Å)	IIb (Å)	III (Å)
Hydrated	h	3.7(1)	3.2(1)		3.0(1)
Dehydrated	dh	1.1(1)*	1.4(1)*	3.1(1)	1.1(1)*

6.5 Dehydrated $Li_{6.2-x}M_x$-MER (4.2) structures

Incorporation of other cations into $Li_{6.2}$-MER (4.2) was found to have significant effects. This is not apparent from examination of the hydrated patterns given in Figure 6.3.1, which shows that all samples within the series described here are single phase. Upon dehydration, however, this is no longer the case, as seen in Figure 6.3.2. Samples containing more K and Cs cations than $Li_{4.0}K_{2.2}$- and $Li_{3.4}Cs_{2.8}$-MER (4.2), respectively, exhibit additional peaks at lower angles, indicating an additional, expanded merlinoite material, shown in Section 6.3. This could not be attributed to incomplete dehydration and is consistent with exsolution, the process in which a homogenous solid separates into multiple phases. In this case it refers to uniformly dispersed cations in the hydrated material redistributing upon dehydration to 2 separate phases which better accommodate the different cation types (e.g. Li-rich and K-rich phases) and different associated crystallographic properties. This is a known phenomenon in zeolites, with Pakhomova *et al*. reporting its occurrence in Na,K-amicite (**GIS**) and Lozinska *et al*. detailing such behaviour in Cu,Na-Rho (3.9).[38,39] In both cases, these are examples of flexible zeolites containing cations with conflicting site preferences. In both amicite and Rho, Na^+ species direct more distorted frameworks, with narrower 8-ring sites, whilst K^+ favours wider 8-rings in amicite and Cu^{2+} preferentially binds to 6-ring sites in undistorted Rho (3.9).

The same is true for these materials, with Li cations directing an extremely distorted framework structure, forming very narrow 8-rings, which would be expected to be unfavourable for bulkier K and Cs cations. Therefore, upon dehydration, materials form Li- and K- or Cs-rich phases, with different degrees of framework distortion. Conversely, the $Li_{6.2-x}Na_x$-MER (4.2) series shows no such obvious behaviour due to the relative similarities in site preference of small Li and Na cations. Samples with 4.2 and 5.2 cations per unit cell began to show progressively large shoulder effects on peaks at *ca*. 18 and 28°, suggesting either an additional phase or an alternative symmetry. Given the inability to describe the pure Na-form of the MER (4.2) material, this is perhaps unsurprising. From here on, this chapter deals solely with pure-phase materials, excluding the $Li_{6.2-x}Na_x$-samples with the peak shoulders mentioned.

Rietveld plots of selected $Li_{6.2-x}M_x$-MER (4.2) samples are shown in Figure 6.5.1. Only M cations were refined, due to the use of PXRD data alone and the poor X-ray scattering of

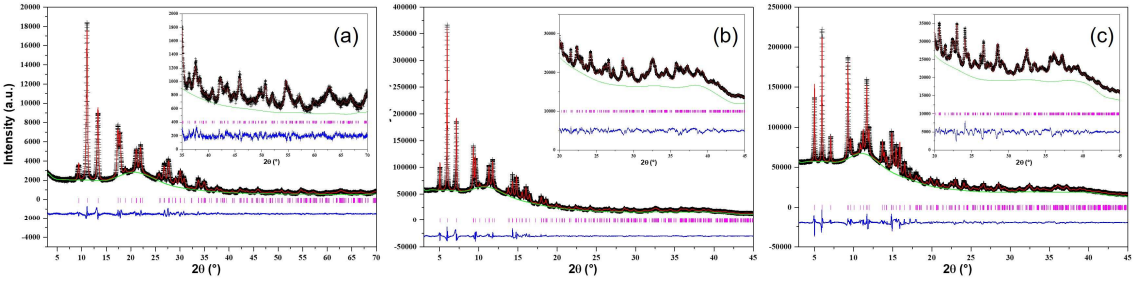

Figure 6.5.1. Rietveld plots of dehydrated (a) $Li_{4.0}Na_{2.2}$-, (b) $Li_{4.0}K_{2.2}$-, and (c) $Li_{3.4}Cs_{2.8}$-MER (4.2), with the expansion of higher angle data shown inset. ((a) Stoe, λ = 1.54056 Å, (b, c) I11, DLS, λ = 0.826398 Å).

Li^+ species. The refined structures of the partially-exchanged materials are given in Figure 6.5.2 and structural details of the materials are given in Table 6.5.1. All materials investigated here possess similar framework structures upon dehydration, with distortions resembling those of $Li_{6.2}$-MER (4.2) and adopting the mode I distortion also observed in $Na_{6.7}$-MER (3.8) and $Na_{5.2}K_{1.0}$-MER (4.2), discussed in Chapters 4 and 5, respectively.

*Table 6.5.1. Unit cell parameters and volumes for $Li_{6.2-x}M_x$-MER (4.2) samples, with space groups (SGs) and Rietveld R_{wp} and χ^2 values. *The Li-form was refined using combined PXRD and PND data.*

Cation form	SG	*a* (Å)	*b* (Å)	c (Å)	V (Å^3)	R_{wp} (%)	χ^2
$Li_{6.2}$*	*Immm*	13.201(1)	13.114(1)	10.007(1)	1732(1)	4.1	17
$Li_{5.0}Na_{1.2}$	*Immm*	13.240(1)	13.172(1)	9.985(1)	1741(1)	4.6	1.6
$Li_{4.0}Na_{2.2}$	*Immm*	13.297(1)	13.263(1)	9.946(1)	1754(1)	4.1	1.7
$Li_{3.0}Na_{3.2}$	*Immm*	13.339(1)	13.343(1)	9.948(1)	1771(1)	4.1	1.6
$Li_{5.0}K_{1.2}$	*Immm*	13.225(1)	13.179(1)	9.938(1)	1732(1)	4.5	2.2
$Li_{4.0}K_{2.2}$	*Immm*	13.275(1)	13.244(1)	9.907(1)	1742(1)	2.9	5.5
$Li_{3.4}Cs_{2.8}$	*Immm*	13.337(1)	13.377(1)	9.837(1)	1755(1)	3.0	5.8

A graphical comparison of unit cell volume is given in Figure 6.5.3. From this it can be seen that all samples reported here are smaller than their pure-cation MER (4.2) analogues. As Li content decreases, unit cell volumes increases, and therefore the addition of larger cations does indeed reduce framework distortion. Surprisingly, $Li_{6.2-x}K_x$- and $Li_{6.2-x}Cs_x$-MER (4.2) samples possess more distorted frameworks than $Li_{6.2-x}Na_x$-materials with similar Li content. This highlights the importance of cation siting, as well

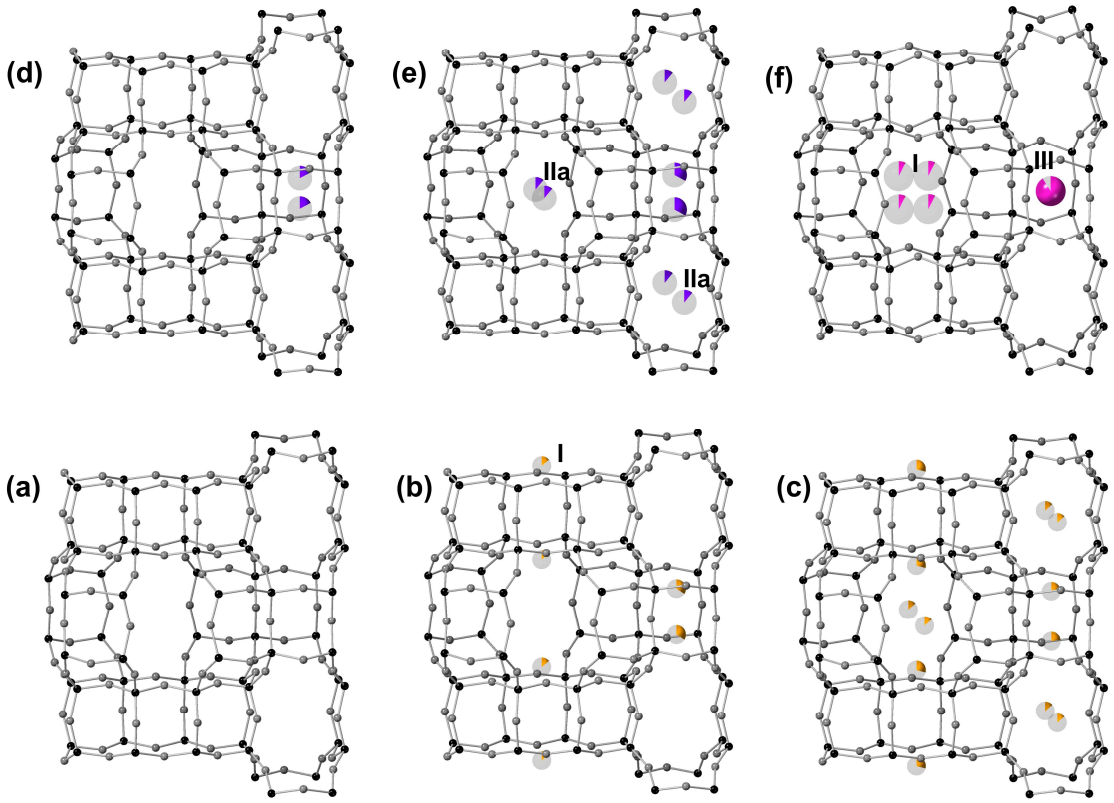

Figure 6.5.2. Extended structures of dehydrated forms of $Li_{6.2-x}M_x$-MER (4.2): (a) $Li_{5.0}Na_{1.2}$-, (b) $Li_{4.0}Na_{2.2}$-, (c) $Li_{3.0}Na_{3.2}$-, (d) $Li_{5.0}K_{1.2}$-, (e) $Li_{4.0}K_{2.2}$- and (f) $Li_{3.4}Cs_{2.8}$-MER (4.2). T and O sites are shown in black and grey, with Na^+, K^+, and Cs^+ shown in orange, purple, and pink, respectively, with fractional occupancies indicated by partial shading. Example cations sites are labelled.

as cation type, as the introduction of progressively larger cations does not increase the unit cell volume, as may be initially expected.

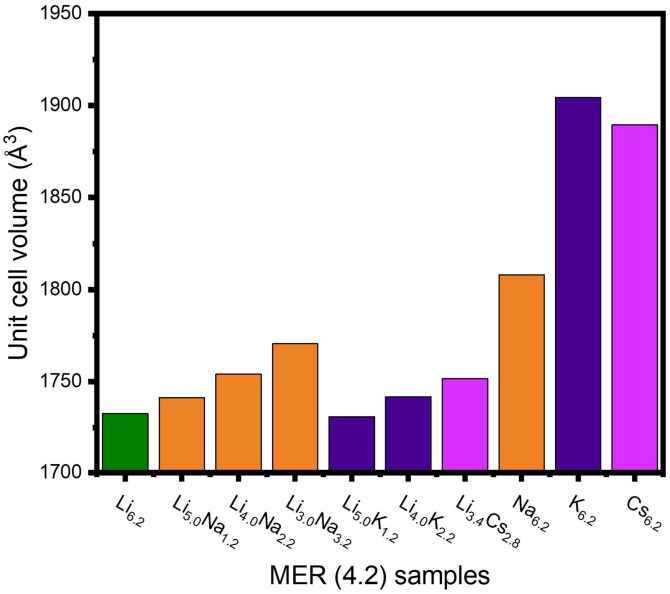

Figure 6.5.3. Unit cell volumes of $Li_{6.2-x}M_x$-MER (4.2) materials. The cation form is shown underneath. Values for other pure cation forms are shown for comparison.

Just as the X-ray scattering from Li cations is too poor for unambiguous refinement of these species from PXRD data, the low Na content in $Li_{5.0}Na_{1.2}$-MER did not allow definitive refinement of the relatively light Na^+ species. Table 6.5.2 lists cation sitings derived from Rietveld refinement for the other samples. Site III is preferentially occupied by the non-Li cations in almost all materials investigated and is particularly favourable for K^+ and Cs^+ species. This site was previously found to be preferentially occupied by Cs cations in MER (4.2). Na-containing samples exhibit higher occupancies in site I than the other forms, which may be expected to have implications for the *d8r* window size.

*Table 6.5.2. Site occupancies of M cations within $Li_{6.2-x}M_x$-MER (4.2) materials. Ω, Frac and Abs denote multiplicity, fractional and absolute occupancy, respectively. The total number of cations per unit cell refined, and their type, is also shown. *The Li-form was refined using combined PXRD and PND data.*

Cation form	**I**			**IIa**			**III**			**Total**
	Frac	Ω	Abs	Frac	Ω	Abs	Frac	Ω	Abs	
$Li_{6.2}$*	0.50(3)	8	4.0(2)	0.28(3)	8	2.2(2)				6.2(3) Li^+
$Li_{4.0}Na_{2.2}$	0.14(2)	4	0.6(1)				0.34(2)	4	1.4(1)	2.0(2) Na^+
$Li_{3.0}Na_{3.2}$	0.29(2)	4	1.2(1)	0.14(2)	4	0.6(1)	0.23(2)	4	0.9(1)	2.7(2) Na^+
$Li_{5.0}K_{1.2}$							0.17(1)	4	0.7(1)	0.7(1) K^+
$Li_{4.0}K_{2.2}$				0.11(1)	4	0.4(1)	0.33(1)	4	1.3(1)	1.7(2) K^+
$Li_{3.4}Cs_{2.8}$	0.08(1)	8	0.6(1)				0.91(1)	2	1.8(1)	2.4(2) Cs^+

Window sizes of the materials are given in Table 6.5.3. The $Li_{6.2}$-MER (4.2) material shows an exceptionally large range of window sizes in its dehydrated form, due to the assembly of extremely narrow 8-rings and the large channel that this demands, previously discussed for materials with mode I distortions in Chapter 5. Similar behaviour is observed for the other materials, with window sizes marginally larger as the Li content decreases for a given series and $Li_{6.2-x}Na_x$-MER (4.2) samples possessing generally larger windows than their K- and Cs-containing analogues. $Li_{3.4}Cs_{2.8}$-MER (4.2) exhibits some anomalous behaviour, with window IIa narrower than in the pure Li-form, and the largest window III size. These may be due to the high occupation of site III by bulky cations and the interconnected nature of the framework. It is notable that with such minor differences between samples, all structures here would be expected to

possess only 1-dimensional channel connectivity, as previously mentioned in Chapters 4 and 5.

*Table 6.5.3. Window sizes within $Li_{6.2-x}M_x$-MER (4.2) materials. Windows that would be closed to CO_2 percolation (<2.3 Å) are denoted by *.*

Cation form	I (Å)	IIa (Å)	IIb (Å)	III (Å)
$Li_{6.2}$	1.4(1)*	1.3(1)*	3.0(1)	1.1(1)*
$Li_{5.0}Na_{1.2}$	1.4(1)*	1.3(1)*	3.0(1)	1.1(1)*
$Li_{4.0}Na_{2.2}$	1.6(1)*	1.4(1)*	3.1(1)	1.3(1)*
$Li_{3.0}Na_{3.2}$	1.6(1)*	1.4(1)*	3.0(1)	1.4(1)*
$Li_{5.0}K_{1.2}$	1.4(1)*	1.4(1)*	2.8(1)	1.2(1)*
$Li_{4.0}K_{2.2}$	1.5(1)*	1.3(1)*	3.1(1)	1.3(1)*
$Li_{3.4}Cs_{2.8}$	1.5(1)*	1.1(1)*	3.0(1)	1.6(1)*

6.6 $Li_{6.2-x}M_x$MER (4.2) materials as CO_2 sorbents

Experimental data shown in Section 6.3 illustrates the CO_2 adsorption behaviour of the $Li_{6.2}$-MER (4.2) sample. A step in adsorption occurs above ambient pressure, at *ca*. 3 bar. This is very different from the isotherms seen for other pure cation forms of MER (4.2), discussed in Chapter 5, which saw any such steps at much reduced pressure. To better understand how the Li-materials behaves under CO_2 adsorption, VPXRD experiments were carried out on a laboratory instrument by Dr Georgieva with assistance from Dr Andreev. The results of these experiments are shown in Figure 6.6.1. It can be seen that

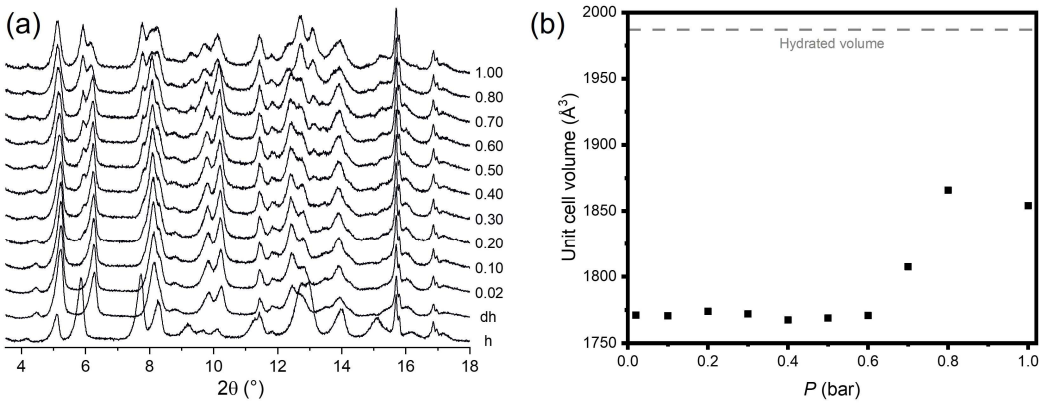

Figure 6.6.1. Laboratory VPXRD experiments at 25 °C for $Li_{6.2}$-MER (4.2): (a) collected patterns and (b) refined unit cell volumes with pressure. CO_2 pressures in bar are indicated on the right of (a) and h and dh correspond to hydrated and dehydrated, respectively. (PANalytical, Mo $K\alpha_{1,2}$, λ = 0.711 Å).

at 0.02 bar of CO_2, the material adopts a structure very similar to that of the dehydrated form. In addition to this pattern, shoulders begin to appear on the peaks at *ca*. 6 and 8° possibly at pressures as low as 0.10 bar and are obvious by 0.30 bar of CO_2. These are evidence of an expanded structure, relative to the dehydrated form, but do not align well with the hydrated pattern and occurs well below 3 bar, the pressure at which a kink in the adsorption isotherm is observed. This suggests the presence of an intermediate structure, which occurs concurrently with the narrow-pore form.

From Figure 6.6.1, it can be seen that as pressure increases, the proportion of the sample in this intermediate form increases. Due to the low quality of the VPXRD data, the structure of this phase could not be refined, but at higher pressure (> 0.5 bar) the unit cell parameters of this phase could be fitted, between 1910 and 1950 $Å^3$ which approaches the hydrated unit cell volume of 1987 $Å^3$. As the framework is expected to be more open, with larger windows, the degree of connectivity may increase above the 1-dimensional channel system of the activated material.

The initial aim of these binary series was to increase the adsorption uptakes at lower partial pressure of CO_2 compared to the pure Li-form. As shown in the previous section, the introduction of larger cations causes marginally increased window sizes along with expanded unit cell volumes. All dehydrated samples investigated here retain the 1-dimensional pore system present in dehydrated $Li_{6.2}$-MER (4.2) however, and this would suggest that kinetic properties of the materials remain poor. Indeed, the isotherm metadata shown in Figure 6.3.5 suggests that there is no improvement in adsorption kinetics for the $Li_{4.0}K_{2.2}$- and $Li_{3.4}Cs_{2.8}$-MER (4.2) samples, with the data looking particularly slow for the latter, taking a long time to reach equilibrium for a given dose of pressure. This can be attributed to bulky Cs cations occupying the centre of *ste* cavities in site III, adding further hindrance by blocking the single open channel system. For uptake to occur in this material, a cation gating mechanism is therefore required.

It can be seen however that inclusion of larger cations does shift the step in adsorption to lower pressure. In Figure 6.3.4, it is shown that progressively decreasing Li content causes the adsorption step to move to lower pressure in $Li_{6.2-x}Na_x$- and $Li_{6.2-x}K_x$-MER (4.2). The effect is most marked with initial doping, as ever more M cations have less of an influence. Comparison of different cation forms is shown in Figure 6.3.6. Here it can

be seen that, whilst $Li_{4.0}Na_{2.2}$- and $Li_{4.0}K_{2.2}$-materials behave in a very similar way in significantly reducing the step pressure, Cs cations in $Li_{3.4}Cs_{2.8}$-MER (4.2) have a much smaller effect on the position of the step. Instead, the main effect appears to be the lowering of CO_2 uptake in the lower pressure regime, likely due to Cs^+ species occupying appreciable pore volume in the greatly distorted material.

The pressure at which the adsorption step occurs in previous materials studied is understood to be due to relative energetic favourabilities of narrow- and wide-pore forms. As such, it appears that relatively small amounts of Na^+ and K^+ exchange greatly improves the favourability of the wide-pore form, as these larger cations are better accommodated than Li cations by expanded 8-rings. By contrast, this concentration of Cs cations has no such effect and this is likely due to little difference in energetics between the preferred *ste* sites in the dehydrated and expanded structures.

These materials were also studied under laboratory VPXRD experiments, shown in Figure 6.6.2. Just as for the Li-form, other samples appear to show the presence of an intermediate. $Li_{4.0}Na_{2.2}$-MER (4.2) shows such a phase between 0.10 – 0.50 bar of CO_2, before expansion to an single wide-pore form, which is similar to the step in adsorption for this material, although this is rather muted for this material. A minor additional phase is also seen in the data for $Li_{4.0}K_{2.2}$-MER (4.2) at 0.02 bar which does not align with peak positions of the wide-pore phase at higher pressure. An intermediate phase is isolated for the $Li_{2.0}Na_{4.2}$-sample between 0.10 and 0.50 bar. The features of the pattern may be more reminiscent of the wide-pore form, yet it is not identical, and for this sample, the unit cell volume remains near constant at *ca*. 1950 $Å^3$ before expansion to the wide-pore form at 0.60 bar of CO_2, with a unit cell volume of *ca*. 1980 $Å^3$. Looking at the other materials, such features can also be observed in these, complicated by the existence of multiple phases simultaneously.

From the relative phase content of each sample, shown in Figure 6.6.2, some observations can be made, despite the poor quality of the data. First, the intermediate has a limited effect on adsorption uptake, as highlighted by comparison of $Li_{4.0}Na_{2.2}$- and $Li_{2.0}Na_{4.2}$-MER (4.2). The former exhibits a gradual conversion of the initial narrow-pore phase to the intermediate form, whilst the latter shows a clear change between the 2 forms at low

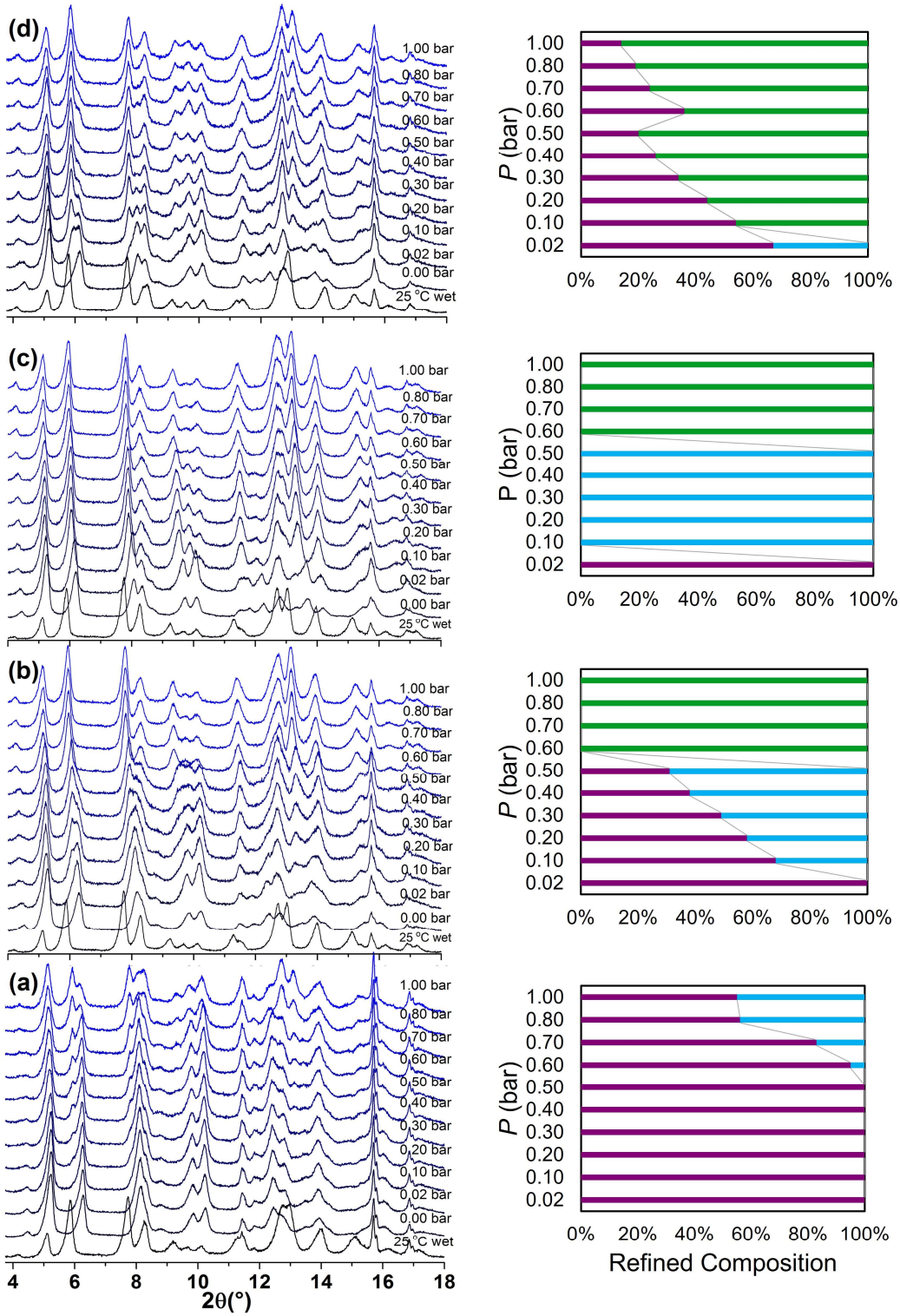

Figure 6.6.2. (Left) VPXRD experiments at 25 °C for (a) $Li_{6.2}$-, (b) $Li_{4.0}Na_{2.2}$-, (c) $Li_{2.0}Na_{4.2}$-, and (d) $Li_{4.0}K_{2.2}$-MER (4.2). (Right) Relative fitted phase compositions for each pressure. Narrow-, intermediate-, and wide-pore phases are indicated in purple, blue, and green, respectively. (PANalytical, Mo K$\alpha_{1,2}$, λ = 0.711 Å).

pressure. Despite this, their respective isotherms show smoothed steps at very similar

CO_2 pressure, the pressure at which transition to the wide-pore structure occurs.

A second observation is that the nature of structural transitions in the materials is not identical. As described for $Li_{4.0}Na_{2.2}$-MER (4.2), increasingly more of the intermediate form is observed before a threshold partial pressure is reached, and only the wide-pore form is seen. The $Li_{2.0}Na_{4.2}$-sample could be said to behave in a similar way, with full conversion at low pressure of CO_2. By contrast, both narrow- and wide-pore forms can be observed simultaneously in the $Li_{4.0}K_{2.2}$-form, as can the narrow-pore and intermediate form at low pressure of CO_2. This suggests that the transition from the intermediate to the wide-pore form is more readily achieved than from the narrow-pore form to the intermediate. Taken with the presence of a step in the CO_2 adsorption isotherm, it is possible that a cooperative effect may be responsible for the expansion from the intermediate to the wide-pore form. This would occur with expansion in one local region of a crystal improving the favourability of the same expansion in adjacent regions. Potential additional evidence of such a mechanism is the lack of any concurrent observation of intermediate and wide-pore forms.

Finally, the increased unit cell volume of the intermediate structures may ease transition to the wide-pore form compared to the extremely distorted framework present in the dehydrated material. The changing behaviour with cation type present also suggests that the cation content allows modulation of the transition and may therefore by impacted by cation siting or mobility. Similar behaviour has been suggested to occur in zeolite Rho by Balestra *et al*., with modelling suggesting that long-lived metastable structures arose due to the inhibition of cation hopping and the trapping of cations in crystallographic sites.[23] This would also explain why no such phase is observed for other merlinoite materials investigated in this work, as upon dehydration their framework structures are more relaxed than those described here.

In addition to the laboratory data described, synchrotron data was obtained for $Li_{3.4}Cs_{2.8}$-MER (4.2) on beamline I11 at Diamond Light Source, Oxfordshire by Drs Georgieva, Lozinska and Prof Wright. As previously stated, Cs cations did not reduce the pressure at which a step in the adsorption isotherm occurred and as such, high pressures of CO_2 achieved at the synchrotron source enabled study of this materials before and after pore

opening. Patterns obtained are shown in Figure 6.6.3, along with Rietveld plots and refined structures of the dehydrated and high-pressure regimes.

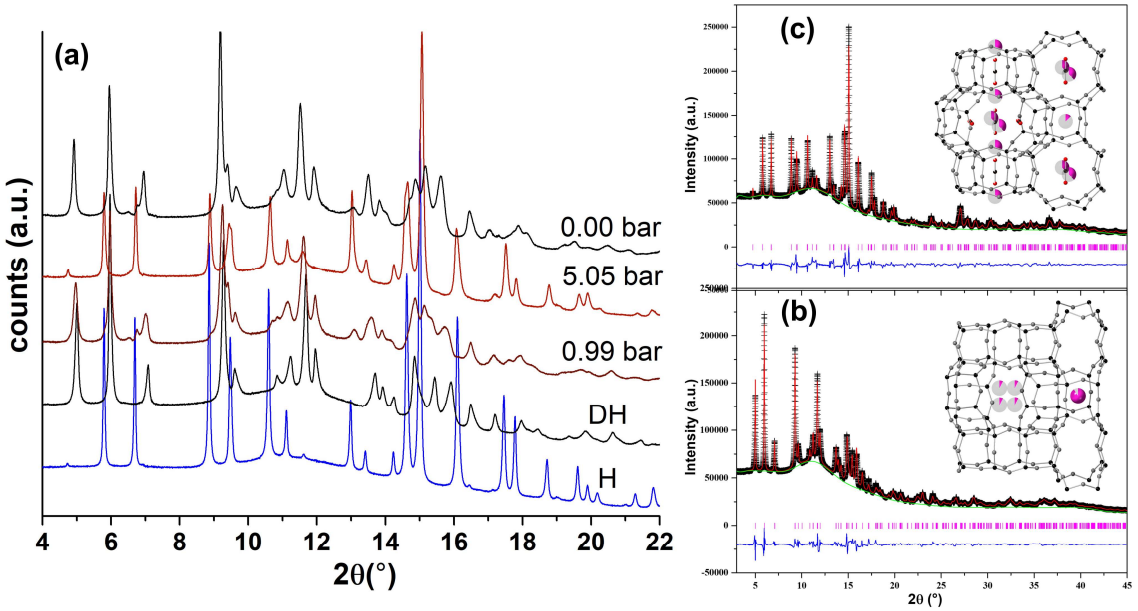

Figure 6.6.3. (a) Synchrotron VPXRD data for $Li_{3.4}Cs_{2.8}$-MER (4.2). Conditions are as labelled (H and DH correspond to hydrated and dehydrated; 0.00 bar indicates the evacuated sample after desorption). Rietveld plots of (b) DH and (c) 5.05 bar data, with refined structures inset. T and O sites are shown in black and grey, Cs cations in pink, and CO_2 in black and red, with fractional occupancies indicated by partial filling of spheres. (I11, DLS, λ = 0.826398 Å).

From this data, it can be seen that at 0.99 bar of CO_2, the material consists of 2 phases, a dehydrated-like, narrow-pore phase and another more similar to, though not matching, the hydrated pattern. Fitting the pattern gives a unit cell volume of 1952 $Å^3$ for this phase, in keeping with the intermediate forms observed for other $Li_{6.2-x}M_x$-materials. Furthermore, isotherm data suggests that a wide-pore form would not be expected until higher pressure. This suggests that the material behaves somewhat like $Li_{6.2}$-MER (4.2), with the appearance of an intermediate phase close to 1 bar of CO_2. Unfortunately, the broad peak shapes arising from this 2-phase pattern, as well as the presence of additional minor peaks, made confident refinement unfeasible.

At the higher pressure of 5.05 bar of CO_2, above the step in the adsorption isotherm, a single phase was present which more closely aligns with the hydrated pattern and with a larger unit cell volume of 1995 $Å^3$. Framework expansion is clear by comparison of the structures shown in Figure 6.6.3, as is cation relocation, with Cs^+ concentrated in site III in the centre of the *ste* cavity redistributed to sites I and II in the *pau* cavity.

Upon subsequent evacuation to 0.00 bar of CO_2, the pattern resembles that acquired at 0.99 bar of CO_2. This suggests that CO_2 is encapsulated within the structure upon desorption. This was further evidenced by cyclical adsorption experiments carried out by Dr Georgieva. In these, each experiment is followed by another without heating the sample. As can be seen in Figure 6.3.7, the shape of the CO_2 adsorption isotherm changes with each experiment, with the step in adsorption occurring at progressively lower pressure. This may suggest that successively more of the material is trapped in an intermediate form by encapsulation of CO_2 species. Such guest molecules likely act to reduce the energetic barrier to expansion and cation movement, such as water molecules were found to in Cs-Rho by Xu *et al*.[40] This also raises an issue of the additional complexity that may arise in flexible materials such as merlinoite in understanding which phases are relevant during industrial application. Looking at the gradients present in isotherm metadata presented in Figure 6.3.5, it can also be seen that such cycling greatly alters the kinetic behaviour of the material, with more rapid CO_2 adsorption occurring for a sample that has undergone such treatment. Therefore, such behaviour provides another method to manipulate equilibrium and kinetic adsorption properties of merlinoite materials, though not without its challenges.

6.7 Conclusion

In this section, the structures of Li- and related $Li_{6.2-x}M_x$-forms of MER (4.2) were investigated. $Li_{6.2-x}Na_x$-samples gave an uninterrupted range of single-phase materials, with cells expanding as the mean cation size increased, although not linearly. In Chapter 5, it was seen that large and small cations prefer different sites in the MER (4.2) material, modifying framework contraction upon dehydration. As such, limited K^+ and Cs^+ could be incorporated into $Li_{6.2}$-MER (4.2) before exsolution occurred to form Li-rich and poor phases. This was driven by the lack of availability of sufficiently large sites for these cations in the heavily distorted $Li_{6.2}$-MER (4.2) framework. Such observations limit the extent to which cation exchange can be viewed as simple solid solutions. Adsorption isotherms of materials tended to show shifting behaviour between the end members of their respective series but there were complications. The $Li_{3.4}Cs_{2.8}$-form, although possessing a framework structure larger than many of the other $Li_{6.2-x}M_x$-MER (4.2)

materials, failed to shift the position of the isotherm adsorption step seen for the pure-Li parent. Intermediate structures were also observed in VPXRD experiments, unlike in previously examined merlinoite samples, highlighting the rich structural chemistry of the zeolite and the nuances present in the study of these materials.

6.8 References

(1) Passaglia, E.; Pongiluppi, D.; Rinaldi, R. Merlinoite, a New Mineral of the Zeolite Group. *Neues Jahrb. Fur Mineral. - Monatshefte* **1977**, *8*, 355–364.

(2) Galli, E.; Gottardi, G.; Pongiluppi, D. The Crystal Structure of the Zeolite Merlinoite. *Neues Jahrb. Fur Mineral. - Monatshefte* **1979**, *10*, 1–9.

(3) Sherman, J. D. Identification and Characterization of Zeolites Synthesized in the K_2O-Al_2O_3-SiO_2-H_2O System. In *Molecular Sieves-II*; Katzer, J. R., Ed.; American Chemical Society: Washington DC, 1977; pp 30–42.

(4) Barrer, R. M.; Baynham, J. W. The Hydrothermal Chemistry of the Silicates. Part VII. Synthetic Potassium Aluminosilicates. *J. Chem. Soc.* **1956**, 2882–2891.

(5) Barrer, R. M.; Baynham, J. W.; Bultitude, F. W.; Meier, W. M. Hydrothermal Chemistry of the Silicates. Part VIII. Low-Temperature Crystal Growth of Aluminosilicates, and of Some Gallium and Germanium Analogues. *J. Chem. Soc.* **1959**, 195–208.

(6) Galli, E.; Passaglia, E.; Pongiluppi, D.; Rinaldi, R. Mazzite, a New Mineral, the Natural Counterpart of the Synthetic Zeolite Ω. *Contrib. to Mineral. Petrol.* **1974**, *45*, 99–105.

(7) Pakhomova, A. S.; Armbruster, T.; Krivovichev, S. V.; Yakovenchuk, V. N. Dehydration of the Zeolite Merlinoite from the Khibiny Massif, Russia: An *in Situ* Temperature-Dependent Single-Crystal X-Ray Study. *Eur. J. Mineral.* **2014**, *26* (3), 371–380.

(8) Kakutani, Y.; Weerachawanasak, P.; Hirata, Y.; Sano, M.; Suzuki, T.; Miyake, T. Highly Effective K-Merlinoite Adsorbent for Removal of Cs^+ and Sr^{2+} in Aqueous Solution. *RSC Adv.* **2017**, *7*, 30919–30928.

(9) Chen, W.; Song, G.; Lin, Y.; Qiao, J.; Wu, T.; Yi, X.; Kawi, S. A Green and Efficient Strategy for Utilizing of Coal Fly Ash to Synthesize K-MER Zeolite as Catalyst for Cyanoethylation and Adsorbent of CO_2. *Microporous Mesoporous Mater.* **2021**, *326*, 111353.

(10) Cheong, Y.; Rigolet, S.; Daou, T. J.; Wong, K.; Chuan, T.; Ng, E. Crystal Growth Study of Nanosized K-MER Zeolite from Bamboo Leaves Ash and Its Catalytic Behaviour in Knoevenagel Condensation of Benzaldehyde with Ethyl Cyanoacetate. *Mater. Chem. Phys.* **2020**, *251* (April), 123100.

(11) Seo, Y.; Adi, E.; Jiang, N.; Oh, S.; Park, S. Catalytic Dehydration of Methanol over Synthetic Zeolite W. *Microporous Mesoporous Mater.* **2010**, *128*, 108–114.

(12) Li, J.; Zhuang, X.; Font, O.; Moreno, N.; Vallejo, V. R.; Querol, X.; Tobias, A. Synthesis of Merlinoite from Chinese Coal Fly Ashes and Its Potential Utilization as Slow Release K-Fertilizer. *J. Hazard. Mater.* **2014**, *265*, 242–252.

(13) Estevam, S. T.; Fernandes, T.; Tainá, D. A.; Raiane, S. Synthesis of K - Merlinoite Zeolite from Coal Fly Ash for Fertilizer Application. *Brazilian J. Chem. Eng.* **2021**, 0123456789.

(14) Hermassi, M.; Valderrama, C.; Font, O.; Moreno, N.; Querol, X.; Harrouch, N.; Luis, J. Science of the Total Environment Phosphate Recovery from Aqueous Solution by K-Zeolite Synthesized from Fly Ash for Subsequent Valorisation as Slow Release Fertilizer. *Sci. Total Environ.* **2020**, *731*, 139002.

(15) Mirfendereski, S. M. Synthesis and Application of High-Permeable Zeolite MER Membrane for Separation of Carbon Dioxide from Methane. *J. Aust. Ceram. Soc.* **2019**, *55*, 103–114.

(16) Choi, H. J.; Jo, D.; Min, J. G.; Hong, S. B. The Origin of Selective Adsorption of CO_2 on Merlinoite Zeolites. *Angew. Chemie - Int. Ed.* **2020**, *60* (8), 4307–4314.

(17) Yeo, Z. Y.; Chai, S. P.; Zhu, P. W.; Mah, S. K.; Mohamed, A. R. Preparation of Self-Supported Crystalline Merlinoite-Type Zeolite W Membranes through Vacuum Filtration and Crystallization for CO_2/CH_4 Separations. *New J. Chem.* **2015**, *39* (5), 4135–4140.

(18) KR Pat. 20170137999A, 2017.

(19) JP Pat. 2006150239, 2006.

(20) WIPO Pat. 2021024045A1, 2021.

(21) IZA Database of Zeolite Structures http://europe.iza-structure.org, accessed October 2023.

(22) Lozinska, M. M.; Mangano, E.; Greenaway, A. G.; Fletcher, R.; Thompson, S. P.; Murray, C. A.; Brandani, S.; Wright, P. A. Cation Control of Molecular Sieving by Flexible Li-Containing Zeolite Rho. *J. Phys. Chem. C* **2016**, *120* (35), 19652–19662.

(23) Balestra, S. R. G.; Hamad, S.; Ruiz-Salvador, A. R.; Domínguez-García, V.; Merkling, P. J.; Dubbeldam, D.; Calero, S. Understanding Nanopore Window Distortions in the Reversible Molecular Valve Zeolite RHO. *Chem. Mater.* **2015**, *27* (16), 5657–5667.

(24) Solov'eva, L. P.; Borisov, S. V.; Bakakin, V. V. New Skeletal Structure in the Crystal Structure of Barium Chloroaluminosilicate $BaAlSi_2O_6(Cl,OH)$ -> $Ba_2[X]BaCl_2[(Si,Al)_8O_{18})$. *Kristallografiya* **1971**, *16*, 1179.

(25) Baturin, S. V.; Malinovskii, Y. A.; Runovoa, I. B. Crystalline Structure of the Low-Silica Merlinoite from the Kola Peninsula. *Mineral. Zhurnal* **1985**, *7*, 67–74.

(26) Bieniok, A.; Bornholdt, K.; Brendel, U.; Baur, W. H. Synthesis and Crystal Structure of Zeolite W, Resembling the Mineral Merlinoite. *J. Mater. Chem.* **1996**, *6* (2), 271.

(27) Barrett, P. A.; Valencia, S.; Camblor, M. A. Synthesis of a Merlinoite-Type Zeolite with an Enhanced Si/Al Ratio via Pore Filling with Tetraethylammonium Cations. *J. Mater. Chem.* **1998**, *23* (10), 2263–2268.

(28) Yakubovich, O. V.; Massa, W.; Pekov, I. V.; Kucherinenko, Y. V. Crystal Structure of a Na,K-Variety of Merlinoite. *Crystallogr. Reports* **1999**, *44*, 776–782.

(29) Skofteland, B. M.; Ellestad, O. H.; Lillerud, K. P. Potassium Merlinoite: Crystallization, Structural and Thermal Properties. *Microporous Mesoporous Mater.* **2001**, *43* (1), 61–71.

(30) Wang, J. Y.; Mangano, E.; Brandani, S.; Ruthven, D. M. A Review of Common Practices in Gravimetric and Volumetric Adsorption Kinetic Experiments. *Adsorption* **2021**, *27* (3), 295–318.

(31) Lozinska, M. M.; Mangano, E.; Mowat, J. P. S.; Shepherd, A. M.; Howe, R. F.; Thompson, S. P.; Parker, J. E.; Brandani, S.; Wright, P. A. Understanding Carbon Dioxide Adsorption on Univalent Cation Forms of the Flexible Zeolite Rho at Conditions Relevant to Carbon Capture from Flue Gases. *J. Am. Chem. Soc.* **2012**, *134* (42), 17628–17642.

(32) Cook, M.; Conner, W. C. How Big Are the Pores of Zeolites? In *Proceedings of the 12th International Zeolite Conference*; Treacy, M. M. J., Marcus, B. K., Bisher, M. E., Higgins, J. B., Eds.; Materials Research Society: Warrendale, PA, USA, 1999; pp 409–414.

(33) Smith, L. J.; Eckert, H.; Cheetham, A. K. Site Preferences in the Mixed Cation Zeolite, Li,Na-Chabazite: A Combined Solid-State NMR and Neutron Diffraction Study. *J. Am. Chem. Soc.* **2000**, *122* (8), 1700–1708.

(34) Smith, L. J.; Eckert, H.; Cheetham, A. K. Potassium Cation Effects on Site Preferences in the Mixed Cation Zeolite Li, Na-Chabazite. *Chem. Mater.* **2001**, *13* (2), 385–391.

(35) Lozinska, M. M.; Mowat, J. P. S.; Wright, P. A.; Thompson, S. P.; Jorda, J. L.; Palomino, M.; Valencia, S.; Rey, F. Cation Gating and Relocation during the Highly Selective "Trapdoor" Adsorption of CO_2 on Univalent Cation Forms of Zeolite Rho. *Chem. Mater.* **2014**, *26* (6), 2052–2061.

(36) Shang, J.; Li, G.; Singh, R.; Gu, Q.; Nairn, K. M.; Bastow, T. J.; Medhekar, N.; Doherty, C. M.; Hill, A. J.; Liu, J. Z.; Webley, P. A. Discriminative Separation of Gases by a "Molecular Trapdoor" Mechanism in Chabazite Zeolites. *J. Am. Chem. Soc.* **2012**, *134* (46), 19246–19253.

(37) Mace, A.; Hedin, N.; Laaksonen, A. Role of Ion Mobility in Molecular Sieving of CO_2 over N_2 with Zeolite NaKA. *J. Phys. Chem. C* **2013**, *117* (46), 24259–24267.

(38) Pakhomova, A. S.; Danisi, R. M.; Armbruster, T.; Lazic, B.; Gfeller, F.; Krivovichev,

S. V.; Yakovenchuk, V. N. High-Temperature Induced Dehydration, Phase Transition and Exsolution in Amicite: A Single-Crystal X-Ray Study. *Microporous Mesoporous Mater.* **2013**, *182*, 207–219.

(39) Lozinska, M. M.; Jamieson, S.; Verbraeken, M. C.; Miller, D. N.; Bode, B. E.; Murray, C. A.; Brandani, S.; Wright, P. A. Cation Ordering and Exsolution in Copper-Containing Forms of the Flexible Zeolite Rho (Cu,M-Rho; M=H, Na) and Their Consequences for CO_2 Adsorption. *Chem. - A Eur. J.* **2021**, *27* (51), 13029–13039.

(40) Xu, L.; Okrut, A.; Tate, G. L.; Ohnishi, R.; Wu, K. L.; Xie, D.; Kulkarni, A.; Takewaki, T.; Monnier, J. R.; Katz, A. Cs-RHO Goes from Worst to Best as Water Enhances Equilibrium CO_2 Adsorption via Phase Change. *Langmuir* **2021**, *37*, 13903-13908.

(41) Bieniok, A.; Bürgi, H.-B. Deformation Analysis of the D8R-Unit in Zeolite Structures. In *Studies in Surface Science and Catalysis*; Weitkamp, J., Karge, H. G., Pfeifer, H., Hölderich, W., Eds.; Elsevier B.V.: Amsterdam, 1994; Vol. 84, pp 567–574.

(42) Greenaway, A. G.; Shin, J.; Cox, P. A.; Shiko, E.; Thompson, S. P.; Brandani, S.; Hong, S. B.; Wright, P. A. Structural Changes of Synthetic Paulingite (Na,H-ECR-18) upon Dehydration and CO_2 Adsorption. *Zeitschrift fur Krist.* **2015**, *230* (4), 223–231.

(43) Newsam, J. M.; Jarman, R. H.; Jacobson, A. J. A Study of the Mixed $Na_{1-x}Li_x$ Zeolite A System by Powder X-Ray Diffraction. *J. Solid State Chem.* **1985**, *58* (3), 325–334.

(44) Johnson, G. M.; Reisner, B. A.; Tripathi, A.; Corbin, D. R.; Toby, B. H.; Parise, J. B. Flexibility and Cation Distribution upon Lithium Exchange of Aluminosilicate and Aluminogermanate Materials with the RHO Topology. *Chem. Mater.* **1999**, *11* (10), 2780–2787.

(45) Norby, P.; Poshni, F. I.; Gualtieri, A. F.; Hanson, J. C.; Grey, C. P. Cation Migration in Zeolites: An in Situ Powder Diffraction and MAS NMR Study of the Structure of Zeolite Cs(Na)−Y during Dehydration. *J. Phys. Chem. B* **1998**, *102* (5), 839–856.

(46) Su, B.; Martens, J. A. An Infrared Study on the Location of Benzene Molecules and Cations in Cs^+-Exchanged EMT Zeolite. **1998**, *25*, 151–167.

(47) Vance, T. B. J.; Seff, K. Hydrated and Dehydrated Crystal Structures of Seven-Twelfths Cesium-Exchanged Zeolite A. *J. Phys. Chem.* **1975**, *79* (20), 2163–2167.

(48) Choi, H. J.; Hong, S. B. Effect of Framework Si/Al Ratio on the Mechanism of CO_2 Adsorption on the Small-Pore Zeolite Gismondine. *Chem. Eng. J.* **2022**, *433* (P3), 133800.

(49) Vrabec, J.; Stoll, J.; Hasse, H. A Set of Molecular Models for Symmetric Quadrupolar Fluids. *J. Phys. Chem. B* **2001**, *105* (48), 12126–12133.

7 Zeolite Phillipsite

7.1 Introduction

Phillipsite is a naturally occurring zeolite discovered by crystallographer Armand Lévy in 1825 in specimens from Aci Reale in Sicily, Italy, and named by him for "Mr W. Phillips, whose contributions to minerology are so numerous and so valuable".[1] Early structural work, using a range of space groups, was carried out by Steinfink,[2] Sadanaga *et al*.,[3] and Rinaldi *et al*.,[4] with the monoclinic description of the latter the most commonly used by subsequent work.

Zeolite phillipsite has been the subject of interest for a range of potential applications. This includes those typical for any zeolite including ion exchange, such as for removal of Sr or Cs cations from nuclear waste,[5–7] ammonium removal,[8] and Na and K cation removal from lignin wastewater.[9] Additional suggested applications include ethanol purification,[10] use as a fungicide,[11] or selective CO_2 adsorption.[12,13]

The phillipsite framework structure (framework type code **PHI**) is composed of 8-rings connected by 4-rings and related to that of the **MER** structure, discussed in Chapters 4-6. Zeolites with these frameworks, in addition to gismondine (**GIS**), can be described as being formed of double crankshaft chains (dccs), with the framework type dependent on the relative orientation of these chains, as shown in Figure 7.1.1.[14] The structural similarity of phillipsite and merlinoite is such that they have been reported as naturally

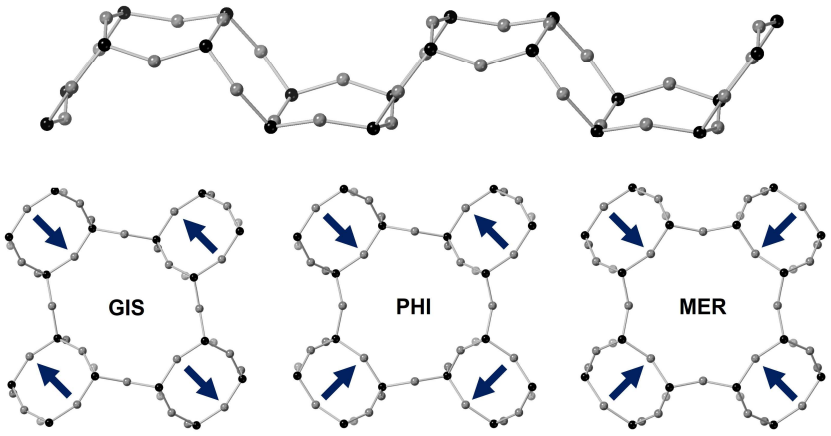

Figure 7.1.1. A double crankshaft chain (dcc) and framework types composed of dccs, as labeled. The dccs can be rotated relative to each other, and blue arrows indicate the relative orientation of neighbouring dccs. T and O sites are depicted in black and grey, respectively.

occurring intergrowths.[15] The framework is composed of *phi* and *oto* cavities, as shown in Figure 7.1.2. As for **MER**, a 3-dimensionally connected channel system is the result of cavity tiling in **PHI**, enabling percolation of small guest species throughout the material. The empty framework structure can be described by the orthorhombic *Cmcm* space group, but upon the inclusion of cations, this is typically reduced to the monoclinic space group of Rinaldi *et al.*, $P2_1/m$.[4,14]

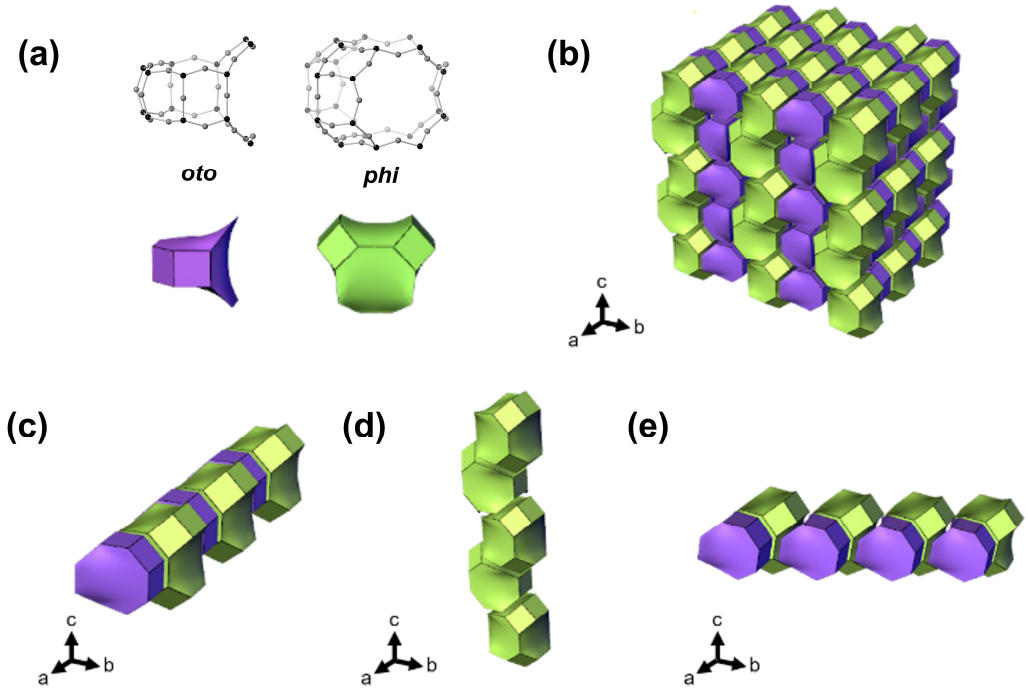

*Figure 7.1.2. Structural representation of zeolite phillipsite (framework type **PHI**). (a) Cavity types present in **PHI** and (b) tiling of those cavities within the extended framework. (c, d, e) the 3 channel systems in the **PHI** framework, the linear oto-phi, phi-phi and stepped oto-phi channels. Tetrahedral and O atoms are represented in black and grey, and oto and phi cavities depicted in purple and green, respectively, with axes relative to the Cmcm framework unit cell. Figure adapted from Choi et al.*[16]

As for zeolites Rho and merlinoite, phillipsite is flexible and distorts upon dehydration as the framework adapts to better coordinate extra-framework cations within the material.[17–19] The consequences for cation siting and window size has associated implications for gas adsorption behaviour. As has been found by Choi *et al.*, the exact nature of flexible zeolite frameworks, even amongst polytypes, has a large impact on structural and adsorption behaviour.[20,21]

Although the **PHI** framework has a rather small unit cell, with a volume of *ca.* 1000 Å^3 in the $P2_1/m$ description, and only possesses 2 types of cavity, multiple potential cation

sites are available, and the description used in this work is shown in Figure 7.1.3. Windows between *oto* and *phi* cavities following the linear *oto-phi-oto* channel form sites I and Ia (together I*), whilst site II is located between adjacent *phi* cavities along the *phi-phi* channel. The remaining 8-ring between *oto* and *phi* cavities constitutes site III, and site IV is similar to site Ia, but displaced away from the 8-ring, towards the centre of the *phi* cage. Cations sitting in these sites can inhibit percolation of gas molecules along their respective channels and fill otherwise available pore space. The exact nature of cation siting is dependent on cation size and charge density, and this has repercussions on framework distortion, as well as adsorbate dispersal. This has already been seen to be the case for Rho and merlinoite zeolites in previous chapters.

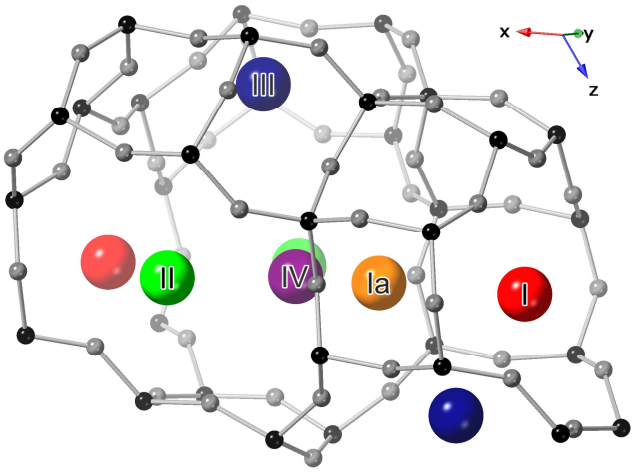

Figure 7.1.3. Framework structure of PHI with labelling schemes used for cation sites. Tetrahedral and O sites are shown in black and grey, respectively. Extra-framework cation sites are shown as I and Ia (red and orange, respectively), S8Rs between phi and oto cavities along the a axis; II, S8R between adjacent phi cavities (green); III, S8R between phi and oto cavities, aligned normal to the ab plane (blue); and IV, proud of the S8R, displaced from site Ia towards the centre of the phi cavity (purple).

Much work has been carried out in investigating naturally occurring forms of phillipsite, including those with heavy alkaline earth metals, Sr and Ba. These works however focus on hydrated materials. For example, natural forms of K,Na,Ca-PHI (1.7-2.2) were found to have K cations in site III whilst Ca or Na occupied site II. Gualtieri *et al*. looked at both natural and synthetic forms of zeolite phillipsite with Si/Al *ca*. 2.2.[6] In these studies, they found Na, K and Cs cations in sites close to Ia/IV, with further Na^+ sitting in site II and additional K^+ and Cs^+ species in site III, though these were again all hydrated samples. Further studies by the authors found K cations also sitting in site I, along with Ba and

Sr^{2+} species occupying sites I and III preferentially, with further Sr cations found in site II.[7] Structural investigations of multiple cation forms of the same phillipsite material had not been carried out before this work.

The only other study of gas adsorption on a range of cation forms of phillipsite zeolites was published simultaneously with this work by Higuchi *et al*., on materials with Si/Al = 2.5.[12] They found unusual adsorption behaviour in multiple cation forms of their material, specifically sigmoidal isotherms, but the investigation was largely focussed on synthesis and did not provide a structural understanding of the observed behaviour. The work presented here is based on samples synthesised by collaborators in the group of Prof Suk Bong Hong at POSTECH, Pohang, South Korea. Multiple cation forms of these materials, with Si/Al = 2.5 and 3.6, had been synthesised and this chapter aims to provide a structural basis for the adsorption behaviour observed in these samples.

7.2 Acknowledgements

Work reported here is entirely based on the work and dedication of Dr Hyun June Choi, from the group of Prof Suk Bong Hong at the Center for Ordered Nanoporous Materials Synthesis, Pohang University of Science and Technology (POSTECH), South Korea. Dr Choi, Ms Hyeryoen Kim and Ms Min Ji Baek synthesised all materials investigated in this chapter. Adsorption isotherms were obtained by Dr Choi, with additional data aided by Dr Magdalena M. Lozinska. Initial PXRD patterns were collected by Dr Choi, with Drs Dohyun Moon, Hyun Hwi Lee, Docheon Ahn and Young Hwa Jung running synchrotron experiments carried out at Pohang Accelerator Laboratory (PAL), South Korea. Dr Choi also collected *in situ* VPXRD data with aid from Dr Yuri Andreev at the University of St Andrews.

Again, work carried out personally in this chapter is entirely structural. Although all final structures presented in this work have been refined by myself, Dr Choi is also responsible for identifying site IV as a potential site for Cs cations in these samples, which is significant in the unusual adsorption behaviour described below. As for previous chapters, relevant experimental results, collected by collaborators as described, are detailed at the beginning of sections within this chapter.

7.3 Si/Al = 2.5

7.3.1 Underlying experimental work

Zeolite phillipsite with Si/Al = 2.5, hence denoted PHI (2.5), was synthesised by Dr Choi as described in Choi *et al.*,[16] and found to have the chemical composition $Na_{1.9}K_{2.7}[Si_{11.4}Al_{4.6}O_{32}].(H_2O)_{9.9}$ through a combination of elemental analysis, TGA and NMR analysis.

Subsequent ion exchange created a range of cation forms of the PHI (2.5) material, $M_{4.6}$-PHI (2.5), where M indicates a cation, which included Na-, K-, Rb- and Cs- forms. PXRD patterns of these samples under hydrated and dehydrated conditions are shown in Figure 7.3.1. $Li_{4.6}$-PHI (2.5) was also produced but found to be unstable upon dehydration and so is not included here.

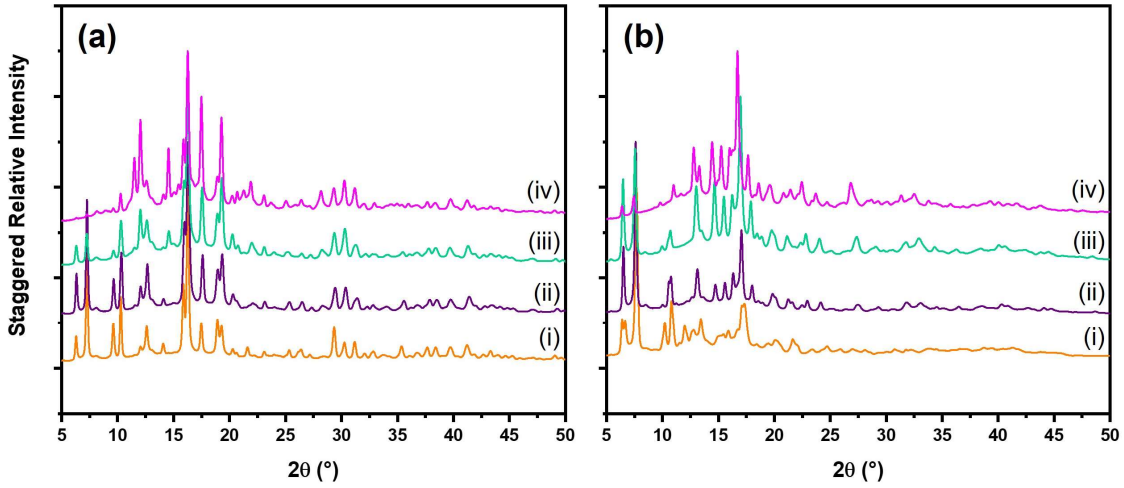

Figure 7.3.1. PXRD patterns of (a) hydrated and (b) dehydrated PHI (2.5) materials at 298 K: (i) $Na_{4.6}$-, (ii) $K_{4.6}$-, (iii) $Rb_{4.6}$-, (iv) $Cs_{4.6}$-PHI (2.5). (9B, PAL, λ = 0.900 Å).

CO_2 adsorption isotherms up to 1 bar were collected at various temperatures for different cation forms, as shown in Figure 7.3.2. Higher pressure isotherms up to 5 bar at varying temperatures were also collected for the Na- and Cs-forms of PHI (2.5), shown in Figure 7.3.3. $Cs_{4.6}$-PHI (2.5) clearly shows a step in its adsorption isotherm at relatively low pressure, with a plateau at high pressure. By contrast, the Na-material shows a muted kink at higher pressures of CO_2. The other cation forms are more similar to the Cs-sample, though the inflection is not so steep.

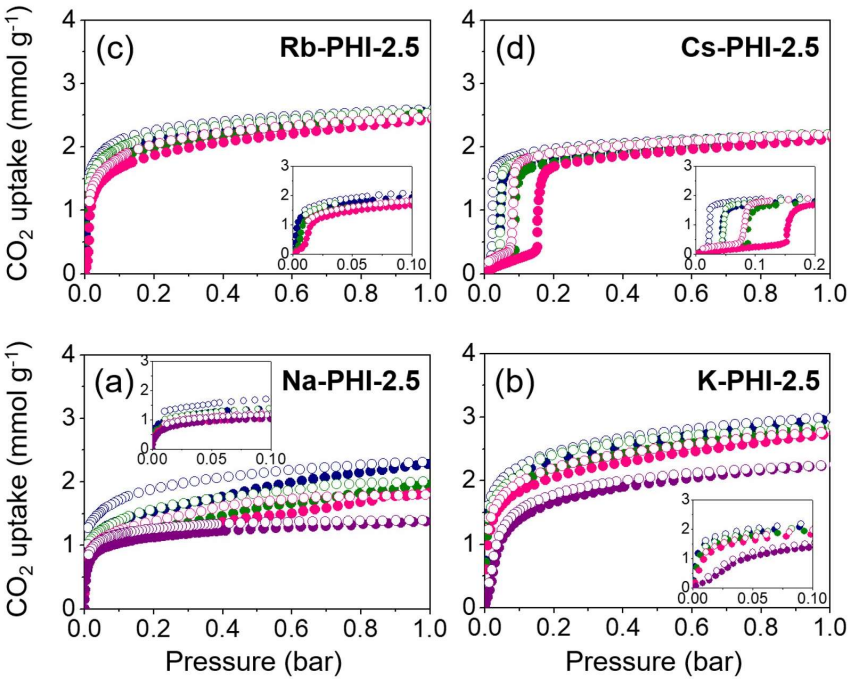

Figure 7.3.2. CO_2 adsorption isotherms up to 1 bar for PHI (2.5) samples: (a) $Na_{4.6}$-, (b) $K_{4.6}$-, (c) $Rb_{4.6}$-, (d) $Cs_{4.6}$-PHI (2.5). Adsorption and desorption branches are indicated by closed and open symbols; respectively. Lower pressures isotherm regions (up to 0.1 bar) are shown inset. Isotherm temperatures are (blue) 298, (green) 308, (pink) 318 and (purple) 348 K. Adapted from Choi et al.[16]

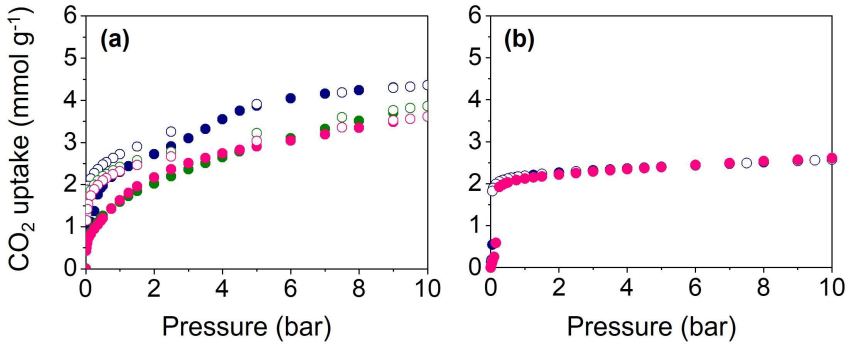

Figure 7.3.3. CO_2 adsorption isotherms up to 10 bar for PHI (2.5) samples: (a) $Na_{4.6}$- and (b) $Cs_{4.6}$-PHI (2.5). Adsorption and desorption branches are indicated by closed and open symbols; respectively. Isotherm temperatures are (blue) 298, (green) 308 and (pink) 318 K.

7.3.2 Structural studies of PHI (2.5) materials

7.3.2.1 Hydrated $M_{4.6}$-PHI (2.5)

As for the merlinoite materials, samples are created in a hydrated form. As such, the hydrated PHI (2.5) samples are discussed first here, having been investigated using Rietveld refinement and the patterns given in Figure 7.3.1. Rietveld plots of hydrated

$M_{4.6}$-PHI (2.5) materials are shown in Figure 7.3.4 and further crystallographic details are given in Appendix VI.III.I.

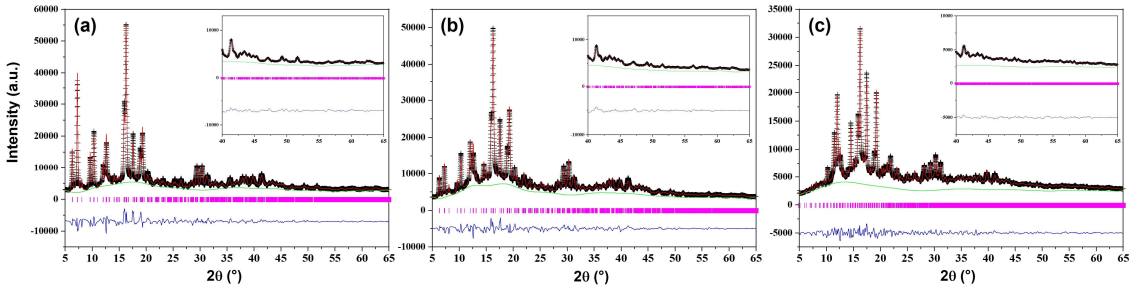

Figure 7.3.4. Rietveld plots of hydrated $M_{4.6}$-PHI (2.5) samples, with M = (a) K, (b) Rb and (c) Cs. (9B, PAL, λ = 0.900 Å).

As has been discussed, the typical space group used to fit phillipsite materials in the literature is the monoclinic $P2_1/m$, and most of the materials studies here were in keeping with this description. Exceptions to this were Na- and Cs- forms of the material, both of which could be fitted using a 2 × 1 × 2 supercell in the $P2_1/c$ space group. This enabled the refinement of the $Cs_{4.6}$-PHI (2.5) data but the Na-equivalent could not be adequately described, due to the additional water content, relatively poor X-ray scattering of Na cations and unit cell size. Fitting of unit cell parameters however, shows $Na_{4.6}$-PHI (2.5) to have a reduced unit cell volume (a quarter of the refined 2 × 1 × 2 supercell volume) of *ca.* 1015 Å^3 in its hydrated form. The unit cell parameters and measures of fit of the other hydrated PHI (2.5) materials are given in Table 7.3.1, and their refined structures are shown in Figure 7.3.5.

As for merlinoite and Rho,[22] the unit cell volumes of all hydrated samples are very similar, including the reduced unit cell of $Cs_{4.6}$-PHI (2.5) (1018 Å^3). The need for a supercell description for this material appears to be due to relative cation ordering, as discussed later, and this is likely the case for the Na-form too.

Table 7.3.1. Space group (SG), unit cell parameters and R_{wp} from refinement of hydrated $M_{4.6}$-PHI (2.5) samples.

Material	SG	*a* (Å)	*b* (Å)	*c* (Å)	*β* (°)	*V* (Å^3)	R_{wp}
$K_{4.6}$	$P2_1/m$	9.963(1)	14.170(2)	8.700(2)	125.0(1)	1006(1)	7.6%
$Rb_{4.6}$	$P2_1/m$	9.992(1)	14.201(2)	8.716(2)	125.1(1)	1012(1)	5.2%
$Cs_{4.6}$	$P2_1/c$	20.082(3)	14.223(3)	17.475(4)	125.3(1)	4072(1)	4.7%

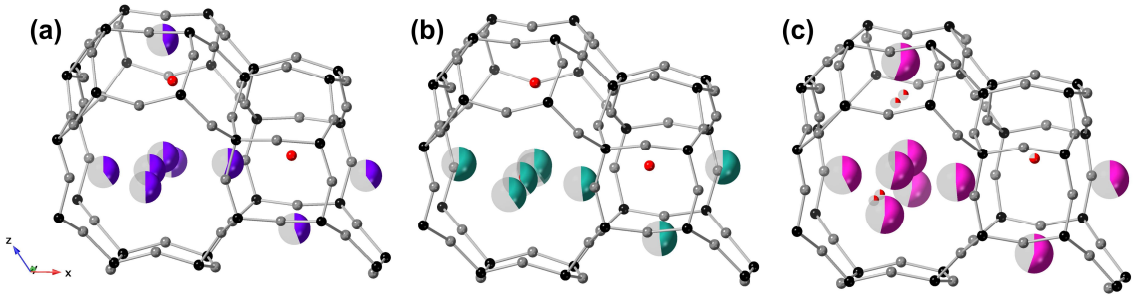

Figure 7.3.5. Refined structures of hydrated $M_{4.6}$-PHI (2.5) materials. M = (a) K, (b) Rb and (c) Cs. Framework T and O sites are shown in black and grey, respectively. K, Rb and Cs cations are shown in purple, cyan and pink, with extraframework O shown in red, respectively. The Cs-form is a reduced average of the supercell. Partial shading of spheres indicates fractional occupancy.

7.3.2.2 *Dehydrated $M_{4.6}$-PHI (2.5)*

The hydrated forms are not the most relevant to adsorption, as materials are initially exposed to CO_2 after activation in a dehydrated state. Rietveld plots of $M_{4.6}$-PHI (2.5) materials after dehydration are shown in Figure 7.3.6 and additional crystallographic details are given in Appendix VI.III.I.

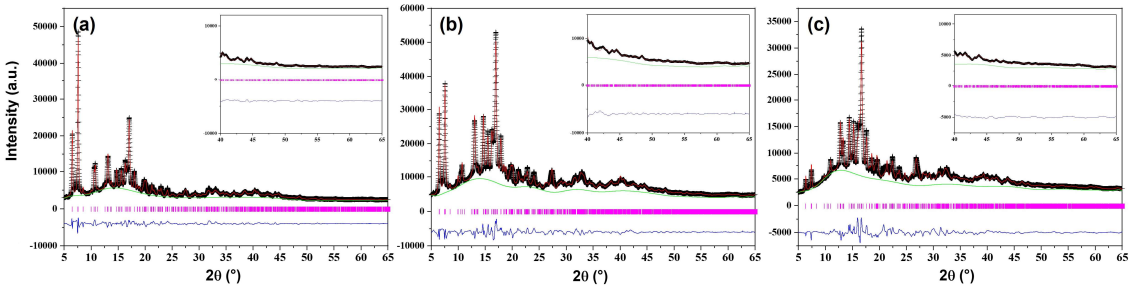

Figure 7.3.6. Rietveld plots of dehydrated $M_{4.6}$-PHI (2.5) samples, with M = (a) K, (b) Rb and (c) Cs. (9B, PAL, λ = 0.900 Å).

As for the hydrated samples, these materials were best fitted with $P2_1/m$, and there was no need to introduce a supercell description for the Cs-form upon dehydration. The $Na_{4.6}$-PHI (2.5) sample again exhibited additional peaks, such as those present at 6.4 and 6.7°, where other samples only showed a single peak. This was best fitted in *Pc* symmetry using a $1 \times 1 \times 2$ supercell, with a reduced unit cell volume of 837 Å^3, a decrease of almost 18% relative to its hydrated form. Confident refinement of the structure within this description proved unattainable, largely due to the lack of a good starting model for such a greatly distorted framework. Furthermore, peaks in the pattern quickly broaden at higher angle, reducing the information available for confident refinement. Future

computational work may enable a better starting model, and there may be another, more valid, space group that could be used for this material.

The other cation forms of the material also observed reductions in unit cell volume upon dehydration, and unit cell parameters and refinement details are presented in Table 7.3.2. As for most merlinoite samples, the degree of contraction increased as cation size decreased, with a 10, 9 and 6% reduction in unit cell volume for K-, Rb- and Cs-forms, respectively, all much lower than that apparent for the Na-sample. The refined structures of the dehydrated $M_{4.6}$-PHI (2.5) samples are shown in Figure 7.3.7.

Table 7.3.2. Space group (SG), unit cell parameters and R_{wp} from refinement of dehydrated $M_{4.6}$-PHI (2.5) samples.

Material	SG	a (Å)	b (Å)	c (Å)	β (°)	V (Å^3)	R_{wp}
$K_{4.6}$	$P2_1/m$	9.795(1)	13.580(2)	8.370(1)	125.8(1)	902(1)	4.7%
$Rb_{4.6}$	$P2_1/m$	9.854(1)	13.657(2)	8.385(1)	125.7(1)	917(1)	4.5%
$Cs_{4.6}$	$P2_1/m$	10.000(1)	13.889(2)	8.529(1)	125.8(1)	961(1)	5.1%

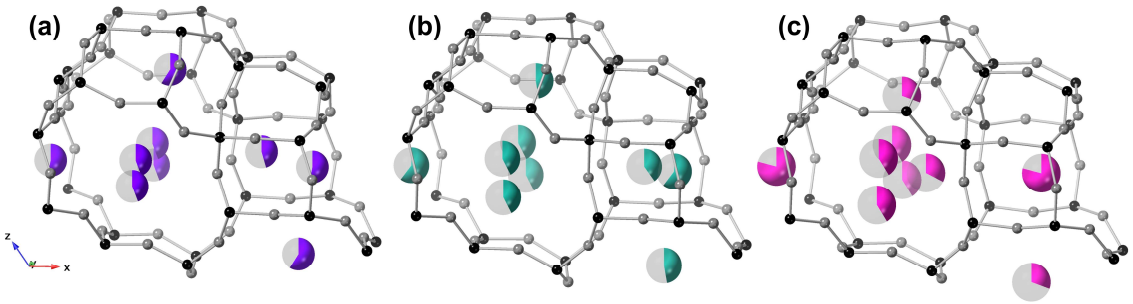

Figure 7.3.7. Refined structures of dehydrated $M_{4.6}$-PHI (2.5) materials. M = (a) K, (b) Rb and (c) Cs. Framework T and O sites are shown in black and grey, respectively. K, Rb and Cs cations are shown in purple, cyan and pink, respectively. Partial shading of spheres indicates fractional occupancy.

7.3.2.3 *Comparison of PHI (2.5) structures*

Cation sitings in PHI (2.5) materials are given in Table 7.3.3. Cation occupancies are broadly similar across all materials and their hydrated and dehydrated states, with the exception of $Cs_{4.6}$-PHI (2.5), which sees a lower occupancy of site III and higher occupancy of site I. Additionally, and more noticeably, site Ia is abandoned upon dehydration as Cs cations shift to site IV, a site displaced from site Ia further into the *phi* cavity. This site has previously been reported as occupied by Ba^{2+} in work by Sani *et al*.

in a natural, Ba-containing phillipsite at elevated temperature.[19] At 528 K, site IV was found to be 47% occupied by Ba cations, making it the second most favoured after site I (97% occupancy). It should be noted that the size of the elemental neighbours, Ba^{2+} and Cs^{+}, are not as similar as those of the larger Cs and Rb cations. Site IV was not found to be occupied by either K or Rb cations in the materials investigated here, however.

*Table 7.3.3. Absolute site occupancies of M^{+} in PHI (2.5) materials. *denotes merging of related but symmetry inequivalent positions within the $P2_1/c$ 2 × 1 × 2 supercell.*

Cation form	dh/h	I	Ia	II	III	IV	Total
$K_{4.6}$	h	0.9(1)	1.0(1)	1.9(1)	1.0(1)		4.8(2)
	dh	1.0(1)	0.9(1)	1.8(1)	1.2(1)		4.9(1)
$Rb_{4.6}$	h	1.0(1)	1.0(1)	1.6(1)	0.9(1)		4.6(1)
	dh	1.2(1)	0.9(1)	1.7(1)	0.9(1)		4.6(1)
$Cs_{4.6}$	h*	0.9(1)	1.0(1)	2.1(1)	1.2(1)		5.1(2)
	dh	1.6(1)		1.6(1)	0.6(1)	0.6(1)	4.5(1)

The exact nature of cation distribution within the hydrated form of $Cs_{4.6}$-PHI (2.5) is complicated by the need for a supercell description. This gives rise to formerly related sites, such that in addition to sites I, Ia, II and III, there is I′, Ia′, II′, II′′, II′′′ and III′. These are a consequence of 2 symmetry inequivalent sets of *phi* and *oto* cavities, and the loss of mirror symmetry across each *phi* cavity. Cation occupancies for these sites are detailed in Table 7.3.4. For related sites within adjacent *phi* cavities, occupancies are broadly similar, suggesting that the need for a supercell description is predominantly due to the breaking of similarity of sites II within the same *phi* cavity and hence the ordering of cations along the *phi-phi* channel.

Table 7.3.4. Fractional site occupancies of Cs^{+} in hydrated $Cs_{4.6}$-PHI (2.5). Sites in the same row share phi cavities.

I	Ia	II	II′	III
0.42(5)	0.41(5)	0.77(4)	0.37(4)	0.49(4)
I′	**Ia′**	**II′′**	**II′′′**	**III′**
0.43(5)	0.56(5)	0.61(4)	0.40(4)	0.62(4)

The unit cell volume is also related to the window sizes present within the **PHI** structure. Windows are labelled according to their corresponding cation sites, as for **MER** in previous chapters, and free window diameters are given in Table 7.3.5, again calculated as the shortest distance between O sites across the centre of an 8-ring, less the 2 O radii (2 × 1.35 Å).[23] As before, free diameters less than 2.3 Å would be expected to stop CO_2 diffusion, after considering thermal vibration of the framework as suggested by Cook and Conner.[24] Both dehydrated $K_{4.6}$- and $Rb_{4.6}$-PHI (2.5) possess Ia windows with a free diameter of 2.2 Å, limiting access between the *oto* and *phi* cavities, although other, sufficiently large, windows continue to allow access. As previously discussed for zeolites Rho and merlinoite, flexible zeolites may see thermal vibration of windows additional to that of Cook and Conner, and so 2.2 Å may still allow the passage of CO_2 but at a much-reduced rate than that of larger windows. Regardless, cation occupancies may be of greater importance when considering the adsorption properties of these more constrained materials.

A graphical summary of window sizes in PHI (2.5) materials is shown in Figure 7.3.8. The mean window size of hydrated materials is very similar across the 3 cation forms examined here, although window II increases from 3.1 to 3.8 Å from the K- to Cs-forms, and the Cs-analogue also exhibits a narrower window III than the other materials. Dehydrated $K_{4.6}$- and $Rb_{4.6}$-PHI (2.5) samples possess very similar window sizes, whilst the $Cs_{4.6}$-form has larger windows, although over a similar range.

*Table 7.3.5. Free window diameters in PHI (2.5) materials. Windows that would be closed to CO_2 percolation (<2.3 Å) are denoted by *.*

Cation form	dh/h	I (Å)	Ia (Å)	II (Å)	III (Å)
$K_{4.6}$	h	3.5(1)	3.6(1)	3.1(1)	3.3(1)
	dh	2.8(1)	2.2(1)*	2.7(1)	2.9(1)
$Rb_{4.6}$	h	3.6(1)	3.6(1)	3.4(1)	3.3(1)
	dh	2.7(1)	2.2(1)*	2.9(1)	2.8(1)
$Cs_{4.6}$	h	3.7(1)	3.7(1)	3.8(1)	2.9(1)
	dh	3.3(1)	2.6(1)	3.1(1)	3.1(1)

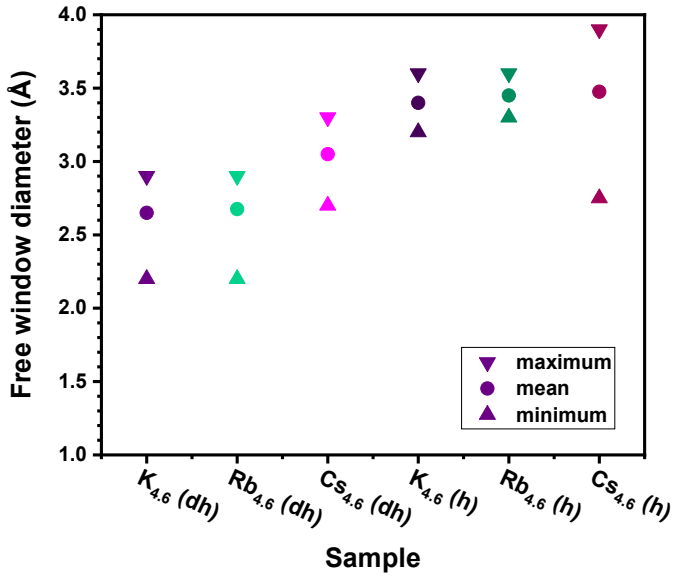

Figure 7.3.8. Free window diameters of PHI (2.5) samples. Mean, maximum and minimum values are depicted as shown in the key. Samples and conditions are as indicated on the x axis.

7.3.2.4 PHI (2.5) materials as CO_2 sorbents

Equilibrium adsorption data showed very different behaviour for each of the samples investigated *via* Rietveld refinement, most notably $Cs_{4.6}$-PHI (2.5). In the dehydrated material, Cs^+ occupies site I, within the *oto* cavity, as well as occupancy of site IV which sits within the *phi* cavity and may be thought to fill available pore volume. The low Si/Al ratio of this material fills the structure with monovalent extra-framework cations, and so cation motion must be highly important for these materials.

In order to better understand how these materials behave under CO_2 adsorption, VPXRD and synchrotron experiments were carried out. The former was carried out by Dr Choi on a laboratory instrument, aided by Dr Andreev. This yielded low quality PXRD data across a range of pressures of CO_2. Synchrotron data was obtained under 1 bar of CO_2, to give high quality data but only at a single pressure.

VPXRD data is shown in Figure 7.3.9. As was the case for other materials, the poor quality of the data still allows some conclusions about the structural behaviour to be made. $K_{4.6}$-PHI (2.5) shows peaks shifting to lower angles over the range of pressures investigated, indicating the gradual expansion, or breathing, of the structure. Similar can be said of the Rb-sample, though there is a greater change in intensities between patterns obtained at low pressures. Both samples appear to have type I isotherms at 298 K, though

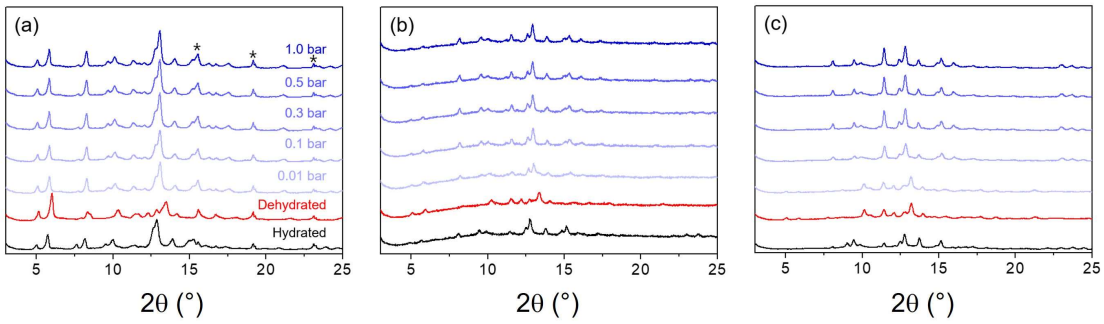

Figure 7.3.9. VPXRD data for (a) $K_{4.6}$-, (b) $Rb_{4.6}$- and (c) $Cs_{4.6}$-PHI (2.5) at 298 K under hydrated, dehydrated and CO_2 adsorption, with conditions as labelled. Peaks from the sample holder are as indicated in (a). (PANalytical, Mo K$\alpha_{1,2}$, λ = 0.711 Å).

at higher temperature there is a step for $Rb_{4.6}$-PHI (2.5) that occurs at very low pressure which may explain the change in pattern in this region. By contrast, the Cs-material seems to adopt 1 of 2 structures, switching between pattern acquisition at 0.01 and 0.10 bar of CO_2. At 298 K, the CO_2 adsorption isotherm shows a steep step at *ca.* 0.04 bar, as seen in Figure 7.3.2. For all materials, the higher-pressure data is more similar to that of the relevant hydrated form than the initial pattern of the dehydrated sample. Expansion behaviour can be more readily observed with structured fits of the patterns, in order to obtain unit cell volume data, as shown in Figure 7.3.10. As for merlinoite data, these VPXRD plots serve to show the trend in unit cell volume and should not be taken as an accurate measure due to the low data quality. All patterns appear to be those of single phases, with the possible exception of $Rb_{4.6}$-PHI (2.5) at 0.01 bar of CO_2. This suggests that expansion is typically rapid on the timescale of equilibration and data acquisition.

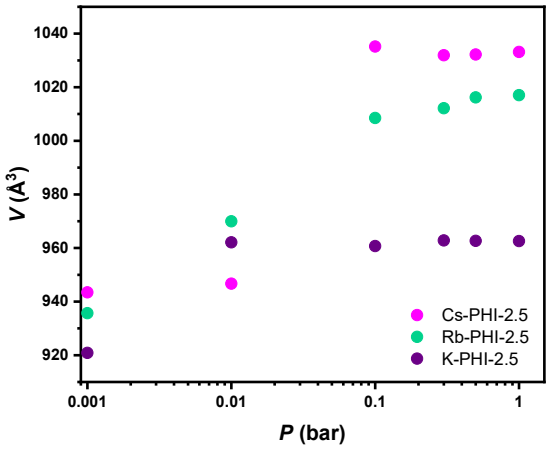

Figure 7.3.10. Unit cell volumes of $M_{4.6}$-PHI (2.5) materials obtained from VPXRD analysis. M = K, Rb and Cs is plotted in purple, cyan and pink, respectively. Data is plotted against a logarithmic axis with dehydrated data shown at 0.001 bar for ease of comparison.

Synchrotron data obtained at 1 bar of CO_2, shown in Figure 7.3.11, allows the refinement of structures under adsorption conditions. Again, the structure of $Na_{4.6}$-PHI (2.5) could not be resolved, although comparison of the patterns shown in Figure 7.3.11 show that at 1 bar of CO_2 the sample is similar to the dehydrated structure, though with obvious differences in peak intensities indicating the structures are not identical. This is perhaps in keeping with the isotherm data, which shows that $Na_{4.6}$-PHI (2.5) accesses additional pore volume above 1 bar of CO_2 at 298 K, suggesting the material opens to a wide-pore form above the pressure examined here. Selected refinement data is given in Table 7.3.6 and Rietveld plots are shown in Figure 7.3.12.

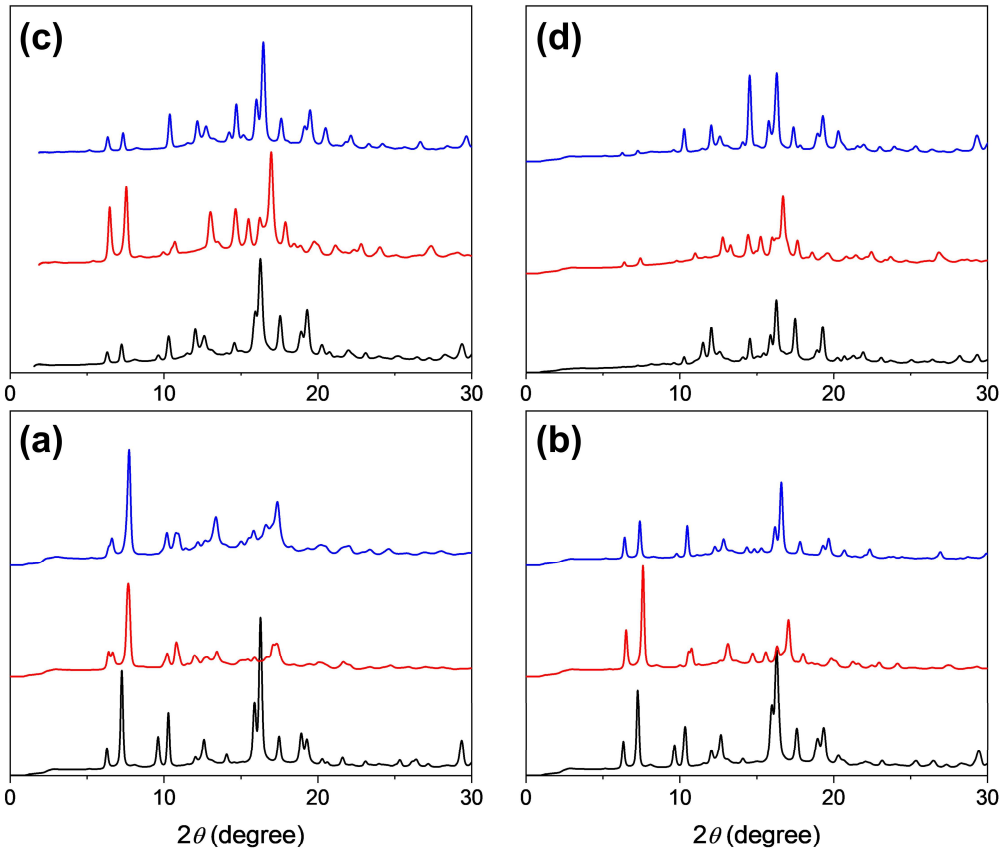

Figure 7.3.11. Synchrotron PXRD patterns of (a) $Na_{4.6}$-, (b) $K_{4.6}$-, (c) $Rb_{4.6}$- and (d) $Cs_{4.6}$-PHI (2.5) collected at 1 bar of CO_2 (blue) with hydrated and dehydrated patterns given for comparison, in black and red, respectively. All patterns obtained at 298 K. (9B, PAL, λ = 0.900 Å).

All samples refined observed an increased unit cell volume, with structures closer to that of their hydrated forms, as shown in Figure 7.3.13, though there was no need to use a supercell description in the refinement of the $Cs_{4.6}$-PHI (2.5) data, as was the case for the sample under hydrated conditions. $K_{4.6}$-PHI (2.5) does not come as close to the unit cell

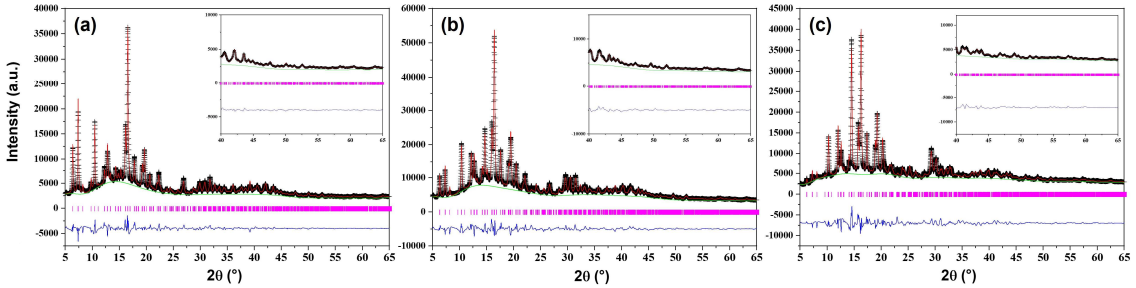

Figure 7.3.12. Rietveld plots of $M_{4.6}$-PHI (2.5) samples under 1 bar of CO_2, with M = (a) K, (b) Rb and (c) Cs. (9B, PAL, λ = 0.900 Å).

volume of its hydrated form as the Rb- and Cs-samples, consistent with that observed in the VPXRD experiments. This suggests there may be further pore volume accessible at higher pressure of CO_2 or at lower temperature.

Table 7.3.6. Space group (SG), unit cell parameters and R_{wp} from refinement of $M_{4.6}$-PHI (2.5) under 1 bar of CO_2.

Material	SG	*a* (Å)	*b* (Å)	*c* (Å)	*β* (°)	*V* (Å³)	R_{wp}
$K_{4.6}$	$P2_1/m$	9.860(1)	13.924(2)	8.534(1)	125.0(1)	959(1)	5.1%
$Rb_{4.6}$	$P2_1/m$	9.999(1)	14.061(2)	8.630(2)	125.2(1)	992(1)	6.7%
$Cs_{4.6}$	$P2_1/m$	10.107(1)	14.149(2)	8.702(1)	125.3(1)	1016(1)	6.2%

Cation occupancies of different sites within materials under 1 bar of CO_2 are given in Table 7.3.7. Values are reasonably similar for all materials in comparison to their hydrated and dehydrated forms, given in Table 7.3.3, with the notable exception of $Cs_{4.6}$-PHI (2.5). For this material the structure agrees well with the hydrated form only, especially considering the higher-than-expected cation content found with the earlier

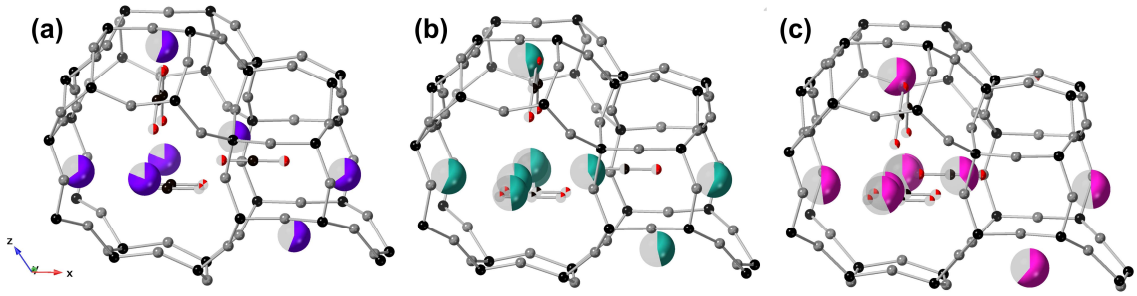

Figure 7.3.13. Refined structures of $M_{4.6}$-PHI (2.5) materials under 1 bar of CO_2. M = (a) K, (b) Rb and (c) Cs. Framework T and O sites are shown in black and grey, respectively. K, Rb and Cs cations are shown in purple, cyan and pink and CO_2 molecules in black and red, respectively. Fractional occupancies are shown by the partial shading of spheres.

refinement. The structure under 1 bar of CO_2, just as that of the hydrated form, shows no Cs^+ sitting in site IV, with increased Cs^+ occupancy observed in site III and additional occupancy within the *oto* cavity split across sites I and Ia.

Table 7.3.7. Absolute site occupancies of M^+ in PHI (2.5) materials under 1 bar of CO_2.

Cation form	I	Ia	II	III	Total
$K_{4.6}$	1.3(1)	0.6(1)	1.6(1)	1.1(1)	4.6(2)
$Rb_{4.6}$	1.1(1)	0.8(1)	1.9(1)	0.9(1)	4.8(1)
$Cs_{4.6}$	0.9(1)	0.9(1)	1.6(1)	1.2(1)	4.6(1)

Free window diameters are given in Table 7.3.8, and comparison with values in Table 7.3.5 show that all materials possess larger windows than their dehydrated forms, as is to be expected from their expanded unit cell volumes. For $K_{4.6}$- and $Rb_{4.6}$-PHI (2.5), window Ia becomes large enough to allow the passage of CO_2 molecules, as the diameter increases from 2.2 Å to 3.1 and 3.3 Å, respectively. Nonetheless, windows are not as wide under 1 bar of CO_2 as in their hydrated form, again with the exception of the $Cs_{4.6}$-form, for which they are typically larger. This may be accredited to the monoclinic supercell description required for the refinement of the hydrated form of this material, which may provide less reliable values than the refinements of the simpler unit cells of the other materials.

Table 7.3.8. Free window diameters in PHI (2.5) materials under 1 bar of CO_2.

Cation form	I (Å)	Ia (Å)	II (Å)	III (Å)
$K_{4.6}$	3.4(1)	3.1(1)	3.3(1)	2.9(1)
$Rb_{4.6}$	3.7(1)	3.3(1)	3.4(1)	3.3(1)
$Cs_{4.6}$	3.4(1)	4.2(1)	3.4(1)	3.6(1)

From the window sizes and cation locations found using synchrotron data, and evidence provided by VPXRD experiments, the materials can be described as behaving in 2 separate ways. For $K_{4.6}$- and $Rb_{4.6}$-PHI (2.5), gradual expansion of the unit cell occurs with increasing pressure of CO_2, causing larger window diameters but no change in cation location. By contrast, the $Cs_{4.6}$-material, undergoes a stepwise expansion accompanied by a marked increase in window diameter and significant cation

relocation. The abandonment of site IV opens up space within the *phi* cavity for CO_2 adsorption, where previously the material was overly crowded with Cs cations. This is discussed in greater detail in Section 7.5.

7.4 Si/Al = 3.6

Further to the PHI (2.5) materials described above, Dr Choi also synthesised materials with Si/Al = 3.6. As these materials possess a lower framework charge, the number of extra-framework cations drops from 4.6 to 3.5 per unit cell. This corresponds to 31% fewer cations to interact with the **PHI** framework and gas molecules. It has already been shown how an even smaller change can impact the adsorption and structural behaviour of merlinoite materials in Chapters 4 and 5. Background experimental details and subsequent structural analysis of these PHI (3.6) materials are given below.

7.4.1 Underlying experimental work

A Na,K-form of a PHI (3.6) was synthesised by Dr Choi and found to have the chemical composition $Na_{1.5}K_{2.0}[Si_{12.5}Al_{3.5}O_{32}].(H_2O)_{10.1}$, as described in Choi *et al*.[16]

Multiple cation forms of the material, $M_{3.5}$-PHI (3.6), were synthesised through ion exchange, where M = Na, K, Rb, Cs and their PXRD patterns under hydrated and dehydrated conditions are shown in Figure 7.4.1. $Li_{3.5}$-PHI (3.6) was also produced but, whilst stable upon dehydration, adsorption of CO_2 was extremely slow and so was not

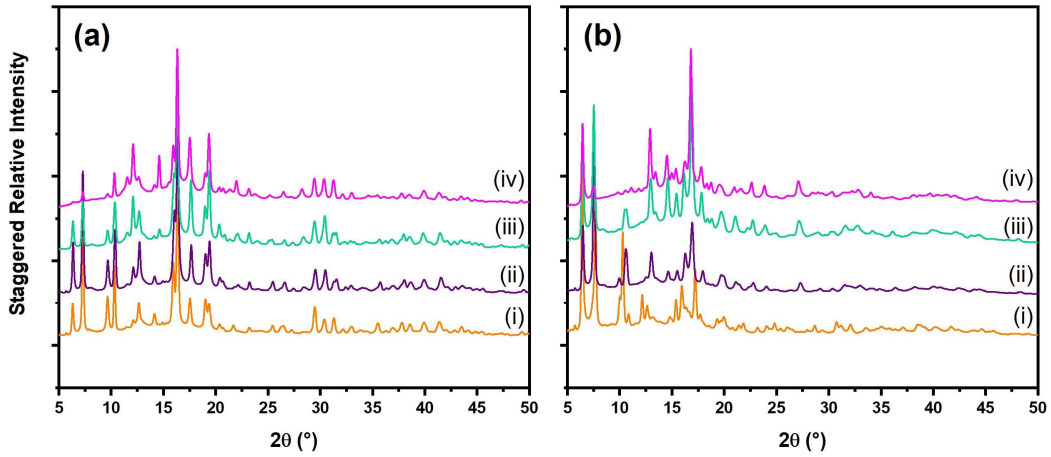

Figure 7.4.1. PXRD patterns of (a) hydrated and (b) dehydrated PHI (3.6) materials at 298 K: (i) $Na_{3.5}$-, (ii) $K_{3.5}$-, (iii) $Rb_{3.5}$-, (iv) $Cs_{3.5}$-PHI (3.6). (9B, PAL, λ = 0.900 Å).

further investigated. As was the case for merlinoite and Rho materials, a detailed study of this sample would also require PND data which was unavailable. CO_2 sorption isotherms up to 1 bar were collected at various temperatures for different cation forms, as shown in Figure 7.4.2.

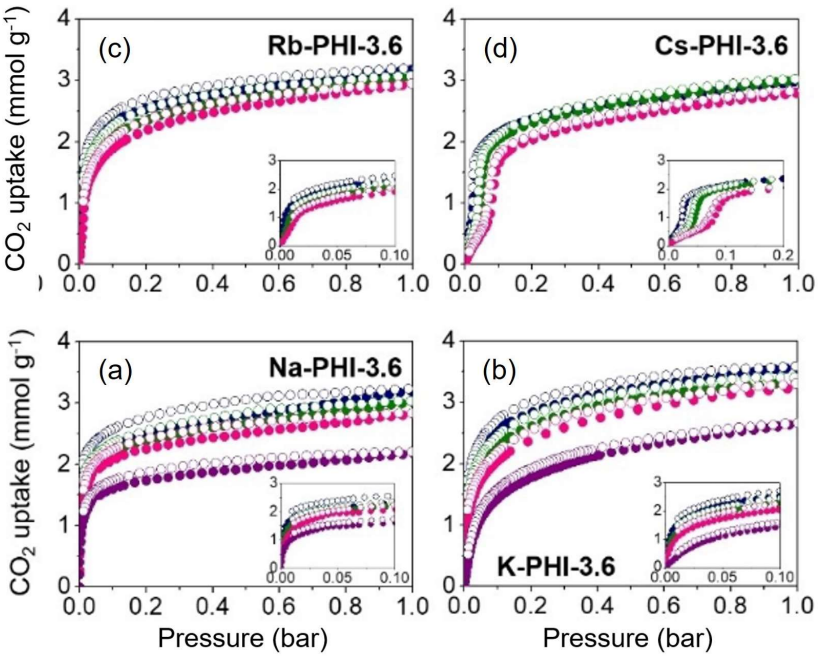

Figure 7.4.2. CO_2 adsorption isotherms up to 1 bar for PHI (3.6) samples: (a) $Na_{3.5}$-, (b) $K_{3.5}$-, (c) $Rb_{3.5}$-, (d) $Cs_{3.5}$-PHI (3.6). Adsorption and desorption branches are indicated by closed and open symbols; respectively. Lower pressures isotherm regions (up to 0.1 bar) are shown inset. Isotherm temperatures are (blue) 298, (green) 308, (pink) 318 and (purple) 348 K. Adapted from Choi et al.[16]

7.4.2 Structural studies of PHI (3.6) materials

7.4.2.1 Hydrated $M_{3.5}$-PHI (3.6)

The Rietveld plots of hydrated $M_{3.5}$-PHI (3.6) materials are shown in Figure 7.4.3 with further crystallographic details given in Appendix VI.III.II. As for the PHI (2.5) materials,

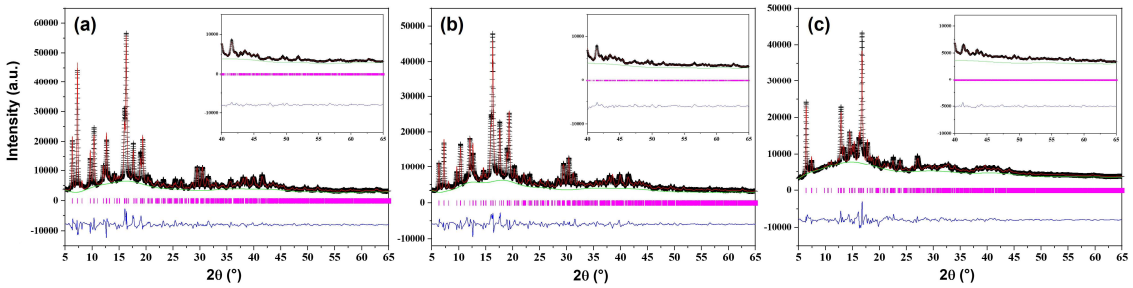

Figure 7.4.3. Rietveld plots of hydrated $M_{3.5}$-PHI (3.6) samples, with M = (a) K, (b) Rb and (c) Cs. (9B, PAL, λ = 0.900 Å).

K- and Rb-forms of the material adopted $P2_1/m$ whilst the Cs-equivalent was fitted using a $P2_1/c$ 2 × 1 × 2 supercell and fitting of the Na-analogue remained elusive. The unit cell parameters and measures of fit of the refined hydrated materials are given in Table 7.4.1, and their refined structures are shown in Figure 7.4.4.

Table 7.4.1. Space group (SG), unit cell parameters and R_{wp} from refinement of hydrated $M_{3.5}$-PHI (3.6) samples.

Material	SG	*a* (Å)	*b* (Å)	*c* (Å)	*β* (°)	*V* (Å³)	R_{wp}
$K_{3.5}$	$P2_1/m$	9.922(1)	14.138(2)	8.674(2)	125.1(1)	995(1)	7.7%
$Rb_{3.5}$	$P2_1/m$	9.941(1)	14.175(2)	8.675(2)	125.1(1)	1001(1)	6.8%
$Cs_{3.5}$	$P2_1/c$	20.024(3)	14.171(3)	17.395(4)	125.5(1)	4018(1)	4.0%

The values presented here are similar to those of the Si/Al = 2.5 samples, although slightly smaller for each comparable cation form, and again similar to each other when considering the supercell description of $Cs_{3.5}$-PHI (3.6) (reduced unit cell volume of 1005 Å³).

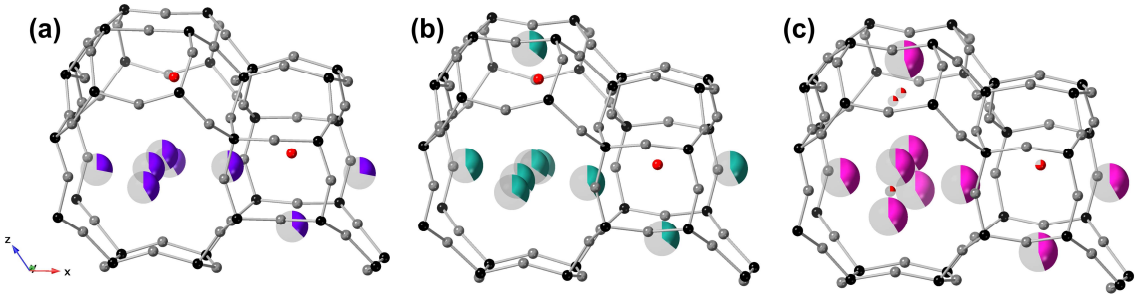

Figure 7.4.4. Structures of hydrated (a) $K_{3.5}$-, (b) $Rb_{3.5}$-, (c) $Cs_{3.5}$-PHI (3.6). K, Rb and Cs cations are shown in purple, cyan and pink, respectively, with the fractional occupancy indicated by filled proportion of sphere. Framework T and O sites are shown in black and grey, respectively, whilst water O sites are shown in red. The Cs-form is a reduced average of the supercell. Fractional occupancies are shown by the partial filling of spheres.

7.4.2.2 Dehydrated $M_{3.5}$-PHI (3.6)

Upon dehydration these materials also show framework distortions, as their unit cell volume decreases. Figure 7.4.5 shows Rietveld plots of the dehydrated $M_{3.5}$-PHI (3.6) sample data with crystallographic details given in Appendix VI.III.II.

Here all samples could be fitted best with $P2_1/m$ but the $Na_{3.5}$-PHI (3.6) material could not be described due to the presence of additional peaks, just as for the $Na_{4.6}$-PHI (2.5)

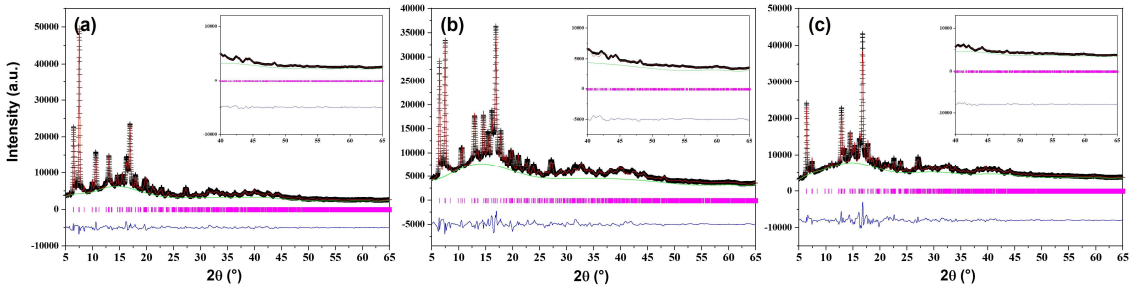

Figure 7.4.5. Rietveld plots of dehydrated $M_{3.5}$-PHI (3.6) samples, with M = (a) K, (b) Rb and (c) Cs. (9B, PAL, λ = 0.900 Å).

sample. Unit cell parameters and refinement details of the other cation forms are given in Table 7.4.2, and show a reduction in unit cell volume corresponding to 8, 7 and 6% for K-, Rb- and Cs-forms, respectively. Whilst this continues the trend seen for previous samples of larger reductions observed for smaller cation forms, here the difference is subdued and each value is smaller than for their PHI (2.5) analogues. The refined structures of the dehydrated $M_{3.5}$-PHI (3.6) materials are presented in Figure 7.4.6.

Table 7.4.2. Space group (SG), unit cell parameters and R_{wp} from refinement of dehydrated $M_{3.5}$-PHI (3.6) samples.

Material	SG	*a* (Å)	*b* (Å)	*c* (Å)	*β* (°)	*V* (Å³)	R_{wp}
$K_{3.5}$	$P2_1/m$	9.820(1)	13.703(2)	8.434(2)	125.9(1)	919(1)	4.4%
$Rb_{3.5}$	$P2_1/m$	9.903(1)	13.733(2)	8.450(2)	126.0(1)	930(1)	4.8%
$Cs_{3.5}$	$P2_1/m$	9.903(1)	13.822(2)	8.435(2)	125.4(1)	941(1)	5.4%

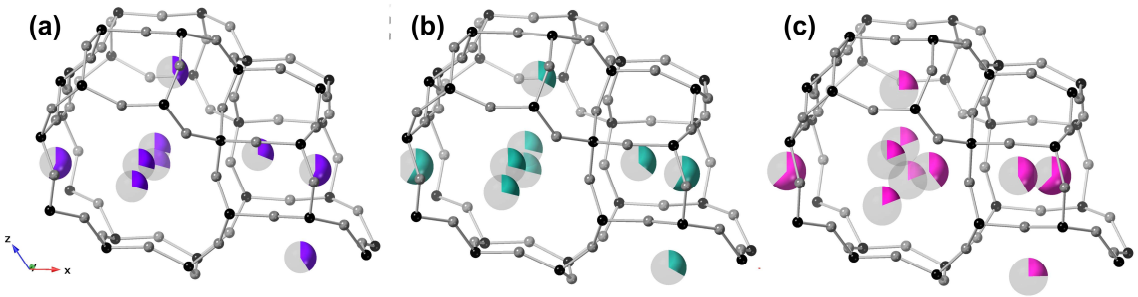

Figure 7.4.6. Structures of dehydrated (a) $K_{3.5}$-, (b) $Rb_{3.5}$-, (c) $Cs_{3.5}$-PHI (3.6). K, Rb and Cs cations are shown in purple, cyan and pink, respectively, with the fractional occupancy indicated by filled proportion of sphere. Framework T and O sites are shown in black and grey, respectively. Partial shading of spheres indicate fractional occupancies.

7.4.2.3 Comparison of PHI (3.6) structures

Table 7.4.3 gives cation occupancies per unit cell in the $M_{3.5}$-PHI (3.6) materials. There is a greater degree of variation for these materials than their PHI (2.5) relatives, though

hydrated forms are similar across the 3 cation forms, and K and Rb cations are spread near identically across sites. As for $Cs_{4.6}$-PHI (2.5), the dehydrated Cs-form of this material exhibits Cs^+ species in site IV, although here site Ia is also occupied. For all materials, fewer cations are found in site II and III compared to their PHI (2.5) counterparts, whilst sites I, Ia and IV more closely match between the different Si/Al materials, indicating these are preferentially occupied by all of the cations examined here. As window sizes in PHI (3.6) materials are larger than in the Si/Al = 2.5 samples and there are fewer cations to hinder percolation of gas molecules, these materials would be expected to possess more rapid sorption kinetics in any PSA or VSA application, though perhaps less selective.

*Table 7.4.3. Absolute site occupancies of M^+ in PHI (3.6) materials. *denotes merging of related but symmetry inequivalent positions within the $P2_1/c$ 2 × 1 × 2 supercell.*

Cation form	dh/h	I	Ia	II	III	IV	Total
$K_{3.5}$	h	0.6(1)	0.9(1)	1.6(1)	0.7(1)		3.8(2)
	dh	1.1(1)	0.6(1)	1.2(1)	0.8(1)		3.7(1)
$Rb_{3.5}$	h	0.8(1)	0.8(1)	1.4(1)	0.7(1)		3.8(1)
	dh	1.2(1)	0.7(1)	1.2(1)	0.7(1)		3.7(1)
$Cs_{3.5}$	h*	0.8(1)	0.9(1)	1.6(1)	1.0(1)		4.3(2)
	dh	0.8(1)	1.2(1)	0.8(1)	0.5(1)	0.8(1)	4.1(1)

The finer details of siting within the hydrated Cs-material are given in Table 7.4.4, as the supercell description gives rise to a more complex site description. As for the Cs-PHI (2.5) material, the ordering of cations within the *phi-phi* channel appears to be the cause of symmetry breaking, both the loss of symmetry between adjacent *phi* cavities and the loss of mirror symmetry across each *phi* cavity, as evidenced by differences in occupancy of site II and its relations.

Free window diameters are given in

Table 7.4.5. Here all windows investigated were found to be sufficiently wide to permit CO_2 diffusion when considering the additional 0.7 Å afforded by thermal vibration as described by Cook and Conner.[24] For each material, windows tend to be wider and more

accessible than comparable PHI (2.5) materials. Furthermore, the range of window diameters is reduced, whilst the mean window diameter for the 3 materials is very similar under identical conditions, as shown graphically in Figure 7.4.7.

Table 7.4.4. Fractional site occupancies of Cs^+ in hydrated $Cs_{3.5}$-PHI (3.6). Sites in the same row share phi cavities.

I	Ia	II	II′	III
0.40(5)	0.42(5)	0.61(4)	0.36(4)	0.35(4)
I′	**Ia′**	**II″**	**II‴**	**III′**
0.43(5)	0.48(5)	0.42(4)	0.26(4)	0.54(4)

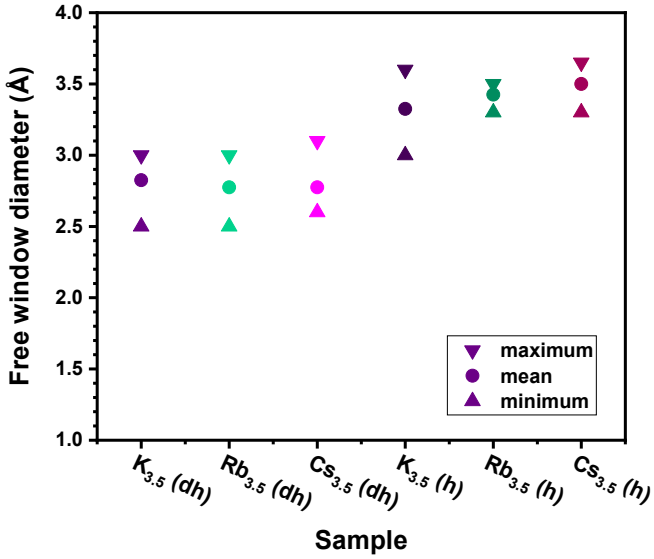

Figure 7.4.7. Free window diameters of PHI (3.6) samples. Mean, maximum and minimum values are depicted as shown in the key. Samples and conditions are as indicated on the x axis.

Table 7.4.5. Free window diameters in PHI (3.6) materials.

Cation form	dh/h	I (Å)	Ia (Å)	II (Å)	III (Å)
$K_{3.5}$	h	3.6(1)	3.5(1)	3.2(1)	3.0(1)
	dh	2.9(1)	2.5(1)	2.9(1)	3.0(1)
$Rb_{3.5}$	h	3.5(1)	3.5(1)	3.4(1)	3.3(1)
	dh	3.0(1)	2.5(1)	2.9(1)	2.7(1)
$Cs_{3.5}$	h	3.5(1)	3.7(1)	3.5(1)	3.3(1)
	dh	2.7(1)	2.7(1)	2.6(1)	3.1(1)

7.4.2.4 *PHI (3.6) materials as CO_2 sorbents*

As for previous PHI (2.5) samples, Drs Choi and Andreev collected VPXRD data, and further synchrotron experiments were run to reveal how these samples respond to gas adsorption. VPXRD patterns are shown in Figure 7.4.8 and the differences between trends in cell expansion for the 3 samples are evidenced in Figure 7.4.9, based on structured fits of the materials.

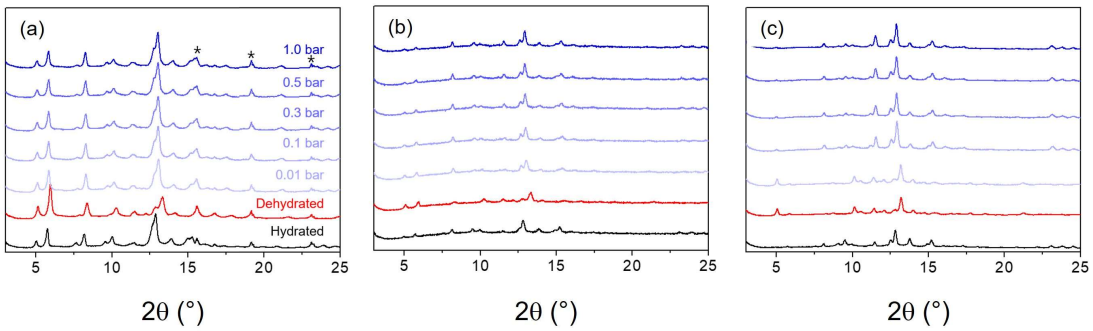

Figure 7.4.8. VPXRD data for (a) $K_{3.5}$-, (b) $Rb_{3.5}$- and (c) $Cs_{3.5}$-PHI (3.6) at 298 K under hydrated, dehydrated and CO_2 adsorption, with conditions as labelled. Peaks from the sample holder are as indicated in (a). (PANalytical, Mo K$\alpha_{1,2}$, λ = 0.711 Å).

From the low-resolution data, the K-form of the material appears to undergo a gradual cell expansion with increasing CO_2 pressure, and similar is observed for Rb-PHI (3.6) though there is more of a step change between the dehydrated pattern and the 0.01 bar data. This matches the equilibrium CO_2 isotherms which shows the K-material to exhibit

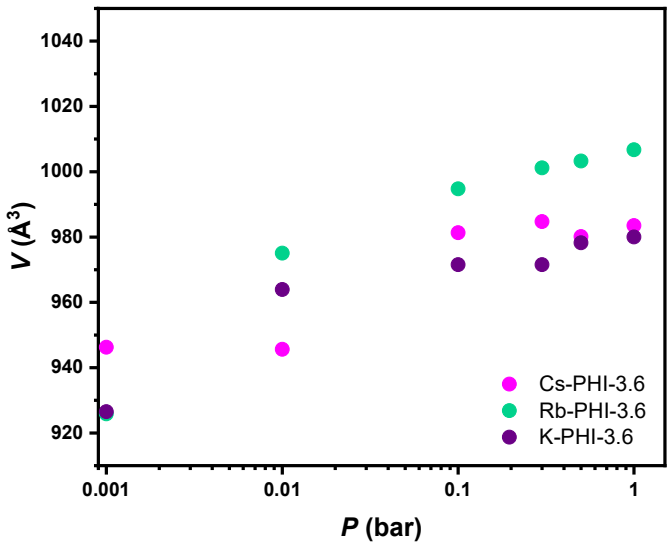

Figure 7.4.9. Unit cell volumes of $M_{3.5}$-PHI (3.6) materials obtained from VPXRD analysis. M = K, Rb and Cs is plotted in purple, cyan and pink, respectively. Data is plotted against a logarithmic axis with dehydrated data shown at 0.001 bar for ease of comparison.

Type I behaviour, whilst the Rb-form has a potential minor step evident at elevated temperatures and at very low pressures. As for the $Cs_{4.6}$-PHI (2.5) sample, here the Cs-form adopts 2 different phases with a boundary found between 0.01 and 0.1 bar of CO_2, matching the step in the CO_2 adsorption isotherm at *ca*. 0.02 bar at 298 K. All samples show patterns that more closely resemble those of their hydrated forms at higher pressure of CO_2.

Synchrotron data acquired under 1 bar of CO_2 is shown in Figure 7.4.10. Again, refinement of the Na-exchanged material could not be carried out, though it appears to be more closely related to the dehydrated structure than the relaxed, hydrated form, matching the behaviour of its PHI (2.5) relation. A summary of refinement data is provided in Table 7.4.6 with associated Rietveld plots given in Figure 7.4.11.

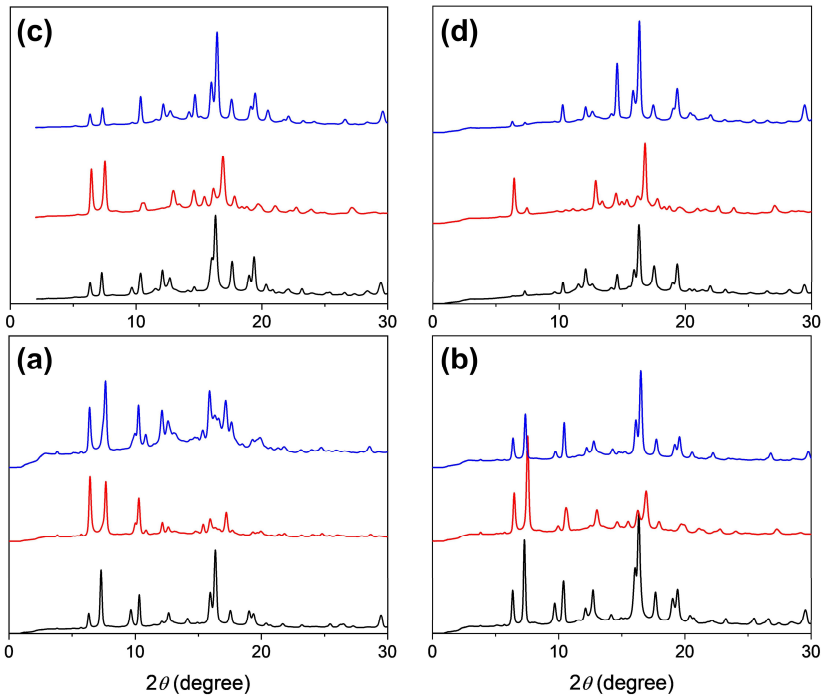

Figure 7.4.10. Synchrotron PXRD patterns of (a) $Na_{3.5}$-, (b) $K_{3.5}$-, (c) $Rb_{3.5}$- and (d) $Cs_{3.5}$-PHI (3.6) collected at 1 bar of CO_2 (blue) with hydrated and dehydrated patterns given for comparison, in black and red, respectively. All patterns obtained at 298 K. (9B, PAL, λ = 0.900 Å).

Unit cell volumes expanded relative to dehydrated materials for all samples and more closely match those of the hydrated forms, even more so than their PHI (2.5) counterparts. This suggests there is limited additional pore volume available for CO_2 adsorption.

Table 7.4.6. Space group (SG), unit cell parameters and R_{wp} from refinement of $M_{3.5}$-PHI (3.6) under 1 bar of CO_2.

Material	SG	*a* (Å)	*b* (Å)	*c* (Å)	*β* (°)	*V* (Å³)	R_{wp}
$K_{3.5}$	$P2_1/m$	9.888(1)	14.007(2)	8.573(1)	124.9(1)	974(1)	5.9%
$Rb_{3.5}$	$P2_1/m$	10.003(1)	14.063(2)	8.641(2)	125.2(1)	993(1)	6.4%
$Cs_{3.5}$	$P2_1/m$	10.083(1)	14.150(3)	8.668(2)	125.2(1)	1011(1)	6.5%

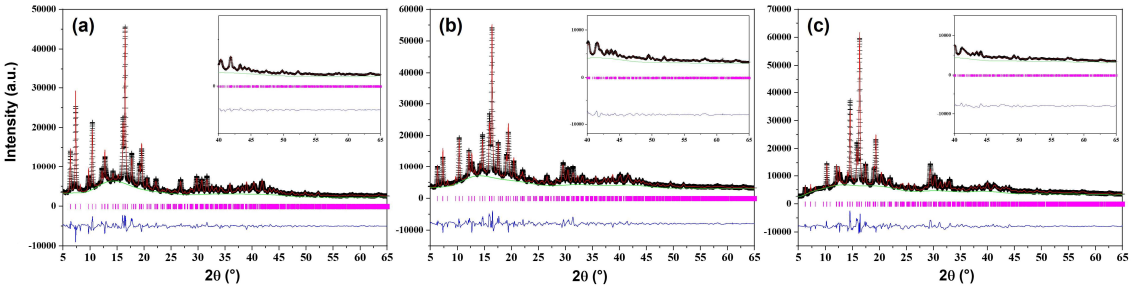

Figure 7.4.11. Rietveld plots of $M_{3.5}$-PHI (3.6) samples under 1 bar of CO_2, with M = (a) K, (b) Rb and (c) Cs. (9B, PAL, λ = 0.900 Å).

Table 7.4.7 gives cation occupancies within the PHI (3.6) materials under 1 bar of CO_2, the structures of which are shown in Figure 7.4.12. For the Cs-material, values more closely resemble that of the hydrated form, presented in Table 7.4.3, with site IV vacated. For the other samples, whilst occupancies of sites I and Ia match those of their dehydrated forms, occupancies of site II and III appear inverted relative to both samples shown earlier, signifying that the energetics of these sites are altered with the presence of CO_2. Site II, located between adjacent *phi* cavities, is less favourable with cations relocated to site III at the base of the *oto* cavity.

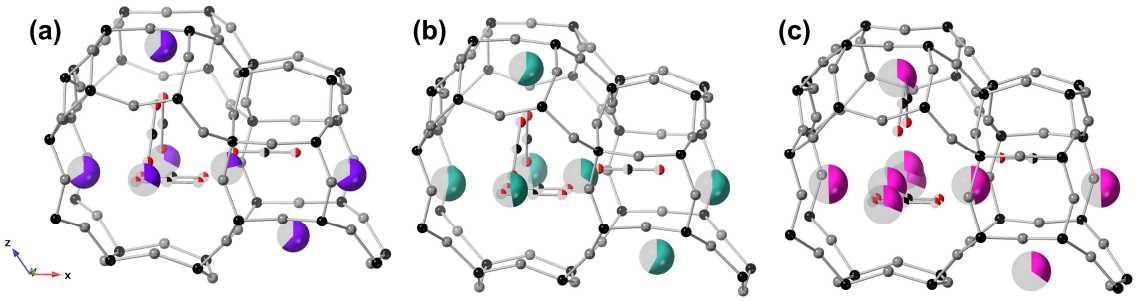

Figure 7.4.12. Refined structures of $M_{3.5}$-PHI (3.6) materials under 1 bar of CO_2. M = (a) K, (b) Rb and (c) Cs. Framework T and O sites are shown in black and grey, respectively. K, Rb and Cs cations are shown in purple, cyan and pink and CO_2 molecules in black and red, respectively. Fractional occupancies are shown by the partial shading of spheres.

Table 7.4.7. Absolute site occupancies of M^+ in PHI (3.6) materials under 1 bar of CO_2.

Cation form	I	Ia	II	III	Total
$K_{4.6}$	1.3(1)	0.4(1)	0.7(1)	1.2(1)	3.6(2)
$Rb_{4.6}$	1.1(1)	0.7(1)	0.9(1)	1.2(1)	3.9(1)
$Cs_{4.6}$	0.9(1)	1.0(1)	1.2(1)	0.7(1)	3.9(1)

The free window diameters listed in Table 7.4.8 more closely resemble those of the hydrated forms given in

Table 7.4.5, as may be expected from the similarity in unit cell volumes. Whilst some of the individual values vary, the mean for each sample matches that of their hydrated form. As for their PHI (2.5) counterparts, samples here fit 2 different behaviours best described as gradual breathing or stepwise expansion upon adsorption. This is discussed further in the following section.

Table 7.4.8. Free window diameters in PHI (3.6) materials under 1 bar of CO_2.

Cation form	I (Å)	Ia (Å)	II (Å)	III (Å)
$K_{3.5}$	3.4(1)	3.5(1)	3.1(1)	3.0(1)
$Rb_{3.5}$	3.3(1)	3.9(1)	3.2(1)	3.1(1)
$Cs_{3.5}$	3.8(1)	3.5(1)	3.5(1)	3.0(1)

7.5 Comparison of materials

7.5.1 Overview

Work presented in this chapter examines multiple cation forms of phillipsite zeolites with different Si/Al ratios. These materials demonstrate different adsorption behaviour to each other and to merlinoite zeolites discussed in Chapters 4-6, which possess the related **MER** framework type. The differences between the structures of these materials and their effects on adsorption behaviour is detailed below.

7.5.2 Comparison of PHI structures

As for Rho and merlinoite zeolites, the unit cell volumes of phillipsite materials under various conditions are dependent on the cations present within the material. As shown in Figure 7.5.1, unit cell volumes increase with cation size, as has been typically observed for previous zeolites discussed, and is most obvious for the dehydrated PHI (2.5) zeolites. In these materials, not only is the Cs-form larger than the smaller-cation forms, it is also larger than its Si/Al = 3.6 analogue, which is not the case for the other cation forms. This and the higher level of distortion for $K_{4.6}$- and $Rb_{4.6}$-PHI (2.5) compared to their higher silica counterparts are likely both caused by higher cation loading leading to greater impact of cations on the framework. For the smaller cations, this leads to a further narrowing of 8-rings to better coordinate the extraframework species, whilst in the case of Cs^+, the structure has to accommodate a high number of bulky cations within the material. Cs cation occupancy of site II is much higher in the material with Si/Al =

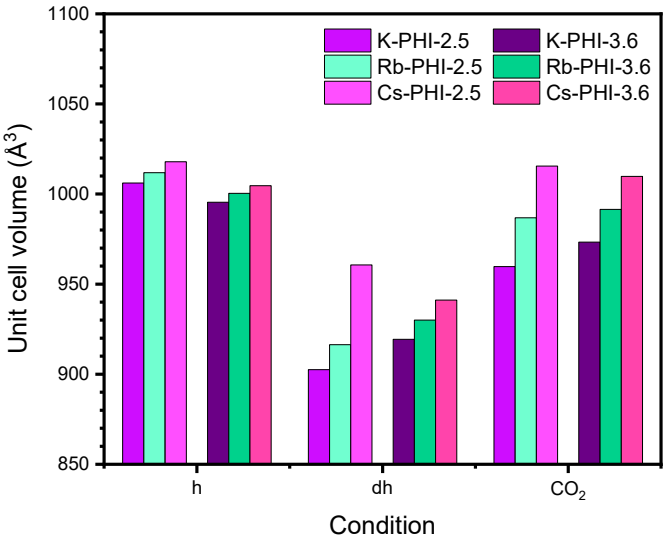

Figure 7.5.1. Unit cell volume of PHI materials under different conditions. Materials are as identified in the legend.

2.5 than that with 3.6, as seen in Tables 7.3.3 and 7.4.3, which may force the *phi* cavity to be propped open, similar to the rationale used to describe the behaviour of Cs-exchanged Rho samples.[25]

The type and number of cations within materials also affect window deformation and this behaviour is similar to that of unit cell volume, as shown in Figure 7.5.2. $Cs_{4.6}$-PHI (2.5) shows anomalously high window diameters, whilst for the other cation forms, the

higher Si/Al material has more relaxed, larger windows. Whilst $K_{4.6}$- and $Rb_{4.6}$-PHI (2.5) possess window Ia sizes below 2.3 Å, all other windows appear sufficiently large for CO_2 percolation once considering thermal vibration, suggesting that there would be limited impact of window size on blocking percolation, though there may still be differences in kinetic selectivity for adsorption processes.

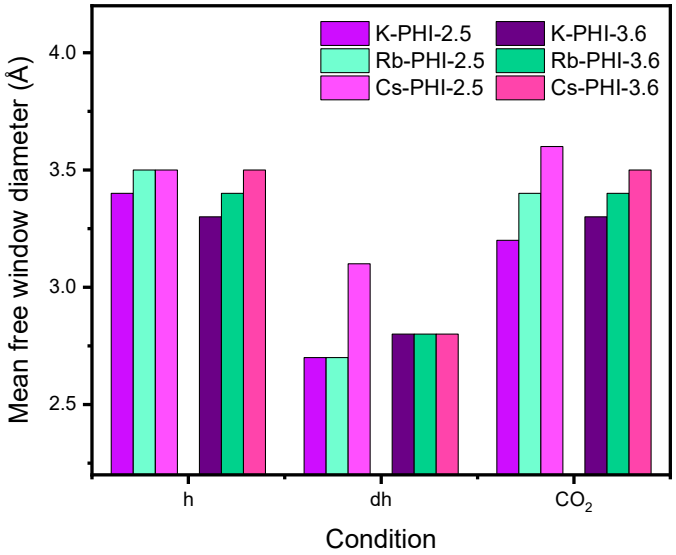

Figure 7.5.2. Mean free window diameter of PHI materials under different conditions. Materials are as identified in the legend.

7.5.3 Mechanisms of adsorption

As has been discussed, K- and Rb- forms adopt a gentle expansion of unit cell upon adsorption of CO_2, although the latter also shows evidence of a minor step change in behaviour at very low pressures, similar to that observed earlier for $K_{6.7}$-MER (3.8). For the smaller-cation forms, whilst the framework is distorted there is sufficient space for the cations to remain labile despite the high cation content of the samples. This requires a cation-gating mechanism to allow CO_2 percolation through the material.[26] As CO_2 is adsorbed, the framework gently breaths to allow sufficient space to hold additional adsorbate species and cations adopt sites that most favourably balance interactions between cations, framework and CO_2.

Cs-exchanged materials however display significant step-like behaviour in their adsorption isotherms and in VPXRD analysis. Whilst the higher Si/Al sample possesses a sigmoidal step, not unlike some of those observed in merlinoite zeolites previously discussed, the $Cs_{4.6}$-PHI (2.5) material exhibits a near rectilinear step, unlike any other

related material such as those with frameworks **GIS** or **MER**,[20,21,27] or indeed any other zeolite. The sharp nature of this step suggested cooperativity and so analysis following Hill's method was carried out as follows.

From adsorption isotherms recorded by Dr Choi, fractional uptake, f, was found by normalising CO_2 adsorption relative to the maximum observed at 1 bar of CO_2 and $\log_{10}(f/(1-f))$ was plotted against $\log_{10}(p/p_0)$, where p_0 = 1 bar, at all temperatures examined. Linear fits were obtained for the step regions such that a reasonable slope was obtained. The gradient of the slope gives the Hill coefficient, n_H, where $n_H > 1$ shows cooperativity. The value of n_H was found to be 18 and remained unchanged with temperature over the range investigated. This suggests that adsorption at 1 site within the structure promotes adsorption at another 17 sites. The resulting Hill plot is given in Figure 7.5.3.

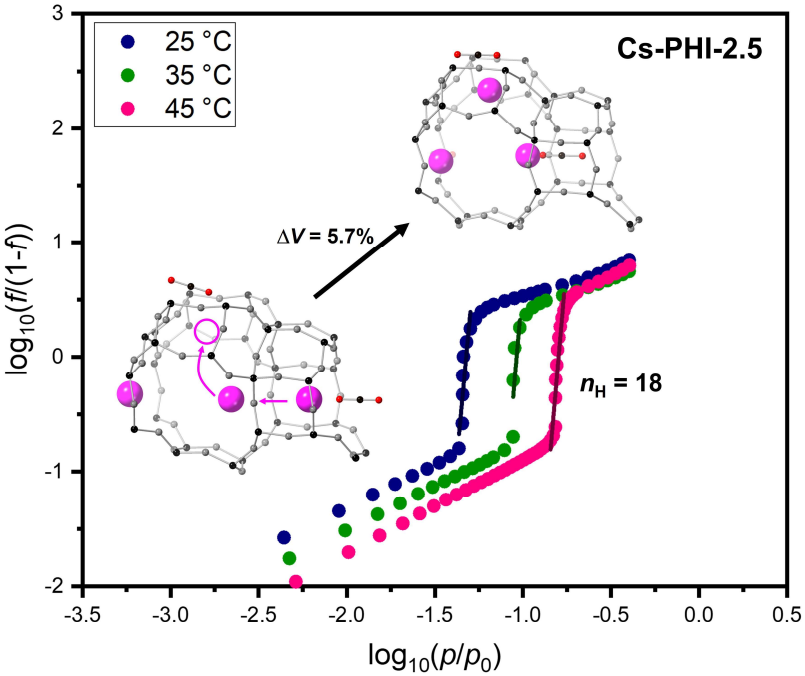

Figure 7.5.3. Hill plot of $Cs_{4.9}$-PHI (2.5) from CO_2 adsorption isotherms at different temperatures. A possible mechanism of pore opening is shown, with structures upon dehydration and subsequent exposure to 1 bar of CO_2 produced at relevant parts of the plot. Framework T and O atoms are shown in black and grey, Cs cations in pink and CO_2 molecules in black and red, respectively.

Such behaviour is unheard of in zeolites and is more well known in some metal-organic frameworks (MOFs) and soft porous crystals.[28,29] In particular, the behaviour of this

sample is reminiscent of the gate opening mechanism of Krause *et al*.[30] The precise nature of pore opening is not the same but could be generalised as the initial material locked in a closed-pore form before a supercritical condition is met, at which point the structure expands to an open-pore form, with an associated increase in available pore volume.

The low uptake of CO_2 by $Cs_{4.6}$-PHI (2.5) can be rationalised based on the large number of Cs cations and their positions within the structure. The high occupancy of site I takes up much of the space within *oto* cavities but more important are the remaining sites, which fill the *phi* cavities. The large size of the Cs cations means that sites III and IV are each placed such that only 1 cation can occupy the *phi* cavity, whilst adoption of site II allows only a single additional cation to be sited across the pore in another site of type II. Further to this, the 2 sites across a given 8-ring between adjacent *phi* cavities can only hold a single Cs cation, as these sites of type II are too close together. As such, the maximum number of cations supported within a given *phi* cavity is 1.5 on average. For the $Cs_{4.6}$-PHI (2.5) material, the value from structural refinement is found to be 1.4 and hence near to full capacity, enforcing a strict local ordering of cations, an example of which is given in Figure 7.5.4. In this ordering, 2 Cs cations would occupy every second *phi* cavity in type II sites, and the *phi* cavities in between would possess only 1 Cs cation in either site III or IV.

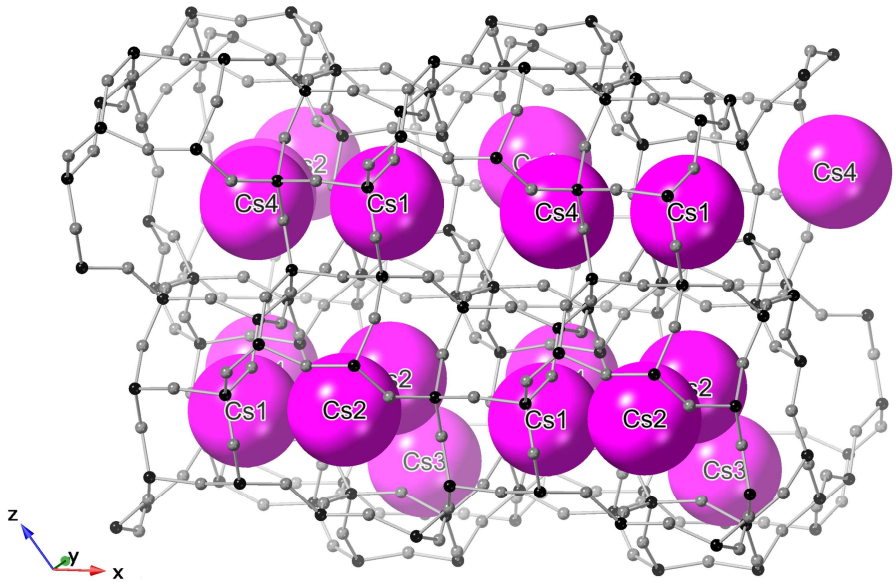

Figure 7.5.4. An example of Cs cation ordering within dehydrated $Cs_{4.6}$-PHI (2.5). T and O sites are shown in black and grey, respectively, with Cs cations depicted in pink using a space filling model. The excessive size of Cs cations prohibits a mix of sites II, III, and IV being occupied in the same t-phi cage.

As both *oto* and *phi* cavities are so highly occupied by large Cs cations, there is little space remaining to adsorb guest species. Similarly, the structure is too crowded to allow Cs^+ to move due to neighbouring "sentinel" cations, blocking any potential cation gating mechanism.[22,31] For the higher Si/Al material, the average occupancy of *phi* cavities is 1.1, allowing some space for CO_2 adsorption and Cs movement, as evidenced by a small uptake of CO_2 at low pressure before a more shallow, sigmoidal step in the adsorption isotherm.

Upon expansion to the open-pore form, Cs cations are redistributed, vacating site IV and occupying site III, at the base of the *oto* cavity, whilst other cations in the *oto* cavity are dispersed across both sites I and Ia. All of this occurs whilst increasing pore space available to CO_2 molecules in both *phi* and *oto* cavities. It may be the presence of CO_2 within the *oto* cavity that provides a trigger for the expansion of the local structure, enabling the movement of further Cs cations and percolation of CO_2 to drive neighbouring regions to expand in a cascade-like manner. Such a model is shown inset within Figure 7.5.3. This mechanism was termed 'cation crowding–dispersal', or 'cation crowding' for short due to the effect of repulsive Cs cation-cation interactions blocking adsorption of CO_2.

The desorption branch in CO_2 isotherms for the Cs-PHI materials also show steps, suggesting a similar mechanism occurring in reverse, with a cooperative closing of pores as CO_2 is expelled from the material. These desorption steps also occur at higher pressure than observed for other zeolite materials presented in this work, which together with the sharp adsorption step makes these materials promising for application as CO_2 sorbents. Further work is required to examine the selectivity of these materials under conditions relevant to applications.

7.6 Conclusion

The response of various cation forms of flexible zeolite phillipsite to CO_2 adsorption was examined through PXRD analysis and Rietveld refinement. With different Si/Al ratios, these materials included $Cs_{4.6}$-PHI (2.5), which possessed an extraordinary CO_2 adsorption isotherm with a sharp step in uptake. This was shown to be due to a sudden change in unit cell volume with sufficient CO_2 caused by blocking of adsorption sites at

low pressure by large Cs cations. Similar behaviour was observed for the material's higher silica equivalent, with other materials undergoing a gentler breathing upon adsorption of CO_2. Stepwise behaviour was found to be linked to cooperative expansion of the **PHI** framework leading to a promising sample for CO_2 adsorption, with behaviour unlike that of other zeolites and more similar to that of selected MOFs or soft porous crystals.

7.7 References

(1) Levy, A. Descriptions of Two New Minerals. *Ann. Philos. New Ser.* **1825**, *10*, 361–363.

(2) Steinfink, H. The Crystal Structure of the Zeolite, Phillipsite. *Acta Crystallogr.* **1962**, *15*, 644–651.

(3) Sadanaga, R.; Marumo, F.; Takeuchi, Y. The Crystal Structure of Harmotome, $Ba_2Al_4Si_{12}O_{32}.12H_2O$. *Acta Crystallogr.* **1961**, *14*, 1153.

(4) Rinaldi, R.; Pluth, J. J.; Smith, J. V. Zeolites of the Phillipsite Family. Refinement of the Crystal Structures of Phillipsite and Harmotome. *Acta Crystallogr. Sect. B Struct. Sci. Cryst. Eng. Mater.* **1974**, *30*, 2426–2433.

(5) EU Pat. 0243557A1, 1987.

(6) Gualtieri, A. F.; Caputo, D.; Colella, C. Ion Exchange Selectivity of Phillipsite for Cs^+: A Structural Investigation Using the Rietveld Method. *Microporous Mesoporous Mater.* **1999**, *32* (3), 319–329.

(7) Gualtieri, A. F.; Passaglia, E.; Galli, E.; Viani, A. Rietveld Structure Refinement of Sr-Exchanged Phillipsites. *Microporous Mesoporous Mater.* **1999**, *31*, 33–43.

(8) GB Pat. 1510018A, 1975.

(9) Zhuang, X.; Shin, M. C.; Jeong, B. J.; Lee, S. H.; Park, J. H. Fabrication of K-PHI Zeolite Coated Alumina Hollow Fiber Membrane and Study on Removal Characteristics of Metal Ions in Lignin Wastewater. *Hwahak Konghak* **2021**, *59* (2), 174–179.

(10) Kiyozumi, Y.; Nemoto, Y.; Nishide, T.; Nagase, T.; Hasegawa, Y.; Mizukami, F. Synthesis of Acid-Resistant Phillipsite (PHI) Membrane and Its Pervaporation Performance. *Microporous Mesoporous Mater.* **2008**, *116* (1–3), 485–490.

(11) JP Pat. JPH01156905A, 1987.

(12) Higuchi, Y.; Miyagawa, S.; Tanaka, S. OSDA-Free and Steam-Assisted Synthesis of PHI Type Zeolite Showing a Unique CO_2 Adsorption Behaviour. *CrystEngComm* **2022**, *24*, 3859.

(13) Bayat, M.; Nabavi, M. S.; Mohammadi, T. An Experimental Study for Finding the Best Condition for PHI Zeolite Synthesis Using Taguchi Method for Gas Separation. *Chem. Pap.* **2018**, *72* (5), 1139–1149.

(14) Baerlocher, C.; McCusker, L. B. IZA Database of Zeolite Structures, http://www.iza-structure.org/databases/, accessed October 2023.

(15) Danisi, R. M.; Armbruster, T.; Nagashima, M. Structural Intergrowth of Merlinoite/Phillipsite and Its Temperature-Dependent Dehydration Behaviour: A Single-Crystal X-Ray Study. *Mineral. Mag.* **2015**, *79* (1), 191–203.

(16) Choi, H. J.; Bruce, E. L.; Kencana, K. S.; Hong, J.; Wright, P. A.; Hong, S. B. Highly Cooperative CO_2 Adsorption via a Cation Crowding Mechanism on a Cesium-Exchanged Phillipsite Zeolite. *Angew. Chemie Int. Ed.* **2023**, *62* (36), e202305816.

(17) Lozinska, M. M.; Mangano, E.; Greenaway, A. G.; Fletcher, R.; Thompson, S. P.; Murray, C. A.; Brandani, S.; Wright, P. A. Cation Control of Molecular Sieving by Flexible Li-Containing Zeolite Rho. *J. Phys. Chem. C* **2016**, *120* (35), 19652–19662.

(18) Georgieva, V. M.; Bruce, E. L.; Verbraeken, M. C.; Scott, A. R.; Casteel, Jr, W. J.; Brandani, S.; Wright, P. A. Triggered Gate Opening and Breathing Effects during Selective CO_2 Adsorption by Merlinoite Zeolite. *J. Am. Chem. Soc.* **2019**, *141* (32), 12744–12759.

(19) Sani, A.; Cruciani, G.; Gualtieri, A. F. Dehydration Dynamics of Ba-Phillipsite: An in Situ Synchrotron Powder Diffraction Study. *Phys. Chem. Miner.* **2002**, *29* (5), 359–361.

(20) Choi, H. J.; Jo, D.; Hong, S. B. Effect of Framework Si/Al Ratio on the Adsorption

Mechanism of CO_2 on Small-Pore Zeolites: II. Merlinoite. *Chem. Eng. J.* **2022**, *446* (P2), 137100.

(21) Choi, H. J.; Min, J. G.; Ahn, S. H.; Shin, J.; Hong, S. B.; Radhakrishnan, S.; Chandran, C. V.; Bell, R. G.; Breynaert, E.; Kirschhock, C. E. A. Framework Flexibility-Driven CO_2 Adsorption on a Zeolite. *Mater. Horizons* **2020**, *7* (6), 1528–1532.

(22) Lozinska, M. M.; Mangano, E.; Mowat, J. P. S.; Shepherd, A. M.; Howe, R. F.; Thompson, S. P.; Parker, J. E.; Brandani, S.; Wright, P. A. Understanding Carbon Dioxide Adsorption on Univalent Cation Forms of the Flexible Zeolite Rho at Conditions Relevant to Carbon Capture from Flue Gases. *J. Am. Chem. Soc.* **2012**, *134* (42), 17628–17642.

(23) Shannon, R. D. Revised Effective Ionic Radii and Systematic Studies of Interatomic Distances in Halides and Chalcogenides. *Acta Crystallogr. Sect. A* **1976**, *32* (5), 751–767.

(24) Cook, M.; Conner, W. C. How Big Are the Pores of Zeolites? In *Proceedings of the 12th International Zeolite Conference*; Treacy, M. M. J., Marcus, B. K., Bisher, M. E., Higgins, J. B., Eds.; Materials Research Society: Warrendale, PA, USA, 1999; pp 409–414.

(25) Lozinska, M. M.; Mowat, J. P. S.; Wright, P. A.; Thompson, S. P.; Jorda, J. L.; Palomino, M.; Valencia, S.; Rey, F. Cation Gating and Relocation during the Highly Selective "Trapdoor" Adsorption of CO_2 on Univalent Cation Forms of Zeolite Rho. *Chem. Mater.* **2014**, *26* (6), 2052–2061.

(26) Shang, J.; Li, G.; Singh, R.; Gu, Q.; Nairn, K. M.; Bastow, T. J.; Medhekar, N.; Doherty, C. M.; Hill, A. J.; Liu, J. Z.; Webley, P. A. Discriminative Separation of Gases by a "Molecular Trapdoor" Mechanism in Chabazite Zeolites. *J. Am. Chem. Soc.* **2012**, *134* (46), 19246–19253.

(27) Choi, H. J.; Hong, S. B. Effect of Framework Si/Al Ratio on the Mechanism of CO_2 Adsorption on the Small-Pore Zeolite Gismondine. *Chem. Eng. J.* **2022**, *433* (P3), 133800.

(28) McDonald, T. M.; Mason, J. A.; Kong, X.; Bloch, E. D.; Gygi, D.; Dani, A.; Crocellà, V.; Giordanino, F.; Odoh, S. O.; Drisdell, W. S.; Vlaisavljevich, B.; Dzubak, A. L.; Poloni, R.; Schnell, S. K.; Planas, N.; Lee, K.; Pascal, T.; Wan, L. F.; Prendergast, D.; Neaton, J. B.; Smit, B.; Kortright, J. B.; Gagliardi, L.; Bordiga, S.; Reimer, J. A.; Long, J. R. Cooperative Insertion of CO_2 in Diamine-Appended Metal-Organic Frameworks. *Nature* **2015**, *519* (7543), 303–308.

(29) Sen, S.; Hosono, N.; Zheng, J. J.; Kusaka, S.; Matsuda, R.; Sakaki, S.; Kitagawa, S. Cooperative Bond Scission in a Soft Porous Crystal Enables Discriminatory Gate Opening for Ethylene over Ethane. *J. Am. Chem. Soc.* **2017**, *139* (50), 18313–18321.

(30) Krause, S.; Hosono, N.; Kitagawa, S. Chemistry of Soft Porous Crystals: Structural Dynamics and Gas Adsorption Properties. *Angew. Chemie - Int. Ed.* **2020**, *59* (36), 15325–15341.

(31) Mace, A.; Hedin, N.; Laaksonen, A. Role of Ion Mobility in Molecular Sieving of CO_2 over N_2 with Zeolite NaKA. *J. Phys. Chem. C* **2013**, *117* (46), 24259–24267.

Appendix I. Experimental and characterisation details

I.I Ion exchange of samples

The calcined Na,Cs-Rho (3.9) material was repeatedly ion exchanged in aqueous 3 M NH_4Cl solution at *ca.* 353 K, filtered and dried at *ca.* 363 K until the desired NH_4-Rho (3.9) form was reached, as determined by the absence of Na and Cs peaks in EDX analysis.

I.II EDX analysis

Energy dispersive X-ray spectroscopy (EDX) analysis was obtained using a JEOL JSM 5600 SEM with an Oxford INCA Energy 200 EDX analyser or a JEOL JSM-IT200 SEM with a JEOL DrySD EDX analyser.

I.III Laboratory X-ray diffractometers

Laboratory PXRD data was obtained on multiple machines, primarily in capillaries in Debye−Scherrer (transmission) geometry, on a Stoe STADI P diffractometer using monochromated Cu $K\alpha_1$ X-rays (1.54056 Å), typically from 3-70° in steps of 0.01°. Some hydrated data was collected on flat plates in Bragg-Brentano (reflection) geometry, on a PANalytical Empyrean using Cu $K\alpha_1$ X-rays (1.54056 Å), from 3-50° in steps of 0.017°.

Laboratory VPXRD data was acquired on a PANalytical Empyrean using Mo $K\alpha_{1,2}$ X-rays (0.711 Å) and an X'celerator RTMS detector, again working in Bragg-Brentano (reflection) geometry, from 3.5-25° in steps of 0.008°. The instrument was equipped with an Anton Paar HTK1200N stage and the sample loaded on an alumina disk and placed within a cell with a furnace. Samples were initially activated *in situ* under a vacuum of 10^{-6} mbar before exposure to desired pressures of CO_2.

Appendix III. Additional PXRD data

III.I The RHO family of materials

III.I.I ZSM-25

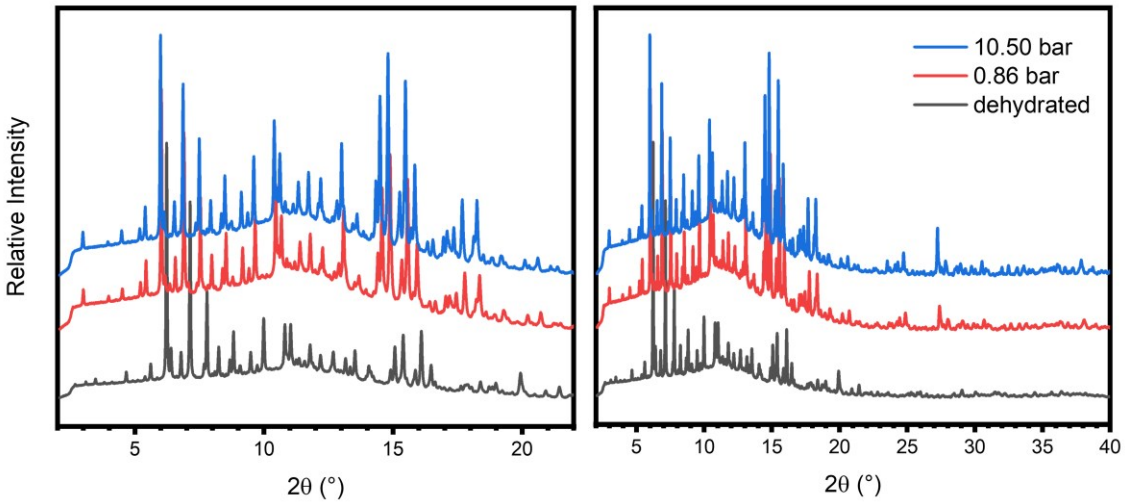

Figure III.I.I. PXRD patterns of Na,TEA-ZSM-25 after dehydration and subsequent exposure to CO_2. Pressures of CO_2 are as indicated in the top right. (I11, DLS, λ = 0.826956 Å)

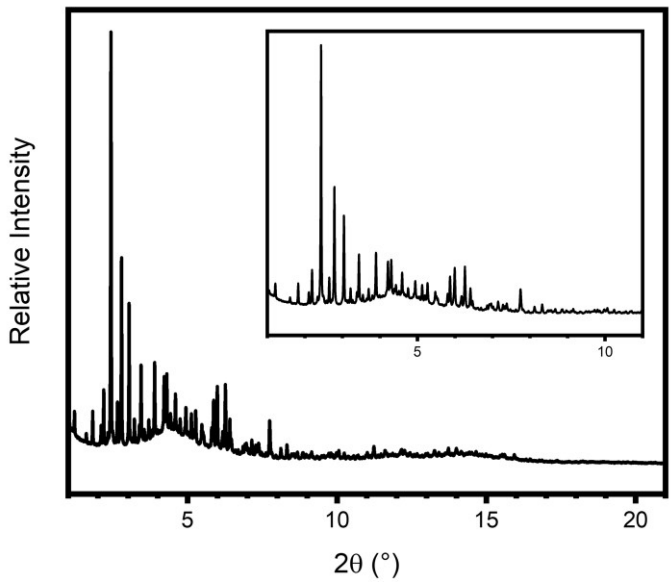

Figure III.I.II. PXRD pattern of dehydrated, calcined Na,H-ZSM-25. (ID31, ESRF, λ = 0.320012 Å)

III.I.II PST-20

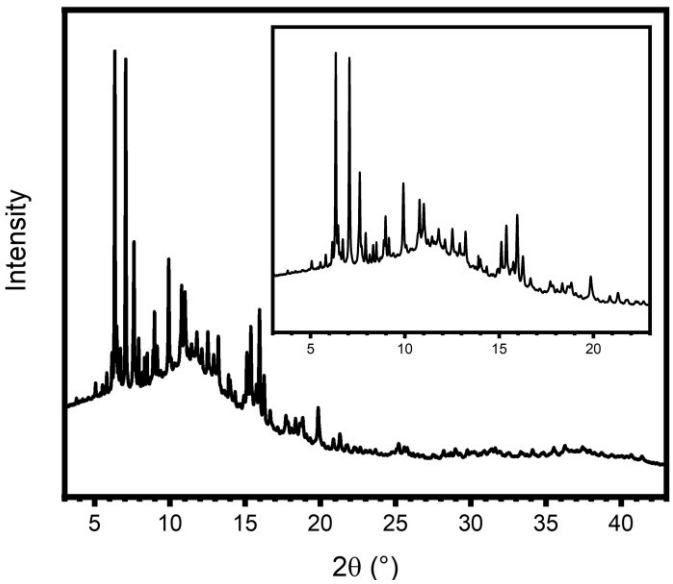

Figure III.I.III. PXRD pattern of dehydrated Na,TEA-PST-20. (I11, DLS, λ = 0.826956 Å)

III.II Merlinoite

III.II.I MER (3.8) VPXRD data

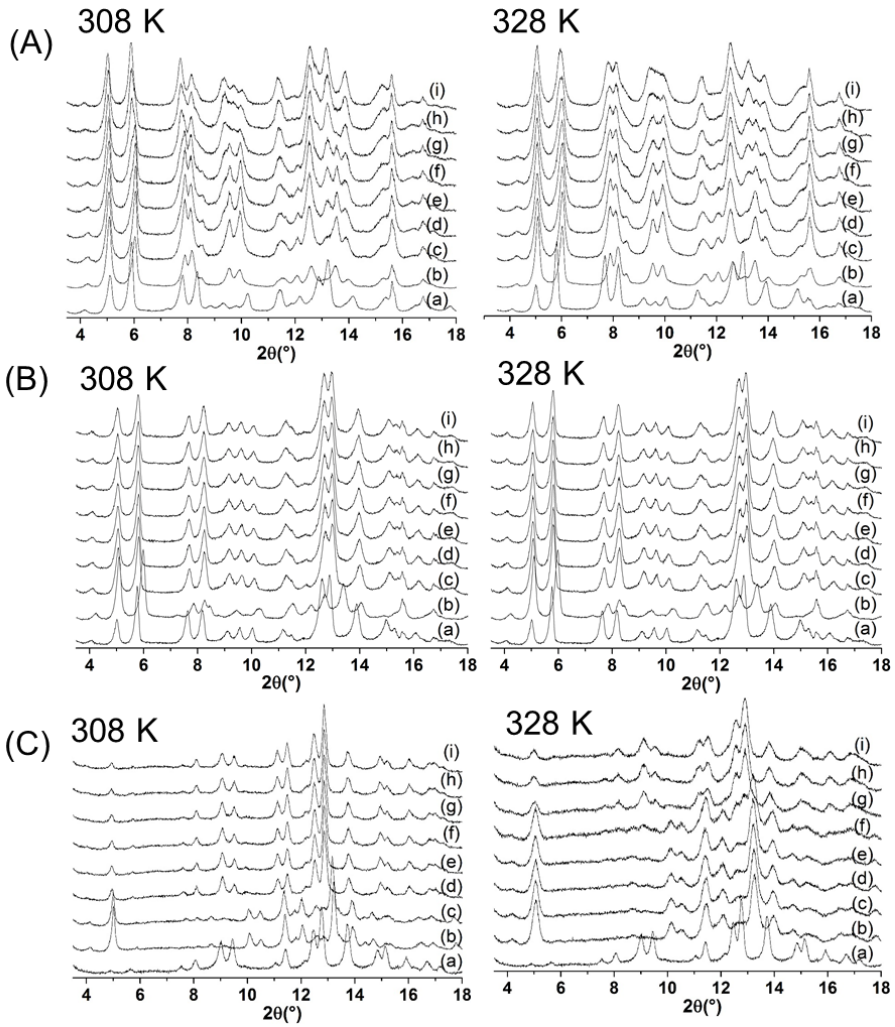

Figure III.II.I. Laboratory VPXRD patterns of MER (3.8) materials: (A) $Na_{6.7}$-, (B) $K_{6.7}$- and (C) $Cs_{6.7}$-MER (3.8). Conditions are (a) hydrated, (b) dehydrated and CO_2 pressures of (c) 0.1, (d) 0.2, (e) 0.3, (f) 0.4, (g) 0.6, (h) 0.8, (i) 1.0 bar. Temperatures are as labelled. Reproduced from Georgieva et al.[1] (PANalytical, Mo $K\alpha_{1,2}$, λ = 0.711 Å).

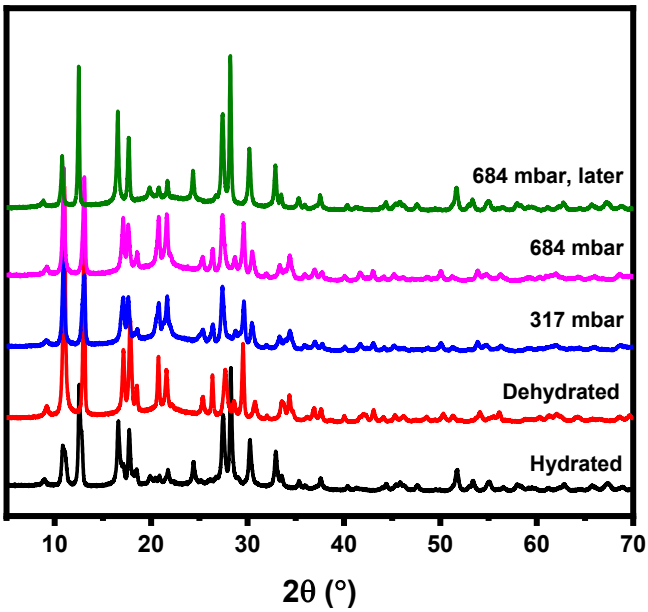

Figure III.II.II. PXRD patterns of $Na_{6.7}$-MER (3.8) collected under various conditions, including sealed in a capillary under 684 mbar of CO_2 immediately after sealing and 1 month later. (Stoe, λ = 1.54056 Å).

III.III References

(1) Georgieva, V. M.; Bruce, E. L.; Verbraeken, M. C.; Scott, A. R.; Casteel, Jr, W. J.; Brandani, S.; Wright, P. A. Triggered Gate Opening and Breathing Effects during Selective CO_2 Adsorption by Merlinoite Zeolite. *J. Am. Chem. Soc.* **2019**, *141* (32), 12744–12759.

Appendix IV. Additional Rietveld plots

IV.I $Li_{9.8}$-Rho (3.9)

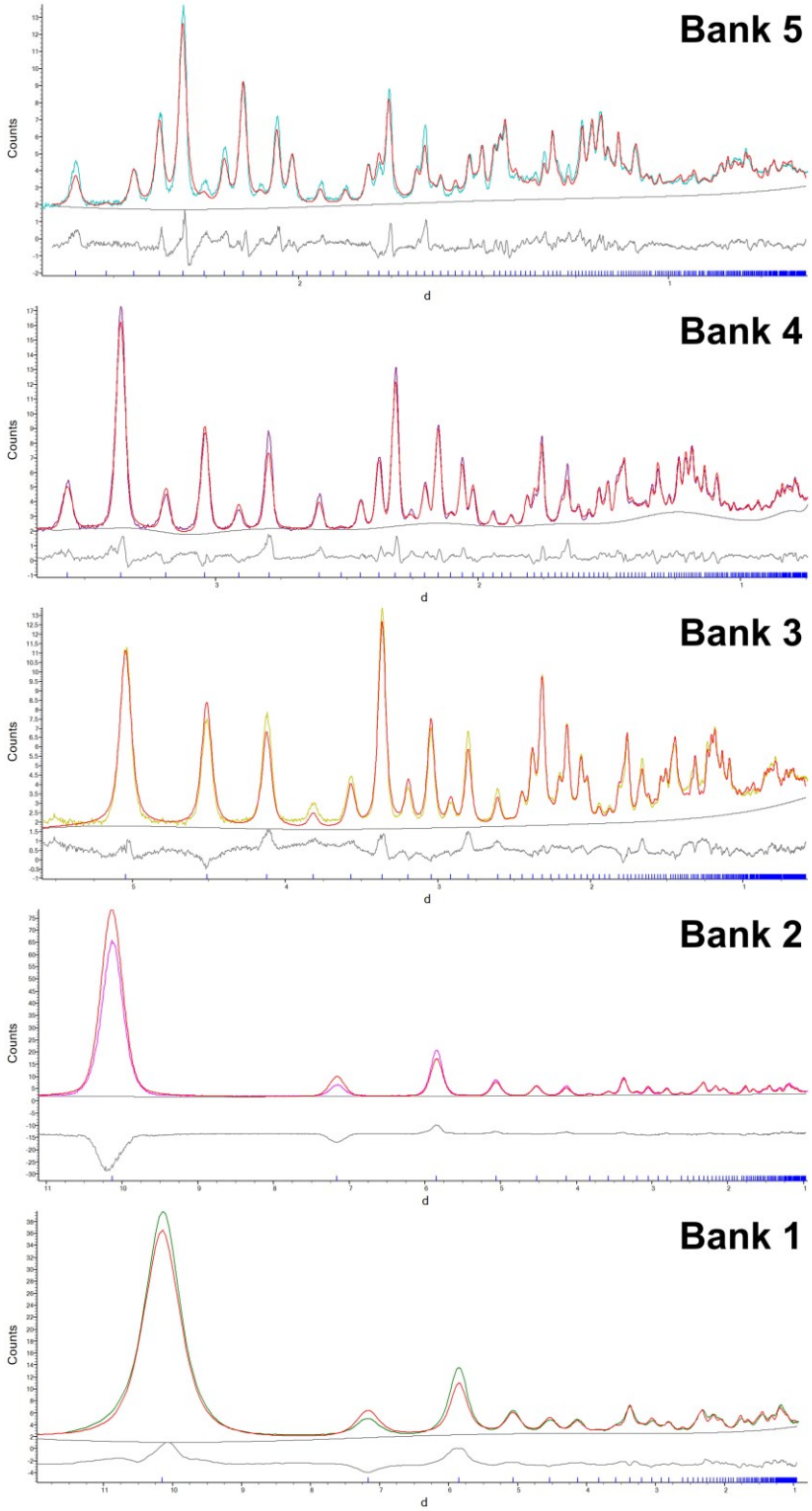

Figure III.III.I. PND data for $Li_{9.8}$-Rho (3.9) under 26 mbar of CO_2. Datasets are as identified.

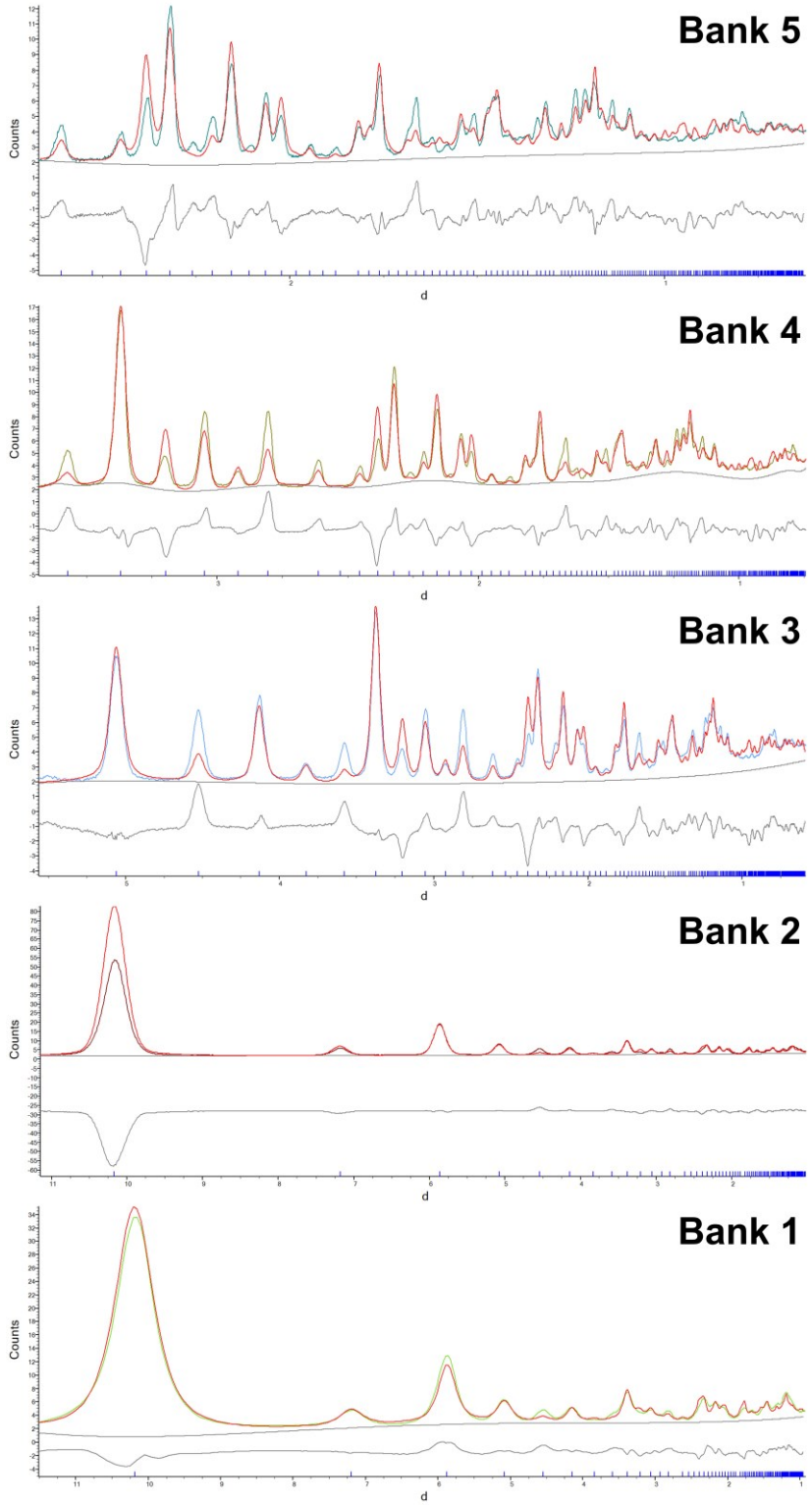

Figure IV.I.II. PND data for $Li_{9.8}$-Rho (3.9) under 70 mbar of CO_2. Datasets are as identified.

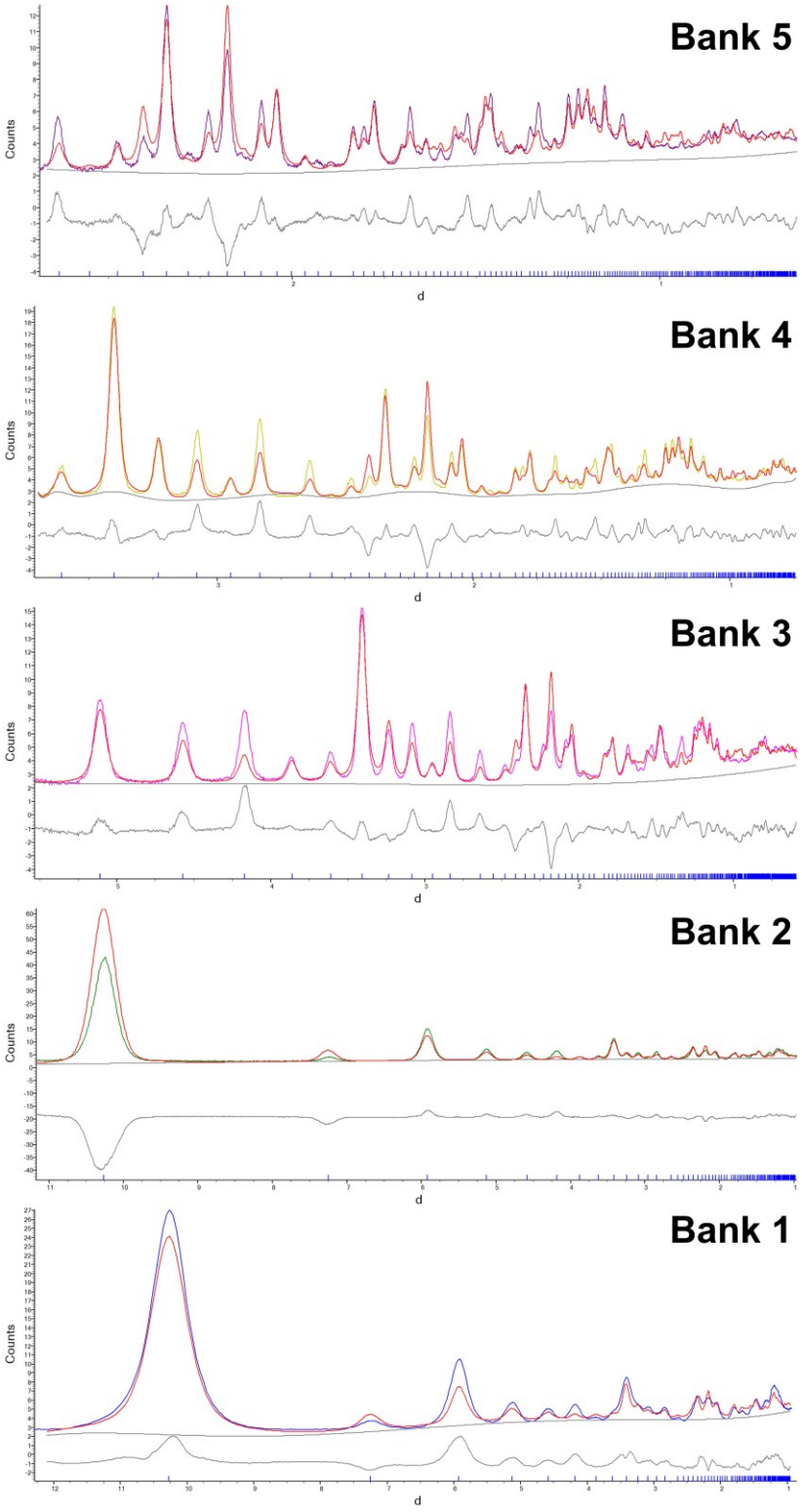

Figure IV.I.III. PND data for $Li_{9.8}$-Rho (3.9) under 175 mbar of CO_2. Datasets are as identified.

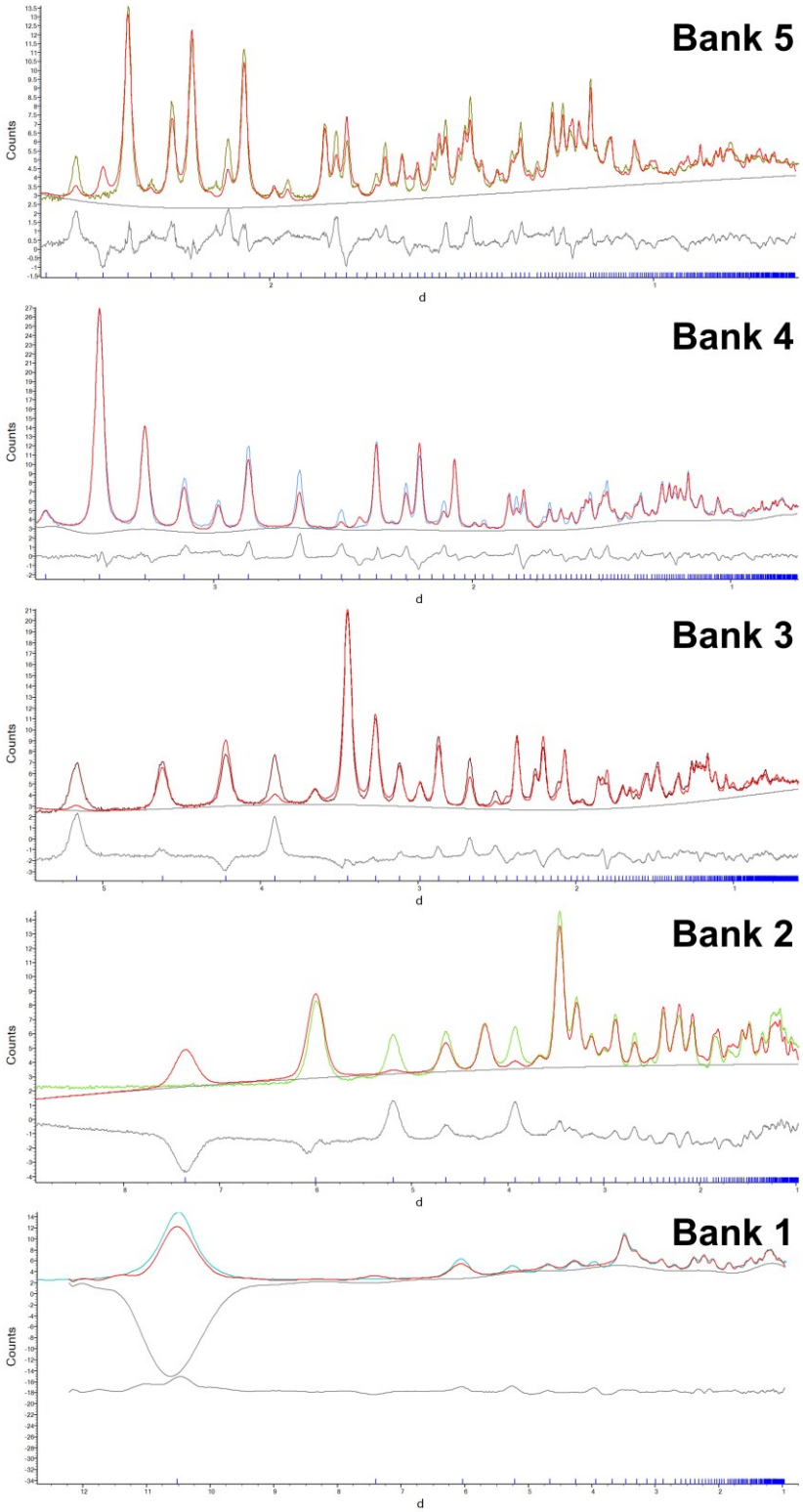

Figure IV.I.IV. PND data for $Li_{9.8}$-Rho (3.9) under 1.2 bar of CO_2. Datasets are as identified.

IV.II $Li_{7.3}Cs_{2.5}$-Rho (3.9)

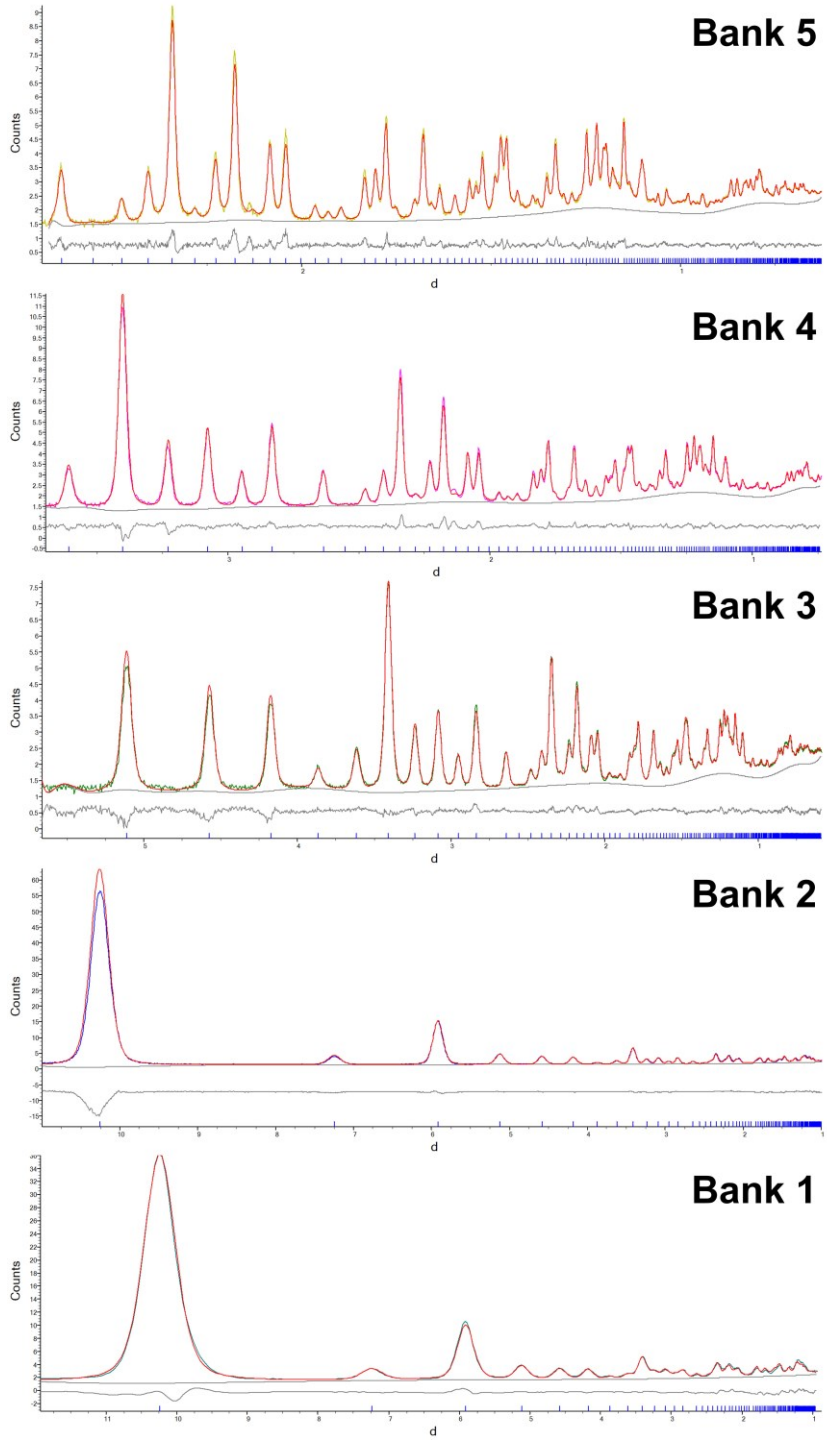

Figure IV.II.I. PND data for $Li_{7.3}Cs_{2.5}$-Rho (3.9) under 1 mbar of CO_2. Datasets are as identified.

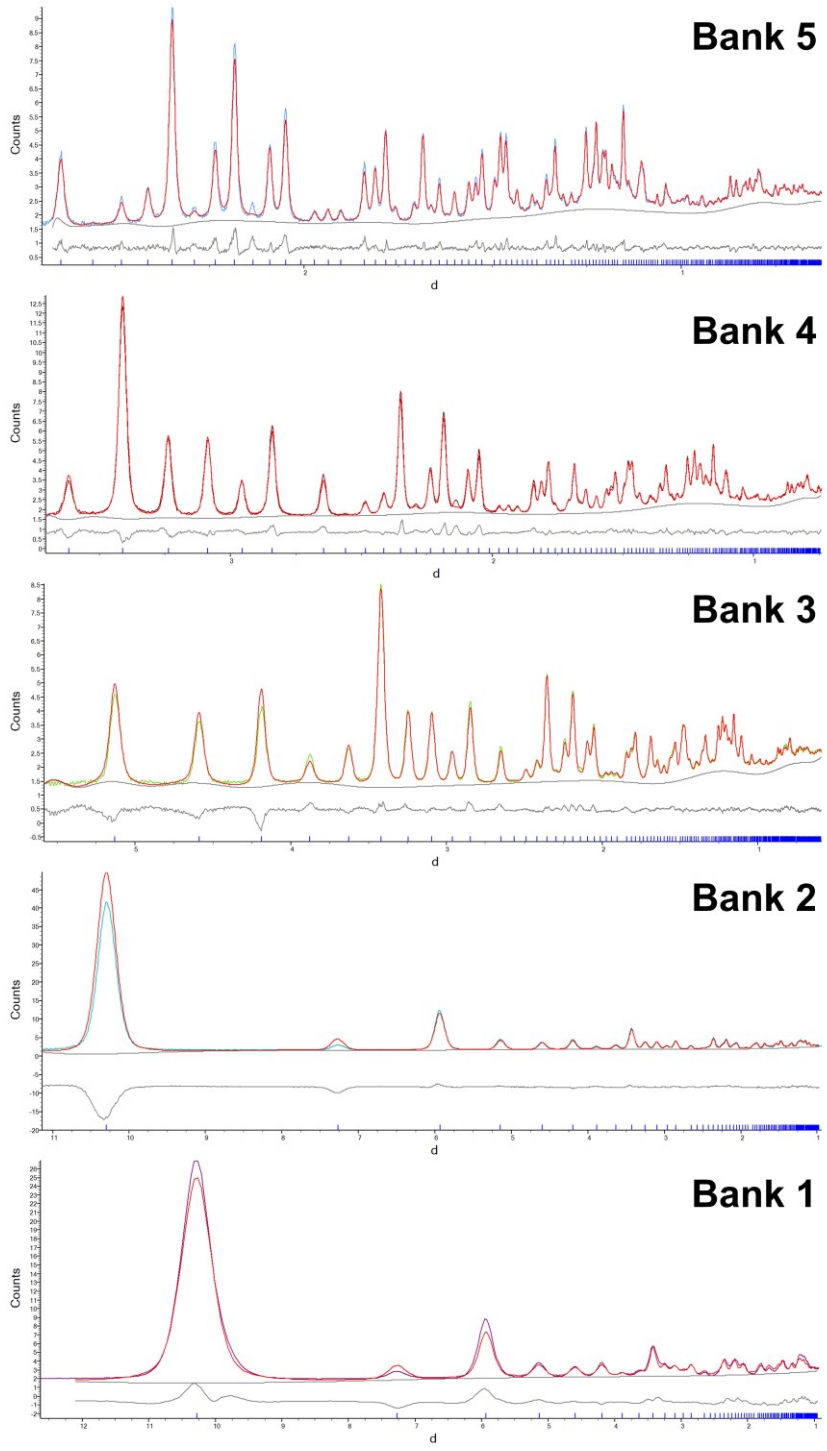

Figure IV.II.II. PND data for $Li_{7.3}Cs_{2.5}$-Rho (3.9) under 25 mbar of CO_2. Datasets are as identified.

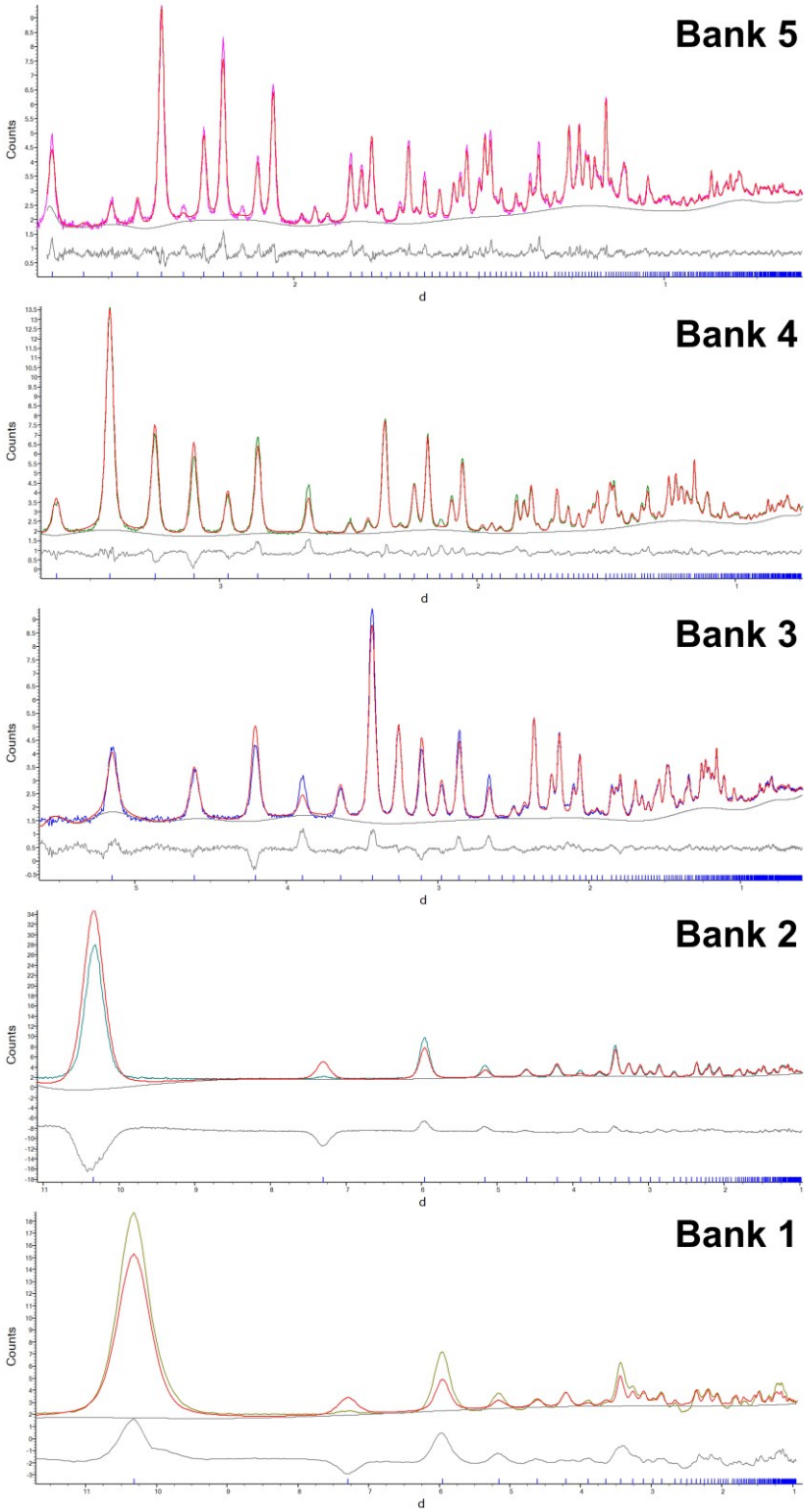

Figure IV.II.III. PND data for $Li_{7.3}Cs_{2.5}$-Rho (3.9) under 190 mbar of CO_2. Datasets are as identified.

IV.III $Li_{5.5}Zn_{2.2}$-Rho (3.9)

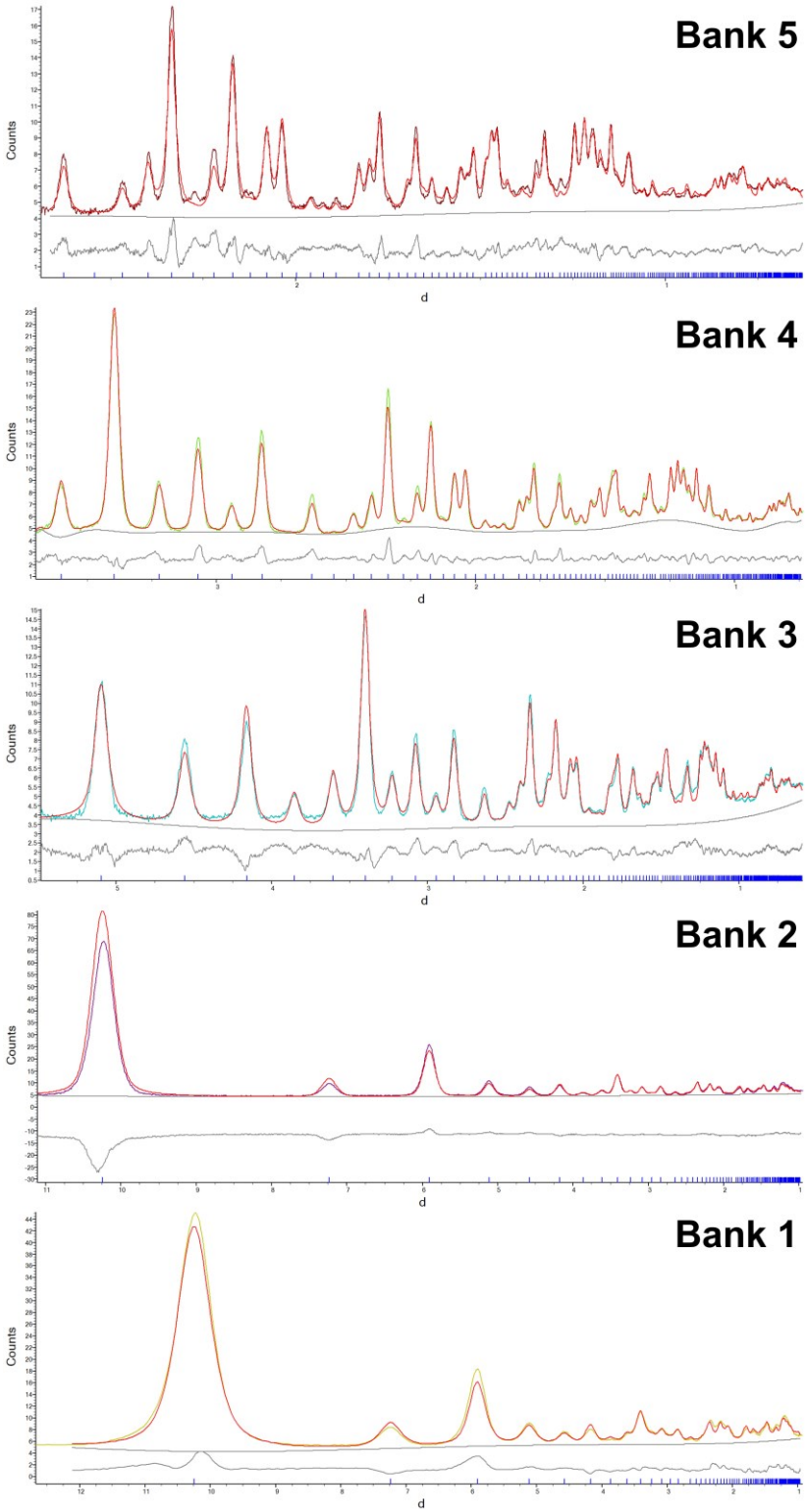

Figure IV.III.I. PND data for $Li_{5.5}Zn_{2.2}$-Rho (3.9) under 24 mbar of CO_2. Datasets are as identified.

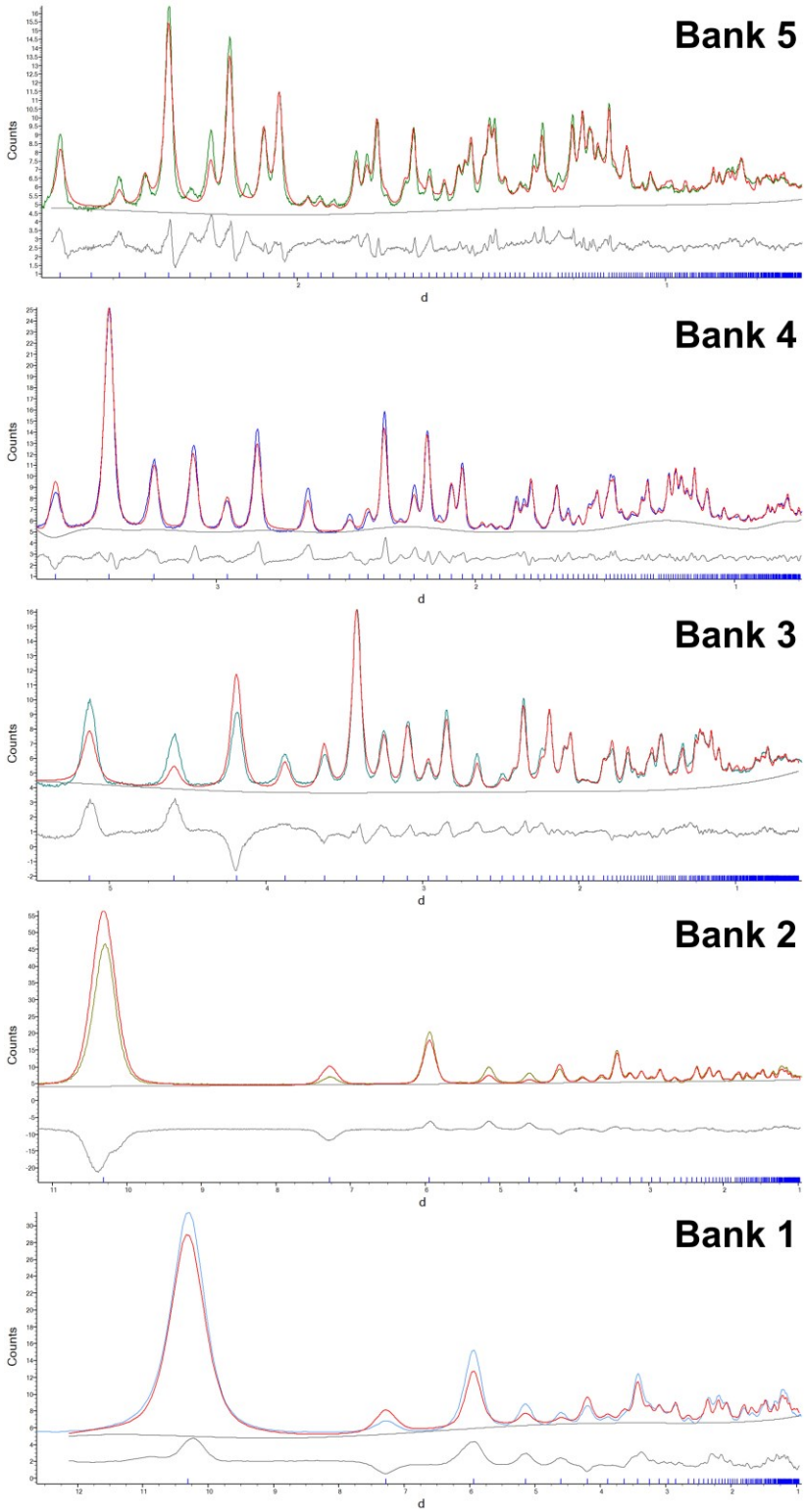

Figure IV.III.II. PND data for $Li_{5.5}Zn_{2.2}$-Rho (3.9) under 159 mbar of CO_2. Datasets are as identified.

IV.IV $Li_{9.8-x}Zn_x$-Rho (3.9)

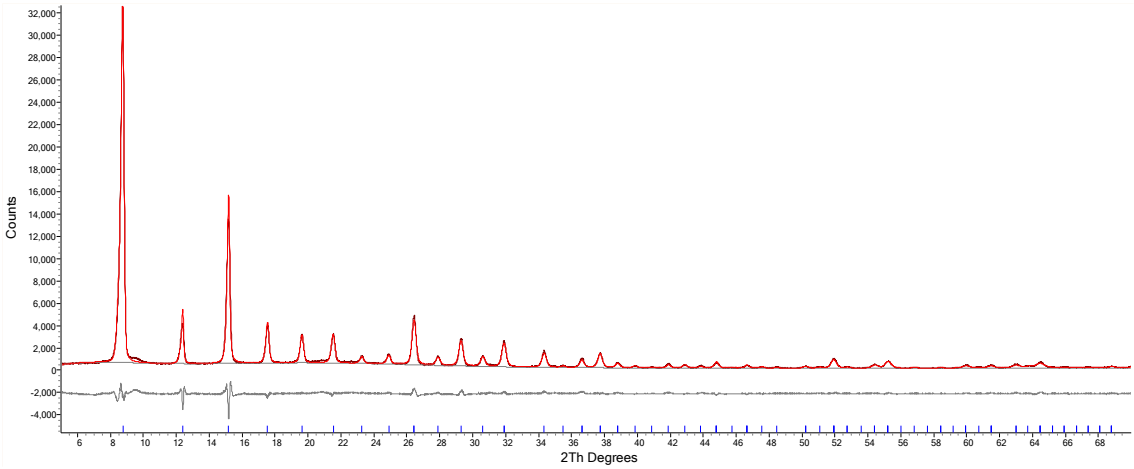

Figure IV.IV.I. Rietveld plot of dehydrated $Li_{7.4}Zn_{1.2}$-Rho (3.9). (Stoe, λ = 1.54056 Å).

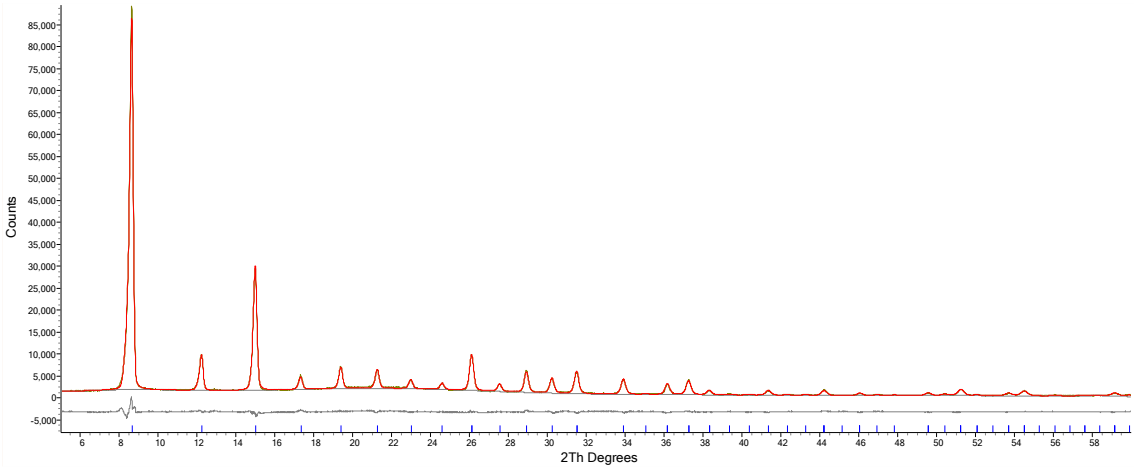

Figure IV.IV.II. Rietveld plot of dehydrated $Li_{1.2}Zn_{4.3}$-Rho (3.9). (Stoe, λ = 1.54056 Å).

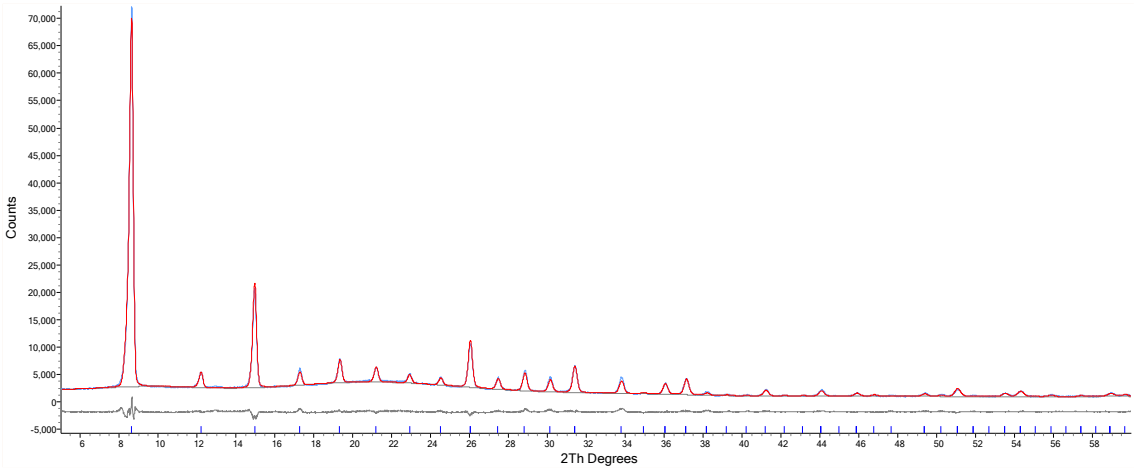

Figure IV.IV.III. Rietveld plot of dehydrated $Zn_{4.9}$-Rho (9.8). (Stoe, λ = 1.54056 Å).

IV.V PST-20

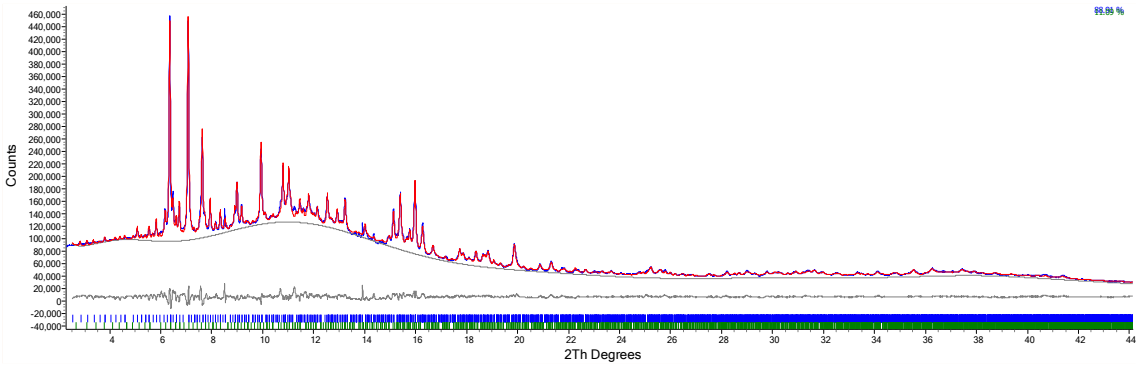

Figure IV.V.I. Rietveld plot of PST-20 fit, containing a ZSM-25 impurity. (I11, DLS, λ = 0.826956 Å).

IV.VI MER (4.2)

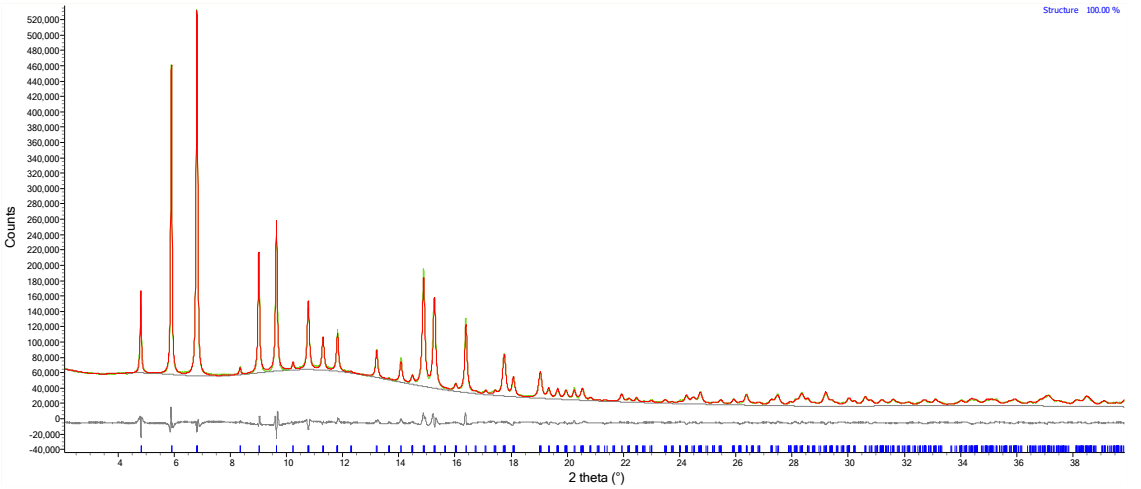

Figure IV.VI.I. Rietveld fit for $K_{6.2}$-MER (4.2) at 20 mbar. (I11, DLS, λ = 0.826956 Å).

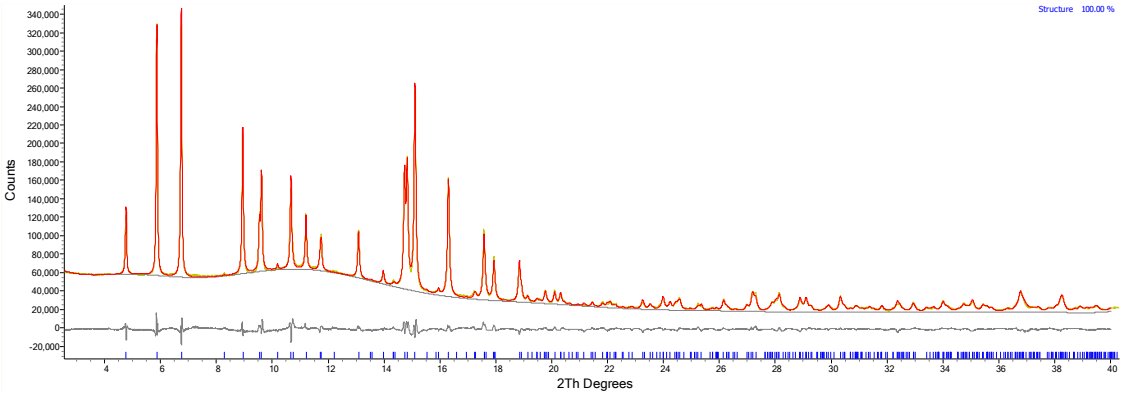

Figure IV.VI.II. Rietveld fit for $K_{6.2}$-MER (4.2) at 100 mbar. (I11, DLS, λ = 0.826956 Å).

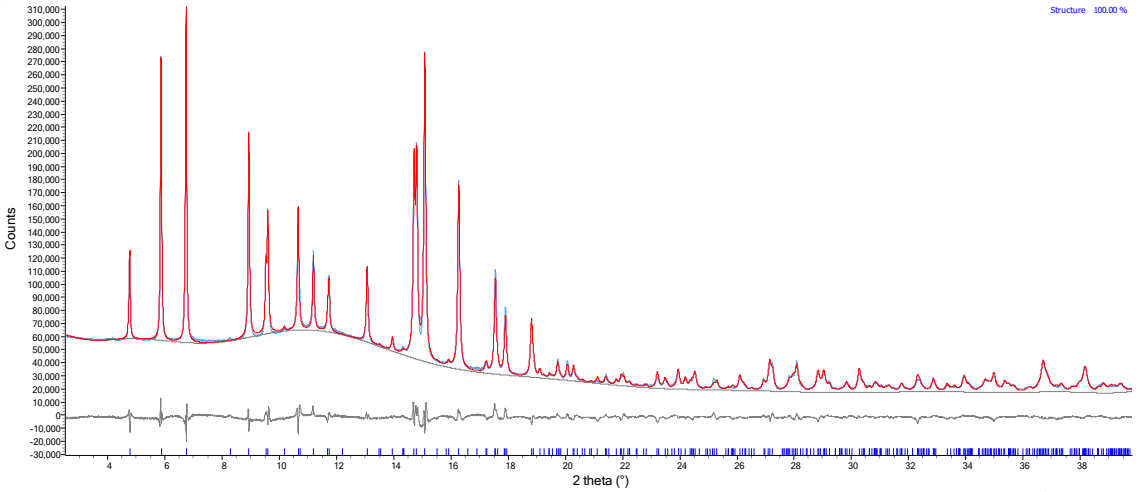

Figure IV.VI.III. Rietveld fit for $K_{6.2}$-MER (4.2) at 300 mbar. (I11, DLS, λ = 0.826956 Å).

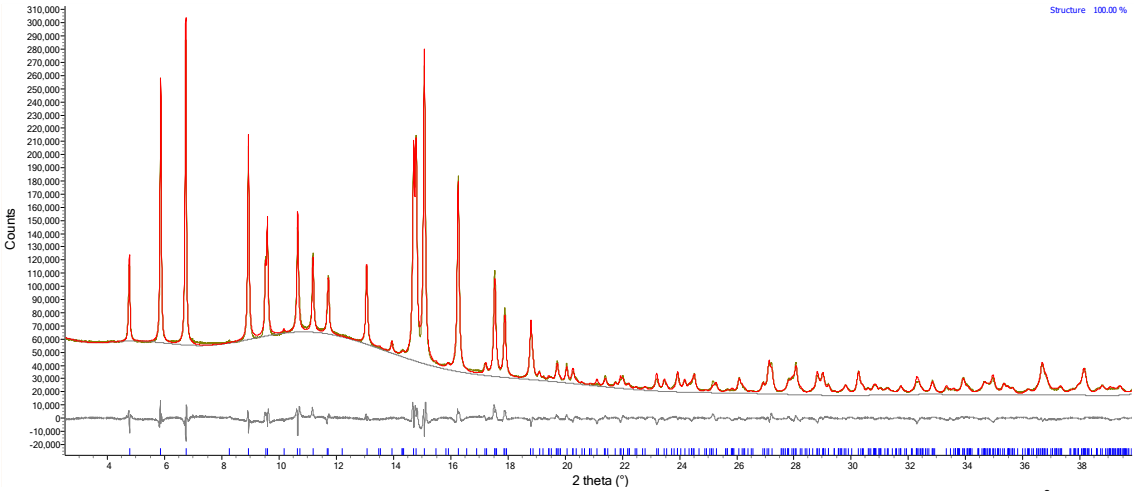

Figure IV.VI.IV. Rietveld fit for $K_{6.2}$-MER (4.2) at 510 mbar. (I11, DLS, λ = 0.826956 Å).

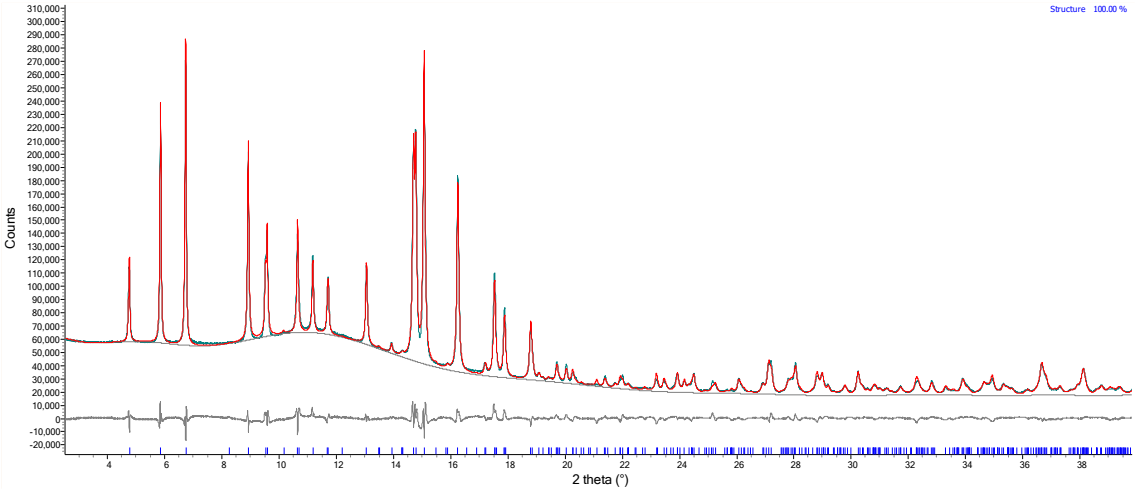

Figure IV.VI.V. Rietveld fit for $K_{6.2}$-MER (4.2) at 990 mbar. (I11, DLS, λ = 0.826956 Å).

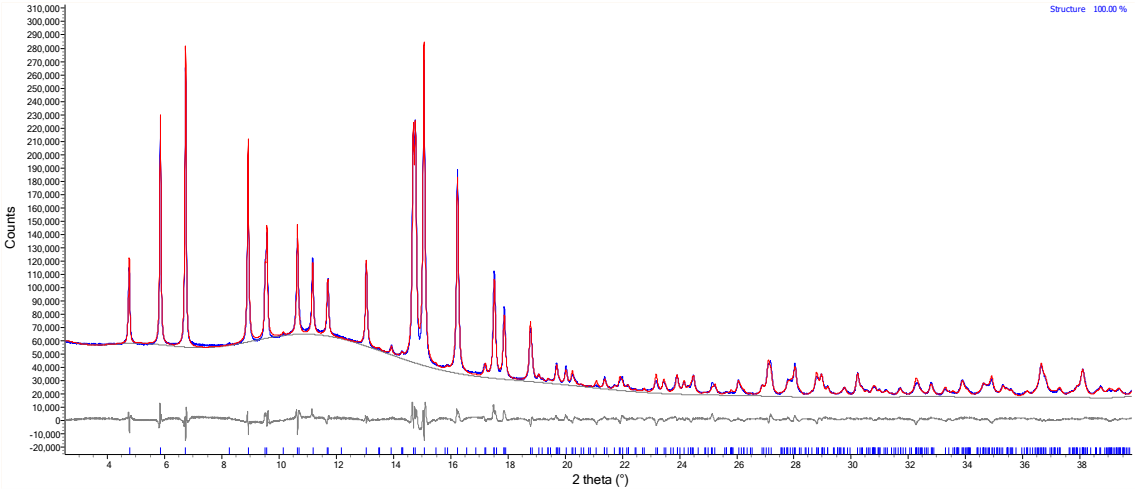

Figure IV.VI.VI. Rietveld fit for $K_{6.2}$-MER (4.2) at 1810 mbar. (I11, DLS, λ = 0.826956 Å).

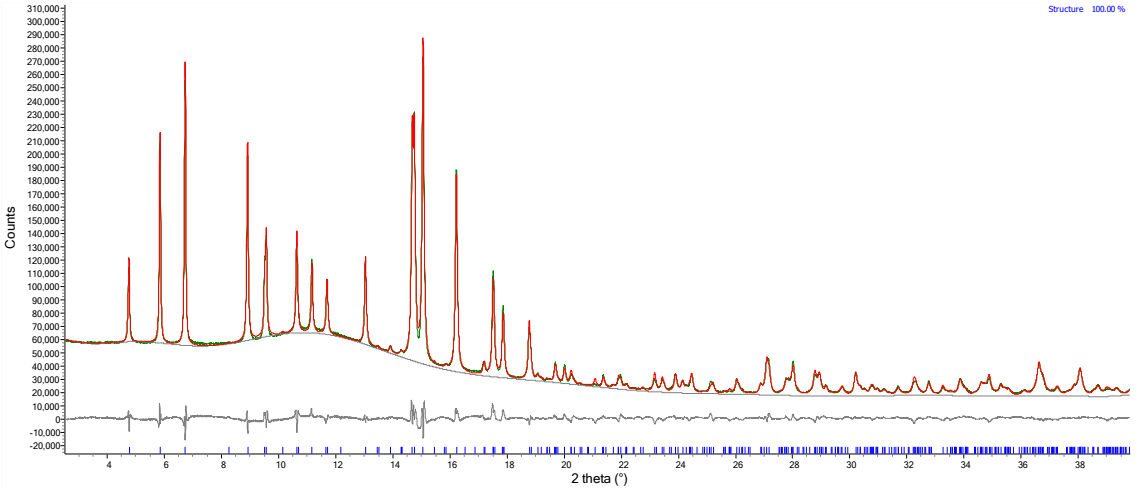

Figure IV.VI.VII. Rietveld fit for $K_{6.2}$-MER (4.2) at 4240 mbar. (I11, DLS, λ = 0.826956 Å).

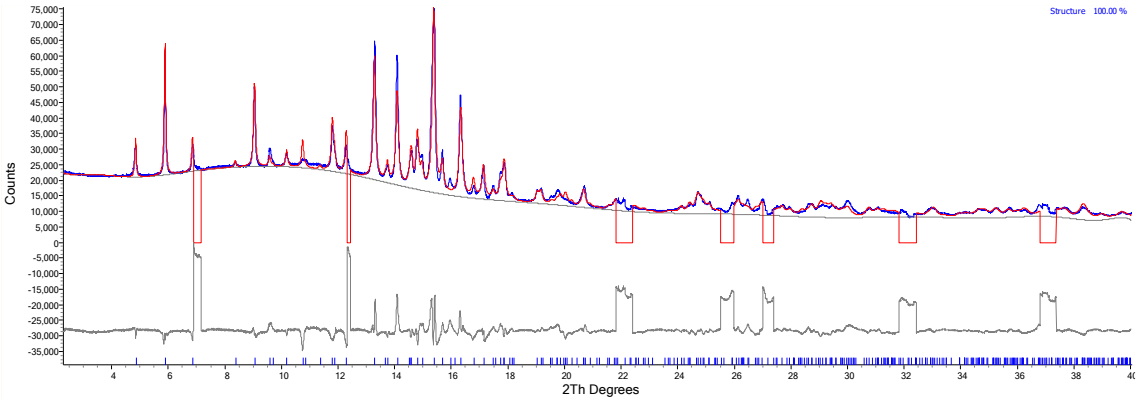

Figure IV.VI.VIII. Rietveld fit for $Cs_{6.2}$-MER (4.2) at 20 mbar. Note sections are cut out due to background effects. (I11, DLS, λ = 0.826956 Å).

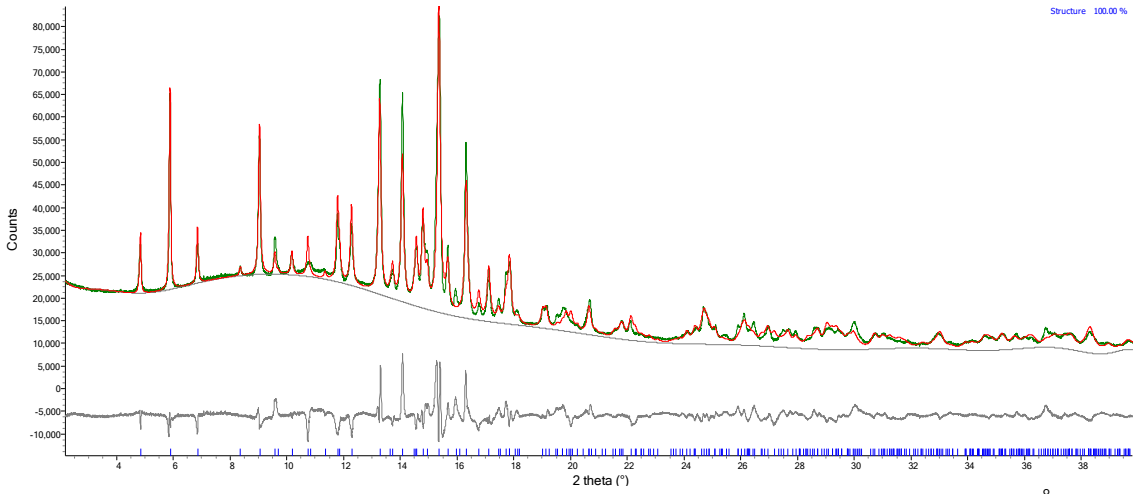

Figure IV.VI.IX. Rietveld fit for $Cs_{6.2}$-MER (4.2) at 40 mbar. (I11, DLS, λ = 0.826956 Å).

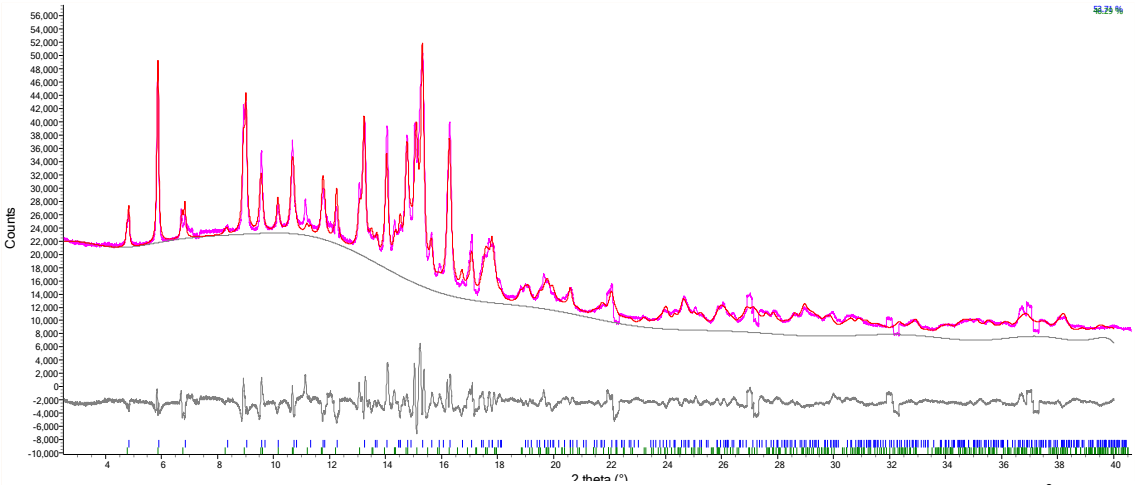

Figure IV.VI.X. Rietveld fit for $Cs_{6.2}$-MER (4.2) at 100 mbar. (I11, DLS, λ = 0.826956 Å).

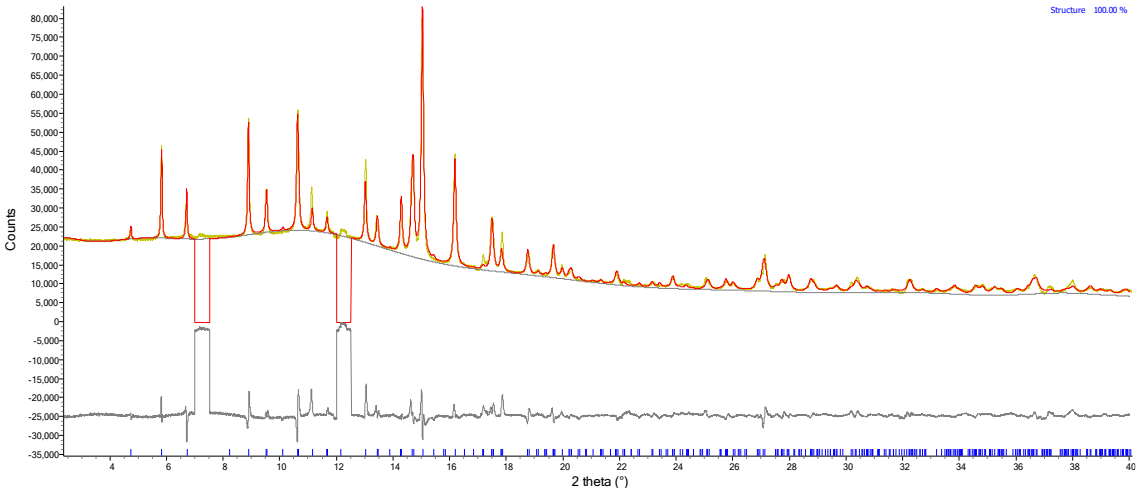

Figure IV.VI.XI. Rietveld fit for $Cs_{6.2}$-MER (4.2) at 230 mbar. Note sections are cut out due to background effects. (I11, DLS, λ = 0.826956 Å).

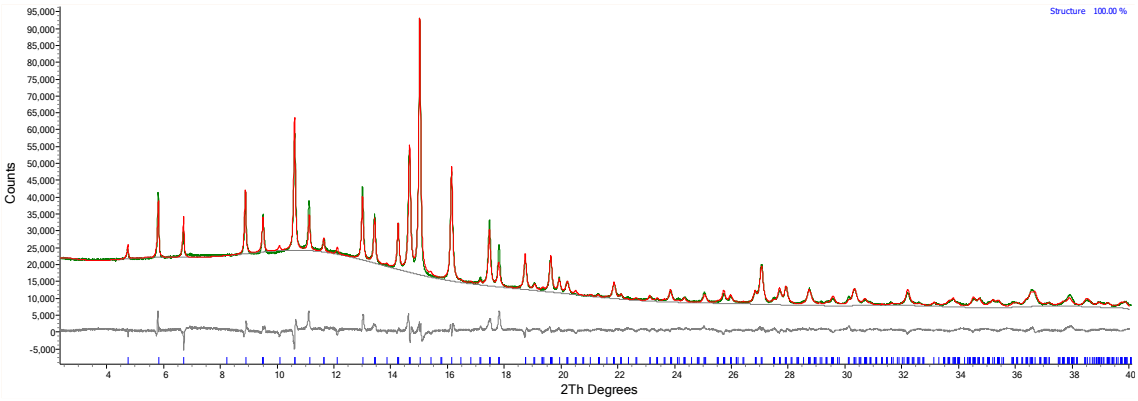

Figure IV.VI.XII. Rietveld fit for $Cs_{6.2}$-MER (4.2) at 880 mbar. (I11, DLS, λ = 0.826956 Å).

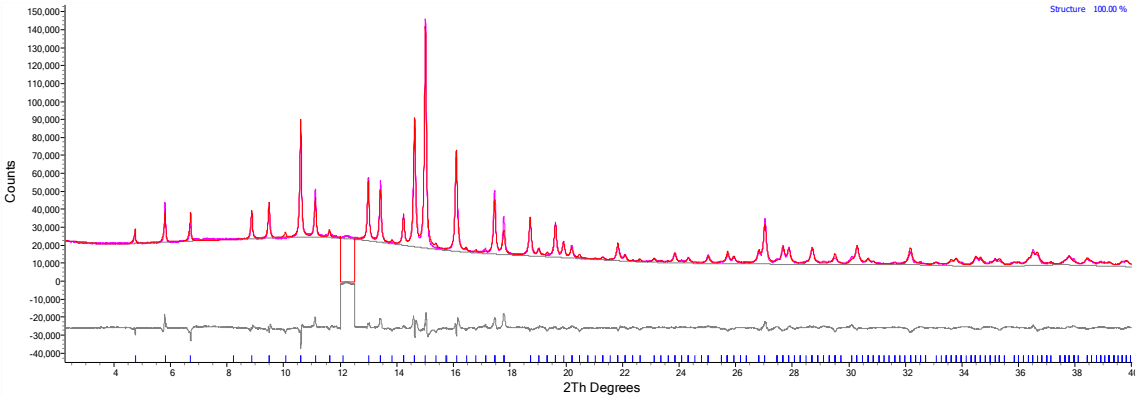

Figure IV.VI.XIII. Rietveld fit for $Cs_{6.2}$-MER (4.2) at 2980 mbar. Note sections are cut out due to background effects. (I11, DLS, λ = 0.826956 Å).

IV.VII Li-MER (4.2)

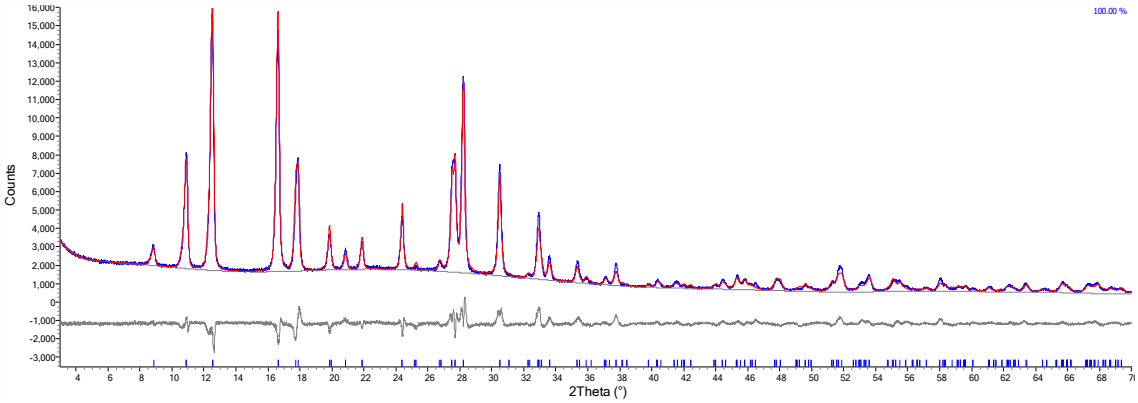

Figure IV.VII.I. Rietveld plot of hydrated $Li_{6.2}$-MER (4.2). (I11, DLS, λ = 0.826956 Å).

Appendix V. Refinement details

V.I The RHO family of materials

V.I.I Zeolite Rho

Table V.I.I. Refinement details of dehydrated Rho materials investigated through combined PND and PXRD.

Sample	**$Li_{9.8}$-Rho (3.9)**	**$Li_{7.3}Cs_{2.5}$-Rho (3.9)**	**$Li_{5.5}Zn_{2.2}$-Rho (3.9)**
Unit Cell	$Li_{10.1}[Si_{38.2}Al_{9.8}O_{96}]$	$Li_{7.8}Cs_{2.3}[Si_{38.2}Al_{9.8}O_{96}]$	$Li_{5.8}Zn_{1.9}[Si_{38.2}Al_{9.8}O_{96}]$
T (K)	298	298	298
Space Group	*I-43m*	*I-43m*	*I-43m*
X-ray Source	Stoe	Stoe	Stoe
λ_{PXRD} (Å)	1.54056	1.54056	1.54056
Neutron Source	Polaris	Polaris	Polaris
***a* (Å)**	14.255(1)	14.444(1)	14.365(1)
***V* (Å^3)**	2897(1)	3013(1)	2964(1)
R_p (PXRD)	*4.7%*	*4.2%*	*6.9%*
R_{wp} (PXRD)	*6.1%*	*5.4%*	*8.9%*
χ^2 (PXRD)	*5.3*	*2.6*	*9.2*
R_p (Bank 1)	3.4%	*3.5%*	2.9%
R_{wp} (Bank 1)	3.8%	*4.1%*	3.2%
χ^2 (Bank 1)	32	*35*	49
R_p (Bank 2)	5.0%	4.4%	5.1%
R_{wp} (Bank 2)	3.9%	3.8%	4.2%
χ^2 (Bank 2)	21	18	51
R_p (Bank 3)	2.4%	2.1%	3.7%
R_{wp} (Bank 3)	2.5%	2.1%	3.8%
χ^2 (Bank 3)	10	5.1	40
R_p (Bank 4)	2.8%	2.0%	2.1%
R_{wp} (Bank 4)	2.6%	1.9%	2.1%
χ^2 (Bank 4)	20	9.6	27
R_p (Bank 5)	3.1%	2.3%	3.7%
R_{wp} (Bank 5)	2.9%	2.2%	3.5%
χ^2 (Bank 5)	8.6	4.4	25
R_p (Total)	4.7%	4.2%	6.8%
R_{wp} (Total)	3.3%	2.9%	3.6%
χ^2 (Total)	*11*	*7.0*	*25*

Table V.I.II. Refinement details of Rho (3.9) materials under CO_2 pressure investigated via PND data.

Sample	**$Li_{9.8}$-Rho (3.9)**	**$Li_{9.8}$-Rho (3.9)**	**$Li_{9.8}$-Rho (3.9)**
Pressure (mbar)	26	70	175
Unit Cell	$Li_{9.9}[Si_{38.2}Al_{9.8}O_{96}].(CO_2)_{3.6}$	$Li_{10.0}[Si_{38.2}Al_{9.8}O_{96}].(CO_2)_{6.5}$	$Li_{9.8}[Si_{38.2}Al_{9.8}O_{96}].(CO_2)_{8.9}$
T (K)	298	298	298
Space Group	*I-43m*	*I-43m*	*I-43m*
Neutron Source	Polaris	Polaris	Polaris
***a* (Å)**	14.296(2)	14.340(3)	14.480(3)
***V* (Å^3)**	2922(1)	2949(2)	3036(2)
R_p (Bank 1)	4.7%	6.1%	6.5%
R_{wp} (Bank 1)	5.6%	7.4%	7.3%
χ^2 (Bank 1)	66	420	154
R_p (Bank 2)	10.4%	12.5%	14.1%
R_{wp} (Bank 2)	7.0%	8.7%	9.7%
χ^2 (Bank 2)	66	376	193
R_p (Bank 3)	4.6%	5.0%	4.9%
R_{wp} (Bank 3)	4.6%	5.0%	5.0%
χ^2 (Bank 3)	32	146	59
R_p (Bank 4)	3.4%	3.9%	3.8%
R_{wp} (Bank 4)	3.1%	3.3%	3.1%
χ^2 (Bank 4)	28	114	44
R_p (Bank 5)	4.5%	4.5%	4.2%
R_{wp} (Bank 5)	4.2%	4.1%	3.7%
χ^2 (Bank 5)	17	59	20
R_p (Total)	6.1%	6.8%	7.1%
R_{wp} (Total)	4.9%	5.7%	5.9%
χ^2 (Total)	37	185	83

Table V.I.II.(continued) Refinement details of Rho (3.9) materials under CO_2 pressure investigated via PND data.

Sample	**$Li_{9.8}$-Rho (3.9)**	**$Li_{7.3}Cs_{2.5}$-Rho (3.9)**	**$Li_{7.3}Cs_{2.5}$-Rho (3.9)**
Pressure (mbar)	1200	1	25
Unit Cell	$Li_{9.8}[Si_{38.2}Al_{9.8}O_{96}].(CO_2)_{14.0}$	$Li_{8.0}Cs_{2.5}[Si_{38.2}Al_{9.8}O_{96}]$	$Li_{8.3}Cs_{2.5}[Si_{38.2}Al_{9.8}O_{96}].(CO_2)_{3.5}$
T (K)	298	298	298
Space Group	*I-43m*	*I-43m*	*I-43m*
Neutron Source	Polaris	Polaris	Polaris
***a* (Å)**	14.641(3)	14.470(1)	14.517(1)
***V* (Å³)**	3138(2)	3030(1)	3059(1)
R_p (Bank 1)	3.2%	3.5%	4.7%
R_{wp} (Bank 1)	4.7%	4.1%	5.3%
χ^2 (Bank 1)	64	35	117
R_p (Bank 2)	9.3%	4.9%	7.7%
R_{wp} (Bank 2)	10.2%	4.0%	5.1%
χ^2 (Bank 2)	266	19	69
R_p (Bank 3)	5.4%	2.1%	2.0%
R_{wp} (Bank 3)	5.1%	2.1%	2.0%
χ^2 (Bank 3)	69	5.3	10
R_p (Bank 4)	3.8%	2.0%	2.0%
R_{wp} (Bank 4)	3.4%	1.9%	1.9%
χ^2 (Bank 4)	58	9.6	21
R_p (Bank 5)	4.3%	2.1%	2.1%
R_{wp} (Bank 5)	3.5%	1.9%	2.0%
χ^2 (Bank 5)	21	3.6	7.8%
R_p (Total)	5.6%	3.0%	3.8%
R_{wp} (Total)	6.0%	2.7%	3.2%
χ^2 (Total)	98	10	31

Table V.I.II.(continued) Refinement details of Rho (3.9) materials under CO_2 pressure investigated via PND data.

Sample	**$Li_{7.3}Cs_{2.5}$-Rho (3.9)**	**$Li_{5.5}Zn_{2.2}$-Rho (3.9)**	**$Li_{5.5}Zn_{2.2}$-Rho (3.9)**
Pressure (mbar)	190	24	159
Unit Cell	$Li_{7.6}Cs_{2.5}[Si_{38.2}Al_{9.8}O_{96}].(CO_2)_{8.6}$	$Li_{5.5}Zn_{2.1}[Si_{38.2}Al_{9.8}O_{96}].(CO_2)_{3.1}$	$Li_{5.5}Zn_{2.1}[Si_{38.2}Al_{9.8}O_{96}].(CO_2)_{7.1}$
T (K)	298	298	298
Space Group	*I-43m*	*I-43m*	*I-43m*
Neutron Source	Polaris	Polaris	Polaris
***a* (Å)**	14.566(2)	14.438(2)	14.523(3)
***V* (Å^3)**	3091(1)	3010(1)	3063(2)
R_p (Bank 1)	7.3%	3.5%	4.1%
R_{wp} (Bank 1)	8.1%	3.8%	4.5%
χ^2 (Bank 1)	114	72	243
R_p (Bank 2)	11.4%	7.0%	7.7%
R_{wp} (Bank 2)	7.5%	5.1%	6.7%
χ^2 (Bank 2)	72	83	361
R_p (Bank 3)	2.7%	3.1%	3.9%
R_{wp} (Bank 3)	2.7%	3.5%	3.9%
χ^2 (Bank 3)	9.0	36	114
R_p (Bank 4)	2.7%	2.2%	2.7%
R_{wp} (Bank 4)	2.3%	2.1%	2.4%
χ^2 (Bank 4)	15	28	96
R_p (Bank 5)	2.5%	3.4%	3.6%
R_{wp} (Bank 5)	2.2%	3.2%	3.2%
χ^2 (Bank 5)	4.4	22	56
R_p (Total)	5.3%	4.2%	4.7%
R_{wp} (Total)	4.6%	3.6%	4.3%
χ^2 (Total)	29	44	161

Table V.I.III. Refinement details of dehydrated $Li_{9.8-x}Zn_x$-Rho (3.9) samples.

Sample	**$Li_{7.4}Zn_{1.2}$-Rho (3.9)**	**$Li_{1.2}Zn_{4.3}$-Rho (3.9)**	**$Zn_{4.9}$-Rho (3.9)**
Unit Cell	$Zn_{1.4}Si_{38.2}Al_{9.8}O_{96}$	$Zn_{4.2}Si_{38.2}Al_{9.8}O_{96}$	$Zn_{4.9}Si_{38.2}Al_{9.8}O_{96}$
T (K)	298	298	298
Space Group	*I*-43*m*	*I*-43*m*	*I*-43*m*
X-ray Source	Stoe	Stoe	Stoe
λ (Å)	1.54056	1.54056	1.54056
***a* (Å)**	14.303(1)	14.481(1)	14.533(1)
***V* (Å^3)**	2926(1)	3037(1)	3069(1)
R_p	6.5%	3.2%	3.3%
R_{wp}	8.6%	4.1%	4.3%
χ^2	6.0	3.8	4.9

V.I.II ZSM-25

Table V.I.IV. Refinement summary for dehydrated calcined (Na,H)-ZSM-25 and templated (Na,TEA)-ZSM-25.

Sample	**(Na,H)-ZSM-25 (dehydrated)**	**(Na,TEA)-ZSM-25 (dehydrated)**
Measured Chemical Formula	$Na_{285}H_{40}[Si_{1106}Al_{325}O_{2880}]$	$Na_{285}N_{40}C_{320}[Si_{1115}Al_{325}O_{2880}]$
Refined Chemical Formula	$Na_{282}[Si_{1106}Al_{325}O_{2880}]$	$Na_{273}N_{38}C_{304}[Si_{1106}Al_{325}O_{2880}]$
T (K)	298	298
Space Group	*I*$\bar{4}$3*m*	*I*$\bar{4}$3*m*
X-ray Source	ID-31, ESRF	I-11, DLS
λ (Å)	0.320012	0.826956
***a* (Å)**	42.631(1)	42.980(1)
***V* (Å^3)**	77480(5)	79396(6)
R_p	1.9%	2.3%
R_{wp}	2.4%	3.1%
χ^2	1.7	0.7

V.II Merlinoite

V.II.I MER (3.8)

Table V.II.I. Crystallographic details of the refinements of hydrated $M_{5.9}TEA_{0.8}$-MER (3.8) samples.

Sample	**$Li_{5.9}TEA_{0.8}$-MER (3.8)**	**$Na_{5.9}TEA_{0.8}$-MER (3.8)**	**$K_{5.9}TEA_{0.8}$-MER (3.8)**	**$Cs_{5.9}TEA_{0.8}$-MER (3.8)**
Unit Cell	$(NC_8H_{20})_{0.8}$ $Si_{32}O_{64}$	$Na_{6.0}(NC_8H_{20})_{0.8}$ $Si_{32}O_{64}$	$K_{6.1}(NC_8H_{20})_{0.8}$ $Si_{32}O_{64}$	$Cs_{5.7}(NC_8H_{20})_{0.8}$ $Si_{32}O_{64}$
T (K)	298	298	298	298
Space Group	*I*4/*mmm*	*I*4/*mmm*	*I*4/*mmm*	*I*4/*mmm*
X-ray Source	Stoe	Stoe	Stoe	Stoe
λ (Å)	1.54056	1.54056	1.54056	1.54056
***a* (Å)**	14.157(1)	14.132(1)	14.166(1)	14.193(1)
***c* (Å)**	10.016(1)	10.067(1)	9.989(1)	10.042(1)
***V* (Å^3)**	2008(1)	2011(1)	2005(1)	2023(1)
R_p	9.6%	7.3%	7.1%	8.5%
R_{wp}	12.7%	9.9%	9.3%	11.1%
χ^2	12	8.9	5.8	1.5

Table V.II.II. Crystallographic details of refinements of hydrated $M_{6.7}$-MER (3.8) samples.

Sample	**$Na_{6.7}$-MER (3.8)**	**$K_{6.7}$-MER (3.8)**	**$Cs_{6.2}K_{0.5}$-MER (3.8)**
Unit Cell	$Na_{6.7}Si_{32}O_{64}.O_{20.0}$	$K_{6.5}Si_{32}O_{64}.O_{18.5}$	$Cs_{6.3}Si_{32}O_{64}.O_{12.9}$
T (K)	298	298	298
Space Group	*Immm*	$P4_2/nmc$	$P4_2/nmc$
X-ray Source	Stoe	Stoe	Panalytical
λ (Å)	1.54056	1.54056	1.54056
***a* (Å)**	14.139(2)	14.114(1)	14.219(1)
***b* (Å)**	14.145(2)	-	-
***c* (Å)**	10.023(1)	9.916(1)	10.015(1)
***V* (Å^3)**	2005(1)	1975(1)	2025(1)
R_p	7.2%	7.4%	6.2%
R_{wp}	9.4%	9.4%	8.0%
χ^2	4.9	2.3	3.4

Table V.II.III. Crystallographic details of the refinements of dehydrated $M_{5.9}TEA_{0.8}$-MER (3.8) samples.

Sample	**$Li_{5.9}TEA_{0.8}$-MER (3.8)**	**$Na_{5.9}TEA_{0.8}$-MER (3.8)**	**$K_{5.9}TEA_{0.8}$-MER (3.8)**	**$Cs_{5.9}TEA_{0.8}$-MER (3.8)**
Unit Cell	$(NC_8H_{20})_{0.8}$ $Si_{32}O_{64}$	$Na_{6.0}(NC_8H_{20})_{0.8}$ $Si_{32}O_{64}$	$K_{5.9}(NC_8H_{20})_{0.8}$ $Si_{32}O_{64}$	$Cs_{6.0}(NC_8H_{20})_{0.8}$ $Si_{32}O_{64}$
T (K)	298	298	298	298
Space Group	*Immm*	*Immm*	$P4_2/nmc$	$P4_2/nmc$
X-ray Source	Stoe	Stoe	Stoe	Stoe
λ (Å)	1.54056	1.54056	1.54056	1.54056
***a* (Å)**	13.262(2)	13.554(1)	13.652(1)	13.789(1)
***b* (Å)**	13.198(2)	13.525(1)	-	-
***c* (Å)**	10.142(1)	10.100(1)	9.998(1)	10.039(1)
***V* (Å³)**	1775(1)	1852(1)	1863(1)	1909(1)
R_p	7.0%	5.5%	6.7%	5.0%
R_{wp}	8.9%	7.2%	8.8%	6.5%
χ^2	6.1	4.6	5.3	1.4

Table V.II.IV. Crystallographic details of the refinements of dehydrated $M_{6.7}$-MER (3.8) samples.

Sample	**$Na_{6.7}$-MER (3.8)**	**$K_{6.7}$-MER (3.8)**	**$Cs_{6.2}K_{0.5}$-MER (3.8)**
Unit Cell	$Na_{6.7}Si_{32}O_{64}$	$K_{6.4}Si_{32}O_{64}$	$Cs_{6.0}Si_{32}O_{64}$
T (K)	298	298	298
Space Group	*Immm*	$P4_2/nmc$	$P4_2/nmc$
X-ray Source	Stoe	Stoe	Stoe
λ (Å)	1.54056	1.54056	1.54056
***a* (Å)**	13.493(1)	13.586(1)	13.751(1)
***b* (Å)**	13.520(1)	-	-
***c* (Å)**	9.915(1)	9.876(1)	9.950(1)
***V* (Å^3)**	1809(1)	1823(1)	1881(1)
R_p	6.3%	6.3%	7.3%
R_{wp}	8.5%	8.1%	9.3%
χ^2	6.8	2.8	1.4

Table V.II.V. Crystallographic details of the refined dehydrated $M_{6.7}$-MER (3.8) samples with adsorbed CO_2.

Sample	**$Na_{6.7}$-MER (317 mbar)**	**$Na_{6.7}$-MER (684 mbar)**	**$K_{6.7}$-MER (500 mbar)**	**$Cs_{6.2}K_{0.5}$-MER (500 mbar)**
Unit Cell	$Na_{6.7}Si_{32}O_{64}.(CO_2)_{4.9}$	$Na_{6.8}Si_{32}O_{64}.(CO_2)_{7.6}$	$K_{7.0}Si_{32}O_{64}.(CO_2)_{5.8}$	$Cs_{6.7}Si_{32}O_{64}.(CO_2)_{7.4}$
T (K)	298	298	298	298
Space Group	*Immm*	*Immm*	$P4_2/nmc$	$P4_2/nmc$
X-ray Source	Stoe	Stoe	Stoe	Stoe
λ (Å)	1.54056	1.54056	1.54056	1.54056
***a* (Å)**	13.476(1)	14.120(1)	14.007(1)	14.197(1)
***b* (Å)**	13.440(2)	14.122(1)	-	-
***c* (Å)**	10.013(1)	10.031(1)	9.845(1)	10.016(1)
***V* (Å³)**	1814(1)	2000(1)	1932(1)	2019(1)
R_p	5.9%	5.4%	6.8%	6.0%
R_{wp}	7.8%	7.1%	8.7%	7.5%
χ^2	5.5	4.7	3.2	1.4

V.II.II MER (4.2)

Table V.II.VI. Crystallographic details of refinement of $K_{6.2-x}Na_x$-MER (4.2) materials.

Sample	**$K_{5.7}Na_{0.5}$-MER (4.2)**	**$K_{5.2}Na_{1.0}$-MER (4.2)**	**$K_{4.2}Na_{1.0}$-MER (4.2)**
Unit Cell	$K_{5.4}Si_{25.8}Al_{6.2}O_{64}$	$K_{6.1}Si_{25.8}Al_{6.2}O_{64}$	$K_{4.3}Si_{25.8}Al_{6.2}O_{64}$
T (K)	298	298	298
Space Group	*Pmmn*	*Pmmn*	*Pmmn*
X-ray Source	I11	Stoe	Stoe
λ (Å)	0.826398	1.540560	1.540560
***a* (Å)**	13.978(1)	13.918(1)	13.753(1)
***b* (Å)**	13.913(1)	13.746(1)	13.647(1)
***c* (Å)**	9.820(1)	9.862(1)	9.851(1)
***V* (Å³)**	1910(1)	1887(1)	1849(1)
R_{wp}	3.3	6.1	5.7
R_p	2.4	4.7	4.5
χ^2	48	8	5
Sample	**$K_{3.2}Na_{3.0}$-MER (4.2)**	**$K_{2.2}Na_{4.0}$-MER (4.2)**	**$K_{1.2}Na_{5.0}$-MER (4.2)**
Unit Cell	$K_{3.0}Na_{1.5}Si_{25.8}Al_{6.2}O_{64}$	$K_{1.5}Na_{4.1}Si_{25.8}Al_{6.2}O_{64}$	$K_{1.2}Na_{4.2}Si_{25.8}Al_{6.2}O_{64}$
T (K)	298	298	298
Space Group	*Pmmn*	*Pmmn*	*Pmmn*
X-ray Source	I11	Stoe	I11
λ (Å)	0.826398	1.540560	0.826398
***a* (Å)**	13.671(1)	13.629(1)	13.606(1)
***b* (Å)**	13.598(1)	13.564(1)	13.551(1)
***c* (Å)**	9.864(1)	9.846(1)	9.845(1)
***V* (Å³)**	1833(1)	1820(1)	1815(1)
R_{wp}	3.3	5.8	3.4
R_p	2.4	4.5	2.4
χ^2	48	7	47

Table V.II.VII. Crystallographic details of refinement of $K_{6.2}$-MER (4.2) under exposure to CO_2.

Sample	**$K_{6.2}$-MER (4.2) (dh)**	**$K_{6.2}$-MER (4.2) (20 mbar)**	**$K_{6.2}$-MER (4.2) (100 mbar)**
Unit Cell	$K_{6.1}Si_{25.8}Al_{6.2}O_{64}$	$K_{6.4}Si_{25.8}Al_{6.2}O_{64}$	$K_{6.2}Si_{25.8}Al_{6.2}O_{64}.(CO_2)_{5.7}$
T (K)	298	298	298
Space Group	*Pmmn*	*Pmmn*	$P4_2/nmc$
X-ray Source	I11	I11	I11
λ (Å)	0.826398	0.826398	0.826398
***a* (Å)**	13.950(1)	13.948(1)	14.069(1)
***b* (Å)**	13.894(1)	13.901(1)	
***c* (Å)**	9.831(1)	9.834(1)	9.873(1)
***V* (Å³)**	1905(1)	1907(1)	1954(1)
R_{wp}	2.4	2.8	2.8
R_p	1.9	2.1	2.1
χ^2	24	34	33
Sample	**$K_{6.2}$-MER (4.2) (300 mbar)**	**$K_{6.2}$-MER (4.2) (510 mbar)**	**$K_{6.2}$-MER (4.2) (990 mbar)**
Unit Cell	$K_{6.3}Si_{25.8}Al_{6.2}O_{64}.(CO_2)_{7.1}$	$K_{6.4}Si_{25.8}Al_{6.2}O_{64}.(CO_2)_{7.4}$	$K_{6.3}Si_{25.8}Al_{6.2}O_{64}.(CO_2)_{7.8}$
T (K)	298	298	298
Space Group	$P4_2/nmc$	$P4_2/nmc$	$P4_2/nmc$
X-ray Source	I11	I11	I11
λ (Å)	0.826398	0.826398	0.826398
***a* (Å)**	14.094(1)	14.102(1)	14.107(1)
***c* (Å)**	9.896(1)	9.904(1)	9.912(1)
***V* (Å³)**	1966(1)	1970(1)	1973(1)
R_{wp}	2.9	2.9	2.9
R_p	2.2	2.2	2.2
χ^2	35	37	36
Sample	**$K_{6.2}$-MER (4.2) (1810 mbar)**		**$K_{6.2}$-MER (4.2) (4240 mbar)**
Unit Cell	$K_{6.3}Si_{25.8}Al_{6.2}O_{64}.(CO_2)_{8.1}$		$K_{6.3}Si_{25.8}Al_{6.2}O_{64}.(CO_2)_{8.5}$
T (K)	298		298
Space Group	$P4_2/nmc$		$P4_2/nmc$
X-ray Source	I11		I11
λ (Å)	0.826398		0.826398
***a* (Å)**	14.113(1)		14.112(1)
***c* (Å)**	9.918(1)		9.928(1)
***V* (Å³)**	1975(1)		1977(1)
R_{wp}	3.0		2.9
R_p	2.2		2.1
χ^2	38		36

Table V.II.VIII. Crystallographic details of refinement of $Cs_{6.2}$-MER (4.2) under exposure to CO_2.

Sample	**$Cs_{6.2}$-MER (4.2) (dh)**	**$Cs_{6.2}$-MER (4.2) (20 mbar)**	**$Cs_{6.2}$-MER (4.2) (40 mbar)**
Unit Cell	$Cs_{5.9}Si_{25.8}Al_{6.2}O_{64}$	$Cs_{5.5}Si_{25.8}Al_{6.2}O_{64}$ $.(CO_2)_{1.6}$	$Cs_{5.5}Si_{25.8}Al_{6.2}O_{64}$ $.(CO_2)_{1.8}$
T (K)	298	298	298
Space Group	*Pmmn*	$P4_2/nmc$	$P4_2/nmc$
X-ray Source	I11	I11	I11
λ (Å)	0.826398	0.826398	0.826398
***a* (Å)**	13.794(1)	13.819(1)	13.833(1)
***b* (Å)**	13.776(1)	-	-
***c* (Å)**	9.940(1)	9.897(1)	9.898(1)
***V* (Å³)**	1889(1)	1890(1)	1894(1)
R_{wp}	5.5	5.5	5.5
R_p	3.8	3.7	3.7
χ^2	54	53	53
Sample	**$Cs_{6.2}$-MER (4.2) (100 mbar, narrow)**		**$Cs_{6.2}$-MER (4.2) (100 mbar, wide)**
Unit Cell	$Cs_{5.5}Si_{25.8}Al_{6.2}O_{64}.(CO_2)_{2.0}$		$Cs_{4.8}Si_{25.8}Al_{6.2}O_{64}.(CO_2)_{7.7}$
T (K)	298		
Space Group	$P4_2/nmc$		
X-ray Source	I11		
λ (Å)	0.826398		
***a* (Å)**	13.874(1)		14.077(1)
***c* (Å)**	9.921(1)		9.903(1)
***V* (Å³)**	1910(1)		1962(1)
R_{wp}	4.8		
R_p	3.3		
χ^2	38		
Sample	**$Cs_{6.2}$-MER (4.2) (230 mbar)**	**$Cs_{6.2}$-MER (4.2) (880 mbar)**	**$Cs_{6.2}$-MER (4.2) (2980 mbar)**
Unit Cell	$Cs_{4.8}Si_{25.8}Al_{6.2}O_{64}$ $.(CO_2)_{6.1}$	$Cs_{5.3}Si_{25.8}Al_{6.2}O_{64}$ $.(CO_2)_{6.4}$	$Cs_{5.8}Si_{25.8}Al_{6.2}O_{64}$ $.(CO_2)_{7.1}$
T (K)	298	298	298
Space Group	$P4_2/nmc$	$P4_2/nmc$	$P4_2/nmc$
X-ray Source	I11	I11	I11
λ (Å)	0.826398	0.826398	0.826398
***a* (Å)**	14.129(1)	14.143(1)	14.152(1)
***c* (Å)**	9.949(1)	9.978(1)	10.007(1)
***V* (Å³)**	1986(1)	1996(1)	2004(1)
R_{wp}	4.2	3.3	4.3
R_p	2.8	2.2	2.9
χ^2	27	17	32

V.II.III Li,M-MER (4.2)

Table V.II.IX. Crystallographic details of refinement of hydrated $Li_{6.2}$-MER (4.2).

Sample	**$Li_{6.2}$-MER (4.2) (h)**
Unit Cell	$Si_{25.9}Al_{6.1}O_{64}.O_{18.2}$
***T* (K)**	298
Space Group	*Immm*
X-ray Source	Stoe
λ (Å)	1.54056
***a* (Å)**	14.150(1)
***b* (Å)**	14.145(1)
***c* (Å)**	9.926(1)
***V* (Å^3)**	1986.6(2)
R_p	4.7%
R_{wp}	6.4%
χ^2	1.9

Table V.II.X. Crystallographic details of refinement of dehydrated $Li_{6.2}$-MER (4.2) using combined PXRD and PND data.

Sample	**$Li_{6.2}$-MER (4.2)**						
Unit Cell	$Li_{6.2}Si_{25.9}Al_{6.1}O_{64}$						
T (K)	298						
Space Group	*Immm*						
***a* (Å)**	13.201(2)						
***b* (Å)**	13.114(2)						
***c* (Å)**	10.007(2)						
***V* (Å^3)**	1732(1)						
X-ray Source	Stoe						
λ_{PXRD} (Å)	1.54056						
Neutron Source	Polaris						
Dataset	PXRD	Bank 1	Bank 2	Bank 3	Bank 4	Bank 5	Total
R_p	7.4%	1.5%	4.5%	5.7%	3.8%	4.0%	7.4%
R_{wp}	11.1%	1.6%	4.4%	4.9%	3.1%	3.3%	4.1%
χ^2	4.0	5.8	31	44	30	12	18

Table V.II.XI. Crystallographic details of refinement of dehydrated $Li_{6.2-x}Na_x$-MER (4.2) samples.

Sample	**$Li_{5.0}Na_{1.2}$-MER (4.2)**	**$Li_{4.0}Na_{2.2}$-MER (4.2)**	**$Li_{3.0}Na_{3.2}$-MER (4.2)**
Unit Cell	$[Si_{25.9}Al_{6.1}O_{64}]$	$Na_{1.9}[Si_{25.9}Al_{6.1}O_{64}]$	$Na_{2.6}[Si_{25.9}Al_{6.1}O_{64}]$
***T* (K)**	298	298	298
Space Group	*Immm*	*Immm*	*Immm*
X-ray Source	Stoe	Stoe	Stoe
λ (Å)	1.54056	1.54056	1.54056
***a* (Å)**	13.240(1)	13.297(1)	13.339(1)
***b* (Å)**	13.172(1)	13.263(1)	13.343(1)
***c* (Å)**	9.985(1)	9.946(1)	9.948(1)
***V* (Å^3)**	1741.3(3)	1754.1(2)	1770.6(2)
R_p	3.5%	3.1%	3.2%
R_{wp}	4.6%	4.1%	4.1%
χ^2	1.7	1.7	1.6

Table V.II.XII. Crystallographic details of refinement of dehydrated $Li_{6.2-x}K_x$-MER (4.2) samples.

Sample	**$Li_{5.0}K_{1.2}$-MER (4.2)**	**$Li_{4.0}K_{2.2}$-MER (4.2)**
Unit Cell	$K_{0.7}[Si_{25.9}Al_{6.1}O_{64}]$	$K_{1.7}[Si_{25.9}Al_{6.1}O_{64}]$
***T* (K)**	298	298
Space Group	*Immm*	*Immm*
X-ray Source	Stoe	I11, DLS
λ (Å)	1.54056	0.826398
***a* (Å)**	13.225(1)	13.275(1)
***b* (Å)**	13.179(1)	13.244(1)
***c* (Å)**	9.938(1)	9.907(1)
***V* (Å^3)**	1732.2(2)	1741.7(2)
R_p	3.4%	2.0%
R_{wp}	4.5%	2.9%
χ^2	1.8	2.1

Table V.II.XIII. Crystallographic details of refinement of $Li_{3.4}Cs_{2.8}$-MER (4.2) under varying conditions.

Sample	**$Li_{3.4}Cs_{2.8}$-MER (4.2)**		
Condition	Hydrated	Dehydrated	5.05 bar CO_2
Unit Cell	$Cs_{3.1}Si_{25.9}Al_{6.1}O_{64}.O_{15.2}$	$Cs_{2.4}Si_{25.9}Al_{6.1}O_{64}$	$Cs_{2.9}Si_{25.9}Al_{6.1}O_{64}.(CO_2)_{8.3}$
***T* (K)**	298	298	298
Space Group	*Immm*	*Immm*	*Immm*
X-ray Source	I11, DLS	I11, DLS	I11, DLS
λ (Å)	0.826398	0.826398	0.826398
***a* (Å)**	14.153(1)	13.337(1)	14.088(1)
***b* (Å)**	14.154(1)	13.377(1)	14.099(1)
***c* (Å)**	10.003(1)	9.837(1)	10.028(1)
***V* (Å^3)**	2003.8(2)	1755.0(2)	1991.8(2)
R_p	3.0%	2.0%	2.4%
R_{wp}	4.7%	3.0%	3.3%
χ^2	2.5	2.3	1.9

V.III Phillipsite

V.III.I PHI (2.5)

Table V.III.I. Crystallographic details of refinement of $K_{4.6}$-PHI (2.5) under varying conditions.

Sample	**$K_{4.6}$-PHI (2.5)**		
Condition	Hydrated	Dehydrated	1 bar CO_2
Unit Cell	$K_{4.8}Si_{11.4}\ Al_{4.6}O_{32}.O_{6.0}$	$K_{4.9}Si_{11.4}\ Al_{4.6}O_{32}$	$K_{4.6}Si_{11.4}\ Al_{4.6}O_{32}.(CO_2)_{3.6}$
***T* (K)**	298	298	298
Space Group	$P2_1/m$	$P2_1/m$	$P2_1/m$
X-ray Source	2D, PAL	2D, PAL	2D, PAL
λ (*Å*)	0.9	0.9	0.9
***a* (Å)**	9.961(1)	9.795(1)	9.860(1)
***b* (Å)**	14.174(2)	13.580(2)	13.924(2)
***c* (Å)**	8.718(2)	8.370(1)	8.534(1)
β (°)	125.18(1)	125.84(1)	125.04(1)
***V* (Å^3)**	1006.1(3)	902.5(2)	959.3(3)
R_p	7.7	4.7	5.1
R_{wp}	5.6	3.5	3.6
χ^2	33	10	11

Table V.III.II. Crystallographic details of refinement of $Rb_{4.6}$-PHI (2.5) under varying conditions.

Sample	**$Rb_{4.6}$-PHI (2.5)**		
Condition	Hydrated	Dehydrated	1 bar CO_2
Unit Cell	$Rb_{4.6}Si_{11.4}\ Al_{4.6}O_{32}.O_{5.9}$	$Rb_{4.6}Si_{11.4}\ Al_{4.6}O_{32}$	$Rb_{4.8}Si_{11.4}\ Al_{4.6}O_{32}.(CO_2)_{3.6}$
***T* (K)**	298	298	298
Space Group	$P2_1/m$	$P2_1/m$	$P2_1/m$
X-ray Source	2D, PAL	2D, PAL	2D, PAL
λ (*Å*)	0.9	0.9	0.9
***a* (Å)**	9.992(1)	9.854(1)	9.978(1)
***b* (Å)**	14.203(2)	13.658(2)	14.030(2)
***c* (Å)**	8.714(2)	8.385(1)	8.616(1)
β (°)	125.08(1)	125.68(1)	125.10(1)
***V* (Å^3)**	1012.0(3)	916.6(2)	986.8(3)
R_p	5.2	4.5	4.9
R_{wp}	3.9	3.3	3.7
χ^2	18	17	16

Table V.III.III. Crystallographic details of refinement of $Cs_{4.6}$-PHI (2.5) under varying conditions.

Sample	**$Cs_{4.6}$-PHI (2.5)**		
Condition	Hydrated	Dehydrated	1 bar CO_2
Unit Cell	$Cs_{20.4}Si_{45.6}Al_{18.4}O_{128}.O_{16}$	$Cs_{4.5}Si_{11.4}\ Al_{4.6}O_{32}$	$Cs_{4.7}Si_{11.4}\ Al_{4.6}O_{32}.(CO_2)_{3.5}$
***T* (K)**	298	298	298
Space Group	$P2_1/c$	$P2_1/m$	$P2_1/m$
X-ray Source	2D, PAL	2D, PAL	2D, PAL
λ (*Å*)	0.9	0.9	0.9
***a* (Å)**	20.082(3)	10.000(1)	10.110(1)
***b* (Å)**	14.223(3)	13.889(2)	14.150(2)
***c* (Å)**	17.475(4)	8.528(1)	8.705(1)
β (°)	125.35(2)	125.81(1)	125.27(1)
***V* (Å^3)**	4071(2)	960.5(3)	1016.7(3)
R_p	4.7	5.2	6.2
R_{wp}	3.6	3.8	4.5
χ^2	11	15	20

V.III.II PHI (3.6)

Table V.III.IV. Crystallographic details of refinement of $K_{3.5}$-PHI (3.6) under varying conditions.

Sample	**$K_{3.5}$-PHI (3.6)**		
Condition	Hydrated	Dehydrated	1 bar CO_2
Unit Cell	$K_{3.8}Si_{12.5}\ Al_{3.5}O_{32}.O_{6.0}$	$K_{3.7}Si_{12.5}\ Al_{3.5}O_{32}$	$K_{3.6}Si_{12.5}\ Al_{3.5}O_{32}.(CO_2)_{3.9}$
***T* (K)**	298	298	298
Space Group	$P2_1/m$	$P2_1/m$	$P2_1/m$
X-ray Source	2D, PAL	2D, PAL	2D, PAL
λ (*Å*)	0.9	0.9	0.9
***a* (Å)**	9.922(1)	9.820(1)	9.888(1)
***b* (Å)**	14.138(2)	13.703(2)	14.007(2)
***c* (Å)**	8.674(2)	8.434(2)	8.573(1)
β (°)	125.13(1)	125.92(1)	124.93(1)
***V* (Å^3)**	995.1(3)	919.0(3)	973.5(2)
R_p	7.7	4.4	5.9
R_{wp}	5.7	3.3	4.4
χ^2	35	9	16

Table V.III.V. Crystallographic details of refinement of $Rb_{3.5}$-PHI (3.6) under varying conditions.

Sample	**$Rb_{3.5}$-PHI (3.6)**		
Condition	Hydrated	Dehydrated	1 bar CO_2
Unit Cell	$Rb_{3.8}Si_{12.5}\ Al_{3.5}O_{32}.O_{6.0}$	$Rb_{3.7}Si_{12.5}\ Al_{3.5}O_{32}$	$Rb_{3.9}Si_{12.5}\ Al_{3.5}O_{32}.(CO_2)_{4.0}$
***T* (K)**	298	298	298
Space Group	$P2_1/m$	$P2_1/m$	$P2_1/m$
X-ray Source	2D, PAL	2D, PAL	2D, PAL
λ (*Å*)	0.9	0.9	0.9
***a* (Å)**	9.941(1)	9.903(1)	10.003(1)
***b* (Å)**	14.175(2)	13.733(2)	14.063(2)
***c* (Å)**	8.675(2)	8.450(2)	8.641(2)
β (°)	125.06(2)	125.95(1)	125.24(2)
***V* (Å^3)**	1000.6(3)	930.3(3)	992.8(3)
R_p	6.8	4.8	6.4
R_{wp}	5.0	3.6	4.8
χ^2	27	15	25

Table V.III.VI. Crystallographic details of refinement of $Cs_{3.5}$-PHI (3.6) under varying conditions.

Sample	**$Cs_{3.5}$-PHI (3.6)**		
Condition	Hydrated	Dehydrated	1 bar CO_2
Unit Cell	$Cs_{17.2}Si_{50}$ $Al_{14}O_{128}.O_{16}$	$Cs_{4.1}Si_{12.5}$ $Al_{3.5}O_{32}$	$Cs_{3.9}Si_{12.5}$ $Al_{3.5}O_{32}.(CO_2)_{4.3}$
***T* (K)**	298	298	298
Space Group	$P2_1/c$	$P2_1/m$	$P2_1/m$
X-ray Source	2D, PAL	2D, PAL	2D, PAL
λ (*Å*)	0.9	0.9	0.9
***a* (Å)**	20.024(3)	9.903(1)	10.083(1)
***b* (Å)**	14.171(3)	13.822(2)	14.150(3)
***c* (Å)**	17.395(3)	8.435(2)	8.668(2)
β (°)	125.50(1)	125.38(1)	125.16(1)
***V* (Å^3)**	4018(1)	941.3(3)	1011.1(3)
R_p	4.0	5.4	6.5
R_{wp}	2.9	3.8	4.9
χ^2	10	18	26

Appendix VI. Crystallographic information

VI.I The RHO family of materials

VI.I.I Zeolite Rho

Table VI.I.I. Refined structure of dehydrated $Li_{9.8}$-Rho (3.9).

Site	Type	x	y	z	Occ.	Ω	B_{iso}
Si1	Si	0.278(1)	0.127(1)	0.427(1)	0.8	48	3.6(1)
Al1	Al	0.278(1)	0.127(1)	0.427(1)	0.2	48	3.6(1)
O1	O	0.227(1)	0.227(1)	0.397(1)	1	24	1.0(1)
O2	O	0.117(1)	0.117(1)	0.629(1)	1	24	1.0(1)
O3	O	0.041(1)	0.215(1)	0.384(1)	1	48	1.0(1)
Li1	Li	0.294(1)	0.294(1)	0.294(1)	0.82(1)	8	2
Li2	Li	0.956(1)	0.044(1)	0.653(1)	0.15(1)	24	2

Table VI.I.II. Refined structure of dehydrated $Li_{7.3}Cs_{2.5}$-Rho (3.9).

Site	Type	x	y	z	Occ.	Ω	B_{iso}
Si1	Si	0.273(1)	0.123(1)	0.423(1)	0.8	48	1
Al1	Al	0.273(1)	0.123(1)	0.423(1)	0.2	48	1
O1	O	0.219(1)	0.219(1)	0.393(1)	1	24	1.1(1)
O2	O	0.124(1)	0.124(1)	0.629(1)	1	24	1.1(1)
O3	O	0.035(1)	0.215(1)	0.382(1)	1	48	1.1(1)
Li1	Li	0.283(1)	0.283(1)	0.283(1)	0.72(1)	8	0.5
Li2	Li	0.958(2)	0.042(2)	0.875(14)	0.08(1)	24	0.5
Cs3	Cs	0	0	0.5	0.38(1)	6	1

Table VI.I.III. Refined structure of dehydrated $Li_{5.5}Zn_{2.2}$-Rho (3.9).

Site	Type	x	y	z	Occ.	Ω	B_{iso}
Si1	Si	0.277(1)	0.127(1)	0.424(1)	0.8	48	1
Al1	Al	0.277(1)	0.127(1)	0.424(1)	0.2	48	1
O1	O	0.221(1)	0.221(1)	0.396(1)	1	24	1
O2	O	0.121(1)	0.121(1)	0.633(1)	1	24	1
O3	O	0.033(1)	0.215(1)	0.381(1)	1	48	1
Li1	Li	0.287(1)	0.287(1)	0.287(1)	0.47(2)	8	0.5
Li2	Li	0.041(4)	0.959(4)	0.640(4)	0.07(1)	24	0.5
Zn1	Zn	0.318(2)	0.318(2)	0.318(2)	0.07(1)	8	0.5
Zn2	Zn	0.080(1)	0.920(1)	0.561(1)	0.06(1)	24	0.5

Table VI.I.IV. Refined structure of dehydrated $Li_{7.4}Zn_{1.2}$-Rho (3.9).

Site	Type	x	y	z	Occ.	Ω	B_{iso}
Si1	Si	0.277(1)	0.125(1)	0.427(1)	0.8	48	1
Al1	Al	0.277(1)	0.125(1)	0.427(1)	0.2	48	1
O1	O	0.224(1)	0.224(1)	0.393(1)	1	24	2
O2	O	0.115(1)	0.115(1)	0.629(1)	1	24	2
O3	O	0.040(1)	0.212(1)	0.382(1)	1	48	2
Zn1	Zn	0.284(2)	0.284(2)	0.284(2)	0.07(1)	8	2
Zn2	Zn	0.929(3)	0.071(3)	0.807(3)	0.03(1)	24	2

Table VI.I.V. Refined structure of dehydrated $Li_{1.2}Zn_{4.3}$-Rho (3.9).

Site	Type	x	y	z	Occ.	Ω	B_{iso}
Si1	Si	0.274(1)	0.124(1)	0.422(1)	0.8	48	1
Al1	Al	0.274(1)	0.124(1)	0.422(1)	0.2	48	1
O1	O	0.214(1)	0.214(1)	0.397(1)	1	24	2
O2	O	0.127(1)	0.127(1)	0.629(1)	1	24	2
O3	O	0.032(1)	0.214(1)	0.376(1)	1	48	2
Zn1	Zn	0.270(1)	0.270(1)	0.270(1)	0.22(1)	8	2
Zn2	Zn	0.937(1)	0.063(1)	0.541(1)	0.11(1)	24	2

Table VI.I.VI. Refined structure of dehydrated $Zn_{4.9}$-Rho (3.9).

Site	Type	x	y	z	Occ.	Ω	B_{iso}
Si1	Si	0.272(1)	0.121(1)	0.421(1)	0.8	48	1
Al1	Al	0.272(1)	0.121(1)	0.421(1)	0.2	48	1
O1	O	0.211(1)	0.211(1)	0.402(1)	1	24	2
O2	O	0.129(1)	0.129(1)	0.621(1)	1	24	2
O3	O	0.033(1)	0.212(1)	0.383(1)	1	48	2
Zn1	Zn	0.284(1)	0.284(1)	0.284(1)	0.19(1)	8	2
Zn2	Zn	0.964(1)	0.036(1)	0.591(1)	0.14(1)	24	2

VI.I.II ZSM-25

Table VI.I.VII. Crystallographic sites as determined from Rietveld refinements for dehydrated, calcined (Na,H)-ZSM-25

Site	Type	x	y	z	Occ	Mult	Biso
Si1	Si	0.847(2)	0.574(2)	0.525(2)	0.77	48	0.71
Si1	Al	0.847(2)	0.574(2)	0.525(2)	0.23	48	0.71
Si2	Si	0.860(2)	0.593(2)	0.457(2)	0.77	48	0.71
Si2	Al	0.860(2)	0.593(2)	0.457(2)	0.23	48	0.71
Si3	Si	0.807(2)	0.628(2)	0.542(2)	0.77	48	0.71
Si3	Al	0.807(2)	0.628(2)	0.542(2)	0.23	48	0.71
Si4	Si	0.819(2)	0.648(2)	0.470(2)	0.77	48	0.71
Si4	Al	0.819(2)	0.648(2)	0.470(2)	0.23	48	0.71
Si5	Si	0.737(2)	0.644(2)	0.529(2)	0.77	48	0.71
Si5	Al	0.737(2)	0.644(2)	0.529(2)	0.23	48	0.71
Si6	Si	0.749(2)	0.629(2)	0.456(2)	0.77	48	0.71
Si6	Al	0.749(2)	0.629(2)	0.456(2)	0.23	48	0.71
Si7	Si	0.695(2)	0.591(2)	0.541(2)	0.77	48	0.71
Si7	Al	0.695(2)	0.591(2)	0.541(2)	0.23	48	0.71
Si8	Si	0.711(2)	0.576(2)	0.473(2)	0.77	48	0.71
Si8	Al	0.711(2)	0.576(2)	0.473(2)	0.23	48	0.71
Si9	Si	0.627(2)	0.575(2)	0.525(2)	0.77	48	0.71

Table VI.I.VII. (continued) Crystallographic sites as determined from Rietveld refinements for dehydrated, calcined (Na,H)-ZSM-25.

Site	Type	x	y	z	Occ	Mult	Biso
Si9	Al	0.627(2)	0.575(2)	0.525(2)	0.23	48	0.71
Si10	Si	0.644(2)	0.593(2)	0.458(2)	0.77	48	0.71
Si10	Al	0.644(2)	0.593(2)	0.458(2)	0.23	48	0.71
Si11	Si	0.569(2)	0.076(2)	0.025(2)	0.77	48	0.71
Si11	Al	0.569(2)	0.076(2)	0.025(2)	0.23	48	0.71
Si12	Si	0.583(2)	0.092(2)	0.959(2)	0.77	48	0.71
Si12	Al	0.583(2)	0.092(2)	0.959(2)	0.23	48	0.71
Si13	Si	0.529(2)	0.132(2)	0.040(2)	0.77	48	0.71
Si13	Al	0.529(2)	0.132(2)	0.040(2)	0.23	48	0.71
Si14	Si	0.543(2)	0.149(2)	0.973(2)	0.77	48	0.71
Si14	Al	0.543(2)	0.149(2)	0.973(2)	0.23	48	0.71
Si15	Si	0.704(2)	0.652(2)	0.808(2)	0.77	48	0.71
Si15	Al	0.704(2)	0.652(2)	0.808(2)	0.23	48	0.71
Si16	Si	0.686(2)	0.638(2)	0.180(2)	0.77	48	0.71
Si16	Al	0.686(2)	0.638(2)	0.180(2)	0.23	48	0.71
Si17	Si	0.751(2)	0.566(2)	0.703(2)	0.77	48	0.71
Si17	Al	0.751(2)	0.566(2)	0.703(2)	0.23	48	0.71
Si18	Si	0.737(2)	0.582(2)	0.316(2)	0.77	48	0.71
Si18	Al	0.737(2)	0.582(2)	0.316(2)	0.23	48	0.71
Si19	Si	0.689(2)	0.639(2)	0.737(2)	0.77	48	0.71
Si19	Al	0.689(2)	0.639(2)	0.737(2)	0.23	48	0.71
Si20	Si	0.701(2)	0.652(2)	0.249(2)	0.77	48	0.71
Si20	Al	0.701(2)	0.652(2)	0.249(2)	0.23	48	0.71
Si21	Si	0.685(2)	0.820(2)	0.581(2)	0.77	48	0.71
Si21	Al	0.685(2)	0.820(2)	0.581(2)	0.23	48	0.71
Si22	Si	0.702(2)	0.807(2)	0.431(2)	0.77	48	0.71
Si22	Al	0.702(2)	0.807(2)	0.431(2)	0.23	48	0.71
Si23	Si	0.960(2)	0.688(2)	0.639(2)	0.77	48	0.71
Si23	Al	0.960(2)	0.688(2)	0.639(2)	0.23	48	0.71

Table VI.I.VII. (continued) Crystallographic sites as determined from Rietveld refinements for dehydrated, calcined (Na,H)-ZSM-25.

Site	Type	x	y	z	Occ	Mult	Biso
Si24	Si	0.972(2)	0.706(2)	0.345(2)	0.77	48	0.71
Si24	Al	0.972(2)	0.706(2)	0.345(2)	0.23	48	0.71
Si25	Si	0.916(2)	0.814(2)	0.541(2)	0.77	48	0.71
Si25	Al	0.916(2)	0.814(2)	0.541(2)	0.23	48	0.71
Si26	Si	0.930(2)	0.796(2)	0.469(2)	0.77	48	0.71
Si26	Al	0.930(2)	0.796(2)	0.469(2)	0.23	48	0.71
Si27	Si	0.929(2)	0.360(2)	0.759(2)	0.77	48	0.71
Si27	Al	0.929(2)	0.360(2)	0.759(2)	0.23	48	0.71
Si28	Si	0.918(2)	0.348(2)	0.258(2)	0.77	48	0.71
Si28	Al	0.918(2)	0.348(2)	0.258(2)	0.23	48	0.71
Si29	Si	0.759(2)	0.359(2)	0.153(2)	0.77	48	0.71
Si29	Al	0.759(2)	0.359(2)	0.153(2)	0.23	48	0.71
Si30	Si	0.260(2)	0.918(2)	0.570(2)	0.77	48	0.71
Si30	Al	0.260(2)	0.918(2)	0.570(2)	0.23	48	0.71
O1	O	0.818(3)	0.592(3)	0.541(3)	1	48	0.29
O2	O	0.850(3)	0.629(3)	0.457(3)	1	48	0.29
O3	O	0.768(3)	0.628(3)	0.543(3)	1	48	0.29
O4	O	0.788(3)	0.632(3)	0.455(3)	1	48	0.29
O5	O	0.707(3)	0.627(3)	0.542(3)	1	48	0.29
O6	O	0.741(3)	0.592(3)	0.457(3)	1	48	0.29
O7	O	0.657(3)	0.592(3)	0.539(3)	1	48	0.29
O8	O	0.681(3)	0.596(3)	0.462(3)	1	48	0.29
O9	O	0.101(3)	0.591(3)	0.537(3)	1	48	0.29
O10	O	0.121(3)	0.591(3)	0.464(3)	1	48	0.29
O11	O	0.539(3)	0.096(3)	0.038(3)	1	48	0.29
O12	O	0.571(3)	0.128(3)	0.959(3)	1	48	0.29
O13	O	0.688(3)	0.620(3)	0.818(3)	1	48	0.29
O14	O	0.685(3)	0.599(3)	0.179(3)	1	48	0.29
O15	O	0.705(3)	0.768(3)	0.652(3)	1	48	0.29

Table VI.I.VII. (continued) Crystallographic sites as determined from Rietveld refinements for dehydrated, calcined (Na,H)-ZSM-25.

Site	Type	x	y	z	Occ	Mult	Biso
O16	O	0.704(3)	0.789(3)	0.351(3)	1	48	0.29
O17	O	0.740(3)	0.688(3)	0.601(3)	1	48	0.29
O18	O	0.739(3)	0.682(3)	0.379(3)	1	48	0.29
O19	O	0.631(3)	0.572(3)	0.487(3)	1	48	0.29
O20	O	0.789(3)	0.565(3)	0.701(3)	1	48	0.29
O21	O	0.768(3)	0.5692)	0.299(3)	1	48	0.29
O24	O	0.351(3)	0.570(3)	0.179(3)	1	48	0.29
O25	O	0.316(3)	0.538(3)	0.820(3)	1	48	0.29
O26	O	0.318(3)	0.539(3)	0.264(3)	1	48	0.29
O27	O	0.351(3)	0.570(3)	0.733(3)	1	48	0.29
O28	O	0.817(3)	0.356(3)	0.492(3)	1	48	0.29
O29	O	0.931(3)	0.761(3)	0.682(3)	1	48	0.29
O30	O	0.931(3)	0.797(3)	0.351(3)	1	48	0.29
O31	O	0.959(3)	0.815(3)	0.456(3)	1	48	0.29
O32	O	0.928(3)	0.851(3)	0.540(3)	1	48	0.29
O33	O	0.931(3)	0.798(3)	0.509(3)	1	48	0.29
O34	O	0.759(3)	0.932(3)	0.460(3)	1	48	0.29
O35	O	0.796(3)	0.930(3)	0.571(4)	1	48	0.29
O36	O	0.796(3)	0.650(3)	0.848(3)	1	48	0.29
O37	O	0.760(3)	0.681(3)	0.157(3)	1	48	0.29
O38	O	0.744(3)	0.120(3)	0.348(3)	1	48	0.29
O39	O	0.744(3)	0.103(3)	0.654(3)	1	48	0.29
O40	O	0.620(3)	0.069(3)	0.241(3)	1	48	0.29
O41	O	0.602(3)	0.070(3)	0.757(3)	1	48	0.29
O42	O	0.898(3)	0.542(3)	0.189(3)	1	48	0.29
O43	O	0.878(3)	0.540(3)	0.812(3)	1	48	0.29
O44	O	0.848(3)	0.511(3)	0.208(3)	1	48	0.29
O47	O	0.344(3)	0.259(3)	0.042(3)	1	48	0.29
O48	O	0.346(3)	0.295(3)	0.929(3)	1	48	0.29

Table VI.I.VII. (continued) Crystallographic sites as determined from Rietveld refinements for dehydrated, calcined (Na,H)-ZSM-25.

Site	Type	x	y	z	Occ	Mult	Biso
O65	O	0.568(3)	0.073(3)	-0.013(3)	1	48	0.29
O66	O	0.546(3)	0.150(3)	0.011(3)	1	48	0.29
O67	O	0.491(3)	0.134(3)	0.037(3)	1	48	0.29
O68	O	0.844(3)	0.575(3)	0.487(3)	1	48	0.29
O69	O	0.739(3)	0.642(3)	0.491(3)	1	48	0.29
O70	O	0.711(3)	0.574(3)	0.511(3)	1	48	0.29
O45	O	0.315(3)	0.315(3)	0.036(4)	1	24	0.29
O46	O	0.348(3)	0.348(3)	0.963(4)	1	24	0.29
O49	O	0.682(3)	0.682(3)	0.818(5)	1	24	0.29
O50	O	0.650(3)	0.650(3)	0.182(4)	1	24	0.29
O51	O	0.738(3)	0.738(3)	0.564(3)	1	24	0.29
O52	O	0.705(3)	0.705(3)	0.426(4)	1	24	0.29
O53	O	0.595(3)	0.595(3)	0.531(4)	1	24	0.29
O54	O	0.627(3)	0.627(2)	0.460(4)	1	24	0.29
O55	O	0.707(3)	0.651(4)	0.707(3)	1	24	0.29
O56	O	0.736(3)	0.652(4)	0.264(3)	1	24	0.29
O22	O	0.735(5)	0.653(3)	0.653(3)	1	24	0.29
O23	O	0.741(4)	0.683(3)	0.317(3)	1	24	0.29
O57	O	0.565(3)	0.040(3)	0.040(3)	1	24	0.29
O58	O	0.575(4)	0.074(3)	0.926(3)	1	24	0.29
O59	O	0.847(4)	0.537(3)	0.537(3)	1	24	0.29
O60	O	0.852(4)	0.575(3)	0.425(3)	1	24	0.29
O61	O	0.705(4)	0.573(3)	0.573(3)	1	24	0.29
O62	O	0.707(3)	0.540(3)	0.460(3)	1	24	0.29
O63	O	0.622(4)	0.541(3)	0.541(3)	1	24	0.29
O64	O	0.636(3)	0.575(2)	0.425(2)	1	24	0.29
Na1	Na	0.067(4)	0.067(4)	0.067(4)	0.5(2)	8	1.36
Na2	Na	0.364(3)	0	0	1.0(2)	12	1.36
Na3	Na	0.157(4)	0	0	0.9(2)	12	1.36

Table VI.I.VII. (continued) Crystallographic sites as determined from Rietveld refinements for dehydrated, calcined (Na,H)-ZSM-25.

Site	Type	x	y	z	Occ	Mult	Biso
Na4	Na	0.074(2)	0.257(2)	0.074(2)	1.0(1)	24	1.36
Na5	Na	0.107(3)	0.401(4)	0.107(3)	0.5(1)	24	1.36
Na6	Na	0.502(3)	0.064(3)	0.064(3)	0.7(1)	24	1.36
Na7	Na	0.423(3)	0.232(2)	0.232(2)	0.7(2)	24	1.36
Na8	Na	0.068(5)	0.402(4)	0.402(4)	0.4(1)	24	1.36
Na9	Na	0.167(4)	0.393(3)	0.393(3)	0.6(1)	24	1.36
Na10	Na	0.363(7)	0.168(5)	0.168(5)	0.3(2)	24	1.36
Na11	Na	0.048(3)	0.172(2)	0.172(2)	0.9(1)	24	1.36
Na12	Na	0.143(3)	0.265(2)	0.265(2)	0.9(2)	24	1.36
Na13	Na	0.169(2)	0.169(2)	-0.035(2)	1.0(2)	24	1.36
Na14	Na	0.212(4)	0.212(4)	0.356(5)	0.5(1)	24	1.36
Na15	Na	0.211(2)	0.561(2)	0.016(2)	0.8(1)	48	1.36
Na16	Na	0.236(2)	0.339(2)	-0.010(3)	0.8(1)	48	1.36

Table VI.I.VIII. Crystallographic sites as determined from Rietveld refinements for dehydrated, templated (Na,TEA)-ZSM-25.

Site	Type	x	y	z	Occ	Mult	Biso
Si1	Si	0.850(3)	0.578(3)	0.526(3)	0.77	48	0.71
Si1	Al	0.850(3)	0.578(3)	0.526(3)	0.23	48	0.71
Si2	Si	0.859(3)	0.591(3)	0.460(4)	0.77	48	0.71
Si2	Al	0.859(3)	0.591(3)	0.460(4)	0.23	48	0.71
Si3	Si	0.809(3)	0.633(3)	0.538(3)	0.77	48	0.71
Si3	Al	0.809(3)	0.633(3)	0.538(3)	0.23	48	0.71
Si4	Si	0.820(3)	0.647(3)	0.469(3)	0.77	48	0.71
Si4	Al	0.820(3)	0.647(3)	0.469(3)	0.23	48	0.71
Si5	Si	0.737(3)	0.643(3)	0.534(3)	0.77	48	0.71
Si5	Al	0.737(3)	0.643(3)	0.534(3)	0.23	48	0.71
Si6	Si	0.745(3)	0.634(3)	0.463(3)	0.77	48	0.71
Si6	Al	0.745(3)	0.634(3)	0.463(3)	0.23	48	0.71

Table VI.I.VIII. (continued) Crystallographic sites as determined from Rietveld refinements for dehydrated, templated (Na,TEA)-ZSM-25.

Site	Type	x	y	z	Occ	Mult	Biso
Si7	Si	0.697(3)	0.587(3)	0.542(3)	0.77	48	0.71
Si7	Al	0.697(3)	0.587(3)	0.542(3)	0.23	48	0.71
Si8	Si	0.709(3)	0.577(3)	0.469(3)	0.77	48	0.71
Si8	Al	0.709(3)	0.577(3)	0.469(3)	0.23	48	0.71
Si9	Si	0.626(3)	0.575(3)	0.527(3)	0.77	48	0.71
Si9	Al	0.626(3)	0.575(3)	0.527(3)	0.23	48	0.71
Si10	Si	0.642(3)	0.592(3)	0.461(3)	0.77	48	0.71
Si10	Al	0.642(3)	0.592(3)	0.461(3)	0.23	48	0.71
Si11	Si	0.570(3)	0.077(3)	0.028(3)	0.77	48	0.71
Si11	Al	0.570(3)	0.077(3)	0.028(3)	0.23	48	0.71
Si12	Si	0.581(3)	0.091(3)	0.960(4)	0.77	48	0.71
Si12	Al	0.581(3)	0.091(3)	0.960(4)	0.23	48	0.71
Si13	Si	0.533(3)	0.136(3)	0.040(3)	0.77	48	0.71
Si13	Al	0.533(3)	0.136(3)	0.040(3)	0.23	48	0.71
Si14	Si	0.543(3)	0.149(3)	0.972(3)	0.77	48	0.71
Si14	Al	0.543(3)	0.149(3)	0.972(3)	0.23	48	0.71
Si15	Si	0.700(3)	0.652(3)	0.810(3)	0.77	48	0.71
Si15	Al	0.700(3)	0.652(3)	0.810(3)	0.23	48	0.71
Si16	Si	0.689(3)	0.640(3)	0.182(3)	0.77	48	0.71
Si16	Al	0.689(3)	0.640(3)	0.182(3)	0.23	48	0.71
Si17	Si	0.751(3)	0.572(4)	0.703(4)	0.77	48	0.71
Si17	Al	0.751(3)	0.572(4)	0.703(4)	0.23	48	0.71
Si18	Si	0.736(3)	0.579(3)	0.314(3)	0.77	48	0.71
Si18	Al	0.736(3)	0.579(3)	0.314(3)	0.23	48	0.71
Si19	Si	0.690(3)	0.639(3)	0.743(3)	0.77	48	0.71
Si19	Al	0.690(3)	0.639(3)	0.743(3)	0.23	48	0.71
Si20	Si	0.700(3)	0.645(3)	0.248(3)	0.77	48	0.71
Si20	Al	0.700(3)	0.645(3)	0.248(3)	0.23	48	0.71
Si21	Si	0.690(3)	0.822(3)	0.581(3)	0.77	48	0.71

Table VI.I.VIII. (continued) Crystallographic sites as determined from Rietveld refinements for dehydrated, templated (Na,TEA)-ZSM-25.

Site	Type	x	y	z	Occ	Mult	Biso
Si21	Al	0.690(3)	0.822(3)	0.581(3)	0.23	48	0.71
Si22	Si	0.701(3)	0.810(3)	0.432(4)	0.77	48	0.71
Si22	Al	0.701(3)	0.810(3)	0.432(4)	0.23	48	0.71
Si23	Si	0.963(3)	0.685(3)	0.635(3)	0.77	48	0.71
Si23	Al	0.963(3)	0.685(3)	0.635(3)	0.23	48	0.71
Si24	Si	0.968(3)	0.703(3)	0.349(3)	0.77	48	0.71
Si24	Al	0.968(3)	0.703(3)	0.349(3)	0.23	48	0.71
Si25	Si	0.917(3)	0.815(3)	0.542(3)	0.77	48	0.71
Si25	Al	0.917(3)	0.815(3)	0.542(3)	0.23	48	0.71
Si26	Si	0.927(3)	0.798(3)	0.469(3)	0.77	48	0.71
Si26	Al	0.927(3)	0.798(3)	0.469(3)	0.23	48	0.71
Si27	Si	0.932(3)	0.360(3)	0.758(3)	0.77	48	0.71
Si27	Al	0.932(3)	0.360(3)	0.758(3)	0.23	48	0.71
Si28	Si	0.919(3)	0.351(3)	0.259(3)	0.77	48	0.71
Si28	Al	0.919(3)	0.351(3)	0.259(3)	0.23	48	0.71
Si29	Si	0.757(3)	0.360(3)	0.153(3)	0.77	48	0.71
Si29	Al	0.757(3)	0.360(3)	0.153(3)	0.23	48	0.71
Si30	Si	0.259(4)	0.918(3)	0.572(3)	0.77	48	0.71
Si30	Al	0.259(4)	0.918(3)	0.572(3)	0.23	48	0.71
O1	O	0.822(6)	0.598(6)	0.540(7)	1	48	0.29
O2	O	0.847(6)	0.626(6)	0.540(7)	1	48	0.29
O3	O	0.771(6)	0.630(5)	0.541(5)	1	48	0.29
O4	O	0.786(6)	0.637(5)	0.461(5)	1	48	0.29
O5	O	0.707(5)	0.625(6)	0.545(6)	1	48	0.29
O6	O	0.736(5)	0.598(6)	0.459(6)	1	48	0.29
O7	O	0.659(5)	0.588(5)	0.537(6)	1	48	0.29
O8	O	0.678(5)	0.590(5)	0.462(5)	1	48	0.29
O9	O	0.102(6)	0.592(6)	0.537(5)	1	48	0.29
O10	O	0.118(5)	0.592(7)	0.464(6)	1	48	0.29

Table VI.I.VIII. (continued) Crystallographic sites as determined from Rietveld refinements for dehydrated, templated (Na,TEA)-ZSM-25.

Site	Type	x	y	z	Occ	Mult	Biso
O11	O	0.544(5)	0.100(5)	0.038(6)	1	48	0.29
O12	O	0.569(5)	0.128(7)	0.960(7)	1	48	0.29
O13	O	0.688(6)	0.620(5)	0.823(6)	1	48	0.29
O14	O	0.687(6)	0.601(6)	0.179(7)	1	48	0.29
O15	O	0.702(6)	0.774(5)	0.649(6)	1	48	0.29
O16	O	0.707(6)	0.790(5)	0.354(6)	1	48	0.29
O17	O	0.743(6)	0.683(6)	0.601(6)	1	48	0.29
O18	O	0.742(6)	0.682(6)	0.382(5)	1	48	0.29
O19	O	0.631(5)	0.570(5)	0.489(7)	1	48	0.29
O20	O	0.790(7)	0.569(6)	0.705(5)	1	48	0.29
O21	O	0.771(6)	0.571(6)	0.297(6)	1	48	0.29
O24	O	0.346(6)	0.567(6)	0.179(5)	1	48	0.29
O25	O	0.318(6)	0.542(6)	0.822(6)	1	48	0.29
O26	O	0.320(5)	0.545(5)	0.264(7)	1	48	0.29
O27	O	0.346(5)	0.566(6)	0.737(5)	1	48	0.29
O28	O	0.818(6)	0.351(6)	0.492(6)	1	48	0.29
O29	O	0.933(6)	0.762(5)	0.676(5)	1	48	0.29
O30	O	0.933(7)	0.792(6)	0.350(6)	1	48	0.29
O31	O	0.957(7)	0.816(5)	0.456(6)	1	48	0.29
O32	O	0.930(7)	0.847(6)	0.542(6)	1	48	0.29
O33	O	0.928(6)	0.799(6)	0.509(7)	1	48	0.29
O34	O	0.762(6)	0.927(5)	0.457(7)	1	48	0.29
O35	O	0.794(6)	0.929(6)	0.571(6)	1	48	0.29
O36	O	0.792(5)	0.652(7)	0.847(6)	1	48	0.29
O37	O	0.761(6)	0.681(6)	0.154(6)	1	48	0.29
O38	O	0.742(6)	0.119(7)	0.349(6)	1	48	0.29
O39	O	0.745(5)	0.101(6)	0.650(6)	1	48	0.29
O40	O	0.619(6)	0.072(6)	0.242(6)	1	48	0.29
O41	O	0.602(5)	0.070(6)	0.756(6)	1	48	0.29

Table VI.I.VIII. (continued) Crystallographic sites as determined from Rietveld refinements for dehydrated, templated (Na,TEA)-ZSM-25.

Site	Type	x	y	z	Occ	Mult	Biso
O42	O	0.900(6)	0.542(6)	0.185(6)	1	48	0.29
O43	O	0.878(5)	0.542(6)	0.814(6)	1	48	0.29
O44	O	0.851(6)	0.508(6)	0.203(6)	1	48	0.29
O47	O	0.349(6)	0.262(6)	0.041(6)	1	48	0.29
O48	O	0.350(6)	0.293(6)	0.932(5)	1	48	0.29
O65	O	0.567(5)	0.075(6)	-0.011(6)	1	48	0.29
O66	O	0.546(5)	0.150(6)	0.010(5)	1	48	0.29
O67	O	0.492(6)	0.137(5)	0.039(6)	1	48	0.29
O68	O	0.846(6)	0.576(6)	0.489(7)	1	48	0.29
O69	O	0.735(5)	0.647(6)	0.494(6)	1	48	0.29
O70	O	0.714(5)	0.575(5)	0.511(5)	1	48	0.29
O45	O	0.318(6)	0.318(6)	0.042(10)	1	24	0.29
O46	O	0.348(6)	0.348(6)	0.960(9)	1	24	0.29
O49	O	0.683(6)	0.683(6)	0.820(9)	1	24	0.29
O50	O	0.657(6)	0.657(6)	0.182(9)	1	24	0.29
O51	O	0.736(6)	0.736(6)	0.572(8)	1	24	0.29
O52	O	0.707(5)	0.707(5)	0.427(9)	1	24	0.29
O53	O	0.596(5)	0.596(5)	0.532(8)	1	24	0.29
O54	O	0.625(5)	0.625(5)	0.46110)	1	24	0.29
O55	O	0.711(6)	0.648(10)	0.711(6)	1	24	0.29
O56	O	0.732(6)	0.652(8)	0.268(6)	1	24	0.29
O22	O	0.741(8)	0.654(7)	0.654(7)	1	24	0.29
O23	O	0.748(8)	0.678(5)	0.322(5)	1	24	0.29
O57	O	0.567(7)	0.043(6)	0.043(6)	1	24	0.29
O58	O	0.570(8)	0.070(5)	0.930(5)	1	24	0.29
O59	O	0.852(7)	0.544(7)	0.544(7)	1	24	0.29
O60	O	0.850(8)	0.570(6)	0.430(6)	1	24	0.29
O61	O	0.705(8)	0.572(6)	0.572(6)	1	24	0.29
O62	O	0.711(7)	0.542(5)	0.458(5)	1	24	0.29

Table VI.I.VIII. (continued) Crystallographic sites as determined from Rietveld refinements for dehydrated, templated (Na,TEA)-ZSM-25.

Site	Type	x	y	z	Occ	Mult	Biso
O63	O	0.623(8)	0.544(6)	0.544(6)	1	24	0.29
O64	O	0.627(7)	0.570(5)	0.430(5)	1	24	0.29
Na1	Na	0.040(4)	0.040(4)	0.040(4)	1	8	1.36
Na2	Na	0.234(4)	0.234(4)	0.234(4)	0.99998	8	1.36
Na3	Na	0.282(5)	0.282(5)	0.282(5)	0.99998	8	1.36
Na4	Na	0.438(5)	0.438(5)	0.438(5)	1	8	1.36
Na5	Na	0.14(13)	0	0	0.49861	12	1.36
Na6	Na	0.051(3)	0.519(5)	0.051(3)	0.9378	24	1.36
Na7	Na	0.426(5)	0.231(3)	0.231(3)	1	24	1.36
Na8	Na	0.074(5)	0.212(3)	0.212(3)	1	24	1.36
Na9	Na	0.191(5)	0.409(3)	0.409(3)	0.8475	24	1.36
Na10	Na	0.033(6)	0.159(4)	0.159(4)	1	24	1.36
Na11	Na	0.144(6)	0.262(3)	0.262(3)	0.99859	24	1.36
Na12	Na	0.102(3)	0.102(3)	0.470(4)	1	24	1.36
Na13	Na	0.224(3)	0.224(3)	0.372(5)	1	24	1.36
Na14	Na	0.224(3)	0.587(3)	0.013(3)	1	48	1.36
N1	N	0.5	0	0	0.4(2)	6	2.00
C1a	C	0.478	0	0.030	0.2(1)	48	2.00
C1b	C	0.5	0	0.061	0.4(2)	24	2.00
N2	N	0.340	0	0	0.9(2)	12	2.00
C2a	C	0.318	0	0.030	0.4(1)	48	2.00
C2b	C	0.340	0	0.061	0.9(1)	48	2.00
C2c	C	0.362	0	0.030	0.4(1)	48	2.00
N3x	N	0.136	0.136	0.136	0.5(1)	8	2.00
C31ax	C	0.114	0.114	0.114	0.5(1)	8	2.00
C31bx	C	0.136	0.093	0.093	0.2(1)	24	2.00
C32ax	C	0.157	0.157	0.114	0.5(1)	24	2.00
C32bx	C	0.150	0.150	0.079	0.5(1)	24	2.00
N3y	N	0.119	0.119	0.119	0.5(1)	8	2.00

Table VI.I.VIII. (continued) Crystallographic sites as determined from Rietveld refinements for dehydrated, templated (Na,TEA)-ZSM-25.

Site	Type	x	y	z	Occ	Mult	Biso
C31ay	C	0.140	0.140	0.140	0.5(1)	8	2.00
C31by	C	0.162	0.162	0.119	0.2(1)	24	2.00
C32ay	C	0.141	0.098	0.098	0.5(1)	24	2.00
C32by	C	0.176	0.105	0.105	0.5(1)	24	2.00
N4x	N	0.266	0.266	0.266	0.5(1)	8	2.00
C41ax	C	0.244	0.244	0.244	0.5(1)	8	2.00
C41bx	C	0.266	0.223	0.223	0.2(1)	24	2.00
C42ax	C	0.287	0.287	0.244	0.5(1)	24	2.00
C42bx	C	0.280	0.280	0.209	0.5(1)	24	2.00
N4y	N	0.200	0.200	0.200	0.5(1)	8	2.00
C41ay	C	0.222	0.222	0.222	0.5(1)	8	2.00
C41by	C	0.243	0.243	0.200	0.2(1)	24	2.00
C42ay	C	0.222	0.179	0.179	0.5(1)	24	2.00
C42by	C	0.257	0.186	0.186	0.5(1)	24	2.00
N5x	N	0.377	0.377	0.377	0.5(1)	8	2.00
C51ax	C	0.355	0.355	0.355	0.5(1)	8	2.00
C51bx	C	0.377	0.334	0.334	0.2(1)	24	2.00
C52ax	C	0.398	0.398	0.355	0.5(1)	24	2.00
C52bx	C	0.390	0.390	0.319	0.5(1)	24	2.00
N5y	N	0.343	0.343	0.343	0.5(1)	8	2.00
C51ay	C	0.364	0.364	0.364	0.5(1)	8	2.00
C51by	C	0.385	0.385	0.342	0.2(1)	24	2.00
C52ay	C	0.364	0.321	0.321	0.5(1)	24	2.00
C52by	C	0.400	0.329	0.329	0.5(1)	24	2.00

VI.II Merlinoite

VI.II.I MER (3.8)

Table VI.II.I. Refined structure of hydrated $Li_{5.9}TEA_{0.8}$-MER (3.8).

Site	Type	x	y	z	Occ	Mult	Biso
O1	O	0.161(1)	0.161(1)	0.212(1)	1	16	2
O2	O	0.125(1)	0.288(1)	0	1	16	2
O3	O	0	0.243(1)	0.197(1)	1	16	2
O4	O	0.148(1)	0.352(1)	0.25	1	16	2
Si1	Si	0.112(1)	0.261(1)	0.159(1)	1	32	2
Ow1	O	0	0	0	0.84(2)	2	2
Ow4	O	0	0	0.5	0.31(2)	2	2
Ow2	O	0.5	0	0.834(2)	0.84(1)	8	2
Ow3	O	0.5	0.188(1)	0	0.73(1)	8	2
N1	N	0.5	0.5	0	0.4	2	2
C1	C	0.561	0.561	0.087	0.2	16	2
C2	C	0.622	0.622	0.000	0.4	8	2
H1	H	0.600	0.516	0.156	0.4	32	2
H1a	H	0.516	0.600	0.156	0.4	32	2
H2	H	0.666	0.666	0.063	0.4	16	2
H2a	H	0.577	0.666	-0.062	0.4	32	2
H2b	H	0.666	0.577	-0.062	0.4	32	2

Table VI.II.II. Refined structure of hydrated $Na_{5.9}TEA_{0.8}$-MER (3.8).

Site	Type	x	y	z	Occ	Mult	Biso
Na1	Na	0	0	0.823(4)	0.40(1)	4	2
Na2	Na	0.5	0.861(2)	0	0.35(1)	8	2
Na3	Na	0	0.5	0.75	0.39(3)	4	2
O1	O	0.165(1)	0.165(1)	0.196(1)	1	16	2
O2	O	0.123(1)	0.290(1)	0	1	16	2
O3	O	0	0.249(1)	0.193(1)	1	16	2
O4	O	0.154(1)	0.347(1)	0.25	1	16	2
Si1	Si	0.111(1)	0.261(1)	0.158(1)	1	32	2
Ow1	O	0	0	0	0.60(3)	2	2
Ow2	O	0.5	0	0.868(3)	0.67(2)	8	2
Ow3	O	0.5	0.259(1)	0	0.75(2)	8	2
Ow4	O	0	0	0.5	0.48(2)	2	2
N1	N	0.5	0.5	0	0.4	2	2
C1	C	0.561	0.561	0.087	0.2	16	2
C2	C	0.622	0.622	0.000	0.4	8	2
H1	H	0.600	0.516	0.155	0.4	32	2
H1a	H	0.516	0.600	0.155	0.4	32	2
H2	H	0.667	0.667	0.063	0.4	16	2
H2a	H	0.577	0.666	-0.062	0.4	32	2
H2b	H	0.666	0.577	-0.062	0.4	32	2

Table VI.II.III. Refined structure of hydrated $K_{5.9}TEA_{0.8}$-MER (3.8).

Site	Type	x	y	z	Occ	Mult	Biso
O1	O	0.161(1)	0.161(1)	0.206(1)	1	16	2
O2	O	0.125(1)	0.297(1)	0	1	16	2
O3	O	0	0.242(1)	0.203(1)	1	16	2
O4	O	0.157(1)	0.343(1)	0.25	1	16	2
Si1	Si	0.110(1)	0.260(1)	0.156(1)	0.8	32	2
Si1	Al	0.110(1)	0.260(1)	0.156(1)	0.2	32	2
Ow1	O	0	0	0	0.66(2)	2	2
Ow2	O	0.5	0	-0.113(2)	0.77(2)	8	2
Ow3	O	0.5	0.278(2)	0	0.36(1)	8	2
K1	K	0	0	0.777(2)	0.34(1)	4	2
K2	K	0.5	0.849(1)	1	0.54(1)	8	2
K3	K	0	0.5	0.75	0.10(1)	4	2
N1	N	0.5	0.5	0	0.4	2	2
C1	C	0.561	0.561	0.087	0.2	16	2
C2	C	0.622	0.622	0.000	0.4	8	2
H1	H	0.600	0.516	0.157	0.4	32	2
H1a	H	0.516	0.600	0.157	0.4	32	2
H2	H	0.666	0.666	0.063	0.4	16	2
H2a	H	0.577	0.666	-0.063	0.4	32	2
H2b	H	0.666	0.577	-0.063	0.4	32	2

Table VI.II.IV. Refined structure of hydrated $Cs_{5.9}TEA_{0.8}$-MER (3.8).

Site	Type	x	y	z	Occ	Mult	Biso
O1	O	0.156(2)	0.156(2)	0.216(3)	1	16	2
O2	O	0.139(3)	0.278(2)	0	1	16	2
O3	O	0	0.240(3)	0.174(4)	1	16	2
O4	O	0.154(2)	0.346(2)	0.25	1	16	2
Si1	Si	0.110(1)	0.245(1)	0.161(1)	1	32	2
Ow1	O	0	0	0	0.72(11)	2	2
Ow2	O	0.5	0	0	0.93(6)	8	2
Ow3	O	0.5	0.298(4)	0	1.00(7)	8	2
Ow4	O	0	0	0.5	0.30(11)	2	2
Cs1	Cs	0	1	0.752(2)	0.28(1)	4	2
Cs2	Cs	0.5	0.810(2)	1	0.30(1)	8	2
Cs3	Cs	0	0.5	0.75	0.55(1)	4	2
N1	N	0.5	0.5	0	0.4	2	2
C1	C	0.561	0.561	0.087	0.2	16	2
C2	C	0.622	0.622	0.000	0.4	8	2
H1	H	0.600	0.516	0.156	0.4	32	2
H1a	H	0.516	0.600	0.156	0.4	32	2
H2	H	0.666	0.666	0.063	0.4	16	2
H2a	H	0.577	0.666	-0.062	0.4	32	2
H2b	H	0.666	0.577	-0.062	0.4	32	2

Table VI.II.V. Refined structure of dehydrated $Li_{5.9}TEA_{0.8}$-MER (3.8).

Site	Type	x	y	z	Occ	Mult	Biso
O1	O	0.124(1)	0.203(1)	0.183(2)	1	16	1
O2	O	0.259(1)	0.129(1)	0	1	8	1
O5	O	0.147(2)	0.648(2)	0	1	8	1
O3	O	0.161(1)	0	0.149(2)	1	8	1
O6	O	0	0.641(1)	0.188(2)	1	8	1
O4	O	0.301(2)	0.115(1)	0.262(2)	1	16	1
Si1	Si	0.212(1)	0.110(1)	0.159(1)	0.79	16	1
Si1	Al	0.212(1)	0.110(1)	0.159(1)	0.21	16	1
Si2	Si	0.109(1)	0.678(1)	0.154(1)	0.79	16	1
Si2	Al	0.109(1)	0.678(1)	0.154(1)	0.21	16	1
N1	N	0.5	0.5	0	0.4	2	2
C1	C	0.565	0.565	0.086	0.2	16	2
C2	C	0.630	0.631	0.000	0.4	8	2
H1	H	0.607	0.517	0.154	0.4	16	2
H1a	H	0.517	0.607	0.154	0.4	16	2
H2	H	0.678	0.678	0.062	0.4	16	2
H2a	H	0.582	0.678	-0.062	0.4	16	2
H2b	H	0.677	0.582	-0.062	0.4	16	2

Table VI.II.VI. Refined structure of dehydrated $Na_{5.9}TEA_{0.8}$-MER (3.8).

Site	Type	x	y	z	Occ	Mult	Biso
Na1	Na	0	0.035(2)	0.865(3)	0.37(1)	8	2
Na2	Na	0.777(3)	0.5	0	0.36(2)	4	2
Na3	Na	0.422(4)	0	0.748(8)	0.21(1)	8	2
O1	O	0.132(1)	0.178(1)	0.206(1)	1	16	1
O2	O	0.264(1)	0.126(2)	0	1	8	1
O5	O	0.150(1)	0.663(2)	0	1	8	1
O3	O	0.169(1)	0	0.170(2)	1	8	1
O6	O	0	0.683(1)	0.197(2)	1	8	1
O4	O	0.298(1)	0.127(1)	0.271(1)	1	16	1
Si1	Si	0.225(1)	0.112(1)	0.159(1)	1	16	1
Si2	Si	0.107(1)	0.698(1)	0.157(1)	1	16	1
N1	N	0.5	0.5	0	0.4	2	2
C1	C	0.564	0.564	0.086	0.2	16	2
C2	C	0.627	0.628	0.000	0.4	8	2
H1	H	0.604	0.517	0.155	0.4	16	2
H1a	H	0.517	0.605	0.155	0.4	16	2
H2	H	0.674	0.674	0.063	0.4	16	2
H2a	H	0.580	0.674	-0.062	0.4	16	2
H2b	H	0.673	0.580	-0.062	0.4	16	2
Na1	Na	0	0.035(2)	0.865(3)	0.37(1)	8	2
Na2	Na	0.777(3)	0.5	0	0.36(2)	4	2

Table VI.II.VII. Refined structure of dehydrated $K_{5.9}TEA_{0.8}$-MER (3.8).

Site	Type	x	y	z	Occ	Mult	Biso
O1	O	0.134(1)	0.699(1)	0.537(2)	1	16	1
O2	O	0.134(1)	-0.173(1)	0.320(1)	1	16	1
O3	O	-0.694(1)	-0.131(1)	0.197(2)	1	16	1
O4	O	0	0.701(1)	0.312(2)	1	8	1
O5	O	0.184(1)	0	0.344(2)	1	8	1
Si1	Si	0.114(1)	0.718(1)	0.360(1)	0.8	16	1
Si1	Al	0.114(1)	0.718(1)	0.360(1)	0.2	16	1
Si2	Si	0.243(1)	-0.107(1)	0.328(1)	0.8	16	1
Si2	Al	0.243(1)	-0.107(1)	0.328(1)	0.2	16	1
K1	K	0.5	0.5	-0.095(1)	0.54(1)	4	2
K2	K	0.261(1)	0.5	0.544(2)	0.33(1)	8	2
K3	K	0	0.5	0.166(5)	0.28(1)	4	2
N1	N	0.5	0.5	0.5	0.4	2	2
C1	C	0.563	0.563	0.587	0.2	16	2
C2	C	0.627	0.627	0.500	0.4	8	2
H1	H	0.604	0.517	0.656	0.4	16	2
H1a	H	0.517	0.604	0.656	0.4	16	2
H2	H	0.672	0.672	0.563	0.4	16	2
H2a	H	0.580	0.672	0.437	0.4	16	2
H2b	H	0.672	0.580	0.437	0.4	16	2

Table VI.II.VIII. Refined structure of dehydrated $Cs_{5.9}TEA_{0.8}$-MER (3.8).

Site	Type	x	y	z	Occ	Mult	Biso
O1	O	0.127(2)	0.702(2)	0.525(3)	1	16	1
O2	O	0.146(2)	-0.176(2)	0.323(2)	1	16	1
O3	O	-0.685(2)	-0.136(2)	0.209(2)	1	16	1
O4	O	0	0.702(2)	0.323(3)	1	8	1
O5	O	0.212(2)	0	0.318(3)	1	8	1
Si1	Si	0.113(1)	0.717(1)	0.356(2)	0.8	16	1
Si1	Al	0.113(1)	0.717(1)	0.356(2)	0.2	16	1
Si2	Si	0.253(1)	-0.114(1)	0.328(1)	0.8	16	1
Si2	Al	0.253(1)	-0.114(1)	0.328(1)	0.2	16	1
Cs1	Cs	0.5	0.5	-0.047(1)	0.42(1)	4	2
Cs2	Cs	0.266(2)	0.5	0.548(2)	0.18(1)	8	2
Cs3	Cs	0	0.5	0.119(1)	0.73(1)	4	2
N1	N	0.5	0.5	0.5	0.4	2	2
C1	C	0.563	0.563	0.587	0.2	16	2
C2	C	0.625	0.625	0.500	0.4	8	2
H1	H	0.603	0.517	0.656	0.4	16	2
H1a	H	0.517	0.603	0.656	0.4	16	2
H2	H	0.671	0.671	0.563	0.4	16	2
H2a	H	0.579	0.670	0.438	0.4	16	2
H2b	H	0.670	0.579	0.438	0.4	16	2

Table VI.II.IX. Refined structure of hydrated $Na_{6.7}$-MER (3.8).

Site	Type	x	y	z	Occ	Mult	Biso
Na1	Na	0	1	0.805(15)	0.38(13)	4	2
Na2	Na	0.5	0.718(2)	1	0.95(5)	4	2
Na3	Na	0	0.5	0.711(16)	0.36(3)	4	2
Ow1	O	0	1	0.725(10)	0.97(17)	4	2
Ow2	O	0.5	0	0	1.00(8)	2	2
Ow3	O	0.5	0.5	0.5	0.94(5)	2	2
Ow4	O	0.301(3)	0.385(2)	0	0.96(3)	8	2
Ow5	O	0.428(3)	0.377(3)	0	0.64(4)	8	2
O1	O	0.160(2)	0.160(2)	0.209(2)	1	16	1
O2	O	0.112(3)	0.290(3)	0	1	8	1
O5	O	0.707(3)	0.128(2)	0	1	8	1
O3	O	0	0.247(2)	0.198(2)	1	8	1
O6	O	0.757(2)	0	0.178(3)	1	8	1
O4	O	0.150(2)	0.354(2)	0.244(3)	1	16	1
Si1	Si	0.111(1)	0.258(1)	0.150(1)	0.8	16	1
Al1	Al	0.111(1)	0.258(1)	0.150(1)	0.2	16	1
Si2	Si	0.738(1)	0.103(1)	0.171(1)	0.8	16	1
Al2	Al	0.738(1)	0.103(1)	0.171(1)	0.2	16	1

Table VI.II.X. Refined structure of hydrated $K_{6.7}$-MER (3.8).

Site	Type	x	y	z	Occ	Mult	Biso
K1	K	0	1	0.775(4)	0.40(3)	4	2
K2	K	0.5	0.825(1)	1	0.55(1)	8	2
K3	K	0	0.5	0.806(11)	0.13(1)	4	2
Ow1	O	0	1	0.675(4)	1.00(6)	4	2
Ow2	O	0.5	0	0	0.43(3)	4	2
Ow3	O	0.5	0.5	0.5	1.00(3)	2	2
Ow4	O	0.425(1)	0.340(1)	0	0.67(1)	16	2
O1	O	0.145(1)	0.163(1)	0.192(1)	1	16	1
O2	O	0.119(1)	0.286(1)	0	1	16	1
O3	O	0	0.270(2)	0.218(2)	1	8	1
O5	O	0.789(2)	0	0.189(2)	1	8	1
O4	O	0.175(1)	0.350(1)	0.241(2)	1	16	1
Si1	Si	0.110(1)	0.268(1)	0.163(1)	0.8	16	1
Al1	Al	0.110(1)	0.268(1)	0.163(1)	0.2	16	1
Si2	Si	0.753(1)	0.111(1)	0.156(1)	0.8	16	1
Al2	Al	0.753(1)	0.111(1)	0.156(1)	0.2	16	1

Table VI.II.XI. Refined structure of hydrated $Cs_{6.2}K_{0.5}$-MER (3.8).

Site	Type	x	y	z	Occ	Mult	Biso
O2	O	0.130(1)	0.289(1)	0	1	16	1
O3	O	0	0.252(5)	0.186(9)	1	8	1
O5	O	0.751(6)	0	0.183(9)	1	8	1
O1	O	0.163(5)	0.164(5)	0.189(2)	1	16	1
O4	O	0.16(2)	0.350(2)	0.250(6)	1	16	1
Si1	Si	0.112(2)	0.261(3)	0.160(2)	0.8	16	1
Al1	Al	0.112(2)	0.261(3)	0.160(2)	0.2	16	1
Si2	Si	0.741(3)	0.111(2)	0.161(2)	0.8	16	1
Al2	Al	0.741(3)	0.111(2)	0.161(2)	0.2	16	1
Cs1	Cs	0	1	0.733(1)	0.59(1)	4	2
Cs2	Cs	0.5	0.812(1)	1	0.46(1)	8	2
Cs3	Cs	0	0.5	0.801(2)	0.25(1)	4	2
Ow1	O	0.5	0	0	0.79(5)	4	2
Ow2	O	0.5	0.5	0.5	1.00(6)	2	2
Ow3	O	0.5	0.5	0	0.85(6)	2	2
Ow4	O	0.375(1)	0.375(1)	0	0.74(2)	8	2

Table VI.II.XII. Refined structure of dehydrated $Na_{6.7}$-MER (3.8).

Site	Type	x	y	z	Occ	Mult	Biso
Na1	Na	0.054(2)	1	0.796(2)	0.40(2)	8	2
Na2	Na	0.5	0.784(2)	0.973(8)	0.33(1)	8	2
Na3	Na	0	0.5	0.843(9)	0.22(2)	4	2
O1	O	0.189(1)	0.127(1)	0.184(1)	1	16	1
O2	O	0.114(2)	0.260(1)	0	1	8	1
O5	O	0.661(1)	0.126(1)	0	1	8	1
O3	O	0	0.177(2)	0.201(2)	1	8	1
O6	O	0.663(2)	0	0.229(2)	1	8	1
O4	O	0.127(1)	0.296(1)	0.273(2)	1	16	1
Si1	Si	0.111(1)	0.224(1)	0.154(1)	0.8	16	1
Al1	Al	0.111(1)	0.224(1)	0.154(1)	0.2	16	1
Si2	Si	0.690(1)	0.110(1)	0.165(1)	0.8	16	1
Al2	Al	0.690(1)	0.110(1)	0.165(1)	0.2	16	1

Table VI.II.XIII. Refined structure of dehydrated $K_{6.7}$-MER (3.8)

Site	Type	x	y	z	Occ	Mult	Biso
O1	O	0.131(1)	0.691(1)	0.525(2)	1	16	1
O2	O	0.145(1)	-0.180(1)	0.332(2)	1	16	1
O3	O	-0.693(1)	-0.125(1)	0.207(2)	1	16	1
O4	O	0	0.690(1)	0.309(2)	1	8	1
O5	O	0.187(1)	0	0.380(2)	1	8	1
Si1	Si	0.110(1)	0.710(1)	0.350(1)	0.8	16	1
A11	Al	0.110(1)	0.710(1)	0.350(1)	0.2	16	1
Si2	Si	0.242(1)	-0.117(1)	0.328(1)	0.8	16	1
Al2	Al	0.242(1)	-0.117(1)	0.328(1)	0.2	16	1
K1	K	0.5	0.5	-0.088(2)	0.38(1)	4	2
K2	K	0.222(1)	0.5	0.572(2)	0.48(1)	8	2
K3	K	0	0.5	0.177(5)	0.28(1)	4	2

Table VI.II.XIV. Refined structure of dehydrated $Cs_{6.2}K_{0.5}$-MER (3.8)

Site	Type	x	y	z	Occ	Mult	Biso
O1	O	0.122(2)	0.701(2)	0.527(3)	1	16	1
O2	O	0.149(2)	-0.180(2)	0.320(2)	1	16	1
O3	O	-0.682(2)	-0.134(2)	0.208(3)	1	16	1
O4	O	0	0.698(2)	0.319(4)	1	8	1
O5	O	0.206(2)	0	0.314(3)	1	8	1
Si1	Si	0.113(1)	0.713(1)	0.361(2)	0.8	16	1
Al1	Al	0.113(1)	0.713(1)	0.361(2)	0.2	16	1
Si2	Si	0.245(1)	-0.110(1)	0.331(2)	0.8	16	1
Al2	Al	0.245(1)	-0.110(1)	0.331(2)	0.2	16	1
Cs1	Cs	0.5	0.5	0	0.78(1)	2	2
Cs2	Cs	0.288(1)	0.5	0.525(2)	0.24(1)	8	2
Cs3	Cs	0	0.5	0.120(1)	0.62(1)	4	2

VI.II.II MER (4.2)

Table VI.II.XV. Refined structure of dehydrated $K_{6.2}$-MER (4.2).

Site	Type	x	y	z	Occ.	Mult.	B_{iso}
K1	K	0	0	0.497(2)	0.32(1)	2	2
K11	K	0	0	0.121(3)	0.30(1)	2	2
K2a	K	0.5	-0.208(1)	0.260(1)	0.59(1)	4	2
K2b	K	0.657(1)	0	0.790(1)	0.64(1)	4	2
O1	O	-0.176(1)	0.155(1)	0.068(2)	1	8	1
O2	O	0.157(1)	0.181(1)	0.433(2)	1	8	1
O3	O	-0.120(1)	-0.298(1)	0.230(3)	1	8	1
O4	O	0	-0.212(2)	0.058(3)	1	4	1
O5	O	0	-0.286(2)	0.440(3)	1	4	1
O6	O	0.140(1)	-0.328(1)	-0.031(2)	1	8	1
O7	O	-0.329(1)	0.134(1)	0.532(2)	1	8	1
O8	O	0.297(1)	-0.119(1)	0.271(2)	1	8	1
O9	O	-0.208(2)	0	0.443(2)	1	4	1
O10	O	-0.280(2)	0	0.059(2)	1	4	1
Si1	Si	-0.111(1)	0.291(1)	0.391(1)	0.81	8	1
Al1	Al	-0.111(1)	0.291(1)	0.391(1)	0.19	8	1
Si2	Si	-0.108(1)	-0.246(1)	0.085(1)	0.81	8	1
Al2	Al	-0.108(1)	-0.246(1)	0.085(1)	0.19	8	1
Si3	Si	-0.226(1)	0.386(1)	-0.108(1)	0.81	8	1
Al3	Al	-0.226(1)	0.386(1)	-0.108(1)	0.19	8	1
Si4	Si	0.251(1)	0.394(1)	0.578(1)	0.81	8	1
Al4	Al	0.251(1)	0.394(1)	0.578(1)	0.19	8	1

Table VI.II.XVI. Refined structure of dehydrated $Cs_{6.2}$-MER (4.2).

Site	Type	x	y	z	Occ.	Mult.	B_{iso}
Cs1a	Cs	0	0	0.235(1)	0.80(1)	2	2
Cs2	Cs	-0.286(1)	0.5	0.277(1)	0.37(1)	4	2
Cs3	Cs	0	0.5	0.847(1)	0.64(1)	2	2
Cs31	Cs	0	0.5	0.390(1)	0.73(1)	2	2
O1	O	0.146(2)	-0.182(2)	0.068(3)	1	8	1
O2	O	0.180(2)	0.154(2)	0.434(3)	1	8	1
O3	O	-0.292(2)	-0.126(2)	0.224(3)	1	8	1
O4	O	-0.203(3)	0	0.062(4)	1	4	1
O5	O	-0.292(3)	0	0.430(4)	1	4	1
O6	O	-0.318(2)	0.134(2)	-0.042(3)	1	8	1
O7	O	0.130(2)	-0.322(2)	0.544(3)	1	8	1
O8	O	-0.114(2)	0.296(2)	0.276(3)	1	8	1
O9	O	0	-0.198(3)	0.444(4)	1	4	1
O10	O	0	-0.307(3)	0.060(4)	1	4	1
Si1	Si	0.283(1)	-0.119(1)	0.386(1)	0.81	8	1
Al1	Al	0.283(1)	-0.119(1)	0.386(1)	0.19	8	1
Si2	Si	-0.242(1)	-0.110(1)	0.081(1)	0.81	8	1
Al2	Al	-0.242(1)	-0.110(1)	0.081(1)	0.19	8	1
Si3	Si	0.389(1)	-0.207(1)	-0.117(1)	0.81	8	1
Al3	Al	0.389(1)	-0.207(1)	-0.117(1)	0.19	8	1
Si4	Si	0.395(1)	0.254(1)	0.577(2)	0.81	8	1
Al4	Al	0.395(1)	0.254(1)	0.577(2)	0.19	8	1

Table VI.II.XVII. Refined structure of dehydrated $K_{5.7}Na_{0.5}$-MER (4.2).

Site	Type	x	y	z	Occ.	Mult.	B_{iso}
K1	K	0	0	0.494(3)	0.22(1)	2	2
K11	K	0	0	0.129(2)	0.30(1)	2	2
K2a	K	0.5	-0.199(1)	0.250(1)	0.47(1)	4	2
K2b	K	0.656(1)	0	0.788(1)	0.61(1)	4	2
O1	O	-0.175(1)	0.158(1)	0.068(2)	1	8	1
O2	O	0.157(1)	0.182(1)	0.431(2)	1	8	1
O3	O	-0.118(1)	-0.297(1)	0.229(2)	1	8	1
O4	O	0	-0.216(1)	0.053(2)	1	4	1
O5	O	0	-0.287(1)	0.444(2)	1	4	1
O6	O	0.137(1)	-0.333(1)	-0.028(2)	1	8	1
O7	O	-0.331(1)	0.132(1)	0.531(2)	1	8	1
O8	O	0.301(1)	-0.119(1)	0.270(2)	1	8	1
O9	O	-0.206(1)	0	0.439(2)	1	4	1
O10	O	-0.276(1)	0	0.056(2)	1	4	1
Si1	Si	-0.109(1)	0.292(1)	0.395(1)	0.81	8	1
Al1	Al	-0.109(1)	0.292(1)	0.395(1)	0.19	8	1
Si2	Si	-0.108(1)	-0.247(1)	0.082(1)	0.81	8	1
Al2	Al	-0.108(1)	-0.247(1)	0.082(1)	0.19	8	1
Si3	Si	-0.228(1)	0.384(1)	-0.105(1)	0.81	8	1
Al3	Al	-0.228(1)	0.384(1)	-0.105(1)	0.19	8	1
Si4	Si	0.251(1)	0.393(1)	0.578(1)	0.81	8	1
Al4	Al	0.251(1)	0.393(1)	0.578(1)	0.19	8	1

Table VI.II.XVIII. Refined structure of dehydrated $K_{5.2}Na_{1.0}$-MER (4.2).

Site	Type	x	y	z	Occ.	Mult.	B_{iso}
K11	K	0	0	0.014(2)	0.81(2)	2	2
K2a	K	0.5	-0.183(3)	0.153(4)	0.37(2)	4	2
K2b	K	0.680(1)	0	0.780(2)	0.78(1)	4	2
O1	O	-0.180(2)	0.170(2)	0.070(3)	1	8	1
O2	O	0.145(2)	0.184(2)	0.421(3)	1	8	1
O3	O	-0.112(2)	-0.317(2)	0.232(3)	1	8	1
O4	O	0	-0.211(2)	0.074(4)	1	4	1
O5	O	0	-0.305(3)	0.446(4)	1	4	1
O6	O	0.129(2)	-0.339(2)	-0.027(3)	1	8	1
O7	O	-0.317(2)	0.133(3)	0.527(3)	1	8	1
O8	O	0.289(2)	-0.123(2)	0.266(3)	1	8	1
O9	O	-0.195(3)	0	0.428(5)	1	4	1
O10	O	-0.277(3)	0	0.060(4)	1	4	1
Si1	Si	-0.110(1)	0.291(1)	0.394(2)	1	8	1
Al1	Al	-0.110(1)	0.291(1)	0.394(2)	0.19	8	1
Si2	Si	-0.113(1)	-0.260(1)	0.090(2)	0.81	8	1
Al2	Al	-0.113(1)	-0.260(1)	0.090(2)	0.19	8	1
Si3	Si	-0.227(1)	0.384(1)	-0.092(2)	0.81	8	1
Al3	Al	-0.227(1)	0.384(1)	-0.092(2)	0.19	8	1
Si4	Si	0.273(1)	0.390(1)	0.592(2)	0.81	8	1
Al4	Al	0.273(1)	0.390(1)	0.592(2)	0.19	8	1

Table VI.II.XIX. Refined structure of dehydrated $K_{4.2}Na_{2.0}$-MER (4.2).

Site	Type	x	y	z	Occ.	Mult.	B_{iso}
K11	K	0	0	0.100(3)	0.39(1)	2	2
K2a	K	0.5	-0.068(1)	0.185(2)	0.41(1)	4	2
K2b	K	0.711(1)	0	0.732(4)	0.46(1)	4	2
O1	O	0	0.195(2)	0.060(3)	1	8	1
O2	O	0.132(2)	0.181(2)	0.420(3)	1	8	1
O3	O	-0.111(1)	-0.329(1)	0.246(4)	1	8	1
O4	O	0	-0.310(3)	0.025(4)	1	4	1
O5	O	0	-0.318(3)	0.466(4)	1	4	1
O6	O	0.178(2)	-0.383(2)	0.006(3)	1	8	1
O7	O	-0.311(2)	0.145(2)	0.509(3)	1	8	1
O8	O	0.269(1)	-0.121(1)	0.250(4)	1	8	1
O9	O	-0.198(3)	0	0.432(5)	1	4	1
O10	O	-0.180(3)	0	0.085(5)	1	4	1
Si1	Si	-0.108(1)	0.293(1)	0.406(2)	1	8	1
Al1	Al	-0.108(1)	0.293(1)	0.406(2)	0.19	8	1
Si2	Si	-0.112(1)	-0.303(1)	0.083(2)	0.81	8	1
Al2	Al	-0.112(1)	-0.303(1)	0.083(2)	0.19	8	1
Si3	Si	-0.271(2)	0.390(1)	-0.091(2)	0.81	8	1
Al3	Al	-0.271(2)	0.390(1)	-0.091(2)	0.19	8	1
Si4	Si	0.275(2)	0.390(1)	0.593(2)	0.81	8	1
Al4	Al	0.275(2)	0.390(1)	0.593(2)	0.19	8	1

Table VI.II.XX. Refined structure of dehydrated $K_{3.2}Na_{3.0}$-MER (4.2).

Site	Type	x	y	z	Occ.	Mult.	B_{iso}
Na1	Na	0	0	0.445(3)	0.45(2)	2	2
Na11	Na	0	0	0.201(4)	0.30(1)	2	2
K2a	K	-0.209(1)	0.5	0.207(2)	0.37(1)	4	2
K2b	K	0	0.559(1)	0.690(2)	0.38(1)	4	2
O1	O	0.135(1)	-0.187(2)	0.071(2)	1	8	1
O2	O	0.144(1)	0.191(2)	0.427(2)	1	8	1
O3	O	-0.270(1)	-0.122(1)	0.240(2)	1	8	1
O4	O	-0.182(2)	0	0.060(2)	1	4	1
O5	O	-0.186(1)	0	0.404(2)	1	4	1
O6	O	-0.311(1)	0.133(2)	-0.014(2)	1	8	1
O7	O	0.185(1)	-0.376(2)	0.492(2)	1	8	1
O8	O	-0.118(1)	0.333(1)	0.257(2)	1	8	1
O9	O	0	-0.317(2)	0.470(2)	1	4	1
O10	O	0	-0.321(2)	0.033(2)	1	4	1
Si1	Si	0.234(1)	-0.114(1)	0.399(1)	0.81	8	1
Al1	Al	0.234(1)	-0.114(1)	0.399(1)	0.19	8	1
Si2	Si	-0.219(1)	-0.106(1)	0.088(1)	0.81	8	1
Al2	Al	-0.219(1)	-0.106(1)	0.088(1)	0.19	8	1
Si3	Si	0.391(1)	-0.206(1)	-0.102(1)	0.81	8	1
Al3	Al	0.391(1)	-0.206(1)	-0.102(1)	0.19	8	1
Si4	Si	0.390(1)	0.189(1)	0.577(1)	0.81	8	1
Al4	Al	0.390(1)	0.189(1)	0.577(1)	0.19	8	1

Table VI.II.XXI. Refined structure of dehydrated $K_{2.2}Na_{4.0}$-MER (4.2).

Site	Type	x	y	z	Occ.	Mult.	B_{iso}
Na11	Na	0	0	0.081(3)	0.60(2)	2	2
K2b	K	0.5	-0.062(1)	0.189(2)	0.37(1)	4	2
Na2a	Na	0.707(1)	0	0.718(3)	0.73(2)	4	2
O1	O	-0.150(2)	0.196(2)	0.062(3)	1	8	1
O2	O	0.130(2)	0.187(2)	0.422(3)	1	8	1
O3	O	-0.111(1)	-0.333(1)	0.243(3)	1	8	1
O4	O	0	-0.319(3)	0.021(4)	1	4	1
O5	O	0	-0.330(3)	0.463(4)	1	4	1
O6	O	0.182(2)	-0.385(2)	0.005(3)	1	8	1
O7	O	-0.308(2)	0.137(2)	0.514(3)	1	8	1
O8	O	0.262(1)	-0.115(1)	0.253(3)	1	8	1
O9	O	-0.183(3)	0	0.437(4)	1	4	1
O10	O	-0.171(3)	0	0.084(4)	1	4	1
Si1	Si	-0.109(1)	0.298(1)	0.398(2)	1	8	1
Al1	Al	-0.109(1)	0.298(1)	0.398(2)	0.19	8	1
Si2	Si	-0.113(1)	-0.309(1)	0.081(2)	0.81	8	1
Al2	Al	-0.113(1)	-0.309(1)	0.081(2)	0.19	8	1
Si3	Si	-0.272(1)	0.390(1)	-0.096(2)	0.81	8	1
Al3	Al	-0.272(1)	0.390(1)	-0.096(2)	0.19	8	1
Si4	Si	0.280(1)	0.389(1)	0.588(2)	0.81	8	1
Al4	Al	0.280(1)	0.389(1)	0.588(2)	0.19	8	1

Table VI.II.XXII. Refined structure of dehydrated $K_{1.2}Na_{5.0}$-MER (4.2).

Site	Type	x	y	z	Occ.	Mult.	B_{iso}
Na11	Na	0	0	-0.040(2)	0.09(3)	2	2
Na1	Na	0	0	0.445(3)	0.67(3)	2	2
K2a	K	0.5	-0.070(1)	0.189(3)	0.31(1)	4	2
Na2b	Na	0.706(1)	0	0.704(2)	0.66(2)	4	2
O1	O	0.134(2)	-0.190(2)	0.068(3)	1	8	1
O2	O	0.141(2)	0.189(2)	0.422(3)	1	8	1
O3	O	-0.263(1)	-0.118(1)	0.239(3)	1	8	1
O4	O	-0.174(3)	0	0.061(4)	1	4	1
O5	O	-0.184(3)	0	0.418(4)	1	4	1
O6	O	-0.307(2)	0.124(2)	-0.018(2)	1	8	1
O7	O	0.185(2)	-0.372(2)	0.497(3)	1	8	1
O8	O	-0.117(1)	0.335(1)	0.246(3)	1	8	1
O9	O	0	-0.319(3)	0.470(3)	1	4	1
O10	O	0	-0.332(3)	0.025(3)	1	4	1
Si1	Si	0.231(1)	-0.107(1)	0.391(1)	0.81	8	1
Al1	Al	0.231(1)	-0.107(1)	0.391(1)	0.19	8	1
Si2	Si	-0.219(1)	-0.111(1)	0.090(1)	0.81	8	1
Al2	Al	-0.219(1)	-0.111(1)	0.090(1)	0.19	8	1
Si3	Si	0.386(2)	-0.196(1)	-0.076(1)	0.81	8	1
Al3	Al	0.386(2)	-0.196(1)	-0.076(1)	0.19	8	1
Si4	Si	0.386(2)	0.193(1)	0.602(1)	0.81	8	1
Al4	Al	0.386(2)	0.193(1)	0.602(1)	0.19	8	1

Table VI.II.XXIII. Refined structure of $K_{6.2}$-MER (4.2) at 20 mbar of CO_2.

Site	Type	x	y	z	Occ.	Mult.	B_{iso}
K1	K	0	0	0.531(3)	0.24(1)	2	2
K11	K	0	0	0.082(2)	0.46(1)	2	2
K2a	K	0.5	-0.212(1)	0.260(1)	0.59(1)	4	2
K2b	K	0.657(1)	0	0.789(1)	1	4	2
O1	O	-0.177(1)	0.156(1)	0.067(2)	1	8	1
O2	O	0.157(1)	0.183(1)	0.435(2)	1	8	1
O3	O	-0.119(1)	-0.300(1)	0.231(2)	1	8	1
O4	O	0	-0.211(1)	0.060(2)	1	4	1
O5	O	0	-0.287(1)	0.441(2)	1	4	1
O6	O	0.139(1)	-0.329(1)	-0.032(2)	1	8	1
O7	O	-0.330(1)	0.132(1)	0.529(2)	1	8	1
O8	O	0.296(1)	-0.118(1)	0.272(2)	1	8	1
O9	O	-0.204(1)	0	0.441(1)	1	4	1
O10	O	-0.282(1)	0	0.061(1)	1	4	1
Si1	Si	-0.110(1)	0.291(1)	0.395(1)	0.81	8	1
Al1	Al	-0.110(1)	0.291(1)	0.395(1)	0.19	8	1
Si2	Si	-0.107(1)	-0.247(1)	0.084(1)	0.81	8	1
Al2	Al	-0.107(1)	-0.247(1)	0.084(1)	0.19	8	1
Si3	Si	-0.228(1)	0.385(1)	-0.112(1)	0.81	8	1
Al3	Al	-0.228(1)	0.385(1)	-0.112(1)	0.19	8	1
Si4	Si	0.252(1)	0.393(1)	0.578(1)	0.81	8	1
Al4	Al	0.252(1)	0.393(1)	0.578(1)	0.19	8	1

Table VI.II.XXIV. Refined structure of $K_{6.2}$-MER (4.2) at 100 mbar of CO_2.

Site	Type	x	y	z	Occ.	Mult.	B_{iso}
K1	K	0	0	0.752(1)	0.30(1)	4	2
K2	K	0.5	0.824(1)	0.021(1)	0.63(1)	8	2
O1	O	0.160(1)	0.175(1)	0.185(1)	1	16	1
O2	O	0.124(1)	0.298(1)	0	1	16	1
O3	O	0	0.266(1)	0.201(1)	1	8	1
O5	O	0.780(1)	0	0.194(1)	1	8	1
O4	O	0.162(1)	0.366(1)	0.235(1)	1	16	1
Si1	Si	0.112(2)	0.277(2)	0.153(1)	1	16	1
Al1	Al	0.112(2)	0.277(2)	0.153(1)	1	16	1
Si2	Si	0.745(1)	0.109(1)	0.164(1)	1	16	1
Al2	Al	0.745(1)	0.109(1)	0.164(1)	1	16	1
C1	C	0.5	0.5	0	0.37(1)	2	4
OC1	O	0.5	0.5	0.117	0.37(1)	4	4
C2	C	0.148(1)	0	0.5	0.22(2)	8	4
OC2	O	0.148(1)	-0.082	0.5	0.22(2)	16	4
C3	C	0	0.5	0.208(2)	0.47(1)	4	4
OC3	O	0	0.5	0.325(2)	0.47(1)	4	4
OC3a	O	0	0.5	0.090(2)	0.47(1)	4	4
C4	C	0	0	0	0.66(1)	2	4
OC4	O	0	0	0.117	0.66(1)	4	4

Table VI.II.XXV. Refined structure of $K_{6.2}$-MER (4.2) at 300 mbar of CO_2.

Site	Type	x	y	z	Occ.	Mult.	B_{iso}
K1	K	0	0	0.744(1)	0.27(1)	4	2
K2	K	0.5	0.826(1)	0.020(1)	0.65(1)	8	2
O1	O	0.160(1)	0.177(1)	0.185(1)	1	16	1
O2	O	0.1252)	0.298(1)	0	1	16	1
O3	O	0	0.260(1)	0.202(1)	1	8	1
O5	O	0.780(1)	0	0.195(1)	1	8	1
O4	O	0.159(1)	0.366(1)	0.237(1)	1	16	1
Si1	Si	0.111(1)	0.276(1)	0.154(1)	1	16	1
Al1	Al	0.111(1)	0.276(1)	0.154(1)	1	16	1
Si2	Si	0.744(1)	0.109(1)	0.163(1)	1	16	1
Al2	Al	0.744(1)	0.109(1)	0.163(1)	1	16	1
C1	C	0.5	0.5	0	0.41(1)	2	4
OC1	O	0.5	0.5	0.117	0.41(1)	4	4
C2	C	0.152(1)	0	0.5	0.33(1)	8	4
OC2	O	0.152(1)	-0.082	0.5	0.33(1)	16	4
C3	C	0	0.5	0.213(2)	0.54(1)	4	4
OC3	O	0	0.5	0.330(2)	0.54(1)	4	4
OC3a	O	0	0.5	0.096(2)	0.54(1)	4	4
C4	C	0	0	0	0.76(1)	2	4
OC4	O	0	0	0.117	0.76(1)	4	4

Table VI.II.XXVI. Refined structure of $K_{6.2}$-MER (4.2) at 510 mbar of CO_2.

Site	Type	x	y	z	Occ.	Mult.	B_{iso}
K1	K	0	0	0.742(1)	0.27(1)	4	2
K2	K	0.5	0.827(1)	0.019(1)	0.66(1)	8	2
O1	O	0.159(1)	0.177(1)	0.185(1)	1	16	1
O2	O	0.126(1)	0.298(1)	0	1	16	1
O3	O	0	0.258(1)	0.203(1)	1	8	1
O5	O	0.778(1)	0	0.195(1)	1	8	1
O4	O	0.158(1)	0.365(1)	0.239(1)	1	16	1
Si1	Si	0.111(1)	0.275(1)	0.155(1)	1	16	1
Al1	Al	0.111(1)	0.275(1)	0.155(1)	1	16	1
Si2	Si	0.743(1)	0.109(1)	0.162(1)	1	16	1
Al2	Al	0.743(1)	0.109(1)	0.162(1)	1	16	1
C1	C	0.5	0.5	0	0.42(1)	2	4
OC1	O	0.5	0.5	0.117	0.42(1)	4	4
C2	C	0.151(1)	0	0.5	0.35(1)	8	4
OC2	O	0.151(1)	-0.082	0.5	0.35(1)	16	4
C3	C	0	0.5	0.208(2)	0.56(1)	4	4
OC3	O	0	0.5	0.325(2)	0.56(1)	4	4
OC3a	O	0	0.5	0.091(2)	0.56(1)	4	4
C4	C	0	0	0	0.78(1)	2	4
OC4	O	0	0	0.117	0.78(1)	4	4

Table VI.II.XXVII. Refined structure of $K_{6.2}$-MER (4.2) at 990 mbar of CO_2.

Site	Type	x	y	z	Occ.	Mult.	B_{iso}
K1	K	0	0	0.740(1)	0.26(1)	4	2
K2	K	0.5	0.827(1)	0.019(1)	0.66(1)	8	2
O1	O	0.159(1)	0.176(1)	0.185(1)	1	16	1
O2	O	0.126(1)	0.298(1)	0	1	16	1
O3	O	0	0.257(1)	0.203(1)	1	8	1
O5	O	0.777(1)	0	0.195(1)	1	8	1
O4	O	0.157(1)	0.365(1)	0.241(1)	1	16	1
Si1	Si	0.111(1)	0.275(1)	0.155(1)	1	16	1
Al1	Al	0.111(1)	0.275(1)	0.155(1)	1	16	1
Si2	Si	0.743(1)	0.109(1)	0.162(1)	1	16	1
Al2	Al	0.743(1)	0.109(1)	0.162(1)	1	16	1
C1	C	0.5	0.5	0	0.42(1)	2	4
OC1	O	0.5	0.5	0.117	0.42(1)	4	4
C2	C	0.152(1)	0	0.5	0.38(1)	8	4
OC2	O	0.152(1)	-0.082	0.5	0.38(1)	16	4
C3	C	0	0.5	0.207(2)	0.58(1)	4	4
OC3	O	0	0.5	0.324(2)	0.58(1)	4	4
OC3a	O	0	0.5	0.089(2)	0.58(1)	4	4
C4	C	0	0	0	0.80(1)	2	4
OC4	O	0	0	0.117	0.80(1)	4	4

Table VI.II.XXVIII. Refined structure of $K_{6.2}$-MER (4.2) at 1810 mbar of CO_2.

Site	Type	x	y	z	Occ.	Mult.	B_{iso}
K1	K	0	0	0.739(1)	0.26(1)	4	2
K2	K	0.5	0.827(1)	0.018(1)	0.66(1)	8	2
O1	O	0.159(1)	0.177(1)	0.185(1)	1	16	1
O2	O	0.126(1)	0.298(1)	0	1	16	1
O3	O	0	0.256(1)	0.203(1)	1	8	1
O5	O	0.776(1)	0	0.195(1)	1	8	1
O4	O	0.156(1)	0.364(1)	0.242(1)	1	16	1
Si1	Si	0.111(1)	0.275(1)	0.155(1)	1	16	1
Al1	Al	0.111(1)	0.275(1)	0.155(1)	1	16	1
Si2	Si	0.743(1)	0.109(1)	0.162(1)	1	16	1
Al2	Al	0.743(1)	0.109(1)	0.162(1)	1	16	1
C1	C	0.5	0.5	0	0.42(1)	2	4
OC1	O	0.5	0.5	0.117	0.42(1)	4	4
C2	C	0.152(1)	0	0.5	0.41(1)	8	4
OC2	O	0.152(1)	-0.082	0.5	0.41(1)	16	4
C3	C	0	0.5	0.207(2)	0.61(1)	4	4
OC3	O	0	0.5	0.324(2)	0.61(1)	4	4
OC3a	O	0	0.5	0.090(2)	0.61(1)	4	4
C4	C	0	0	0	0.81(1)	2	4
OC4	O	0	0	0.117	0.81(1)	4	4

Table VI.II.XXIX. Refined structure of $K_{6.2}$-MER (4.2) at 4240 mbar of CO_2.

Site	Type	x	y	z	Occ.	Mult.	B_{iso}
K1	K	0	0	0.738(1)	0.26(1)	4	2
K2	K	0.5	0.827(1)	0.017(1)	0.66(1)	8	2
O1	O	0.159(1)	0.177(1)	0.185(1)	1	16	1
O2	O	0.127(1)	0.298(1)	0	1	16	1
O3	O	0	0.254(1)	0.203(1)	1	8	1
O5	O	0.775(1)	0	0.195(1)	1	8	1
O4	O	0.155(1)	0.363(1)	0.244(1)	1	16	1
Si1	Si	0.111(1)	0.274(1)	0.155(1)	1	16	1
Al1	Al	0.111(1)	0.274(1)	0.155(1)	1	16	1
Si2	Si	0.742(1)	0.109(1)	0.161(1)	1	16	1
Al2	Al	0.742(1)	0.109(1)	0.161(1)	1	16	1
C1	C	0.5	0.5	0	0.43(1)	2	4
OC1	O	0.5	0.5	0.117	0.43(1)	4	4
C2	C	0.153(1)	0	0.5	0.43(1)	8	4
OC2	O	0.153(1)	-0.082	0.5	0.43(1)	16	4
C3	C	0	0.5	0.209(2)	0.65(1)	4	4
OC3	O	0	0.5	0.326(2)	0.65(1)	4	4
OC3a	O	0	0.5	0.092(2)	0.65(1)	4	4
C4	C	0	0	0	0.82(1)	2	4
OC4	O	0	0	0.117	0.82(1)	4	4

Table VI.II.XXX. Refined structure of $Cs_{6.2}$-MER (4.2) at 20 mbar of CO_2.

Site	Type	x	y	z	Occ.	Mult.	B_{iso}
Cs1a	Cs	0	0	0	0.48(1)	2	2
Cs2	Cs	0.5	0.695(1)	0	0.30(1)	8	2
Cs3	Cs	0	0.5	0.119(1)	0.58(1)	4	2
O1	O	0.177(1)	0.150(1)	0.191(1)	1	16	1
O2	O	0.129(1)	0.299(1)	0	1	16	1
O3	O	0	0.202(1)	0.174(2)	1	8	1
O5	O	0.705(1)	0.000	0.198(2)	1	8	1
O4	O	0.129(1)	0.318(1)	0.280(1)	1	16	1
Si1	Si	0.107(1)	0.243(1)	0.152(1)	0.81	16	1
Al1	Al	0.107(1)	0.243(1)	0.152(1)	0.19	16	1
Si2	Si	0.713(1)	0.115(1)	0.150(1)	0.81	16	1
Al2	Al	0.713(1)	0.115(1)	0.150(1)	0.19	16	1
C1	C	0.5	0.5	0	0.81(1)	2	4
OC1	O	0.5	0.5	0.117	0.81(1)	4	4

Table VI.II.XXXI. Refined structure of $Cs_{6.2}$-MER (4.2) at 40 mbar of CO_2.

Site	Type	x	y	z	Occ.	Mult.	B_{iso}
Cs1a	Cs	0	0	0	0.47(1)	2	2
Cs2	Cs	0.5	0.695(1)	0	0.29(1)	8	2
Cs3	Cs	0	0.5	0.122(1)	0.59(1)	4	2
O1	O	0.177(1)	0.150(1)	0.190(1)	1	16	1
O2	O	0.130(1)	0.299(1)	0	1	16	1
O3	O	0	0.203(1)	0.174(2)	1	8	1
O5	O	0.712(1)	0.000	0.201(2)	1	8	1
O4	O	0.128(1)	0.321(1)	0.280(1)	1	16	1
Si1	Si	0.108(1)	0.244(1)	0.154(1)	0.81	16	1
Al1	Al	0.108(1)	0.244(1)	0.154(1)	0.19	16	1
Si2	Si	0.715(1)	0.114(1)	0.150(1)	0.81	16	1
Al2	Al	0.715(1)	0.114(1)	0.150(1)	0.19	16	1
C1	C	0.5	0.5	0	0.88(1)	2	4
OC1	O	0.5	0.5	0.117	0.88(1)	4	4

Table VI.II.XXXII. Refined structure of narrow-pore $Cs_{6.2}$-MER (4.2) at 100 mbar CO_2.

Site	Type	x	y	z	Occ.	Mult.	B_{iso}
Cs1a	Cs	0	0	0	0.47(1)	2	2
Cs2	Cs	0.5	0.698(1)	0	0.28(1)	8	2
Cs3	Cs	0	0.5	0.122(1)	0.59(1)	4	2
O1	O	0.175(2)	0.144(2)	0.177(2)	1	16	1
O2	O	0.130(1)	0.301(2)	0	1	16	1
O3	O	0	0.207(2)	0.168(4)	1	8	1
O5	O	0.696(3)	0	0.197(3)	1	8	1
O4	O	0.132(2)	0.315(2)	0.277(2)	1	16	1
Si1	Si	0.109(1)	0.239(1)	0.149(2)	0.81	16	1
Al1	Al	0.109(1)	0.239(1)	0.149(2)	0.19	16	1
Si2	Si	0.711(1)	0.113(1)	0.151(1)	0.81	16	1
Al2	Al	0.711(1)	0.113(1)	0.151(1)	0.19	16	1
C1	C	0.5	0.5	0	1.00(1)	2	4
OC1	O	0.5	0.5	0.117	1.00(1)	4	4

Table VI.II.XXXIII. Refined structure of wide-pore $Cs_{6.2}$-MER (4.2) at 100 mbar CO_2.

Site	Type	x	y	z	Occ.	Mult.	B_{iso}
Cs1aa	Cs	0	0	0	0.44(1)	4	2
Cs2a	Cs	0.5	0.789(2)	0	0.24(1)	8	2
Cs3a	Cs	0	0.5	0.089(4)	0.27(1)	4	2
O1a	O	0.173(4)	0.173(4)	0.163(4)	1	16	1
O2a	O	0.102(3)	0.303(2)	0	1	16	1
O3a	O	0	0.227(6)	0.206(7)	1	8	1
O5a	O	0.768(7)	0	0.204(7)	1	8	1
O4a	O	0.146(4)	0.348(4)	0.258(6)	1	16	1
Si1a	Si	0.102(3)	0.267(2)	0.160(3)	0.81	16	1
Al1a	Al	0.102(3)	0.267(2)	0.160(3)	0.19	16	1
Si2a	Si	0.733(2)	0.104(3)	0.160(4)	0.81	16	1
Al2a	Al	0.733(2)	0.104(3)	0.160(4)	0.19	16	1
C1a	C	0.5	0.5	0	0.41(6)	2	4
OC1a	O	0.5	0.5	0.117	0.41(6)	4	4
C2a	C	0.172(2)	0	0.5	0.69(2)	8	4
OC2a	O	0.172(2)	-0.082	0.5	0.69(2)	16	4
C3a	C	0	0	0	0.67(4)	2	4
OC3a	O	0	0	0.117	0.67(4)	4	4

Table VI.II.XXXIV. Refined structure of $Cs_{6.2}$-MER (4.2) at 230 mbar CO_2.

Site	Type	x	y	z	Occ.	Mult.	B_{iso}
Cs1	Cs	0	0	-0.264(1)	0.48(1)	4	2
Cs2	Cs	0.5	0.795(1)	0.013(2)	0.21(1)	8	2
Cs3	Cs	0	0.5	0.046(1)	0.31(1)	4	2
O1	O	0.167(2)	0.168(2)	0.175(1)	1	16	1
O2	O	0.114(1)	0.297(1)	0	1	16	1
O3	O	0	0.249(3)	0.200(4)	1	8	1
O5	O	0.753(3)	0	0.198(4)	1	8	1
O4	O	0.155(4)	0.346(4)	0.250(2)	1	16	1
Si1	Si	0.109(1)	0.265(1)	0.157(1)	0.81	16	1
Al1	Al	0.109(1)	0.265(1)	0.157(1)	0.19	16	1
Si2	Si	0.737(1)	0.110(1)	0.156(1)	0.81	16	1
Al2	Al	0.737(1)	0.110(1)	0.156(1)	0.19	16	1
C1	C	0.5	0.5	0	0.33(2)	2	4
OC1	O	0.5	0.5	0.117	0.33(2)	4	4
C2	C	0.167(1)	0	0.5	0.49(1)	8	4
OC2	O	0.167(1)	-0.082	0.5	0.49(1)	16	4
C3	C	0	0	0	0.76(1)	2	4
OC3	O	0	0	0.117	0.76(1)	4	4

Table VI.II.XXXV. Refined structure of $Cs_{6.2}$-MER (4.2) at 880 mbar CO_2.

Site	Type	x	y	z	Occ.	Mult.	B_{iso}
Cs1	Cs	0	0	-0.256(1)	0.47(1)	4	2
Cs2	Cs	0.5	0.792(1)	0.002(1)	0.28(2)	8	2
Cs3	Cs	0	0.5	0.055(1)	0.30(1)	4	2
O1	O	0.166(1)	0.166(1)	0.180(1)	1	16	1
O2	O	0.117(1)	0.294(1)	0	1	16	1
O3	O	0	0.249(2)	0.195(3)	1	8	1
O5	O	0.751(2)	0	0.196(3)	1	8	1
O4	O	0.154(16)	0.346(16)	0.250(2)	1	16	1
Si1	Si	0.111(1)	0.263(1)	0.157(1)	0.81	16	1
Al1	Al	0.111(1)	0.263(1)	0.157(1)	0.19	16	1
Si2	Si	0.737(1)	0.111(1)	0.157(1)	0.81	16	1
Al2	Al	0.737(1)	0.111(1)	0.157(1)	0.19	16	1
C1	C	0.5	0.5	0	0.50(1)	2	4
OC1	O	0.5	0.5	0.116	0.50(1)	4	4
C2	C	0.169(1)	0	0.5	0.48(1)	8	4
OC2	O	0.169(1)	-0.082	0.5	0.48(1)	16	4
C3	C	0	0	0	0.81(1)	2	4
OC3	O	0	0	0.116	0.81(1)	4	4

Table VI.II.XXXVI. Refined structure of $Cs_{6.2}$-MER (4.2) at 2980 mbar CO_2.

Site	Type	x	y	z	Occ.	Mult.	B_{iso}
Cs1	Cs	0	0	-0.250(1)	0.46(1)	4	2
Cs2	Cs	0.5	0.790(1)	0.001(1)	0.35(1)	8	2
Cs3	Cs	0	0.5	0.069(1)	0.29(1)	4	2
O1	O	0.163(1)	0.163(1)	0.182(1)	1	16	1
O2	O	0.115(1)	0.295(1)	0	1	16	1
O3	O	0	0.248(2)	0.197(3)	1	8	1
O5	O	0.755(2)	0	0.191(4)	1	8	1
O4	O	0.149(4)	0.3494)	0.254(2)	1	16	1
Si1	Si	0.112(1)	0.263(1)	0.158(1)	0.81	16	1
Al1	Al	0.112(1)	0.263(1)	0.158(1)	0.19	16	1
Si2	Si	0.739(1)	0.112(1)	0.155(1)	0.81	16	1
Al2	Al	0.739(1)	0.112(1)	0.155(1)	0.19	16	1
C1	C	0.5	0.5	0	0.60(1)	2	4
OC1	O	0.5	0.5	0.116	0.60(1)	4	4
C2	C	0.177(1)	0	0.5	0.52(1)	8	4
OC2	O	0.177(1)	-0.082	0.5	0.52(1)	16	4
C3	C	0	0	0	0.86(1)	2	4
OC3	O	0	0	0.116	0.86(1)	4	4

VI.II.III Li,M-MER (4.2)

Refined structure of hydrated $Li_{6.2}$-MER (4.2)

Site	Type	x	y	z	Occ.	W	B_{iso}
Ow1	O	0	0	0.719(1)	1.00	4	2
Ow2	O	0.5	0.5	0.5	1.00	2	2
Ow3	O	0.313(1)	0.439(1)	0.000(1)	0.50(1)	16	2
Ow4	O	0.452(2)	0.402(2)	0	0.53(2)	8	2
O1	O	0.168(2)	0.159(1)	0.202(1)	1	16	1
O2	O	0.115(2)	0.278(2)	0	1	8	1
O5	O	0.696(1)	0.129(2)	0	1	8	1
O3	O	0	0.226(1)	0.196(3)	1	8	1
O6	O	0.752(2)	0	0.187(3)	1	8	1
O4	O	0.142(1)	0.350(1)	0.248(3)	1	16	1
Si1	Si	0.106(1)	0.254(1)	0.158(1)	0.81	16	1
Al1	Al	0.106(1)	0.254(1)	0.158(1)	0.19	16	1
Si2	Si	0.731(1)	0.109(1)	0.157(1)	0.81	16	1
Al2	Al	0.731(1)	0.109(1)	0.157(1)	0.19	16	1

Table VI.II.XXXVII. Refined structure of dehydrated $Li_{6.2}$-MER (4.2).

Site	Type	x	y	z	Occ.	W	B_{iso}
O1	O	0.198(1)	0.125(1)	0.186(1)	1	16	1
O2	O	0.118(1)	0.245(1)	0	1	8	1
O5	O	0.661(1)	0.141(1)	0	1	8	1
O3	O	0	0.149(1)	0.173(2)	1	8	1
O6	O	0.645(1)	0	0.203(1)	1	8	1
O4	O	0.118(1)	0.305(1)	0.250(1)	1	16	1
Si1	Si	0.106(1)	0.206(1)	0.152(1)	0.81	16	1
Al1	Al	0.106(1)	0.206(1)	0.152(1)	0.19	16	1
Si2	Si	0.675(1)	0.105(1)	0.161(1)	0.81	16	1
Al2	Al	0.675(1)	0.105(1)	0.161(1)	0.19	16	1
Li1	Li	0.50(9)	0.5	0.331(13)	0.38(3)	8	2
Li2	Li	0.5	0.101(11)	0.164(16)	0.39(3)	8	2

Table VI.II.XXXVIII. Refined structure of dehydrated $Li_{5.0}Na_{1.2}$-MER (4.2).

Site	Type	x	y	z	Occ.	W	B_{iso}
O1	O	0.202(1)	0.123(1)	0.180(1)	1	16	1
O2	O	0.115(1)	0.245(1)	0	1	8	1
O5	O	0.650(2)	0.127(1)	0	1	8	1
O3	O	0	0.154(1)	0.178(2)	1	8	1
O6	O	0.643(1)	0	0.216(3)	1	8	1
O4	O	0.127(1)	0.302(1)	0.253(2)	1	16	1
Si1	Si	0.114(1)	0.207(1)	0.151(1)	0.81	16	1
Al1	Al	0.114(1)	0.207(1)	0.151(1)	0.19	16	1
Si2	Si	0.679(1)	0.113(1)	0.159(1)	0.81	16	1
Al2	Al	0.679(1)	0.113(1)	0.159(1)	0.19	16	1

Table VI.II.XXXIX. Refined structure of dehydrated $Li_{4.0}Na_{2.2}$-MER (4.2).

Site	Type	x	y	z	Occ.	W	B_{iso}
O1	O	0.198(1)	0.127(1)	0.182(1)	1	16	1
O2	O	0.121(1)	0.251(1)	0	1	8	1
O5	O	0.654(1)	0.127(1)	0	1	8	1
O3	O	0	0.161(1)	0.178(2)	1	8	1
O6	O	0.650(1)	0	0.208(2)	1	8	1
O4	O	0.124(1)	0.306(1)	0.254(1)	1	16	1
Si1	Si	0.110(1)	0.210(1)	0.154(1)	0.81	16	1
Al1	Al	0.110(1)	0.210(1)	0.154(1)	0.19	16	1
Si2	Si	0.683(1)	0.113(1)	0.158(1)	0.81	16	1
Al2	Al	0.683(1)	0.113(1)	0.158(1)	0.19	16	1
Na1	Na	0	0	0.767(1)	0.14(2)	4	2
Na2	Na	0	0.5	0.885(1)	0.34(2)	4	2

Table VI.II.XL. Refined structure of dehydrated $Li_{3.0}Na_{3.2}$-MER (4.2).

Site	Type	x	y	z	Occ.	W	B_{iso}
O1	O	0.196(1)	0.128(1)	0.180(1)	1	16	1
O2	O	0.118(1)	0.253(1)	0	1	8	1
O5	O	0.654(1)	0.126(1)	0	1	8	1
O3	O	0	0.161(1)	0.179(1)	1	8	1
O6	O	0.652(1)	0	0.212(1)	1	8	1
O4	O	0.123(1)	0.307(1)	0.252(1)	1	16	1
Si1	Si	0.110(1)	0.213(1)	0.154(1)	0.81	16	1
Al1	Al	0.110(1)	0.213(1)	0.154(1)	0.19	16	1
Si2	Si	0.683(1)	0.114(1)	0.158(1)	0.81	16	1
Al2	Al	0.683(1)	0.114(1)	0.158(1)	0.19	16	1
Na1	Na	0	0	0.760(1)	0.29(2)	4	2
Na2	Na	0.5	0.213(1)	0	0.14(2)	4	2
Na3	Na	0	0.5	0.875(1)	0.23(2)	4	2

Table VI.II.XLI. Refined structure of dehydrated $Li_{5.0}K_{1.2}$-MER (4.2).

Site	Type	x	y	z	Occ.	W	B_{iso}
O1	O	0.203(1)	0.123(1)	0.179(1)	1	16	1
O2	O	0.122(1)	0.249(1)	0	1	8	1
O5	O	0.649(1)	0.128(1)	0	1	8	1
O3	O	0	0.151(1)	0.171(2)	1	8	1
O6	O	0.650(1)	0	0.223(2)	1	8	1
O4	O	0.123(1)	0.301(1)	0.257(1)	1	16	1
Si1	Si	0.112(1)	0.211(1)	0.146(1)	0.81	16	1
Al1	Al	0.112(1)	0.211(1)	0.146(1)	0.19	16	1
Si2	Si	0.676(1)	0.113(1)	0.162(1)	0.81	16	1
Al2	Al	0.676(1)	0.113(1)	0.162(1)	0.19	16	1
K1	K	0	0.5	0.076(1)	0.17(1)	4	2

Table VI.II.XLII. Refined structure of dehydrated $Li_{4.0}K_{2.2}$-MER (4.2).

Site	Type	x	y	z	Occ.	W	B_{iso}
O1	O	0.200(1)	0.122(1)	0.172(1)	1	16	1
O2	O	0.123(1)	0.245(1)	0	1	8	1
O5	O	0.649(1)	0.133(1)	0	1	8	1
O3	O	0	0.158(1)	0.177(2)	1	8	1
O6	O	0.650(1)	0.000	0.207(2)	1	8	1
O4	O	0.125(1)	0.301(1)	0.257(1)	1	16	1
Si1	Si	0.113(1)	0.209(1)	0.149(1)	0.81	16	1
Al1	Al	0.113(1)	0.209(1)	0.149(1)	0.19	16	1
Si2	Si	0.678(1)	0.112(1)	0.162(1)	0.81	16	1
Al2	Al	0.678(1)	0.112(1)	0.162(1)	0.19	16	1
K1	K	0	0.154(1)	0.5	0.11(1)	4	2
K2	K	0	0.5	0.086(1)	0.33(1)	4	2

Table VI.II.XLIII. Refined structure of dehydrated $Li_{3.4}Cs_{2.8}$-MER (4.2).

Site	Type	x	y	z	Occ.	W	B_{iso}
O1	O	0.196(1)	0.128(1)	0.169(1)	1	16	1
O2	O	0.117(1)	0.249(1)	0	1	8	1
O5	O	0.645(1)	0.117(1)	0	1	8	1
O3	O	0	0.159(1)	0.203(1)	1	8	1
O6	O	0.660(1)	0	0.206(2)	1	8	1
O4	O	0.128(1)	0.304(1)	0.254(1)	1	16	1
Si1	Si	0.109(1)	0.207(1)	0.151(1)	1	16	1
Al1	Al	0.109(1)	0.207(1)	0.151(1)	1	16	1
Si2	Si	0.681(1)	0.116(1)	0.154(1)	1	16	1
Al2	Al	0.681(1)	0.116(1)	0.154(1)	1	16	1
Cs2	Cs	0	0.5	0	0.91(1)	2	2
Cs1	Cs	0.446(1)	0.5	0.082(2)	0.08(1)	8	2

Table VI.II.XLIV. Refined structure of hydrated $Li_{3.4}Cs_{2.8}$-MER (4.2).

Site	Type	x	y	z	Occ.	W	B_{iso}
Cs1	Cs	0	0	0.247(1)	0.35(1)	4	2
Cs2	Cs	0	0.5	0	0.30(1)	2	2
Cs3	Cs	0.5	0.181(1)	0	0.28(1)	4	2
Ow1	O	0	0	0.663(1)	1	4	2
Ow2	O	0.5	0.5	0.5	1	2	2
Ow3	O	0.296(1)	0.385(1)	0.026(1)	0.24(1)	16	2
Ow4	O	0.420(1)	0.358(1)	0	0.67(1)	8	2
O1	O	0.168(1)	0.156(1)	0.199(1)	1	16	1
O2	O	0.124(1)	0.306(1)	0	1	8	1
O5	O	0.703(1)	0.113(1)	0	1	8	1
O3	O	0	0.232(1)	0.171(2)	1	8	1
O6	O	0.745(1)	0	0.207(1)	1	8	1
O4	O	0.140(1)	0.344(1)	0.258(2)	1	16	1
Si1	Si	0.108(1)	0.261(1)	0.165(1)	0.81	16	1
Al1	Al	0.108(1)	0.261(1)	0.165(1)	0.19	16	1
Si2	Si	0.733(1)	0.110(1)	0.156(1)	0.81	16	1
Al2	Al	0.733(1)	0.110(1)	0.156(1)	0.19	16	1

Table VI.II.XLV. Refined structure of $Li_{3.4}Cs_{2.8}$-MER (4.2) under 5.05 bar of CO_2.

Site	Type	x	y	z	Occ.	W	B_{iso}
Cs1	Cs	0	0	0.245(1)	1	4	2
Cs2	Cs	0	0.5	0	1	2	2
Cs3	Cs	0.5	0.232(1)	0	1	4	2
O1	O	0.160(1)	0.170(1)	0.188(1)	1	16	1
O2	O	0.124(1)	0.307(1)	0	1	8	1
O5	O	0.714(1)	0.119(1)	0	1	8	1
O3	O	0	0.256(2)	0.210(1)	1.00	8	1
O6	O	0.770(1)	0	0.197(1)	1.00	8	1
O4	O	0.160(1)	0.359(1)	0.237(1)	1.00	16	1
Si1	Si	0.111(1)	0.269(1)	0.160(1)	0.81	16	1
Al1	Al	0.111(1)	0.269(1)	0.160(1)	0.19	16	1
Si2	Si	0.742(1)	0.108(1)	0.161(1)	0.81	16	1
Al2	Al	0.742(1)	0.108(1)	0.161(1)	0.19	16	1
C1	C	0.5	0.5	0	0.61(1)	2	2
OC1	O	0.5	0.5	0.116	0.61(1)	4	2
C2	C	0.172(1)	0	0.5	0.91(1)	4	2
OC2	O	0.172(1)	0.918	0.5	0.91(1)	8	2
C3	C	0	0.5	0.5	1.00(2)	2	2
OC3	O	0	0.5	0.616	1.00(2)	4	2
C4	C	0	0.5	0	0.81(1)	2	2
OC4	O	0	0	0.116	0.81(1)	4	2

VI.III Phillipsite

VI.III.I PHI (2.5)

Table VI.III.I. Refined structure of hydrated $K_{4.6}$-PHI (2.5).

Site	Type	*x*	*y*	*z*	Occ	M	B_{iso}
K1	K	0.716(5)	0.75	0.521(6)	0.40(3)	2	2
K1a	K	0.214(4)	0.75	0.465(5)	0.55(3)	2	2
K2	K	0.489(5)	0.579(1)	0.471(3)	0.50(1)	4	2
K3	K	0.866(5)	0.25	0.189(5)	0.44(2)	2	2
O1	O	0.082(5)	0.105(4)	0.188(6)	1	4	2
O2	O	0.647(6)	0.588(4)	0.188(7)	1	4	2
O3	O	0.611(6)	0.106(4)	0.193(8)	1	4	2
O4	O	0.030(6)	0.916(4)	0.181(7)	1	4	2
O5	O	0.888(6)	0.040(2)	0.273(4)	1	4	2
O6	O	0.303(4)	0.374(2)	0.082(3)	1	4	2
O7	O	0.798(4)	0.499(6)	0.501(7)	1	4	2
O8	O	0.538(7)	0.75	0.017(10)	1	2	2
O9	O	0.053(8)	0.25	0.963(8)	1	2	2
Si1	Si	0.738(2)	0.010(2)	0.293(3)	0.71	4	2
Al1	Al	0.738(2)	0.010(2)	0.293(3)	0.29	4	2
Si2	Si	0.431(2)	0.140(2)	0.015(3)	0.71	4	2
Al2	Al	0.431(2)	0.140(2)	0.015(3)	0.29	4	2
Si3	Si	0.050(3)	0.013(2)	0.280(3)	0.71	4	2
Al3	Al	0.050(3)	0.013(2)	0.280(3)	0.29	4	2
Si4	Si	0.112(2)	0.137(2)	0.021(3)	0.71	4	2
Al4	Al	0.112(2)	0.137(2)	0.021(3)	0.29	4	2
wO1	O	0.5	0.75	0.5	1.00(3)	2	2
wO2	O	0.948(6)	0.75	0.419(4)	1.00(4)	2	2
wO3	O	0.206(5)	0.75	0.030(6)	1.00(6)	2	2

Table VI.III.II. Refined structure of dehydrated $K_{4.6}$-PHI (2.5).

Site	Type	*x*	*y*	*z*	Occ	M	B_{iso}
K1	K	0.851(4)	0.75	0.493(4)	0.52(2)	2	2
K1a	K	0.008(4)	0.75	0.417(4)	0.45(2)	2	2
K2	K	0.534(3)	0.031(2)	0.565(3)	0.44(1)	4	2
K3	K	0.860(3)	0.25	0.026(3)	0.59(2)	2	2
O1	O	0.178(3)	0.063(2)	0.253(4)	1	4	2
O2	O	0.678(4)	0.569(2)	0.226(4)	1	4	2
O3	O	0.618(4)	0.113(2)	0.111(5)	1	4	2
O4	O	-0.004(4)	0.900(2)	0.126(5)	1	4	2
O5	O	0.925(4)	0.043(2)	0.283(4)	1	4	2
O6	O	0.334(4)	0.384(2)	0.088(4)	1	4	2
O7	O	0.806(4)	0.432(2)	0.496(5)	1	4	2
O8	O	0.608(5)	0.75	0.095(6)	1	2	2
O9	O	0.158(5)	0.25	0.125(6)	1	2	2
Si1	Si	0.758(2)	0.038(1)	0.290(2)	0.71	4	2
Al1	Al	0.758(2)	0.038(1)	0.290(2)	0.29	4	2
Si2	Si	0.428(2)	0.135(1)	-0.024(2)	0.71	4	2
Al2	Al	0.428(2)	0.135(1)	-0.024(2)	0.29	4	2
Si3	Si	0.072(2)	-0.016(1)	0.294(3)	0.71	4	2
Al3	Al	0.072(2)	-0.016(1)	0.294(3)	0.29	4	2
Si4	Si	0.165 (2)	0.131(1)	0.079(2)	0.71	4	2
Al4	Al	0.165(2)	0.131(1)	0.079(2)	0.29	4	2

Table VI.III.III. Refined structure of $K_{4.6}$-PHI (2.5) under 1 bar of CO_2.

Site	Type	*x*	*y*	*z*	Occ	M	B_{iso}
K1	K	0.795(5)	0.75	0.517(5)	0.65(4)	2	5.2
K1a	K	0.113(11)	0.75	0.323(12)	0.30(3)	2	5.2
K2	K	0.5	0	0.5	0.81(2)	2	5.2
K3	K	0.853(6)	0.25	0.155(6)	0.56(4)	2	5.2
O1	O	0.142(4)	0.082(2)	0.232(5)	1	4	1
O2	O	0.674(4)	0.576(2)	0.211(5)	1	4	1
O3	O	0.612(4)	0.110(2)	0.126(5)	1	4	1
O4	O	-0.003(4)	0.908(2)	0.145(4)	1	4	1
O5	O	0.916(4)	0.048(2)	0.291(4)	1	4	1
O6	O	0.326(4)	0.375(2)	0.085(4)	1	4	1
O7	O	0.798(4)	0.458(2)	0.502(6)	1	4	1
O8	O	0.592(6)	0.75	0.084(7)	1	2	1
O9	O	0.110(7)	0.25	0.064(7)	1	2	1
Si1	Si	0.750(2)	0.032(1)	0.291(3)	0.71	4	1
Al1	Al	0.750(2)	0.032(1)	0.291(3)	0.29	4	1
Si2	Si	0.426(2)	0.143(1)	-0.010(2)	0.71	4	1
Al2	Al	0.426(2)	0.143(1)	-0.010(2)	0.29	4	1
Si3	Si	0.063(2)	-0.006(1)	0.287(2)	0.71	4	1
Al3	Al	0.063(2)	-0.006(1)	0.287(2)	0.29	4	1
Si4	Si	0.143(2)	0.140(1)	0.053(2)	0.71	4	1
Al4	Al	0.143(2)	0.140(1)	0.053(2)	0.29	4	1
C1	C	0.49(3)	0.799(11)	0.590(17)	0.15(2)	4	8
OC1	O	0.60(3)	0.799(11)	0.590(17)	0.15(2)	4	8
OC1a	O	0.37(3)	0.799(11)	0.590(17)	0.15(2)	4	8
C2	C	0.105(14)	0.75	0.45	0.50(4)	2	8
OC2	O	0.223(14)	0.75	0.45	0.50(4)	2	8
OC2a	O	-0.012(14)	0.75	0.45	0.50(4)	2	8
C3	C	0.291(8)	0.816(4)	0.120(13)	0.50(3)	4	8
OC3	O	0.371(8)	0.857(4)	0.263(13)	0.50(3)	4	8

Table VI.III.III.(continued) Refined structure of $K_{4.6}$-PHI (2.5) under 1 bar of CO_2.

Site	Type	*x*	*y*	*z*	Occ	M	B_{iso}
OC3a	O	0.211(8)	0.774(4)	-0.023(13)	0.50(3)	4	8

Table VI.III.IV. Refined structure of hydrated $Rb_{4.6}$-PHI (2.5).

Site	Type	*x*	*y*	*z*	Occ	M	B_{iso}
Rb1	Rb	0.714(2)	0.75	0.432(3)	0.55(2)	2	2
Rb1a	Rb	0.301(3)	0.75	0.531(2)	0.48(2)	2	2
Rb2	Rb	0.476(3)	0.569(1)	0.474(2)	0.40(1)	4	2
Rb3	Rb	0.854(3)	0.25	0.183(3)	0.48(1)	2	2
O1	O	0.084(6)	0.104(5)	0.184(7)	1	4	2
O2	O	0.644(8)	0.590(5)	0.194(8)	1	4	2
O3	O	0.610(7)	0.102(5)	0.187(7)	1	4	2
O4	O	0.036(7)	0.914(5)	0.182(7)	1	4	2
O5	O	0.877(8)	0.038(2)	0.258(4)	1	4	2
O6	O	0.300(6)	0.379(3)	0.076(4)	1	4	2
O7	O	0.806(4)	0.500(6)	0.504(5)	1	4	2
O8	O	0.543(8)	0.75	0.028(9)	1	2	2
O9	O	0.069(8)	0.25	0.968(9)	1	2	2
Si1	Si	0.735(3)	0.011(2)	0.287(3)	0.71	4	2
Al1	Al	0.735(3)	0.011(2)	0.287(3)	0.29	4	2
Si2	Si	0.426(2)	0.141(2)	0.009(4)	0.71	4	2
Al2	Al	0.426(2)	0.141(2)	0.009(4)	0.29	4	2
Si3	Si	0.046(3)	0.010(2)	0.286(3)	0.71	4	2
Al3	Al	0.046(3)	0.010(2)	0.286(3)	0.29	4	2
Si4	Si	0.111(2)	0.137(2)	0.017(3)	0.71	4	2
Al4	Al	0.111(2)	0.137(2)	0.017(3)	0.29	4	2
wO1	O	0.5	0.75	0.5	0.93(4)	2	2
wO2	O	0.991(5)	0.75	0.430(6)	1.00(4)	2	2
wO3	O	0.209(7)	0.75	0.997(8)	1.00(7)	2	2

Table VI.III.V. Refined structure of dehydrated $Rb_{4.6}$-PHI (2.5).

Site	Type	*x*	*y*	*z*	Occ	M	B_{iso}
Rb1	Rb	0.882(2)	0.75	0.495(2)	0.60(2)	2	2
Rb1a	Rb	0.985(4)	0.75	0.473(3)	0.40(1)	2	2
Rb2	Rb	0.539(2)	0.045(1)	0.596(2)	0.42(1)	4	2
Rb3	Rb	0.826(2)	0.25	0.986(2)	0.47(1)	2	2
O1	O	0.175(4)	0.072(3)	0.262(5)	1	4	2
O2	O	0.672(4)	0.566(2)	0.220(5)	1	4	2
O3	O	0.622(5)	0.117(2)	0.116(5)	1	4	2
O4	O	0.985(4)	0.902(2)	0.126(5)	1	4	2
O5	O	0.922(5)	0.048(2)	0.282(4)	1	4	2
O6	O	0.341(5)	0.384(2)	0.087(5)	1	4	2
O7	O	0.815(4)	0.430(3)	0.499(5)	1	4	2
O8	O	0.589(5)	0.750()	0.117(7)	1	2	2
O9	O	0.161(6)	0.250()	0.098(6)	1	2	2
Si1	Si	0.752(2)	0.039(1)	0.285(2)	0.71	4	2
Al1	Al	0.752(2)	0.039(1)	0.285(2)	0.29	4	2
Si2	Si	0.429(2)	0.138(1)	0.973(2)	0.71	4	2
Al2	Al	0.429(2)	0.138(1)	0.973(2)	0.29	4	2
Si3	Si	0.066(2)	0.988(1)	0.283(3)	0.71	4	2
Al3	Al	0.066(2)	0.988(1)	0.283(3)	0.29	4	2
Si4	Si	0.170(2)	0.130(1)	0.085(3)	0.71	4	2
Al4	Al	0.170(2)	0.130(1)	0.085(3)	0.29	4	2

Table VI.III.VI. Refined structure of $Rb_{4.6}$-PHI (2.5) at 1 bar of CO_2.

Site	Type	*x*	*y*	*z*	Occ	M	B_{iso}
Rb1	Rb	0.777(3)	0.75	0.501(4)	0.57(3)	2	5.2
Rb1a	Rb	0.236(4)	0.75	0.466(6)	0.41(4)	2	5.2
Rb2	Rb	0.512(3)	0.046(1)	0.522(3)	0.48(1)	4	5.2
Rb3	Rb	0.823(4)	0.25	0.125(4)	0.46(3)	2	5.2
O1	O	0.118(4)	0.079(3)	0.195(5)	1	4	1
O2	O	0.667(5)	0.581(3)	0.201(5)	1	4	1
O3	O	0.616(4)	0.103(2)	0.135(5)	1	4	1
O4	O	0.021(5)	0.900(3)	0.169(5)	1	4	1
O5	O	0.910(5)	0.035(2)	0.281(5)	1	4	1
O6	O	0.299(5)	0.370(2)	0.069(4)	1	4	1
O7	O	0.795(4)	0.465(2)	0.488(6)	1	4	1
O8	O	0.577(7)	0.75	0.056(7)	1	2	1
O9	O	0.087(7)	0.25	0.050(8)	1	2	1
Si1	Si	0.753(2)	0.017(1)	0.280(2)	0.71	4	1
Al1	Al	0.753(2)	0.017(1)	0.280(2)	0.29	4	1
Si2	Si	0.421(2)	0.142(1)	-0.007(3)	0.71	4	1
Al2	Al	0.421(2)	0.142(1)	-0.007(3)	0.29	4	1
Si3	Si	0.061(2)	-0.005(1)	0.290(3)	0.71	4	1
Al3	Al	0.061(2)	-0.005(1)	0.290(3)	0.29	4	1
Si4	Si	0.125(2)	0.144(1)	0.026(3)	0.71	4	1
Al4	Al	0.125(2)	0.144(1)	0.026(3)	0.29	4	1
C1	C	0.50(3)	0.814(10)	0.591(12)	0.18(3)	4	8
OC1	O	0.62(3)	0.814(10)	0.591(12)	0.18(3)	4	8
OC1a	O	0.39(3)	0.814(10)	0.591(12)	0.18(3)	4	8
C2	C	0.09(2)	0.75	0.45	0.50(6)	2	8
OC2	O	0.20(2)	0.75	0.45	0.50(6)	2	8
OC2a	O	-0.03(2)	0.75	0.45	0.50(6)	2	8
C3	C	0.209(7)	0.810(5)	0.013(11)	0.50(4)	4	8
OC3	O	0.288(7)	0.852(5)	0.155(11)	0.50(4)	4	8

Table VI.III.VI.(continued) Refined structure of $Rb_{4.6}$-PHI (2.5) at 1 bar of CO_2.

Site	Type	*x*	*y*	*z*	Occ	M	B_{iso}
OC3a	O	0.130(7)	0.769(5)	-0.129(11)	0.50(4)	4	8

Table VI.III.VII. Refined structure of hydrated $Cs_{4.6}$-PHI (2.5).

Site	Type	*x*	*y*	*z*	Occ	M	B_{iso}
Cs1	Cs	0.338(5)	0.738(6)	0.220(6)	0.42(5)	4	2
Cs1_1	Cs	0.859(4)	0.730(5)	0.244(5)	0.43(5)	4	2
Cs1a	Cs	0.144(3)	0.755(5)	0.238(4)	0.41(5)	4	2
Cs1a_1	Cs	0.642(3)	0.769(4)	0.253(3)	0.56(5)	4	2
Cs2	Cs	0.240(2)	0.593(3)	0.248(2)	0.77(4)	4	2
Cs2_1	Cs	0.239(5)	0.602(4)	0.714(4)	0.37(4)	4	2
Cs2_2	Cs	0.733(3)	0.553(2)	0.232(3)	0.61(4)	4	2
Cs2_3	Cs	0.679(6)	0.619(5)	0.609(5)	0.40(4)	4	2
Cs3	Cs	0.396(3)	0.210(3)	0.039(3)	0.62(4)	4	2
Cs3_1	Cs	0.926(4)	0.228(4)	0.100(3)	0.49(4)	4	2
O1	O	0.03(2)	0.10(2)	0.07(2)	1	4	2
O2	O	0.02(2)	0.10(2)	0.58(2)	1	4	2
O3	O	0.54(2)	0.13(2)	0.09(2)	1	4	2
O4	O	0.54(2)	0.10(2)	0.59(2)	1	4	2
O5	O	0.33(2)	0.59(2)	0.09(2)	1	4	2
O6	O	0.34(2)	0.58(2)	0.60(2)	1	4	2
O7	O	0.83(2)	0.60(2)	0.10(2)	1	4	2
O8	O	0.83(2)	0.61(2)	0.59(2)	1	4	2
O9	O	0.28(2)	0.11(2)	0.09(2)	1	4	2
O10	O	0.29(2)	0.08(2)	0.59(2)	1	4	2
O11	O	0.81(2)	0.09(2)	0.08(2)	1	4	2
O12	O	0.79(2)	0.10(2)	0.58(2)	1	4	2
O13	O	0.04(2)	0.90(2)	0.11(2)	1	4	2
O14	O	0.03(2)	0.92(2)	0.60(2)	1	4	2
O15	O	0.50(2)	0.93(2)	0.09(2)	1	4	2

Table VI.III.VII.(continued). Refined structure of hydrated $Cs_{4.6}$-PHI (2.5).

Site	Type	*x*	*y*	*z*	Occ	M	B_{iso}
O16	O	0.52(2)	0.92(2)	0.59(2)	1	4	2
O17	O	0.43(2)	0.09(2)	0.13(2)	1	4	2
O18	O	0.43(2)	0.02(2)	0.62(2)	1	4	2
O19	O	0.93(2)	-0.01(2)	0.11(2)	1	4	2
O20	O	0.93(2)	0.04(2)	0.62(2)	1	4	2
O21	O	0.14(2)	0.38(2)	0.04(2)	1	4	2
O22	O	0.11(2)	0.34(2)	0.51(2)	1	4	2
O23	O	0.63(2)	0.40(2)	0.02(2)	1	4	2
O24	O	0.66(2)	0.38(2)	0.54(2)	1	4	2
O25	O	0.40(2)	0.52(2)	0.25(2)	1	4	2
O26	O	0.42(2)	0.51(2)	0.75(2)	1	4	2
O27	O	0.90(2)	0.49(2)	0.24(2)	1	4	2
O28	O	0.91(2)	0.53(2)	0.75(2)	1	4	2
O29	O	0.280(14)	0.75(2)	0.52(2)	1	4	2
O30	O	0.78(2)	0.76(2)	0.49(2)	1	4	2
O31	O	-0.01(2)	0.27(2)	-0.02(2)	1	4	2
O32	O	0.54(2)	0.25(2)	-0.01(2)	1	4	2
Si1	Si	0.367(8)	0.028(8)	0.147(8)	0.71	4	2
Al1	Al	0.367(8)	0.028(8)	0.147(8)	0.29	4	2
Si2	Si	0.370(7)	0.003(10)	0.637(9)	0.71	4	2
Al2	Al	0.370(7)	0.003(10)	0.637(9)	0.29	4	2
Si3	Si	0.871(7)	-0.001(8)	0.143(8)	0.71	4	2
Al3	Al	0.871(7)	-0.001(8)	0.143(8)	0.29	4	2
Si4	Si	0.858(7)	0.012(9)	0.627(8)	0.71	4	2
Al4	Al	0.858(7)	0.012(9)	0.627(8)	0.29	4	2
Si5	Si	0.197(8)	0.129(9)	0.503(10)	0.71	4	2
Al5	Al	0.197(8)	0.129(9)	0.503(10)	0.29	4	2
Si6	Si	0.192(7)	0.156(8)	1.005(8)	0.71	4	2
Al6	Al	0.192(7)	0.156(8)	1.005(8)	0.29	4	2

Table VI.III.VII.(continued). Refined structure of hydrated $Cs_{4.6}$-PHI (2.5).

Site	Type	*x*	*y*	*z*	Occ	M	B_{iso}
Si7	Si	0.703(8)	0.143(9)	0.514(7)	0.71	4	2
Al7	Al	0.703(8)	0.143(9)	0.514(7)	0.29	4	2
Si8	Si	0.717(7)	0.364(8)	0.506(8)	0.71	4	2
Al8	Al	0.717(7)	0.364(8)	0.506(8)	0.29	4	2
Si9	Si	0.024(8)	0.014(7)	0.144(9)	0.71	4	2
Al9	Al	0.024(8)	0.014(7)	0.144(9)	0.29	4	2
Si10	Si	0.024(8)	0.013(9)	0.647(9)	0.71	4	2
Al10	Al	0.024(8)	0.013(9)	0.647(9)	0.29	4	2
Si11	Si	0.514(9)	0.038(8)	0.137(8)	0.71	4	2
Al11	Al	0.514(9)	0.038(8)	0.137(8)	0.29	4	2
Si12	Si	0.519(8)	0.010(9)	0.633(9)	0.71	4	2
Al12	Al	0.519(8)	0.010(9)	0.633(9)	0.29	4	2
Si13	Si	0.037(7)	0.127(9)	0.503(9)	0.71	4	2
Al13	Al	0.037(7)	0.127(9)	0.503(9)	0.29	4	2
Si14	Si	0.020(7)	0.158(8)	0.988(8)	0.71	4	2
Al14	Al	0.020(7)	0.158(8)	0.988(8)	0.29	4	2
Si15	Si	0.549(7)	0.132(9)	0.516(8)	0.71	4	2
Al15	Al	0.549(7)	0.132(9)	0.516(8)	0.29	4	2
Si16	Si	0.554(8)	0.139(7)	0.999(9)	0.71	4	2
Al16	Al	0.554(8)	0.139(7)	0.999(9)	0.29	4	2
wO1_1	O	0.81(2)	0.82(2)	0.29(2)	1.0(3)	4	4
wO2	O	0.43(2)	0.75(3)	0.12(2)	1.0(3)	4	4
wO2_1	O	0.98(2)	0.74(2)	0.21(2)	1.0(3)	4	4
wO3	O	0.14(2)	0.85(2)	0.03(2)	1.0(2)	4	4

Table VI.III.VIII. Refined structure of dehydrated $Cs_{4.6}$-PHI (2.5).

Site	Type	*x*	*y*	*z*	Occ	M	B_{iso}
Cs1	Cs	0.911(1)	0.75	0.484(1)	0.79(1)	2	2
Cs2	Cs	0.454(1)	0.922(1)	0.390(2)	0.41(1)	4	2
Cs4	Cs	0.760(3)	0.25	0.920(4)	0.31(1)	2	2
Cs3	Cs	0.354(3)	0.75	0.499(4)	0.33(1)	2	2
O1	O	0.168(6)	0.076(4)	0.253(7)	1	2	2
O2	O	0.662(6)	0.569(4)	0.205(7)	1	2	2
O3	O	0.628(6)	0.119(3)	0.138(8)	1	4	2
O4	O	0.991(6)	0.910(4)	0.123(7)	1	4	2
O5	O	0.902(6)	0.041(4)	0.257(7)	1	4	2
O6	O	0.336(6)	0.373(3)	0.093(8)	1	4	2
O7	O	0.818(7)	0.445(3)	0.501(9)	1	4	2
O8	O	0.575(8)	0.75	0.072(12)	1	4	2
O9	O	0.127(10)	0.25	0.086(11)	1	4	2
Si1	Si	0.747(3)	0.034(2)	0.281(3)	0.71	4	2
Al1	Al	0.747(3)	0.034(2)	0.281(3)	0.29	4	2
Si2	Si	0.435(3)	0.139(2)	0.991(3)	0.71	4	2
Al2	Al	0.435(3)	0.139(2)	0.991(3)	0.29	4	2
Si3	Si	0.064(4)	0.997(2)	0.285(4)	0.71	4	2
Al3	Al	0.064(4)	0.997(2)	0.285(4)	0.29	4	2
Si4	Si	0.168(3)	0.135(1)	0.083(3)	0.71	4	2
Al4	Al	0.168(3)	0.135(1)	0.083(3)	0.29	4	2

Table VI.III.IX. Refined structure of $Cs_{4.6}$-PHI (2.5) at 1 bar of CO_2.

Site	Type	*x*	*y*	*z*	Occ	M	B_{iso}
Cs1	Cs	0.775(3)	0.75	0.515(3)	0.48(2)	2	5
Cs1a	Cs	0.233(3)	0.75	0.455(4)	0.39(3)	2	5
Cs2	Cs	0.503(5)	0.035(1)	0.504(3)	0.43(8)	4	5
Cs3	Cs	0.791(3)	0.25	0.065(3)	0.61(2)	2	5
O1	O	0.093(6)	0.099(4)	0.194(8)	1	2	1
O2	O	0.662(7)	0.591(4)	0.204(7)	1	2	1
O3	O	0.600(6)	0.089(4)	0.161(7)	1	4	1
O4	O	0.020(6)	0.916(4)	0.164(7)	1	4	1
O5	O	0.899(7)	0.036(3)	0.289(5)	1	4	1
O6	O	0.300(7)	0.376(2)	0.068(5)	1	4	1
O7	O	0.799(5)	0.491(6)	0.502(8)	1	4	1
O8	O	0.565(9)	0.75	0.029(12)	1	4	1
O9	O	0.085(9)	0.25	0.978(11)	1	4	1
Si1	Si	0.743(3)	0.013(3)	0.287(4)	0.71	4	1
Al1	Al	0.743(3)	0.013(3)	0.287(4)	0.29	4	1
Si2	Si	0.422(3)	0.136(2)	0.001(4)	0.71	4	1
Al2	Al	0.422(3)	0.136(2)	0.001(4)	0.29	4	1
Si3	Si	0.048(3)	0.013(3)	0.281(3)	0.71	4	1
Al3	Al	0.048(3)	0.013(3)	0.281(3)	0.29	4	1
Si4	Si	0.122(3)	0.137(2)	0.030(4)	0.71	4	1
Al4	Al	0.122(3)	0.137(2)	0.030(4)	0.29	4	1
C1	C	0.50(3)	0.826(7)	0.57(2)	0.25(4)	4	8
OC1	O	0.62(3)	0.826(7)	0.57(2)	0.25(4)	4	8
OC1a	O	0.39(3)	0.826(7)	0.57(2)	0.25(4)	4	8
C2	C	0.27(2)	0.75	0.45	0.50(10)	2	8
OC2	O	0.38(2)	0.75	0.45	0.50(10)	2	8
OC2a	O	0.15(2)	0.75	0.45	0.50(10)	2	8
C3	C	0.28(2)	0.855(8)	0.12(2)	0.39(3)	4	8
OC3	O	0.36(2)	0.896(8)	0.26(2)	0.39(3)	4	8

Table VI.III.IX.(continued) Refined structure of $Cs_{4.6}$-PHI (2.5) at 1 bar of CO_2.

Site	Type	*x*	*y*	*z*	Occ	M	B_{iso}
OC3a	O	0.20(2)	0.814(8)	0.98(2)	0.39(3)	4	8

VI.III.II PHI (3.6)

Table VI.III.X. Refined structure of hydrated $K_{3.5}$-PHI (3.6).

Site	Type	*x*	*y*	*z*	Occ	M	B_{iso}
K1	K	0.732(8)	0.75	0.513(11)	0.28(4)	2	2
K1a	K	0.221(6)	0.75	0.487(7)	0.44(4)	2	2
K2	K	0.485(6)	0.581(2)	0.466(3)	0.41(1)	4	2
K3	K	0.866(7)	0.25	0.197(6)	0.37(2)	2	2
O1	O	0.086(6)	0.103(4)	0.184(7)	1	4	2
O2	O	0.649(7)	0.588(4)	0.189(8)	1	4	2
O3	O	0.612(7)	0.105(4)	0.193(8)	1	4	2
O4	O	0.036(7)	0.914(4)	0.191(8)	1	4	2
O5	O	0.895(6)	0.040(2)	0.278(4)	1	4	2
O6	O	0.297(5)	0.371(2)	0.080(3)	1	4	2
O7	O	0.797(5)	0.500(5)	0.500(10)	1	4	2
O8	O	0.533(8)	0.75	0.026(11)	1	2	2
O9	O	0.040(9)	0.25	0.971(10)	1	2	2
Si1	Si	0.739(3)	0.005(1)	0.288(3)	0.71	4	2
Al1	Al	0.739(3)	0.005(1)	0.288(3)	0.29	4	2
Si2	Si	0.432(2)	0.140(2)	0.015(3)	0.71	4	2
Al2	Al	0.432(2)	0.140(2)	0.015(3)	0.29	4	2
Si3	Si	0.052(3)	0.015(1)	0.279(3)	0.71	4	2
Al3	Al	0.052(3)	0.015(1)	0.279(3)	0.29	4	2
Si4	Si	0.109(2)	0.141(2)	0.014(3)	0.71	4	2
Al4	Al	0.109(2)	0.141(2)	0.014(3)	0.29	4	2
wO1	O	0.5	0.75	0.5	1.00(3)	2	2
wO2	O	0.939(7)	0.75	0.411(4)	1.00(4)	2	2
wO3	O	0.187(6)	0.75	0.014(7)	1.00(7)	2	2

Table VI.III.XI. Refined structure of dehydrated $K_{3.5}$-PHI (3.6).

Site	Type	*x*	*y*	*z*	Occ	M	B_{iso}
K1	K	0.842(4)	0.75	0.497(4)	0.57(2)	2	2
K1a	K	0.026(6)	0.75	0.418(6)	0.31(2)	2	2
K2	K	0.532(5)	0.041(2)	0.551(5)	0.29(1)	4	2
K3	K	0.863(4)	0.25	0.022(5)	0.41(3)	2	2
O1	O	0.170(4)	0.067(3)	0.247(4)	1	4	2
O2	O	0.679(4)	0.573(2)	0.223(4)	1	4	2
O3	O	0.617(5)	0.110(2)	0.118(6)	1	4	2
O4	O	-0.002(5)	0.900(2)	0.134(4)	1	4	2
O5	O	0.924(4)	0.042(2)	0.288(4)	1	4	2
O6	O	0.331(4)	0.380(2)	0.087(4)	1	4	2
O7	O	0.800(4)	0.438(2)	0.495(5)	1	4	2
O8	O	0.596(5)	0.75	0.088(6)	1	2	2
O9	O	0.145(6)	0.25	0.113(7)	1	2	2
Si1	Si	0.759(2)	0.031(1)	0.296(2)	0.78	4	2
Al1	Al	0.759(2)	0.031(1)	0.296(2)	0.22	4	2
Si2	Si	0.429(2)	0.136(1)	-0.021(2)	0.78	4	2
Al2	Al	0.429(2)	0.136(1)	-0.021(2)	0.22	4	2
Si3	Si	0.073(2)	-0.012(1)	0.296(2)	0.78	4	2
Al3	Al	0.073(2)	-0.012(1)	0.296(2)	0.22	4	2
Si4	Si	0.159(2)	0.135(1)	0.073(2)	0.78	4	2
Al4	Al	0.159(2)	0.135(1)	0.073(2)	0.22	4	2

Table VI.III.XII. Refined structure of $K_{3.5}$-PHI (3.6) at 1 bar of CO_2.

Site	Type	*x*	*y*	*z*	Occ	M	B_{iso}
K1	K	0.772(5)	0.75	0.516(5)	0.66(4)	2	5.2
K1a	K	0.22(2)	0.75	0.49(2)	0.21(5)	2	5.2
K2	K	0.5	0	0.5	0.33(4)	2	5.2
K3	K	0.852(5)	0.25	0.157(4)	0.62(2)	2	5.2
O1	O	0.126(4)	0.094(3)	0.224(5)	1	4	1
O2	O	0.667(4)	0.585(2)	0.202(5)	1	4	1
O3	O	0.622(4)	0.109(2)	0.156(6)	1	4	1
O4	O	0.015(4)	0.905(3)	0.172(4)	1	4	1
O5	O	0.910(4)	0.045(2)	0.291(4)	1	4	1
O6	O	0.313(4)	0.375(2)	0.083(3)	1	4	1
O7	O	0.791(4)	0.473(3)	0.497(5)	1	4	1
O8	O	0.562(7)	0.75	0.067(7)	1	2	1
O9	O	0.075(6)	0.25	0.017(6)	1	2	1
Si1	Si	0.745(2)	0.019(1)	0.285(2)	0.78	4	1
Al1	Al	0.745(2)	0.019(1)	0.285(2)	0.22	4	1
Si2	Si	0.433(2)	0.144(1)	0.003(2)	0.78	4	1
Al2	Al	0.433(2)	0.144(1)	0.003(2)	0.22	4	1
Si3	Si	0.063(2)	0.002(1)	0.289(2)	0.78	4	1
Al3	Al	0.063(2)	0.002(1)	0.289(2)	0.22	4	1
Si4	Si	0.126(2)	0.138(1)	0.042(2)	0.78	4	1
Al4	Al	0.126(2)	0.138(1)	0.042(2)	0.22	4	1
C1	C	0.47(2)	0.814(7)	0.550(10)	0.23(2)	4	8
OC1	O	0.58(2)	0.814(7)	0.550(10)	0.23(2)	4	8
OC1a	O	0.35(2)	0.814(7)	0.550(10)	0.23(2)	4	8
C2	C	0.036(13)	0.75	0.400(8)	0.50(4)	2	8
OC2	O	0.153(13)	0.75	0.400(8)	0.50(4)	2	8
OC2a	O	0.919(13)	0.75	0.400(8)	0.50(4)	2	8
C3	C	0.379(8)	0.883(4)	0.281(10)	0.50(2)	4	8
OC3	O	0.459(8)	0.924(4)	0.423(10)	0.50(2)	4	8

Table VI.III.XII.(continued) Refined structure of $K_{3.5}$-PHI (3.6) at 1 bar of CO_2.

Site	Type	*x*	*y*	*z*	Occ	M	B_{iso}
OC3a	O	0.300(8)	0.842(4)	0.138(10)	0.50(2)	4	8

Table VI.III.XIII. Refined structure of hydrated $Rb_{3.5}$-PHI (3.6).

Site	Type	*x*	*y*	*z*	Occ	M	B_{iso}
Rb1	Rb	0.695(4)	0.75	0.444(4)	0.42(3)	2	2
Rb1a	Rb	0.277(3)	0.75	0.529(4)	0.41(3)	2	2
Rb2	Rb	0.493(5)	0.572(1)	0.485(3)	0.35(1)	4	2
Rb3	Rb	0.859(4)	0.25	0.180(4)	0.36(2)	2	2
O1	O	0.068(7)	0.106(5)	0.175(9)	1	4	2
O2	O	0.647(8)	0.592(5)	0.202(9)	1	4	2
O3	O	0.611(7)	0.104(5)	0.190(9)	1	4	2
O4	O	0.043(7)	0.915(5)	0.196(7)	1	4	2
O5	O	0.878(8)	0.037(2)	0.258(4)	1	4	2
O6	O	0.297(6)	0.371(2)	0.066(4)	1	4	2
O7	O	0.807(4)	0.504(7)	0.502(7)	1	4	2
O8	O	0.545(9)	0.75	0.024(12)	1	2	2
O9	O	0.060(10)	0.25	0.963(11)	1	2	2
Si1	Si	0.736(3)	0.010(2)	0.288(3)	0.78	4	2
Al1	Al	0.736(3)	0.010(2)	0.288(3)	0.22	4	2
Si2	Si	0.429(2)	0.141(2)	0.002(4)	0.78	4	2
Al2	Al	0.429(2)	0.141(2)	0.002(4)	0.22	4	2
Si3	Si	0.044(3)	0.014(2)	0.280(3)	0.78	4	2
Al3	Al	0.044(3)	0.014(2)	0.280(3)	0.22	4	2
Si4	Si	0.105(2)	0.137(2)	0.009(4)	0.78	4	2
Al4	Al	0.105(2)	0.137(2)	0.009(4)	0.22	4	2
wO1	O	0.5	0.75	0.5	0.99(4)	2	2
wO2	O	0.961(10)	0.75	0.428(6)	1.00(4)	2	2
wO3	O	0.188(7)	0.75	0.983(9)	1.00(8)	2	2

Table VI.III.XIV. Refined structure of dehydrated $Rb_{3.5}$-PHI (3.6).

Site	Type	*x*	*y*	*z*	Occ	M	B_{iso}
Rb1	Rb	0.870(2)	0.75	0.498(2)	0.58(1)	2	2
Rb1a	Rb	0.008(3)	0.75	0.446(3)	0.36(1)	2	2
Rb2	Rb	0.539(3)	0.033(1)	0.565(3)	0.29(1)	4	2
Rb3	Rb	0.831(3)	0.25	0.994(3)	0.33(1)	2	2
O1	O	0.173(4)	0.068(3)	0.248(5)	1	4	2
O2	O	0.673(4)	0.572(3)	0.220(4)	1	4	2
O3	O	0.629(5)	0.116(3)	0.125(6)	1	4	2
O4	O	0.995(5)	0.898(2)	0.140(5)	1	4	2
O5	O	0.926(5)	0.053(2)	0.284(5)	1	4	2
O6	O	0.334(4)	0.382(2)	0.086(5)	1	4	2
O7	O	0.809(5)	0.438(2)	0.499(6)	1	4	2
O8	O	0.571(6)	0.75	0.084(8)	1	2	2
O9	O	0.156(6)	0.25	0.104(8)	1	2	2
Si1	Si	0.757(2)	0.033(1)	0.286(3)	0.78	4	2
Al1	Al	0.757(2)	0.033(1)	0.286(3)	0.22	4	2
Si2	Si	0.435(2)	0.136(1)	0.987(2)	0.78	4	2
Al2	Al	0.435(2)	0.136(1)	0.987(2)	0.22	4	2
Si3	Si	0.065(2)	0.989(1)	0.287(3)	0.78	4	2
Al3	Al	0.065(2)	0.989(1)	0.287(3)	0.22	4	2
Si4	Si	0.163(2)	0.132(1)	0.075(2)	0.78	4	2
Al4	Al	0.163(2)	0.132(1)	0.075(2)	0.22	4	2

Table VI.III.XV. Refined structure of $Rb_{3.5}$-PHI (3.6) at 1 bar of CO_2.

Site	Type	*x*	*y*	*z*	Occ	M	B_{iso}
Rb1	Rb	0.784(4)	0.75	0.525(4)	0.53(3)	2	5.2
Rb1a	Rb	0.257(4)	0.75	0.473(7)	0.35(4)	2	5.2
Rb2	Rb	0.5	0	0.5	0.47(2)	2	5.2
Rb3	Rb	0.819(3)	0.25	0.098(3)	0.58(2)	2	5.2
O1	O	0.089(5)	0.113(3)	0.189(7)	1	4	1
O2	O	0.683(6)	0.588(3)	0.218(6)	1	4	1
O3	O	0.608(5)	0.097(3)	0.140(7)	1	4	1
O4	O	0.010(5)	0.929(3)	0.152(6)	1	4	1
O5	O	0.909(6)	0.044(2)	0.301(5)	1	4	1
O6	O	0.309(5)	0.368(2)	0.074(4)	1	4	1
O7	O	0.801(5)	0.486(4)	0.509(8)	1	4	1
O8	O	0.561(8)	0.75	0.042(8)	1	2	1
O9	O	0.060(8)	0.25	0.924(9)	1	2	1
Si1	Si	0.749(3)	0.017(2)	0.293(3)	0.78	4	1
Al1	Al	0.749(3)	0.017(2)	0.293(3)	0.22	4	1
Si2	Si	0.425(3)	0.137(2)	0.991(4)	0.78	4	1
Al2	Al	0.425(3)	0.137(2)	0.991(4)	0.22	4	1
Si3	Si	0.055(3)	0.019(2)	0.281(3)	0.78	4	1
Al3	Al	0.055(3)	0.019(2)	0.281(3)	0.22	4	1
Si4	Si	0.121(3)	0.145(2)	0.021(3)	0.78	4	1
Al4	Al	0.121(3)	0.145(2)	0.021(3)	0.22	4	1
C1	C	0.47(2)	0.826(6)	0.560(12)	0.25(3)	4	8
OC1	O	0.59(2)	0.826(6)	0.560(12)	0.25(3)	4	8
OC1a	O	0.36(2)	0.826(6)	0.560(12)	0.25(3)	4	8
C2	C	0.06(2)	0.75	0.434(9)	0.50(5)	2	8
OC2	O	0.17(2)	0.75	0.434(9)	0.50(5)	2	8
OC2a	O	0.94(2)	0.75	0.434(9)	0.50(5)	2	8
C3	C	0.397(12)	0.882(5)	0.304(12)	0.50(2)	4	8
OC3	O	0.472(12)	0.929(5)	0.439(12)	0.50(2)	4	8

Table VI.III.XV.(continued) Refined structure of $Rb_{3.5}$-PHI (3.6) at 1 bar of CO_2.

Site	Type	*x*	*y*	*z*	Occ	M	B_{iso}
OC3a	O	0.322(12)	0.835(5)	0.170(12)	0.50(2)	4	8

Table VI.III.XVI. Refined structure of hydrated $Cs_{3.5}$-PHI (3.6).

Site	Type	*x*	*y*	*z*	Occ	M	B_{iso}
Cs1	Cs	0.349(4)	0.730(6)	0.239(5)	0.40(4)	4	2
Cs1_1	Cs	0.871(3)	0.735(4)	0.244(4)	0.43(4)	4	2
Cs1a	Cs	0.143(3)	0.751(4)	0.252(4)	0.42(4)	4	2
Cs1a_1	Cs	0.643(3)	0.774(4)	0.256(3)	0.48(4)	4	2
Cs2	Cs	0.244(3)	0.575(3)	0.250(3)	0.61(3)	4	2
Cs2_1	Cs	0.235(4)	0.601(4)	0.705(4)	0.36(3)	4	2
Cs2_2	Cs	0.720(4)	0.544(3)	0.206(4)	0.42(3)	4	2
Cs2_3	Cs	0.687(6)	0.621(5)	0.613(6)	0.26(3)	4	2
Cs3	Cs	0.397(3)	0.214(3)	0.048(3)	0.54(4)	4	2
Cs3_1	Cs	0.932(4)	0.248(5)	0.095(4)	0.35(3)	4	2
O1	O	0.02(2)	0.09(2)	0.08(2)	1	4	2
O2	O	0.03(2)	0.10(2)	0.58(2)	1	4	2
O3	O	0.54(2)	0.12(2)	0.09(2)	1	4	2
O4	O	0.54(2)	0.10(2)	0.59(2)	1	4	2
O5	O	0.33(2)	0.60(2)	0.10(2)	1	4	2
O6	O	0.34(2)	0.58(2)	0.60(2)	1	4	2
O7	O	0.833(13)	0.59(2)	0.10(2)	1	4	2
O8	O	0.82(2)	0.61(2)	0.60(2)	1	4	2
O9	O	0.29(2)	0.10(2)	0.10(2)	1	4	2
O10	O	0.29(2)	0.08(2)	0.60(2)	1	4	2
O11	O	0.81(2)	0.09(2)	0.08(2)	1	4	2
O12	O	0.79(2)	0.09(2)	0.58(2)	1	4	2
O13	O	0.04(2)	0.90(2)	0.10(2)	1	4	2
O14	O	0.02(2)	0.91(2)	0.60(2)	1	4	2
O15	O	0.50(2)	0.93(2)	0.08(2)	1	4	2

Table VI.III.XVI.(continued) Refined structure of hydrated $Cs_{3.5}$-PHI (3.6).

Site	Type	*x*	*y*	*z*	Occ	M	B_{iso}
O16	O	0.523(2)	0.91(2)	0.60(2)	1	4	2
O17	O	0.431(14)	0.07(2)	0.6(2)	1	4	2
O18	O	0.437(14)	0.03(2)	0.63(2)	1	4	2
O19	O	0.93(2)	-0.01(2)	0.11(2)	1	4	2
O20	O	0.934(14)	0.04(2)	0.62(2)	1	4	2
O21	O	0.13(2)	0.37(2)	0.04(2)	1	4	2
O22	O	0.12(2)	0.341(13)	0.51(2)	1	4	2
O23	O	0.63(2)	0.39(2)	0.01(2)	1	4	2
O24	O	0.658(12)	0.37(2)	0.55(2)	1	4	2
O25	O	0.41(2)	0.51(2)	0.26(2)	1	4	2
O26	O	0.41(2)	0.51(2)	0.75(2)	1	4	2
O27	O	0.90(2)	0.48(2)	0.25(2)	1	4	2
O28	O	0.90(2)	0.51(2)	0.75(2)	1	4	2
O29	O	0.280(12)	0.751(14)	0.52(2)	1	4	2
O30	O	0.772(13)	0.76(2)	0.495(14)	1	4	2
O31	O	-0.006(13)	0.26(2)	-0.02(2)	1	4	2
O32	O	0.528(13)	0.25(2)	-0.02(2)	1	4	2
Si1	Si	0.364(7)	0.022(7)	0.138(8)	0.78	4	2
Al1	Al	0.364(7)	0.022(7)	0.138(8)	0.22	4	2
Si2	Si	0.368(7)	0.004(7)	0.638(7)	0.78	4	2
Al2	Al	0.368(7)	0.004(7)	0.638(7)	0.22	4	2
Si3	Si	0.870(6)	0.003(8)	0.141(7)	0.78	4	2
Al3	Al	0.870(6)	0.003(8)	0.141(7)	0.22	4	2
Si4	Si	0.862(7)	0.011(8)	0.637(8)	0.78	4	2
Al4	Al	0.862(7)	0.011(8)	0.637(8)	0.22	4	2
Si5	Si	0.202(7)	0.131(7)	0.501(8)	0.78	4	2
Al5	Al	0.202(7)	0.131(7)	0.501(8)	0.22	4	2
Si6	Si	0.194(6)	0.160(6)	0.998(7)	0.78	4	2
Al6	Al	0.194(6)	0.160(6)	0.998(7)	0.22	4	2

Table VI.III.XVI.(continued) Refined structure of hydrated $Cs_{3.5}$-PHI (3.6).

Site	Type	*x*	*y*	*z*	Occ	M	B_{iso}
Si7	Si	0.705(6)	0.144(8)	0.511(7)	0.78	4	2
Al7	Al	0.705(6)	0.144(8)	0.511(7)	0.22	4	2
Si8	Si	0.713(7)	0.140(7)	0.004(8)	0.78	4	2
Al8	Al	0.713(7)	0.140(7)	0.004(8)	0.22	4	2
Si9	Si	0.018(5)	-0.002(8)	0.135(7)	0.78	4	2
Al9	Al	0.018(5)	-0.002(8)	0.135(7)	0.22	4	2
Si10	Si	0.026(6)	0.010(7)	0.648(8)	0.78	4	2
Al10	Al	0.026(6)	0.010(7)	0.648(8)	0.22	4	2
Si11	Si	0.516(7)	0.020(7)	0.139(8)	0.78	4	2
Al11	Al	0.516(7)	0.020(7)	0.139(8)	0.22	4	2
Si12	Si	0.518(7)	0.011(8)	0.638(7)	0.78	4	2
Al12	Al	0.518(7)	0.011(8)	0.638(7)	0.22	4	2
Si13	Si	0.036(7)	0.130(7)	0.502(8)	0.78	4	2
Al13	Al	0.036(7)	0.130(7)	0.502(8)	0.22	4	2
Si14	Si	0.028(6)	0.155(7)	0.999(6)	0.78	4	2
Al14	Al	0.028(6)	0.155(7)	0.999(6)	0.22	4	2
Si15	Si	0.548(6)	0.141(7)	0.509(7)	0.78	4	2
Al15	Al	0.548(6)	0.141(7)	0.509(7)	0.22	4	2
Si16	Si	0.547(7)	0.144(7)	1.000(7)	0.78	4	2
Al16	Al	0.547(7)	0.144(7)	1.000(7)	0.22	4	2
wO1_1	O	0.784(11)	0.75(2)	0.28(2)	1.0(2)	4	4
wO2	O	0.436(14)	0.75(2)	0.13(2)	1.0(3)	4	4
wO2_1	O	0.982(13)	0.74(2)	0.24(2)	1.0(2)	4	4
wO3	O	0.148(17)	0.849(14)	0.03(2)	1.0(3)	4	4

Table VI.III.XVII. Refined structure of dehydrated $Cs_{3.5}$-PHI (3.6).

Site	Type	*x*	*y*	*z*	Occ	M	B_{iso}
Cs1	Cs	0.035(2)	0.75	0.504(3)	0.41(1)	2	2
Cs2	Cs	0.450(3)	0.579(2)	0.392(3)	0.19(1)	4	2
Cs1a	Cs	0.906(2)	0.75	0.500(2)	0.62(1)	2	2
Cs4	Cs	0.363(3)	0.75	0.489(3)	0.39(1)	2	2
Cs3	Cs	0.739(3)	0.25	-0.047(4)	0.25(1)	2	2
O8	O	0.595(8)	0.75	0.077(9)	1	2	2
O9	O	0.130(10)	0.25	0.095(10)	1	2	2
O1	O	0.162(7)	0.073(4)	0.243(7)	1	4	2
O2	O	0.673(7)	0.573(4)	0.214(7)	1	4	2
O3	O	0.612(7)	0.111(4)	0.132(8)	1	4	2
O4	O	0.002(5)	0.905(4)	0.133(7)	1	4	2
O5	O	0.908(7)	0.044(4)	0.266(5)	1	4	2
O6	O	0.321(6)	0.380(3)	0.082(6)	1	4	2
O7	O	0.812(6)	0.448(3)	0.499(8)	1	4	2
Si1	Si	0.746(3)	0.031(2)	0.282(3)	0.78	4	2
Al1	Al	0.746(3)	0.031(2)	0.282(3)	0.22	4	2
Si2	Si	0.422(3)	0.136(2)	-0.021(3)	0.78	4	2
Al2	Al	0.422(3)	0.136(2)	-0.021(3)	0.22	4	2
Si3	Si	0.065(3)	-0.003(2)	0.280(4)	0.78	4	2
Al3	Al	0.065(3)	-0.003(2)	0.280(4)	0.22	4	2
Si4	Si	0.154(3)	0.133(2)	0.069(4)	0.78	4	2
Al4	Al	0.154(3)	0.133(2)	0.069(4)	0.22	4	2

Table VI.III.XVIII. Refined structure of $Cs_{3.5}$-PHI (3.6) at 1 bar of CO_2.

Site	Type	*x*	*y*	*z*	Occ	M	B_{iso}
Cs1	Cs	0.218(3)	0.75	0.492(3)	0.47(2)	2	2
Cs2	Cs	0.480(4)	0.541(1)	0.462(3)	0.31(1)	4	2
Cs1a	Cs	0.744(2)	0.75	0.496(3)	0.49(2)	2	2
Cs3	Cs	0.785(5)	0.25	0.064(4)	0.35(2)	2	2
O8	O	0.554(11)	0.75	0.999(15)	1	2	1
O9	O	0.042(11)	0.25	0.996(15)	1	2	1
O1	O	0.082(7)	0.091(7)	0.176(9)	1	4	1
O2	O	0.657(7)	0.588(6)	0.180(9)	1	4	1
O3	O	0.593(8)	0.091(7)	0.178(10)	1	4	1
O4	O	0.026(7)	0.911(7)	0.184(10)	1	4	1
O5	O	0.887(8)	0.047(3)	0.274(7)	1	4	1
O6	O	0.283(7)	0.368(2)	0.077(6)	1	4	1
O7	O	0.807(7)	0.501(8)	0.500(10)	1	4	1
Si1	Si	0.743(4)	0.012(3)	0.284(5)	0.78	4	1
Al1	Al	0.743(4)	0.012(3)	0.284(5)	0.22	4	1
Si2	Si	0.411(4)	0.136(3)	0.013(6)	0.78	4	1
Al2	Al	0.411(4)	0.136(3)	0.013(6)	0.22	4	1
Si3	Si	0.043(4)	0.010(3)	0.284(5)	0.78	4	1
Al3	Al	0.043(4)	0.010(3)	0.284(5)	0.22	4	1
Si4	Si	0.091(4)	0.139(2)	0.006(5)	0.78	4	1
Al4	Al	0.091(4)	0.139(2)	0.006(5)	0.22	4	1
C1	C	0.50	0.706(7)	0.576(12)	0.33(3)	4	8
OC1	O	0.61	0.706(7)	0.576(12)	0.33(3)	4	8
OC1a	O	0.38	0.706(7)	0.576(12)	0.33(3)	4	8
C2	C	0.92(3)	0.75	0.347(10)	0.50(6)	2	8
OC2	O	0.04(3)	0.75	0.347(10)	0.50(6)	2	8
OC2a	O	0.81(3)	0.75	0.347(10)	0.50(6)	2	8
C3	C	0.247(10)	0.811(7)	0.056(12)	0.50(4)	4	8
OC3	O	0.322(10)	0.858(7)	0.189(12)	0.50(4)	4	8

Table VI.III.XVIII.(continued) Refined structure of $Cs_{3.5}$-PHI (3.6) at 1 bar of CO_2.

Site	Type	*x*	*y*	*z*	Occ	M	B_{iso}
OC3a	O	0.173(10)	0.764(7)	0.922(12)	0.50(4)	4	8

Appendix VII. Model for Zn and Li siting in $Li_{9.8-2x}Zn_x$-Rho (3.9) materials

The 2 samples measured with PND data, $Li_{9.8}$- and $LiZn_{2.2}$-Rho, both show *ca.* 67% of Li sitting in the S6R site and the remaining 33% sitting in the S8R. We assume this to be constant across the series, as the unit cell does not drastically increase in size with higher Zn^{2+} content. For the $Li_{9.8-2x}Zn_x$-Rho (3.9) series, this then gives:

$$Li_{8R} = 0.33(9.8 - 2x).$$

PXRD data gives more accurate measurements of Zn sitings across the whole series and fitting this data, forcing through the origin as shown in Figure VI.III.I gives the following expression for Zn^{2+} 8R content:

$$Zn_{8R} = 0.0336x^2 + 0.5034x.$$

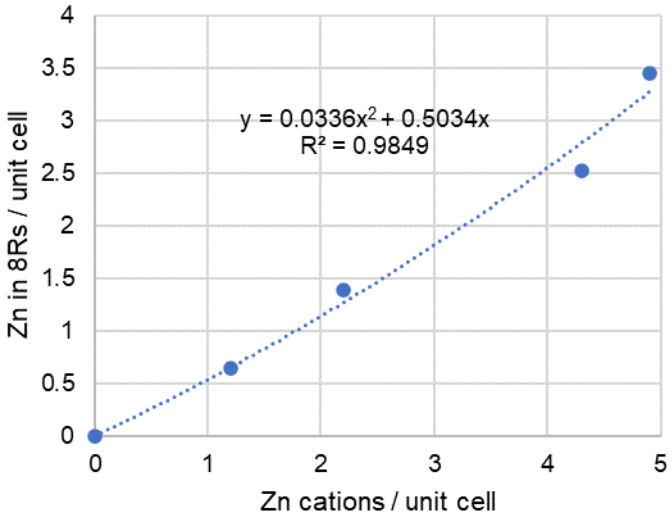

Figure VI.III.I. Zn S8R content in the $Li_{9.8-2x}Zn_x$-Rho (3.9) series.

A quadratic equation was found to improve the fit over a linear approximation and could be rationalised as due to limited 6-rings with 2 or more associated negative charges available for the divalent Zn^{2+}. The number of open windows, n_{ow} could thus be given as:

$$n_{ow} = -0.0336x^2 + 0.1566x + 2.766.$$

This could be compared with experimental values, as shown in Figure VI.III.II, where the approximation for Li is used to fill in missing data. The maximum number of open windows is 2.9 and occurs at x = 2, very close to the sample investigated $LiZn_{2.2}$-Rho.

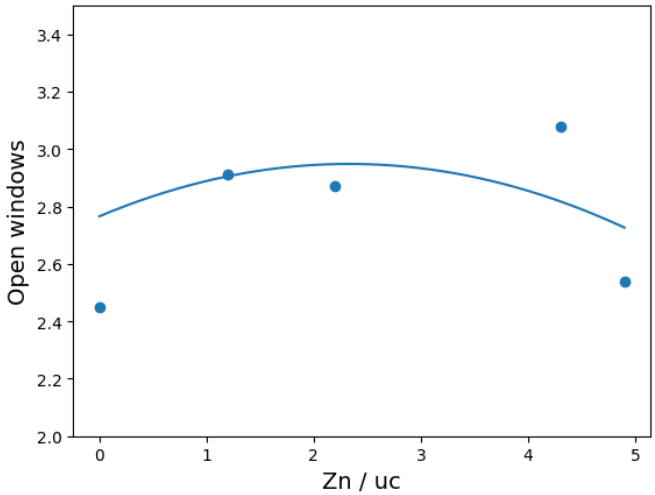

Figure VI.III.II. Experimental and modelled open windows with Zn content.

Values for individual samples are given in Table VI.III.I.

Table VI.III.I. Structural and adsorption data for Li,Zn-Rho materials. Occupancy values are from refinements, with extrapolated Li values indicated by italics.

Sample	***a* (Å)**	**6R occupancy**	**8R occupancy**	**O_2 D/r^2 (s^{-1})**	**Kinetic O_2/Ar selectivity**
Li-Rho	14.255(1)	6.6(1) Li	3.6(2) Li	6.7×10^{-3}	3600
$LiZn_{1.2}$-Rho	14.303(1)	*5.0 Li*, 0.6(1) Zn	*2.4 Li*, 0.6(1) Zn	3.52×10^{-2}	1760
$LiZn_{2.2}$-Rho	14.365(1)	3.8(2) Li, 0.6(1) Zn	1.7(2) Li, 1.5 (1) Zn	3.70×10^{-1}	813
$LiZn_{4.3}$-Rho	14.481(1)	*0.8 Li*, 1.8(1) Zn	*0.4 Li*, 2.5(1) Zn	9.73×10^{-1}	45
Zn-Rho	14.533(1)	1.5(1) Zn	3.5(1) Zn	3.70×10^{-1}	45

Appendix VIII. Fits of Li-MER (4.2) VPXRD data

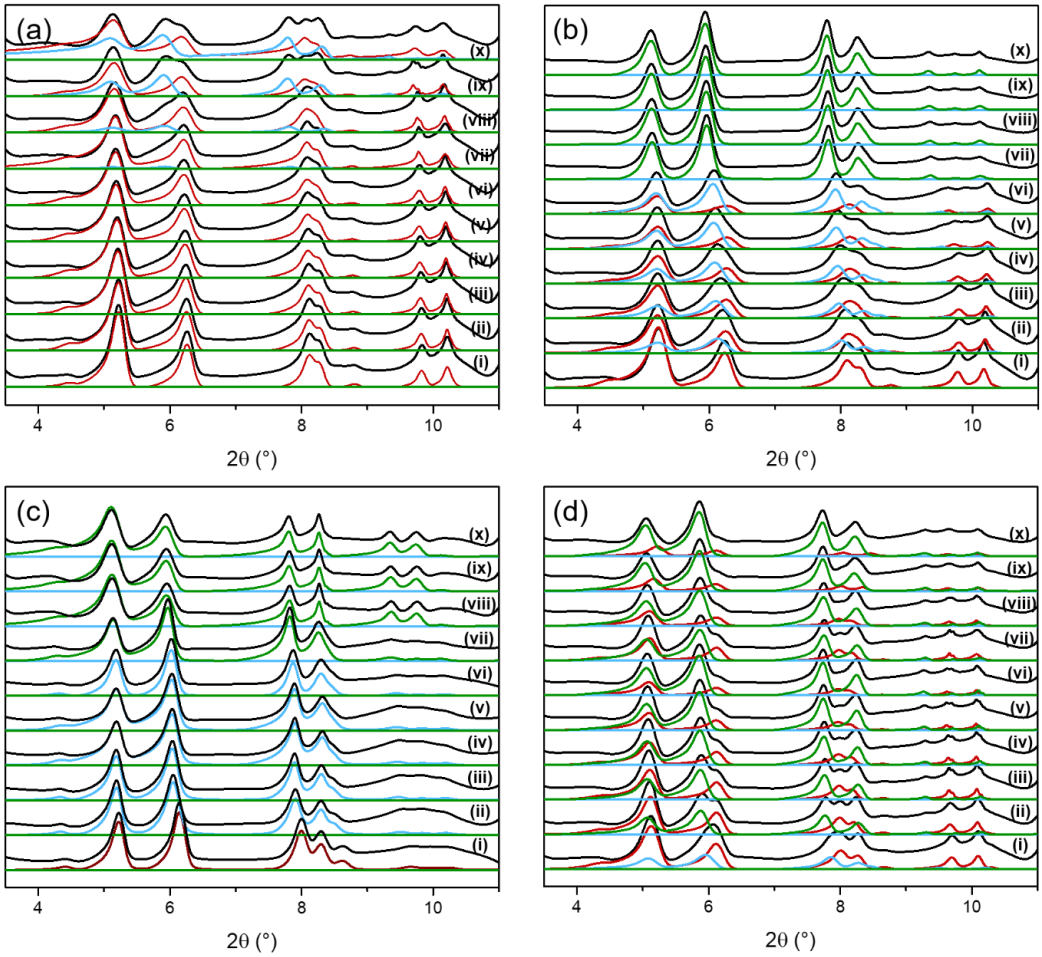

Figure VI.III.I. Calculated VPXRD patterns of (a) $Li_{6.2}$-, (b) $Li_{4.0}Na_{2.2}$-, (c) $Li_{2.0}Na_{4.2}$- and (d) $Li_{4.0}K_{2.2}$-MER (4.2). Patterns corresponding to the total, narrow-pore, intermediate and wide-pore phases are shown in black, red, blue and green, respectively. Partial pressures of CO_2 during acquisition were (i) 20, (ii) 100, (iii) 200, (iv) 300, (v) 400, (vi) 500, (vii) 600, (viii) 700, (ix) 800 and (x) 1000 mbar. (PANalytical, Mo $K\alpha_{1,2}$, λ = 0.711 Å). Reproduced from Georgieva et al.[1]

VIII.I References

(1) Georgieva, V. M.; Bruce, E. L.; Chitac, R. G.; Lozinska, M. M.; Hall, A. M.; Murray, C. A.; Smith, R. I.; Turrina, A.; Wright, P. A. Cation Control of Cooperative CO_2 Adsorption in Li-Containing Mixed Cation Forms of the Flexible Merlinoite Zeolite. *Chem. Mater.* **2021**, 33, 1157–1173.

Appendix IX. Reproduced Figures

In addition to the papers described in the front matter, co-authored by myself, the following figures have also been reproduced, or adapted, as referenced in the main body of this work.

Figure 2.1.2: Reprinted with permission from Waseda, Y.; Matsubara, E.; Shinoda, K. *X-Ray Diffraction Crystallography; Introduction, Examples and Solved Problems*; Springer: Heidelberg, 2011, Copyright 2011 Springer.

Figure 2.1.6: Reproduced https://www.diamond.ac.uk, Diamond Light Source.

Figure 2.1.15: ***I11 schematic***: Reprinted with permission from Thompson, S. P.; Parker, J. E.; Potter, J.; Hill, T. P.; Birt, A.; Cobb, T. M.; Yuan, F.; Tang, C. C. Beamline I11 at Diamond: A New Instrument for High Resolution Powder Diffraction. *Rev. Sci. Instrum*. **2009**, *80*, 075107., Copyright 2009 AIP Publishing. ***MAC and PSD analysers*:** Reproduced https://www.diamond.ac.uk, Copyright Diamond Light Source.

Figure 2.1.16: Reprinted with permission from Smith, R. I.; Hull, S.; Tucker, M. G. The Upgraded Polaris Powder Diffractometer at the ISIS Neutron Source. *Rev. Sci. Instrum*. **2019**, *90* (11), 115101. Copyright 2009 AIP Publishing.

Figure 3.1.1: Reprinted with permission from Shin, J.; Xu, H.; Seo, S.; Guo, P.; Min, J. G.; Cho, J.; Wright, P. A.; Zou, X.; Hong, S. B. Targeted Synthesis of Two Super-Complex Zeolites with Embedded Isoreticular Structures. *Angew. Chemie - Int. Ed*. **2016**, *128* (16), 5012–5016. Copyright 2016 Wiley.